Dynamics and Model-Based Control of Balance Recovery in Humans Using Lower-Limb Exoskeletons

by

Keaton A. Inkol

A thesis
presented to the University of Waterloo
in fulfillment of the
thesis requirement for the degree of
Doctor of Philosophy
in
Systems Design Engineering

Waterloo, Ontario, Canada, 2023

© Keaton A. Inkol 2023

Examining Committee Membership

The following served on the Examining Committee for this thesis. The decision of the Examining Committee is by majority vote.

External Examiner:	Mickaël Begon Professeur titulaire, Faculté de Médecine, École de Kinésiologie et des Sciences de l'Activité Physique, Université de Montréal
Internal Member:	Katja Mombaur Professor, Systems Design Engineering, University of Waterloo
Internal-External Member:	Andrew Laing Associate Professor, Kinesiology and Health Sciences, University of Waterloo
Other Member(s):	James Tung Associate Professor, Mechanical and Mechatronics Engineering, University of Waterloo
Supervisor(s):	John McPhee Professor, Systems Design Engineering, University of Waterloo

Author's Declaration

I hereby declare that I am the sole author of this thesis. This is a true copy of the thesis, including any required final revisions, as accepted by my examiners.

I understand that my thesis may be made electronically available to the public.

Abstract

In the past decade, powered robotic lower-limb exoskeletons have emerged as an exciting technological advancement, offering enhancements in mobility and quality of life for individuals with physical impairments. While the potential benefits of these systems are vast, the practical implementation of exoskeletons is not without its challenges: it is difficult to remain upright and balanced without assistance from a device like crutches. Therefore, the current dissertation investigated how to address this concern through computational methods and experimental testing.

To tackle the issue of poor exoskeleton balance and to address the relatively limited existing work on integrated human-biomechantronic models, especially those specific to lower-limb exoskeletons, an approach centered on predictive multibody dynamic computer simulations, full-state feedback control, optimal control, and optimization was undertaken. The research goals were broadly organized into four categories: **i)** Generation of novel simulations of human-only feet-in-place balance recovery in the sagittal plane; **ii)** Creation of an integrated symbolic model of human-exoskeleton multibody dynamics that does not rely on rigid coupling between human and exoskeleton; **iii)** Generation of novel dynamic simulations of human-exoskeleton balance with and without the presence of novel feet-in-place balance assistance; **iv)** Testing the proposed assistance algorithms in experiments with healthy young adults.

The human model was represented in the sagittal plane as a 5 degree-of-freedom inverted pendulum driven by computationally-efficient and C^2 continuous muscle torque generators. The exoskeleton model was designed as a floating-base biped with 9 degrees of freedom; dynamic parameters were identified separately using a combination of physical experiments and optimization approaches. Coupling the human and exoskeleton models required the development of a constitutive model of compliant human-exoskeleton interactions, in addition to a rigid-coupling formulation for efficient control-oriented model development. Predictive open-loop and closed-loop simulations of human motion were produced using a symbolic direct-collocation approach; the closed loop method introduced a novel model of central nervous system behaviour via nonlinear model predictive control. Open-loop simulations of human-only and human-exoskeleton feet-in-place balance were used to assess how human physiology and device hardware could impact the end-user's capacity for responding to external perturbations without requiring a step or falling (the feasible stability region). Novel methods for feet-in-place balance recovery assistance were

derived using optimal full-state-feedback with constraints (model predictive control) paired with a nonlinear moving horizon estimator of joint angles, velocities, motor torques, and external torques — all from noisy onboard measurements.

Findings from simulations were important in providing a mechanical assessment of human and human-exoskeleton feet-in-place balance recovery, i.e., how certain mechanical qualities impact system motion and balance regulation. For example, optimized arm motion did not provide an improvement in the size of human-only feet-in-place feasible stability region. Additionally, minimizing "effort" during estimations of the stability region suggested that an ankle strategy is more efficient than a hip strategy, differing from existing literature. Furthermore, the simulation of human-only motion using nonlinear model predictive control suggested that performance criteria featuring displacements of the center of mass (COM) and trunk pitch (from reference values) prompted different human postural strategies (this was consistent with open-loop simulations). Wearing an exoskeleton, while advantageous in altering net mass distribution, did reduce the size of the end-user stability region indicating a lower capacity for responding to perturbations when wearing the device. Parameter identification using physical experiments and inverse dynamics-based optimization approaches both provided reasonable replication of experimental joint angles and actuator torques, though a final validation was difficult; the accuracy of the onboard sensor measurements must be assessed. Dynamics simulations also provided a means of assessing the capabilities of different balance regulating control algorithms. Simulations employing various full-state feedback control laws demonstrated their feasibility in introducing assistive or autonomous balancing torques for the hip, knee, and ankle. Notably, the model predictive approach outperformed others by providing optimal regulation while considering important constraints, e.g., regulating the zero-moment point in the support polygon. Lastly, experimental results indicated that friction compensation alone was sufficient for reasonable feet-in-place balance control when the end-user was a healthy young adult; the proposed COM assist-as-needed algorithm proved less effective.

Acknowledgements

First and foremost, I want to express my deepest gratitude to my supervisor, Professor John McPhee. Throughout my tenure with the Motion Research Group, John has consistently provided invaluable support, sharing his wisdom and offering feedback in a constructive manner. I am genuinely appreciative of his composure during stressful times and for his role in my personal and professional growth. I would also like to acknowledge my committee members: Professors Katja Mombaur, James Tung, and Andrew Laing. I am thankful to each of you for imparting wisdom and offering support throughout my journey as a PhD student, as well as for fostering a collaborative environment. Thank you also to my external examiner, Professor Mickaël Begon for taking the time to be a part of my PhD thesis examination.

Second, I would like to thank all current members of the Motion Research Group for their friendship, support and for pushing me towards continuous improvement ... and of course, for those chats over a cold beer! I would like to extend special recognition to former group members Dr. Brokoslaw Laschowski, Dr. Valerie Norman-Gerum, and Dr. Behzad Danaei, along with current member Dr. Ali Nasr. Our discussions have played a crucial role in shaping the content of this thesis and providing the inspiration to persevere through the challenges of writing.

Thirdly, I wish to acknowledge my fellow collaborators at the University of Waterloo. I would like to express my appreciation to Christian Mele from Professor James Tung's group for providing both the exoskeleton test-bench and invaluable assistance with the motion capture during the parameter identification experiment. I am also thankful for your friendship and willingness to collaborate on a multitude of projects. I wholeheartedly wish you success as you continue your journey through graduate school. Finally, I would express gratitude to both Claudia Town and Taylor Winberg from Professor Andrew Laing's group for their exceptional support with data acquisition during experimental testing of the exoskeleton balance controller. Your dedication and effort went above and beyond. I would also like to thank Taylor for dragging me out to play a game basketball from time to time; achieving work-life balance can be hard and this certainly helped.

Fourth, I want to thank the Natural Sciences and Engineering Research Council of Canada (NSERC), the Waterloo Engineering Excellence PhD Fellowship program, and the Canada Research Chairs (CRC) program for funding this research. I would also like to

thank RoboHub staff at the University of Waterloo (Brandon DeHart and Robert Wagner) as well as the engineering staff at Technaid (Elkyn Balcazar) for their assistance with the robotic exoskeleton testing.

Finally, I would like to acknowledge my family and friends who have been there to support me through the challenges that I have endured during my time at University of Waterloo. Words alone cannot truly capture how grateful I am for you all. Special thanks to Alisha for keeping the apartment from falling apart and putting up with me while I was completing this work, Mom and Dad for the late-night phone calls, and Jordon and Kelsey for helping me find some much needed distractions.

Table of Contents

List of Figures xiii

List of Tables xxx

List of Abbreviations xxxiii

1 Introduction 1

1.1 Problem Identification 2

1.2 Contributions 3

2 Literature Review 7

2.1 Lower-Limb Exoskeletons and Orthoses 7

2.1.1 State-of-the-Art 7

2.1.2 Design and Control 11

2.2 Human Control of Balance 12

2.2.1 Control of Walking versus Stance 12

2.2.2 Feet-In-Place (FIP) Balance Recovery Strategies 14

2.2.3 Addressing Redundancies in Human Balance Recovery 15

2.3 Approaches Towards Assistive Balance Control 18

2.3.1 Dynamic Modeling and Simulation of Human-Exoskeleton Motion . 18

2.3.2 Autonomous Balance Control Methods 20
2.3.3 Human-In-Charge and Assist-As-Needed Methods 22

3 Simulating the Biomechanics of Human Balance Recovery 24
3.1 Multibody System Dynamic Model 25
3.2 Assessing the Boundaries of Upright Stance 29
3.2.1 Assessing the Feasible Stability Region of FIP Balance 32
3.2.2 Simulation Experiments and Results 37
3.3 Human-Only NMPC Feet-In-Place Balance Regulation 51
3.3.1 Background 51
3.3.2 Feedback Optimal Control 53
3.3.3 Biomimetic Cost Functions and Constraints 54
3.3.4 Simulation Experiments and Results 56

4 Dynamic Modeling of Lower-Limb Exoskeletons 62
4.1 Planar Model of Biomechatronic Devices 62
4.1.1 Multibody System Dynamics 62
4.1.2 Electric Actuator Modeling 66
4.2 Identification of Multibody Dynamic and Actuator Parameters 68
4.2.1 Background 68
4.2.2 Physical Measurements and Computer-Aided Design 71
4.2.3 Optimizing the Experimental Design for Identification 76
4.2.4 Parameter Identification Methods 88
4.3 Identification Results and Discussion 92

5 Modeling Integrated Human-Exoskeleton Systems **106**

5.1 Background . . . 106

5.2 Interactions via Nonlinear Compliance . . . 107

5.2.1 Human-Cuff Hunt-Crossley Interactions . . . 108

5.2.2 Human-Strap Interaction Elements . . . 110

5.3 Proof of Concept Simulations . . . 114

5.4 Merging Human- Exoskeleton Models for FIP Simulations . . . 120

6 Dynamic Simulations of Model-Based Assisted Balance Control **124**

6.1 The Human-Exoskeleton Feet-In-Place FSR . . . 124

6.1.1 FIP Stability with Exoskeleton Assistance . . . 125

6.1.2 Simulation Experiments and Results . . . 127

6.2 Real-Time Feet-In-Place Balance Control . . . 136

6.2.1 Control-Oriented Nonlinear Dynamics . . . 136

6.2.2 Balance Regulation: Full-State Feedback . . . 137

6.2.3 Optimal Balance Regulation: Linear Quadratic Regulator . . . 138

6.2.4 Optimal Balance Regulation: Model Predictive Control . . . 143

6.2.5 Nonlinear State Estimation and Intent Detection . . . 151

6.3 Proof-of-Concept Simulations . . . 156

6.3.1 Effect of Optimal Regulation Parameters and Constraints . . . 157

6.3.2 Autonomous State Estimation during Balance Recovery . . . 166

7 Experimental Testing of Model-Based Feet-in-Place Balance Control **174**

7.1 Background . . . 174

7.2 Control Architecture . . . 177

7.2.1 Model Predictive Control . . . 177

7.2.2 Novel COM-Dependent Assistance . . . 179
7.2.3 Nonlinear Friction Compensation and Saturation . . . 182
7.3 Methods . . . 184
7.3.1 Participants . . . 184
7.3.2 Experimental Protocol . . . 185
7.3.3 Outcome Measures and Statistical Analyses . . . 189
7.3.4 Predictive Simulations . . . 192
7.4 Experimental Results . . . 193
7.5 Discussion . . . 203

8 Conclusions **213**
8.1 Summary of Contributions . . . 213
8.2 Recommendations for Future Research . . . 218

Letter of Copyright Permission **224**

References **227**

APPENDICES **266**

A Example: Human Parameter Values **267**

B Background: Muscle Torque Generators **270**

C Muscle Torque Generator Functions **275**

D Smoothing Muscle Torque Generator Functions **281**
D.1 Background . . . 281
D.2 Curve Fitting Routine . . . 284

E Background: Feasible Stability Region and Capturability **286**

F Supplementary Human-Only FSR Simulations **290**

F.1 Effect of Different FSR Candidate Functions 290

F.2 Influence of Adding Degrees of Freedom for Initial COM Velocity 292

F.3 Influence of Muscle Strength 297

G Obtaining the Set of Minimum Parameters **301**

H Minimal Parameter Equations of Motion (Exoskeleton Leg) **306**

I Offline Moving Horizon Estimation **308**

I.1 Overview 308

I.2 Results 311

J Background: Interactions via Kinematic Constraints **316**

K Supplementary Human-Exoskeleton FSR Simulations **320**

K.1 Influence of Adding Degrees of Freedom to Pendulum: Human-Exoskeleton 320

K.2 Effect of Added Mass at Different Locations 326

L Full-State Feedback: Computed Torque Control) **328**

L.1 Overview 328

L.2 Balance Recovery Simulations 330

M Extended Kalman Filtering for FIP Balance **335**

N Supplementary Human-Exoskeleton Simulations of Assisted Balance **340**

O Participant Screening Questionnaire **347**

List of Figures

3.1 **A**) Schematic of the planar MTG-driven model; balance recovery was evoked via unexpected fore aft accelerations of the support surface ($\ddot{x}_{\text{plat}}$) or a horizontal push to the pelvis F_{push}. **B**) Model of the base of support (for a single leg/foot) used to derive the toe/heel constraint forces that dictated the domain of feasibility for feet-in-place balance. Symbols include the following: $a_{*\text{e/f}}$, extensor/flexor muscle torque activation; θ, joint angle; τ_{mtg}, net joint muscle torque produced by activations; F_{push} and $\ddot{x}_{\text{plat}}$, horizontal push force applied to pelvis and support-surface acceleration respectively; λ_{h} and λ_{t}, the normal ground reaction force $\mathbf{F}_{\text{gf}} \cdot \hat{\jmath}$ resolved at two contact ponts (heel and toe); and ν, the horizontal position of the zero moment point (ZMP). . 26

3.2 The feasible stability region (FSR) for the human-only FIP balance model generated with different constraints on the model degrees of freedom, i.e., which joints were to be "locked" during simulations. Conditions are as follows: only ankle movement (DOF=1); ankle+knee+hip movement permitted (DOF=3); ankle+knee+hip and upper limbs movement permitted (DOF=5). Additionally, the analytical results from Hof et al. [154] are shown (FSR derived from linear inverted pendulum) to validate the results of the DOF=1 simulation, i.e., the nonlinear inverted pendulum FSR. . . . 39

3.3 COM and ZMP trajectories that result in the **anterior** FSR boundary for the human-only balance model when different constraints are imposed on the model degrees of freedom, i.e., which joints were to be "locked" during simulations. Results are shown for an initial normalized AP COM position of 0.25, 0.50, and 0.75. 40

3.4 COM and ZMP trajectories that result in the **posterior** FSR boundary for the human-only balance model when different constraints are imposed on the model degrees of freedom, i.e., which joints were to be "locked" during simulations. Results are shown for an initial normalized AP COM position of 0.25, 0.50, and 0.75. 40

3.5 Joint angles that result in the **anterior** FSR boundary for the human-only balance model when different constraints are imposed on the model degrees of freedom, i.e., which joints were to be "locked" during simulations. Conditions are as follows: only ankle movement (DOF=1); ankle+knee+hip movement permitted (DOF=3); ankle+knee+hip and upper limbs movement permitted (DOF=5). Results are shown for an initial normalized AP COM position of 0.25, 0.50, and 0.75. 41

3.6 Joint angles that result in the **posterior** FSR boundary for the human-only balance model when different constraints are imposed on the model degrees of freedom, i.e., which joints were to be "locked" during simulations. Conditions are as follows: only ankle movement (DOF=1); ankle+knee+hip movement permitted (DOF=3); ankle+knee+hip and upper limbs movement permitted (DOF=5). Results are shown for an initial normalized AP COM position of 0.25, 0.50, and 0.75. 42

3.7 The feasible stability region (FSR) for the human-only FIP balance model generated with different time delays (dead time, δ) imposed during simulations, i.e., muscle activations could not shift from their value measured the initial time until δ ms had passed (Equation 3.38). Arm movement was restricted in these simulations. Conditions are as follows: 0 ms dead time (baseline); 75 ms dead time (short delay in [158, 344]); 150 ms dead time (longer delay reported in [50]). 44

3.8 Active hip, knee, and ankle muscle torques that resulted in the **anterior** FSR boundary for the human-only balance model when different time delays (dead time, δ) were imposed during simulations (right boundary in Fig. 3.7). 45

3.9 Active hip, knee, and ankle muscle torques that resulted in the **posterior** FSR boundary for the human-only balance model when different time delays (dead time, δ) were imposed during simulations (left boundary in Fig. 3.7). 45

3.10 The Pareto front of the evaluated squared torque cost against the A) maximal forward COM velocity that could be terminated, i.e., anterior FSR boundary, and B) maximal backward COM velocity that could be terminated, i.e., posterior FSR boundary. Both costs were normalized to their values at $\rho = 0$, i.e., maximal balance effort. A colour gradient was used to highlight the shift in FSR boundary for a given normalized AP COM position and a given value of ρ. 48

3.11 Hip, knee, and ankle joint angles (*left*) and active hip, knee, and ankle muscle torques (*right*) that resulted in the **forward** FSR boundary for the human-only balance model given different values of the homotopy parameter ρ (see Fig. 3.10A). 49

3.12 Hip, knee, and ankle joint angles (*left*) and active hip, knee, and ankle muscle torques (*right*) that resulted in the **backward** FSR boundary for the human-only balance model given different values of the homotopy parameter ρ (see Fig. 3.10B). 50

3.13 Simulated postural responses following backward (left, initial fall forward) and forward (right, initial fall backward) support-surface perturbations with the arm joints locked (dotted figure) or free (solid figure). Responses were generated using the six optimality criteria shown. Perturbation initiation is marked by * on the time axis. 58

3.14 Simulated postural responses following A) backward and B) forward support-surface perturbations with the arm joints locked or free. Responses were generated using the six optimality criteria shown. Note: ankle $> 0°$ during dorsiflexion, knee $> 0°$ during extension, hip $> 0°$ during flexion. 59

3.15 . Simulated upper limb responses following forward and backward perturbations. Responses were generated using one of the six optimality criteria shown. Note: both shoulder and elbow are $> 0°$ during flexion. 59

4.1 **A**) Schematic of the planar floating-base lower-limb exoskeleton model highlighting individual segment COM positions (and respective reference frames), geometry, and the location of revolute joints, i.e., where revolute kinematic constraints were imposed [141]. **B**) Schematic highlighting the nine multi-body exosekeleton model degrees of freedom (DOF; 3 floating-base coordinates and 6 joint coordinates) and the location of applied actuator torques $T_{\text{ac},i}$. 63

4.2 Example of the construction of the EXO-H3 thigh rigid body segment from a combination of welded rigid bodies, each shown by their custom CAD approximation developed for this dissertation, e.g., cuffs, rotor/stator/gearing, etc. Weld constraint topology is highlighted through the use of dashed blue arrows, i.e., the rotor/gearing output shaft is welded to a link that is subsequently welded to another adjustable link as well as a cuff element. These cuff elements are designed to interact with the human end-user. An image of the EXO-H3, obtained from the owner's manual (Technaid, Spain) is shown to the right for reference. 64

4.3 **A)** Image of the Technaid EXO-H3 obtained from their owner's manual (Technaid, Spain) and **B)** the custom CAD model of the Technaid EXO-H3 developed for this dissertation. This CAD model was created using a combination of physical measurements taken by the current author (via digital calipers) along with some existing .stl files of EXO-H3 component models provided by the manufacturer (Technaid). In **C)**, the CAD model is shown in the pose displayed in the earlier device schematics (Fig. 4.1). . 75

4.4 Condition number of the normalized (*left axis*) and untransformed (*right axis*) observation matrix Ξ_{obs} following each iteration of the novel algorithm described in Algorithm 1. Note that each iteration adds an additional trial to the overall parameter identification experiment. 82

4.5 Desired (optimal exciting) and experimental segment angles for a lower-limb exoskeleton parameter identification experiment consisting of 6 trials (T1-6). Segments include the thigh (*left*), shank (*centre*), and foot (*right*). The root mean square error (RMSE) between experimental and desired trajectories are indicated on each plot. 83

4.6 Desired (optimal exciting) and experimental joint angles (obtained from Vicon motion capture and EXO-H3 rotary encoders separately) for a lower-limb exoskeleton parameter identification experiment consisting of 6 trials (T1-6). Joints include the hip (*left*), knee (*centre*), and ankle (*right*). The root mean square error (RMSE) between experimental and Vicon trajectories are indicated on each plot. 84

4.7 The EXO-H3 trunk pitch angle measured during each of the 6 trials (T1-6) in the lower-limb exoskeleton parameter identification experiment. Note that a negative angle indicates a forward/anterior pitch. 86

4.8 Experimental amplified joint motor torques (scaled by the gear ratio; obtained from EXO-H3 motor current sensors) for a lower-limb exoskeleton parameter identification experiment consisting of 6 trials (T1-6). Joints include the hip (*left*), knee (*centre*), and ankle (*right*). 87

4.9 Results of fitting Equation (4.10) to the passive torques measured in the EXO-H3 knee joint. Experimental data was analyzed only for the extension direction of knee velocity (positive values). 93

4.10 Measured and simulated joint angles for the lower-limb exoskeleton parameter identification trials (T1-6), i.e., hip (*left*), knee (*centre*), and ankle (*right*) angles. Simulated trajectories were obtained using the parameters obtained via physical experiments (PhyExp), inverse dynamics optimization (InvDyn), and forward dynamics optimization (ForDyn). For parameter values, see Table 4.8. 97

4.11 Measured and simulated motor torques angles for the lower-limb exoskeleton parameter identification trials (T1-6). Motors were included at the following joints: hip (*left*), knee (*centre*), and foot (*right*). Simulated trajectories were obtained using the parameters obtained via physical experiments (PhyExp) and inverse dynamics optimization (InvDyn). Note that the results obtained with parameters from forward dynamics optimization were not included due to their poor fit (see Table 4.10). For parameter values, see Table 4.8. . . 98

4.12 Measured and simulated joint angles for the forward step validation trial, i.e., hip (*left*), knee (*centre*), and ankle (*right*) angles. Simulated trajectories were obtained using the parameters obtained via physical experiments (PhyExp), inverse dynamics optimization (InvDyn), and forward dynamics optimization (ForDyn). 103

4.13 Measured and simulated motor torques for the forward step validation trial. Motors were included at the following joints: hip (*left*), knee (*centre*), and foot (*right*). Simulated trajectories were obtained using the parameters obtained via physical experiments (PhyExp) and inverse dynamics optimization (InvDyn). Note that the results obtained with parameters from forward dynamics optimization were not included due to their poor fit (see Table 4.12). 103

5.1 **A)** Overview of the compliant cuff interaction geometry where the human segment is approximated as a cylinder and cuff geometry is approximated as a rectangular prism. **B)** Geometry of the intersecting bodies during contact events (δ =depth of penetration). Note that the rightmost figure shows a single infinitesimal cross-sectional ellipse for a given value of x. **C)** An example of cuff element located on the real EXO-H3 and the model designed in the current dissertation. 109

5.2 **A)** Overview of the compliant strapping interaction geometry where the human segment is approximated as a cylinder. **B)** Geometry of the intersecting bodies in both the (x, y) and (z, x) planes during contact events with the resulting strapping geometry shown by the red/green lines. Note that the contact geometry was exaggerated to better highlight the variables of interest. **C)** An example of a Velcro strap element located on the real EXO-H3 and the model designed in the current dissertation. 111

5.3 Schematic showing naming conventions for the strapping and cuff elements of interest within the MapleSim interface: straps 1-2 (Velcro) acting on the anterior shank; cuffs 1-2 acting on the posterior shank; straps 3-4 acting on the dorsal/posterior aspects on the foot. The misalignment between the EXO-H3 and human knee joint that occurred shortly after simulation onset is also highlighted for the readers interest. Note that the CAD models of the human leg segments used to estimate cylinder parameters and visualizations were provided by Christian Mele from his work in his MASc thesis [241]. . 115

5.4 **A)** The desired EXO-H3 hip and knee trajectories controlled via joint-level PD control; the ankle joint received no controller inputs, i.e. motor torques. The hip was held motionless while the knee underwent an extension ramp followed by a flexion ramp. **B)** Simulated strapping tensions F_{str} (Equation (5.19)) for each of three Velcro types listed in Table 5.1 ("Standard", "Kric Krac", "Elasticated") using parameters obtained from the data in Bader and Pearcy [38]. 116

5.5 Simulated human hip, knee, and ankle joint angles for each type of Velcro strap (Standard, Kric Krac, and Elasticated) under the **A)** "loose" condition (baseline strap resting length) and the **B)** "secured" condition (strap resting length reduced by 5-10 cm). For reference, the exoskeleton joint angle trajectories are shown by the black line. 118

5.6 Simulated **A)** tension for each shank strapping element (Velcro 1-2), **B)** applied normal forces due to contact at each shank cuff element (Cuffs 1-2), and **C)** corresponding constraint forces (applied to the shank) evaluated when using kinematic constraints to combine human and exoskeleton in simulation rather than compliant elements. 119

5.7 Schematic of the floating-base human-only (A) and lower-limb exoskeleton dynamic models (B, based on the Technaid Exo-H3), with each systems' nine degrees of freedom highlighted. Note that the human is shown transparently in B to highlight how the exoskeleton fits the user. 121

6.1 The feasible stability region (FSR) for the human-exoskeleton FIP balance model generated with **no** reflected inertia in the actuators (direct-drive) and varying values of actuator Coulomb friction τ_c. Actuator parameters were consistent between joints. 128

6.2 The feasible stability region (FSR) for the human-exoskeleton FIP balance model generated with **with** reflected inertia in the actuators (gearing present) and varying values of actuator Coulomb friction τ_c. Actuator parameters were consistent between joints. 129

6.3 The feasible stability region (FSR) for the human-exoskeleton FIP balance model generated with **with** reflected inertia in the actuators (gearing present), a set actuator Coulomb friction torque ($\tau_c = 6$ Nm), and varying values of actuator viscous friction μ_o. Actuator parameters were consistent between joints. 129

6.4 The feasible stability region (FSR) for the human-exoskeleton FIP balance model generated following repositioning of the battery rigid body with respect to the trunk-fixed longitudinal axis, i.e., -25 cm (baseline), 0 cm, +15 cm. 131

6.5 The feasible stability region (FSR) for the human-exoskeleton FIP balance model generated with different constraints imposed on the maximum muscle activation, i.e., muscle activations could not surpass 10, 25, or 100%, with the 10% condition representing the individual with the lowest muscle strength. Arm movement was restricted in these simulations. 132

6.6 Hip, knee, and ankle joint angles that resulted in the **anterior** FSR boundary for the human-exoskeleton balance model when different constraints were imposed on the maximum muscle activation during simulations, i.e., muscle activations could not surpass 10, 25, or 100%. 133

6.7 Hip, knee, and ankle joint angles that resulted in the **posterior** FSR boundary for the human-exoskeleton balance model when different constraints were imposed on the maximum muscle activation during simulations, i.e., muscle activations could not surpass 10, 25, or 100%. 134

6.8 The feasible stability region (FSR) for the human-exoskeleton FIP balance model generated with different constraints imposed on the maximum amplified motor torque, i.e., τ_{mtr} for each joint could not surpass ±15 Nm, ±30 Nm (baseline), or ±60 Nm. 135

6.9 Control schematic for simulation set 2: optimal regulation of FIP balance recovery via linear quadratic regulator (LQR; unconstrained) or model predictive control (MPC; constrained). 157

6.10 Balance recovery (with FIP) joint angle trajectories obtained with a linear quadratic regulator (LQR) and model predictive control architecture (MPC) with variations in the objective homotopy parameter ρ. 159

6.11 Balance recovery (with FIP) motor torque trajectories obtained with a linear quadratic regulator (LQR) and model predictive control architecture (MPC) with variations in the objective homotopy parameter ρ. 159

6.12 Balance recovery (with FIP) anteroposterior (AP) COM/ZMP trajectories obtained with a linear quadratic regulator (LQR) and model predictive control architecture (MPC) with variations in the objective homotopy parameter ρ. Where necessary, the relevant support polygon boundary is highlighted by a dotted line. 160

6.13 Balance recovery (with FIP) joint angle trajectories obtained with a linear quadratic regulator (LQR) and model predictive control architecture (MPC) with variations in the objective weighing parameter σ. 161

6.14 Balance recovery (with FIP) motor torque trajectories obtained with a linear quadratic regulator (LQR) and model predictive control architecture (MPC) with variations in the objective weighing parameter σ. 161

6.15 Balance recovery (with FIP) anteroposterior (AP) COM/ZMP trajectories obtained with a linear quadratic regulator (LQR) and model predictive control architecture (MPC) with variations in the objective weighing parameter σ. Where necessary, the relevant support polygon boundary is highlighted by a dotted line. 162

6.16 Balance recovery (with FIP) joint angle trajectories obtained via model predictive control (MPC) with (constrained) and without (unconstrained) inclusion of the ZMP-BOS constraint in Equation (6.73). 164

6.17 Balance recovery (with FIP) anteroposterior (AP) COM/ZMP trajectories obtained via model predictive control (MPC) with (constrained) and without (unconstrained) inclusion of the ZMP-BOS constraint in Equation (6.73). . 164

6.18 Balance recovery (with FIP) joint angle trajectories obtained via model predictive control (MPC) with (constrained) and without (unconstrained) inclusion of the terminal constraints in Equation (6.78). Support polygon boundaries exceeded the limits chose for the vertical axis. 165

6.19 Balance recovery (with FIP) anteroposterior (AP) COM/ZMP trajectories obtained via model predictive control (MPC) with (constrained) and without (unconstrained) inclusion of the terminal constraints in Equation (6.78). . . 165

6.20 Balance recovery (with FIP) joint angle trajectories obtained via model predictive control (MPC) with variations in the prediction horizon length, i.e., 300 ms, 500 ms, or 700 ms. 166

6.21 Control schematic for simulation set 3: optimal regulation of FIP balance recovery via model predictive control (MPC) with concurrent nonlinear state estimation via the extended Kalman filter (EKF) or moving horizon estimation (MHE). 167

6.22 Balance recovery (with FIP) anteroposterior (AP) COM/ZMP trajectories obtained via MPC control paired with either an extended Kalman filter (EKF) or a moving horizon estimator (MHE) for each of the test cases introduced in the current section. Simulation tests were as follows: no friction in plant/EKF (TEST 1); model-mismatch with no friction in EKF, but friction in plant (TEST 2); friction in both EKF and plant (TEST 3). 168

6.23 Balance recovery (with FIP) joint angle trajectories obtained via MPC control paired with either an extended Kalman filter (EKF) or a moving horizon estimator (MHE) for each of the test cases introduced in the current section. 169

6.24 Balance recovery (with FIP) motor torque trajectories obtained via MPC control paired with either an extended Kalman filter (EKF) or a moving horizon estimator (MHE) for each of the test cases introduced in the current section. 169

6.25 True and estimated balance recovery (with FIP) joint angle trajectories obtained via MPC control paired with either an extended Kalman filter (EKF) or a moving horizon estimator (MHE) for TEST 3. 170

6.26 True and estimated balance recovery (with FIP) motor torque trajectories obtained via MPC control paired with either an extended Kalman filter (EKF) or a moving horizon estimator (MHE) for TEST 3. 171

6.27 Balance recovery (with FIP) human MTG torque trajectories obtained via MPC control paired with either an extended Kalman filter (EKF) or a moving horizon estimator (MHE) for TEST 3. 171

6.28 True and estimated balance recovery (with FIP) joint angle trajectories obtained via MPC control paired with either an extended Kalman filter (EKF) or a moving horizon estimator (MHE) for TEST 3. Signals were quantized for the current simulations (rounded to nearest 0.1 deg or Nm) . 173

6.29 Balance recovery (with FIP) motor (EXO) and human MTG (HUM) torque trajectories obtained via MPC control paired with a moving horizon estimator (MHE) for TEST 3. Signals were quantized for the current simulations (rounded to nearest 0.1 deg or Nm) 173

7.1 Model predictive control (MPC) and center of mass (COM) position/velocity-based assistance control architecture used in experiments. Note that the finite-state machine (FSM) used the hip angles to determine whether or not the user was in upright stance with the feet approximately symmetrical (FSM == 1). 176

7.2 A) Anteroposterior (AP) COM position scaling function (χ_x) and B) AP COM velocity (χ_v) scaling function for $\mathcal{B} = [-0.06, 0.00, 0.05, 0.21]$ m, $\delta_{\text{ant}} = 0.05$ m, $\delta_{\text{post}} = 0.02$ m, $F = 1$, $\omega_0 = 3$ Hz, $\ell_{\text{c2h}} = 0.06$ m, and $\ell_{\text{c2t}} = 0.21$ m. 182

7.3 Representative mean human-only COM and XCOM position (in the Exo condition, H-E [blue], and no Exo condition, H-NE [purple], condition) as well as the combined human-exoskeleton COM and XCOM (in the Exo condition, HE-E [red]) for balance recovery in response to backward and forward support-surface translations. Shaded areas indicate ±1 SD. Also shown are the temporal profiles of the AP platform velocity for each condition, where positive values correspond to the anterior direction. 193

7.4 Representative mean human joint angles for balance recovery in response to backward and forward support-surface translations. Shaded areas indicate ±1 SD. 194

7.5 Representative mean MPC-derived assistive torque $\tau_{\text{mtr}}*$, following scaling by COM position-velocity scaling function in Section 7.2.2, for balance recovery in response to backward and forward support-surface translations. Shaded areas indicate ±1 SD. 195

7.6 **A**) Maximum hand speed and **B**) maximum COP speed measured following each direction of perturbation (backward B, forward F, left L, right R). * indicates a statistically significant main effect ($p < 0.05$, only a direction main effect present in A). 196

7.7 Experimental and predicted (via human-NMPC) anteroposterior (AP) COM trajectories during human-only balance recovery (No Exo), i.e., induced falling forward or backward. 200

7.8 Experimental and predicted (via human-NMPC) anteroposterior (AP) COP (assumed coincident with ZMP) trajectories during human-only balance recovery (Exo), i.e., induced falling forward or backward. 200

7.9 Experimental and predicted (via human-NMPC or exoskeleton-MPC) anteroposterior (AP) COM trajectories during human-exoskeleton balance recovery (No Exo), i.e., induced falling forward or backward. 201

7.10 Experimental and predicted (via human-NMPC or exoskeleton-MPC) anteroposterior (AP) COP (assumed coincident with ZMP) trajectories during human-exoskeleton balance recovery (Exo), i.e., induced falling forward or backward. 201

7.11 Experimental and predicted (via human-NMPC) hip, knee, and joint angle trajectories during human-only balance recovery (No Exo), i.e., induced falling forward or backward. 202

7.12 Experimental and predicted (via human-NMPC or exoskeleton-MPC) hip, knee, and joint angle trajectories during human-exoskeleton balance recovery (Exo), i.e., induced falling forward or backward. 202

7.13 Revised model predictive control (MPC) assistance architecture using simpler assistance parameterization via χ_{ff} and χ_{fb}. 209

7.14 Simulated human-exoskeleton joint angles (left) and control torques (right; desired torques input to the friction compensation block) for tests 1-3 where the simulated end-user experienced a forward perturbation. 211

7.15 Simulated human-exoskeleton anteroposterior COM position (with respect to the ankle) for tests 1-3 where the simulated end-user experienced a forward perturbation. 212

B.1 Schematic of the knee, ankle, and hip joint within Norman-Gerum's sit-to-stand model [262], actuated by (a) Hill-type muscles and (b) muscle torque generators (MTGs). Note the complex wrapping geometry and redundancy encountered when using muscles. MTGs permit multibody system reduction by approximating the force-length/velocity curves and passive elements (shown *bottom*) directly at the joint level (scaling torques using joint rotations). Note the analogs between the MTG parameters and Hill-type parameters (e.g. optimal muscle length ℓ_0 and joint angle θ_0). Eccentric and concentric phases of muscle/torque scaling are indicated by "con." and "ecc." respectively. Adapted with permission from author V. Norman-Gerum [262] 272

F.1 A) Plots of the three feasible stability region (FSR) candidate functions introduced in F.1 (experiment 1; $k = 1$, $d = 1$, $\epsilon = 1$) in addition to B) the FSR for the human-only FIP balance model generated using each function candidate (arm movement was restricted). As a reminder, for a given COM position normalized to foot length (vertical axis; 0 = toe, 1 = heel), if the COM velocity is within the FSR boundaries (shaded region), then the biped can terminate this velocity such that quiet, upright stance can still be captured. If the velocity goes beyond these boundaries, then the model must take a step (not analyzed herein) or fall. The rightmost and leftmost boundary represent the anterior (forward) and posterior (backward) fall limit respectively. 291

F.2 The feasible stability region (FSR) for the human-only FIP balance model generated with different constraints on the initial velocity, i.e., which joints could contribute to generating the maximal COM velocity at onset. Arm movement was **NOT** restricted in these simulations. Conditions are as follows: only ankle velocity (DOF=1); ankle+hip permitted (DOF=2); ankle+knee+hip permitted (DOF=3); ankle+knee+hip and upper limbs permitted (DOF=5). 293

F.3 Joint angles that result in the **anterior** FSR boundary for the human-only balance model when different constraints are imposed on the initial velocity, i.e., which joints could contribute to generating the maximal COM velocity at onset (right boundary in Fig. F.2). Shown are the results for simulations in which the initial normalized COM position is 0.25 (*left*), 0.50 (*middle*), and 0.75 units (*right*). Arm movement was **NOT** restricted in these simulations. Conditions are as follows: only ankle velocity (DOF=1); ankle+hip permitted (DOF=2); ankle+knee+hip permitted (DOF=3); ankle+knee+hip and upper limbs permitted (DOF=5). 294

F.4 Joint angles that result in the **posterior** FSR boundary for the human-only balance model when different constraints are imposed on the initial velocity, i.e., which joints could contribute to generating the maximal COM velocity at onset (left boundary in Fig. F.2). Shown are the results for simulations in which the initial normalized COM position is 0.25 (*left*), 0.50 (*middle*), and 0.75 units (*right*). Arm movement was **NOT** restricted in these simulations. 295

F.5 The feasible stability region (FSR) for the human-only FIP balance model generated with different constraints imposed on the maximum muscle activation, i.e., muscle activations could not surpass 25, 50, 75, or 100%, with the 25% condition representing the individual with the lowest muscle strength. Arm movement was restricted in these simulations. 296

F.6 Active hip, knee, and ankle muscle torques that resulted in the **anterior** FSR boundary for the human-only balance model when different time delays (dead time, δ) were imposed during simulations (right boundary in Fig. 3.7). 298

F.7 Hip, knee, and ankle joint angles that resulted in the **posterior** FSR boundary for the human-only balance model with different constraints imposed on the maximum muscle activation simulations (left boundary in Fig. F.5). . . 299

I.1 Estimated minimal MOI parameters, i.e., $\mathbf{p}_{\text{Md},1}$ (*left*; thigh), $\mathbf{p}_{\text{Md},2}$ (*centre*; shank), and $\mathbf{p}_{\text{Md},3}$ (*right*; foot), using the proposed MHE scheme over multiple iterations. The MHE algorithm was tested under two conditions: EXP 1 (*top*), the MHE window length was adjusted (M=2, M=5, M=10) for a given measurement noise covariance (cov(v) = 10^{-6}); EXP 2 (*bottom*), the measurement noise covariance was adjusted (cov(v) = 10^{-6}, cov(v) = 10^{-6}, cov(v) = 10^{-1}) for a given MHE window (M=5). 313

I.2 Estimated Coulomb friction parameters, i.e., $\mu_{\text{h},0}$ (*left*; hip), $\mu_{\text{k},0}$ (*centre*; knee), and $\mu_{\text{a},0}$ (*right*; ankle), using the proposed MHE scheme over multiple iterations. The MHE algorithm was tested under two conditions: EXP 1 (*top*), the MHE window length was adjusted (M=2, M=5, M=10) for a given measurement noise covariance (cov(v) = 10^{-6}); EXP 2 (*bottom*), the measurement noise covariance was adjusted (cov(v) = 10^{-6}, cov(v) = 10^{-6}, cov(v) = 10^{-1}) for a given MHE window (M=5). 314

I.3 Trace of the estimated parameter error covariance $\mathbf{P}$ using the proposed MHE scheme over multiple iterations. The MHE algorithm was tested under two conditions: **A)** EXP 1, the MHE window length was adjusted (M=2, M=5, M=10) for a given measurement noise covariance (cov(v) = 10^{-6}); **B)** EXP 2, the measurement noise covariance was adjusted (cov(v) = 10^{-6}, cov(v) = 10^{-6}, cov(v) = 10^{-1}) for a given MHE window (M=5). 315

K.1 The feasible stability region (FSR) for the human-exoskeleton FIP balance model generated with different constraints on the model degrees of freedom, i.e., which joints were to be "locked" during simulations. Conditions are as follows: only ankle movement (DOF=1); ankle+knee+hip movement permitted (DOF=3); ankle+knee+hip and upper limbs movement permitted (DOF=5). Additionally, the analytical results from Hof et al. [154] are shown (FSR derived from linear inverted pendulum) to validate the results of the DOF=1 simulation, i.e., the nonlinear inverted pendulum FSR. . . . 321

K.2 COM and ZMP position that result in the **anterior** FSR boundary for the human-exoskeleton balance model when different constraints are imposed on the model degrees of freedom, i.e., which joints were to be "locked" during simulations. 322

K.3 COM and ZMP position that result in the **posterior** FSR boundary for the human-exoskeleton balance model when different constraints are imposed on the model degrees of freedom, i.e., which joints were to be "locked" during simulations. 323

K.4 Joint angles that result in the **anterior** FSR boundary for the human-exoskeleton balance model when different constraints are imposed on the model degrees of freedom, i.e., which joints were to be "locked" during simulations. Conditions are as follows: only ankle movement (DOF=1); ankle+knee+hip movement permitted (DOF=3); ankle+knee+hip and upper limbs movement permitted (DOF=5). 324

K.5 Joint angles that result in the **posterior** FSR boundary for the human-exoskeleton balance model when different constraints are imposed on the model degrees of freedom, i.e., which joints were to be "locked" during simulations. Conditions are as follows: only ankle movement (DOF=1); ankle+knee+hip movement permitted (DOF=3); ankle+knee+hip and upper limbs movement permitted (DOF=5). 325

K.6 The feasible stability region (FSR) for the human-exoskeleton FIP balance model generated following addition of 10 kg mass to the centroid of different segments (5 kg to left and right segments; along the longitudinal axis). Mass was added to the following segments: the trunk, thighs, shanks, and feet. The baseline condition used the EXO-H3 multibody parameters obtained in Chapter 4. 327

L.1 Control schematic for simulation set 1: computed torque control (CTC) of FIP balance recovery in joint space (JCTC), COM-space (CCTC), or a combination of the two (COMB). 331

L.2 Feed-forward nonlinear friction compensation block incorporated in the simulated control schemes in Chapter 6. 332

L.3 Balance recovery (with FIP) joint angle trajectories obtained for each variation of computed torque control formulated in joint space (JCTC), COM-space (CCTC), or a combination of the two (COMB). 333

L.4 Balance recovery (with FIP) motor torque trajectories obtained for each variation of computed torque control formulated in joint space (JCTC), COM-space (CCTC), or a combination of the two (COMB). 333

L.5 Balance recovery (with FIP) anteroposterior (AP) COM/ZMP trajectories obtained for each variation of computed torque control formulated in joint space (JCTC), COM-space (CCTC), or a combination of the two (COMB). 334

N.1 Control schematic for simulation set 4: assisted FIP balance recovery via model predictive control (MPC) with concurrent nonlinear state estimation (moving horizon estimation; MHE). The human end-user CNS is modelled using the LQR from Chapter 6 to capture performance of the MHE when there is a mismatch between the exoskeleton and human feedback control law. Assistive torques derived from the MPC were scaled by factor $\chi \in [0, 1]$ 341

N.2 Anteroposterior (AP) COM/ZMP trajectories obtained via MPC control paired with a moving horizon estimator (MHE) to assist a simulated 40%-strength end-user with FIP balance recovery. 343

N.3 Anteroposterior (AP) COM/ZMP trajectories obtained via MPC control paired with a moving horizon estimator (MHE) to assist a simulated 70%-strength end-user with FIP balance recovery. 343

N.4 True and estimated joint angle trajectories obtained via MPC control paired with a moving horizon estimator (MHE) to assist a simulated 40%-strength end-user with FIP balance recovery. 344

N.5 True and estimated motor (EXO) and human MTG (HUM) torque trajectories obtained via MPC control paired with a moving horizon estimator (MHE) to assist a simulated 40%-strength end-user with FIP balance recovery. 344

N.6 True and estimated joint angle trajectories obtained via MPC control paired with a moving horizon estimator (MHE) to assist a simulated 70%-strength end-user with FIP balance recovery. 345

N.7 True and estimated motor (EXO) and human MTG (HUM) torque trajectories obtained via MPC control paired with a moving horizon estimator (MHE) to assist a simulated 70%-strength end-user with FIP balance recovery. 345

List of Tables

2.1 Examples of commercial powered lower-limb exoskeletons and orthoses available and approved for research purposes. Passive devices are not considered here. 8

3.1 Evaluated Logarithmic Cost Ratios (CR). Bolded values indicate negative CRs, i.e., using the upper limbs further reduced the cost of balancing according to the associated criteria. 60

4.1 EXO-H3 Joint Ranges of Motion. 65

4.2 EXO-H3 Actuator Parameters Provided by Manufacturer (Technaid, Spain) 68

4.3 EXO-H3 isolated joint module and foot segment components, final physical measurements (mass and MOI about the COM), and name of subsegments that the component is comprised of. Note that stator/rotor links are links specifically connected to the fixed/output shaft of the actuator respectively. Masses were measured via scale (calibrated to 4 kg), while MOIs were measured using an MOI tester (MOI-025-004, Inertia Dynamics, USA). 73

4.4 EXO-H3 isolated subsegment components and final physical measurements (mass and MOI about the COM). As noted in the rightmost column of the table, each component listed below represents a single subsegment within the EXO-H3 CAD and rigid body analysis (unlike the components listed in Table 4.3). Masses were measured via scale (calibrated to 4 kg), while MOIs were measured using an MOI tester (MOI-025-004, Inertia Dynamics, USA). 74

4.5 EXO-H3 subsegments, shown in Tables 4.3 and 4.4, assigned to each of the trunk, thigh, shank, and foot segments defined in Fig. 4.1. 74

4.6 Trunk multibody dynamic parameters obtained for the EXO-H3 via CAD analysis paired with physical measurements. 92

4.7 Nonlinear friction parameters obtained for the EXO-H3 using the two optimization methods presented in Chapter 4.2.4: an inverse dynamics approach (Inv-Dyn) and a forward dynamics approach (For-Dyn). The results generated from the physical dynamometer experiment with the EXO-H3 knee are also presented (PhyExp). 94

4.8 Minimal multibody dynamic parameters obtained for the EXO-H3 using the two optimization methods presented in Chapter 4.2.4: an inverse dynamics approach (Inv-Dyn) and a forward dynamics approach (For-Dyn). The results generated from the physical experiment (direct measurements and CAD analysis) are also presented (PhyExp). 95

4.9 Redundant multibody dynamic parameters obtained for the EXO-H3 using the two optimization methods presented in Chapter 4.2.4: an inverse dynamics approach (Inv-Dyn) and a forward dynamics approach (For-Dyn). The results generated from the physical experiment (direct measurements and CAD analysis) are also presented (PhyExp). 96

4.10 Root mean square error (RMSE) between the joint angles measured during the 6 exciting experimental identification trials (T1-6) and simulated values using identified parameters from inverse dynamics optimization (InvDyn), forward dynamics optimization (ForDyn), and physical experiments (PhyExp). 99

4.11 Root mean square error (RMSE) between the joint motor torques measured during the 6 exciting experimental identification trials (T1-6) and simulated values using identified parameters from inverse dynamics optimization (InvDyn), forward dynamics optimization (ForDyn), and physical experiments (PhyExp). 100

4.12 Root mean square error (RMSE) between the experimental step validation joint angles/ motor torques and simulated values using identified parameters from inverse dynamics optimization (InvDyn), forward dynamics optimization (ForDyn), and physical experiments (PhyExp). 104

5.1 Estimated strapping parameters for three types of Velcro® based on Bader and Pearcy [38]. 114

7.1 Parameters used for real-time MPC. Parameter arrays like in the case of $\mathbf{u}_{\min}$ are written in the order hip, knee, and ankle. 178

7.2 COM-assistance parameters used in experiments. 183

7.3 Nonlinear friction compensation parameters used in experiments. 183

7.4 Support-surface translation parameters 186

7.5 Statistical analysis (two-way repeated measures ANOVA) of a perturbation main effect (p_{Dir}), exoskeleton main effect (p_{Exo}), and interaction (p_{Int}) for the kinematic outcome measures (mean ± SD). Note that statistical significance was reached at $p < 0.05$ (main or interaction effect indicated by *). 197

7.6 Statistical analyses (one-way repeated measures ANOVAs) for an exoskeleton main effect (p_{Exo}) on the COM/COP-based outcome measures (mean ± SD). Note that statistical significance was reached at $p < 0.05$ (exoskeleton main effect indicated by *). 198

A.1 Example of human multibody dynamic parameters for the thigh, shank, upper arm and forearm+hand 268

A.2 Example of human multibody dynamic parameters for the lumped head, trunk, pelvis in addition to the lumped foot segment. The $\hat{\mathbf{j}}$-direction corresponds to the corresponding segment longitudinal axis (positive = superior); the $\hat{\mathbf{i}}$-direction describes the segment-fixed anteroposterior axis (positive = anterior). 269

I.1 Root mean square error (RMSE) between the experimental step validation segment angles and values estimated using the MHE scheme iteratively under the conditions outlined in the leftmost columns. 315

List of Abbreviations

AAN Assist-as-needed. Appears on pages: 22, 23, 136, 179, 180, 196, 203, 206, 208, 213, 217, 222, 223, 346

AC Alternating current. Appears on pages: 10

AF Arms free (unconstrained in simulations). Appears on pages: 57, 61

AJM Average joint misalignment. Appears on pages: 117

AL Arms "locked" (constrained in simulations). Appears on pages: 57, 60, 61

ANOVA Analysis of variance. Appears on pages: xxxii, 191, 197

AP Anteroposterior. Appears on pages: xiii–xv, xxi–xxiv, xxix, 27, 30, 38, 40–42, 44, 46–48, 128, 130, 132, 135, 160, 162, 164, 165, 168, 182, 193, 196, 198, 200, 201, 205, 291, 293, 297, 321, 326, 331, 334, 343

BOS Base of support. Appears on pages: xxi, xxii, 13, 14, 27, 30, 31, 162–164, 183, 210, 211, 342

CAD Computer-aided design. Appears on pages: xvi, xix, xxx, xxxi, 64, 68, 69, 71, 72, 74, 75, 89, 92, 95, 96, 114, 115, 156, 219

CAN Controller area network. Appears on pages: 82, 85, 105

CCTC COM-space computed torque control. Appears on pages: xxviii, xxix, 329–334

CNS Central nervous system. Appears on pages: xxix, 12–17, 22, 37, 43, 47, 51–54, 61, 138, 152, 174, 175, 181, 188, 192, 204–207, 209, 222, 340–342

COM Centre of mass. Appears on pages: v, xi–xvi, xxi–xxx, xxxii, 13–17, 20–22, 25, 30–32, 34–43, 46–49, 51, 55–57, 60, 63, 68, 69, 71–75, 92, 96, 110, 124–126, 128, 130–135, 137, 139, 141, 142, 146–148, 158, 160, 162–165, 168, 176–183, 189–193, 195, 196, 198–201, 203–206, 208, 210, 212, 213, 217, 221, 222, 268, 269, 286–288, 290–299, 303, 321–323, 326, 327, 329–334, 342, 343, 346

COMB Combined COM-space and joint-space computed torque control. Appears on pages: xxviii, xxix, 330–334

COP Centre of pressure. Appears on pages: xxiv, xxxii, 13, 14, 16, 23, 190, 191, 193, 196–201, 204, 205, 207, 322

CTC Computed torque control. Appears on pages: xxviii, 138, 143, 328, 330–332

DAE Differential algebraic equation(s). Appears on pages: 122, 123, 137, 317, 318

DC Direct current. Appears on pages: 8–10, 66, 68, 176

DOF Degree(s) of freedom. Appears on pages: xiii, xiv, xvi, xxvi–xxviii, 8, 9, 24, 25, 37–39, 41–43, 46, 63, 65, 79, 106, 114, 127, 157, 207, 211, 219, 292–294, 296, 297, 301, 316, 317, 319–326

EKF Extended Kalman filter. Appears on pages: xxii, xxiii, 152, 153, 155, 156, 166–171, 173, 215, 310, 335–339

EMF Electromotive Force. Appears on pages: 66, 72, 75, 92

EMG Electromyography. Appears on pages: 11, 16, 17, 186–188, 207

FFT Fast Fourier transform. Appears on pages: 85, 86

FIP Feet-in-place balance recovery strategy. Appears on pages: ix, x, xiii, xiv, xx–xxiii, xxv–xxix, 13, 14, 17, 20, 23, 24, 30, 32, 33, 37, 39, 44, 46, 88, 120, 122–125, 127–132, 135, 136, 138–141, 143, 145, 147, 148, 152–154, 156, 157, 159–173, 175, 180, 182, 188, 203, 206–208, 212–218, 220–222, 289, 291, 293, 296, 297, 320–323, 326–328, 330, 331, 333–335, 338, 340–346

FPE Foot placement estimator. Appears on pages: 21, 220

FSM Finite-state machine. Appears on pages: xxiii, 176

FSR Feasible stability region. Appears on pages: xiii–xv, xx, xxi, xxv–xxviii, 32–35, 37–50, 57, 120, 123–125, 127–136, 156, 177, 180, 182, 204, 205, 208, 214, 217, 221, 222, 286, 288–299, 320–327, 346

IIR Infinite impulse response. Appears on pages: 178, 212

IMU Inertial measurement unit. Appears on pages: 208, 222, 346

IRED Infrared-emitting diode. Appears on pages: 188

JCTC Joint-space computed torque control. Appears on pages: xxviii, xxix, 328, 330–334

KKT Karush-Kuhn-Tucker. Appears on pages: 179

LQR Linear quadratic regulator. Appears on pages: xxi, xxix, 5, 16, 138–143, 146, 153, 156–163, 330, 340–342

MHE Moving Horizon Estimation (Estimator). Appears on pages: xxii, xxiii, xxvii, xxix, xxxii, 6, 71, 152–154, 156, 157, 166–173, 215, 217, 220–222, 308–315, 340–346

MOI Moment of inertia. Appears on pages: xxvii, xxx, 25, 63, 66, 68, 69, 71–74, 89, 92, 96, 102, 128, 268, 269, 303, 311, 313

MPC Model predictive control. Appears on pages: xxi–xxiv, xxix, xxxii, 5, 22, 57, 61, 143–148, 150, 153, 156–173, 175–179, 181–183, 189, 195, 196, 198, 201–203, 205–210, 212, 340–346

MTG Muscle torque generator. Appears on pages: xiii, xxiii, xxv, xxix, 26–28, 31, 33, 34, 37, 38, 43, 44, 46, 47, 49–51, 55, 58, 122, 131–135, 138, 150, 154, 157, 158, 160, 168, 170, 171, 173, 179, 200, 206, 210, 214, 218, 221, 270, 272–278, 280–282, 284, 297–299, 330, 342, 344–346

MVC Maximum voluntary contraction. Appears on pages: 187

NLP Nonlinear programming. Appears on pages: 33, 34, 37, 43, 54, 55, 60, 80–82, 90, 91, 93, 127, 154, 155, 284, 290, 308–310, 323

NMPC Nonlinear model predictive control. Appears on pages: ix, xxiv, 51–55, 57, 58, 60, 61, 143, 147, 148, 158, 192, 193, 200–202, 205, 206, 214, 220, 221

ODE Ordinary differential equation(s). Appears on pages: 27, 34, 36, 69, 90, 91, 106, 117, 121–123, 126, 137, 144, 154, 192, 302, 304, 308, 310, 312, 316–318

PD Proportional-derivative (control). Appears on pages: xix, 20, 23, 116, 175, 177, 180, 206, 209, 217

QP Quadratic programming. Appears on pages: 88, 143, 148, 149, 163, 179, 221

RMSE Root-mean-square error. Appears on pages: xvi, xvii, xxxi, xxxii, 83, 84, 86, 94, 99–101, 104, 168, 170, 311, 312, 315, 342

SCI Spinal cord injury. Appears on pages: 7, 341

UKF Unscented Kalman filter. Appears on pages: 309, 310

XCOM Extrapolated centre of mass from Hof et al. [154]. Appears on pages: xxiii, 22, 23, 55–58, 60, 148, 178, 180, 190–193, 196, 198, 199, 204, 205, 207, 217, 220, 222, 346

ZMP Zero-moment point. Appears on pages: xiii, xiv, xxi, xxii, xxiv, xxvii–xxix, 13, 16, 20, 21, 24, 30, 31, 36, 38, 40, 126, 143, 145, 146, 158, 160, 162–165, 167, 168, 178, 200, 201, 205, 206, 210, 287, 321–323, 331, 332, 334, 342, 343, 346

Chapter 1

Introduction

The World Health Organization estimates that approximately 1.3 billion individuals globally have experienced some form of physical disability [21]. Addressing deficits in human mobility is a non-trivial challenge, given the multitude of conditions that can significantly impact a person's ability to move [52, 103, 182, 297, 333]. For example, stroke is most typically recognized as the leading cause of disability globally [52]. In a recent study of community dwelling older adult stroke survivors in South Korea, Ju et al. [182] reported that an individual's stroke was the biggest cause of disability when compared to secondary issues like musculoskeletal problems, e.g., back or neck problems, arthritis, etc. Traumatic brain injuries are also responsible for a large number of disabilities. For example, Schneider et al. [297] reported that in the United States, approximately 47.4% of individuals over 40 years of age that have a history of head injuries are living with disability. Furthermore, the risk of experiencing mobility issues has a tendency to increase with age [225], which is concerning given the currently aging population for many countries; it is expected that over 25% of Canada's population will be at least 65 years of age by 2068 [20].

Modern mobility aids that are widely available to the public tend to be passive in nature (e.g., seated wheelchairs, crutches/walkers) with motorized devices being the exception, e.g., powered wheelchairs. Regarding wheelchairs, worldwide there are an estimated 65 million users [190]; in Canada alone, nearly 300,000 community-dwelling individuals are reported to require a wheelchair or scooter [312]. Tools like crutches, walkers, and wheelchairs dominate the medical-device space because their performance is well-established and relatively reliable; the end-user has a good understanding of how the tool functions with

respect to their own biomechanics. Although common, they are not without issue. For example, the experiments by Bateni et al. [44] identified the negative impact that walker-use can have on compensatory stepping following an external perturbation, thus increasing the likelihood of falling. In regards to wheelchairs, many people that are reliant on these devices often wish to regain the ability to stand and walk independently, secondary to wishes like the regain of urinary and/or sexual functions [66, 96]. However, that is not possible if relying on a wheelchair alone; other interventions like physical rehabilitation are required [187, 303, 377]. In fact, wheelchair reliance is often associated with conditions like muscle atrophy that further reduce the feasibility of independent movement [251]. Additionally, use of these specialized devices can incur a large cost due to limitations in interactions with the environment, i.e., the end-user often require modifications to living and/or workspace, e.g., access ramps [96].

Existing and widely-available mobility aids are limited in the scope of their ability to provide rehabilitative function, end-user assistance, and automation due to a minimal level of adaptability for a variety of tasks of daily living. Alternatively, active and passive robotic devices have the potential to be tuned continuously to provide the user with assistance as needed for multiple tasks. Thus, an alternative solution for correcting mobility deficits gaining rapid traction in both academic and industry settings involves the development and use of robotic exoskeletons and orthoses. Briefly, lower-limb exoskeletons are active or passive biomechatronic devices designed to mimic the anatomy of the human end-user in order to deliver device actuator torques about the ankle, knee, and/or hip joints [334]. Actuators are typically motors and gearing in the active case [214] and spring-dampers in the passive case [162, 311, 325]. Exoskeletons are sometimes defined differently from orthoses in that orthoses fully replace the muscle torques of the end-user rather than simply augment them [334].

1.1 Problem Identification

While exciting in their prospects, there are still numerous drawbacks and limitations with current exoskeleton technology. For example, actuator hardware (reflected inertia, friction losses, and backdrivability), energy limits (require heavy onboard batteries), kinematic mismatches, poor interfacing, or lack of actuated degrees of freedom are all problems commonly found in a variety of exoskeletons (discussed further in Section 2.1.1). Interestingly,

many of these limitations contribute to a major problem with wearable lower-limb robotics: **they are difficult to remain balanced in without assistance from a device like crutches**. In response to this, over the past decade, researchers have begun to investigate different means of addressing the concern of reduced upright stability when an exoskeleton is donned. Some solutions posed utilize a kinematic [103, 284], inverse dynamics model [106, 103, 105] or forward dynamics model [134, 138] of the human-exoskeleton system dynamics; however, many of exoskeleton control systems ultimately tend to base the final control law around simpler model-free approaches, e.g., proportional-integral-derivative (PID) control [103, 105, 284].

With the primary gap in the literature identified (**poor balance when wearing an exoskeleton**), the focus of the current dissertation is to present a novel approach to studying human-exoskeleton balance control via computationally-efficient dynamic simulations and nonlinear optimal control methods (Chapters 3 and 6). Optimized symbolic multibody dynamics models of both the human musculoskeletal system and lower-limb robotic exoskeleton (based on the Technaid EXO-H3, Spain) were designed to carry out simulations and provide control-oriented models for real-time control implementations (Chapters 3-5). The simulation interface designed in Chapters 3 and 6 is used to design and test novel full-state feedback control and state estimation algorithms capable of automating or assisting the end-user of a lower-limb exoskeleton in staying balanced (Chapter 6). The final portion of this dissertation involves implementing the proposed controllers within an experimental setting (Chapter 7). Specifically, investigations into real-time assisted balance control were conducted with a novel model predictive control scheme that made decisions according to predictions made using the proposed forward dynamics standing balance model (Chapter 7).

1.2 Contributions

The primary contributions of the current dissertation can be lumped into the following four categories:

1. To generate novel simulations of **human-only** balance recovery in the sagittal plane using nonlinear optimal control methods that utilize both feedforward and feedback control.

2. To create an integrated symbolic model of **human-exoskeleton** multibody dynamics to study human-exoskeleton balance control and limits; the model is suitable for derivative-based optimal control algorithms (constituent equations are C^2 continuous). The exoskeleton model will be specific to the lower limbs.

3. To generate novel dynamic simulations of **human-exoskeleton** balance with and without the presence of exoskeleton assistance. This will involve the study and design of different novel control and state-estimation architectures for standing feet-in-place balance control.

4. To test a novel approach in assisting the end-user of a lower-limb exoskeleton in staying balanced with their feet-in-place following perturbations in a variety of directions.

The following list outlines the novel contributions of this dissertation according to each chapter:

- Chapter 3
  - Reformulation of the feasible stability region problem [264, 370] using constrained single-objective nonlinear programming based around direct collocation with symbolic derivatives [172].
  - Pareto optimization assessing trade-offs in the feasible stability region [264] with minimization of human "effort", e.g., input torques [172].
  - Curve-fitting approximation method for piecewise muscle torque generator functions, motivated by the approach by Millard et al. [244]
  - Dynamic simulations of human feet-in-place balance recovery using nonlinear model predictive control (feedback nonlinear optimal control) [170]
  - Investigation of arm strategies in balance recovery as they emerge from optimal control, e.g., can arm movement increase the size of the feasible stability region or do they assist in reducing other costs of balancing? [170]
- Chapter 4
  - Development of a lower-limb robotic exoskeleton model, based on the Technaid EXO-H3, featuring nonlinear joint impedance via a regularized friction model

[65]. The model designed herein is used to study human-exoskeleton balance control, but its generalized formulation can be employed in the study of a variety of human-exoskeleton tasks, e.g., sit-to-stand, sagittal walking, etc.

  - Extension of the parameter identification experiment design method by Swevers et al. [318] used in industrial robotics; a mathmetical approach to designing a sequence of multibody parameter identification experimental joint trajectories to be used to identify parameters in commercial lower-limb exoskeletons (Swevers proposed a method with a single experiment).
  - Comparison of inverse and forward dynamics approaches, including proposal of a novel moving horizon estimation method, in experimental parameter identification of a commercial exoskeleton (EXO-H3, Technaid, Spain).

- Chapter 5

  - Development of a combined human-exoskeleton model to be used within control-oriented dynamic simulations (merging the human and exoskeleton systems) using rigid and compliant contact principles.
  - Preliminary design of a point-contact (Hunt-Crossley [161]) human-exoskeleton contact model to capture unilateral interactions between rigid cuffing elements and soft human tissue, i.e., the contact force can "push", but cannot "pull".
  - Preliminary design of human-exoskeleton contact model to capture unilateral interactions between elastic strapping elements and soft human tissue, i.e., the strap can can "push" push back on user segment but cannot "pull".

- Chapter 6

  - Assessment of human-exoskeleton feasible stability region (primarily estimated for humans alone, [264, 370]) to quantify how certain features of the exoskeleton system design can impact the stability of the end-user under ideal scenarios.
  - Development of a multitude of model-based full-state feedback control schemes for autonomous or assistive human-exoskeleton balance recovery, including real-time control schemes based around unconstrained, i.e., linear quadratic regulator (LQR), and constrained optimal control, i.e., model predictive control (MPC).

  - Development of real-time state and disturbance estimation algorithms for standing human-exoskeleton balance; the approaches are based on Kalman filtering and nonlinear moving horizon estimation (MHE) [310].

- Chapter 7

  - Experimental testing of the novel model-predictive assistive balance control scheme in Chapter 6 with a model-based center of mass (COM) assistance profile; testing took place with young adult participants in Dr. Andrew Laing's laboratory at University of Waterloo [358].
  - Experimental comparison of healthy young adult balance recovery kinematics with and without wearing a lower-limb exoskeleton. Only Mileti et al. [243] has investigated this effect; though they did so after uncoupling the device actuators, i.e., the device was completely passive.

Chapter 2

Literature Review

2.1 Lower-Limb Exoskeletons and Orthoses

2.1.1 State-of-the-Art

For many individuals with mobility deficits, such as those who have experienced a spinal cord injury (SCI), wearable robotic exoskeletons offer a potentially life-changing improvement in the ability to stand, ambulate, and complete tasks of daily living independently. These systems can augment or replace the end-user's own muscle forces [334] to assist the individual in executing a variety of complex motor tasks like sit-to-stand, walking, stair-climbing, etc [97, 101, 138, 214, 334].

In addition to many laboratories around the world working towards building custom upper-limb and lower-limb exoskeleton and orthosis devices [103, 349], there are now a number of commercially available devices. The focus in this dissertation will be on the lower-limb variety of exoskeletons. Some examples of these commercial lower-limb systems are listed in Table 2.1. Typically, these lower-limb devices are built and sold for therapeutic or research purposes, though there has been an increase in those available for personal use (see [46] and [325] for an in-depth review of available technologies).

Table 2.1: Examples of commercial powered lower-limb exoskeletons and orthoses available and approved for research purposes. Passive devices are not considered here.

	Device Information			
DOF	Name	Manufacturer	Actuation	Resources
Ankle	1) EasyWalk Soft Exo-Suit	Syrebo	Powered cable-driven mechanism (Bowden cables).	Home Page: [17] Seen In: N/A
	2) ReStore Soft Exo-Suit	ReWalk Robotics	Powered cable-driven mechanism (Bowden cables).	Home Page: [13] Seen In: [143, 144, 322]
Knee	1) Keeogo	B-Temia	Electric motors (no information on transmission).	Home Page: [3] Seen In: [110, 232, 235]
Hip	1) Walking Assist	Honda	Electric motors with plantetary gearing.	Home Page: N/A Seen In: [113]
	2) Myosuit	MyoSwiss	Novel artificial tendon/ligament actuation (tension manipulated via brushless DC motor).	Home Page: [11] Seen In: [111, 139, 140]
	3) PhoeniX	SuitX (US Bionics, Inc)	Electric motors (no information on transmission).	Home Page: [16] Seen In: [194]
Knee, Hip	1) Indego	Parker Hannifin (now Ekso Bionics)	Electric motors (no information on transmission).	Home Page: [12] Seen In: [209, 307, 324]
	2) H-MEX	Hyundai	Brushless DC motors with strain-wave gearing.	Home Page: N/A Seen In: [163]
	3) HAL Lower Limb	CYBERDYNE	Brushless DC motors with strain-wave gearing.	Home Page: [5] Seen In: [86, 164]
	4) ExoMotus (Industrial)	Fourier Intelligence International	Electric motors with plantetary gearing.	Home Page: [8] Seen In: [76]
	5) EksoNR	Ekso Bionics	Electric motors (no information on transmission). Ankle passively actuated via spring.	Home Page: [6] Seen In: [317]

	6) ReWalk Personal	ReWalk Robotics	Brushless DC motors (no information on transmission). Ankle passively actuated via spring.	Home Page: [14] Seen In: [322, 375]
	7) Lokomat (Fixed)	Hocoma	Precision ball screws connected to brushless DC motors	Home Page: [10] Seen In: [42]
	8) RoboGait (Fixed)	Bama Technology	Electric motors (no information on transmission).	Home Page: [4] Seen In: [107]
	9) ExoAtlet II	ExoAtlet	Electric motors (no information on transmission).	Home Page: [7] Seen In: [199, 265]
	10) Angel Suit	Angel Robotics	Brushless DC motors with spring-embedded gearing	Home Page: [2] Seen In: [79, 178]
	11) ABLE Exoskeleton	ABLE Human Motion	Brushless DC motors with strain-wave gearing.	Home Page: [1] Seen In: [319, 364]
Ankle, Knee, Hip	1) EXO-H3	Technaid	Brushless DC motors with strain-wave gearing.	Home Page: [18] Seen In: [169, 172, 243]
	2) HANK	GOGOA	Electric motors (no information on transmission).	Home Page: [9] Seen In: [29, 126, 238]
Ankle, Knee, Hip*	1) Atalante X (Self-balancing)	Wandercraft	Electric motors (no information on transmission).	Home Page: [19] Seen In: [134, 135, 138]
	2) REX (Self-balancing)	REX Bionics	Brushless DC motors (no information on transmission).	Home Page: [15] Seen In: [41, 277]
	3) ExoLite X (Self-balancing)	ExoMed	Electric motors (no information on transmission) with joystick interface.	Home Page: N/A Seen In: [176]

* DOF span both sagittal and frontal plane.

In general, the state-of-the-art lower-limb exoskeletons are constructed as follows: electric actuators are placed in parallel with the end-user joints of interest, specifically to deliver power along a specific axis of rotation, e.g., knee flexion and extension. The specific joints and axes of rotation targeted by the device can vary widely between manufacturer/model,

e.g., ankle, knee, and hip [18, 19]; knee and hip [12, 6]; or just the ankle [13]. In almost all cases, these lower-limb devices deliver actuator torques to assist the user with movement in the sagittal plane only, although devices like the Atalante X (Wandercraft [19]) and REX (REX Bionics [15]) can deliver important hip abduction torques to allow for a higher degree of control over the integrated human-exoskeleton via features like a step width modulation [45, 348]. The trade-off in this case is that the size and complexity of these devices spanning multiple planes of motion are quite cumbersome in relation to other planar commercial devices like the Indego (Parker-Hannifin [12]) and the EXO-H3 (Technaid [18]). Modern electric actuators used in these devices are typically comprised of brushless direct-current (DC) or alternating-current (AC) motors paired with a medium to high-ratio gearing system [214, 325]. Often, the latter includes strain-wave (harmonic drive) or planetary gearing due to their relatively "flat" geometry requiring less space to operate [214]. Recently, there has also been a push to employ series-elastic and flexible-cable actuators to generate more "muscle-like" control [210].

To connect and maintain the position of the lower-limb exoskeleton's actuators, a network of rigid or soft links is often constructed with the goal of closely mimicking end-user anatomy [156, 162]. Lightweight rigid materials have historically been used for creating a biomimetic structure that will not collapse under the end-user's weight, e.g., aluminum and stainless steel [162, 296, 18]. Recently, the work in labs like the Harvard Biodesign Lab have focused on implementing soft robotics materials in exoskeleton construction to better follow the compliant nature of the musculoskeletal system and the soft tissue that surrounds it [156]. To power any electric actuators being used, some modern systems rely on separate power supply units not fixed to the exoskeleton e.g., the Lokomat [10]. However, a mobile exoskeleton unit capable of being used outside of rehabilitation or research environments requires an onboard power supply. In many of these cases, this onboard power supply is a heavy Lithium-ion battery that can have a profound effect on the distribution of mass in the device [162, 214, 334]. If the device makes use of passive actuation, this problem is removed, though at the cost of limiting the scope of device manipulation by any control engineers.

In the scientific literature, there have been a variety of issues identified with the current state-of-the-art exoskeleton technology. Some of these problems include the following: high-ratio gearing reflecting substantial rotational inertia onto the end-user in addition to introducing large amounts of energy dissipation (difficult for user to back-drive); limited degrees of freedom relative to the end-user's anatomy; introduction of kinematic errors (e.g.,

joint misalignment) due to use of rigid materials [214, 313]. Another notable issue is that the current state-of-the-art devices have rather poor balancing capabilities, i.e., upright bipedal postures tend to be unstable [105, 138, 169, 305, 343]. In fact, the designers of these devices (e.g., Technaid, Parker Hannifin) often mandate that the end-user uses an additional device to prevent falls, e.g., crutches or a walker. Evidently, this solution reduces functionality by removing free use of the arms during device operation, which intrinsically impacts the user's decision to use an exoskeleton. Additionally, control methods such as finite-state architectures, often employed in state-of-the-art exoskeletons [46, 101, 334], can induce balance-loss by perturbing the system during periods of state transition. Lastly, the hardware is often designed to assist the user in one plane of motion, i.e., the sagittal plane; however, models in the literature suggest that medio-lateral stability in tasks like walking explicitly requires active high-level neural control [45]. This is a major point of interest in the proprietary self-balancing systems featured only in the Atalante X [135, 138] and the REX exoskeletons; both exoskeletons include a hip abduction degree of freedom.

2.1.2 Design and Control

Classically, control of lower-limb exoskeletons has focused on reducing metabolic energy expenditure of the end-user during ambulation. A review of common control approaches in the literature is given in [46, 334]. Foremost, exoskeleton controls are typically broken down into three levels: high-level, mid-level, and low-level. High-level controls are typically concerned with features like environment recognition [206] and end-user intent detection [159, 191, 255, 372]. Often, especially in the context of rehabilitation, control engineers must consider whether the device behaves fully autonomously or provides human-in-charge assistance according to the interpretations of this level [46, 283, 334]. Mid-level controls typically use information from the high-level controller and involve estimation of the necessary actuator torques/positions that provide assistance or automation (typically the former). In the review by Baud et al. [46], the authors discuss the wide-use of impedance control in lower-limb exoskeleton mid-level controls, especially when partial assistance is desired. In a recent study, Arami et al. [33] investigated a data-driven approach to controlling leg impedance during walking with a powered ankle orthosis. This technique aims to develop a gait cycle controller that can effectively adapt to perturbations in the overall gait pattern. Mid-level actuator position and/or torque estimations can also emerge from model-based approaches [24, 49, 103, 105] including those derived from EMG and reflex-

driven neuromuscular models [35, 99, 100]. Lastly, the mid-level torque/position is sent to the low-level controller which is responsible for end-performance of the actuators, e.g., matching the desired output torque from the mid-level control via motor current control.

In recent literature, there has been a concerted effort to delve into the challenges of maintaining balance while utilizing robotic exoskeletons. Effective control of standing balance often employs variations of model-based [103, 169] or joint-level control strategies [103, 105, 284], which take into account a range of human balance techniques as documented in the literature, e.g., the ankle and hip strategies [158, 359]. Additionally, researchers like Gurriet et al. [134, 138] have proposed model-based control schemes based on hybrid zero dynamics, capable of establishing stable locomotor patterns in individuals with paraplegia. As previously mentioned, this system is implemented in the Atalante X [19], for its self-balancing feature, catering to individuals with limited lower-limb motor control, such as paraplegics (see Section 2.1.1). Balance control within the framework of lower-limb exoskeletons will be discussed further in Section 2.3.

To this point, many of the control laws discussed are designed with experimental observations of human motor control in mind, for instance, employing end-effector impedance control to minimize jerk [114] or endeavoring to induce a hip or ankle strategy for maintaining stationary foot positions [158]. On the other hand, balance controllers focusing on step placement are primarily preoccupied with the precise location of foot placement and the initiation/control of stepping [134, 245, 343]. The following section will discuss the neural control mechanisms governing human balance. This exploration will serve as a foundation for our own investigations into human-exoskeleton balance control, rooted in optimal control principles.

2.2 Human Control of Balance

2.2.1 Control of Walking versus Stance

After experiencing a significant external perturbation, such as a push or a sudden support-surface acceleration, the central nervous system (CNS) deploys a sophisticated array of multi-joint motor strategies to prevent a fall [158]. The response to such disturbances varies depending on whether the individual is engaged in activities like walking or maintaining a stationary posture, each demanding unique adjustments. During walking, the CNS

may strive to regain balance in a manner that sustains desired whole-body momentum and returns the body to a predefined trajectory in joint phase space, i.e., the gait cycle [94, 95, 245]. Conversely, when the goal is to maintain upright stance without continuing ambulation, CNS-mediated balance recovery typically involves the methodical return of the body's position to a specific equilibrium state, or a static pose [202, 252, 344, 361]. Often, this static pose entails symmetrical foot placement, with the center of mass positioned just anterior to the ankle joint [242]. However, exceptions arise, as seen in postures resembling double-support in gait, like the tandem stance in the Romberg test [115].

During quiet standing, researchers have likened the behavior of the musculoskeletal system to that of an inverted pendulum. In this model, the whole-body center of mass (COM) is carefully regulated within the boundaries of the support polygon, primarily through the active manipulation of bilateral ankle torques by the CNS [122, 361, 359]. These torques lead to characteristic shifts in the foot-ground center of pressure (COP), a variable frequently analysed to evaluate an individual's ability to maintain balance [361]. This inverted pendulum model classically assumes that the feet remain stationary during balancing (feet-in-place; FIP). Assuming no lifting of the heel or toes, this requires that the frictional force between the foot and the ground remains within the "friction cone" [133, 264] and that the zero-moment point (ZMP) stays within the confines of the support polygon [264, 346]. Briefly, the ZMP is the theoretical location of the foot-ground reaction force point of application that produces a rotationally static base of support (BOS; assuming the foot is flat against the ground). In some situations, the ZMP and COP are considered synonymous, i.e., integrated point of pressure acting on the foot; however, this is only true when the ZMP is within the confines of the support polygon. On paper, the ZMP can exist outside the support polygon, while the COP in reality cannot. Owing to these foundational studies, the inverted pendulum model has become a widely-used framework in the literature for modeling human balance control and recovery for both walking [25, 26, 154, 153, 174, 242, 245, 252, 264, 351, 353, 354]. Furthermore, it has been instrumental in the development of control algorithms for automating balance recovery in humanoid robots [148, 279, 278].

If maintaining an FIP stance is not feasible for balance recovery, the CNS has alternative strategies. These include altering the geometry of the support polygon and adjusting interactions with the environment to redistribute forces around the body, effectively regulating the COM kinematics. Crucially, braking impulses resulting from changes in human-environment interactions can play a pivotal role in halting or reversing COM

momentum after an external perturbation [285]. These tactics fall under the category of "change in support" strategies and may involve taking a step (or multiple steps) toward the direction of impending imbalance or utilizing the hands to grab a supporting object, such as a railing or crutches/walker [223]. To understand the features the CNS employs to scale and adapt reactive step parameters, various theoretical models have been proposed [25, 26, 154, 245, 278]. Intriguingly, much like quiet standing, these models often revolve around the concept of an inverted pendulum, utilizing factors like the state of the COM (velocity, kinetic energy) and overall body angular momentum (e.g., pinwheel motion) to provide estimations [130]. In contrast, determinants of reach-and-grasp responses may be more constrained, relying on factors like the fixed position of a supporting object in the environment, e.g., railing, and the visuospatial map stored within the CNS [233]

2.2.2 Feet-In-Place (FIP) Balance Recovery Strategies

The classification of different FIP-based balance recovery strategies was disseminated in the study by Horak and Nashner [158]. Briefly, controlled translations of the support-surface (support-surface perturbations) were used to perturb upright balance in young, healthy adults. By imposing different environmental conditions (narrowing the support polygon), the authors were able to identify two unique control strategies used by the CNS: the *ankle* and *hip* strategy. To reduce any ambiguity in characterizing these strategies, their kinematic definitions will be used [27, 202, 344, 359]. The ankle strategy is effectively a linear scaling of quiet standing control; postural stability is maintained through ankle rotations (other joints are kept straight). This strategy is often conflated with the response to small perturbations and is the strategy best captured by the inverted pendulum model, i.e., ankle torques (reflected by the COP displacement) are used to "corral" the COM to the confines of the BOS [361]. Conversely, the hip strategy operates the body similar to a double pendulum whose segments rotate about the ankles and hips (other joints remain fixed/straight). Note that the descriptions provided assume a forward loss-of-balance. Backward balance recovery has similar strategies, though display some direction-dependence [166], likely due to asymmetry of the support polygon about the ankle joint in the sagittal plane. The review by Maki and McIlroy [223] outlines four factors that determine the characteristics and adaptability of CNS-driven balance recovery: 1) the features of the perturbation (e.g. direction and magnitude); 2) the "central set" of the individual; 3) ongoing cognitive or motor activity; and 4) environmental constraints. Of

interest herein are the effects of perturbation parameters [222], e.g., an unexpected large magnitude perturbation will have a greater probability of inducing a hip strategy compared to an ankle strategy assuming the feet can be kept in-place.

An additional strategy that should be acknowledged is the *knee* strategy, which has been observed experimentally [27, 61] and within simulations of standing balance control [77, 175, 342, 341]. By definition, this strategy entails the flexion of the knees during balance recovery; however, other joints are not required to be fixed as required by the ankle and hip strategy. In the robotics literature, this is often referred to as the squat strategy, and is defined according to the lowering of the COM [36]. Similar to muscle synergies [302], Alexandrov et al. [27] suggested that the kinematics from all three balance recovery strategies can act as a basis to reconstruct the inter- and intra-subject variations in observed balance recovery. Often, the knee strategy is ignored due to infrequent or minor observations within experiments; usually, the knees remain relatively locked for the typical case of human balance recovery. However, movement of the knees during balancing maneuvers can theoretically expand the margins of stability, i.e. stable regions within the inverted pendulum COM phase space [175, 77].

A common feature of many biomechanical studies, not just those regarding balance control, is the exclusion of arm motion, e.g. arms are to be fixed to trunk [169, 202, 227, 243, 342, 344]. Those simulations that do include arms often have a particular component of the motor task that requires goal-oriented arm movement, e.g. pointing [240]. For a task like balance recovery, arm responses tend to be most overt following exposure to a novel and/or unexpected perturbation [168, 229], and have quite a few hypothesized roles, e.g., reduction of trunk extension velocity according to impulse momentum theory [332], countermovement of COM [229], or alteration of net centroidal angular momentum [26, 130, 152]. However, it remains unclear how experimentally-observed arm strategies might provide assistance when considering all the possible criteria the CNS weighs when recovering balance. In this case, dynamic simulations based on optimal control principles could be of benefit [55, 250].

2.2.3 Addressing Redundancies in Human Balance Recovery

The following section will address how humans remain balanced in the presence of many system redundancies. Bernstein, a Soviet neurophysiologist, posed the "degree-of-freedom

problem": how is the CNS capable of sufficiently controlling the large number of degrees of freedom of the musculoskeletal system [54]? One particular solution to this problem of motor redundancy that is of particular interest is that of optimal control [202, 268, 344]. In this approach, we assume that over long periods of evolution, the CNS has adapted to solve the redundancy problem by utilizing motions that extremise some set of meaningful performance criteria. For example, the work of Neville Hogan suggests that the CNS moves the human-upper limb during a pointing task in such a way that minimizes end-effector (hand) jerk over the horizon of interest [55, 114, 155].

In this optimal framework, we wish to address the question of which criteria the CNS uses to generate the appropriate balance recovery strategies following a perturbation. As introduced prior, research by Winter popularized the inverted pendulum model of quiet stance [361, 359]. In this case, the CNS regulates changes in COM kinematics through ankle muscle control (COP/ZMP control) alone (assuming no pinwheel). As such, control of balance is often considered within the COM space, which suggests that the CNS could be trying to minimize displacements of the COM from a reference point over the horizon of interest. This is further strengthened by observations like those of Welch and Ting [353], who were able to reconstruct experimental electromyography (EMG) measurements from the ankle during balance recovery using a delayed feedback control law based on COM kinematics only. This idea has been a motivating factor behind many recent exoskeleton balance approaches [24, 49, 105, 103]. Many optimal control studies of human and human-exoskeleton balance control and recovery have also hence utilized the COM in developing performance criteria [26, 169, 172, 185, 202, 344]. For example, Afschrift et al. [24] recently proposed modulation of a local neuromuscular feedback controller to provide assistive ankle torques during human-exoskeleton walking through COM-dependent ankle activations.

Early work by Kuo [202, 203] examined how adjusting the cost function within a linear quadratic regulator (LQR), and applying the linear control law to a planar, torque-driven double pendulum (degrees of freedom = ankle and hip rotations), would result in evocation of different postural strategies following a lean-and-release perturbation. Recently, Versteeg et al. [344] expanded this work to detailed musculoskeletal models. Using a human model designed in SIMM and direct shooting optimal control, they observed that following a support-surface perturbation, the model would use a hip-strategy if the COM objective was highly-weighted; in contrast, highly weighing the minimization of trunk pitch (i.e. segment-space goal) resulted in the ankle strategy. This could suggest that the CNS either varies cost function weights (and thus task space) with repeated exposure to perturbations

to change the strategy evoked, or that the task space remains the same, but the CNS shifts towards more inverted pendulum-like COM control.

Attention should also drawn to the very limited work on predictive simulations of standing change in support balance recovery. Two studies investigated the possible shift in postural strategy through reweighting of objective criteria. Aftab et al. [25, 26] predicted human multi-step responses using a simple inverted pendulum model and an objective function that included the COM velocity. To our knowledge, only the paper by Hemami et al. [147] tried to create a biomechanical bipedal model with multiple recovery strategies in mind. Others like the one proposed by Aftab [26] utilize a variation of the linear inverted pendulum model. Bayon et al. [48] used centroidal angular momentum (i.e., whole-body angular momentum with respect to the COM) to try and predict human balance recovery strategies. This approach draws upon principles of FIP balance discussed by Goswami [130] and Hof [152]. This approach was not as reliable in predicting human balance recovery kinematics relative to optimal full-state feedback [202, 203, 342] or feedforward optimal control methods [344].

Another point of interest in discussing the issues of motor redundancy in generating human balance recovery is the addition of constraints. Typically, in the absence of constraints (environmental, instructions, etc.), humans will often default to change in support recovery. In a laboratory environment, humans may attempt fixed-support balance until it is no longer perceived as feasible, either due to mechanical limits [154, 174, 264] or perceptual limits [74]. In many studies examining fixed support balance recovery, the verbal instructions "*... try not to take a step*" are therefore provided [27, 158, 167, 224]. In the review by Maki and McIlroy [223], the authors discussed how constraints applied to the "central set" [157], e.g. fear of falling, instructions, prior experience [57, 58, 230, 344], and/or the addition of ongoing motor activity, e.g. concurrently executing a volitional task [331], can determine the motor patterns used for balance recovery, i.e., they reduce the search space usable by the CNS for optimal control.

Before moving on, it is also of importance to consider how the CNS might be constrained in responding to a perturbation temporally. The delay observed between perturbation onset and the beginning of muscle activity (based on EMG measurements) is typically 80-100 ms [158] or up to 130 ms according to the recent experimental study of human-exoskeleton balance control by Beck et al. [50]. Note that this is only the latency between perturbation onset and the first pronounced burst of *any* muscle activity; the duration of this initial

burst in muscle activity is approximately 100 ms [223]. Based on the time delays reported by [158], it would make sense that polysynaptic reflex pathways (response times ≈ 70-90 ms [267]), which exist within the spinal cord and brainstem, would be responsible for driving these postural responses rather than the motor cortex (response times ≈ 100-200 ms [223, 267]). With that said, cortical input has been suggested to modulate late phases of fixed support recovery in addition to reactive stepping using dual-task paradigms, i.e. a simultaneous performance of a cognitive task and balance recovery [64, 166, 223, 263]. In recent studies involving forward dynamic computer simulations of human balance, this characteristic 80-100 ms time delay was applied as a constant for all muscles [344, 353].

2.3 Approaches Towards Assistive Balance Control

2.3.1 Dynamic Modeling and Simulation of Human-Exoskeleton Motion

Recently, the U.S. Food and Drug Administration began encouraging engineers and researchers in health/medicine to implement computational modelling within the medical device design process [254]. Coincidentally, simulations of human musculoskeletal biomechanics have been gaining ground over the decade as a tool for investigating topics like injury risk and human motor control; this information can then be integrated into assistive device hardware and software design. Typically, biomechanical simulations fall into one of two categories: inverse and forward dynamics. The latter is of noted interest as it facilitates construction of predictive *what-if* scenarios, which can provide insight into device control robustness, human-device interactions, etc., without putting the end-user at risk.

There are relatively few multibody dynamic models that unify lower-limb exoskeleton dynamics with human biomechanics – even fewer if forward dynamics and predictive simulations are desired. The review by Grabke et al. [131] provides a summary of Hill-type muscle actuated musculoskeletal models that have been combined with lower-limb exoskeletons. Nearly all models highlighted in [131] pertained to gait and were not predictive in nature; no models of balance recovery were noted. Forward dynamic walking models designed by Ames' research group have been used primarily to assist paraplegics; thus, there is little to no input from a simultaneous human control model [134, 138]. Research from Mombaur has recently examined dynamic simulations of human-exoskeleton push recovery

during walking. To our knowledge, only data tracking simulations have been published for the combined models as a means of analyzing exoskeleton design and input requirements [193, 295]. The human-exoskeleton sit-to-stand simulations by Bottin-Noonan and Sreenivasa [63] (driven by inverse dynamics-derived torques) involved a passive human and a hip-knee-ankle exoskeleton driven by ideal actuators, i.e., no friction and no muscle modelling. The recent work by Emmens et al. [106, 104, 105] and Bayon [48, 49] utilized an inverse dynamics model of a human-exoskeleton to derive control-oriented torques from their momentum-based control approach; however, forward dynamic simulations are of limited investigation [106]. Likewise, this model was control-oriented, and thus did not consider features like muscle torque generation and passive versus active muscle control. Furthermore, researchers tend to lump exoskeleton inertia to the human model in parallel rather than investigating non-rigid human-device couplings (*see next paragraph*) [105, 134, 226, 295].

To connect the human and exoskeleton models, the exoskeleton geometric and inertial parameters are commonly lumped into the human parameters. For a detailed description of lumping inertial parameters, see [295]. Likewise, Millard et al. [246], Manns et al. [226] and others [63, 135, 138, 295] used holonomic constraint equations to generate reaction forces that bound the systems together in the form of differential-algebraic equations. Inherently, these formulations assume perfect joint-alignment of the orthosis and are drastically sensitive to this assumption, i.e. misalignment can cause lock-up and infeasible kinematic solutions. Alternative to these rigid connections, compliant connections offer the ability to adjust the force transmission between exoskeleton and human. Sanchez-Villamanan [293] investigated the use of spring connections with stiffness coefficients derived from experimental evaluations of lower limb soft tissue compliance [75]. The authors observed variable power transmission to a modelled shank when the spring attaching the segment to the exoskeleton had low stiffness. This suggested that anatomical regions with higher soft tissue compliance would benefit from redesigns that improved connection rigidity. Duong et al. [98, 183] proposed a multibody exoskeleton model (no human) in which, during operation, interaction torques on the physical system were inferred from differences between measured end-user and device joint angles, i.e., human and device were coupled via ideal rotational spring-dampers. The basis of their design however was pairing this simple interaction torque model with a neural network to improve gait control performance. Huang et al. [160] also used a simple rotational spring-damper approach for interaction torque estimation, though the authors used this model to improve walking control performance via

reinforcement learning. Lastly, Serrancoli et al. [301] proposed a human-exoskeleton contact model with three linear and rotational spring and-damper systems (bushing elements in OpenSim); one between shank, thigh, and trunk segments. This model is basically an extension of the model proposed by Sanchez-Villamanan [293]. Notably, the authors performed motion-driven simulations in OpenSim and compared the results to measurements of interaction pressure. The model performed reasonably well in estimations of applied pelvis and thigh forces; though, had trouble with shank estimates. The authors made note that without calibration, contact forces estimated by the model were not accurate. For more information on human-exoskeleton coupling, we refer to the reader to the recent review by Scherb et al. [296].

2.3.2 Autonomous Balance Control Methods

As mentioned prior, control engineers for exoskeletons must consider whether the device behaves fully autonomously or provides human-in-charge assistance , e.g., "assist-as-needed" [46, 49, 283, 334]. We will first discuss the case of autonomous control, in which we treat the integrated human-exoskeleton system as a robotic humanoid (like we do in the case of purely humanoid robotics):

Stephens [314, 315] investigated humanoid balance through full-state feedback methods and integral control of the ZMP. The methods disseminated easily reproduced the ankle and hip FIP strategy in experiments with the robot by using nonlinear feedback regulation of the COM. A notable feature of this approach is the real-time provision of corrective ankle, knee, and hip torques. Emmens et al. [103, 105] suggested autonomous control of quiet standing and fixed-support balance recovery using proportional-derivative (PD) control of whole-body COM sway or momentum. The controller would try to lock the knees in an extended position, while scaling input ankle torques by COM sway error. These control methods draw parallels to the previously mentioned study by Winter [361] and others [253, 272] in which human balance control is framed within the inverted pendulum COM-task space. Emmens et al. [106, 103, 105] also proposed a momentum-based controller, based on the principles outlined in [130], capable of yielding input torques for the ankle, knee, and hip (the last was not used in [103]). This approach involved a constrained quadratic programming approach that would rapidly solve for joint accelerations that regulate whole-body momentum subject to constraints, e.g., kinematic limits. With that said, this controller performed worse than the COM PD controller in terms of recovery

times, i.e., the duration until the COM was brought back to rest. Lastly, in systems like those proposed and tested by Emmens et al. [103, 105] and others [109, 134, 138], high-level intent recognition is ignored; therefore, authors sometimes have participants undergo a training protocol in order to effectively and confidently use the device, especially when those individuals must rely on the device in some capacity, e.g., individuals with paraplegia [340]. These systems are also inherently limited as the user adapts and subsequently relies on the device for actuation, i.e., "slacking" [69, 102, 287, 334].

In the case that a physical or modelled humanoid requires a step(s) to prevent a fall, often due to physical constraints (e.g. limited size of support polygon, motor torque limits), additional control schemes must be implemented. As these are not of primary focus herein, we will only briefly discuss these. Often to obtain autonomous humanoid stepping that maintains upright balance, a tool to estimate step parameters is necessary, e.g. number and length of steps. Outside of ZMP-driven stepping strategies, optimal control (e.g. dynamic optimization, model predictive control, [148, 211, 259, 294]) and the N-step capture point method [279, 278] provide a means of using reduced, control-oriented models to estimate the steps parameters required by a complex biped. For example, consider the use of a linear inverted pendulum model, i.e. the COM is a point mass with a constant height maintained by a telescoping "leg", to assess the balance of a more complex biped. Necessary foot placement(s) can derived from the conditions that attenuate linear kinetic energy as time tends towards infinity [184]: this necessary foot placement is the capture point. Mathematically, these conditions represent movement along stable eigenvectors that force the inverted pendulum to move towards an equilibrium state. Frequently, researchers will make alterations to the control-oriented inverted pendulum, e.g. addition of a flywheel to mimic changes in angular momentum about the COM (trunk and arm counter-rotations) [130, 152, 278]. These modifications result in the generation of capture regions, which present feasible locations for foot-placement and hence greater robustness. Inspired by the general N-step capture points, researchers subsequently derived foot placement estimators (FPEs) [92, 245, 248, 356]. Briefly, these FPEs are similar to the one-step capture point, but include rotational kinetic energy terms, energy dissipation following step impact, and do not require the biped to be in contact with ground prior to step estimation. For example, Millard et al. [245] observed high correlations between the the actual sagittal step placements made by a human during natural gait and the bipedal foot placements estimated via FPE. Recent research into FPEs have been concerned with expanding to 3D balance control, e.g., estimation of step width and length [92, 245]. A final note, capture

point methods have been used to predict human stepping characteristics during walking and following perturbations, e.g. using model predictive control (MPC) of a linear inverted pendulum with flywheel [25, 26]. In fact, these methods draw distinct similarities to balance assessment measures designed with human biomechanics in mind, e.g. the extrapolated COM [154, 153, 174]. The extrapolated COM (XCOM) has been recently proposed in step estimation and assistive procedures for stabilizing the lateral plane of gait for those wearing lower-limb robotic exoskeletons [343, 197, 339, 348].

2.3.3 Human-In-Charge and Assist-As-Needed Methods

The nature of exoskeleton control is intrinsically different from that of humanoid robots: the control design must integrate itself within the human's motor plans. The review by Tucker et al. [334] provides an overview of the hierarchical systems typically utilized for control of exoskeletons. This hierarchy features three tiers: high, middle, and low-level. When considering how human motor control interacts with the exoskeleton control system, it is important to examine high-level control, which effectively recognizes the intent of the user (e.g. locomotion modes [334]) by processing and analyzing data measured from wearable or embedded sensors, e.g. electromyography and force transducers. Signal-based [191, 374] or model-based [98, 99, 195, 255, 320] intent recognition systems and myoneural interfaces [83] can provide a link between human and exoskeleton that allows the human to directly influence the exoskeleton's desired actions. However, as noted by Herr and Wilkenfield [149], the plasticity of the CNS can cause a "spiral of adaptations" as the user adapts to the new conditions imposed by the exoskeleton [102]; thus, the devices may also need to simultaneously adapt to the evolving user requirements. Evidently, the state of human awareness of exoskeleton dynamics and control should be taken into consideration when designing controllers and dynamic simulations of this integrated system [49, 98, 159, 191, 257, 256, 307, 372, 376].

The assist-as-needed (AAN) concept in lower-limb exoskeleton control has gained significant attention [102]. AAN control algorithms are designed to exert minimal assistance while providing precise control over the user's limbs, thereby presenting a challenging yet effective approach. Research indicates that encouraging active user participation in exoskeleton-driven physical therapy significantly enhances patient outcomes, as comprehensively reviewed by Hogan et al. [155]. Emken et al. [102] introduced a transformative perspective on the AAN concept by framing it as an optimization problem. This shift has

spurred researchers to explore methods for adapting controllers to evolving patient needs, yielding varying degrees of success [198, 217, 218].

Among AAN control strategies, joint or task-space impedance is the most straightforward. It derives exoskeleton joint torques based on the system's kinematics. This approach is widely employed in exoskeleton research because it allows for easy tuning of control parameters, known as gains, to deliver the desired level of assistance, as thoroughly reviewed by Tucker et al. [334]. For instance, in gait assistance, PD control laws track desired trajectories corresponding to specific phases (e.g., the swing phase, often selected using a finite state machine). The control gains influence the vigor with which actuators drive the joints toward these reference trajectories. AAN algorithms in walking control often iteratively adjust parameters using methods rooted in human motor learning, such as step-by-step evaluations of error. If the error during assistance remains low, the assistance parameters are reduced for the subsequent step [102]. This reduction can also be regulated using a forgetting factor [102, 217, 218], preventing over-reliance on assistance [72, 287].

Currently, there are limited instances of published AAN balance control systems specifically tailored for the stance phase or FIP configuration of lower-limb exoskeletons. One early assistive controller, put forth by Vallery [338], harnessed an AAN-based approach along with feedforward forces derived from the XCOM position [154] to guide participants back to an upright position. This was implemented through a variable speed gyroscope that could impart changes in whole-body angular momentum as necessary for balance [130]; however, its validation has primarily focused on lateral balance during treadmill walking [339]. Additionally, Rajasekaran et al. [284] proposed an AAN FIP balance method capable of utilizing either an ankle or hip strategy, or a combination of both, achieved through angle-dependent joint stiffness. Nevertheless, concerns have been raised regarding the clarity of the stability limit definition (and its derivation from the COP), the scaling of the stiffness gains as a proportion of an unspecified constant, and the true advantage of an uncoupled ankle-hip angle stability definition. Lastly, Afschrift et al. [24] recently introduced an AAN approach involving an adjustment of applied ankle torque to elicit appropriate balance recovery responses during perturbed forward walking. Notably, this method did not rely on an explicit step length/width estimator that met biped capturability requirements [348].

Chapter 3

Simulating the Biomechanics of Human Balance Recovery

In order to address the goals outlined in the current dissertation, it is necessary to build a dynamic model capable of capturing key components of FIP balance recovery in the sagittal plane. These components may include characteristic joint kinematics, shifting of the ZMP, and muscle forces/activations. To do so, a 5 degree-of-freedom (DOF) multibody dynamic model was designed. The generalized coordinates of the standing model were then adjusted post-hoc to simplify the constituent equations for any control or observation-oriented stance models (see Chapter 6). Computationally efficient muscle models were also included to imitate the limitations of human muscle physiology within simulations without introducing complex factors like musculotendon geometry and mathematical discontinuities featured in many other musculoskeletal models [247, 327]. All models disseminated herein were designed in MapleSim (MapleSoft, Canada) as the constituent symbolic equations and their derivatives could be optimized and exported as a script in one of many languages, e.g., Python, MATLAB, C++, etc. Symbolic equations can allow for rapid dynamic simulations and improved optimal control performance [219]. The current section provides greater detail on the development of the standing human biomechanical model and predictive simulations of fixed-support balance recovery.

3.1 Multibody System Dynamic Model

The 5-DOF sagittal plane model of human upright stance (displayed in Fig. 3.1) consisted of the following 11 rigid bodies designated according to anthropometric definitions provided in the literature: right and left thigh, shank, foot, upper arm, and forearm; lumped trunk, head and pelvis. It was assumed that the pelvis, trunk, head and arms were rigidly welded together. Note that the anthropometrics outlined in de Leva [90] and Winter [360] were used to define the inertial and geometric properties for each body other than the feet; these rigid bodies were rather based on the definitions by Ezati [108]. Briefly, these resources provide scaling of dynamic parameters for each individual segment according to human height, weight, and sex. Parameters include segment length (distance between proximal to distal joint locations), mass, rigid body COM position in addition to moments of inertia (MOI) relative to the COM. In all cases, rigid body parameters were scaled according to the height and weight of the human (or end-user) of interest (see Table A.1 and Table A.2 in Appendix A for an example of parameters values for a young adult male; height = 1.80 m, weight = 75 kg).

Segments were connected using revolute joints to mimic the DOF provided by the bilateral ankle, knee, hip, shoulder and elbow joints. The feet were rigidly fixed to the support-surface with bilateral symmetry akin to a human quietly standing with their feet in the same sagittal position. Note that it is common for the upper limbs to be bound to the users trunk in many experiments regarding human balance control (either via manual resistance from the individual or through separate bindings; [50, 243, 344]). We will briefly explore the use of upper limb movements in balancing later in Chapter 3.2 and 3.3.

When presented with the topology described above, the graph theoretic approach used by MapleSim generates a system with generalized coordinates

$$\mathbf{q}_{\mathrm{h}}(t) = \{\theta_{\mathrm{hip}}(t), \theta_{\mathrm{knee}}(t), \theta_{\mathrm{ankle}}(t), \theta_{\mathrm{shldr}}(t), \theta_{\mathrm{elbow}}(t)\}^{\mathrm{T}} \tag{3.1}$$

where $\mathbf{q}_{\mathrm{h}}(t) \in \mathcal{Q}_{\mathrm{h}}$ and $\mathcal{Q}_{\mathrm{h}} \subseteq \mathbb{R}^5$. Each θ_i listed in (3.1) corresponds to a rotation at each of the lower-limb joints in the sagittal plane, i.e., flexion/extension. Note that generalized joint velocities exist within the tangent space to $\mathcal{Q}_{\mathrm{h}}$ at a given $\mathbf{q}_{\mathrm{h}}(t)$, i.e., $\dot{\mathbf{q}}_{\mathrm{h}}|_{\mathbf{q}_{\mathrm{h}}} \in T_{\mathbf{q}}\mathcal{Q}_{\mathrm{h}}$. Throughout this document, θ will consistently refer to joint coordinates whereas uses of ϕ will relate to the angle of a given segment with respect to the inertial frame. This idea will be revisited in Chapter 4.2.

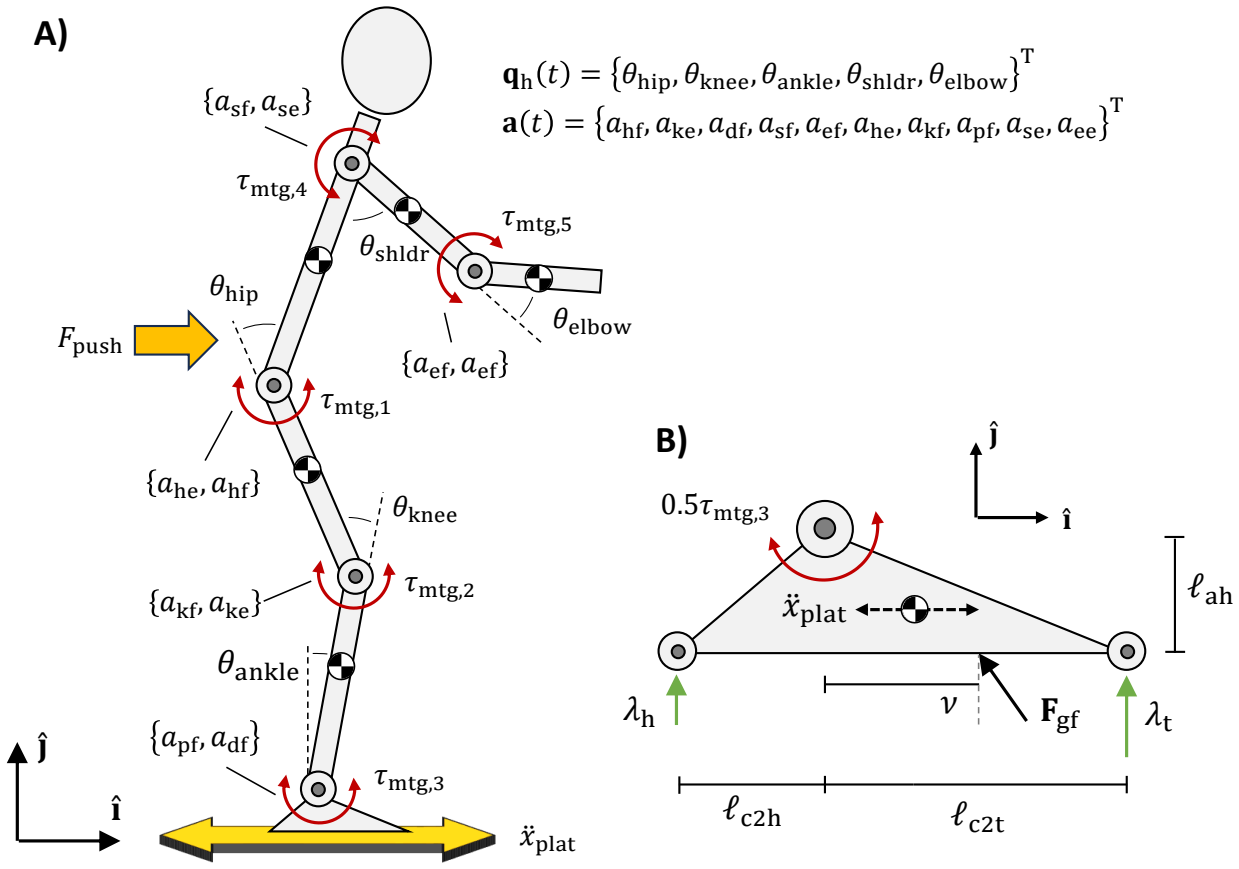


Figure 3.1: **A**) Schematic of the planar MTG-driven model; balance recovery was evoked via unexpected fore aft accelerations of the support surface ($\ddot{x}_{\mathrm{plat}}$) or a horizontal push to the pelvis F_{push}. **B**) Model of the base of support (for a single leg/foot) used to derive the toe/heel constraint forces that dictated the domain of feasibility for feet-in-place balance. Symbols include the following: $a_{*\mathrm{e/f}}$, extensor/flexor muscle torque activation; θ, joint angle; τ_{mtg}, net joint muscle torque produced by activations; F_{push} and $\ddot{x}_{\mathrm{plat}}$, horizontal push force applied to pelvis and support-surface acceleration respectively; λ_{h} and λ_{t}, the normal ground reaction force $\mathbf{F}_{\mathrm{gf}} \cdot \hat{\mathrm{j}}$ resolved at two contact ponts (heel and toe); and ν, the horizontal position of the zero moment point (ZMP).

The dynamics of the standing human model can be represented by the following system of ordinary differential equations (ODEs):

$$\mathbf{M}_{\mathrm{h}}(\mathbf{q}_{\mathrm{h}}(t))\ddot{\mathbf{q}}_{\mathrm{h}} = \mathbf{\Gamma}(\mathbf{q}_{\mathrm{h}}(t), \dot{\mathbf{q}}_{\mathrm{h}}) + \boldsymbol{\tau}_{\mathrm{mtg}}(\mathbf{q}_{\mathrm{h}}(t), \dot{\mathbf{q}}_{\mathrm{h}}, \mathbf{a}(t)) + \mathbf{P}(\mathbf{q}_{\mathrm{h}}(t), F_{\mathrm{push}}(t), \ddot{x}_{\mathrm{plat}}) \tag{3.2}$$

where $\mathbf{M}_{\mathrm{h}} \in \mathbb{R}^{5\times5}$ is the symmetric configuration-dependent inertia matrix and $\mathbf{\Gamma} : \mathcal{Q}_{\mathrm{h}} \times T_{\mathbf{q}}\mathcal{Q}_{\mathrm{h}} \to \mathbb{R}^{5\times1}$ is a function that maps generalized positions and velocities to gravitational potential torques/forces and fictitious centrifugal/coriolis torques/forces. Disturbances to upright balance were induced through the use of time-varying anteroposterior (AP) accelerations of the support surface $\ddot{x}_{\mathrm{plat}}$, i.e., accelerations of the base of support (BOS), and/or an AP push force $F_{\mathrm{push}}(t)$ that is applied just superior ($\approx$ 10 cm) to the hip joint center (i.e., the pelvis, see Fig. 3.1A). The former mimics the experimental protocols implemented by Maki and McIlroy [222] as well as the perturbation modality within a growing number of labs [50, 158, 166, 353, 357, 358]. These translations can be highly regulated through robotic controls such that the size of perturbation applied to the upright human is repeatable within experimental testing. The latter term, i.e., F_{push}, replicates the perturbation modality employed in recent human-exoskeleton balance studies [103, 105]; a human tester would apply a forward or backward push to the participant's pelvis using a device containing a force transducer that allowed the authors to reasonably reproduce the same push each time. All modeled external disturbances were mapped to the joint torque space through $\mathbf{P} : \mathcal{Q}_{\mathrm{h}} \times \mathbb{R} \times \mathbb{R} \to \mathbb{R}^{5\times1}$.

The human model was actuated actively and passively through the use of p muscle torque generators (MTGs) represented by $\boldsymbol{\tau}_{\mathrm{mtg}} \in \mathbb{R}^{5\times1}$ [244]. Among other things, using MTGs allowed us to include biofidelic actuation in dynamic simulations without requiring definition of complex musculoskeletal geometry [165]. The result was a more computationally efficient model [244]. For the current system, there are two MTGs for each joint coordinate: one to deliver flexion torques, and the other to extend the joint, i.e., $p = 10$. The resulting equation for $\boldsymbol{\tau}_{\mathrm{mtg}} : \mathcal{Q}_{\mathrm{h}} \times T_{\mathbf{q}}\mathcal{Q}_{\mathrm{h}} \times \mathcal{A}^2 \to \mathbb{R}^{5\times1}$, as implemented in Equation (3.2), i.e., the muscle torques at each joint in the model, was thus

$$\begin{aligned}\boldsymbol{\tau}_{\mathrm{mtg}}(\mathbf{q}_{\mathrm{h}}(t), \dot{\mathbf{q}}_{\mathrm{h}}, \mathbf{a}(t)) = {} & 2\mathbf{a}^{\mathrm{flex}}(t)\boldsymbol{\tau}_{\mathrm{iso}}^{\mathrm{flex}}\boldsymbol{\tau}_{\theta}(\mathbf{q}_{\mathrm{h}}; \bar{\mathbf{p}}_{\theta}^{\mathrm{flex}})\boldsymbol{\tau}_{\omega}(\dot{\mathbf{q}}_{\mathrm{h}}; \bar{\mathbf{p}}_{\omega}^{\mathrm{flex}}) \\ & + 2\mathbf{a}^{\mathrm{ext}}(t)\boldsymbol{\tau}_{\mathrm{iso}}^{\mathrm{ext}}\boldsymbol{\tau}_{\theta}(\mathbf{q}_{\mathrm{h}}; \bar{\mathbf{p}}_{\theta}^{\mathrm{ext}})\boldsymbol{\tau}_{\omega}(\dot{\mathbf{q}}_{\mathrm{h}}; \bar{\mathbf{p}}_{\omega}^{\mathrm{ext}}) + 2\boldsymbol{\tau}_{\mathrm{psv}}(\mathbf{q}_{\mathrm{h}}, \dot{\mathbf{q}}_{\mathrm{h}}; \bar{\mathbf{p}}_{\mathrm{psv}})\end{aligned} \tag{3.3}$$

or alternatively,

$$\boldsymbol{\tau}_{\mathrm{mtg}}(\mathbf{q}_{\mathrm{h}}(t), \dot{\mathbf{q}}_{\mathrm{h}}, \mathbf{a}(t)) = \boldsymbol{\tau}_{\mathrm{mtg}}^{\mathrm{cns}}(\mathbf{a}, \mathbf{q}_{\mathrm{h}}, \dot{\mathbf{q}}_{\mathrm{h}}; \cdot) + 2\boldsymbol{\tau}_{\mathrm{psv}}(\mathbf{q}_{\mathrm{h}}, \dot{\mathbf{q}}_{\mathrm{h}}; \bar{\mathbf{p}}_{\mathrm{psv}}) \tag{3.4}$$

where $\boldsymbol{\tau}^{\text{cns}}_{\text{mtg}}(\cdot)$ is used to simply identify the torques resulting from an active neural drive and differentiate them with respect to their passive counterpart. Note that the scaling of terms in Equation (3.3) and (3.4) by 2 was due to the assumption of bilateral symmetry in the standing balance model, i.e., right and left groups of MTGs share the same activation profiles [344]. In Equation (3.4), $\mathbf{a}(t) = [\mathbf{a}^{\text{flex}}, \mathbf{a}^{\text{ext}}]^\intercal$ is the concatenation of the flexor $\mathbf{a}^{\text{flex}} \in \mathcal{A}$ and extensor activations $\mathbf{a}^{\text{ext}} \in \mathcal{A}$ ($\mathcal{A} \subset \{\mathbb{R}^5 \,|\, a_i \in [0,1]\}$). We also introduce isometric torque parameter vectors $\boldsymbol{\tau}^{\text{flex}}_{\text{iso}} = [\tau^{\text{flex}}_{\text{iso},1}, \ldots, \tau^{\text{flex}}_{\text{iso},5}]^\intercal$ and $\boldsymbol{\tau}^{\text{ext}}_{\text{iso}} = [\tau^{\text{ext}}_{\text{iso},1}, \ldots, \tau^{\text{ext}}_{\text{iso},5}]^\intercal$ that determine peak MTG output at zero joint-velocity and the optimal joint angle. The former contains maximal isometric torques for the hip flexors, knee extensors, ankle dorsiflexors, shoulder flexors, and elbow flexors; the latter contains values for the hip extensors, knee flexors, ankle plantarflexors, shoulder extensors, and elbow extensors. We refer the reader to Appendix B as well as our review paper in the journal Multibody System Dynamics (Inkol et al. [165]) for background and rationale on why MTGs were implemented in the current dissertation [165]. Appendices C and D discuss the explicit functions used for active joint angle/velocity scaling and passive torque generation in the MTGs, including a smoothing approach designed to guarantee C^2 continuity for optimal control [244].

As mentioned above, the output torque of each MTG was amplified via a time-varying activation variable $a_i(t) \in [0,1], \forall i = 1 \ldots p$ such that $\tau_{\text{mtg},i}(\cdot, 0) = 0$ Nm. This activation variable can be thought of as the state of cross-bridge formation and tension generation triggered by some central stimulus or excitation $u(t) \in [0,1]$. If we assume that any given MTG has identical activation dynamics to that of an individual muscle, then we can reasonably model changes in $a(t)$ as a first-order system like in [327, 328]:

$$\dot{a} = \begin{cases} \frac{u-a}{t_{\text{act}}(0.5+1.5a)} & u > a \\ \frac{u-a(0.5+1.5a)}{t_{\text{deact}}} & u \leq a \end{cases} \tag{3.5}$$

where t_{act} and t_{deact} are the activation and deactivation time constants that define how quickly an MTGs output changes in response to an increase and decrease of u relative to a. Typically, the time constants are set as $t_{\text{act}} = 10$ ms and $t_{\text{deact}} = 40$ ms [88, 327].

As we assumed bilateral symmetry in our model of human upright posture, a total of $p = 10$ MTGs were implemented to drive the human: one flexor and extensor per element of $\mathbf{q}_{\text{h}}$ (see Fig. 5.7). As mentioned prior, researchers often tend to rely on optimal control methods to generate predictive simulations of human movement using a given musculoskeletal dynamic model. Many fast and reliable optimal control methods such as interior-point

methods utilize derivatives of the problem's constituent equations with respect to model inputs, states, etc [219]. Therefore, if we were to use (3.5) within the ensuing state-space dynamic equations, we may encounter problems related to the discontinuity at $u(t) = a(t)$, especially if we wish to use symbolic model equations within the optimization. To address this problem, De Groote [88] recently suggested using smoothed activation dynamics $\breve{\dot{a}}$ instead,

$$\begin{aligned}\breve{\dot{a}} = &(u-a)(\beth(u-a;k_a)+0.5)\cdot t_{\text{act}}^{-1}(0.5+1.5a)^{-1} \\ &+(u-a)(0.5-\beth(u-a;k_a))\cdot(0.5+1.5a)t_{\text{deact}}^{-1}\end{aligned} \tag{3.6}$$

where

$$\beth(\delta;k_a) = 0.5\tanh(k_a\delta) \tag{3.7}$$

is a smoothing function that transitions between activated and deactivated states without requiring an explicit piece-wise definition. The stiffness of this transition is controlled by variable $k_a \in \{\mathbb{R} \,|\, k_a > 0\}$ ($k_a = 0.1$ in [88]) The hyperbolic tangent function is used within this smooth approximation under the assumption that

$$\lim_{k_a\to\infty}\tanh(k_a\delta) = \begin{cases}1 & \delta \geq 0\\ -1 & \delta < 0\end{cases} \tag{3.8}$$

which intrinsically implies

$$\lim_{k_a\to\infty}\breve{\dot{a}} = \dot{a} \tag{3.9}$$

This notion of smoothed approximations is important for the current dissertation in the context of generating symbolic derivatives for optimal control of human-exoskeleton systems, i.e., the necessary optimal control derivatives are bound, always exist, and functions are Lipschitz continuous. Note that moving forward, the diacritic notation $\breve{x}$ will refer to the smoothed approximation of x.

3.2 Assessing the Boundaries of Upright Stance

Domain of Feasibility for Balanced Posture

To quantify the ability of a biped in staying upright and stable, we must identify some subset of $\mathcal{Q}_{\text{h}}$ and its tangent space in which the upright human will always remain balanced.

We will refer to this space as the domain of feasibility for FIP balance. We note that this definition does not imply asymptotic or marginal stability of the nonlinear system, rather providing a binary "fall" or "no-fall" classification. Classically, in analyses and simulations of FIP balance, we can define the domain of feasibility according to the assumptions of the model, i.e. the foot rigid body is flat against the ground and linearly/rotationally static [154, 169, 264] (see Fig. 3.1B). Mathematically, we can say that the biped will remain balanced over some infinite prediction horizon so long as the following conditions are met [264]:

$$\left\{\begin{array}{c} -\mathbf{F}_{\mathrm{gf}} \cdot \hat{\mathbf{j}} \\ \nu(\mathbf{q}_{\mathrm{h}}, \dot{\mathbf{q}}_{\mathrm{h}}, \ddot{\mathbf{q}}_{\mathrm{h}}, \boldsymbol{\tau}_{\mathrm{mtg}}, \ddot{x}_{\mathrm{plat}}) - \ell_{\mathrm{c2t}} \\ -\ell_{\mathrm{c2h}} - \nu(\mathbf{q}_{\mathrm{h}}, \dot{\mathbf{q}}_{\mathrm{h}}, \ddot{\mathbf{q}}_{\mathrm{h}}, \boldsymbol{\tau}_{\mathrm{mtg}}, \ddot{x}_{\mathrm{plat}}) \\ |\mathbf{F}_{\mathrm{gf}} \cdot \hat{\mathbf{i}}| - \mu_{\mathrm{gf}} |\mathbf{F}_{\mathrm{gf}} \cdot \hat{\mathbf{j}}| \end{array}\right\} = \boldsymbol{\Omega}(\cdot) < \mathbf{0}, \quad \forall\, t \in [0, \infty) \tag{3.10}$$

where term 1 is the unilateral contact constraint (ground reaction force cannot pull on foot), terms 2 and 3 relate to maintaining the ZMP within the the support polygon (BOS boundaries) [346], and term 4 is the requirement for the foot to **not** slide against the ground, i.e., friction cone constraint [133]. In Equation (3.10), ℓ_{c2h} and ℓ_{c2t} are the horizontal distance between the foot COM and toe/heel respectively, i.e. the boundaries of the BOS/support polygon.

Briefly, we expand on Equation (3.10). The variable $\mathbf{F}_{\mathrm{gf}} \in \mathbb{R}^3$ is the 3D reaction force between foot and ground evaluated through top-down Newton recursion over the links within the standing model's open kinematic chain,

$$\mathbf{F}_{\mathrm{gf}} = \sum_{i=1}^{n_{\mathrm{rb}}} m_i(-\mathbf{g} + \ddot{\mathbf{r}}_{\mathrm{rcm},i}(\mathbf{q}_{\mathrm{h}})) \tag{3.11}$$

where n_{rb} is the number of rigid bodies in the system, $\mathbf{r}_{\mathrm{rcm},i} \in \mathbb{R}^3$ is the i^{th} rigid body's COM, and $\mathbf{g} = -g \cdot \hat{\mathbf{j}}$ is the acceleration due to gravity. The variable $\nu \in \mathbb{R}$ in (3.10) is the anteroposterior (AP) location of the ZMP (with respect to the ankle center), i.e., assuming a rotationally static BOS,

$$\nu(\cdot) = \frac{-\tau_{\mathrm{mtg},3} - \ell_{\mathrm{ah}} \mathbf{F}_{\mathrm{gf}} \cdot \hat{\mathbf{i}} + m_{\mathrm{ft}}(\ell_{\mathrm{fcx}} g - \ell_{\mathrm{fcy}} \ddot{x}_{\mathrm{plat}})}{\mathbf{F}_{\mathrm{gf}} \cdot \hat{\mathbf{j}}} \tag{3.12}$$

where ℓ_{ah} is the height of the ankle above the ground and m_{ft} is the foot mass, while ℓ_{fcx} and ℓ_{fcy} are the horizontal and vertical position of the foot segment COM with respect

to the ankle (in the foot-fixed frame). The notation $\tau_{\text{mtg},3}$ indicates the 3$^{\text{rd}}$ element of the MTG vector, i.e., the bilateral ankle muscle torque. Note that Equation (3.11) can rewritten in terms of the whole-body COM kinematics, i.e.,

$$\mathbf{r}_{\text{cm}} = \sum_{i=1}^{n_{\text{rb}}} \frac{m_i}{(\sum_{j=1}^{n_{\text{rb}}} m_j)} \mathbf{r}_{\text{rcm},i}(\mathbf{q}_{\text{h}}) \tag{3.13}$$

$$\mathbf{F}_{\text{gf}} = (\ddot{\mathbf{r}}_{\text{cm}} - \mathbf{g}) \sum_{i=1}^{n_{\text{rb}}} m_i, \quad \ddot{\mathbf{r}}_{\text{cm}} \equiv \ddot{\mathbf{r}}_{\text{cm}}(\mathbf{q}_{\text{h}}, \dot{\mathbf{q}}_{\text{h}}, \ddot{\mathbf{q}}_{\text{h}}) \tag{3.14}$$

where $\mathbf{r}_{\text{cm}} \in \mathbb{R}^3$ is the sagittal position of the whole-body COM; $\dot{\mathbf{r}}_{\text{cm}}$ and $\ddot{\mathbf{r}}_{\text{cm}}$ are the velocity and acceleration respectively.

For the sake of computational efficiency, the dimension of Equation (3.10) was reduced by assuming the foot was hinged to the support surface at two anatomical locations: i) toes/head of metatarsals and ii) the heel/calcaneus. This approach is conceptually similar to previous biomechanical simulations of standing balance in which heel-raise was permitted using a torsional spring [78], though this was not a feature studied herein. From the ZMP equations, the following linear system was reached, which assumes that the BOS and inertial frame are parallel:

$$\begin{bmatrix} \ell_{\text{c2t}} & -\ell_{\text{c2h}} & \ell_{\text{ah}} \\ 1 & 1 & 0 \\ 0 & 0 & 1 \end{bmatrix} \begin{Bmatrix} \lambda_{\text{t}} \\ \lambda_{\text{h}} \\ \lambda_{\text{fr}} \end{Bmatrix} = \begin{Bmatrix} -\tau_{\text{mtg},3} + m_{\text{ft}}(\ell_{\text{fcx}} g - \ell_{\text{fcy}} \ddot{x}_{\text{plat}}) \\ \mathbf{F}_{\text{gf}} \cdot \hat{\mathbf{j}} \\ \mathbf{F}_{\text{gf}} \cdot \hat{\mathbf{i}} \end{Bmatrix} \tag{3.15}$$

so that now we can simply rewrite the domain of feasibility as

$$\boldsymbol{\Omega}(\cdot) = \begin{Bmatrix} -\lambda_{\text{t}} \\ -\lambda_{\text{h}} \\ |\lambda_{\text{fr}}| - \mu_{\text{gf}} |\lambda_{\text{t}} + \lambda_{\text{h}}| \end{Bmatrix} < \mathbf{0}, \quad \forall\, t \in [0, \infty) \tag{3.16}$$

where $\lambda_{\text{t}} \in \mathbb{R}$ is the vertical force applied to the toe marker, $\lambda_{\text{h}} \in \mathbb{R}$ is the vertical force applied to the heel marker, and $\lambda_{\text{fr}} \in \mathbb{R}$ is the friction force acting on the plantar surface of the foot. One of λ_{t} or λ_{h} becoming negative would indicate rotation of the foot about the opposing marker, i.e., the ZMP exiting the support polygon. Both variables becoming negative would indicate that the model has become fully airborne, which defies the condition of stability according to Equation (3.10). For example, when $\lambda_{\text{h}} < 0$, the

model should in theory switch to a system mode in which the heel is raised. In this mode, we could instead write the domain of feasibility as

$$\boldsymbol{\Omega}(\cdot) = \left\{ \begin{array}{c} -\mathbf{r}_{\text{heel}} \cdot \hat{\mathrm{j}} \\ -\lambda_{\text{t}} \\ |\lambda_{\text{fr}}| - \mu_{\text{gf}}|\lambda_{\text{t}}| \end{array} \right\} < \mathbf{0}, \quad \forall\, t \in [0, \infty) \tag{3.17}$$

where $\mathbf{r}_{\text{heel}}$ introduces a collision constraint between the heel and ground (assuming level ground). The transition between the two modes is also of interest: a parameter free approach uses impulse-momentum theory to discretely switch the system's state to the new mode [133]. This notion is the basis of hybrid dynamical systems and can be used to explore and simulate/control balance recovery beyond the FIP strategies [134, 135, 138, 294, 295].

3.2.1 Assessing the Feasible Stability Region of FIP Balance

The following section contains content related to the paper "Using Dynamic Simulations to Estimate the Feasible Stability Region of Feet-In-Place Balance Recovery for Lower-Limb Exoskeleton Users" published/presented at the 2022 9th IEEE RAS/EMBS International Conference for Biomedical Robotics and Biomechatronics (Inkol and McPhee [172]).

An *extensively validated* method of analyzing the balancing capabilities of a human in balance recovery is the feasible stability region (FSR) [175, 264, 370]. For balance in the sagittal plane, the concept states that so long as the *horizontal* position and velocity of the whole-body COM are within the "stable" region of COM phase-space, the biped will not fall. These boundaries are intrinsically dependent on the system dynamics and are closely related to concepts like capturability [278] and foot placement estimation [26, 245]: they characterize the domain of feasibility for balanced posture using COM kinematics. For the readers' interest, the derivation of an analytical solution for the FSR boundaries of an inverted pendulum are shown in Appendix E. This derivation is often helpful in conceptualizing the FSR. For more complex models of human stance, we must rely on computer simulations to inform us of the theoretical boundaries of stability and how they may be affected by certain model parameters. For example, Pai and Patton [264] evaluated the boundaries for a nonlinear inverted pendulum model using forward dynamics simulations. Yang et al. [369, 370] continued this work by expanding their examinations of postural stability using computer simulations of a walking model with one foot on the

ground (single-support). However, rather than introducing constraints into their optimization routines, the authors of these most recent simulations have relied on careful tuning of cost functions containing a large number of terms within a direct shooting-formulated optimal control problem.

In the current dissertation, the FSR for the human-only model balancing with FIP was determined through a computationally-efficient symbolic direct collocation optimal control scheme [56]. Briefly, direct collocation involves parameterization of both the continuous state and control trajectories, i.e.,

$$\mathbf{x}_{\mathrm{h}}(t) = \begin{Bmatrix} \mathbf{q}_{\mathrm{h}} \\ \dot{\mathbf{q}}_{\mathrm{h}} \\ \check{\mathbf{a}} \end{Bmatrix}, \quad \mathbf{u}_{\mathrm{h}}(t) = \begin{Bmatrix} \mathbf{u} \\ \ddot{\mathbf{q}}_{\mathrm{h}} \\ \check{\dot{\mathbf{a}}} \end{Bmatrix} \tag{3.18}$$

into discrete arrays or sequences consisting of n nodes or knot points that span the entire prediction horizon $[t_0, t_f]$: $\{\mathbf{x}_{\mathrm{h}}[k]\}_{k=1}^{n} = \mathcal{X} = \{\mathbf{x}_{\mathrm{h}}[1], \mathbf{x}_{\mathrm{h}}[2], ..., \mathbf{x}_{\mathrm{h}}[n]\}^{\intercal}$; $\{\mathbf{u}_{\mathrm{h}}[k]\}_{k=1}^{n} = \mathcal{U} = \{\mathbf{u}_{\mathrm{h}}[1], \mathbf{u}_{\mathrm{h}}[2], ..., \mathbf{u}_{\mathrm{h}}[n]\}^{\intercal}$. Note that the notation $\mathbf{x}[k]$ indicates a continuous function being sampled at the k^{th} instance with the notation $\mathbf{x}[k] = \mathbf{x}(t_0 + (i-1)\Delta t)$ where $\Delta t = (t_f - t_0)(n-1)^{-1}$. Note that we adopted the state-space formulation discussed in the recent article on biomechanical simulations by Puchaud et al. [281]. Specifically, we include the accelerations and derivative of MTG activations in the control variable as controls to be identified alongside the MTG inputs $\mathbf{u} \in \mathbb{R}^p$ $(p = 10)$, with the intent of yielding smooth, human-like motions in simulations.

The reformulation of the FSR optimal control problem through direct collocation was important; numerous simulations were required to estimate the FIP FSR for a single set of parameter values. As direct collocation involves parameterization of both the state and control trajectories as decision variables (not just the controls), the resulting nonlinear programming (NLP) problems are typically large-scale but sparse when compared to direct shooting [56]. The sparsity of the derivatives in the direct collocation formulation allow for simple symbolic formulations to be applied, whereas direct shooting has complex derivatives that contain propagated states. Not only that, but direct collocation has been shown to outperform direct shooting optimal control methods in predictive simulations of human biomechanics [276], though it performs similarly to multiple shooting methods [280].

The discrete finite-horizon formulation of the infinite-horizon optimal control problem

that solves for the anterior FSR boundary was stated mathematically as,

$$\underset{x,u}{\text{argmin}} \{-\dot{\mathbf{r}}_{\text{cm}}[1] \cdot \hat{\mathbf{i}}\} \tag{3.19}$$

subject to

$$\mathbf{h}_{\text{init}}(\mathbf{x}_{\text{h}}[1], \mathbf{u}_{\text{h}}[1]; \mathbf{q}_{\text{max},0}, \mathbf{q}_{\text{min},0}) \leq \mathbf{0} \tag{3.20}$$

$$\mathbf{g}_{\text{init}}(\mathbf{x}_{\text{h}}[1], \mathbf{u}_{\text{h}}[1]; r_0) = \mathbf{0} \tag{3.21}$$

$$\mathbf{h}_{\text{term}}(\mathbf{x}_{\text{h}}[n], \mathbf{u}_{\text{h}}[n]) \leq \mathbf{0} \tag{3.22}$$

$$\mathbf{g}_{\text{term}}(\mathbf{x}_{\text{h}}[n], \mathbf{u}_{\text{h}}[n] = \mathbf{0} \tag{3.23}$$

$$\mathbf{g}_{\text{coll}}(\mathbf{x}_{\text{h}}[k], \mathbf{u}_{\text{h}}[k], \mathbf{x}_{\text{h}}[k+1], \mathbf{u}_{\text{h}}[k+1]) \leq \mathbf{0} \quad \forall\, k = 1 \ldots n-1 \tag{3.24}$$

$$\mathbf{h}_{\text{fsr}}(\mathbf{x}_{\text{h}}[k], \mathbf{u}_{\text{h}}[k]) \leq \mathbf{0} \quad \forall\, k = 1 \ldots n \tag{3.25}$$

$$\mathbf{g}_{\text{fsr}}(\mathbf{x}_{\text{h}}[k], \mathbf{u}_{\text{h}}[k] = \mathbf{0} \quad \forall\, k = 1 \ldots n \tag{3.26}$$

$$\begin{Bmatrix} \mathbf{x}_{\text{min}} \\ \mathbf{u}_{\text{min}} \end{Bmatrix} \leq \begin{Bmatrix} \mathbf{x}_{\text{h}}[k] \\ \mathbf{u}_{\text{h}}[k] \end{Bmatrix} \leq \begin{Bmatrix} \mathbf{x}_{\text{max}} \\ \mathbf{u}_{\text{max}} \end{Bmatrix} \quad \forall\, k = 1 \ldots n \tag{3.27}$$

which looks to identify for the maximum initial COM velocity $\dot{\mathbf{r}}_{\text{cm}}$ in the forward direction $\hat{\mathbf{i}}$ that can be terminated given a set initial horizontal COM position r_0. By solving this problem for the set of COM positions normalized to foot length $\{0, 0.25, ..., 1.00\}$ (0 = COM over toe, 1 = COM over heel), like in [174, 175, 370, 369], we could establish the system's FSR boundaries for when the COM is within the base of support. The prediction horizon was set to 1.5 seconds based on the simulations and observations by [344] and contains 61 nodes ($\Delta t = 25$ ms). Over the prediction horizon, the state was assumed to be a piecewise quadratic spline between states at collocation points (trapezoidal method). Box constraints in (3.27) restricted joint motion to reasonable anatomic values as discussed within the literature [244, 262] in addition to MTG activations to the $[0, 1]$ domain.

Boundary constraints on the solution to the underlying continuous ODEs were enforced through initial and terminal constraint equations (3.20), (3.21), (3.22), (3.23). Briefly, these equations provided the NLP solver a degree of leniency in how the human was configured at the first node, i.e., the initial inequality constraint

$$\mathbf{h}_{\text{init}}(\mathbf{x}_{\text{h}}, \mathbf{u}_{\text{h}}) = \begin{Bmatrix} \mathbf{q}_{\text{h}} - \mathbf{q}_{\text{max},0} \\ \mathbf{q}_{\text{min},0} - \mathbf{q}_{\text{h}} \\ \dot{\mathbf{q}}_{\text{h}} - \boldsymbol{\omega}_{\text{max},0} \\ \boldsymbol{\omega}_{\text{min},0} - \dot{\mathbf{q}}_{\text{h}} \end{Bmatrix} \tag{3.28}$$

where $\mathbf{q}_{\text{max},0}$ and $\mathbf{q}_{\text{min},0}$ are the maximum and minimum initial joint angles; $\boldsymbol{\omega}_{\text{max},0}$ and $\boldsymbol{\omega}_{\text{min},0}$ are maximum and minimum initial velocities. In nearly all simulation experiments conducted for the human FSR estimation (excluding the supplementary experiment in Appendix F.1), the initial velocity boundaries were set so that the initial COM velocity could only be altered through changes in the initial ankle velocity. In a given simulation, this approach limited how the COM could be perturbed at the onset of balance recovery such that we obtained more conservative estimates of the FSR. The ankle joint velocity was selected based on the rationale

$$\left|\frac{\partial \dot{\mathbf{r}}_{\text{cm}} \cdot \hat{\imath}}{\partial \omega_{\text{ankle}}}\right| > \max\left\{\left|\frac{\partial \dot{\mathbf{r}}_{\text{cm}} \cdot \hat{\imath}}{\partial \omega_{\text{hip}}}\right|, \left|\frac{\partial \dot{\mathbf{r}}_{\text{cm}} \cdot \hat{\imath}}{\partial \omega_{\text{knee}}}\right|, \left|\frac{\partial \dot{\mathbf{r}}_{\text{cm}} \cdot \hat{\imath}}{\partial \omega_{\text{shldr}}}\right|, \left|\frac{\partial \dot{\mathbf{r}}_{\text{cm}} \cdot \hat{\imath}}{\partial \omega_{\text{elbow}}}\right|\right\}. \tag{3.29}$$

The initial equality constraint in Equation (3.21) was defined as

$$\mathbf{g}_{\text{init}}(\mathbf{x}_{\text{h}}, \mathbf{u}_{\text{h}}) = \mathbf{r}_{\text{cm}} \cdot \hat{\imath} - r_0 \tag{3.30}$$

which brought the initial COM to a strict desired position r_0, i.e., the COM position for which we wish to evaluate the FSR boundary. Terminal constraints in Equations (3.22) and (3.23) were defined to bring the model to a halt at the final node in the prediction horizon ($t = t_f$ or $k = n$) [77, 78, 175, 264, 344]:

$$\mathbf{h}_{\text{term}}(\mathbf{x}_{\text{h}}, \mathbf{u}_{\text{h}}) = \begin{Bmatrix} \mathbf{r}_{\text{cm}} \cdot \hat{\imath} - \ell_{\text{c2t}} \\ -\ell_{\text{c2h}} - \mathbf{r}_{\text{cm}} \cdot \hat{\imath} \\ \phi_{\text{tr}} - \phi_{\text{max,f}} \\ \phi_{\text{min,f}} - \phi_{\text{tr}} \\ \dot{\phi}_{\text{tr}} - \dot{\phi}_{\text{max,f}} \\ \dot{\phi}_{\text{min,f}} - \dot{\phi}_{\text{tr}} \end{Bmatrix} \tag{3.31}$$

$$\mathbf{g}_{\text{term}}(\mathbf{x}_{\text{h}}, \mathbf{u}_{\text{h}}) = \begin{Bmatrix} \dot{\mathbf{r}}_{\text{cm}} \cdot \hat{\imath} \\ \ddot{\mathbf{r}}_{\text{cm}} \cdot \hat{\imath} \end{Bmatrix} \tag{3.32}$$

To summarize these equations, at t_f, the horizontal COM position was restricted to be within the base of support boundaries marked by the heels at ℓ_{c2h} and head of metatarsals at ℓ_{c2t} (3.31), while its velocity and acceleration were to be 0 (3.32). At t_f ($k = n$), according to Equation (3.31), the trunk was also to be upright and motionless (according to trunk segment angle ϕ_{tr} and velocity $\dot{\phi}_{\text{tr}}$) suggesting a return to quiet stance as observed in human experiments [175, 344].

Equation (3.24) involved numerically solving the system of ODEs that described human standing motion via trapezoidal collocation:

$$\mathbf{g}_{\text{coll}} = \mathbf{x}_{\text{h}}[k+1] - \mathbf{x}_{\text{h}}[k] - \frac{\Delta t}{2}(\mathbf{f}_{\text{h}}[k] + \mathbf{f}_{\text{h}}[k+1]) = \mathbf{0} \tag{3.33}$$

where

$$\mathbf{f}_{\text{h}}[k] \equiv \begin{Bmatrix} \dot{\mathbf{q}}_{\text{h}}[k] \\ \ddot{\mathbf{q}}_{\text{h}}[k] \\ \check{\mathbf{a}}[k] \end{Bmatrix} = \begin{Bmatrix} \mathbf{x}_{\text{h},6..10}[k] \\ \mathbf{u}_{\text{h},11..15}[k] \\ \mathbf{u}_{\text{h},16..25}[k] \end{Bmatrix}, \quad \mathbf{f}_{\text{h}}[k+1] \equiv \begin{Bmatrix} \dot{\mathbf{q}}_{\text{h}}[k+1] \\ \ddot{\mathbf{q}}_{\text{h}}[k+1] \\ \check{\mathbf{a}}[k+1] \end{Bmatrix} \tag{3.34}$$

The implementation of implicit ODE solving methods was intended to improve the numerical stability of the ODE solution obtained over the horizon of interest. While this is of less concern when simulating the viscoelastic mechanics of human motion, the same cannot be guaranteed for stiff ODEs like those observed in robotic systems with high gearing friction (i.e., stiff transitions between "stiction" and sliding friction); this idea is visited in Chapter 6 when we simulate human-exoskeleton balance.

Path inequality constraints in Equation (3.25), were defined as follows:

$$\mathbf{h}_{\text{fsr}}(\mathbf{x}_{\text{h}}, \mathbf{u}_{\text{h}}) = \begin{Bmatrix} \boldsymbol{\Omega}(\mathbf{x}_{\text{h}}, \mathbf{u}_{\text{h}}, \cdot) \\ \phi_{\text{tr}} - \phi_{\max} \\ \phi_{\min} - \phi_{\text{tr}} \\ \dot{\phi}_{\text{tr}} - \dot{\phi}_{\max} \\ \dot{\phi}_{\min} - \dot{\phi}_{\text{tr}} \end{Bmatrix} \tag{3.35}$$

As detailed prior, these inequality constraints were enforced to to prevent the ZMP from existing outside of the physical boundaries of the support polygon, slipping of the feet (assuming a static coefficient of friction of $\mu_{\text{gf}} = 0.80$ [264]), and the vertical ground-reaction forces from "pulling" on the feet. The result is the system remaining within the domain of feasibility for balanced posture over the course of the entire simulation horizon – as the COM is motionless at t_f due to enforcement of (3.32), we assume that the system will always be balanced (as $t \to \infty$). Additionally, to avoid unreasonable solutions featuring excessive head motion, the orientation of the trunk segment was also constrained; at all times, the trunk's angle was to be within $\pm 60^\circ$ with respect to the vertical and its speed could not exceed $|200|^\circ/\text{s}$ [175].

Path equality constraints in Equation 3.26 were defined as

$$\mathbf{g}_{\text{fsr}}(\mathbf{x}_{\text{h}}, \mathbf{u}_{\text{h}}) = \begin{Bmatrix} \mathbf{M}_{\text{h}}(\mathbf{q}_{\text{h}})\ddot{\mathbf{q}}_{\text{h}} - \boldsymbol{\Gamma}(\mathbf{q}_{\text{h}}, \dot{\mathbf{q}}_{\text{h}}) - \boldsymbol{\tau}_{\text{mtg}}(\mathbf{q}_{\text{h}}, \dot{\mathbf{q}}_{\text{h}}, \mathbf{a}(t)) - \mathbf{P}(\mathbf{q}_{\text{h}}, F_{\text{push}}, \ddot{x}_{\text{plat}}) \\ \dot{\mathbf{a}} - \check{\dot{\mathbf{a}}} \\ \omega_{\text{shldr}} \\ \omega_{\text{elbow}} \end{Bmatrix} \tag{3.36}$$

which involves implicitly solving for $\mathbf{q}_{\text{h}}$, as described by Puchaud et al. [281], with $F_{\text{push}} = 0$ and $\ddot{x}_{\text{plat}} = 0$. The inclusion of the upper limb velocities ω_{shldr} and ω_{elbow} indicate our desire to obtain the FSR boundaries assuming no assistance from the arms; exclusion of those terms would allow us to investigate whether arm motion permits higher COM velocities.

The NLP problem posed in this section was solved using the interior-point method within `fmincon` (MATLAB) with analytical gradients and hessians for both cost and constraint functions obtained using custom worksheets developed within MapleSim software. Due to the scale of the NLP, we elected to use the interior-point method (described in [219]) as it tends to show improved scalability when compared to techniques like the active-set method [208]. The algorithm itself was permitted to iterate up to 10,000 times (total number of Newton steps) if it did not yet meet the optimality tolerance (set to $10^{-}6$) or Newton step tolerance (set to $10^{-}10$).

3.2.2 Simulation Experiments and Results

In this section, we assess the 5-DOF human model's anterior and posterior FSR boundaries under a variety of novel conditions to better understand how certain features of human anatomy and physiology impact the ability to balance with FIP. These analyses also provide a baseline quantification of balancing capabilities that we can then use to assess how assistive device features influence the end-user's ability to balance. Lastly, we provide a novel assessment of how trade-offs in the limits of FIP balance control occur with concurrent minimization of active effort by the CNS through Pareto optimization (originally published in Inkol and McPhee [172]). Supplementary experiments investigating cost function structure, initial restrictions on DOF, and constraints on MTG strength are shown in Appendix F.

1) Influence of Adding Degrees of Freedom to Human Model

The first simulation experiment was designed to investigate how imposing different constraints on the model degrees of freedom, i.e., which joints were to be "locked" during simulations. Similar work was done by Iqbal and Pai [175] in their analysis of how knee motion can increase the size of the FSR for a 3-DOF biomechanical stance model that did not use MTGs. However, to our knowledge, no authors have assessed how biomechanical motion of the upper limbs could increase the ability to remain balanced according to the FSR. Therefore, we considered three conditions for the current simulation experiment:

1. Only ankle movement permitted during balance recovery (DOF=1, i.e., inverted pendulum [264, 370])
2. Ankle, knee, and hip movements permitted during balance recovery (DOF=3, i.e., triple inverted pendulum [175])
3. Ankle, knee, and hip movements in addition to upper limbs movements are permitted during balance recovery (DOF=5)

Additionally, the analytical results from Hof et al. [154], with an eigenfrequency $\omega = 2.65$ Hz, were calculated (FSR derived from linear inverted pendulum, according to Equations (E.19) and (E.20)) to validate the results of the DOF=1 simulations, i.e., linear approximation of the nonlinear inverted pendulum FSR [154]. Restrictions on the DOF used were imposed through manipulation of the box constraints in Equation (3.27), i.e., constrained joint velocities could never exceed $\pm 0.005\,^{\circ}/\text{s}$.

The estimated FSR generated over the the set of AP COM positions $\{0, 0.25, ..., 1.00\}$ (normalized to foot length; 0 = COM over toe, 1 = COM over heel) is displayed is Fig. 3.2. In Figs. 3.3 and 3.4, the simulated whole-body COM and ZMP trajectories that yielded the maximum capturable anterior and posterior COM velocities respectively, are shown for an initial normalized COM position of 0.25, 0.50, and 0.75. The joint angles that generated these COM/ZMP trajectories are shown in Figs. 3.5 and 3.6.

In general, the DOF=3 system was able to capture larger anterior and posterior COM velocities for balance recovery in comparison to the DOF=1 system. The DOF=3 system achieved this increase through control of whole-body angular momentum relative to the COM [130]. When falling forward (Fig. 3.5), the DOF=3 system relied on a motor

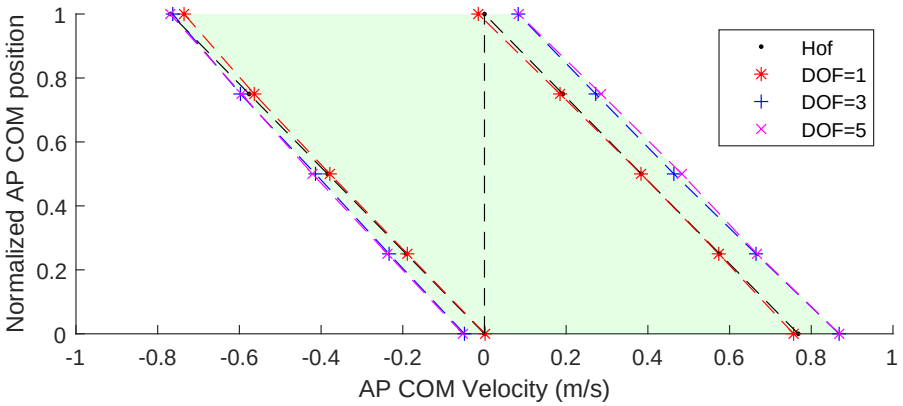


Figure 3.2: The feasible stability region (FSR) for the human-only FIP balance model generated with different constraints on the model degrees of freedom, i.e., which joints were to be "locked" during simulations. Conditions are as follows: only ankle movement (DOF=1); ankle+knee+hip movement permitted (DOF=3); ankle+knee+hip and upper limbs movement permitted (DOF=5). Additionally, the analytical results from Hof et al. [154] are shown (FSR derived from linear inverted pendulum) to validate the results of the DOF=1 simulation, i.e., the nonlinear inverted pendulum FSR.

strategy combining hip flexion, knee extension, and ankle plantarflexion, similar to the hip strategy in [158] and simulated recently by Cheng et al. [78]. The optimal control algorithm obtained strategies that resulted in initialization with a flexed knee like in Iqbal and Pai [175] prior to moving into knee extension; the extended knee posture performs better in COM control according to simulations by Cheng et al. [78]. The differences in FSR between conditions were not surprising given the observations of the triple pendulum by Iqbal and Pai [175] relative to the inverted pendulum by Pai and Patton [264] and Hof et al. More recent models of humanoid standing balance have also highlighted the benefits to balance recovery that angular momentum about the COM can provide [26, 48, 130, 152].

The primary novelty within this simulation experiment was whether the FSR could be increased in a meaningful way with the use of arm motion. Information on this would provide a basis for arm responses in the scope of optimal control in addition to other existing theories, e.g., reducing trunk extension velocity following a slip [332]. From Fig. 3.2, it is quite evident that any gains in anterior and posterior FSR boundaries with the use of the upper limbs was marginal at best. Therefore, at least for perturbations in the

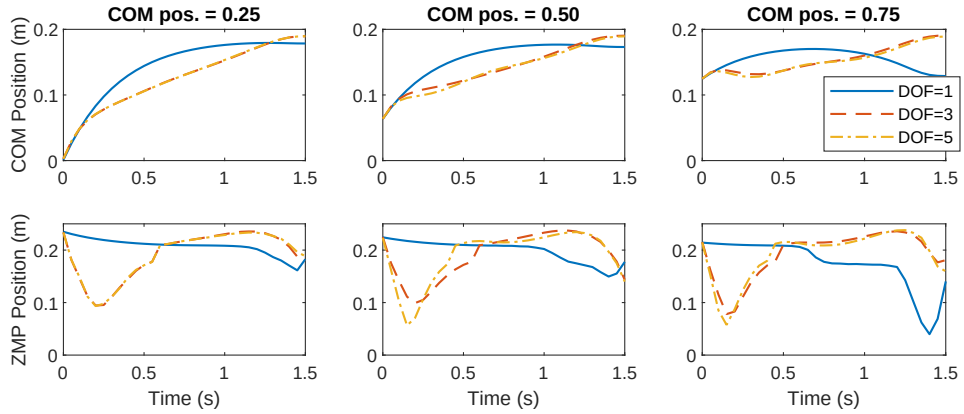


Figure 3.3: COM and ZMP trajectories that result in the **anterior** FSR boundary for the human-only balance model when different constraints are imposed on the model degrees of freedom, i.e., which joints were to be "locked" during simulations. Results are shown for an initial normalized AP COM position of 0.25, 0.50, and 0.75.

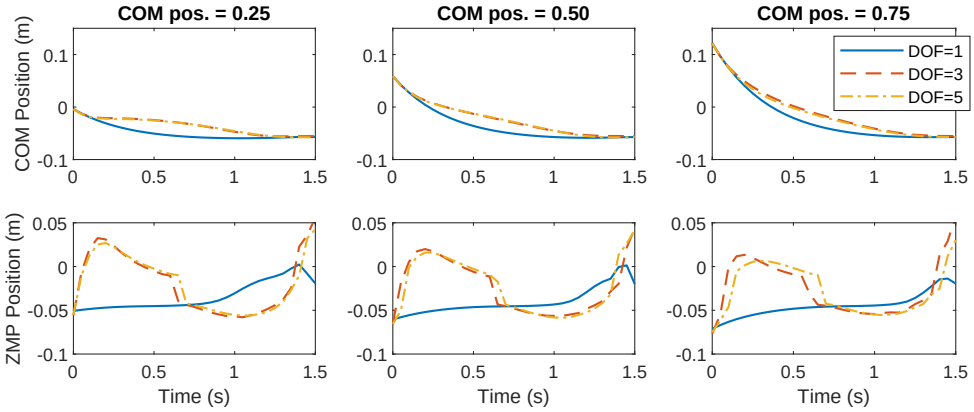


Figure 3.4: COM and ZMP trajectories that result in the **posterior** FSR boundary for the human-only balance model when different constraints are imposed on the model degrees of freedom, i.e., which joints were to be "locked" during simulations. Results are shown for an initial normalized AP COM position of 0.25, 0.50, and 0.75.

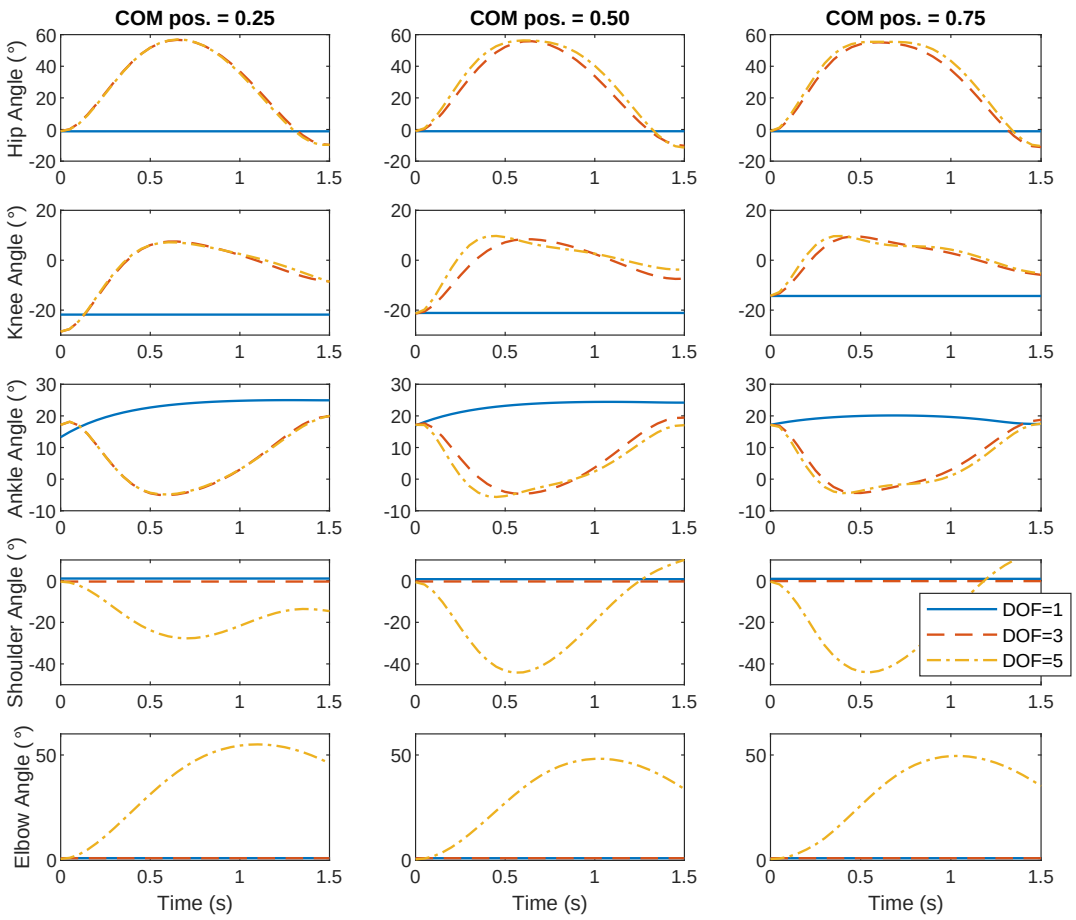


Figure 3.5: Joint angles that result in the **anterior** FSR boundary for the human-only balance model when different constraints are imposed on the model degrees of freedom, i.e., which joints were to be "locked" during simulations. Conditions are as follows: only ankle movement (DOF=1); ankle+knee+hip movement permitted (DOF=3); ankle+knee+hip and upper limbs movement permitted (DOF=5). Results are shown for an initial normalized AP COM position of 0.25, 0.50, and 0.75.

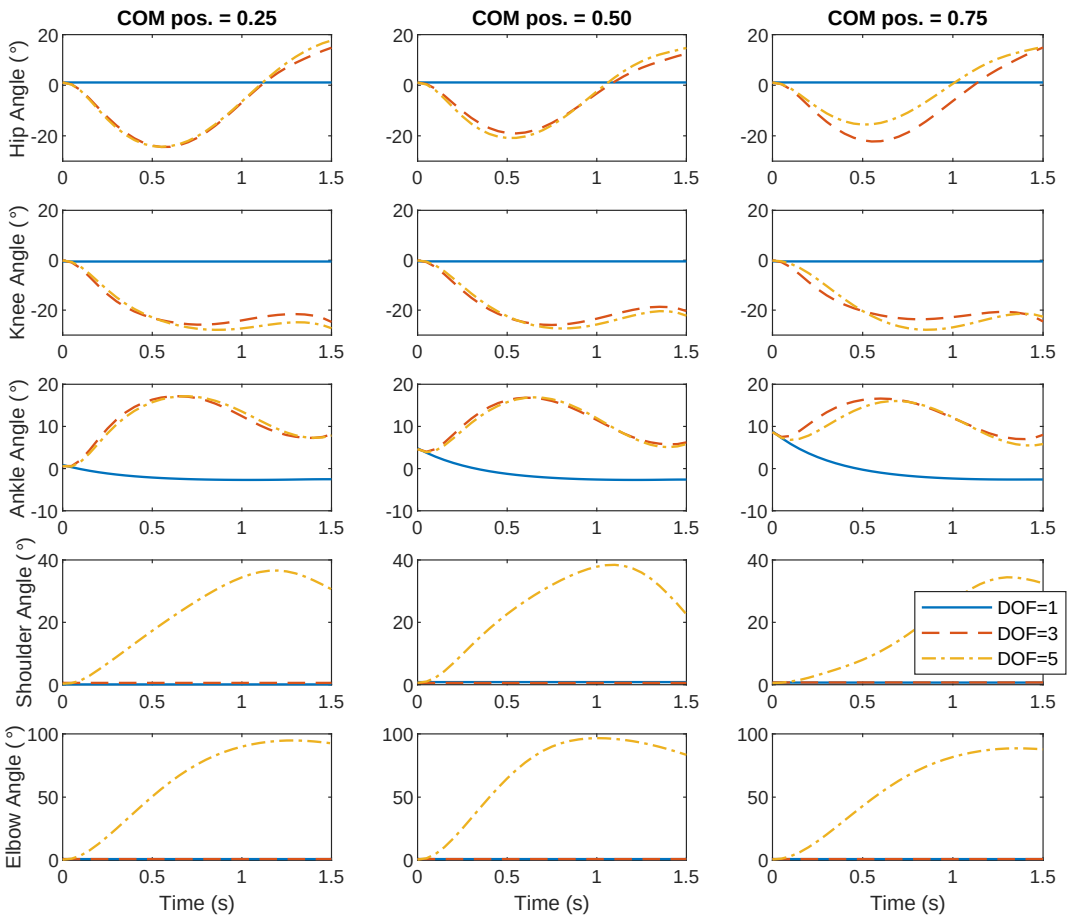


Figure 3.6: Joint angles that result in the **posterior** FSR boundary for the human-only balance model when different constraints are imposed on the model degrees of freedom, i.e., which joints were to be "locked" during simulations. Conditions are as follows: only ankle movement (DOF=1); ankle+knee+hip movement permitted (DOF=3); ankle+knee+hip and upper limbs movement permitted (DOF=5). Results are shown for an initial normalized AP COM position of 0.25, 0.50, and 0.75.

sagittal plane, it does not appear that the use of arm motion can truly improve balancing capabilities if knee and hip motion is also being utilized. We do note that this may not be the case for other combinations of constraints to the model DOF, e.g., how does arm motion increase the FSR when the hips and knees are "locked". When the initial COM velocity was forward, the optimal balance recovery solution was a combined shoulder extension and elbow flexion strategy (Fig. 3.5). Briefly, this action amounts to simply raising the head+arms+trunk segment COM, potentially to improve the net angular momentum with respect to the whole-body COM during balance recovery [130, 152]. When the initial COM velocity was backward, the optimal balance recovery solution suggested was a combined shoulder-elbow flexion strategy (Fig. 3.6). This counter-movement strategy for backwards falls has been observed for experimental cases of walking and slipping [168, 229, 332] in addition to standing balance recovery [85]. In general, the goal is to provide anterior shifting of the COM as it is perturbed posteriorly (Fig. 3.4). Troy and Grabiner [332] also suggested that flexion velocity of the shoulder can reduce the maximum trunk extension velocity used by individuals during slip recovery. In Fig. 3.6, we note that for the COM = 0.75 condition, the magnitude of trunk extension was reduced by $\approx 8^\circ$ with the inclusion of arm motion (DOF=3 vs DOF=5). This result may therefore provide further support for the arguments of Troy and Grabiner [332].

2) Influence of Delays in Initiating Balance Recovery

As established in the literature, following a perturbation to upright stance, the CNS typically responds with a 75-150 ms delay [50, 158, 344, 354]. Naturally, the size of this delay will vary according to an individual's age as well as the presence of many medical conditions [89, 273]. Therefore, the second simulation experiment was designed to investigate the influence of different time delays (dead time, δ) imposed on the initiation of balance recovery during simulations. To elaborate, MTG activations were not permitted to shift from their value set at the initial time until δ ms had passed. Mathematically, this was incorporated through the box constraints in Equation (3.27) as

$$-\varepsilon_1 \mathbf{1} \leq \dot{\mathbf{a}} \leq \varepsilon_1 \mathbf{1}, \quad \forall\, k = 1 \ldots n_{\text{delay}} \tag{3.37}$$

$$\mathbf{0} \leq \mathbf{a} \leq \varepsilon_2 \mathbf{1}, \quad \forall\, k = 1 \ldots n_{\text{delay}} \tag{3.38}$$

where $\varepsilon_1 = 1 \times 10^{-3}$ and $\varepsilon_2 = 0.33$ are the activation boundaries during the delay period and n_{delay} is the number of inactive nodes. These constraints would force the NLP solver

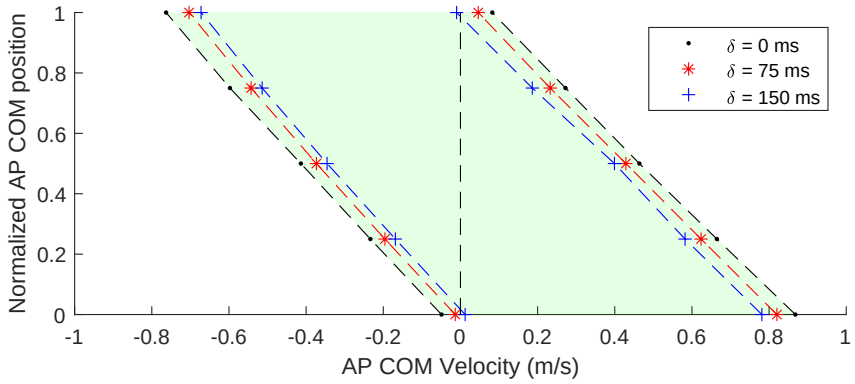


Figure 3.7: The feasible stability region (FSR) for the human-only FIP balance model generated with different time delays (dead time, δ) imposed during simulations, i.e., muscle activations could not shift from their value measured the initial time until δ ms had passed (Equation 3.38). Arm movement was restricted in these simulations. Conditions are as follows: 0 ms dead time (baseline); 75 ms dead time (short delay in [158, 344]); 150 ms dead time (longer delay reported in [50]).

to obtain the best initial MTG activations $< \varepsilon_2$ ($\varepsilon_2 = 0.33$ avoids substantial initial MTG co-activation reducing initial model stiffness [361]) and to set subsequent MTG activations as $\mathbf{a}[k] = \mathbf{a}[1] \, \forall \, k = 2 \ldots n_{\text{delay}}$ due to inclusion of Equation (3.37). For example, for a time step of $\Delta t = 25$ ms in simulations, a 75 ms response delay (dead time) was mimicked by setting $n_{\text{delay}} = 3$; a 150 ms delay would required $n_{\text{delay}} = 6$.

The following conditions were investigated with respect to influence on size of shape of the FSR:

1. $\delta = 0$ ms ($n_{\text{delay}} = 0$) – Ideal
2. $\delta = 75$ ms ($n_{\text{delay}} = 0$) – Based on observations from [158, 344].
3. $\delta = 150$ ms ($n_{\text{delay}} = 0$) – Based on observations from [50, 264]

Because arm movement had little impact on the FSR size in previous experiments, it was restricted in the current simulations. The estimated FSR generated over the the set of AP

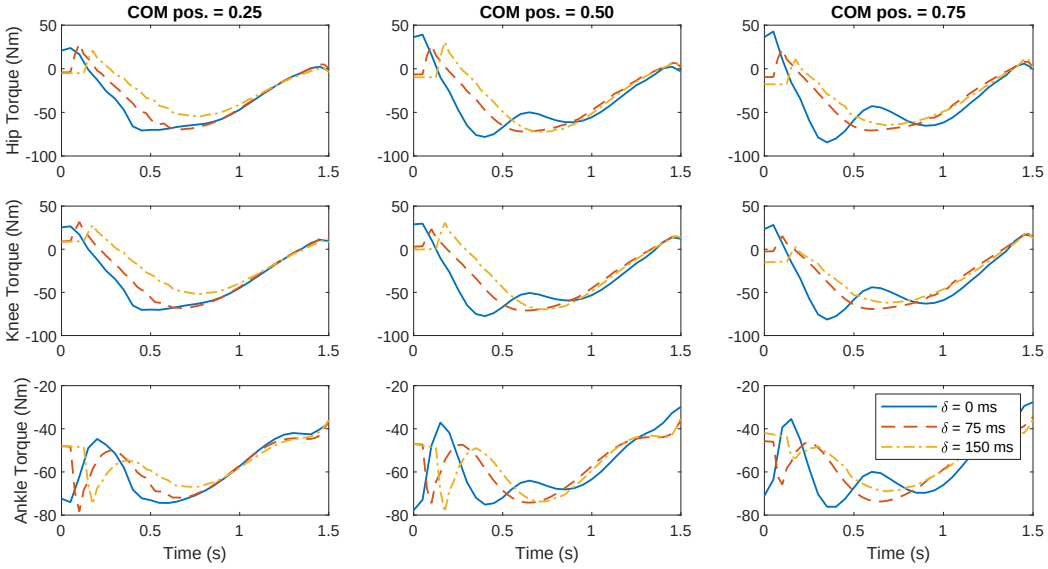


Figure 3.8: Active hip, knee, and ankle muscle torques that resulted in the **anterior** FSR boundary for the human-only balance model when different time delays (dead time, δ) were imposed during simulations (right boundary in Fig. 3.7).

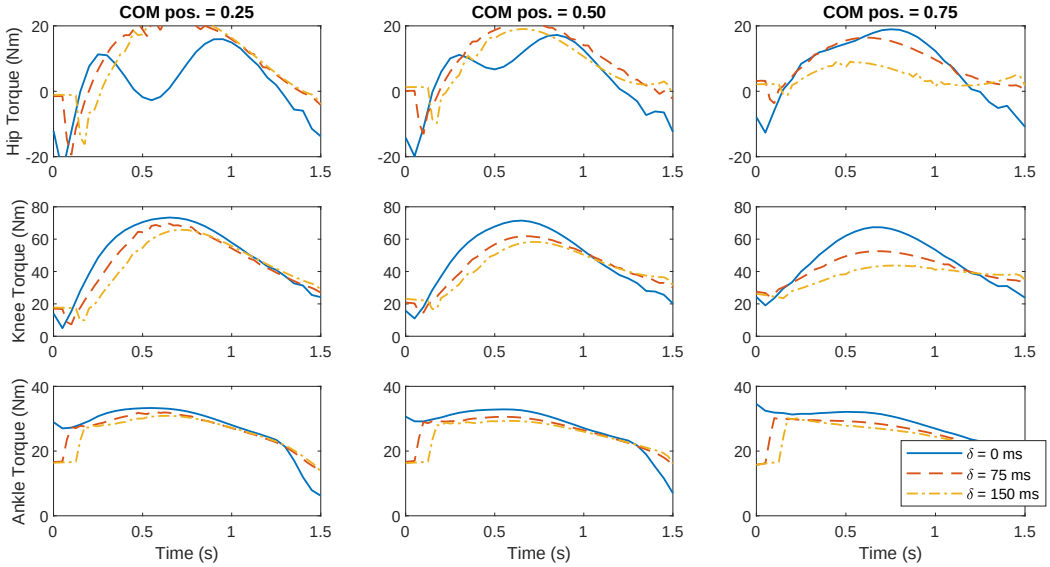


Figure 3.9: Active hip, knee, and ankle muscle torques that resulted in the **posterior** FSR boundary for the human-only balance model when different time delays (dead time, δ) were imposed during simulations (left boundary in Fig. 3.7).

COM positions $\{0, 0.25, ..., 1.00\}$ (normalized to foot length; 0 = COM over toe, 1 = COM over heel) is displayed is Fig. 3.7. In Figs. 3.8 and 3.9, the simulated hip, knee, and ankle active MTG torques, i.e., torque = $0.5\tau_{\text{mtg}}^{\text{cns}}$ Nm, that yielded the maximum capturable anterior and posterior COM velocities respectively, are shown for an initial normalized COM position of 0.25, 0.50, and 0.75.

Evidently, an increase in dead time at the onset of balance recovery consistently reduces booth anterior and posterior boundaries of the FSR for FIP balance (Fig. 3.7). Each successive increase of dead time shifted the anterior and forward boundaries negatively and positively respectively. These observations are consistent with the observations made by Hof et al. [153] who added a neural delay into their linear inverted pendulum model of balance control. For example, using Hof's delayed linear model [153], we obtain a forward FSR estimate of 0.38 m/s at an initial normalized AP COM position of 0.50; this is compared to the 0.42 m/s we obtain in simulations with a 75 ms delay and a 3-DOF pendulum (arms restricted). In Figs. 3.8 and 3.9, it is clear how including the delay constraints in Equations (3.38) and (3.37) affected active muscle torque generation during forward and backward balance recovery. For example, with a normalized AP COM position of 0.50 and an initial forward COM momentum, the delayed human model ($\delta = 75$ ms and $\delta = 150$ ms) is initialized with near-zero hip and knee ankle torques (passively driven at first node) and a reduced magnitude of active plantarflexion (relative to the $\delta = 0$ ms condition). After the dead time has passed, the delayed active muscle torques seemingly begin to track the non-delayed active torques ($\delta = 0$ ms condition), before essentially converging to the non-delayed signals after approximately 1 second.

3) Trade-Offs in Stability with Effort (Pareto Optimization)

In forward dynamic biomechanical simulations of FIP standing balance, minimizing human muscle activations has been suggested to promote balancing strategies that avoid energetically costly deviations of the trunk from the vertical [202, 344]; however, it is not clear how specifically concurrent minimization of muscle torques directly influences that estimation of the FSR. Therefore, the final FSR-based simulation experiment in Chapter 3 assessed the trade-off in torque generation in the human MTGs with the anterior and posterior FIP FSR boundary. To our knowledge, this is the first application of Pareto optimization in identifying human/humanoid balance limits with some quantification of human effort or metabolic energy expenditure. Previous methods of assessing the interaction between

COM control and CNS effort have utilized multi-objective optimization routines that feature trial-and-error tuning of objective weights [202, 344]. In some instances, these weights are not reported in the final publication [77]. A Pareto optimization approach instead limits the manual tuning of weights, and instead introduces a homotopy between two separate objective functions that acts to parameterize the corresponding Pareto frontier [23, 151, 347]. Therefore, the cost function in Equation (3.19) was augmented to solve the following optimization problem:

$$\underset{x,u}{\operatorname{argmin}} \{-(1-\rho)w_1 d\dot{\mathbf{r}}_{\mathrm{cm}}[1] \cdot \hat{\imath} + \rho w_2 \sum_{k=1}^{n} (\boldsymbol{\tau}_{\mathrm{mtg}}^{\mathrm{cns}}[k] \cdot \boldsymbol{\tau}_{\mathrm{mtg}}^{\mathrm{cns}}[k])\} \tag{3.39}$$

subject to the constraints outlined in Equations (3.20), (3.21), (3.22), (3.23), (3.24), (3.25), and (3.26). In Equation (3.39), $\boldsymbol{\tau}_{\mathrm{mtg}}^{\mathrm{cns}}$ is the torque generated in the MTGs by the CNS only (introduced in Equation (3.4)). This alteration effectively scalarizes the two objective criteria, i.e., the two terms in (3.39), which allows us to estimate the Pareto frontier of these objectives by evaluating the equation across the interval $\rho \in [0, 1]$ [23]. Whether to solve for the anterior or posterior FSR boundary at a given COM position was set according to $d \in \{-1, 1\}$ (1 = anterior, -1 = posterior). Numerically, to handle differences in scaling between objectives, weights w_1 and w_2 were set to the inverse of their associated term evaluated at $\rho = 0$, e.g., at normalized AP COM position = 0.50, $w_1 = 0.63^{-1}$s/m, $w_2 = 2.3 \times 10^{-5}$ N^{-2}m^{-2}. The optimal control problem was then solved at a normalized COM positions $\{0, 0.25, \ldots, 1\}$ for each value of $\rho \in \{0, 0.2, \ldots, 1\}$.

Fig. 3.10 displays the results of the Pareto optimization that searched for the trade-offs in FSR size that come with concurrent minimization of active MTG torques. To interpret these surface plots, the vertical axis ($J_{\mathrm{com}}(\%)$) displays the percentage of the maximum possible FSR velocity at a given normalized AP COM position, i.e., the FSR boundary velocity for $\rho = \ldots$ normalized to the FSR boundary velocity at $\rho = 0$, that is capturable given some concurrent minimization of active effort, i.e., the $\boldsymbol{\tau}_{\mathrm{mtg}}^{\mathrm{cns}}$ term in Equation (3.39). The effort cost term, i.e., $J_{\mathrm{effort}}(\%)$, is also normalized to the maximal effort to capture the COM velocity at $\rho = 0$ for a given normalized AP COM pos. Therefore, in Fig. 3.10, when $J_{\mathrm{effort}} = 1$ (or 100%), the resulting J_{com} is always 1, i.e., with maximum effort, we always obtain the ideal human FSR boundary. Reducing the level of effort demanded by the human ($J_{\mathrm{effort}} < 1$) causes characteristic reductions in the anterior and posterior FSR boundaries reflected by monotonic decreases in J_{com}. Notably, for the anterior FSR in Fig. 3.10A, observed that for COM positions close to the anterior boundary of the support polygon

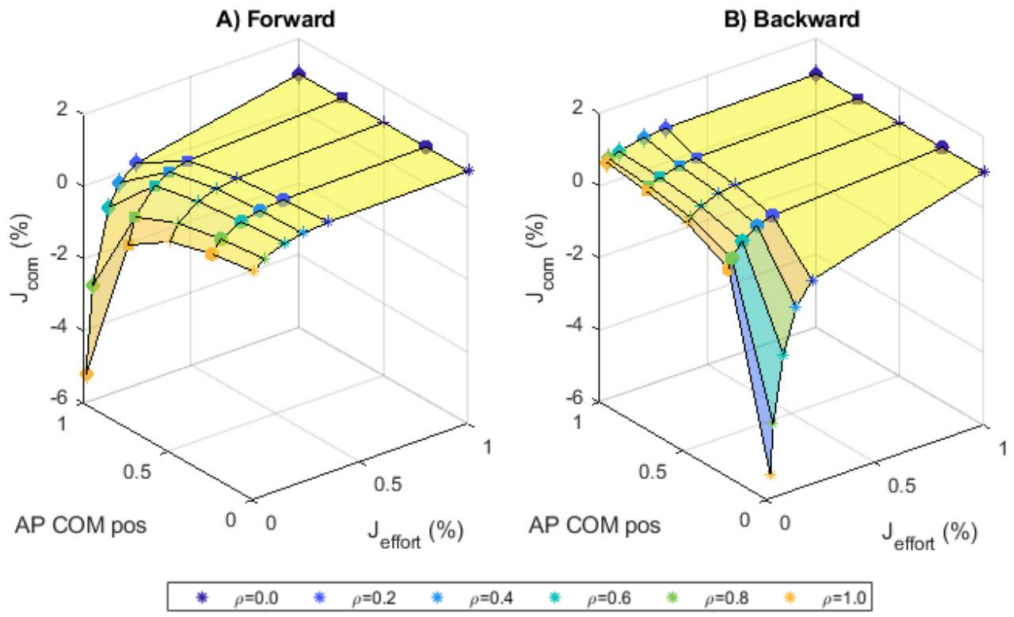


Figure 3.10: The Pareto front of the evaluated squared torque cost against the A) maximal forward COM velocity that could be terminated, i.e., anterior FSR boundary, and B) maximal backward COM velocity that could be terminated, i.e., posterior FSR boundary. Both costs were normalized to their values at $\rho = 0$, i.e., maximal balance effort. A colour gradient was used to highlight the shift in FSR boundary for a given normalized AP COM position and a given value of ρ.

(toes), there was a sharp increase in the effect of reducing effort on reducing capturability. Similar observations were made for the posterior FSR boundary in Fig. 3.10B: for COM positions close to the posterior boundary of the support polygon (heels), there was again a sharp increase in the effect of reducing effort on reducing capturability. The shift in postural strategies the resulted in the values plotted in Fig. 3.10 at a normalized AP COM position of 0.50 are shown in Figs. 3.11 (anterior FSR strategy) and 3.12 (posterior FSR strategy).

In Fig. 3.11, it is evident that for $\rho = 0$ (maximal effort), the strategy requiring most effort to capture forward COM velocities is the hip strategy characterized by hip flexion, knee extension, and ankle plantar flexion [158, 359]. Increasing concurrent effort minimization (reducing ρ from 1), quite drastically shifts the motor strategy towards an ankle strategy that features little hip flexion though still uses knee extension and ankle plantar flexion [154, 158]; these latter features also decreased at $\rho \in \{0.8, 1\}$. In the case of

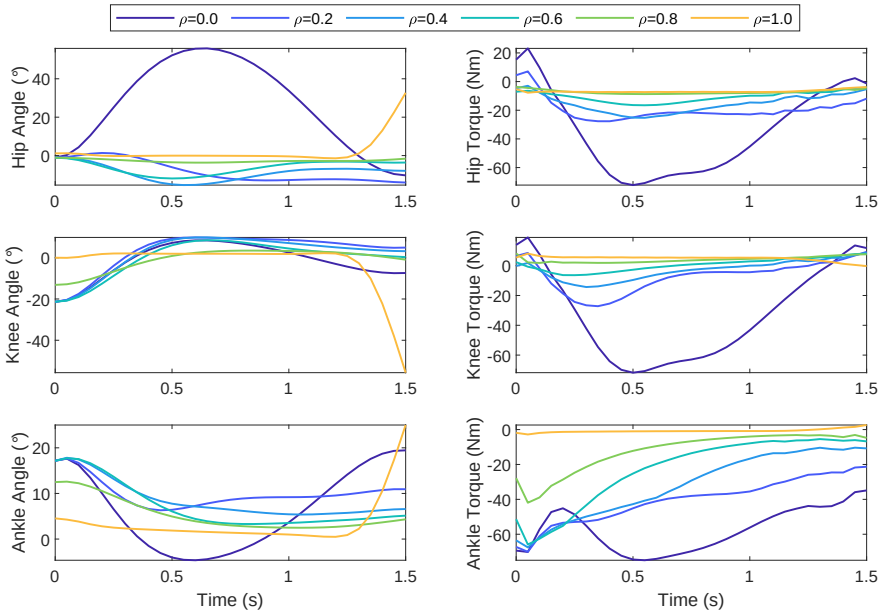


Figure 3.11: Hip, knee, and ankle joint angles (*left*) and active hip, knee, and ankle muscle torques (*right*) that resulted in the **forward** FSR boundary for the human-only balance model given different values of the homotopy parameter ρ (see Fig. 3.10A).

backward COM velocities, there was again a general shift from hip to ankle strategy with increases of ρ (Fig. 3.12); like in Appendix F (experiment F.3), reducing effort in the cost function also shifted the hip trajectory from extension (at $\rho = 0$) to flexion (at $\rho = 0.2$). Therefore, the substantial magnitudes of hip flexion/extension that obviously require large active hip **and** knee MTG torques are not necessary to achieve a high-degree of capturability. Instead, it may be possible to have controls that predominantly utilize ankle and knee motion to offset net torque requirements. With that said, this statement is not necessarily true for COM positions near the toe (for the anterior FSR boundary) and the heel (for the posterior FSR boundary). In these regions of COM phase-space, not using hip motion sufficiently (i.e., the motor strategy used when $\rho = 0$) can substantially impede capturability of the COM. This result is inline with the notion that the ankle strategy shows poor capturabililty in these instances [154]. However, Versteeg et al. [344] observed that increasing the priority to minimize muscle stress in simulations resulted in greater trunk pitch and hip flexion; though, when the objective criteria contained only COM terms with the effort term, the effect of minimizing muscle stresses was quite minimal (little change in postural strategy). We did observe this maintenance of the hip strategy when using

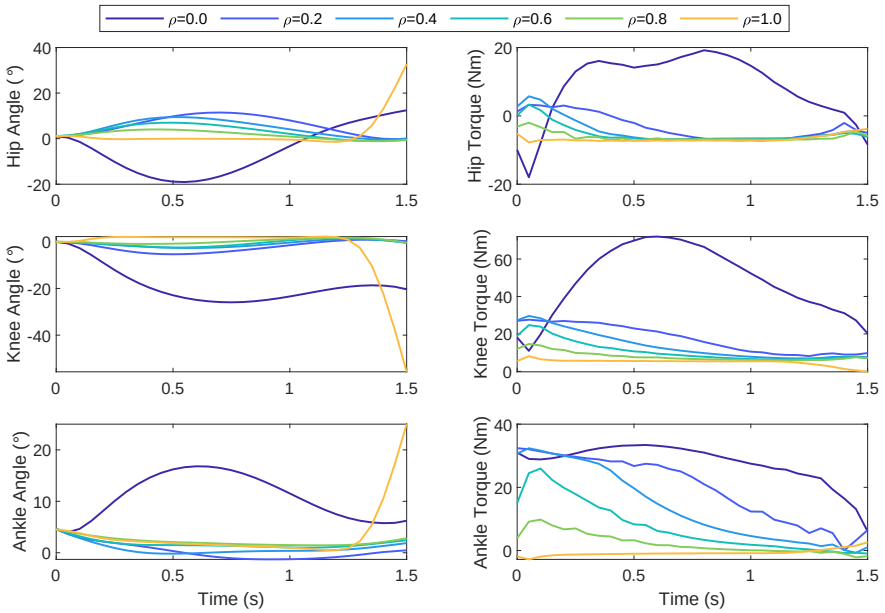


Figure 3.12: Hip, knee, and ankle joint angles (*left*) and active hip, knee, and ankle muscle torques (*right*) that resulted in the **backward** FSR boundary for the human-only balance model given different values of the homotopy parameter ρ (see Fig. 3.10B).

only constraints on the torque generation in our optimal control formulation, but did not observe the same in the case of effort minimization. The possible reasons for this difference are countless: the authors minimized muscle stresses, which can be sensitive to the muscle models used. Interestingly, Versteeg et al. [344] acknowledged that improvements were necessary for the models of trunk musculature used in their simulations. Similarly, it is not clear if their measure of stresses included the parallel elastic tension in each muscle, i.e., the passive MTG contributions that were ignored in Equation (3.39), or how much damping was featured in their simulations (and where) which could influence muscle force requirements. The analysis in the current dissertation was specifically based on the torque generated by each MTG rather than its stress or activation. The intent behind this decision was that in experiment F.3 (Appendix F), the constraining of activations alone allowed the hip flexor/extensors to still generate a large magnitude of torque relative to the requirements of balancing due to the difference in magnitude of maximal isometric torques between MTGs. Finally, the authors in [344] simulated balance recovery in response to a known support-surface perturbation, which could also influence the resulting optimal

strategy, e.g., using an internal CNS model of support-surface accelerations to help control the COM [174]. It is also not clear whether the results they obtained were sensitive to the initial guess provided for the simulations assessing the effect of minimizing muscle stress, i.e., the authors used their results from previous simulation experiments to initialize these optimizations.

A final point of interest in the current simulation experiment is in describing how the disseminated results relate to adaptations made by the CNS following repeated exposures to a specific perturbation. It is reasonable to suggest that the CNS develops an internal model of the system disturbance, e.g., its magnitude, direction, and onset/duration, as it experiences it multiple time [168]. The learning results in experimentally-observed motor adaptions in the context of perturbations to both standing balance [158, 344, 355] and walking balance [57, 58, 146, 168, 230]. In Versteeg et al. [344], the authors noted that during experiments, there was a general shift in postural strategy from a hip strategy to an ankle strategy. However, the results we presented for the current simulation experiment suggest that these adaptations could instead relate to an increased weighing of the joint torques generated actively by the muscles, i.e., the CNS desires lower MTG torques that have the potential to expend metabolic energy. In fact, there are other examples of the CNS adopting motor strategies to reduce energy expenditure, e.g., short-term motor adaptations during walking [112]

3.3 Human-Only NMPC Feet-In-Place Balance Regulation

The following section contains content related to the paper "Simulating Human Upper and Lower Limb Balance Recovery Responses Using Nonlinear Model Predictive Control" published/presented at the 2021 43rd Annual International Conference of the IEEE Engineering in Medicine & Biology Society (Inkol and McPhee [170]).

3.3.1 Background

As established prior, to generate forward dynamic simulations for human balance recovery, inputs to the biomechanical system must be known. Optimal control is often used to form

inputs similar to the activations sent by the CNS. Ideally, human motor control models should feature concurrent feedforward and feedback elements [240]; however, many balance models reliant on feedback elements are limited in complexity [26, 169, 202], use a simple local control scheme [185] or are driven by experimental tracking [227]. More complex musculoskeletal models [77, 88, 344] tend to rely on feedforward optimal control, which inherently requires the perturbation delivered to the system to be a part of the dynamic model within the optimization. A good match between the dynamics of the control-oriented and system models implies that the responses to a truly novel perturbation cannot be captured; rather it is likely that the responses generated mimic those that occur after repeated exposure and habituation [168, 344]. Nonlinear model predictive control (NMPC) offers a novel solution to this problem [240, 256]; it generates the inputs using constrained open-loop optimal control but operates with a receding horizon that subsequently closes the loop.

Discussed in 3.2.1, a common feature of many biomechanical simulations, not just balance, is the exclusion of arm motion, e.g. arms are rigidly fixed to trunk [169, 202, 342, 227, 344]. Those simulations that do include arms often have a particular component of the motor task that requires arms, e.g. pointing [240]. For a task like balance recovery, arm responses tend to be most overt following exposure to a novel and/or unexpected perturbation [168], and have quite a few hypothesized roles [332].

Despite the potential role of arms in balance, experimental protocols will often dictate that these segments are not to be used [344]. In the context of optimal control, this raises questions as to whether arm responses arise to reduce cost of movement according to some performance criteria. Answering this question could be beneficial for those designing predictive dynamic biomechanical simulations rooted in optimal control. Therefore, the current section used *what-if* simulations of balance recovery to assess whether arm strategies arise from a typical set of performance criteria following a novel balance perturbation. How these responses alter the actions at postural joints was also investigated. Key features of this approach included the investigation of multiple perturbation directions (in sagittal plane) and the use of NMPC as a model of the CNS experiencing an unknown disturbance. This novel approach differs from previous methods like in [344] wherein the perturbation was included within the optimal control formulation and thus more likely replicated a learned/well-adapted motor strategy.

3.3.2 Feedback Optimal Control

Nonlinear model predictive control (NMPC) was used to generate forward dynamic simulations of humanoid balance recovery. Briefly, NMPC involves solving a nonlinear optimal control problem for a control-oriented model over a future finite horizon $[t_0, t_f]$. The first controller action is then enacted on the system; the process is subsequently repeated at user-defined time steps *ad infinitum*. The finite-horizon discrete optimal control problem takes the form

$$\arg\min_{x,u} \quad \sum_{k=1}^{n} \mathcal{L}(\mathbf{x}_\mathrm{h}[k], \mathbf{u}_\mathrm{h}[k]) \tag{3.40}$$

subject to:

$$\mathbf{q}_\mathrm{h}[1] = \mathbf{q}_0, \quad \dot{\mathbf{q}}_\mathrm{h}[1] = \dot{\mathbf{q}}_0 \tag{3.41}$$

$$\mathbf{g}_\mathrm{coll}(\mathbf{x}_\mathrm{h}[k], \mathbf{u}_\mathrm{h}[k], \mathbf{x}_\mathrm{h}[k+1], \mathbf{u}_\mathrm{h}[k+1]) \leq \mathbf{0} \quad \forall\, k = 1 \ldots n-1 \tag{3.42}$$

$$\mathbf{h}_\mathrm{fsr}(\mathbf{x}_\mathrm{h}[k], \mathbf{u}_\mathrm{h}[k]) \leq \mathbf{0} \quad \forall\, k = 1 \ldots n \tag{3.43}$$

$$\mathbf{g}_\mathrm{fsr}(\mathbf{x}_\mathrm{h}[k], \mathbf{u}_\mathrm{h}[k]) = \mathbf{0} \quad \forall\, k = 1 \ldots n \tag{3.44}$$

$$\mathbf{h}_\mathrm{term}(\mathbf{x}_\mathrm{h}[n], \mathbf{u}_\mathrm{h}[n]) \leq \mathbf{0} \tag{3.45}$$

$$\begin{Bmatrix} \mathbf{x}_\mathrm{min} \\ \mathbf{u}_\mathrm{min} \end{Bmatrix} \leq \begin{Bmatrix} \mathbf{x}_\mathrm{h}[k] \\ \mathbf{u}_\mathrm{h}[k] \end{Bmatrix} \leq \begin{Bmatrix} \mathbf{x}_\mathrm{max} \\ \mathbf{u}_\mathrm{max} \end{Bmatrix} \quad \forall\, k = 1 \ldots n \tag{3.46}$$

which uses the same definitions of $\mathbf{x}_\mathrm{h}$ and $\mathbf{u}_\mathrm{h}$ from the prior section. The function $\mathcal{L}$ is typically referred to as the Lagrangian term. As the goal in the current study was to assess how individual criteria influence the observed balance recovery strategies, multi-objective costs were ignored. Rather, the balance responses generated by different Lagrangians were compared. This decision circumvented additional issues like manually tuning weights between performance criteria required in other studies [227, 294, 295, 344]. The biomimentic cost functions studied are listed in Chapter 3.3.3.

Equations (3.42), (3.43), (3.44) were identical to those defined in Chapter 3.2; again, the form of the equality path constraint (3.43) depended on whether the NMPC was to keep the arms locked to the trunk segment. Note that again, $F_\mathrm{push} = 0$ and $\ddot{x}_\mathrm{plat} = 0$ within the control-oriented NMPC dynamics as we wished to capture a novel response to a perturbation rather than one in which the CNS is anticipating the disturbance, i.e., has knowledge of onset and magnitude of perturbation. The terminal inequality constraints in

(3.45) will be discussed at the end of Chapter (3.3.3); they had to be modified from the definition to improve convergence of the NMPC.

Like in Chapter 3.2, the optimal control problem given by (3.40) was formulated as a nonlinear programming problem (NLP) via direct collocation, i.e. parameterization of state and control trajectories. Thus, the control signal sent from the NMPC to the plant was a linear interpolation between the first two controller actions (separated by a step duration) returned by the optimization routine, i.e.,

$$\mathbf{u}^*(t) = \mathbf{u}(t_0) + \frac{t - t_0}{\delta t}(\mathbf{u}(t_0 + \delta t) - \mathbf{u}(t_0)) \tag{3.47}$$

3.3.3 Biomimetic Cost Functions and Constraints

Joint/State-Space Criteria

The first cost criteria investigated was related to deviations in joint-space was inspired by an optimized pose controller that could respond to multi-directional perturbations [185]. The corresponding Lagrangian minimizes deviations from some reference pose $\bar{\mathbf{q}} = \{\bar{\theta}_{\text{hip}}, \bar{\theta}_{\text{knee}}, \bar{\theta}_{\text{ankle}}, \bar{\theta}_{\text{shldr}}, \bar{\theta}_{\text{elbow}}\}^T$:

$$\Delta\text{Pose: } \mathcal{L}(\cdot) = (\mathbf{q}_{\text{h}} - \bar{\mathbf{q}})^{\intercal}\mathbf{W}(\mathbf{q}_{\text{h}} - \bar{\mathbf{q}}) \tag{3.48}$$

In the current dissertation, $\mathbf{W}$ was set to identity, $\mathbf{I}_{5\times5}$.

Alternatively, rather than evenly weigh the deviations from reference for all joints, individual joints can also be of priority. For example, motion of the knee joint, often imposed as a constraint in models of humanoid stance [202], can be incorporated within the cost functional:

$$\Delta\text{Knee: } \mathcal{L}(\cdot) = (\theta_{\text{knee}} - \bar{\theta}_{\text{knee}})^2 \tag{3.49}$$

Many simulation studies also have made use of segmental trunk pitch relative to an absolute reference angle $\bar{\phi}_{\text{t}}$ [202, 344]:

$$\Delta\text{Trunk: } \mathcal{L}(\cdot) = (\theta_{\text{ankle}} + \theta_{\text{knee}} + \theta_{\text{hip}} - \bar{\phi}_{\text{tr}})^2 \tag{3.50}$$

This term assumes head, and subsequently eye position, is regulated by the CNS in some optimal fashion.

Center of Mass Criteria

As in Chapter 3.2, criteria related to the control of balance in the whole-body center of mass (COM) space included minimizing horizontal excursions of the COM,

$$\Delta\text{COM: } \mathcal{L}(\cdot) = (\mathbf{r}_{\text{cm}}(\mathbf{q}_{\text{h}}) \cdot \hat{\mathbf{i}} - \bar{r})^2 \tag{3.51}$$

where $\mathbf{r}_{\text{cm}}$ is the COM position. The reference point $\bar{r}$, is the COM position evaluated at $\bar{\mathbf{q}}$. This term can also be expanded to regulate deviations of r_{xcm} which is the COM position extrapolated in the direction of its normalized velocity [154],

$$r_{\text{xcm}} = \left(\mathbf{r}_{\text{cm}}(\mathbf{q}_{\text{h}}) + \frac{\dot{\mathbf{r}}_{\text{cm}}(\mathbf{q}_{\text{h}}, \dot{\mathbf{q}}_{\text{h}})}{\omega_0} \right) \cdot \hat{\imath} \tag{3.52}$$

$$\Delta\text{XCOM: } \mathcal{L}(\cdot) = (r_{\text{xcm}} - \bar{r})^2 \tag{3.53}$$

This objective adds a dynamic velocity-component to the performance criteria unlike the COM criterion alone.

Energy/Effort-Based Criteria

Consistent with the human balance recovery literature [202, 344], effort was also considered in the list of performance criteria. In the current study, effort was quantified using squared MTG activations,

$$\text{ACT: } \mathcal{L}(\cdot) = \mathbf{a}^{\intercal}\mathbf{W}\mathbf{a} \tag{3.54}$$

wherein $\mathbf{W}$ is the identity matrix. Often, this category of terms promotes reasonable movements within dynamic simulations of human motion as discussed by Schulz and Mombaur [298].

Modifying the Domain of Feasibility

For an infinite horizon, Eq. (3.10) alone would be sufficient in guaranteeing stability in the NMPC. However, for receding horizon control, convergence of the controller is not always guaranteed without additional modifications. Therefore, to improve stability, a relaxed terminal inequality constraint $\mathbf{h}_{\text{term}}$ was added to the NLP. Briefly, this constraint utilized a multi-dimensional ellipsoid to try and leave the upright human in a stable or capturable

configuration at the end of each prediction horizon. To elaborate, the horizontal XCOM and vertical COM positions at t_f were constrained to remain within the confines of a small ellipse centered at the reference pose COM position $(\bar{r}, \bar{h})$:

$$\mathbf{h}_{\text{term},1} = \frac{(r_{\text{xcm}}(\mathbf{x}(t_f)) - \bar{r})^2}{s_x^2} + \frac{(\mathbf{r}_{\text{cm}}(\mathbf{q}(t_f)) \cdot \hat{\mathbf{j}} - \bar{h})^2}{s_y^2} - 1 \tag{3.55}$$

Here, s_x and s_y are the horizontal and vertical semiaxes. Constraining COM height encourages a return towards upright posture, whereas doing the same for the XCOM can leave the humanoid in a posture that is theoretically recoverable (assuming the body behaves like an inverted pendulum [154, 264]). Similar criteria have appeared as Mayer terms in previous dynamic simulations of balance recovery [77, 344]. In theory, we could also introduce an ellipsoid terminal constraint to both the generalized joint positions

$$\mathbf{h}_{\text{term},2} = \sum_{i=1}^{5} \frac{(q_{\text{h},i} - \bar{q}_i)^2}{s_{q,i}^2} - 1 \tag{3.56}$$

and joint velocities

$$\mathbf{h}_{\text{term},3} = \sum_{i=1}^{5} \frac{(\dot{q}_{\text{h},i} - \dot{\bar{q}}_i)^2}{s_{\dot{q},i}^2} - 1 \tag{3.57}$$

where $s_{q,i}$ is the semiaxis corresponding to $q_{\text{h},i}$ and $s_{\dot{q},i}$ is the semiaxis corresponding to $\dot{q}_{\text{h},i}$. For the simulations presented herein, only the first terminal constraint was considered (XCOM/COM ellipse).

3.3.4 Simulation Experiments and Results

Simulation Experiments

A series of simulation experiments were conducted to mimic an existing and well-known experimental protocol [222], in which healthy young adults were subjected to support-surface translations in four directions. Perturbations were based on a piecewise acceleration function consisting of a propulsive and braking impulse; the function parameters were tuned according to the differences in recovery difficulty between directions, i.e. the probability of inducing a change in support. In the current study, "small" forward and backward perturbations were selected [222], which in experiments triggers balance recovery with a

low likelihood of stepping. Simulations, spanning a two-second window [344], were then run for each combination of Lagrangian (see 3.3.3), perturbation direction (backward and forward), and upper limb condition (arms locked, AL; arms free, AF). Accelerations of the support surface were initiated 150 ms after the beginning of each simulation.

Like for the FSR, the optimal control problem embedded within the NMPC controller was scaled and solved using an interior-point method in fmincon (MATLAB, MathWorks, USA). Symbolic gradients and Hessians for the cost and constraint functions were generated in MapleSim, exported into optimized MATLAB/C++ functions, and supplied to the solver to improve controller efficacy. Controller step size (sampling interval) and prediction horizon length were set to 25 ms and 800 ms respectively; additional parameters included $\bar{\mathbf{q}} = \{-4.6, 2.9, -2.9, 0, 0\}^\intercal$ degrees and $s_x = s_y = 2.5$ cm. Parameter values were based on the limited literature in modelling human motor control via MPC [26, 240].

Given the interest in the functionality of simulated arm responses, a quantitative measure was introduced to assess whether unlocking the arm joints would improve the performance under each criteria. This measure, the logarithmic cost ratio (CR), was evaluated as, $\mathrm{CR} = \log_{10}(J_{\mathrm{AF}}/J_{\mathrm{AL}})$ which effectively indicated whether the arms reduced the given cost of recovery ($\mathrm{CR} < 0$) while also accounting for the varying orders of magnitude between evaluated cost functions. Variables J_{AF} and J_{AL} simply refer to the cost (for a given criterion) evaluated over the duration of simulation when the arms were free and unlocked respectively.

Results

The postural strategies generated using each performance criteria are shown in Fig. 3.13. Some notable features within the results of the AL condition include the following: When using ΔPose, NMPC relied on a general stiffening strategy to minimize all joint deviations for both perturbation directions. The ΔKnee criteria forced the biomechanical model to adopt a classic double pendulum (combined hip-ankle) strategy [158, 202]. Using ΔCOM and ΔXCOM produced near-identical multi-joint COM lowering strategies with some minor perturbation direction-dependencies, e.g. patterns of ankle and hip sway. Unsurprisingly, the ACT criteria prompted the model to relax the most during the recovery, especially for the backward condition. Versteeg et al. [344] reported that increasing the relative weights on muscle stress criteria in dynamic musculoskeletal simulations prompted a shift towards

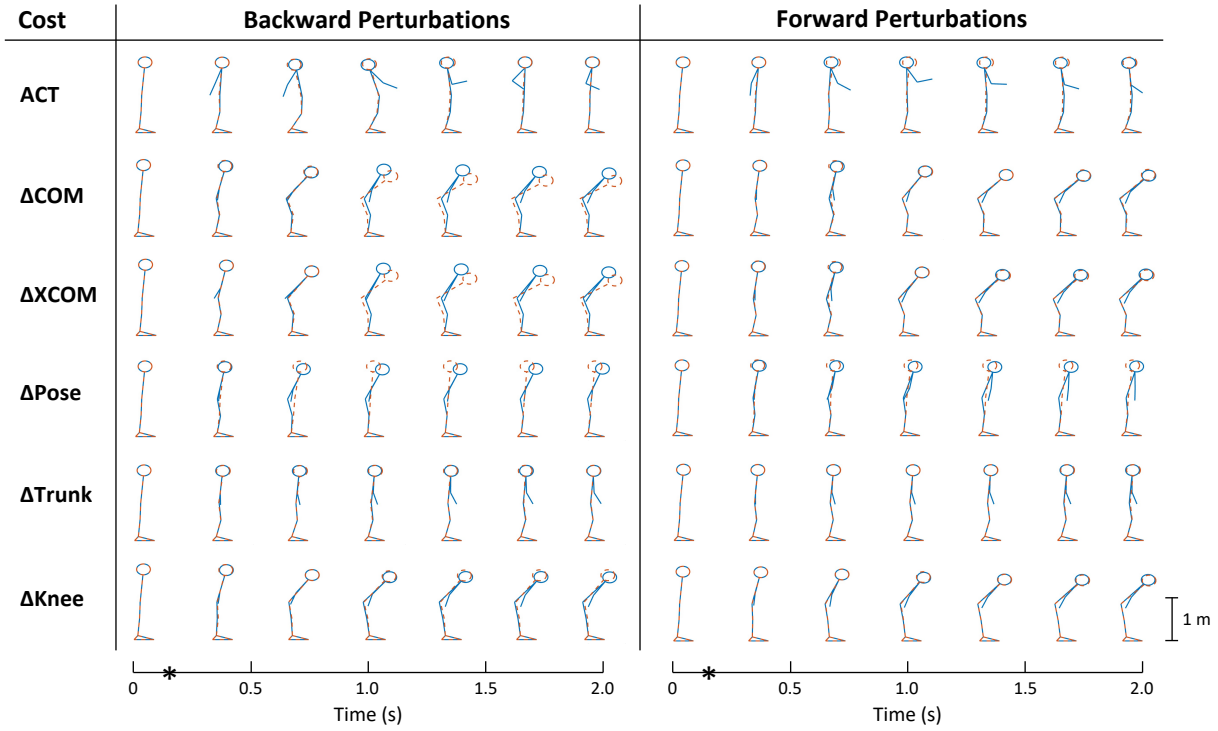


Figure 3.13: Simulated postural responses following backward (left, initial fall forward) and forward (right, initial fall backward) support-surface perturbations with the arm joints locked (dotted figure) or free (solid figure). Responses were generated using the six optimality criteria shown. Perturbation initiation is marked by * on the time axis.

a hip strategy following backward perturbations. In the current study, without additional regulatory criteria [344], the NMPC became reliant on passive MTG terms and moved the model through awkward poses rather than using a defined hip strategy. Formulations using net joint torques may produce more reasonable behaviours as factors like parallel elastic tension and injury limits are considered.

Following a forward perturbation, both ACT and ΔTrunk criteria produced peak backward XCOM excursions relative to the heel (-5.0 to -1.7 cm) that were similar to experimental values using the same perturbation (-4.8 cm [174]). Conversely, XCOM excursions following backward perturbations were consistently underestimated using NMPC, though variables like peak forward trunk pitch did match those in the literature (e.g. -50 to -40° [344]) despite differences in perturbation size. These predictions were best when using

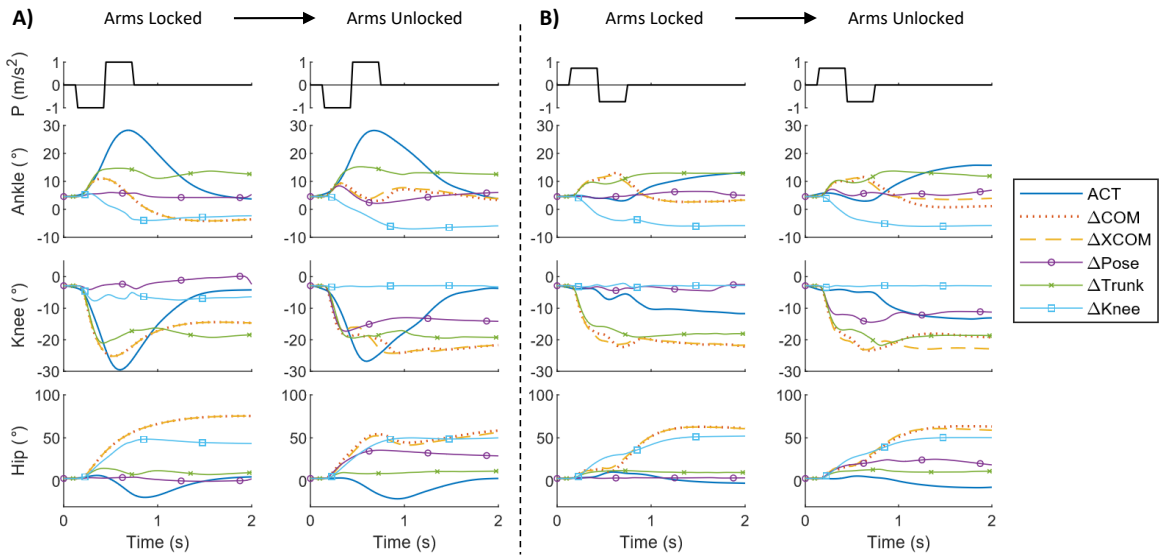


Figure 3.14: Simulated postural responses following A) backward and B) forward support-surface perturbations with the arm joints locked or free. Responses were generated using the six optimality criteria shown. Note: ankle $> 0°$ during dorsiflexion, knee $> 0°$ during extension, hip $> 0°$ during flexion.

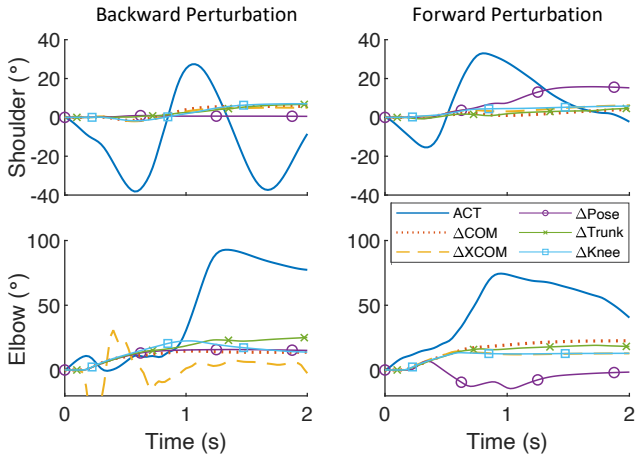


Figure 3.15: . Simulated upper limb responses following forward and backward perturbations. Responses were generated using one of the six optimality criteria shown. Note: both shoulder and elbow are $> 0°$ during flexion.

Table 3.1: Evaluated Logarithmic Cost Ratios (CR). Bolded values indicate negative CRs, i.e., using the upper limbs further reduced the cost of balancing according to the associated criteria.

	Joint-Space			COM-Space		Effort
Dir.	ΔPose	ΔKnee	ΔTrunk	ΔCOM	ΔXCOM	ACT
B	2.13	**-2.61**	**-2.54**	**-1.14**	**-0.82**	**-0.05**
F	2.38	**-0.61**	0.99	0.46	0.04	0.05

ΔCOM or ΔXCOM; ΔKnee provided a markedly close match also (-38.2° with AL). It is likely that using a weighted combination of multiple criteria (e.g. ACT + ΔCOM) would correct these reported prediction errors [202, 298, 344].

Unlocking the arm joints had a handful of interesting effects on the simulated postural kinematics (Fig. 3.13 and Fig. 3.14). Most notably, the ΔPose-predicted balance strategy shifted from stiffening to using pronounced flexion of the knee and hip (occurred for both perturbation directions). Additionally, having the arms locked appeared to make it easier for the NMPC to minimize knee or trunk deviations, as reflected by the CRs in Table 3.1. Most of the observed effects took place in the backward perturbation condition (Table 3.1). For example, unlocking the arms while using ΔCOM and ΔXCOM modified the predicted ankle/hip trajectories in said condition only; no obvious changes exist for the forward condition. In general, unlocking the arms had less of an impact on the forward perturbation responses than anticipated according to experimental observations [85, 168]. This further suggests some element of a "startle" response in terms of motion of the arms following a balance perturbation.

The compensatory arm responses generated for each combination of Lagrangian and perturbation direction are also summarized in Fig. 3.13 and Fig. 3.15. Extremely similar patterns were observed for ΔKnee, ΔTrunk, ΔCOM, ΔXCOM: a slow drift towards flexion in shoulder and elbow following each perturbation. This lack of sizable arm motion could be due to numerous factors, e.g. less arm movement is optimal, local NLP methods and restrictive initial guess not capturing global optimum, too small a perturbation, and the need for a 3D model to capture phenomena [85, 168]. Unfortunately, cases like ΔKnee, where the CR < 0 but there is no unique arm response, make it difficult to assess whether CR improvements were purely coincidental. The exaggerated arm responses observed when

using the ACT criteria is consistent with the corresponding lower-limb responses; an oscillatory behaviour is particularly noticeable in the shoulder. Interestingly, ΔPose had unique arm motions paired with the corresponding *flexed* postural strategy, particularly following forward perturbations. The shoulders were slowly flexed forward and the elbow was maintained nearly straight, i.e. counterbalancing. However, the CR for ΔPose was positive, which suggests that the different control strategy emerged as a byproduct of the relative location of the initial guess within the AF and AL search spaces.

In summary, few cost functions within the NMPC scheme, e.g. ΔPose and ACT, generated substantial compensatory arm movements in a planar biomechanical model of human balance recovery. There are various assumptions, limitations and potential future directions for the current study. Neural delays, notably during 80-130 ms following the perturbation [50, 158, 344], weren't considered to keep the current NMPC iteration simple; future iterations will add delays to improve fidelity. Friction was not considered within the domain of feasibility for balanced posture; though during simulations, the tangential ground reaction force never exceeded a reasonable dry friction threshold (coefficient = 0.20, [264]). It was assumed within the NMPC that the CNS formulates the control problem primarily through Lagrangian terms. The addition of Mayer terms to the embedded problem, as well as any Lagrangian criteria not examined herein, would require further research. Additionally, given the infrequent use of MPC in biomechanical predictive simulations, further system identification may be beneficial in providing direction to biomechanics researchers during MPC design [26, 240]. It is possible that this process would naturally require establishment of the proper optimal control problem formulation.

Chapter 4

Dynamic Modeling of Lower-Limb Exoskeletons

4.1 Planar Model of Biomechatronic Devices

In this chapter, the approach to the general design of a multibody dynamic model for capturing the dynamics of robotic lower-limb exoskeletons is outlined. Subsequently, this mechatronic model is integrated with a human-end user model (Chapter 5) to conduct simulations of integrated human-exoskeleton balance recovery (Chapter 6). It is worth noting that while this model can be adapted to accommodate a wide range of lower-limb exoskeletons operating primarily within the sagittal plane, the primary emphasis was on modeling the dynamics of the EXO-H3 exoskeleton by Technaid® (Spain).

4.1.1 Multibody System Dynamics

To obtain equations of motion for a multibody dynamic lower-limb exoskeleton model, the topology of the rigid bodies from which it is constructed must first be consider (Fig. 4.1). Concisely, the Technaid EXO-H3 is comprised of bilateral leg modules, along with a rigid trunk segment. Each of these segments can be further subdivided into a number of rigid bodies welded together. For example, the trunk segment on the EXO-H3 can be broken down into 3 sub-segments: bilateral orthoses (a soft shell for the user's trunk to fit into), an

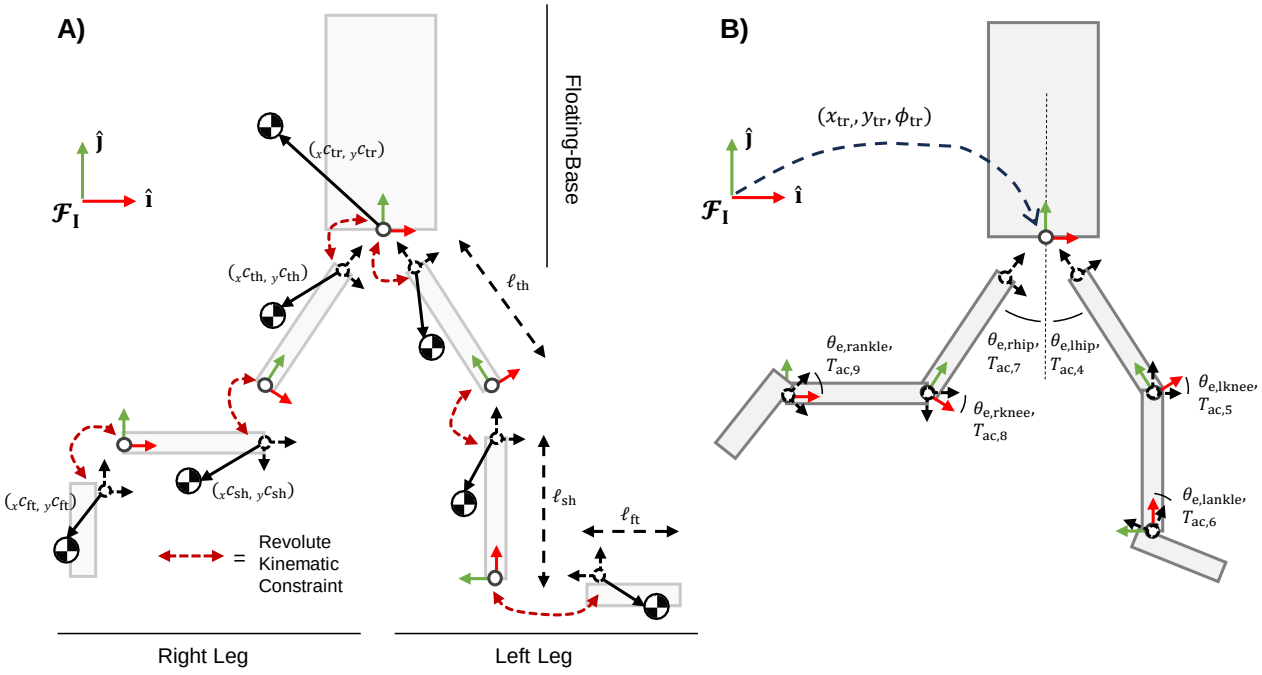


Figure 4.1: **A**) Schematic of the planar floating-base lower-limb exoskeleton model highlighting individual segment COM positions (and respective reference frames), geometry, and the location of revolute joints, i.e., where revolute kinematic constraints were imposed [141]. **B**) Schematic highlighting the nine multibody exosekeleton model degrees of freedom (DOF; 3 floating-base coordinates and 6 joint coordinates) and the location of applied actuator torques $T_{\mathrm{ac},i}$.

assistive attachment connecting right and left leg modules to the orthoses, and a battery fixed to the posterior aspect of the assistive attachment. In the simplified definition of each leg module, each leg consists of three rigid segments connected in series by revolute joints: a thigh, shank, and foot. The revolute joints connecting each segment accordingly are denoted anatomically as the hip, knee, and ankle joint. In reality, these leg modules encompass a range of interconnected elements, e.g., links between joint centers, actuator housings, as well as straps and cuffs that secure the user to the device and introduce additional inertial and gravitational effects (see Fig. 4.2 for example). Similarly, any speed-reduction within the actuators will transmit the input inertia of the actuators (such as the MOI of the rotor and wave generator in strain-wave gearing) back to the end-user, proportional to the square of the gear ratio [335, 336]. All of these considerations must be

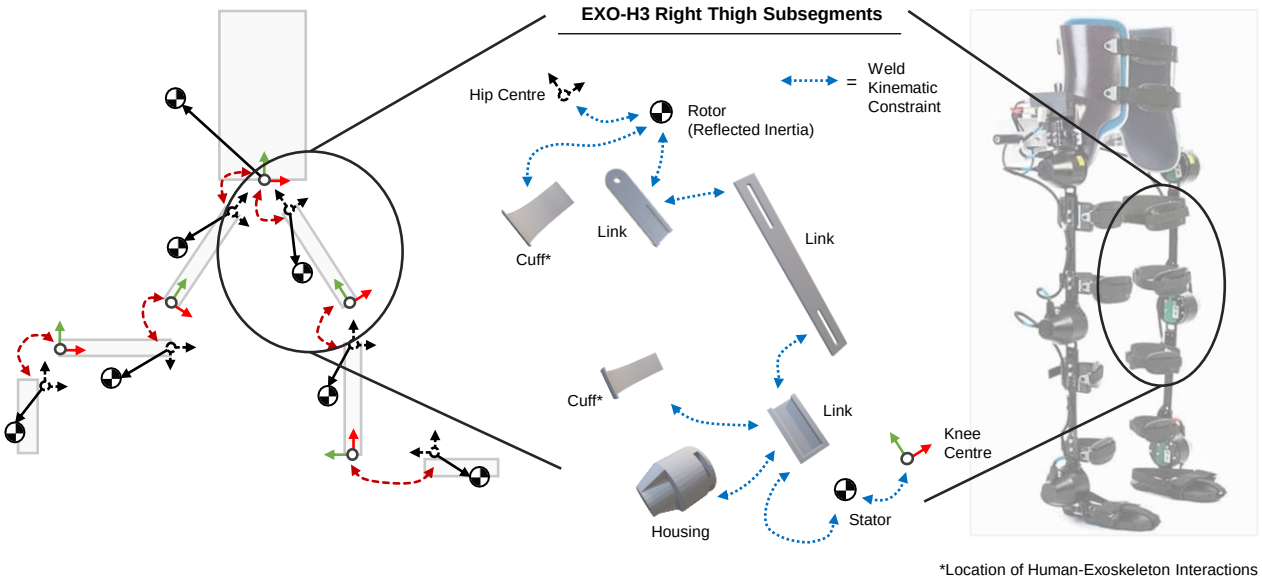


Figure 4.2: Example of the construction of the EXO-H3 thigh rigid body segment from a combination of welded rigid bodies, each shown by their custom CAD approximation developed for this dissertation, e.g., cuffs, rotor/stator/gearing, etc. Weld constraint topology is highlighted through the use of dashed blue arrows, i.e., the rotor/gearing output shaft is welded to a link that is subsequently welded to another adjustable link as well as a cuff element. These cuff elements are designed to interact with the human end-user. An image of the EXO-H3, obtained from the owner's manual (Technaid, Spain) is shown to the right for reference.

taken into account during the multibody design process.

The mathematical framework for constructing a multibody dynamic model according on the rigid body topology described above begins with a general floating-base formulation suited for bipedal/humanoid systems, i.e., we connect the device's hip joint center (expressed in the trunk-fixed frame) to the inertial frame via planar joint [134, 138, 281]. To elaborate further, we introduce the subsequent set of generalized coordinates that define the lower-limb exoskeleton's configuration:

$$\mathbf{q}_{\mathrm{e}}(t) = \{x_{\mathrm{tr}}(t), y_{\mathrm{tr}}(t), \phi_{\mathrm{tr}}(t), \theta_{\mathrm{e,lhip}}(t), \theta_{\mathrm{e,lknee}}(t), \theta_{\mathrm{e,lankle}}(t), \theta_{\mathrm{e,rhip}}(t), \theta_{\mathrm{e,rknee}}(t), \theta_{\mathrm{e,rankle}}(t)\}^{\intercal} \tag{4.1}$$

$$= \{\mathbf{q}_{\mathrm{e,fb}}, \mathbf{q}_{\mathrm{e,ll}}, \mathbf{q}_{\mathrm{e,rl}}\}^{\intercal} \in \mathcal{Q}_{\mathrm{e}}, \quad \mathcal{Q}_{\mathrm{e}} \subseteq \mathbb{R}^{9} \tag{4.2}$$

where $\{x_{\mathrm{tr}}(t), y_{\mathrm{tr}}(t), \phi_{\mathrm{tr}}(t)\}^{\intercal} \in \mathbb{R}^{3\times 1}$ represent the floating base coordinates, i.e., the hip

Table 4.1: EXO-H3 Joint Ranges of Motion.

	Hip	Knee	Ankle
Maximum (°)	105	5	30
Minimum (°)	-30	-105	-30

center's position in the trunk-fixed frame (relative to the inertial frame) in addition to the pitch angle of the trunk segment. Because the EXO-H3 does not feature anatomical DOF like hip ab-/adduction, we do not consider a $z_{\text{tr}}(t)$ coordinate in addition to rotations of the trunk outside the sagittal plane. Inclusion of these features would require redefinition of the floating base coordinates using either three Euler angles or four Euler parameters, i.e., quaternions. Joint coordinates (revolute) are defined for the left (ll) and right leg (rl) as $\mathbf{q}_{\text{e,ll}} \in \mathcal{Q}_{\text{el}}$ and $\mathbf{q}_{\text{e,rl}} \in \mathcal{Q}_{\text{el}}$, where $\mathcal{Q}_{\text{el}} \subseteq \mathbb{R}^3$ signifies the joint angle space constraints attributed to mechanical stops in the exoskeleton hardware (see Table 4.1 for range of motion values pertaining to the EXO-H3). The right and left leg modules share the same generalized coordinate space $\mathcal{Q}_{\text{el}}$ as they share identical actuators.

During assembling of the system topology in MapleSim, it was assumed that the leg modules were manufactured and setup identically, i.e., same hardware and materials, segment lengths and mass distribution. With this assumption, the floating multibody dynamic equations are obtained as

$$\begin{bmatrix} \mathbf{M}_{\text{BB}}(\mathbf{q}_{\text{e,fb}}, \mathbf{q}_{\text{e,ll}}, \mathbf{q}_{\text{e,rl}}) & \mathbf{M}_{\text{JB}}(\mathbf{q}_{\text{e,fb}}, \mathbf{q}_{\text{e,ll}}) & \mathbf{M}_{\text{JB}}(\mathbf{q}_{\text{e,fb}}, \mathbf{q}_{\text{e,rl}}) \\ \mathbf{M}_{\text{JB}}^{\intercal}(\mathbf{q}_{\text{e,fb}}, \mathbf{q}_{\text{e,ll}}) & \mathbf{M}_{\text{JJ}}(\mathbf{q}_{\text{e,ll}}) & \mathbf{0} \\ \mathbf{M}_{\text{JB}}^{\intercal}(\mathbf{q}_{\text{e,fb}}, \mathbf{q}_{\text{e,rl}}) & \mathbf{0} & \mathbf{M}_{\text{JJ}}(\mathbf{q}_{\text{e,rl}}) \end{bmatrix} \begin{Bmatrix} \ddot{\mathbf{q}}_{\text{e,fb}} \\ \ddot{\mathbf{q}}_{\text{e,ll}} \\ \ddot{\mathbf{q}}_{\text{e,rl}} \end{Bmatrix}$$
$$= \begin{Bmatrix} \boldsymbol{\Gamma}_{\text{BB}}(\mathbf{q}_{\text{e,fb}}, \mathbf{q}_{\text{e,ll}}, \mathbf{q}_{\text{e,rl}}, \dot{\mathbf{q}}_{\text{e,fb}}, \dot{\mathbf{q}}_{\text{e,ll}}, \dot{\mathbf{q}}_{\text{e,rl}}) \\ \boldsymbol{\Gamma}_{\text{JB}}(\mathbf{q}_{\text{e,fb}}, \mathbf{q}_{\text{e,ll}}, \dot{\mathbf{q}}_{\text{e,fb}}, \dot{\mathbf{q}}_{\text{e,ll}}) \\ \boldsymbol{\Gamma}_{\text{JB}}(\mathbf{q}_{\text{e,fb}}, \mathbf{q}_{\text{e,rl}}, \dot{\mathbf{q}}_{\text{e,fb}}, \dot{\mathbf{q}}_{\text{e,rl}}) \end{Bmatrix} + \begin{Bmatrix} \mathbf{0} \\ \boldsymbol{\tau}_{\text{ac}}(\dot{\mathbf{q}}_{\text{e,ll}}) \\ \boldsymbol{\tau}_{\text{ac}}(\dot{\mathbf{q}}_{\text{e,rl}}) \end{Bmatrix} \tag{4.3}$$

where $\mathbf{M}_{\text{BB}} : \mathcal{Q}_{\text{e}} \to \mathbb{R}^{3\times3}$ and $\boldsymbol{\Gamma}_{\text{BB}} : \mathcal{Q}_{\text{e}} \times T_{\mathbf{q}}\mathcal{Q}_{\text{e}} \to \mathbb{R}^{3\times1}$ are the symmetrical mass matrix and nonlinear velocity/gravity-dependent torques/forces for the under-actuated base coordinates [281]. These same terms limited to the exoskeleton leg-joint space include mass matrix $\mathbf{M}_{\text{JJ}} : \mathcal{Q}_{\text{el}} \to \mathbb{R}^{3\times3}$. Terms that couple the dynamics of the base and joint coor-

dinates include $\mathbf{M}_{\text{JB}} : \mathcal{Q}_{\text{el}} \times \mathbb{R}^{3\times 1} \to \mathbb{R}^{3\times 3}$ and $\mathbf{\Gamma}_{\text{JB}} : \mathcal{Q}_{\text{el}} \times T_{\mathbf{q}}\mathcal{Q}_{\text{el}} \times \mathbb{R}^{6\times 1} \to \mathbb{R}^{3\times 1}$ [281]. The function $\boldsymbol{\tau}_{\text{ac}}(\cdot) : T_{\mathbf{q}}\mathcal{Q}_{\text{el}} \to \mathbb{R}^{3\times 1}$ returns a column matrix of torques generated by the hip, knee, and ankle joint actuators in a single leg (actively and passively). To improve readability of these equations, they are further condensed to the form

$$\mathbf{M}_{\text{e}}(\mathbf{q}_{\text{e}}(t))\ddot{\mathbf{q}}_{\text{e}} = \mathbf{\Gamma}_{\text{e}}(\mathbf{q}_{\text{e}}(t), \dot{\mathbf{q}}_{\text{e}}) + \mathbf{T}_{\text{ac}}(\dot{\mathbf{q}}_{\text{e}}) \tag{4.4}$$

where $\mathbf{M}_{\text{e}} : \mathcal{Q}_{\text{e}} \to \mathbb{R}^{9\times 9}$ is the net exoskeleton mass matrix and $\mathbf{\Gamma}_{\text{e}} : \mathcal{Q}_{\text{e}} \times T_{\mathbf{q}}\mathcal{Q}_{\text{e}} \to \mathbb{R}^{9\times 1}$ captures all nonlinear torques and forces resulting from the mass/velocity/position of the exoskeleton rigid bodies in addition to the choice of generalized coordinates. Column matrix $\mathbf{T}_{\text{ac}} : T_{\mathbf{q}}\mathcal{Q}_{\text{e}} \to \mathbb{R}^{9\times 1}$ describes the output of the actuator torques across *the entirety* of the floating-based generalized coordinate space (will not touch $\mathbf{q}_{\text{e,fb}}$).

4.1.2 Electric Actuator Modeling

Each actuator in the EXO-H3 consists of the following components in parallel: a brushless DC motor and strain-wave gearing, i.e., a Harmonic Drive®. The latter allows for high torque amplification (high gear ratio) with relatively little space required for transmission [142, 214, 335, 336], and are thus are often used in assistive devices [214]. As mentioned prior, the MOI of the rotor and gearing's wave generator were amplified by the squared gear ratio [335]; these terms are contained within the exoskeleton mass matrix $\mathbf{M}_{\text{e}}$ under the assumption of a constant gear ratio ($N = 160$). If we say that the motor circuit has relatively low inductance, then the *amplified* motor torque for a given joint can be approximated algebraically from the brushed DC motor equations [261]:

$$\tau_{\text{mtr}}(\dot{\theta}_{\text{o}}) = -\frac{KN}{R}(V(t) + KN\dot{\theta}_{\text{o}}), \quad \dot{\theta}_{\text{o}} = -\frac{\dot{\theta}_{\text{r}}}{N} \tag{4.5}$$

where $V(t)$ is the time-varying voltage across the motor's armature, R and K are the motor's winding resistance and torque constant respectively, $\dot{\theta}_{\text{r}}$ is the angular velocity of the rotor, $\dot{\theta}_{\text{o}}$ is the velocity of the gearing's output shaft and N is the drive's gear ratio. If we state that $\tau_{\text{ideal}} = -KNV(t)/R$, then we can reasonably model the amplified battery-dependent component of the actuator as a single ideal torque generator τ_{ideal} with the remaining term being linear damping resulting from the dissipative counter-electromotive force $-K^2N^2\dot{\theta}_{\text{o}}/R$, i.e., back EMF. As we see in subsequent paragraphs, this damping term, along with others emerging between rotor and stator, can also be simply lumped

into the net joint friction resulting from the gearing. In these regards, it is also quite common in the literature to assume that the motor behaves as an ideal actuator rather than considering the electrical domain in design [59, 134, 169, 214, 261].

Given the use of strain-wave gearing in the Exo-H3, it is important to consider the joint-level impedance resulting from friction between the flexspine (free) and circular spine (fixed) [142, 335, 336]. Adopting the Brown and McPhee [65] velocity-dependent friction model, the friction torque resulting from these interactions can be written as

$$\tau_{\mathrm{f}}(\dot{\theta}_{\mathrm{o}}) = -(\tau_{\mathrm{brk}} - \tau_{\mathrm{c}}) \frac{\frac{\dot{\theta}_{\mathrm{o}}}{\omega_{\mathrm{t}}}}{\frac{1}{4}\left(\frac{\dot{\theta}_{\mathrm{o}}}{\omega_{\mathrm{t}}}\right)^2 + \frac{3}{4}} - \tau_{\mathrm{c}} \tanh\left(4\frac{\dot{\theta}_{\mathrm{o}}}{\omega_{\mathrm{t}}}\right) - \mu_{\mathrm{o}}\dot{\theta}_{\mathrm{o}} \tag{4.6}$$

$$= -\alpha_0 \frac{\frac{\dot{\theta}_{\mathrm{o}}}{\omega_{\mathrm{t}}}}{\frac{1}{4}\left(\frac{\dot{\theta}_{\mathrm{o}}}{\omega_{\mathrm{t}}}\right)^2 + \frac{3}{4}} - \alpha_1 \tanh\left(4\frac{\dot{\theta}_{\mathrm{o}}}{\omega_{\mathrm{t}}}\right) - \alpha_2\dot{\theta}_{\mathrm{o}}, \quad \{\alpha_0, \alpha_1, \alpha_2\} \geq 0 \tag{4.7}$$

where τ_{c} and τ_{brk} represent the Coulomb and breakaway torques arising from dry friction, while μ_{o} is the coefficient of viscous friction. The benefit of using this model is its simple implementation and velocity-dependence, C^2 continuity, and ability to mimic (though not fully replicate) static friction ("stiction") forces/torques [269]. Note that (4.7) contains the form of the friction equation that was utilized in parameter identification; (τ_{f} is linear with respect to α_0, α_1 and α_2 (see Chapter 4.2).

The final equation for the actuator torque at a *single* joint was simply the addition of the friction and amplified motor torque:

$$\tau_{\mathrm{ac}}(\dot{\theta}_{\mathrm{o}}) = \tau_{\mathrm{f}}(\dot{\theta}_{\mathrm{o}}) + \tau_{\mathrm{mtr}}(\dot{\theta}_{\mathrm{o}}). \tag{4.8}$$

The final definition for the actuator torque function for a single leg module $\boldsymbol{\tau}_{\mathrm{ac}}$ was therefore

$$\boldsymbol{\tau}_{\mathrm{ac}}(\boldsymbol{\omega}) = \begin{Bmatrix} \tau_{\mathrm{ac}}(\omega_{\mathrm{hip}}) \\ \tau_{\mathrm{ac}}(\omega_{\mathrm{knee}}) \\ \tau_{\mathrm{ac}}(\omega_{\mathrm{ankle}}) \end{Bmatrix} \tag{4.9}$$

where $\boldsymbol{\omega} = \{\omega_{\mathrm{hip}}, \omega_{\mathrm{knee}}, \omega_{\mathrm{ankle}}\}^{\intercal}$ is the vector of joint velocities for a given leg, e.g., $\dot{\mathbf{q}}_{\mathrm{e,ll}}$ and $\dot{\mathbf{q}}_{\mathrm{e,rl}}$ ($\omega = d\theta/dt$ for a given joint). Table 4.2 contains the actuator parameters that were provided by the EXO-H3 manufacturer (Technaid). Estimates of actuator friction parameters were not supplied outside of a reported 88% maximum efficiency for the motor.

Table 4.2: EXO-H3 Actuator Parameters Provided by Manufacturer (Technaid, Spain)

Description	Value
DC Motor	
Nominal Voltage	19 V
Resistance (R)	0.207 Ω
Torque Constant (K)	0.0375 Nms/rad
Rotor Moment of Inertia	4.40×10^{-6} kg m^2
Strain-Wave Gearing	
Mass	0.24 kg
Gear Ratio (N)	160
Moment of Inertia	2.60×10^{-4} kg m^2

4.2 Identification of Multibody Dynamic and Actuator Parameters

4.2.1 Background

With the generalized lower-limb exoskeleton multibody model developed, we now transition into discussions surrounding identification of the dynamic parameters that describe the system of interest. As mentioned prior, in the current dissertation, the system of interest is the Technaid EXO-H3. If we desire to build model-based balance control architectures that can reliably and precisely manipulate the biomechatronic system (see Chapter 6), we must first obtain a reasonable estimate of the system's uncertain parameters; however, this is not without challenges. Likewise, if we wish to generate *what-if* simulations of the combined human-exoskeleton system prior to running in-person tests [169, 172, 226, 246, 295], then device parameters are also required.

The recent literature review by Wu et al. [365] provides an overview of the primary categories of dynamic parameter identification methods: i) physical experiments; ii) computer-aided design (CAD); iii) input/output optimization/identification. The first category of methods typically involves disassembly of the robot and the use of specialized measuring tools to obtain features like rigid body mass and mass distribution (for COM and MOI

estimates). This category of methods can also be extended to phenomena like actuator friction identification [137, 142]. The second category involves estimating the parameters of links (and other rigid bodies) that the robot is comprised of by recreating the 3D geometry of said body(ies) in computer software. By making assumptions regarding material density in the body, its mass, COM location, and MOI can be estimated. In some ways, this category can have overlap with the first category, i.e., using physical measurements of device geometry to inform CAD decisions. The final category iii) involves the use of optimization techniques where measured robot kinematics and/or applied torques are paired with the device mathematical model to obtain optimal parameter values. According to Wu et al. [365], this third category "can achieve high accuracy in identification, and the measurement process is relatively straightforward". It can also yield superior results compared to the first two categories of parameter identification as the system model equations of interest can be used explicitly in the process; however, this assumes that reliable sensor data is available.

In the literature, there are relatively fewer discussions on forward dynamics approaches to parameter identification, especially if on-line dual-estimation methods are not neglected [124, 125, 181, 226, 260, 292, 310, 347, 367]. Conversely to inverse dynamics methods, which only require algebraic manipulations of the underlying mathematical model, forward dynamics methods require identification of sensitivity equations of motion that must be solved alongside system ODEs. These sensitivity equations describe how the generalized positions and velocities vary with perturbations to the dynamic parameter values. Rather than identify according to measurement residuals in the simulated applied torques, the simulated position-error is used. Serban and Freeman [300] discussed the details of this sensitivity analysis when applied to multibody system dynamics. The authors encountered issues with identifiability as seen with the redundant parameters in inverse dynamics methods, i.e., whether different parameters explain similar variance in the measured position data. It is typical in forward dynamics identification schemes to have system equations that are nonlinear in the parameters. Because of issues with identifiability, Vyasarayani et al. [347] merged the methods in [300] with a homotopy approach intended to improve convergence to a global minimum [151]. Ghannadi et al. [124] later adapted this homotopy method successively for mutlibody systems featuring significant gearing backlash discontinuities.

As the forward dynamics approach requires the investigator to solve both the ODEs and sensitivity equations concurrently with the dynamic parameters during identification,

it may not always be computationally tractable, especially for experimental trajectories that span a large time interval. Alternatively, state estimation algorithms (usually lumped with on-line identification methods [365]), can truncate the problem by relying on single time-step iterations rather than using all measurements at once [181]. In general, these approaches utilize a sequence of measurements taken over time, which may be corrupted by statistical noise, and at each time-step (sampling instant), they generate estimations for hidden system variables, such as states, inputs, and/or parameters [310]. By approximating and refining a probability distribution at each time-step that reasonably describes the change in error covariance with each instance of variable estimation, the algorithm is theoretically expected to produce a more-accurate variable estimation [310]. The recent review by Naya et al. [260] provides a detailed description of how the state-estimation algorithms can be used with both constrained and unconstrained multibody systems. In particular, the authors describe the use of dual-estimation, i.e., estimating system states and parameters simultaneously. To date, the majority of on-line state estimation methods used in parameter identification involve variations of the Kalman filter [181, 189, 292, 310], e.g the extended Kalman filter in [292] and unscented Kalman filter in [292]. To our knowledge, few have made use of moving horizon estimation methods for identification [310], especially in the case of nonlinear systems with constraints.

Thus, in the current chapter, the primary goals were as follows:

1. Physical and experimental identification of EXO-H3 parameters using physical measurements and dynamometry [169].

2. Expand experimental design methods of Swevers et al. [318] and Gautier [118, 120] that provide exciting trajectories for dynamic parameter identification; apply these methods to the dynamics of a leg in a commercial lower-limb exoskeleton.

3. Assess EXO-H3 position-control feature with novel test-bench designed and built by Christian Mele [241] (supervisor: Prof. James Tung) in attaining desired experimental trajectories. This was also an opportunity to validate the onboard EXO-H3 rotary encoders using 3D motion capture (Vicon, CO, USA).

4. Compare performance of parameters identified via physical experiments against inverse and forward dynamics-obtained parameters in predictive simulations of both the experimental/training data set and a separate validation data (predictive simulations involved both inverse and forward dynamics).

A novel nonlinear moving horizon estimation (MHE) approach, similar to on-line methods described by Wu et al. [310], was also designed for the current study [260]. However, as results are only preliminary at the time of writing this dissertation, we refer the reader to Appendix I for further details and results.

4.2.2 Physical Measurements and Computer-Aided Design

The first parameter identification experiment conducted for the EXO-H3 utilized direct and indirect physical measurements in addition to a computer aided design (CAD) approach (the first two approaches discussed by Wu et al. [365]). First, the EXO-H3 was disassembled to an extent permissible by the manufacturer, i.e., within limits of warranty; this allowed us to isolate subsegments and clusters of subsegments that could be used to characterize the trunk, thigh, shank, and foot segments described in Fig. 4.1. Refer to Fig. 4.2 for an example of how subsegments were defined to estimate the thigh inertial parameters. The components we were able to isolate in practice, described also in Tables 4.3 and 4.4, were as follows:

1. Bilateral hip (a), knee (b), and ankle (c) joint modules (6 total; each contains an electric actuator);
2. Primary links: links connecting neighboring joint modules (4 total);
3. Foot pads with ankle-attachment links (2 total);
4. Trunk orthosis/shell (2 total; left and right sides);
5. Assistive hip attachment (1 total; connects right and left leg modules to the trunk orthosis);
6. Removable lithium-ion battery (1 total; fixed to posterior aspect of assistive hip attachment).

The mass of each component listed was measured using a scale calibrated up to 4 kg. To approximate the body-fixed sagittal MOI as well as each component's COM position, a calibrated MOI tester was utilized (MOI-025-004, Inertia Dynamics, USA). Several MOIs were recorded for each body; in between each measurement the body was shifted slightly

to measure the MOI about a different parallel axis. Based on parallel axis theorem, it was assumed that the position of the body where the MOI was lowest was the best estimate for local COM position. The measured MOI about the COM for each component are listed in Tables 4.3 and 4.4. Moreover, position of the battery COM, hip attachment COM, and trunk orthosis COM within the trunk-fixed reference frame (i.e., where these components would sit during operation, see Fig 4.1), were obtained using measurements taken after fitting the EXO-H3 to an individual 1.80 m in height alongside the component COM estimates made using the MOI tester.

With physical measurements of the listed components in place, CAD-based approximations were developed to estimate dynamic parameters for individual subsegments within the components that we were able to individually extract from the EXO-H3. This step was necessary in order to find the dynamic parameters highlighted in Fig. 4.1A). To expand, we received STL files of the EXO-H3 from the device manufacturer, Technaid. Using geometric measurements from our specific version of the EXO-H3 device along with the provided STLs, we then manually developed a new CAD model for **all** subsegments identified (AutoCAD 2021, Autodesk). Obtaining these refined CAD models allowed us to obtain volumetric parameters for each subsegment with geometry that closer mimicked the measurements from our particular device. In software, it was assumed that each body was of constant density estimated (when possible) from the measured mass and CAD volume; COM positions estimated from CAD were used to corroborate the COM estimations made using the MOI tester. Subsegment MOIs relative to the COM were estimated using using the geometric radius of gyration. Parameters related to motor/gearing inertia (MOI and mass) were obtained from manufacturer information tables, e.g., Maxon and Harmonic Drive actuation systems (see Table 4.2). For some subsegments, e.g., primary links, we were able to directly validate the CAD-based parameters with the physical measurements. For others, like the link(s) fixed to the actuator output shaft, alternative means were necessary. In this case, the physically measured component that contained the subsegment(s) of interest was constructed using the individual subsegment CAD models. The collective subsegment parameters were then tuned such that they were close to CAD or manufacturer inferred values, whilst producing a component parameters that match the physical measurements.

As a final note, the friction parameters resulting from the energy dissipation in the actuator (both friction and back-EMF) were estimated using a commercial dynamometer (Biodex System 4 Pro, Biodex, USA). The Biodex was responsible for back-driving the

Table 4.3: EXO-H3 isolated joint module and foot segment components, final physical measurements (mass and MOI about the COM), and name of subsegments that the component is comprised of. Note that stator/rotor links are links specifically connected to the fixed/output shaft of the actuator respectively. Masses were measured via scale (calibrated to 4 kg), while MOIs were measured using an MOI tester (MOI-025-004, Inertia Dynamics, USA).

Component	Parameter	Value	Subsegments
1a) Hip Joint Module	Mass (kg)	1.6×10^{0}	i) Hip Stator Link
	MOI (kg m^2)	6.3×10^{-3}	ii) Hip Actuator Housing
			iii) Stator
			iv) Rotor + Gearing
			v) Rotor Link
			vi) Proximal Thigh Cuff
1b) Knee Joint Module	Mass (kg)	1.6×10^{0}	i) Stator Link
	MOI (kg m^2)	6.5×10^{-3}	ii) Distal Thigh Cuff
			iii) Knee Actuator Housing
			iv) Stator
			v) Rotor and Gearing
			vi) Rotor Link
			vii) Proximal Shank Cuff
1c) Ankle Joint Module	Mass (kg)	1.4×10^{0}	i) Stator Link
	MOI (kg m^2)	2.3×10^{-3}	ii) Distal Shank Cuff
			iii) Ankle Actuator Housing
			iv) Stator
			v) Rotor + Gearing
			vi) Ankle Rotor Link
3) Foot Module	Mass (kg)	6.5×10^{-1}	i) Foot Pad
	MOI (kg m^2)	3.8×10^{-3}	ii) Foot Link

exoskeleton knee joint while the device received no external power. The EXO-H3 was fixed to the dynamometer seat and motion of the knee joint was isolated and recorded at 100 Hz. The knee was flexed/extended at a constant velocity $\omega_{\text{test}} \in \{2, 4, 10, 20, 45\}$ deg s^{-1} over the interval $\theta \in [0°, -90°]$, where the knee was fully extended at 0° (see Fig. 4.1B). The

Table 4.4: EXO-H3 isolated subsegment components and final physical measurements (mass and MOI about the COM). As noted in the rightmost column of the table, each component listed below represents a single subsegment within the EXO-H3 CAD and rigid body analysis (unlike the components listed in Table 4.3). Masses were measured via scale (calibrated to 4 kg), while MOIs were measured using an MOI tester (MOI-025-004, Inertia Dynamics, USA).

Component	Parameter	Value	Subsegments
2) Primary Link	Mass (kg)	1.2×10^{-1}	Primary Link
	MOI (kg m^2)	7.2×10^{-4}	
4) Trunk Orthosis	Mass (kg)	5.8×10^{-1}	Trunk Orthosis
	MOI (kg m^2)	7.2×10^{-3}	
5) Hip Attachment	Mass (kg)	1.4×10^{0}	Hip Attachment
	MOI (kg m^2)	3.4×10^{-3}	
6) Battery	Mass (kg)	2.8×10^{0}	Battery
	MOI (kg m^2)	4.6×10^{-3}	

Table 4.5: EXO-H3 subsegments, shown in Tables 4.3 and 4.4, assigned to each of the trunk, thigh, shank, and foot segments defined in Fig. 4.1.

Lower-Limb Exoskeleton Model Segment			
Trunk	Thigh	Shank	Foot
- Trunk Orthosis (×2)	- Rotor + Gearing	- Rotor + Gearing	- Rotor + Gearing
- Hip Attachment	- Rotor Link	- Rotor Link	- Ankle Rotor Link
- Battery	- Proximal Thigh Cuff	- Proximal Shank Cuff	- Foot Link
- Hip Stator Link (×2)	- Primary Link	- Primary Link	- Foot Pad
- Hip Actuator Housing (×2)	- Distal Thigh Cuff	- Distal Shank Cuff	
- Stator (×2)	- Stator Link	- Stator Link	
	- Knee Actuator Housing	- Ankle Actuator Housing	
	- Stator	- Stator	

applied torques recorded for each velocity condition were windowed over periods of constant velocity and then filtered using a zero-lag dual-pass filter (2$^{\text{nd}}$ order low-pass Butterworth,

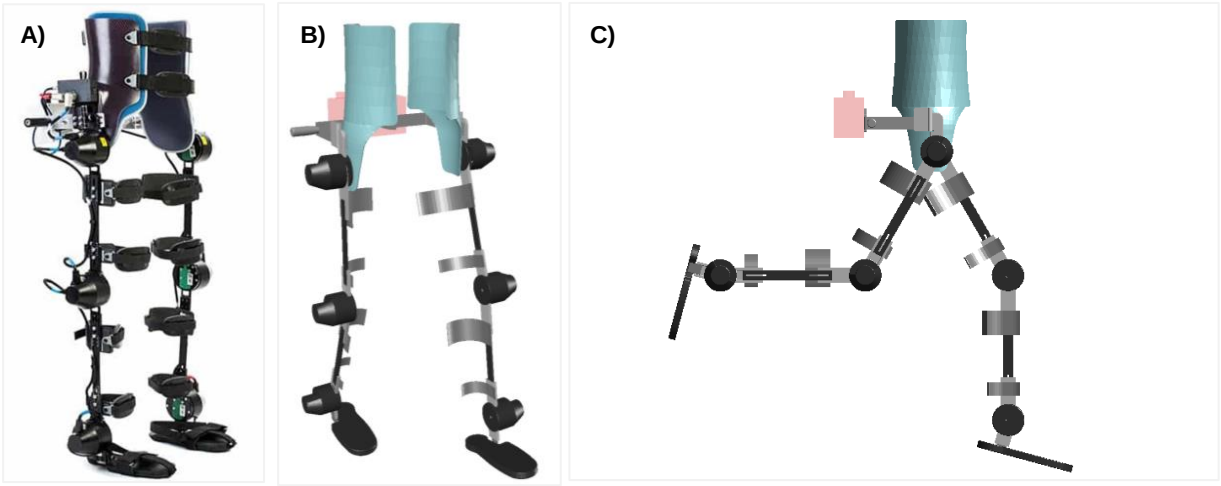


Figure 4.3: **A)** Image of the Technaid EXO-H3 obtained from their owner's manual (Technaid, Spain) and **B)** the custom CAD model of the Technaid EXO-H3 developed for this dissertation. This CAD model was created using a combination of physical measurements taken by the current author (via digital calipers) along with some existing .stl files of EXO-H3 component models provided by the manufacturer (Technaid). In **C)**, the CAD model is shown in the pose displayed in the earlier device schematics (Fig. 4.1).

cut-off = 20 Hz). Components of the remaining constant-velocity torques due to gravity were subsequently removed from the processed data using mass/COM parameters identified previously. A calibration trial using the dynamometer attachment alone was recorded prior to testing with the exoskeleton to remove its associated inertial/gravitational torques from measurements. The nonlinear least squares curve fitting function `lsqnonlin` (MATLAB, USA) was used to fit the final processed torques, across each velocity condition in ω_{test}, to an affine damper function adopted from Equation (4.7):

$$\tau_{\text{f}}(\cdot; \tau_{\text{c}}, \mu_{\text{o}}) = \tau_{\text{c}} - \mu_{\text{o}}\dot{\theta}_{\text{o}} \tag{4.10}$$

where decision variables include τ_{c}, the torque measured at zero speed, i.e., "stiction" torque, and μ_{o}, the coefficient of viscous friction. In the current experiment, the latter parameter was influenced by not only factors like lubrication and temperature, but the motor back EMF as well. For this investigation, we also assumed that that friction behaved identically between the two directions of rotations. To avoid the effects of bias during the curve-fitting process, each velocity condition was provided the same number of data points within the tested range of motion.

4.2.3 Optimizing the Experimental Design for Identification

The second set of parameter identification experiments were focused on using optimization to identify the multibody dynamic parameters specific to the EXO-H3 leg modules. Eventually, the test-bench designed by Christian Mele [241] is used to isolate the leg module during experimental testing (removed ground interactions). The methods used in this section were based on the idea of input-output optimization outlined by Swevers et al. [318], Gautier and Khalil [117, 120], as well as others [282, 365]. In general, this method provides a theoretical basis for identification experimental design according to an inverse dynamics mathematical model. Robot kinematic trajectories are selected/tested according to whether they maximize the "excitation" of the dynamic parameters, i.e., estimates of dynamic parameters are in theory less sensitive when using employing these trajectories with a set of minimal parameters [306]. Therefore, this framework suggests that utilizing optimized kinematic trajectories in identification experiments provides a better understanding of which individual parameter contributes to the variance in the experimental applied torque signals.

Identification Experiment Design via Trajectory Optimization

The trajectory optimization approach for parameter identification required the inverse dynamics equations in Equation (4.4) to be rewritten so as to isolate left leg dynamics (all other bodies held static); the left leg was fixed at the hip joint and behaved like a typical triple pendulum. For ease of analysis, the equations were also transferred to the segment-angle space $\boldsymbol{\phi}(t) = \{\phi_{\text{th}}(t), \phi_{\text{sh}}(t), \phi_{\text{ft}}(t)\}^{\intercal} \in \mathbb{R}^{3\times 1}$, i.e., the angles of the left thigh, shank, and foot segment with respect to the vertical of the inertial-frame $\mathcal{F}_{\text{I}}$ (see Fig. 4.1), and were written in parameter-linear form [118]:

$$\tilde{\boldsymbol{\tau}}_{\text{mtr}} = \boldsymbol{\Lambda}_{\text{obs}}(\boldsymbol{\phi}, \dot{\boldsymbol{\phi}}, \ddot{\boldsymbol{\phi}})\mathbf{p} \tag{4.11}$$

where $\boldsymbol{\Lambda}_{\text{obs}} : \mathbb{R}^{9\times 1} \rightarrow \mathbb{R}^{3\times p}$ (i.e., the observation matrix) maps the full set of EXO-H3 minimal parameters $\mathbf{p} \in \mathbb{R}^{p\times 1}$ to segment motor torques $\tilde{\boldsymbol{\tau}}_{\text{mtr}} \in \mathbb{R}^{3\times 1}$. Since the equations were written with respect to segment angles, the applied torques included actuator torques applied to proximal and distal segment ends (segment motor torques). Parameter column-matrix $\mathbf{p} = \{\mathbf{p}_{\text{Md}}, \mathbf{p}_{\text{Mod}}, \mathbf{p}_{\text{g}}, \mathbf{p}_{\text{f}}\}^{\intercal}$ included inertial parameters found along the diagonal of the mass matrix ($\mathbf{p}_{\text{Md}}$), inertial parameters found elsewhere ($\mathbf{p}_{\text{Mod}}$), parameters describing

the effects of conservative forces ($\mathbf{p}_\text{g}$), and friction parameters from Equation (4.7) ($\mathbf{p}_\text{f}$). Please refer to Appendix G for a detailed derivation of the minimal parameter form of the exoskeleton leg equations of motion.

With the linear-parameter multibody system dynamics, we summarize the process of obtaining optimized experimental kinematic trajectories for parameter identification. First, a method of trajectory parameterization must be defined. While methods like Beziér control point and B-spline parameterization exist (see Chapter 3 and [244, 282]), for convenience, we instead elected to use the simpler Fourier series parameterization proposed by Swevers et al. [318]. These authors provide a great deal of rationale for their use, e.g., signal periodicity reducing spectral leakage, time-series averaging for noise covariance estimations, etc. For the current experiments with the EXO-H3, the desired experimental segment angles, angular velocities, and angular accelerations were written as

$$\boldsymbol{\phi}_\text{exp}(t) = \mathbf{s}_0 + \sum_{i=1}^{n}(\mathbf{s}_i \cos(2\pi i T^{-1} t) + \mathbf{d}_i \sin(2\pi i T^{-1} t)) \tag{4.12}$$

$$\dot{\boldsymbol{\phi}}_\text{exp}(t) = \frac{2\pi}{T}\sum_{i=1}^{n}(i\mathbf{d}_i \cos(2\pi i T^{-1} t) - i\mathbf{s}_i \sin(2\pi i T^{-1} t)) \tag{4.13}$$

$$\ddot{\boldsymbol{\phi}}_\text{exp}(t) = -\frac{4\pi^2}{T^2}\sum_{i=1}^{n}(i^2\mathbf{s}_i \cos(2\pi i T^{-1} t)) + i^2\mathbf{d}_i \sin(2\pi i T^{-1} t))) \tag{4.14}$$

where $\mathbf{s}_i \in \mathbb{R}^{3\times 1}$ and $\mathbf{d}_i \in \mathbb{R}^{3\times 1}$ are real-valued coefficients that amplify the iT^{-1} Hz $\boldsymbol{\phi}_\text{exp}$ signal components ($\mathbf{s}_0$ is a stationary 0 Hz component). Variable T represents the signal's total period (length of experiment) and n is the order of Fourier series.

At a single instance in time for $t \in [0, T]$, at best we can measure three segment motor torque values; however, even if we assume identical friction parameters between joints (see Equation (G.24)), we have $p = 18$ minimal parameters to identify resulting in an ill-posed problem. Taking the Moore–Penrose inverse of $\boldsymbol{\Lambda}_\text{obs}$, one can obtain a least-squares estimation of $\mathbf{p}$ from $\tilde{\boldsymbol{\tau}}_\text{mtr}$, however, the quality of the solution will be poor and sensitive to noise. Instead, we can obtain an improved least-squares estimation of the parameters $\mathbf{p}$ by sampling the system over multiple instances [282, 318], i.e., obtain the value of $\mathbf{p}$ that minimizes the expression

$$\sum_{k=1}^{N_\text{s}} \|\tilde{\boldsymbol{\tau}}_\text{mtr}[k] - \tilde{\boldsymbol{\tau}}_\text{exp}[k]\|^2_{\mathbf{I}_{3\times 3}} = \sum_{k=1}^{N_\text{s}} \|\boldsymbol{\Lambda}_\text{obs}[k]\mathbf{p} - \tilde{\boldsymbol{\tau}}_\text{exp}[k]\|^2_{\mathbf{I}_{3\times 3}} \tag{4.15}$$

where k is the discrete instance at which the continuous time equations and signals are sampled (N_s total samples taken) and $\tilde{\boldsymbol{\tau}}_\text{mtr}[k] \in \mathbb{R}^{3\times 1}$ are the measured segment motor torques at instant k. Equation (4.15) assumes that there is equal and additive zero-mean Gaussian noise with unit covariance $\mathbf{I}_{3\times 3}$ between each measured torque signal $\tilde{\boldsymbol{\tau}}_\text{exp}$, i.e., a special case of maximum likelihood estimator [318]. The summation terms (4.15) in can be simplified by using the "vectorized" inverse dynamics, i.e.,

$$\{\tilde{\boldsymbol{\tau}}_\text{mtr}[k]\}_{k=1}^{N_\text{s}} = \{\boldsymbol{\Lambda}_\text{obs}(\boldsymbol{\phi}_\text{exp}[k], \dot{\boldsymbol{\phi}}_\text{exp}[k], \ddot{\boldsymbol{\phi}}_\text{exp}[k])\mathbf{p}\}_{k=1}^{N_\text{s}} \tag{4.16}$$

$$= \bar{\boldsymbol{\Lambda}}_\text{obs}\mathbf{p} \tag{4.17}$$

where

$$\{\tilde{\boldsymbol{\tau}}_\text{mtr}[k]\}_{k=1}^{N_\text{s}} = \begin{Bmatrix} \tilde{\boldsymbol{\tau}}_\text{mtr}[1] \\ \vdots \\ \tilde{\boldsymbol{\tau}}_\text{mtr}[N_\text{s}] \end{Bmatrix} \quad \text{and} \quad \bar{\boldsymbol{\Lambda}}_\text{obs} = \begin{Bmatrix} \boldsymbol{\Lambda}_\text{obs}(\boldsymbol{\phi}_\text{exp}[1], \dot{\boldsymbol{\phi}}_\text{exp}[1], \ddot{\boldsymbol{\phi}}_\text{exp}[1]) \\ \vdots \\ \boldsymbol{\Lambda}_\text{obs}(\boldsymbol{\phi}_\text{exp}[N_\text{s}], \dot{\boldsymbol{\phi}}_\text{exp}[N_\text{s}], \ddot{\boldsymbol{\phi}}_\text{exp}[N_\text{s}]) \end{Bmatrix} \tag{4.18}$$

are column matrices that contain the N_s samples from measurements and the mathematical model. This change in formatting implies the simpler least-squares optimization of $\mathbf{p}$ from a single experimental trajectory:

$$\mathbf{p}^* = \underset{\mathbf{p}}{\text{argmin}} \ \|\{\tilde{\boldsymbol{\tau}}_\text{exp}[k]\}_{k=1}^{N_\text{s}} - \bar{\boldsymbol{\Lambda}}_\text{obs}\mathbf{p}\|_{\mathbf{I}_{3\times 3}}^2 \tag{4.19}$$

With that said, problems can still be encountered in the identification of Fourier coefficients, i.e., those selected may not sufficiently excite the parameters over the all N_s samples. Furthermore, between each other, individual minimal parameters could still have widely different sensitivities to variations in the motor torque sequence [318]. Therefore, additional steps are necessary.

To address the concerns of ill-conditioning in Equation 4.16, Swevers et al. [318] used nonlinear programming with decision variable $\mathbf{S} = \{\mathbf{s}_0, ..., \mathbf{s}_n, \mathbf{d}_1, ..., \mathbf{d}_n\}$ to obtain experimental trajectories that satisfied

$$\underset{\mathbf{S}}{\text{argmin}} \ \text{cond}(\bar{\boldsymbol{\Lambda}}_\text{obs}^*) \tag{4.20}$$

where

$$\text{cond}(\mathbf{A}) = \frac{\max \varsigma(\mathbf{A})}{\min \varsigma(\mathbf{A})}, \quad \mathbf{A}_{ij}^* = \frac{\mathbf{A}_{ij}}{\|\mathbf{A}_{:j}\|} \, \forall i \tag{4.21}$$

and $\varsigma(\mathbf{X})$ is a function that returns the set of all singular values of $\mathbf{X}$. It was assumed that $\mathbf{u}_{\text{inertial}} = \mathbf{0}$, i.e., we have no way to regulate these floating DOF and thus they can be ignored. Briefly, the condition number of the matrix $\bar{\mathbf{\Lambda}}_{\text{obs}}$ (4.21) quantifies the bound on the accuracy of parameter evaluation from $\mathbf{p} = \bar{\mathbf{\Lambda}}_{\text{obs}}^{-1}\{\tilde{\boldsymbol{\tau}}_{\text{mtr}}[k]\}_{k=1}^{N_{\text{s}}}$. A high condition number implies that small error in the segment torque signal could produce a large error in estimation of the true underlying parameters. Therefore, an experiment with a low condition number should in theory allow us to obtain less sensitive and more accurate parameter estimates from the least-squares estimator [120, 282, 365]. Inclusion of the normalization operation in (4.21) ($\bar{\mathbf{\Lambda}}_{\text{obs}} \rightarrow \bar{\mathbf{\Lambda}}_{\text{obs}}^{*}$) took care of parameter equilibration as recommended by Swevers et al. [318].

In the majority parameter identification optimal experiments designs, trajectories are obtained for a single "experiment", i.e., only one trajectory is solved for [120, 282, 318]. Few studies in parameter identification make it clear that a number of exciting trajectories were used [124]. In the current dissertation, we considered the possibility of using a series of experimental trajectories to increase the number of samples available and potentially improve the conditioning of the observation matrix. Briefly, the custom algorithm used to generate experimental trajectories (described in detail in Algorithm 1) considered a "vectorized" multi-experiment observation matrix,

$$\{\bar{\mathbf{\Lambda}}_{\text{obs}}(\mathbf{S}_j)\}_{j=1}^{N_{\text{e}}} = \begin{Bmatrix} \bar{\mathbf{\Lambda}}_{\text{obs}}(\mathbf{S}_1) \\ \vdots \\ \bar{\mathbf{\Lambda}}_{\text{obs}}(\mathbf{S}_{N_{\text{e}}}) \end{Bmatrix} \tag{4.22}$$

and segment motor torque sequence (simulated and measured),

$$\mathbf{T}_{\text{mtr}} = \begin{Bmatrix} {}_1\{\tilde{\boldsymbol{\tau}}_{\text{mtr}}[k]\}_{k=1}^{N_{\text{s}}} \\ \vdots \\ {}_{N_{\text{e}}}\{\tilde{\boldsymbol{\tau}}_{\text{mtr}}[k]\}_{k=1}^{N_{\text{s}}} \end{Bmatrix}, \quad \mathbf{T}_{\text{exp}} = \begin{Bmatrix} {}_1\{\tilde{\boldsymbol{\tau}}_{\text{exp}}[k]\}_{k=1}^{N_{\text{s}}} \\ \vdots \\ {}_{N_{\text{e}}}\{\tilde{\boldsymbol{\tau}}_{\text{exp}}[k]\}_{k=1}^{N_{\text{s}}} \end{Bmatrix} \tag{4.23}$$

where $\bar{\mathbf{S}} = \{\mathbf{S}_1, \ldots, \mathbf{S}_{N_{\text{e}}}\}$ contains the concatenation of Fourier series coefficients for **all** N_{e} experimental trajectories Each discrete trajectory was assumed to have a constant length of N_{s} nodes. Note that the single experiment observation matrix was rewritten as a function $\bar{\mathbf{\Lambda}}_{\text{obs}} \equiv \bar{\mathbf{\Lambda}}_{\text{obs}}(\mathbf{S}_j)$ to clarify how Fourier coefficients were distributed from $\bar{\mathbf{S}}$.

The associated multi-experiment exciting trajectory optimization was thus defined

mathematically as

$$\mathbf{p}^* = \underset{\mathbf{p}}{\text{argmin}} \quad \sum_{i=1}^{N_\text{e}} \sum_{k=1}^{N_\text{s}} \|\boldsymbol{\Lambda}_\text{obs}[k;\mathbf{S}_i]\mathbf{p} - {}_i\tilde{\boldsymbol{\tau}}_\text{exp}[k]\|^2_{\mathbf{I}_{3\times3}} \tag{4.24}$$

$$= \underset{\mathbf{p}}{\text{argmin}} \quad \|\{\bar{\boldsymbol{\Lambda}}_\text{obs}(\mathbf{S}_i)\}_{i=1}^{N_\text{e}}\mathbf{p} - \mathbf{T}_\text{exp}\|^2 \tag{4.25}$$

$$= \underset{\mathbf{p}}{\text{argmin}} \quad \|\boldsymbol{\Xi}_\text{obs}(\bar{\mathbf{S}})\mathbf{p} - \mathbf{T}_\text{exp}\|^2 \tag{4.26}$$

where the notation ${}_i\tilde{\boldsymbol{\tau}}_\text{exp}[k]$ indicates the experimental segment torque sampled at instance k from experiment i.

The goal of the algorithm proposed is to iteratively add experiments to the observation matrix such that its condition number is reduced (Algorithm 1). When the algorithm reaches a point of diminishing returns, i.e., further experiments will have a marginal effect on conditioning, the algorithm stops its search. This operation requires the end-user to set a desired number of experimental trajectories (*the N_e we hope to reach*) in addition to the order of Fourier series that define them. Starting with $N_\text{e} = 1$ (i.e., experiment 1), the following constrained NLP is solved [318]:

$$\underset{\bar{\mathbf{S}}}{\text{argmin}} \quad \text{cond}(\boldsymbol{\Xi}^*_\text{obs}(\bar{\mathbf{S}})) \tag{4.27}$$

subject to

$$\mathbf{S}_i = \boldsymbol{\varsigma}_i, \quad \forall\, i \in \{i < N_\text{e} \wedge i > 0\} \tag{4.28}$$

$$\dot{\boldsymbol{\phi}}_\text{exp}[1;\mathbf{S}_i] = \mathbf{0}, \quad \forall\, i = 1 \ldots N_\text{e} \tag{4.29}$$

$$\ddot{\boldsymbol{\phi}}_\text{exp}[1;\mathbf{S}_i] = \mathbf{0}, \quad \forall\, i = 1 \ldots N_\text{e} \tag{4.30}$$

$$\boldsymbol{\theta}_\text{min} \leq \mathbf{J}^{-1}(\boldsymbol{\phi}_\text{exp}[k;\mathbf{S}_i] - \boldsymbol{\gamma}[k]) \leq \boldsymbol{\theta}_\text{max}, \quad \forall\, i = 1 \ldots N_\text{e},\, k = 1 \ldots N_\text{s} \tag{4.31}$$

$$\boldsymbol{\omega}_\text{min} \leq \mathbf{J}^{-1}(\dot{\boldsymbol{\phi}}_\text{exp}[k;\mathbf{S}_i] - \dot{\boldsymbol{\gamma}}[k]) \leq \boldsymbol{\omega}_\text{max}, \quad \forall\, i = 1 \ldots N_\text{e},\, k = 1 \ldots N_\text{s} \tag{4.32}$$

$$\boldsymbol{\alpha}_\text{min} \leq \mathbf{J}^{-1}(\ddot{\boldsymbol{\phi}}_\text{exp}[k;\mathbf{S}_i] - \ddot{\boldsymbol{\gamma}}[k]) \leq \boldsymbol{\alpha}_\text{max}, \quad \forall\, i = 1 \ldots N_\text{e},\, k = 1 \ldots N_\text{s} \tag{4.33}$$

where Equations (4.29) and (4.30) force each trajectory to begin and end with the system in static equilibrium; Equations (4.31), (4.32), and (4.33) limit the joint angles to the EXO-H3 range of motion $[\boldsymbol{\theta}_\text{min}, \boldsymbol{\theta}_\text{max}]$ (Table 4.1), joint velocities to manufacturer specified actuator limits $[\boldsymbol{\omega}_\text{min}, \boldsymbol{\omega}_\text{max}]$, and joint accelerations to reasonable values defined the experiment by Swevers et al. [318]. Variable $\boldsymbol{\varsigma}_i$ includes the predefined Fourier coefficients for experiment i, i.e., assumes we know the Fourier coefficients for experiments that occur prior to N_e (assuming $N_\text{e} > 1$). Given the lack of symbolic equations for the observation matrix condition

Algorithm 1 Parameter Identification Experimental Design Algorithm

Input: Desired # of experimental trials: $N_{\text{e,des}} \in \mathbb{I} \geq 1$, Fourier Series Order $n \in \mathbb{I} \geq 1$
Output: Fourier coefficients $\bar{\mathbf{S}}$ and $\text{cond}(\boldsymbol{\Xi}^*_{\text{obs}}(\bar{\mathbf{S}}))$ for N_{e} trials

Initialization $\bar{\mathbf{S}} = \varnothing$
for $i = 1 \dots N_{\text{e,des}}$ **do**
  $N_{\text{e}} \leftarrow i$
  $\mathbf{S}^*_i \leftarrow$ solve (4.27) st. (4.28 – 4.33)
  $\boldsymbol{\varsigma}_i \leftarrow \mathbf{S}^*_i$
  if $i > 1$ **then**
    $\kappa \leftarrow \text{cond}(\bar{\boldsymbol{\Xi}}^*_{\text{obs}}(\bar{\mathbf{S}}))$
    $\bar{\mathbf{S}}_{\text{new}} \leftarrow [\bar{\mathbf{S}}, \mathbf{S}^*_i]$ {Concatenation}
    $\kappa_{\text{new}} \leftarrow \text{cond}(\bar{\boldsymbol{\Xi}}^*_{\text{obs}}(\bar{\mathbf{S}}_{\text{new}}))$ {Condition of observation matrix with new trial}
    if $|\kappa - \kappa_{\text{new}}| < \varepsilon_{\text{tol}}$ **then** {No improvement in observation matrix condition}
      $N_{\text{e}} < N_{\text{e,des}} \iff N_{\text{e}} \neq N_{\text{e,des}}$
      break loop
    else
      $\bar{\mathbf{S}} \leftarrow \bar{\mathbf{S}}_{\text{new}}$
    end if
  else
    $\bar{\mathbf{S}} \leftarrow \mathbf{S}^*_i$
  end if
end for

number (4.20), the NLP had to be solved through numerical methods. With the added computational cost of derivative estimation, the optimization of sequential experimental trajectories was used instead of optimizing N_{e} trajectories simultaneously. Therefore, with the NLP solved, we set $\boldsymbol{\varsigma}_1 = \mathbf{S}^*_1$ and then set $N_{\text{e}} = 2$ before solving Equation (4.27) with constraints (4.28 – 4.33), and the new N_{e} and $\boldsymbol{\varsigma}_1$. Note that this second iteration will obtain $\boldsymbol{\varsigma}_2$. Iterations are continued until $N_{\text{e}} = N_{\text{e,des}}$ and we have obtained $\boldsymbol{\varsigma}_{N_{\text{e}}}$, **or** until we reach a point of diminishing returns in the conditioning of the normalized $\boldsymbol{\Xi}^*_{\text{obs}}$.

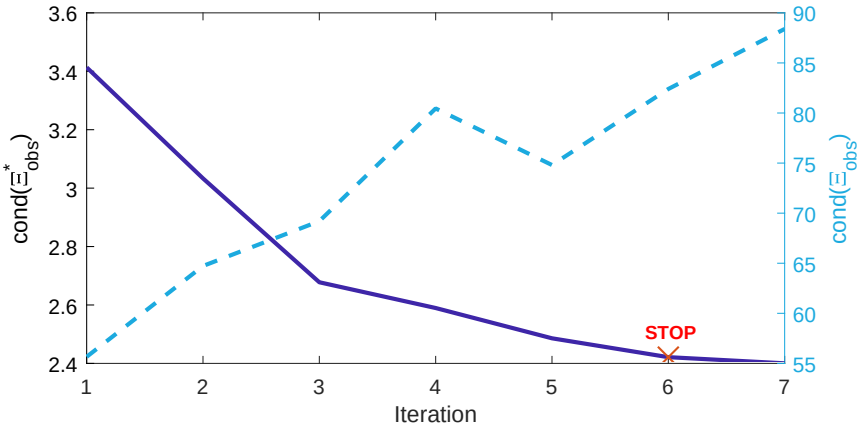


Figure 4.4: Condition number of the normalized (*left axis*) and untransformed (*right axis*) observation matrix Ξ_{obs} following each iteration of the novel algorithm described in Algorithm 1. Note that each iteration adds an additional trial to the overall parameter identification experiment.

Optimized Trajectories and Physical Experiment

For the current dissertation, to obtain a set of exciting experimental trajectories for the exoskeleton leg's minimal parameter set, we set $N_{\text{e,des}} = 8$. Fourier series parameters, i.e., $n = 5$ and $T = 15$ s, were set according to the parameters successfully used by Swevers et al. [318]. The sampling rate was set to the maximum collection rate in the EXO-H3 controller area network (CAN) protocol (100 Hz); thus, having a total signal period of 15 s allowed us to obtain 1501 samples per experiment (same number in [318]). At each step of Algorithm 1, the underlying NLP (4.27) subject to (4.28 – 4.33) was solved using the `fmincon` interior-point solver (MATLAB, Mathworks). The resulting optimal exciting trajectories are shown in terms of the lower-limb segment angles and joint angles (the desired curves in Figs. 4.5 and 4.6 respectively). The final condition number of the normalized observation matrix $\boldsymbol{\Xi}^*_{\text{obs}}$ for all desired experiments combined was 2.40 (see Fig. 4.4). Note that as the normalized observation matrix was decreased with iterations of the proposed algorithm, the untransformed condition number appeared to increase (final value = 88.39).

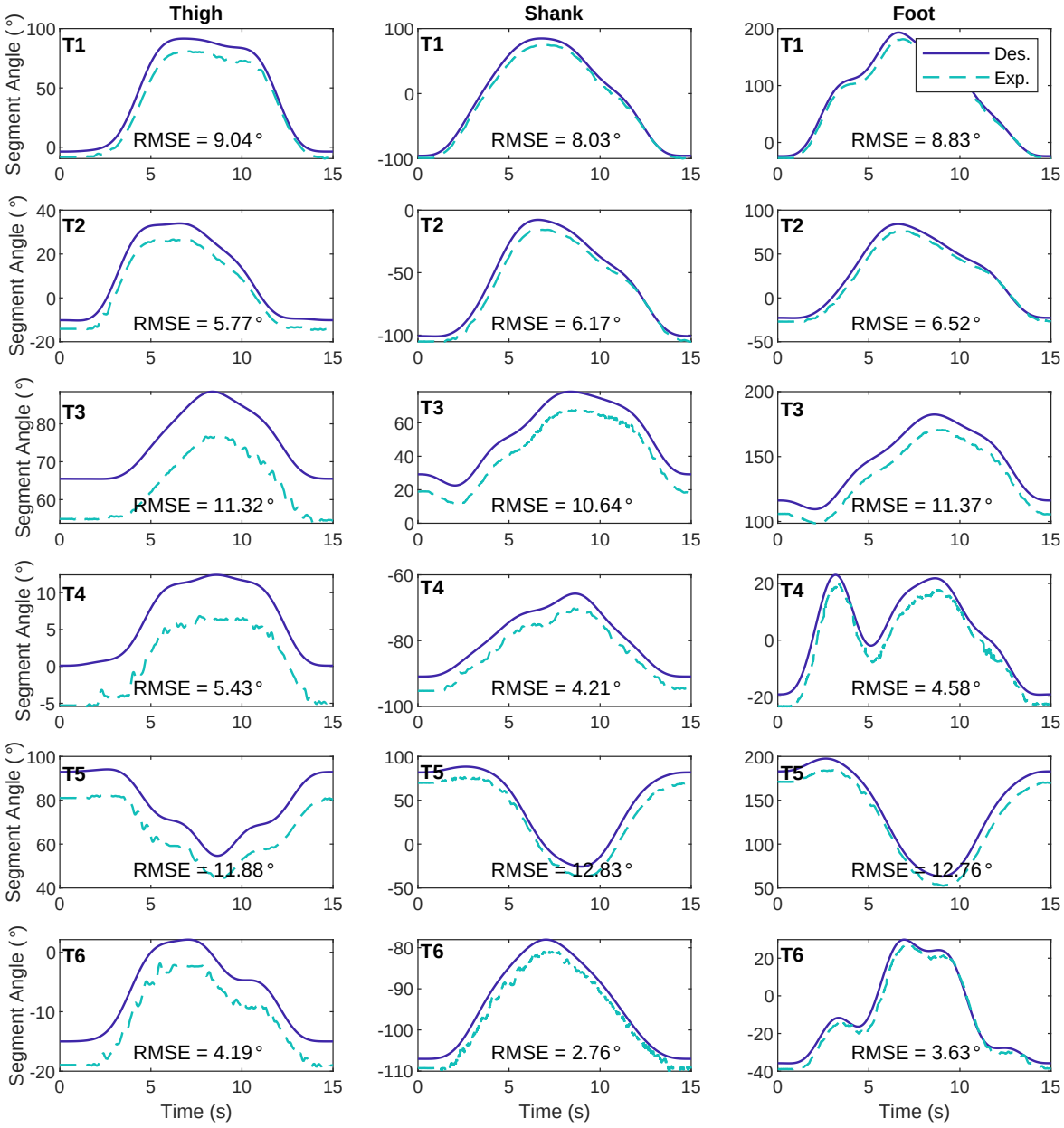


Figure 4.5: Desired (optimal exciting) and experimental segment angles for a lower-limb exoskeleton parameter identification experiment consisting of 6 trials (T1-6). Segments include the thigh (*left*), shank (*centre*), and foot (*right*). The root mean square error (RMSE) between experimental and desired trajectories are indicated on each plot.

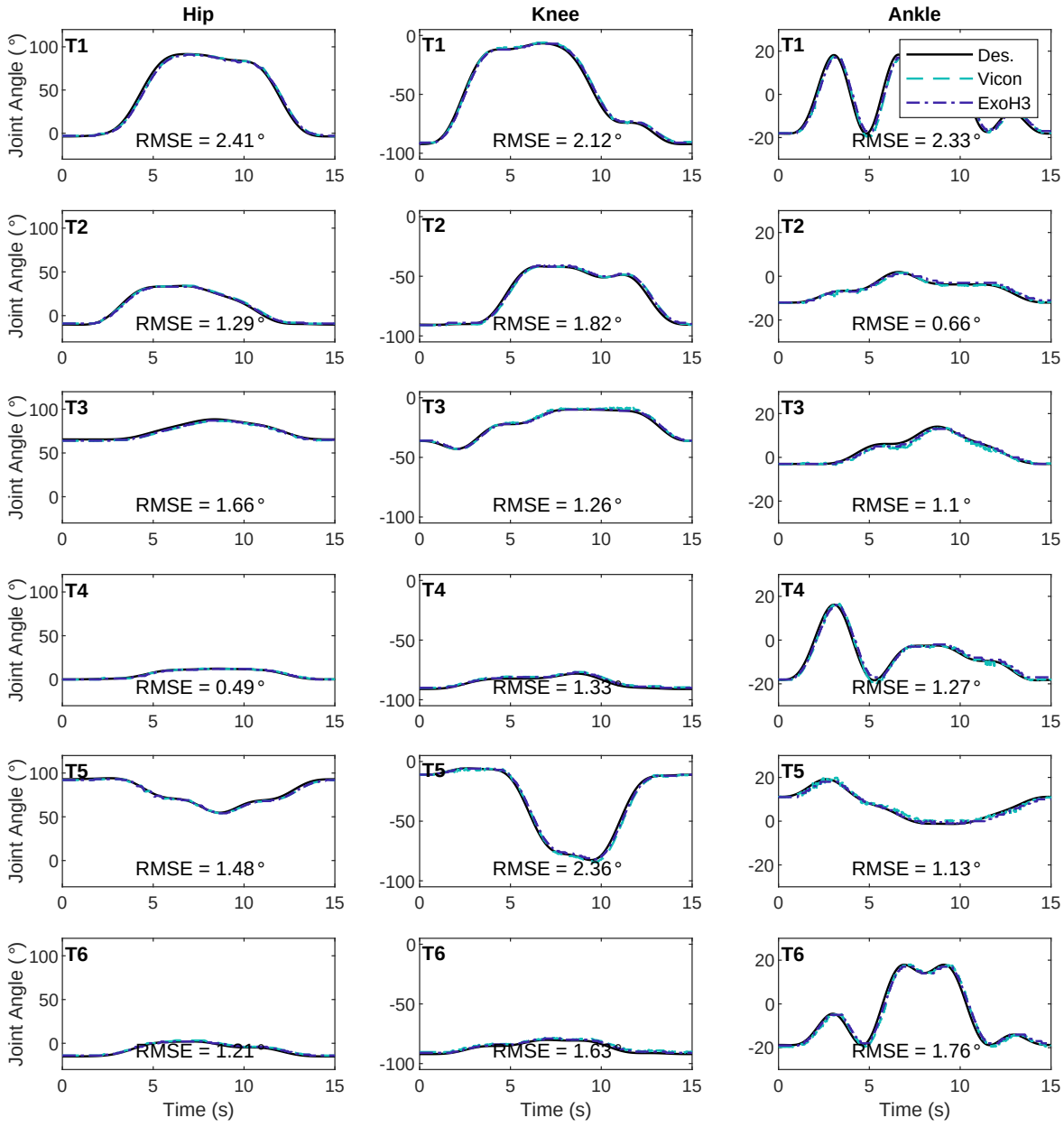


Figure 4.6: Desired (optimal exciting) and experimental joint angles (obtained from Vicon motion capture and EXO-H3 rotary encoders separately) for a lower-limb exoskeleton parameter identification experiment consisting of 6 trials (T1-6). Joints include the hip (*left*), knee (*centre*), and ankle (*right*). The root mean square error (RMSE) between experimental and Vicon trajectories are indicated on each plot.

Each experimental trajectory was replicated in the EXO-H3 by fixing it to a test-bench designed separately by Christian Mele (MASc Thesis [241]; Supervisor: James Tung) and using Technaid's joint position control feature which utilized the joint angle trajectories shown in Fig. 4.6. The sensors onboard the EXO-H3 include joint position encoders and motor current sensors (used to estimate motor torque). Using Technaid's CAN bus protocol, each sensor was able to record data at 100 Hz, though all values measured were quantized to the nearest integer, i.e., nearest degree for joint angles and nearest Nm for motor torques. The 3D motion capture setup available in Waterloo Robohub (University of Waterloo; Vicon Vantage V5 cameras captured at 1000 Hz) was used to obtain high resolution joint kinematics to improve derivative estimations from numerical differentiation as well as to validate the joint angle measurements from the Exo-H3. Individual retroreflective markers were fixed to the EXO-H3 at the actuator joint centers, the midpoint of the primary links, in addition to various other areas on each segment. By using noncollinear marker placements, the 3D marker positions could be used to generate segment-fixed rotation matrices that provided sagittal plane joint angles via conversion to Euler angles [360]. Markers on the trunk orthosis were also included to obtain experimental values for the floating-base inputs; these will be non-zero in physical experiments due to compliance in the interface between device and test-bench.

The motor torque data necessary for identification was obtained purely from the EXO-H3 onboard motor current sensors. In some instances, the sensors were not able to report a value for the CAN bus; in these cases, signal interpolation was necessary. To do this for the quantized torque data, the signal was first interpolated across its entire sampling period via cubic spline followed by re-quantization (data rounded back to nearest integer). Interpolated motor torque data was than low-pass filtered (second-order dual-pass butterworth; cutoff = 20 Hz) after inspection of the signal frequency content via Fast Fourier Transform (FFT); the aim was to reduce the nonlinear effect of signal quantization in this process. The kinematic data required to perform parameter identification was obtained from the 3D motion capture data. Joint marker positions were interpolated (cubic-spline) and low-pass filtered (filter parameters set by inspecting data via FFT; cutoff = 2 Hz) before being used to calculate sagittal trunk (for inertial inputs), thigh, shank, and foot segment angles (Euler angles). Hip, knee, and ankle joint angles were subsequently calculated and shifted so that the first sampled value matched the first angle recorded by the corresponding Exo-H3 rotary encoder. They were then transformed back to segment angle space via Equation (G.6) with the experimental trunk angle. Joint angles were numerically differentiated to

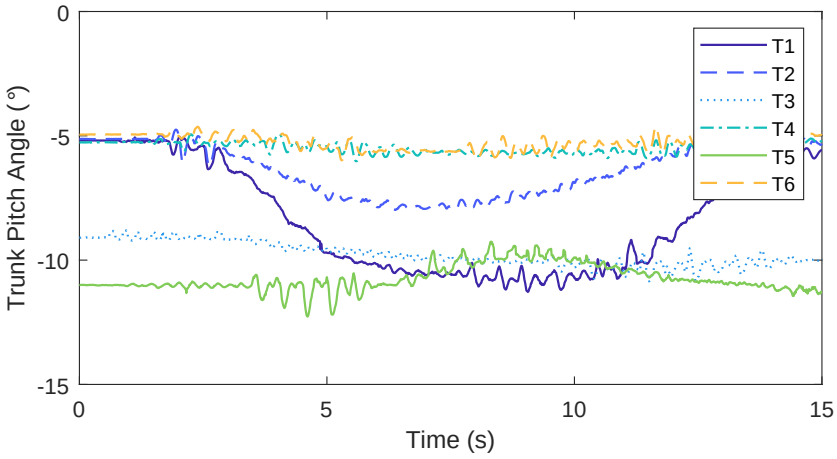


Figure 4.7: The EXO-H3 trunk pitch angle measured during each of the 6 trials (T1-6) in the lower-limb exoskeleton parameter identification experiment. Note that a negative angle indicates a forward/anterior pitch.

obtain velocities and accelerations; note that these signals were also inspected via FFT and filtered as necessary [360].

In Fig. 4.5, the experimental segment kinematics measured via 3D motion capture are plotted against the desired ones for each identification experimental trajectory. Fig. 4.6 rather displays experiment joint kinematics calculated from the segment angles in 4.5 alongside the measured trunk kinematics, e.g., the measured trunk pitch angle during each experimental trial (Fig. 4.7). The amplified hip, knee, and ankle motor torques that were measured by the EXO-H3 during each experiment are shown in Fig. 4.8. In general, experimental joint angles had only small error in attaining the desired joint angles; the highest root mean square error (RMSE) between experiment and desired angles was reported for the first experimental trajectory (Fig. 4.8): hip RMSE = 2.41°, knee RMSE = 2.12°, and ankle RMSE = 2.33°. The RMSE between experimental and desired segment angles was much greater (Fig. 4.5); some segments reported an RMSE of over 10°. This jump in error was due to the EXO-H3 trunk pitch only being softly constrained (Fig. 4.7), which introduced a bias into the distal segments given joint-level position control was used. Due to this trunk pitch in addition to other factors like control error, the final condition number of the normalized observation matrix using experimental segment kinematics instead of de-

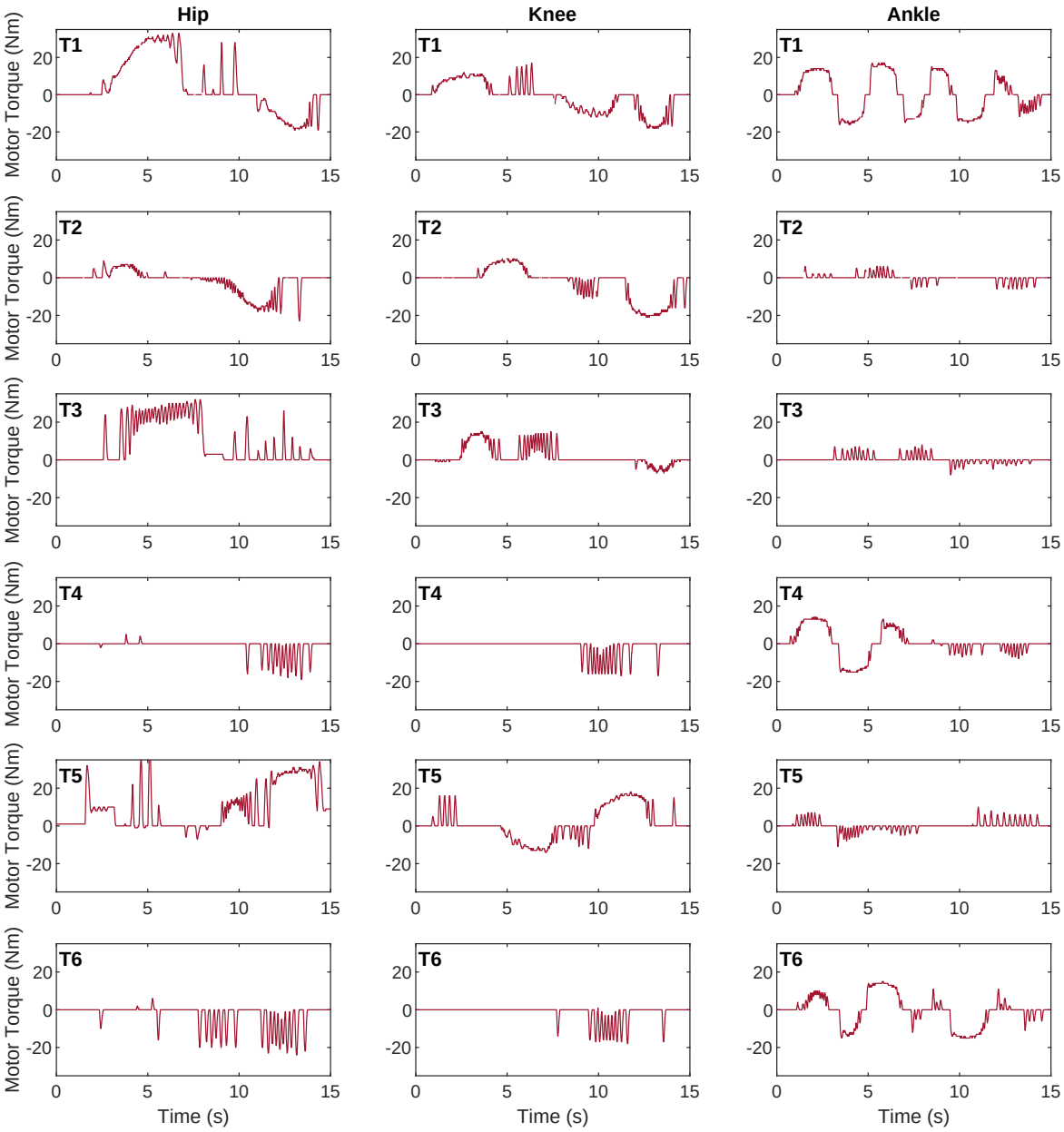


Figure 4.8: Experimental amplified joint motor torques (scaled by the gear ratio; obtained from EXO-H3 motor current sensors) for a lower-limb exoskeleton parameter identification experiment consisting of 6 trials (T1-6). Joints include the hip (*left*), knee (*centre*), and ankle (*right*).

sired was 3.32 (untransformed condition number was 77.62). Swevers et al. [318] reported a substantial increase in the observation matrix condition number when using experimental trajectories due to the presence of an unmodeled gravitational compensation spring. The joint measurements recorded by the rotary encoders included with the EXO-H3 are also plotted against the 3D motion capture joint angles in Fig. 4.6. Disagreements between the two measurement systems were minor, which provides validation for the use of these encoders in our future assistive FIP balance control systems.

4.2.4 Parameter Identification Methods

Inverse Dynamics Analysis

As discussed in the previous section, the inverse dynamics approach to dynamic parameter identification involves the least-squares quadratic programming (QP) problem:

$$\mathbf{p}^* = \underset{\mathbf{p}}{\operatorname{argmin}} \|\boldsymbol{\Xi}_{\text{obs}}(\bar{\mathbf{S}})\mathbf{p} - \mathbf{T}_{\text{exp}}\|^2 \tag{4.34}$$

$$= \underset{\mathbf{p}}{\operatorname{argmin}} \ (\boldsymbol{\Xi}_{\text{obs}}(\bar{\mathbf{S}})\mathbf{p} - \mathbf{T}_{\text{exp}})^\intercal(\boldsymbol{\Xi}_{\text{obs}}(\bar{\mathbf{S}})\mathbf{p} - \mathbf{T}_{\text{exp}}) \tag{4.35}$$

which can be readily solved analytically [282, 318, 365]. First, if we say $\boldsymbol{\Xi}_{\text{obs}}(\bar{\mathbf{S}}) \equiv \boldsymbol{\Xi}_{\text{obs}}$ and expand the cost function from Equation (4.35), i.e.,

$$J(\mathbf{p}) = (\boldsymbol{\Xi}_{\text{obs}}\mathbf{p} - \mathbf{T}_{\text{exp}})^\intercal(\boldsymbol{\Xi}_{\text{obs}}\mathbf{p} - \mathbf{T}_{\text{exp}}) \tag{4.36}$$

$$= \mathbf{p}^\intercal\boldsymbol{\Xi}_{\text{obs}}^\intercal\boldsymbol{\Xi}_{\text{obs}}\mathbf{p} - 2\mathbf{T}_{\text{exp}}^\intercal\boldsymbol{\Xi}_{\text{obs}}\mathbf{p} + \mathbf{T}_{\text{exp}}^\intercal\mathbf{T}_{\text{exp}} \tag{4.37}$$

we then solve (4.35) by finding the critical point of $J(\mathbf{p})$, i.e.,

$$\left.\frac{dJ}{d\mathbf{p}}\right|_{\mathbf{p}^*} = \mathbf{0} \tag{4.38}$$

$$= 2\mathbf{p}^{*\intercal}\boldsymbol{\Xi}_{\text{obs}}^\intercal\boldsymbol{\Xi}_{\text{obs}} - 2\mathbf{T}_{\text{exp}}^\intercal\boldsymbol{\Xi}_{\text{obs}} \tag{4.39}$$

which results in

$$\mathbf{p}^* = (\boldsymbol{\Xi}_{\text{obs}}^\intercal\boldsymbol{\Xi}_{\text{obs}})^{-\intercal}\boldsymbol{\Xi}_{\text{obs}}^\intercal\mathbf{T}_{\text{exp}} \tag{4.40}$$

where $\mathbf{p}^*$ contains the minimum parameter values that minimize the squared-error in motor torque predictions made by the inverse dynamics model.

While simple, one issue in Equation (4.40) is the lack of constraints applied. In reality, we may desire constraints that reduce the parameter search space and limit over-fitting of the dynamic model to the measurement data. For example, box inequality constraints on a subset of the redundant (though meaningful) multibody parameters $\mathbf{p}_\mathrm{r}$,

$$\mathbf{p}_{\mathrm{r,min}} \leq \mathbf{A}_\mathrm{r}\mathbf{p}_\mathrm{r} \leq \mathbf{p}_{\mathrm{r,max}} \tag{4.41}$$

can prevent these parameters from taking on unrealistic values, e.g., negative mass or MOI. Variables $\mathbf{p}_{\mathrm{r,min}}$ and $\mathbf{p}_{\mathrm{r,max}}$ are column matrices containing the parameter bounds; matrix $\mathbf{A}_\mathrm{r}$ isolates the parameters in $\mathbf{p}_\mathrm{r}$ to be box constrained. Box constraints have been included within parameter identification methods like the sigmoidal barrier extended Kalman filter method in Joukov et al. [181]. We may also wish to impose knowledge of certain parameters that are readily measured, such as segment mass and length, during the identification. We thus modify the parameter identification problem to consider "perfect" measurements of the exoskeleton through the constraints

$$\begin{Bmatrix} m_\mathrm{th} \\ m_\mathrm{sh} \\ m_\mathrm{ft} \\ \ell_\mathrm{th} \\ \ell_\mathrm{sh} \\ \ell_\mathrm{ft} \end{Bmatrix} - \mathbf{p}_\mathrm{meas} = \mathbf{R}_{\mathbf{p}_\mathrm{r}}\mathbf{p}_\mathrm{r} - \mathbf{p}_\mathrm{meas} = \mathbf{0} \tag{4.42}$$

where $\mathbf{R}_{\mathbf{p}_\mathrm{r}}$ isolates the redundant parameters that we have said "perfect" measurements of $\mathbf{p}_\mathrm{meas}$. This idea draws many parallels to the cost function in Rackl et al. [282]: the authors aimed to minimize how far their optimized parameter estimations would be from parameter values estimated separately using a 3D CAD model.

To this point, the inverse dynamics model in Equation (G.26) is defined entirely in terms of the set of minimal parameters $\mathbf{p}$; however, our constraints have been placed on the redundant parameters. Therefore, we require an equation that relates these linear parameters back to the nonlinear parameters:

$$\mathbf{g}_\mathbf{p}(\mathbf{p}_\mathrm{r}) - \mathbf{p} = \mathbf{0} \tag{4.43}$$

where $\mathbf{g}_\mathbf{p}(\cdot)$ is obtained from the nonlinear definitions in Equations (G.17), (G.18), and (G.19). If both $\mathbf{p}_\mathrm{r}$ and $\mathbf{p}$ are considered decision variables within the parameter identification, we can then solve the constraints (4.43) with the least-squares minimal parameters

simultaneously. Therefore, the final NLP identification problem for the inverse dynamics EXO-H3 model was:

$$\underset{\mathbf{p},\mathbf{p}_\mathrm{r}}{\operatorname{argmin}} \quad \sum_{i=1}^{N_\mathrm{e}} \sum_{k=1}^{N_\mathrm{s}} \|\boldsymbol{\Lambda}_\mathrm{obs}[k;\mathbf{S}_i]\mathbf{p} - {}_i\tilde{\boldsymbol{\tau}}_\mathrm{exp}[k]\|^2_{\mathbf{I}_{3\times3}} \tag{4.44}$$

subject to

$$\mathbf{R}_{\mathbf{p}_\mathrm{r}}\mathbf{p}_\mathrm{r} - \mathbf{p}_\mathrm{meas} = \mathbf{0} \tag{4.45}$$

$$\mathbf{g}_\mathbf{p}(\mathbf{p}_\mathrm{r}) - \mathbf{p} = \mathbf{0} \tag{4.46}$$

$$\mathbf{p}_\mathrm{r,min} \leq \mathbf{p}_\mathrm{r} \leq \mathbf{p}_\mathrm{r,max} \tag{4.47}$$

which was solved using `fmincon` (interior-point algorithm) with symbolic gradients/Hessians obtained using a custom MapleSim worksheet.

Forward Dynamics Analysis

In the inverse dynamics approach, the measured and simulated applied torques were utilized for least-squares parameter identification. Conversely, for the forward dynamics approach, the variables of interest with regards to model residual error were switched to the thigh, shank, and foot segment angles:

$${}_i\mathbf{y}[k;\mathbf{p}] \equiv {}_i\boldsymbol{\phi}[k;\mathbf{p}] \tag{4.48}$$

where ${}_i\mathbf{y}[k;\mathbf{p}]$ was the model output of interest (sampled at instant k in experiment i) affected by minimal parameters $\mathbf{p}$. As a result, the minimal parameter ODEs in (G.23) had to be rewritten to solve for $\ddot{\boldsymbol{\phi}}$, i.e.,

$$\tilde{\boldsymbol{\tau}}_\mathrm{mtr} = \boldsymbol{\Lambda}_\mathrm{Md}\mathbf{p}_\mathrm{Md} + \boldsymbol{\Lambda}_\mathrm{Mod}\mathbf{p}_\mathrm{Mod} + (\boldsymbol{\Lambda}_\mathrm{g} + \boldsymbol{\Lambda}_\mathrm{fb})\mathbf{p}_\mathrm{g} + \boldsymbol{\Lambda}_\mathrm{f}\mathbf{p}_\mathrm{f} \tag{4.49}$$

$$\Downarrow$$

$$[\mathrm{diag}(\mathbf{p}_\mathrm{Md}) + \nabla_\phi\boldsymbol{\Lambda}]\,\ddot{\boldsymbol{\phi}} = \tilde{\boldsymbol{\tau}}_\mathrm{mtr} + \tilde{\boldsymbol{\tau}}_\mathrm{f} + \tilde{\boldsymbol{\Gamma}}_\mathrm{lin} \tag{4.50}$$

$$\tilde{\mathbf{M}}_\mathrm{lin}\ddot{\boldsymbol{\phi}} = \tilde{\boldsymbol{\tau}}_\mathrm{ac} + \tilde{\boldsymbol{\Gamma}}_\mathrm{lin} \tag{4.51}$$

where

$$\nabla_\phi\boldsymbol{\Lambda} = \frac{\partial\left(\boldsymbol{\Lambda}_\mathrm{Mod}(\boldsymbol{\phi},\dot{\boldsymbol{\phi}},\ddot{\boldsymbol{\phi}})\mathbf{p}_\mathrm{Mod}\right)}{\partial\ddot{\boldsymbol{\phi}}} \tag{4.52}$$

and

$$\tilde{\boldsymbol{\Gamma}}_{\text{lin}} = \nabla_{\phi}\boldsymbol{\Lambda}\ddot{\boldsymbol{\phi}} - \boldsymbol{\Lambda}_{\text{Mod}}\mathbf{p}_{\text{Mod}} - (\boldsymbol{\Lambda}_{\text{g}} + \boldsymbol{\Lambda}_{\text{fb}})\mathbf{p}_{\text{g}} \tag{4.53}$$

$$= -\boldsymbol{\Lambda}^{\circ}_{\text{Mod}}\mathbf{p}_{\text{Mod}} + (\boldsymbol{\Lambda}_{\text{g}} - \boldsymbol{\Lambda}_{\text{fb}})\mathbf{p}_{\text{g}} \tag{4.54}$$

The constrained NLP describing optimal forward dynamics parameter identification was obtained by rewriting the inverse dynamics NLP (4.44) using the forward dynamic equations (4.51):

$$\underset{\mathbf{p},\mathbf{p}_{\text{r}}}{\text{argmin}} \quad \sum_{i=1}^{N_{\text{e}}}\sum_{k=1}^{N_{\text{s}}} \|{}_i\mathbf{y}[k;\mathbf{p}] - {}_i\boldsymbol{\phi}_{\text{exp}}[k]\|^2_{\mathbf{I}_{3\times 3}} \tag{4.55}$$

subject to

$$\mathbf{R}_{\mathbf{p}_{\text{r}}}\mathbf{p}_{\text{r}} - \mathbf{p}_{\text{meas}} = \mathbf{0} \tag{4.56}$$

$$\mathbf{g}_{\mathbf{p}}(\mathbf{p}_{\text{r}}) - \mathbf{p} = \mathbf{0} \tag{4.57}$$

$$\mathbf{p}_{\text{r,min}} \leq \mathbf{p}_{\text{r}} \leq \mathbf{p}_{\text{r,max}} \tag{4.58}$$

$${}_i\boldsymbol{\phi}(0) = {}_i\boldsymbol{\phi}_0, \quad \forall\, i = 1 \ldots N_{\text{e}} \tag{4.59}$$

$${}_i\dot{\boldsymbol{\phi}}(0) = {}_i\dot{\boldsymbol{\phi}}_0, \quad \forall\, i = 1 \ldots N_{\text{e}} \tag{4.60}$$

$$\ddot{\boldsymbol{\phi}} = \tilde{\mathbf{M}}^{-1}_{\text{lin}}(\tilde{\boldsymbol{\tau}}_{\text{ac}} + \tilde{\boldsymbol{\Gamma}}_{\text{lin}}), \quad \forall\, t \in [0, t_f],\, \forall\, i = 1 \ldots N_{\text{e}} \tag{4.61}$$

where Equation (4.61) was solved for each experiment of N_{e} within the cost function via stiff ODE solver `ode15s` in MATLAB; (4.59) and (4.60) are the initial conditions for each experiment being simulated. Note that from the trajectory optimization constraints in (4.29), (4.60) could also be written as ${}_i\dot{\boldsymbol{\phi}}(0) = 0, \forall\, i = 1 \ldots N_{\text{e}}$. The NLP itself was solved using `fmincon` with gradients/Hessians obtained through numerical methods (interior-point algorithm); sensitivity differential equations were not obtained for the current analysis [124, 300, 347]. This iterative approach to parameter identification draws many similarities to the direct shooting approach in optimal control [56]: we guess parameter values, run a simulation of each EXO-H3 experiment with those parameter values, and assess how close to the "target" we were with that first guess (i.e., how large was the squared measurement error). This information is then taken into account as we adjust our guess with the intent of iteratively getting closer to the "target". Note that this method was paired with the global homotopy method described by Vyasarayani et al. [347] to increase the likelihood the we obtain a global optimum for a given initial guess.

4.3 Identification Results and Discussion

First, results of the parameter identification based on physical measurements from the EXO-H3 with CAD analysis are outlined. Table 4.6 displays the estimated "redundant" multibody parameters for the trunk segment, i.e., mass, MOI with respect to the COM, and sagittal COM position relative to the hip joint (in the trunk fixed-frame, see Fig. 4.1). Note the substantial shifting of the trunk COM posteriorly due to the inclusion of the battery. The results of the dynamometer curve-fitting procedure for knee actuator friction are shown in Fig. 4.9. The affine function to which the experimental torque measurements were fit was used to set two friction parameters: $\alpha_{\mathrm{k},0}$ (Coulomb friction) and $\alpha_{\mathrm{k},2}$ (Viscous friction); see Table 4.7. The linear viscous damping coefficient estimated should capture the effects of lubricated friction from the motor and gearing in addition to the motor's back EMF. This result is due to the net actuator torque being measured rather than measurements of motor output only, i.e., voltage input plus back EMF in Equation (4.5). The recorded friction-velocity map was also not sensitive enough to tease out any Stribeck effect [269]; however, previous parameter identifications of strain-wave actuators have suggested that this effect does in fact occur [142]. Therefore, $\alpha_{\mathrm{k},1}$ was set to 0.50 Nm which resulted in a breakaway joint torque that was only marginally higher than the Coulomb torque. As a final note, the spread of data points under each average velocity condition in Fig. 4.9 also suggests that there may be some degree of position-dependence in the actuator output [336]. Likewise, it is possible that experimental error could explain the variance in data points, e.g., joint axis misalignment between device and dynamometer during testing as well faults in the gravity effect calibration.

Second, we summarize the results of the parameter identifications that utilized inverse

Table 4.6: Trunk multibody dynamic parameters obtained for the EXO-H3 via CAD analysis paired with physical measurements.

Parameter	Meaning	Units	CAD/measured Values
m_{tr}	Mass	kg	6.49
I_{tr}	MOI (wrt COM)	kg m^2	1.30×10^{-1}
${}_x c_{\mathrm{tr}}$	$\hat{\mathbf{i}}$ COM position (wrt hip)	cm	-15.41
${}_y c_{\mathrm{tr}}$	$\hat{\mathbf{j}}$ COM position (wrt hip)	cm	10.17

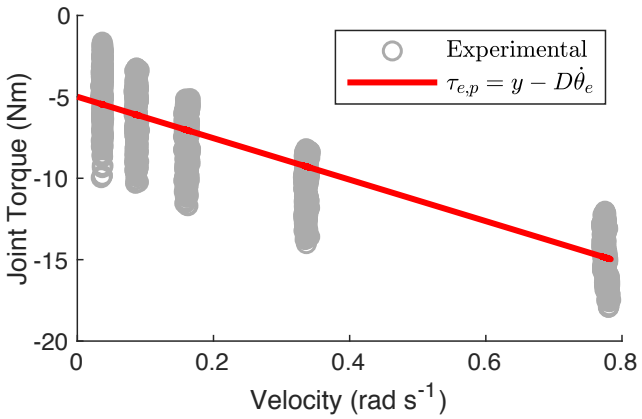


Figure 4.9: Results of fitting Equation (4.10) to the passive torques measured in the EXO-H3 knee joint. Experimental data was analyzed only for the extension direction of knee velocity (positive values).

dynamics modeling (InvDyn) and forward dynamics modeling (ForDyn). Note that when running these identifications, rather than sharing the same parameter values, each joint was prescribed a unique set of friction parameters, i.e., parameters followed Equation (G.25). This assumption was made after experimentation with the motor torque controls to which we gained access with a recent firmware update to the EXO-H3 provided by Technaid (update in Spring 2023; parameter identification collections operated in Summer 2022). Therefore, each joint had the potential for a unique friction profile in simulations; though we do recognize that this in theory could increase conditioning of the resulting inverse dynamics observation matrix. Like the physical experiments, estimated friction parameters from the inverse dynamics (InvDyn) and forward dynamics (ForDyn) optimization approaches are shown in Table 4.7. The estimated dynamic parameters provided by optimization are shown in Tables 4.8 (minimal) and 4.9 (redundant). Note also that these parameters are specific to a single configuration of the EXO-H3 links as they are adjustable for different end-users. The measurements of segment length used as an NLP constraint were obtained directly from the motion capture, i.e., the average distance between markers located at approximate joint centers.

With parameters estimated, we examine the performance of the said estimates in simulating the 6 experimental exciting trajectories used for training. The simulated joint angle trajectories (obtained using separate forward dynamics simulations), for each set of parameter values listed in Tables 4.8 and 4.7, are shown in Fig. 4.10. Calculated root

Table 4.7: Nonlinear friction parameters obtained for the EXO-H3 using the two optimization methods presented in Chapter 4.2.4: an inverse dynamics approach (Inv-Dyn) and a forward dynamics approach (For-Dyn). The results generated from the physical dynamometer experiment with the EXO-H3 knee are also presented (PhyExp).

			Identification Method		
Joint	Parameter	Units	Inv-Dyn	For-Dyn	PhyExp
Hip	$\alpha_{h,0}$	Nm	4.24	9.99	–
	$\alpha_{h,1}$	Nm	0.00	2.89	–
	$\alpha_{h,2}$	Nm s^{-1}	26.34	467.29	–
Knee	$\alpha_{k,0}$	Nm	4.00	9.99	5.50
	$\alpha_{k,1}$	Nm	0.00	0.50	0.50
	$\alpha_{k,2}$	Nm s^{-1}	20.90	0.06	12.80
Ankle	$\alpha_{a,0}$	Nm	4.00	4.98	–
	$\alpha_{a,1}$	Nm	0.00	0.50	–
	$\alpha_{a,2}$	Nm s^{-1}	21.12	8.81	–

mean square error (RMSE) values for each set of joint angles and trial are located in Table 4.10. Similarly, the resulting simulated amplified motor torque trajectories (obtained using separate inverse dynamics simulations), for each set of parameter values are displayed in Fig. 4.11. The RMSE values for the hip, knee, and ankle torque signal estimates for each trial are located in Table 4.11. In general, simulated ankle joint angles were the closest fit to their experimental counterpart across identification methods (Table 4.10). Knee angles were predicted inconsistently within some trials, e.g., T2, showing some substantial divergence for all methods. In general, predictions of hip angles were also quite poor, possibly due to the added weight and inertia of the distal segments acting relative to the hip joint, increasing its sensitivity to parameter errors. Notably, the parameter identified using the forward dynamics method (ForDyn) managed to track the experimental hip angles best, though it still did so with a large margin of error. Its solution was to avoid any substantial deviations of the hip angle from 0, which could be indicative of poor fidelity of actuator torque measurements for the hip.

Looking at simulations of the motor torques for the six exciting identification trials (T1-6 in Fig. 4.11), the simulations generated using PhyExp and InvDyn parameters appeared

Table 4.8: Minimal multibody dynamic parameters obtained for the EXO-H3 using the two optimization methods presented in Chapter 4.2.4: an inverse dynamics approach (Inv-Dyn) and a forward dynamics approach (For-Dyn). The results generated from the physical experiment (direct measurements and CAD analysis) are also presented (PhyExp).

		Identification Method		
Minimal Parameter	Units	Inv-Dyn	For-Dyn	PhyExp
$(m_{\text{ft}} + m_{\text{sh}})\ell_{\text{th}}^2 + ({}_xc_{\text{th}}^2 + {}_yc_{\text{th}}^2)m_{\text{th}} + I_{\text{th}}$	kg m^2	1.93	1.02	1.57
$m_{\text{ft}}\ell_{\text{th}}^2 + ({}_xc_{\text{sh}}^2 + {}_yc_{\text{sh}}^2)m_{\text{sh}} + I_{\text{sh}}$	kg m^2	5.23	8.88	1.21
$({}_xc_{\text{ft}}^2 + {}_yc_{\text{ft}}^2)m_{\text{ft}} + I_{\text{ft}}$	kg m^2	0.44	1.64	0.85
$m_{\text{ft}}\ell_{\text{sh}}\ell_{\text{th}} - {}_yc_{\text{sh}}m_{\text{sh}}\ell_{\text{th}}$	kg m^2	0.25	0.62	0.39
${}_xc_{\text{sh}}m_{\text{sh}}\ell_{\text{th}}$	kg m^2	-0.02	0.07	0.00
${}_yc_{\text{ft}}m_{\text{ft}}\ell_{\text{th}}$	kg m^2	0.00	-0.18	-0.03
${}_xc_{\text{ft}}m_{\text{ft}}\ell_{\text{th}}$	kg m^2	0.00	-0.09	0.03
${}_yc_{\text{ft}}m_{\text{ft}}\ell_{\text{sh}}$	kg m^2	0.00	-0.18	-0.02
${}_xc_{\text{ft}}m_{\text{ft}}\ell_{\text{sh}}$	kg m^2	0.00	-0.09	0.03
$-(m_{\text{ft}} + m_{\text{sh}})\ell_{\text{th}} + {}_yc_{\text{th}}m_{\text{th}}$	kg m	-1.34	-2.19	-1.63
$-{}_yc_{\text{th}}m_{\text{th}}$	kg m	0.05	0.17	0.01
$-m_{\text{ft}}\ell_{\text{sh}} + {}_yc_{\text{sh}}m_{\text{sh}}$	kg m	-0.60	-1.45	-0.85
$-{}_xc_{\text{sh}}m_{\text{sh}}$	kg m	0.04	0.17	0.00
${}_yc_{\text{sh}}m_{\text{ft}}$	kg m	-0.01	-0.43	-0.06
$-{}_xc_{\text{ft}}m_{\text{ft}}$	kg m	0.00	0.21	-0.06

Table 4.9: Redundant multibody dynamic parameters obtained for the EXO-H3 using the two optimization methods presented in Chapter 4.2.4: an inverse dynamics approach (Inv-Dyn) and a forward dynamics approach (For-Dyn). The results generated from the physical experiment (direct measurements and CAD analysis) are also presented (PhyExp).

			Identification Method		
Group	Parameter	Units	Inv-Dyn	For-Dyn	PhyExp
Segment Mass	m_{th}	kg	–	–	1.71
	m_{sh}	kg	–	–	1.71
	m_{ft}	kg	–	–	1.43
MOI wrt COM	I_{th}	kg m^2	1.36	0.00	0.90
	I_{sh}	kg m^2	5.01	8.18	0.91
	I_{ft}	kg m^2	0.44	1.48	0.84
Segment Length	ℓ_{th}	m	–	–	0.43
	ℓ_{sh}	m	–	–	0.42
	ℓ_{ft}	m	–	–	0.28
$\hat{\mathbf{i}}$ COM position*	${}_x c_{\text{th}}$	cm	-3.10	-10.00	-0.30
	${}_x c_{\text{sh}}$	cm	-2.34	10.00	-0.24
	${}_x c_{\text{ft}}$	cm	0.00	-15.00	-3.43
$\hat{\mathbf{j}}$ COM position*	${}_y c_{\text{th}}$	cm	0.00	-50.00	-12.19
	${}_y c_{\text{sh}}$	cm	0.00	-50.00	-13.34
	${}_y c_{\text{ft}}$	cm	-0.57	-30.00	-4.10

* Segment COM position was referenced to a body-fixed frame located at the proximal joint center.

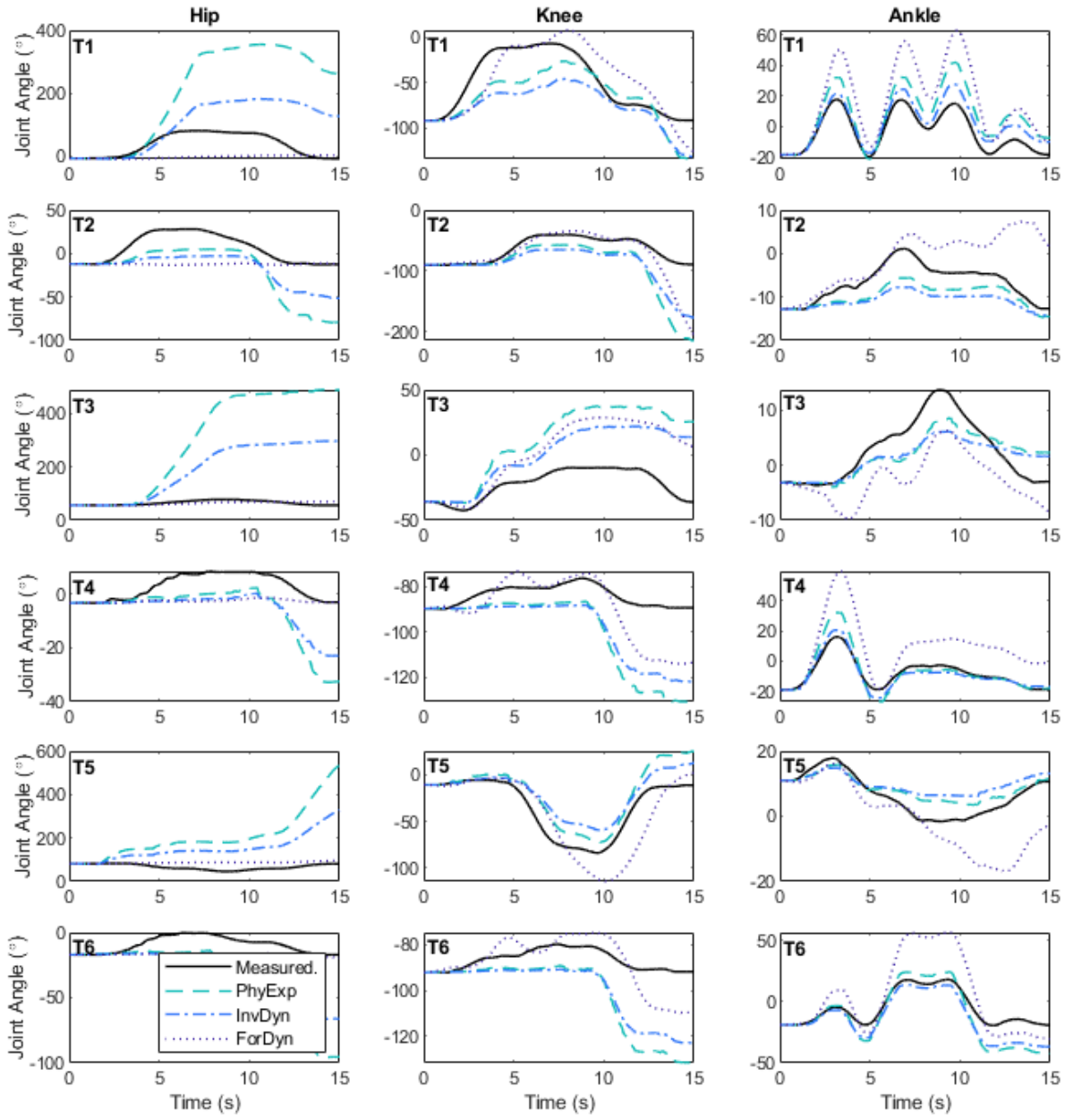


Figure 4.10: Measured and simulated joint angles for the lower-limb exoskeleton parameter identification trials (T1-6), i.e., hip (*left*), knee (*centre*), and ankle (*right*) angles. Simulated trajectories were obtained using the parameters obtained via physical experiments (PhyExp), inverse dynamics optimization (InvDyn), and forward dynamics optimization (ForDyn). For parameter values, see Table 4.8.

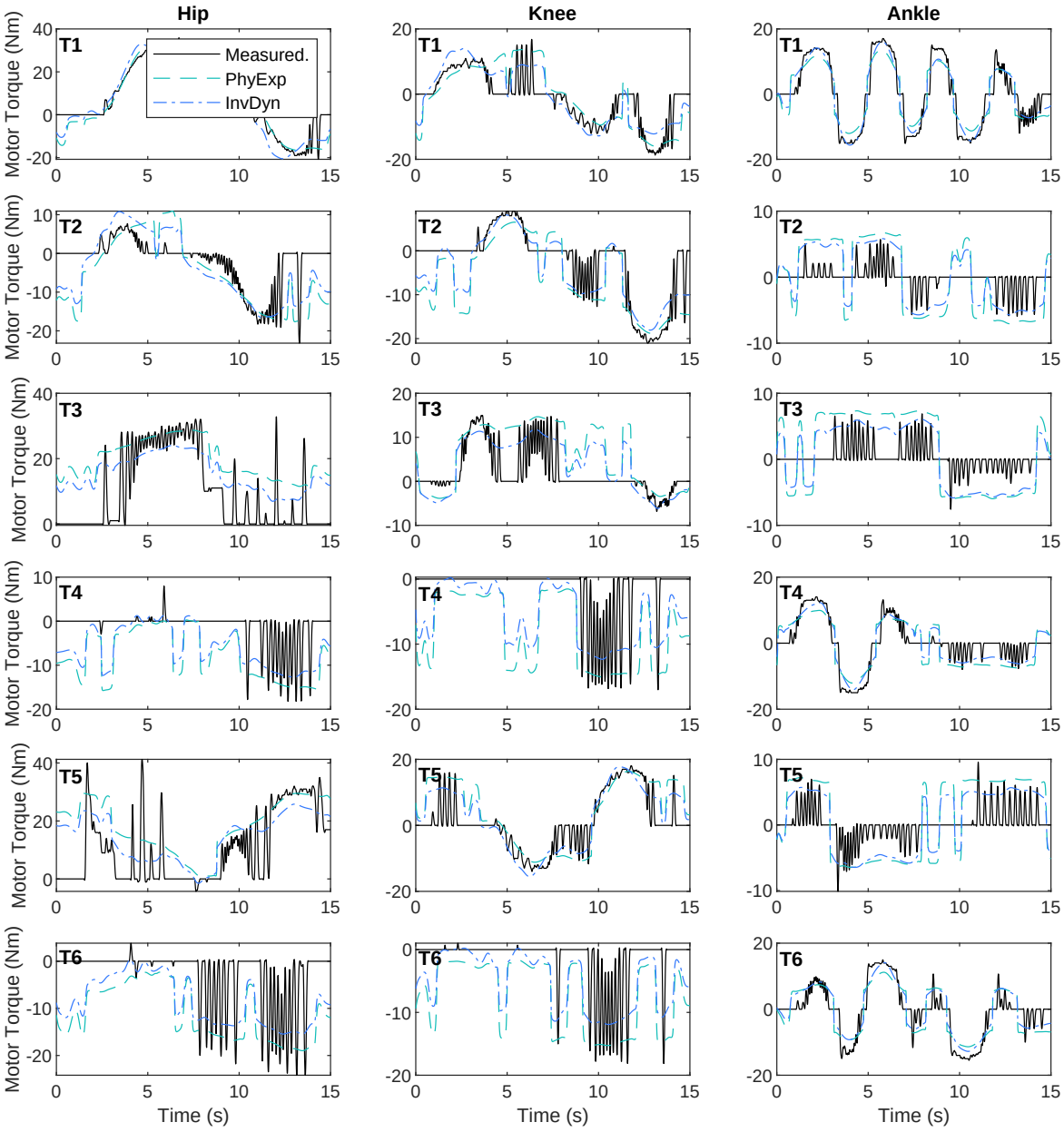


Figure 4.11: Measured and simulated motor torques angles for the lower-limb exoskeleton parameter identification trials (T1-6). Motors were included at the following joints: hip (*left*), knee (*centre*), and foot (*right*). Simulated trajectories were obtained using the parameters obtained via physical experiments (PhyExp) and inverse dynamics optimization (InvDyn). Note that the results obtained with parameters from forward dynamics optimization were not included due to their poor fit (see Table 4.10). For parameter values, see Table 4.8.

Table 4.10: Root mean square error (RMSE) between the joint angles measured during the 6 exciting experimental identification trials (T1-6) and simulated values using identified parameters from inverse dynamics optimization (InvDyn), forward dynamics optimization (ForDyn), and physical experiments (PhyExp).

		Identification Method		
Joint	Trial	Inv-Dyn	For-Dyn	PhyExp
Hip	T1	90.75°	52.52°	211.99°
	T2	25.59°	24.49°	33.18°
	T3	155.76°	7.50°	293.28°
	T4	10.03°	6.78°	12.33°
	T5	102.70°	23.70°	175.41°
	T6	24.01°	9.52°	35.16°
Knee	T1	31.97°	21.56°	24.30°
	T2	33.36°	26.27°	43.37°
	T3	26.41°	28.97°	38.11°
	T4	18.02°	12.07°	22.12°
	T5	17.91°	22.09°	18.34°
	T6	16.75°	8.50°	20.52°
Ankle	T1	6.56°	24.09°	13.18°
	T2	4.92°	7.80°	3.65°
	T3	3.74°	6.03°	3.53°
	T4	3.14°	20.01°	5.74°
	T5	4.80°	10.00°	3.35°
	T6	10.70°	20.41°	12.85°

Table 4.11: Root mean square error (RMSE) between the joint motor torques measured during the 6 exciting experimental identification trials (T1-6) and simulated values using identified parameters from inverse dynamics optimization (InvDyn), forward dynamics optimization (For-Dyn), and physical experiments (PhyExp).

		Identification Method		
Joint	Trial	Inv-Dyn	For-Dyn	PhyExp
Hip Motor	T1	6.88 Nm	161.36 Nm	8.09 Nm
	T2	6.37 Nm	72.74 Nm	8.08 Nm
	T3	9.90 Nm	64.18 Nm	12.74 Nm
	T4	6.48 Nm	55.57 Nm	8.57 Nm
	T5	9.84 Nm	73.56 Nm	12.04 Nm
	T6	8.09 Nm	66.27 Nm	10.40 Nm
Knee Motor	T1	4.92 Nm	34.36 Nm	6.44 Nm
	T2	4.78 Nm	27.05 Nm	6.68 Nm
	T3	4.76 Nm	43.40 Nm	6.88 Nm
	T4	6.02 Nm	33.27 Nm	8.52 Nm
	T5	5.12 Nm	36.15 Nm	7.17 Nm
	T6	5.46 Nm	37.42 Nm	7.76 Nm
Ankle Motor	T1	3.24 Nm	16.03 Nm	4.22 Nm
	T2	3.87 Nm	12.13 Nm	5.07 Nm
	T3	4.10 Nm	18.93 Nm	5.40 Nm
	T4	3.58 Nm	15.07 Nm	4.78 Nm
	T5	4.04 Nm	15.68 Nm	5.27 Nm
	T6	3.70 Nm	16.18 Nm	4.60 Nm

to perform best. The ForDyn-identified parameters performed quite poorly as reflected by the high RMSE values in Table 4.11. Ankle and knee torques were predicted notably well, with the InvDyn parameters performing slightly better than PhyExp. An interesting observation from this plot is that PhyExp and InvDyn parameters performed similarly in simulations despite having some notably different values, e.g., the first three parameters in Table 4.8. This suggests that there may be some issues with the final observation conditioning, i.e., over the experimental trajectories, a large change in some parameters will produce only a small change in required torque. Some remaining misestimations in the hip, knee, and ankle torques could be resulting from the lack of static friction torque output by the Brown and McPhee friction model [65, 269]. For example, the hip torques from T2-T6 were all initially measured at 0; however, in each case, the inverse dynamics model estimates that the actuator should be outputting 10-20 Nm of torque. This required torque could thus be arising from static actuator friction instead of an active torque from the motor. Furthermore, in the measured torque signals, it was common to observe "chatter"-like outputs, i.e., noise but with relatively similar amplitudes between spikes. However, the model predicted relatively constant motor torques over these intervals. This could suggest that the measured torque signals were corrupted with a significant magnitude of white-noise [318]; however, the presence of signal quantization in the EXO-H3 makes it impossible to estimate these underlying noise characteristics.

With the performance of the parameters established within the exciting experimental trial set of data, we now examine performance in a separate validation trial, i.e., a forward step validation. Briefly, hip, knee, and ankle joint angles trajectories of a single stride during natural cadence human gait were obtained from Winter [360]. In Winter [360], these trajectories are given with respect to the percentage of stride; therefore, we set the trajectories to occur over a 3.27 second span (33% slower than the actual trajectory) so that the movement could be easily and safely executed by the EXO-H3. Note that slow gait speeds are fairly typical in exoskeleton systems [135, 138]. Measurements of motor torques and joint angles were obtained using the same protocol utilized for the identification experimental trials. The resulting simulated joint angle trajectories (obtained using forward dynamics) and motor torque trajectories (obtained using inverse dynamics), for each set of parameter values listed in Tables 4.8 and 4.7, are shown in Fig. 4.12 and Fig. 4.13 respectively. Calculated root mean square error (RMSE) values for each joint, trial, and simulation method (InvDyn and ForDyn) are located in Table 4.12. Briefly, as with the six identification trajectories, the simulated hip angle estimates for the step

validation were the poorest regardless of parameter set. Interestingly, for the PhyExp and InvDyn parameters, the initial hip flexion was relatively well-matched; however, the return to extension was not feasible. This could again suggest issues with the measured motor torque signal. The PhyExp parameters performed best in matching knee and ankle trajectories, following by the InvDyn set (Table 4.12). It is likely that case the the dynamics were over-damped with the ForDyn parameters resulting in less hip/knee motion than desired. The motor torques estimates using PhyExp and InvDyn parameter sets were also quite strong (ForDyn results were not shown again in Fig. 4.13 due to poor fit). While the InvDyn parameters performed better in estimating the 6 exciting motor torque trajectories, the PhyExp set performed best in the step validation. This could suggest that the InvDyn results were overfit to the large number of experimental points used in identification optimization, resulting in less generalisability to other motions. In this case, it seems possible that fewer data points, or simply sticking to one exciting experimental trajectory is advantageous for predictive simulations [117, 282, 318]. Regardless, in general, it appears that the physical experiment parameters and inverse dynamics would both be sufficient for model-based assistance applications, especially since assistance infers that they actuators will not be responsible for all required torques [103]. If the controls are to be autonomous, we cannot guarantee perfect performance, though actuator damping should reduce the likelihood of parameter mismatches inducing high-frequency vibrations. Based on Fig. 4.12 and Fig. 4.13 alone, we believe that the PhyExp parameters are most reliable.

Prior to moving to Chapter 5 we must address the limitations of the current investigation. First, trajectories were designed around assumptions of equivalent friction at each joint, though this was not the case in the final optimization for each identification. Again, this change was made following side investigations with the motor control feature introduced late in this research to the EXO-H3. As mentioned prior, this change may affect excitability of the parameters [318]; thus further work should assess the goodness of fit obtained when maintaining the assumption of equivalent friction. Furthermore, the inverse dynamics identification algorithm did not utilize the normalized observation matrix (only used for experiment design), Using this matrix with the appropriate post-hoc transformations could in theory improve the quality of fit according to Swevers et al. [318]. Based on the parameters obtained in Table 4.9, the optimal exciting trajectories obtained may not be sufficiently exciting, especially for the MOI parameters in the forward dynamics case (ForDyn). Rather, a harmonic input signal (motor torques) with known frequency

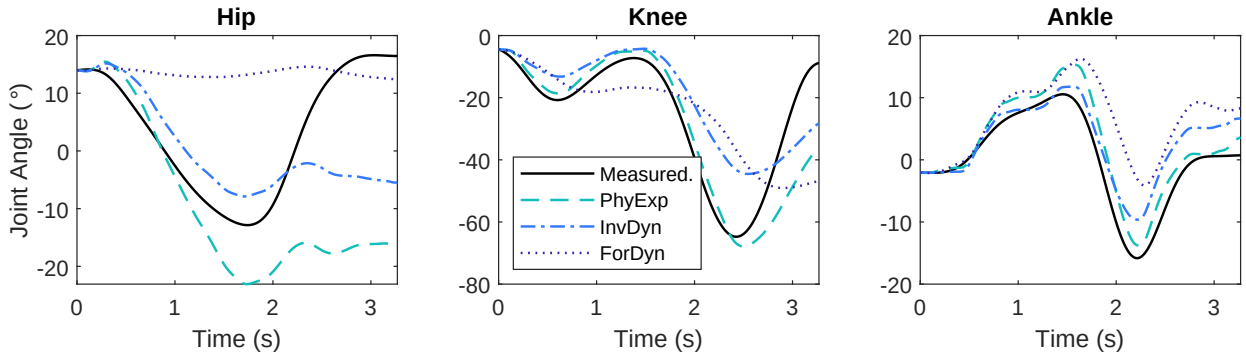


Figure 4.12: Measured and simulated joint angles for the forward step validation trial, i.e., hip (*left*), knee (*centre*), and ankle (*right*) angles. Simulated trajectories were obtained using the parameters obtained via physical experiments (PhyExp), inverse dynamics optimization (InvDyn), and forward dynamics optimization (ForDyn).

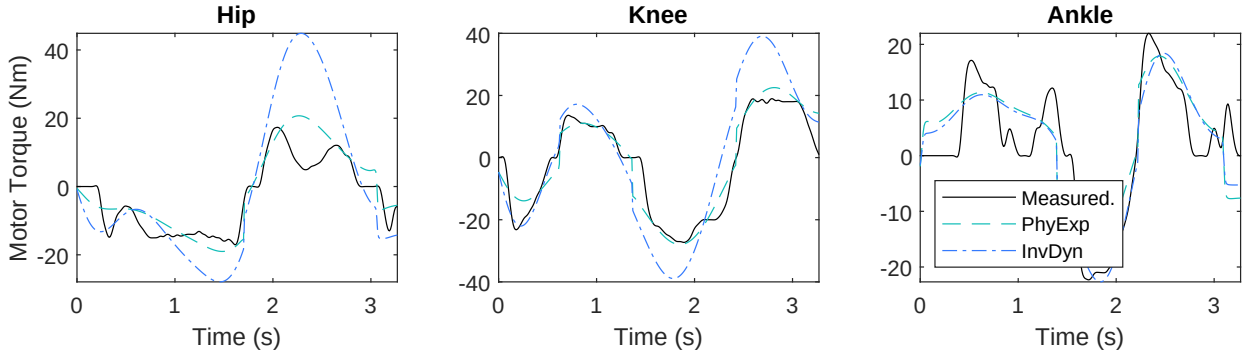


Figure 4.13: Measured and simulated motor torques for the forward step validation trial. Motors were included at the following joints: hip (*left*), knee (*centre*), and foot (*right*). Simulated trajectories were obtained using the parameters obtained via physical experiments (PhyExp) and inverse dynamics optimization (InvDyn). Note that the results obtained with parameters from forward dynamics optimization were not included due to their poor fit (see Table 4.12).

bandwidth may be a better choice [124]. Likewise, the constraints imposed on the system during identification may not have been sufficient in isolating a region of the parameter search space that contained a good local minimum or the global minimum, i.e., there was

Table 4.12: Root mean square error (RMSE) between the experimental step validation joint angles/ motor torques and simulated values using identified parameters from inverse dynamics optimization (InvDyn), forward dynamics optimization (ForDyn), and physical experiments (PhyExp).

	Identification Method		
Joint	Inv-Dyn	For-Dyn	PhyExp
Joint Position			
Hip	10.65°	14.65°	17.8°
Knee	12.05°	16.62°	10.42 °
Ankle	3.99°	7.88°	2.99°
Motor Torques			
Hip	14.71 Nm	183.12 Nm	5.47 Nm
Knee	11.18 Nm	23.27 Nm	4.73 Nm
Ankle	5.55 Nm	13.53 Nm	6.36 Nm

still poor identifiability [300, 347]. In regards to possible modelling error, it could be that the lack of static friction torque created by the Brown and McPhee [65] friction model had a negative impact on the fitting process. Rather, the Brown and McPhee model is designed to mimic the effects of static friction at low velocities through high-gain damping [128, 269]. Alternative methods include a hybrid model of friction [142], which could switch to static friction states discretely, though this could introduce additional error and could make providing the solver with symbolic derivatives challenging. A state-based friction model, e.g., bristle friction [269], could also be implemented in simulations instead [128, 142, 269]. However, this choice is not without drawbacks: the unobserved bristle state is required for inverse dynamics identification methods, otherwise, one must rely on forward dynamics methods with added uncertainty [142].

Lastly, we address the potential limitations of the investigation related to the commercial hardware being used. Foremost, while we are confident in the joint and segment angle measurements, i.e., validated EXO-H3 rotary encoders with high-resolution 3D motion capture, we cannot guarantee the same for motor torque measurements. Additional work is required to validate the motor torque estimates using the EXO-H3 onboard current

sensors, though, doing so could risk losing manufacturer support. It is possible that the quantized motor torque signals obtained via onboard current sensors were not sufficient in accurately providing the true inputs across all trials. Researchers have noted the sometimes poor and noisy quality of motor torque estimations using current sensors [124, 318] as well the possibility of position-dependent gearing ratios for harmonic drives, which could affect estimated actuator output [142, 336]. Furthermore, the EXO-H3 CAN protocol position control scheme used in experiments introduced unwanted high frequencies into the recorded joint angles. In particular, only quantized joint angles could be sent to the joint microcontrollers every 10 ms. The discrete jumps between desired set-points resulted in motion that was not as smooth as desired. Future experiments could benefit from using motor torque control instead of position control now that it is available.

Chapter 5

Modeling Integrated Human-Exoskeleton Systems

5.1 Background

In order to generate predictive dynamic simulations and control-oriented models of a biomechatronic assistive device interacting with an end-user, we must mathematically define how the two systems will be coupled [293, 123, 226, 239, 246, 261, 295]. In the case of merging the human 5-DOF inverted pendulum model with the floating-base exoskeleton , i.e., combining Equation (3.2) and Equation (4.4), we obtain the following second-order ODEs:

$$\begin{bmatrix} \mathbf{M}_{\mathrm{h}} & \mathbf{0} \\ \mathbf{0} & \mathbf{M}_{\mathrm{e}} \end{bmatrix} \begin{Bmatrix} \ddot{\mathbf{q}}_{\mathrm{h}} \\ \ddot{\mathbf{q}}_{\mathrm{e}} \end{Bmatrix} = \begin{Bmatrix} \boldsymbol{\Gamma}_{\mathrm{h}} + \boldsymbol{\tau}_{\mathrm{mtg}} + \mathbf{P} \\ \boldsymbol{\Gamma}_{\mathrm{e}} + \mathbf{T}_{\mathrm{ac}} \end{Bmatrix} + \mathbf{J}^{\intercal} \mathbf{F}_{\mathrm{he}} \tag{5.1}$$

where we introduce n_F human-exoskeleton interaction forces and/or torques in the equations of motion: $\mathbf{F}_{\mathrm{he}} \in \mathbb{R}^{n_F \times 1}$. The interaction forces are mapped to the generalized coordinate space via $\mathbf{J} \in \mathbb{R}^{5 \times n_F}$. To obtain values for $\mathbf{F}_{\mathrm{he}}$, it is most commonly assumed that the human and device are rigidly connected by reaction forces that maintain a set of kinematic constraints [169, 172, 226, 246, 295] (see Chapter 2 for more details). Doing so allows the system designer to estimate interaction forces without needing to define parameters that describe contact mechanics [133]. However, in the context of exoskeleton applications, the assumption of rigidity can overlook crucial phenomena, such as misalignment between the

device's actuator and the human joint axes of rotation, as well as the impaired power transfer that ensues as a result. Despite this limitation, there are relatively few investigations into characterizing and modeling human-exoskeleton compliance. Sánchez-Villamañán et al. [293] and Serrancoli et al. [301] most relevantly simulated compliant human-exoskeleton interactions using ideal spring-dampers. Results to date with this approach have been promising [301]; however, it is limited in its ability to capture any direction-dependence in the interactions. To clarify, the interactions on one aspect of a segment could be different then those experience on another aspect of the same segment due to location-dependent hardware and soft tissue compliance [75, 116, 296, 330]. Recently, we presented our research at the 10$^{\text{th}}$ ECCOMAS Thematic Conference on Multibody Dynamics, where we introduced a novel approach to modeling compliant interactions between humans and exoskeletons (Inkol and McPhee [171]). This involved considering various contact elements such as elastic strapping and rigid cuffs. The aim was to develop simulations capable of accurately representing the asymmetric nature of interactions between humans and the Exo-H3 device, i.e., how force is differently applied to the anterior or posterior aspects of end-user segments. Before delving into this novel approach, please refer to Appendix J for a mathematical description of how parameter-free rigid interactions between humans and exoskeletons are modeled.

5.2 Interactions via Nonlinear Compliance

As mentioned prior, the assumption of rigid human-exoskeleton connections overlooks important phenomena like misalignment between the device's actuator shaft and the human joint axis of rotation. Additionally, without an explicit model, it is difficult to use dynamic simulations to investigate how different pressure distributions during device-use can result in pressure injuries [220, 262]. In reality, like for the EXO-H3, characteristics of the interactions between the device and end-user, e.g., stiffness, can depend on whether the interaction is occurring on the posterior or anterior aspect of the targeted human segment. This direction dependence is the result of the differences in tissue compliance at different regions of the human body [116, 293]. Despite these limitations, there are relatively few investigations into characterizing and modeling human-exoskeleton compliance. Sánchez-Villamañán et al. [293] simulated a compliant human-exoskeleton interaction for the leg using an ideal spring; however, *only* the elasticity due to soft tissue deformation was

considered. Therefore, the purpose of this research was to develop an integrated human-exoskeleton model in which, via unilateral contact equations, the device cuffs and elastic straps (Velcro™) are responsible for the transfer of energy between subsystems. The choice of cuffs and elastics straps as the contact elements was based on the hardware design of the EXO-H3 (Technaid, Spain).

For the leg segments (bilateral thigh, shank, and foot), the EXO-H3 makes contact with the human end-user through the use of a combination of novel models of contact elements. Stiff interactions between rigid segments include the following: i) movement of the posterior aspect of the shank/thigh relative to two stiff "cuffs" attached to an EXO-H3 link and ii) penetration of plantar heel/toe landmarks through the exoskeleton foot pad also modelled as a cuff (see Fig. 5.1). Note that"stiff" in this context refers only to the relatively inelastic material of the exoskeleton cuff; in reality, the contact between human and cuff will be compliant due to the compression of soft tissue on the posterior shank and thigh [293]. The adjustable strapping elements then act to compress the anterior portion of the human shank and thigh against these cuffs (see Fig. 5.2). Strapping also compresses against the dorsal foot surface to ensure contact between the exoskeleton's foot pad and the end-user's plantar foot surface. In total, for each leg, we defined 12 possible sites of contact between the human and exoskeleton segments (thigh, shank, and foot), i.e., 6 strap and 6 cuff contact elements. To obtain the desired proof-of-concept simulations, less attention was directed towards modeling contact between human trunk and exoskeleton trunk orthosis; the trunk was fixed-in-place during simulations.

5.2.1 Human-Cuff Hunt-Crossley Interactions

The proposed approach to modeling human-cuff interactions in a human-exoskeleton system were based on well-established models of contact mechanics with assumptions of simple cylindrical geometry for the human segments [262, 270] and cuffs modelled as rectangular prisms (see Fig. 5.1). For each cuff element, a normal-tangential frame $\mathcal{F}_c = \begin{bmatrix}\hat{\mathbf{t}} & \hat{\mathbf{n}} & \hat{\mathbf{o}}\end{bmatrix}$ was fixed at the centre of the cuff; the contact forces act along the basis vectors that defined this frame. Note that $\hat{\mathbf{n}}$ was always orthogonal to the longitudinal axis of the relevant EXO-H3 segment. The cuff itself was characterized according to its width along $\hat{\mathbf{t}}$ i.e., w_c; it was assumed that the cuff was infinitely long along $\hat{\mathbf{n}}$ and $\hat{\mathbf{o}}$. Each cuff element was associated with a corresponding human rigid body that it was expected to make contact with; it was assumed that this body's geometry could be approximated by an infinitely

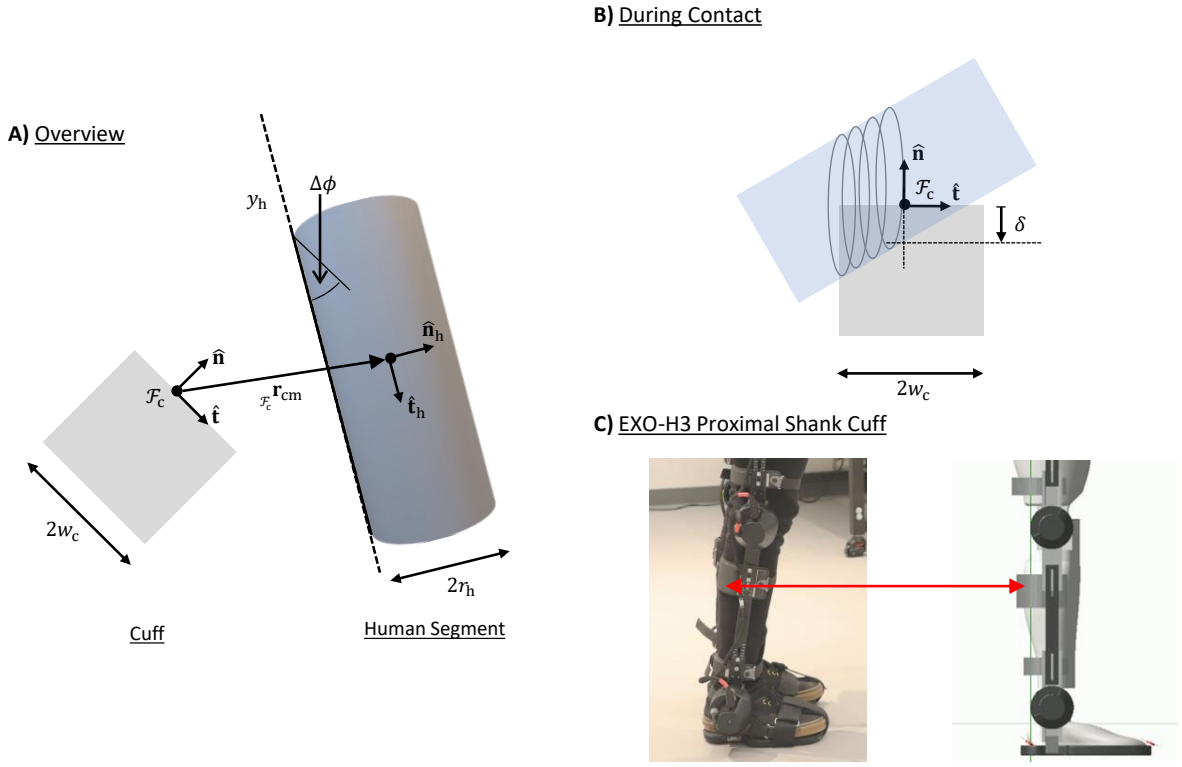


Figure 5.1: **A)** Overview of the compliant cuff interaction geometry where the human segment is approximated as a cylinder and cuff geometry is approximated as a rectangular prism. **B)** Geometry of the intersecting bodies during contact events (δ =depth of penetration). Note that the rightmost figure shows a single infinitesimal cross-sectional ellipse for a given value of x. **C)** An example of cuff element located on the real EXO-H3 and the model designed in the current dissertation.

long cylinder with radius r_h oriented at an angle $\Delta\phi$ with respect to the cuff-fixed frame, i.e., relative angle about $\hat{\mathbf{o}}$ between bodies [262].

The human-cuff interaction model was mathematically defined as follows: the location of the outer surface of cylinder with respect to $\mathcal{F}_c$ was parameterized using the equation of a straight line. To elaborate, the position of the cylinder surface closest to the cuff element was expressed within the contact element frame as

$$y_h = \tan(\Delta\phi)(x - {}_{\mathcal{F}_c}\mathbf{r}_{cm} \cdot \hat{\mathbf{t}}) + {}_{\mathcal{F}_c}\mathbf{r}_{cm} \cdot \hat{\mathbf{n}} - r_h \sec(\Delta\phi) \tag{5.2}$$

where we subtract $r_h \sec(\Delta\phi)$ to ensure that we were tracking the posterior surface of the

cylinder. Note that y_h is a coordinate that travels along $\hat{\mathbf{n}}$; x and z are therefore coordinates along $\hat{\mathbf{t}}$ and $\hat{\mathbf{o}}$ in $\mathcal{F}_\mathrm{c}$ respectively. Because $\sec(\cdot)$ was used, we assumed that $|\Delta\phi| < \frac{\pi}{2}$. To evaluate the contact force between the two bodies (rigid cuff and human segment), it was assumed that the two bodies were elastic and contact between them could be modeled using a Hunt-Crossley model [161, 301, 344]. The depth of penetration between the two bodies was calculated using the straight line described in Equation (5.2) and setting $x = 0$, i.e.,

$$\delta = \tan(\Delta\phi)\,{}_{\mathcal{F}_\mathrm{c}}\mathbf{r}_\mathrm{cm} \cdot \hat{\mathbf{t}} - {}_{\mathcal{F}_\mathrm{c}}\mathbf{r}_\mathrm{cm} \cdot \hat{\mathbf{n}} + r_\mathrm{h} \sec(\Delta\phi) \tag{5.3}$$

where contact is occurring when $\delta > 0$. From this penetration depth, we can calculate a contact force (expressed in the form used by Gonthier et al. [128]) as

$$\mathbf{F}_\mathrm{cuff} \cdot \hat{\mathbf{n}} = \begin{cases} k_\mathrm{c}\delta^{\frac{3}{2}}(1 + d_\mathrm{c}\dot{\delta}_\mathrm{cn}|\dot{\delta}_\mathrm{cn}|) & \delta \geq 0 \\ 0 & \delta < 0 \end{cases} \tag{5.4}$$

where k_c and d_c are element-specific stiffness and damping coefficients. As one can see, this approach to contact modelling treats the interface between the two bodies as a nonlinear spring-damper.

5.2.2 Human-Strap Interaction Elements

The posterior of the human segments were compressed against the cuff elements described above through the use of elastic strapping elements (see Fig. 5.2). At the origin of a given strap, a normal-tangential frame $\mathcal{F}_\mathrm{s} = \begin{bmatrix}\hat{\mathbf{t}} & \hat{\mathbf{n}} & \hat{\mathbf{o}}\end{bmatrix}$ was fixed; deformation of the strap occurred along $\hat{\mathbf{t}}$. Like previously, the location of the longitudinal axis of a cylinder with respect to $\mathcal{F}_\mathrm{s}$ was parameterized using the equation of a straight line and the segment's COM kinematics, i.e.,

$$y_\mathrm{h} = \cot(\Delta\phi)({}_{\mathcal{F}_\mathrm{s}}\mathbf{r}_\mathrm{cm} \cdot \hat{\mathbf{t}} - x_\mathrm{h}) + {}_{\mathcal{F}_\mathrm{c}}\mathbf{r}_\mathrm{cm} \cdot \hat{\mathbf{n}} \tag{5.5}$$

with zero-crossing along the local x,

$$x_\mathrm{xing} = \frac{{}_{\mathcal{F}_\mathrm{s}}\mathbf{r}_\mathrm{cm} \cdot \hat{\mathbf{n}}}{\cot(\Delta\phi)} + {}_{\mathcal{F}_\mathrm{s}}\mathbf{r}_\mathrm{cm} \cdot \hat{\mathbf{t}} \tag{5.6}$$

The penetration depth of the human segment through the strapping element was subsequently calculated as

$$\delta = r_\mathrm{h} \sec(\Delta\phi) + x_\mathrm{xing} \tag{5.7}$$

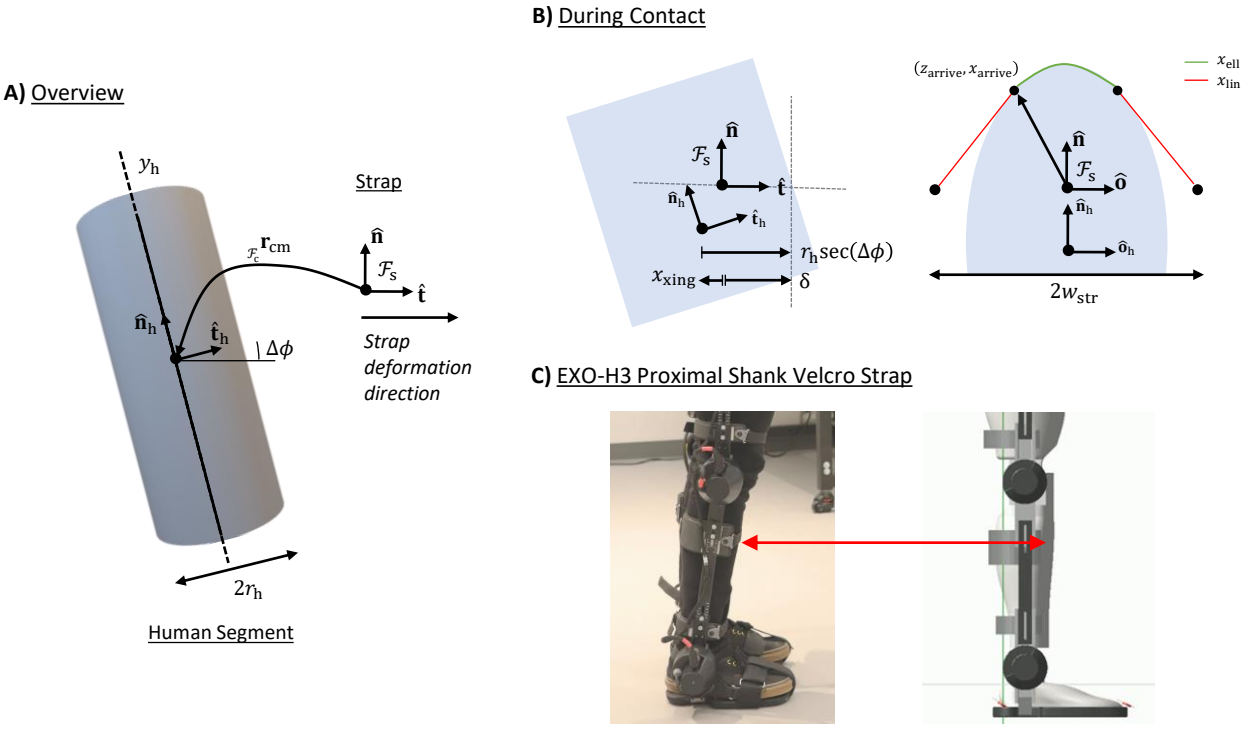


Figure 5.2: **A)** Overview of the compliant strapping interaction geometry where the human segment is approximated as a cylinder. **B)** Geometry of the intersecting bodies in both the (x, y) and (z, x) planes during contact events with the resulting strapping geometry shown by the red/green lines. Note that the contact geometry was exaggerated to better highlight the variables of interest. **C)** An example of a Velcro strap element located on the real EXO-H3 and the model designed in the current dissertation.

where $\delta > 0$ during instances of contact.

We assumed that the strap itself behaved like a massless, deformable cable that conforms to the human cylindrical geometry as the human segment's outer-surface penetrates the strapping element frame. To elaborate, given a strap with symmetrical origin and insertions with respect to $\mathcal{F}_s$, we can represent the curvature of the strap in one-half of the

(z, x)-plane using a spline of the following linear and elliptical curves:

$$x_{\text{lin}} = x_{\text{arrive}} \frac{z + w_{\text{str}}}{z_{\text{arrive}} + w_{\text{str}}} \tag{5.8}$$

$$x_{\text{ell}} = \frac{\cos(\Delta\phi)\, x_{\text{xing}} + \sqrt{r^2 - z^2}}{\cos(\Delta\phi)} \tag{5.9}$$

where $(z_{\text{arrive}}, x_{\text{arrive}})$ are the coordinates pertaining to where the linear strap portion begins making contact with the cylinder surface before transitioning into the elliptical strap interval. The variable w_{str} represents the distance between strap-frame origin and origin of the strap itself, i.e., strap origin is located at $(z, x) = (-w_{\text{str}}, 0)$; the insertion is at $(z, x) = (w_{\text{str}}, 0)$. Note that due to the assumption of symmetry about $\mathbf{t}$ in the (z, x)-plane, the point of departure, or where the elliptical strap transitions back to the linear strap, is simply the mirrored arrival point in the (z, x)-plane. For C^1 strapping curvature, the transition between line segments fulfill the following constraints at the arrival point:

$$\left(\frac{dx_{\text{lin}}}{dz} - \frac{dx_{\text{ell}}}{dz} \right) \Bigg|_{z_{\text{arrive}}} = 0 \tag{5.10}$$

The equation in (5.10) can be expanded using Equations (5.8) and (5.9) and rearranged in order to solve for z_{arrive}, i.e., where the line segments meet and share the same first derivative:

$$z_{\text{arrive}} = -\frac{r\cos(\Delta\phi)\sqrt{w_{\text{str}}^2\left(x_{\text{xing}}^2\cos^2(\Delta\phi) - r^2 + w_{\text{str}}^2\right)}\, x_{\text{xing}} + r^2\, w_{\text{str}}^2}{w_{\text{str}}\left(x_{\text{xing}}^2\cos^2(\Delta\phi) + w_{\text{str}}^2\right)} \tag{5.11}$$

Substituting (5.11) into (5.9) provides an analytical solution for x_{arrive}:

$$x_{\text{arrive}} = \frac{\cos(\Delta\phi)\, x_{\text{xing}} + \sqrt{r^2 - z_{\text{arrive}}^2}}{\cos(\Delta\phi)} \tag{5.12}$$

In simulation, once the arrival coordinates have been determined, the length of entire strap ℓ_{ell} must be evaluated to estimate the tension generated by the internal strains. If we parameterize the Cartesian ellipse coordinates with variable ϑ such that $(z, x - x_{\text{xing}}) = (r_{\text{h}}\cos(\vartheta), r_{\text{h}}\sec(\Delta\phi)\sin(\vartheta))\ \forall\ \vartheta \in [0, 2\pi]$, we obtain an arc length integral that describes

the length of the strap conforming to the penetrating cylinder's surface geometry:

$$\ell_{\text{ell}} = \int_{\vartheta_1}^{\vartheta_2} \sqrt{\frac{dz}{d\vartheta}^2 + \frac{dx}{d\vartheta}^2}\, d\vartheta \tag{5.13}$$

$$= \int_{\vartheta_1}^{\vartheta_2} \sqrt{r\sin^2(\vartheta) + r^2\sec^2\left(\Delta\phi\right)^2\cos^2(\vartheta)}\, d\vartheta \tag{5.14}$$

where the boundaries of integration, i.e.,

$$\vartheta_2 = \cos^{-1}\left(\frac{z_{\text{arrive}}}{r_{\text{h}}}\right) \tag{5.15}$$

$$\vartheta_1 = \frac{\pi}{2} - \vartheta_2 \tag{5.16}$$

are obtained through the assumption of strap arrival/departure symmetry in the (z, x)-plane. Note that the integral in Equation (5.14) must be solved numerically, e.g., quadrature or trapezoidal methods of integration [84], as there is no closed form solution assuming we do not consider elliptical integrals within the set of elementary functions [30]. The length of the strapping components described by the linear function x_{lin}, i.e., portion of straps going from device to point of arrival/departure on human segment, was simply

$$\ell_{\text{lin}} = 2\sqrt{(z_{\text{arrive}} + w_{\text{str}})^2 + x_{\text{arrive}}^2} \tag{5.17}$$

which again accounts for both right and left linear strapping deformations under the assumption of (z, x)-plane contact symmetry.

The tension generated by a strap following changes in the relative kinematic configuration of the human and exoskeleton and stretching of the total strap length

$$\ell(t) = \ell_{\text{lin}} + \ell_{\text{ell}} \tag{5.18}$$

was modelled using a second-order polynomial function,

$$F_{\text{str}}(\ell(t); k_\alpha, k_\beta, \ell_0) = \begin{cases} k_\alpha(\ell(t) - \ell_0) + k_\beta(\ell(t) - \ell_0)^2 & \ell(t) > \ell_0 \\ 0 & \ell(t) \leq \ell_0 \end{cases} \tag{5.19}$$

where ℓ_0 is a resting length parameter that affects tautness, and k_α and k_β are first- and second-order stiffness coefficients. The polynomial itself was selected according to

observations of the stress-strain relationship for different types of Velcro® in response to longitudinal deformations [38]. To balance the forces applied between human and device, the vector forces applied to human and exoskeleton were thus expressed in the element-fixed frame as

$$\mathbf{F}_{\text{str,e}} = -2F_{\text{t}} \sin(\xi) \cdot \hat{\mathbf{t}} \tag{5.20}$$

$$\mathbf{F}_{\text{str,h}} = -\mathbf{F}_{\text{str,e}} \tag{5.21}$$

where

$$\xi = \tan^{-1}\left(\frac{x_{\text{arrive}}}{z_{\text{arrive}} + w_{\text{str}}}\right) \tag{5.22}$$

was the angle of force application dependent on the angle of the linear strap portions with respect to $\hat{\mathbf{t}}$, i.e., no strapping force was delivered along $\hat{\mathbf{n}}$ or $\mathbf{o}$.

5.3 Proof of Concept Simulations

A simulation similar to the dynamometer setup discussed in Chapter 4.2 was used herein to assess the computational performance of the exoskeleton contact model. The trunk and right leg were constrained to a static seated configuration; the left leg was also initialized in a seated position but the hip, knee, and ankle were free to move (see Fig. 5.3). Unlike Chapter 4.2, a three segment, 3-DOF human leg model (used in Chapter 3) was incorporated with the exoskeleton. Kinematic constraints were utilized in all simulations to match the sagittal position of the human and exoskeleton hip joint centers. The 3D CAD models of the human leg segments shown in Fig. 5.3 were used to make estimates of cylinder geometry. These models were created and provided by Christian Mele from his MASc thesis work on human-exoskeleton interfacing [241]. Two strapping elements and two cuff

Table 5.1: Estimated strapping parameters for three types of Velcro® based on Bader and Pearcy [38].

Parameter	Standard	Kric Krac	Elasticated
k_α (N/m)	0	249	121
k_β (N/m^2)	8.59×10^4	1.99×10^4	2.33×10^3

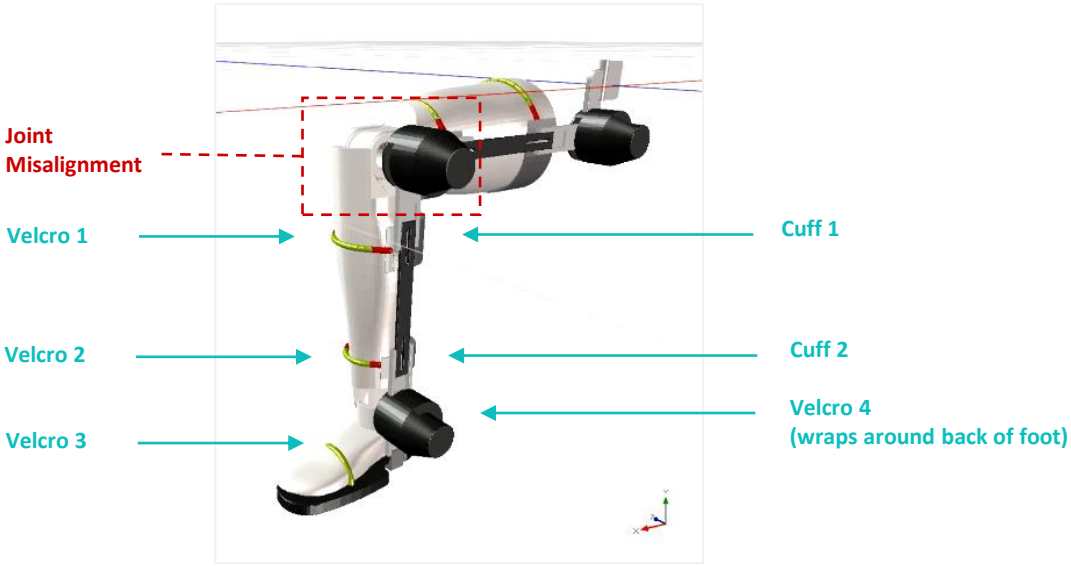


Figure 5.3: Schematic showing naming conventions for the strapping and cuff elements of interest within the MapleSim interface: straps 1-2 (Velcro) acting on the anterior shank; cuffs 1-2 acting on the posterior shank; straps 3-4 acting on the dorsal/posterior aspects on the foot. The misalignment between the EXO-H3 and human knee joint that occurred shortly after simulation onset is also highlighted for the readers interest. Note that the CAD models of the human leg segments used to estimate cylinder parameters and visualizations were provided by Christian Mele from his work in his MASc thesis [241].

elements were included for each of the exoskeleton shank and thigh. For both segments, the straps would compressed against the anterior portion of the human body; cuffs applied force to the posterior aspect. Like in the EXO-H3, straps were wrapped around the leg at the level of each cuff. Two other straps were fixed to the bottom of the exoskeleton foot sole to compress the human foot downward against the exoskeleton foot pad. Lastly, for comparison, we also performed a simulation of the EXO-H3 knee motion with rigid constraints linking the human and device leg segments. The constraint force acting on the shank specifically maintained the kinematic constraint

$$\Phi_{\text{shank}} = \mathbf{r}^{\text{h}}_{\text{cuff}} \cdot \hat{\mathbf{i}}^{\text{se}} = 0 \tag{5.23}$$

where $\mathbf{r}^{\text{h}}_{\text{cuff}} \in \mathbb{R}^3$ is a vector, referenced in the exoskeleton shank coordinate frame, that points toward a position along the longitudinal axis of the human shank that should be maintained at the same height as the proximal shank cuff (Cuff 1 in Fig. 5.3). Variable

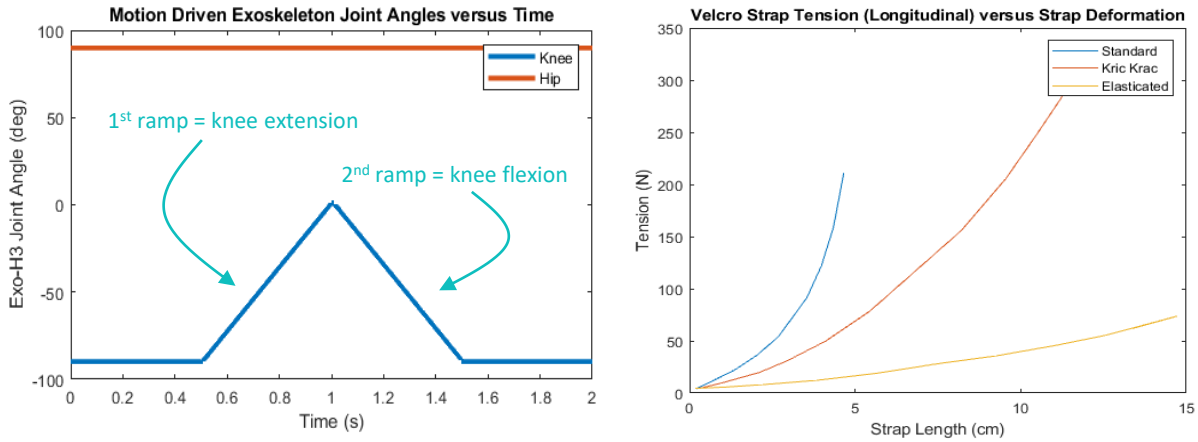


Figure 5.4: **A)** The desired EXO-H3 hip and knee trajectories controlled via joint-level PD control; the ankle joint received no controller inputs, i.e. motor torques. The hip was held motionless while the knee underwent an extension ramp followed by a flexion ramp. **B)** Simulated strapping tensions F_{str} (Equation (5.19)) for each of three Velcro types listed in Table 5.1 ("Standard", "Kric Krac", "Elasticated") using parameters obtained from the data in Bader and Pearcy [38].

$\hat{\mathbf{i}}^{\text{se}} \in \mathbb{R}^3$ is the normal vector in the exoskeleton shank-fixed frame, along which the cuff contact force occurs.

The exoskeleton knee was driven kinematically to match a desired motion (knee extension ramp followed by knee flexion ramp at constant velocity of ± 3.2 °/s; see Fig. 5.4A). Simultaneously, the hip was held at 90° of flexion while the ankle was actuated by passive friction torques (see Chapter 4.1.2). The experimental measurements in Bader and Pearcy [38] were used to identify elastic gains k_α and k_β for three different variations of Velcro® strap materials to be tested: Standard, "Kric Krac", and Elasticated (see Table 5.1 for identified parameter values; Fig. 5.4B for the plotted tension). Additionally, for each of the aforementioned types, a "Loose" and "Secured" condition was tested; the secured condition required the resting length of each Velcro strap be reduced depending on location, i.e., shank and thigh straps reduced by 5 cm; feet straps reduced 5 cm (Velcro 3) and 10 cm (Velcro 4). Rigid cuffs were provided the following arbitrary parameter values to produce stiff contact against the posterior aspect of the shank: $k_c = 10^5$ N/m$^{\frac{3}{2}}$, $d_c = 5 \times 10^4$ Ns/m. For the current simulations, we assumed that there was no tangential friction between cuff and end-user ($f_{\text{f}} = 0$). Note that as we do not have experimental measurements of human-exoskeleton contact pressure during operation, the simulations herein were simply used

to assess computational performance as well as ability of the compliant model to capture phenomena like human-device joint misalignment during simulations.

Simulated hip, knee, and ankle joint angle trajectories for the left human leg, for each of the tested conditions (3 Velcro types $\times$ 2 levels of strap tautness) are shown in Fig. 5.5. In general, the addition of unilateral contact equations to the integrated human-exoskeleton model allowed us to capture the transient phenomenon that are overlooked when assuming the interactions to be rigid. For example, the compliant approach provided the ability to replicate design asymmetries in the exoskeleton, i.e. rigid cuff versus elastic strap on the posterior and anterior aspect of segments. This resulted in the overshoot of the human knee angle in Fig. 5.5A where the elastic strap was unable to halt momentum about the knee quickly, without having a shorter resting length. To try and quantify how the different conditions (Velcro® type and strap tautness) affected joint misalignment, the average ankle joint misalignment (AJM) was evaluated for each simulation. This metric was calculated using the Euclidean distance between human and exoskeleton ankle joint centre positions in the sagittal plane. The ankle was chosen as it was the most distal joint to the hip, and the EXO-H3 and human hip joint centers were always aligned. In general, a lower AJM was observed in response to increases in strap tautness and stiffness parameters. Not surprisingly given its profile in Fig. 5.4B, the secured Standard Velcro was best at minimizing misalignments (AJM = 1.48 mm); making the strap loose substantially increased this error (AJM = 14.6 mm). The worst performance came from the Elasticated straps (loose AJM = 24.0 mm, secured AJM = 12.9 mm) followed by the Kric Krac straps (loose AJM = 16.9 mm, secured AJM = 2.51 mm).

Representative data for the simulated shank strap tension (Standard Velcro®; Secured condition) is shown in Fig. 5.6A. Fig. 5.6B highlights the simulated normal cuff forces recorded under this same condition, while Fig. 5.6C shows the shank constraint force recorded during the constrained simulation, i.e., maintained constraint in Equation (5.23). In MapleSim, solving the dynamic equations with the proposed compliant contact elements and standard parameters over the 2 second period of interest required 22.06 CPU seconds; the constrained model integration required only 0.02 CPU seconds. In all cases, a solution was obtained using a variable step-size stiff Rosenbrock numerical ODE solver. The proximal shank strap (Velcro 1) experienced a decrease in tension during the knee extension (strap shortened). As this decrease occurred, the proximal cuff (Cuff 1) normal force increased due to an increase in gravitational toppling that had to be compensated. Conversely, the distal strap tension (Velcro 2) increased during knee extension

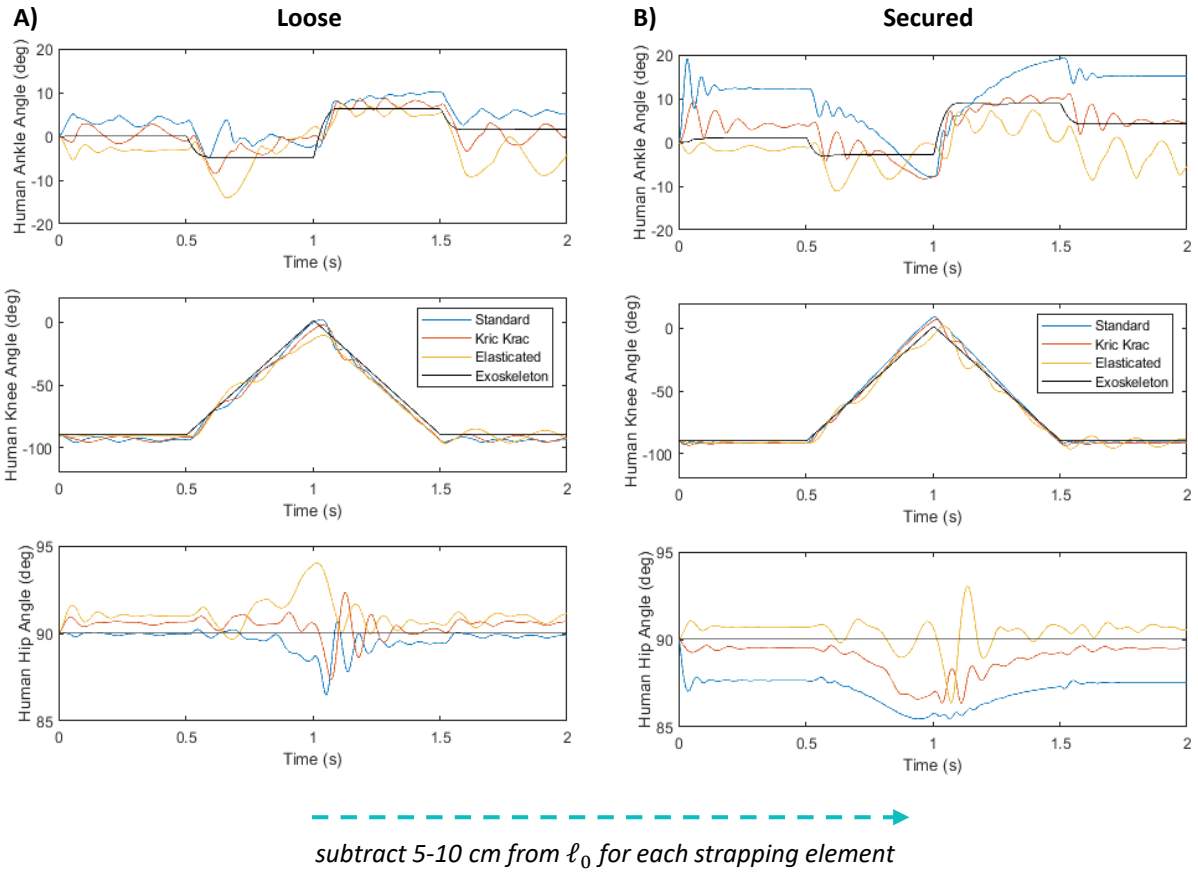


Figure 5.5: Simulated human hip, knee, and ankle joint angles for each type of Velcro strap (Standard, Kric Krac, and Elasticated) under the **A)** "loose" condition (baseline strap resting length) and the **B)** "secured" condition (strap resting length reduced by 5-10 cm). For reference, the exoskeleton joint angle trajectories are shown by the black line.

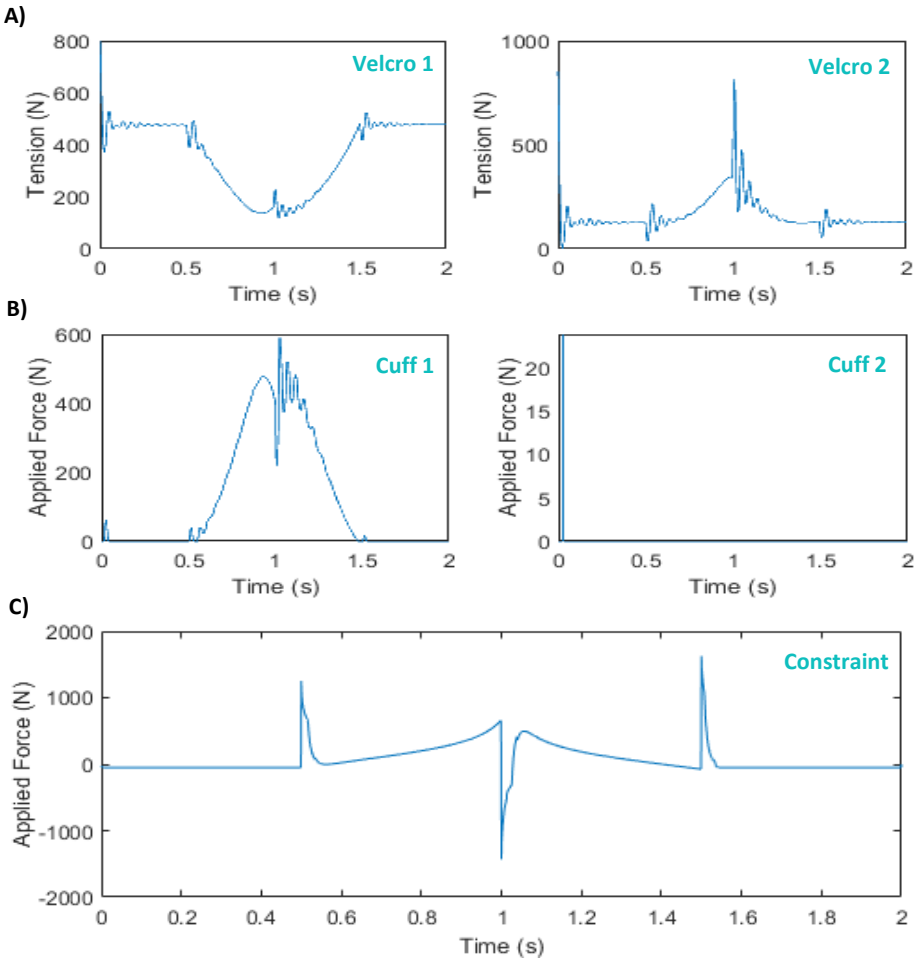


Figure 5.6: Simulated **A)** tension for each shank strapping element (Velcro 1-2), **B)** applied normal forces due to contact at each shank cuff element (Cuffs 1-2), and **C)** corresponding constraint forces (applied to the shank) evaluated when using kinematic constraints to combine human and exoskeleton in simulation rather than compliant elements.

as the shank disengaged from the distal cuff (Cuff 2). In fact, due to the geometry of the shank (larger circumference in proximity to knee than ankle), the distal cuff was never engaged after the first few ms due to engagement with the proximal cuff only. There was good agreement between the applied forces simulated using the constraint method and the compliant cuff method (Fig. 5.6C). The transients observed in the simulated constraint force trajectory, i.e., the jumps in force during sudden changes in knee velocity, were not necessarily observed in the compliant simulations. Rather, in compliant simulations, vibra-

tions were introduced around these events. While oscillatory behaviours were not observed in the constraint force signal, the transients that were observed often exceeded 1000 N and inherently represent high-frequency signal content.

There are numerous limitations to the proposed compliant human-exoskeleton model that should be addressed: first, tangential friction was ignored for both the cuff and strap. The strap tension also had no damping component; both of these factors could be investigated to reduce the magnitude of vibrations observed during simulations [244, 247]. Additionally, motion was restricted to the sagittal plane in the current dissertation, so the contact equations disseminated assume that the human cylinder never rotates with respect to the inertial $\hat{\mathbf{k}}$. Allowing this degree of freedom in compliant human-exoskeleton simulations would require the addition of contact elements that apply forces to the end-user in the frontal plane. Lastly, in their current form, the compliant equations can be quite sensitive to changes in parameters, initial conditions, and choice of solver. Given the similarities between the strapping element equations and models of muscle wrapping [262] as well as the fact that the strap elements were also usually treated as mass-less cables, it may feasible to implement computational methods from the muscle modeling literature to improve performance and reliability [93, 247, 327]. Like in muscle modelling, addition of spring-damper elements in series to each other, e.g., modeling human tissue compression with strapping tension, only adds to this challenge, but is a likely future direction [247].

5.4 Merging Human- Exoskeleton Models for FIP Simulations

As discussed in Chapter 5.1, to create an integrated multibody model of a human wearing a lower-limb exoskeleton, either kinematic constraint equations that couple the two systems together can be defined (i.e., method of Lagrange multipliers), or an explicit model of the interactions between the two systems, according to principles of contact mechanics, can be implemented. In the previous section, we noted that the latter method often resulted in simulations that were substantially slower and more sensitive to their initialization. Therefore, to obtain a computationally efficient model of human-exoskeleton FIP balance for inclusion within control- and observation-oriented models as well as simulations to estimate the human-exoskeleton FIP FSR, the human and exoskeleton were rigidly attached

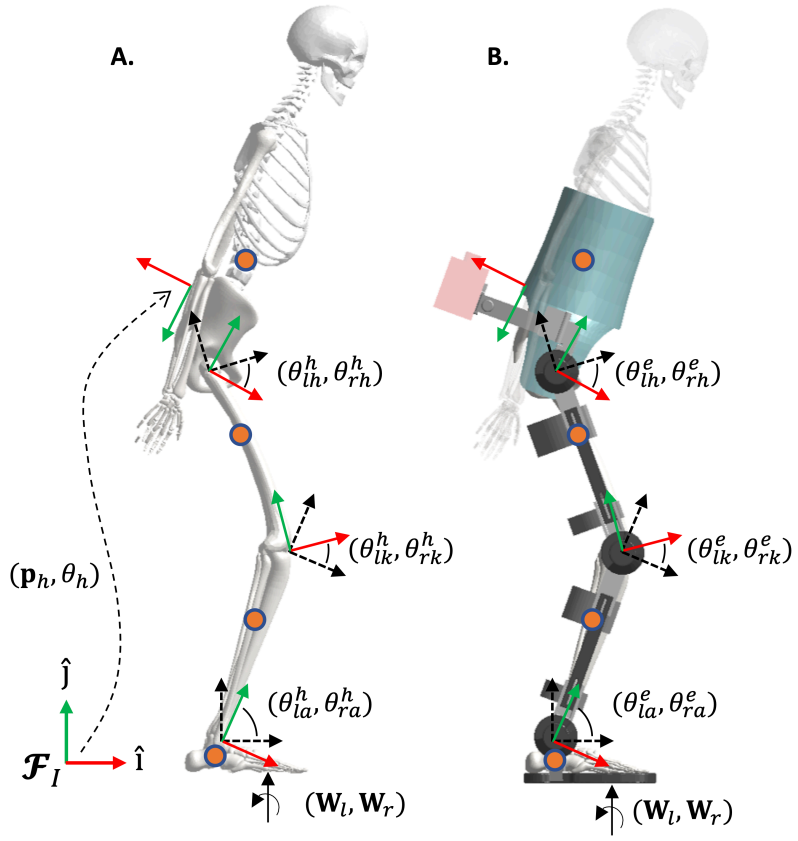


Figure 5.7: Schematic of the floating-base human-only (A) and lower-limb exoskeleton dynamic models (B, based on the Technaid Exo-H3), with each systems' nine degrees of freedom highlighted. Note that the human is shown transparently in B to highlight how the exoskeleton fits the user.

to each other assuming perfect alignment between the joints [134, 169, 172, 246]. In doing so, all constraints forces were removed from the dynamic equations so that we were dealing with ODEs exclusively in the design of controllers and observers for the EXO-H3 [260].

Briefly, to obtain a sagittal upright standing model of the human and exoskeleton, we simply modified the exoskeleton model topology provided in MapleSim. The right and left exoskeleton feet were welded to the ground as done for the human stance model in Chapter 3, i.e., to each foot we applied the constraints

$$\mathbf{r}_{\text{toe,e}} = \mathbf{r}_{\text{toe,h}} = \ell_{\text{c2t}}\hat{\mathbf{i}} - \ell_{\text{ah}}\hat{\mathbf{j}} \tag{5.24}$$

$$\mathbf{r}_{\text{heel,e}} = \mathbf{r}_{\text{toe,h}} = -\ell_{\text{c2h}}\hat{\mathbf{i}} - \ell_{\text{ah}}\hat{\mathbf{j}} \tag{5.25}$$

which assume the exoskeleton foot and human foot are of the same length. In Equations (5.24) and (5.25), $\mathbf{r}_{\text{toe,e}}$ and $\mathbf{r}_{\text{toe,h}}$ were the positions of the exoskeleton and human toe markers respectively as defined in the two-point contact model (Chapter 3.2; $\mathbf{r}_{\text{heel,-}}$ is the position of the heel). The assumption of rigid human-exoskeleton connections, discussed in detail in Appendix J, can then be enforced in dynamic simulations by applying the following constraints between the human and exoskeleton generalized coordinates:

$$\mathbf{q}_{\text{e,ll}} = \mathbf{q}_{\text{e,rl}} = \mathbf{q}_{\text{e3}} \tag{5.26}$$

$$\mathbf{q}_{\text{e3}} = \mathbf{q}_{\text{h,1...3}} \tag{5.27}$$

$$= \mathbf{q}_{\text{h3}} \tag{5.28}$$

$$= \{\theta_{\text{hip}}(t), \theta_{\text{knee}}(t), \theta_{\text{ankle}}(t)\}^{\intercal} \tag{5.29}$$

where $\mathbf{q}_{\text{e3}} \in \mathcal{Q}_{\text{e3}}$ and $\mathcal{Q}_{\text{e3}} \subseteq \mathbb{R}^3$. The notation $\mathbf{x}_{i...j}$ indicates a subset of $\mathbf{x}$, i.e., $\mathbf{x}_{i...j} = \{x_i, \ldots, x_j\}$. Equation (5.26) is an indication that we wish for the exoskeleton model to stand FIP with bilateral symmetry between the lower-limbs.

In MapleSim, the modified exoskeleton model topology yields a system of ODEs that reflect the dynamics of a triple inverted pendulum:

$$\mathbf{M}_{\text{e3}}\ddot{\mathbf{q}}_{\text{e3}} = \boldsymbol{\Gamma}_{\text{e3}}(\mathbf{q}_{\text{e3}}, \dot{\mathbf{q}}_{\text{e3}}) + 2\boldsymbol{\tau}_{\text{ac}}(\dot{\mathbf{q}}_{\text{e3}}) \tag{5.30}$$

where $\mathbf{M}_{\text{e3}} \in \mathbb{R}^{3\times3}$ is the exoskeleton's inertia matrix and $\boldsymbol{\Gamma}_{\text{e3}} \in \mathbb{R}^{3\times1}$ is a column matrix containing gravitational and velocity-dependent torques, and $\boldsymbol{\tau}_{\text{ac}}$ are the lumped actuator torques (introduced in Chapter 4.1.2), but scaled by 2 due to the assumption of bilateral symmetry between the leg segments (similar scaling for MTGs in Chapter 3). Merging these dynamic equations with the standing human equations in Equation (3.2) and the constraints (5.28) result in a system of differential algebraic equations (DAEs):

$$\begin{bmatrix} \mathbf{M}_{\text{h}} & \mathbf{0} \\ \mathbf{0} & \mathbf{M}_{\text{e3}} \end{bmatrix} \begin{Bmatrix} \ddot{\mathbf{q}}_{\text{h}} \\ \ddot{\mathbf{q}}_{\text{e3}} \end{Bmatrix} = \begin{Bmatrix} \boldsymbol{\Gamma}_{\text{h}} + \boldsymbol{\tau}_{\text{mtg}} + \mathbf{P} \\ \boldsymbol{\Gamma}_{\text{e3}} + 2\boldsymbol{\tau}_{\text{ac}} \end{Bmatrix} + (\nabla\Phi)^{\intercal}\boldsymbol{\lambda}_{\text{he}} \tag{5.31}$$

$$\Phi = \mathbf{q}_{\text{e3}} - \mathbf{A}_{\text{he}}\mathbf{q}_{\text{h}} = \mathbf{0}$$

where $\boldsymbol{\lambda}_{\text{he}}$ were the joint reaction torques (Lagrange multipliers) that enforce the kinematic Φ constraints within the dynamic equations. Evaluation of these equations requires definition of the constraint Jacobian,

$$\nabla\Phi = \begin{bmatrix} \frac{\partial\Phi}{\mathbf{q}_{\text{h}}} & \frac{\partial\Phi}{\mathbf{q}_{\text{e3}}} \end{bmatrix} = \begin{bmatrix} -\mathbf{A}_{\text{he}} & \mathbf{I}_{3\times3} \end{bmatrix} \tag{5.32}$$

where $\mathbf{I}_{n\times n}$ is an $n \times n$ identity matrix and

$$\mathbf{A}_{\text{he}} = \begin{bmatrix} \mathbf{I}_{3\times 3} & \mathbf{0}_{3\times 2} \end{bmatrix} \tag{5.33}$$

where $\mathbf{0}_{n\times n}$ is an $n \times n$ matrix of zeros. Equation (5.33) is structured to simply isolate the lower limb joint angles within the human generalized coordinates, i.e., $\mathbf{q}_{\text{h},1..3}$. To further simplify the system, the DAEs in (5.31) are converted to ODEs by solving for the reaction forces from the equations of motion. First, from Equation (5.31), we establish the relation

$$\boldsymbol{\lambda}_{\text{he}} = \mathbf{M}_{\text{e3}}\ddot{\mathbf{q}}_{\text{e3}} - \boldsymbol{\Gamma}_{\text{e3}} - 2\boldsymbol{\tau}_{\text{ac}} \tag{5.34}$$

and then simply substitute (5.34) into (5.31), which yields the system of ODEs

$$\mathbf{M}_{\text{h}}\ddot{\mathbf{q}}_{\text{h}} = \boldsymbol{\Gamma}_{\text{h}} + \boldsymbol{\tau}_{\text{mtg}} + \mathbf{P} - \mathbf{A}_{\text{he}}^{\intercal}(\mathbf{M}_{\text{e3}}\ddot{\mathbf{q}}_{\text{e3}} - \boldsymbol{\Gamma}_{\text{e3}} - 2\boldsymbol{\tau}_{\text{ac}}) \tag{5.35}$$

Expanding Equation (5.35) and substituting in the following kinematic relationships:

$$\mathbf{q}_{\text{e3}} = \mathbf{A}_{\text{he}}\mathbf{q}_{\text{h}} \tag{5.36}$$

$$\dot{\mathbf{q}}_{\text{e3}} = \mathbf{A}_{\text{he}}\dot{\mathbf{q}}_{\text{h}} \tag{5.37}$$

$$\ddot{\mathbf{q}}_{\text{e3}} = \mathbf{A}_{\text{he}}\ddot{\mathbf{q}}_{\text{h}} \tag{5.38}$$

we arrive at the final integrated human-exoskeleton model of the current dissertation:

$$(\mathbf{M}_{\text{h}} + \mathbf{A}_{\text{he}}^{\intercal}\mathbf{M}_{\text{e3}}\mathbf{A}_{\text{he}})\ddot{\mathbf{q}}_{\text{h}} = \boldsymbol{\Gamma}_{\text{h}} + \boldsymbol{\tau}_{\text{mtg}} + \mathbf{P} + \mathbf{A}_{\text{he}}^{\intercal}\boldsymbol{\Gamma}_{\text{e3}} + 2\mathbf{A}_{\text{he}}^{\intercal}\boldsymbol{\tau}_{\text{ac}} \tag{5.39}$$

Note that Equation (5.39) was used to study the human-exoskeleton FSR in Chapter 6. This equation was also the basis of the control-oriented FIP models used within the proposed balance regulation/assistance controllers and state-estimation methods also discussed in Chapter 6.

Chapter 6

Dynamic Simulations of Model-Based Assisted Balance Control

6.1 The Human-Exoskeleton Feet-In-Place FSR

The following section contains content related to the paper "Using Dynamic Simulations to Estimate the Feasible Stability Region of Feet-In-Place Balance Recovery for Lower-Limb Exoskeleton Users" published/presented at the 2022 9th IEEE RAS/EMBS International Conference for Biomedical Robotics and Biomechatronics (Inkol and McPhee [172]).

Typically, when wearing a lower-limb exoskeleton, the net human-exoskeleton COM is lowered (relative to human-only COM) due to distribution of mass in the hardware. In theory, such a change should increase the magnitude of COM velocity that can be recovered from [154]. However, the device's torque generating capabilities, joint-level impedance, and dead times resulting from characteristics of the actuators, sensors, etc. may have the opposite effect. Likewise, constraining torque or power generation in the device's actuators to prevent damage may also affect the device's ability to terminate a forward fall.

Therefore, in the current section, we examined how the human FSR for FIP balance recovery was influenced by the presence of a robotic lower-limb exoskeleton based on the EXO-H3. In particular, we were interested in how features of the hardware, e.g., gearing friction and reflected inertia, changes in mass distribution, and variations in actuator strength, would influence the corresponding FIP margins of stability [154, 175]. The FSR

optimal control problem introduced in Chapter 3 was first reformulated for the human-exoskeleton system. Various simulation experiments of FIP balance were then performed; the results are presented and discussed at the end of this subsection.

6.1.1 FIP Stability with Exoskeleton Assistance

As discussed in Chapter 3, the discrete formulation of the optimal control problem that solved for the anterior human-exoskeleton FSR boundary was stated as

$$\underset{x,u}{\operatorname{argmin}} \{-\dot{\mathbf{r}}_{\text{icm}}[1] \cdot \hat{\imath}\} \tag{6.1}$$

subject to

$$\mathbf{h}_{\text{init}}(\mathbf{x}_{\text{he}}[1], \mathbf{u}_{\text{he}}[1]; \mathbf{q}_{\text{max},0}, \mathbf{q}_{\text{min},0}) \leq \mathbf{0} \tag{6.2}$$

$$\mathbf{g}_{\text{init}}(\mathbf{x}_{\text{he}}[1], \mathbf{u}_{\text{he}}[1]; r_0) = \mathbf{0} \tag{6.3}$$

$$\mathbf{h}_{\text{term}}(\mathbf{x}_{\text{he}}[n], \mathbf{u}_{\text{he}}[n]) \leq \mathbf{0} \tag{6.4}$$

$$\mathbf{g}_{\text{term}}(\mathbf{x}_{\text{he}}[n], \mathbf{u}_{\text{he}}[n] = \mathbf{0} \tag{6.5}$$

$$\mathbf{g}_{\text{coll}}(\mathbf{x}_{\text{he}}[k], \mathbf{u}_{\text{he}}[k], \mathbf{x}_{\text{he}}[k+1], \mathbf{u}_{\text{he}}[k+1]) \leq \mathbf{0} \quad \forall\, k = 1 \ldots n-1 \tag{6.6}$$

$$\mathbf{h}_{\text{fsr}}(\mathbf{x}_{\text{he}}[k], \mathbf{u}_{\text{he}}[k]) \leq \mathbf{0} \quad \forall\, k = 1 \ldots n \tag{6.7}$$

$$\mathbf{g}_{\text{fsr}}(\mathbf{x}_{\text{he}}[k], \mathbf{u}_{\text{he}}[k] = \mathbf{0} \quad \forall\, k = 1 \ldots n \tag{6.8}$$

$$\begin{Bmatrix} \mathbf{x}_{\min} \\ \mathbf{u}_{\min} \end{Bmatrix} \leq \begin{Bmatrix} \mathbf{x}_{\text{he}}[k] \\ \mathbf{u}_{\text{he}}[k] \end{Bmatrix} \leq \begin{Bmatrix} \mathbf{x}_{\max} \\ \mathbf{u}_{\max} \end{Bmatrix} \quad \forall\, k = 1 \ldots n \tag{6.9}$$

where

$$\mathbf{x}_{\text{he}}(t) = \begin{Bmatrix} \mathbf{q}_{\text{h}} \\ \dot{\mathbf{q}}_{\text{h}} \\ \mathbf{a} \end{Bmatrix}, \quad \mathbf{u}_{\text{he}}(t) = \begin{Bmatrix} \mathbf{u} \\ \boldsymbol{\tau}_{\text{mtr}} \\ \ddot{\mathbf{q}}_{\text{h}} \\ \dot{\mathbf{a}} \end{Bmatrix} \tag{6.10}$$

are the modified human-exoskeleton state and control vectors incorporated within the optimal control problem's state-space formulation. As in Chapter 3, the optimal control problem estimates the anterior and posterior boundaries of the FSR according to the COM

kinematics of the combined human-exoskeleton,

$$M_{\mathrm{h}} = \sum_{i=1}^{n_{\mathrm{rb}}} m_i, \quad M_{\mathrm{e}} = \sum_{i=1}^{n_{\mathrm{rb,e}}} m_{\mathrm{e},i} \tag{6.11}$$

$$\mathbf{r}_{\mathrm{icm}} = \frac{M_{\mathrm{h}}}{M_{\mathrm{h}} + M_{\mathrm{e}}} \mathbf{r}_{\mathrm{cm}} + \frac{M_{\mathrm{e}}}{M_{\mathrm{h}} + M_{\mathrm{e}}} \sum_{i=1}^{n_{\mathrm{rb,e}}} \frac{m_{\mathrm{e},i}}{M_{\mathrm{e}}} \mathbf{r}_{\mathrm{ecm},i}(\mathbf{q}_{\mathrm{h}}) \tag{6.12}$$

where $\mathbf{r}_{\mathrm{icm}} \in \mathbb{R}^3$ is the position of the human-exoskeleton COM, $n_{\mathrm{rb,e}}$ is the number of rigid bodies contained within the exoskeleton dynamic model and $m_{\mathrm{e},i}$ and $\mathbf{r}_{\mathrm{ecm}} \in \mathbb{R}^3$ are the mass and COM position of a specific exoskeleton rigid body respectively.

Note that the Equations (6.2– 6.9) were modified from the original descriptions in Chapter 3, i.e., Equations (3.28– 3.36), so as to include the human-exoskeleton dynamics and ranges of motion discussed in Chapters 4 and 5. For example, the trapezoidal collocation constraints were rewritten using the human-exoskeleton states and controls (6.10), i.e.,

$$\mathbf{g}_{\mathrm{coll}} = \mathbf{x}_{\mathrm{he}}[k+1] - \mathbf{x}_{\mathrm{he}}[k] - \frac{\Delta t}{2}(\mathbf{f}_{\mathrm{he}}[k] + \mathbf{f}_{\mathrm{he}}[k+1]) = \mathbf{0} \tag{6.13}$$

where

$$\mathbf{f}_{\mathrm{he}}[k] \equiv \begin{Bmatrix} \dot{\mathbf{q}}_{\mathrm{h}}[k] \\ \ddot{\mathbf{q}}_{\mathrm{h}}[k] \\ \dot{\mathbf{a}}[k] \end{Bmatrix} = \begin{Bmatrix} \mathbf{x}_{\mathrm{he},6..10}[k] \\ \mathbf{u}_{\mathrm{he},14..18}[k] \\ \mathbf{u}_{\mathrm{he},19..28}[k] \end{Bmatrix}, \quad \mathbf{f}_{\mathrm{he}}[k+1] \equiv \begin{Bmatrix} \dot{\mathbf{q}}_{\mathrm{h}}[k+1] \\ \ddot{\mathbf{q}}_{\mathrm{h}}[k+1] \\ \dot{\mathbf{a}}[k+1] \end{Bmatrix} \tag{6.14}$$

Path inequality constraints (6.7) were modified from (3.35) to consider the domain of feasiblity for the human-exoskeleton dynamics $\boldsymbol{\Omega}_{\mathrm{he}}$ rather than the human-only $\boldsymbol{\Omega}$. As a reminder to the reader, these inequality constraints were enforced to to prevent the zero moment point (ZMP) from existing outside of the physical base of support boundaries, slipping of the feet (assuming a static coefficient of friction of 0.80 [264]), and the vertical ground-reaction forces from "pulling" on the feet. Path equality constraints (6.8) were modified from (3.36) to include the ODEs in Equation (5.39) rather than (3.2). Lastly, the initial and terminal constraints (6.2– 6.5) were adjusted from (3.28– 3.32) to consider the initial and final horizontal kinematics of the human-exoskeleton COM ($\mathbf{r}_{\mathrm{icm}}$ rather than the human-only COM $\mathbf{r}_{\mathrm{cm}}$).

6.1.2 Simulation Experiments and Results

Using NLP, the human-exoskeleton model's anterior and posterior FSR boundaries were estimated under a variety of novel conditions with the intention of gaining a better understanding of how features of exoskeleton hardware impact the ability to balance with FIP. Additionally, with the results in Chapter 3, it was possible to assess how the optimal postural strategy in-theory changes from human-only FIP balance to human-exoskeleton balance (originally published in Inkol and McPhee [172]). The following section contains four simulation experiments investigating the effects of end-user capabilities and device hardware on the FIP FSR. For additional FIP FSR simulations investigating factors like restrictions of DOF (like that assessed for the human-only in Section 3) and redistribution/addition of mass to the device, we refer the reader to Appendix K.

1) Influence of Actuator Friction and Reflected Inertia

As noted prior, current state-of-the-art powered exoskeletons are often actuated using small electric motors with high-ratio gear transmissions [214]. Some researchers have suggested that a shift should be made towards actuators with a high-degree of backdrivability, direct-drive systems [205, 214]. Thus, in the first human-exoskeleton FSR simulation experiment, we examined how characteristics of actuator inertia and friction/losses affects the size and shape of the sagittal FIP FSR. This experiment was broken down into three parts involving manipulation of actuator parameters:

1. Reflected inertia removed (direct-drive); variations applied to the joint Coulomb torque τ_c ($\tau_c = 0$ Nm, $\tau_c = 3$ Nm, $\tau_c = 6$ Nm, $\tau_c = 9$ Nm)
2. Reflected inertia included (gear ratio = 160); variations applied to the joint Coulomb torque τ_c ($\tau_c = 0$ Nm, $\tau_c = 3$ Nm, $\tau_c = 6$ Nm, $\tau_c = 9$ Nm)
3. Reflected inertia and joint Coulomb torque included (gear-ratio = 160, $\tau_c = 6$ Nm); variations applied to the joint viscous friction coefficient μ_o ($\mu_o = 0$ Nm rad^{-1}, $\mu_o = 0.5$ Nm rad^{-1}, $\mu_o = 5$ Nm rad^{-1}, $\mu_o = 10$ Nm rad^{-1}, $\mu_o = 20$ Nm rad^{-1})

Note that the friction and inertia parameters used between actuators were consistent to reflect the design of the EXO-H3. Additionally, removal of actuator inertia did not impact

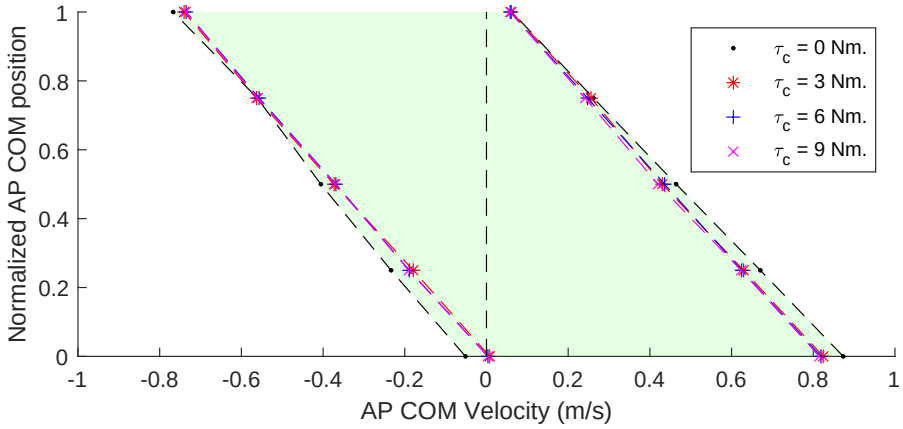


Figure 6.1: The feasible stability region (FSR) for the human-exoskeleton FIP balance model generated with **no** reflected inertia in the actuators (direct-drive) and varying values of actuator Coulomb friction τ_c. Actuator parameters were consistent between joints.

the output of the motors, i.e., the torque generated was still amplified (gear-ratio = 160). As we observed in Chapter 4, dynamic parameters heavily influenced by the actuators, e.g. segment MOI, were quite difficult to obtain and validate. Therefore, these "what-if" simulations acted as an opportunity to assess which parameters are most important to consider to improve human-exoskeleton balancing

The estimated FSR generated over the the set of AP COM positions $\{0, 0.25, ..., 1.00\}$ (normalized to foot length; 0 = COM over toe, 1 = COM over heel) are displayed as follows for each part of the overall experiment: part 1 in Fig. 6.1; part 2 in Fig. 6.2; and part 3 Fig. 6.3. In general, the FSR for the direct-drive condition was larger than the FSR for the condition including reflected inertia; however, as the amount of dry friction in each actuator increased, these differences became lesser. In fact, the direct-drive FSR condition without Coulomb friction produced FSR boundaries that were similar (slightly larger) than the human-only case. This result suggests that the reflected inertia in each actuator is a major influence on the instability felt by end-users during operation. Surprisingly, while the addition of Coulomb torques to the model did reduce the FSR size (both in the direct-drive and reflected inertia case), the effects saturated quickly. In all cases, the greatest FSR reduction came when transitioning from $\tau_c = 0$ Nm to $\tau_c = 3$ Nm; further increases in τ_c resulted in minor changes to the FSR. With that said, this result does still

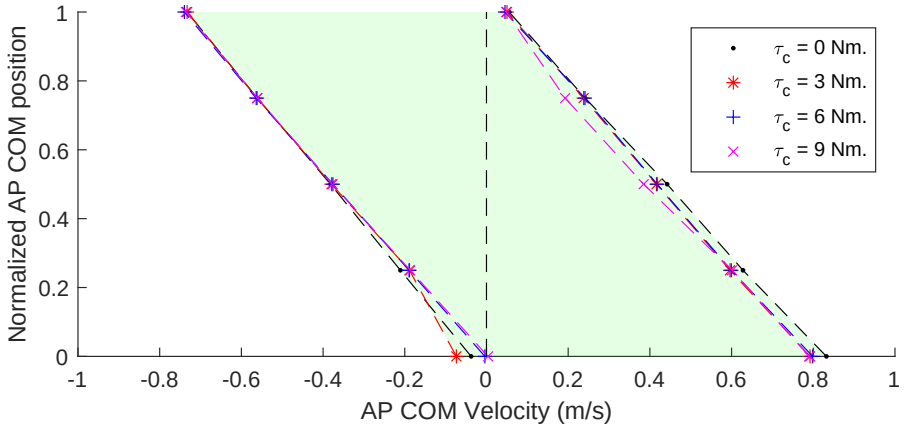


Figure 6.2: The feasible stability region (FSR) for the human-exoskeleton FIP balance model generated with **with** reflected inertia in the actuators (gearing present) and varying values of actuator Coulomb friction τ_c. Actuator parameters were consistent between joints.

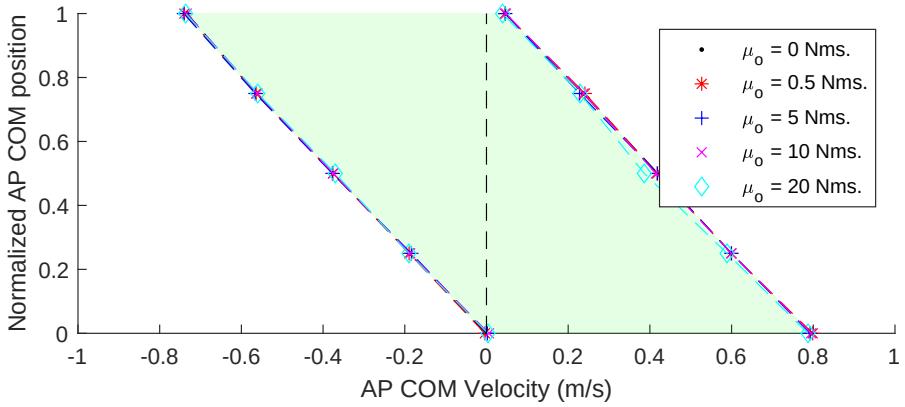


Figure 6.3: The feasible stability region (FSR) for the human-exoskeleton FIP balance model generated with **with** reflected inertia in the actuators (gearing present), a set actuator Coulomb friction torque ($\tau_c = 6$ Nm), and varying values of actuator viscous friction μ_o. Actuator parameters were consistent between joints.

suggest that the presence of Coulomb torques in the actuators reduces end-user balancing capabilities. Lastly, increasing viscous damping in each joint (experiment part 3) produced only marginal effects on the FSR (Fig. 6.3). In fact, only once $\mu_o = 20$ Nm rad^{-1} was there

a noticeable though small decrease in the FSR's anterior boundary. This result suggests that joint damping has little negative effect on the FIP FSR size when dry friction is also present; rather, it is possible that the damping could be used as a possible assistive intervention [338, 339].

2) Effect of Shifting the Battery Position

In Chapter 4, we made note of the posterior positioning of the EXO-H3 within the trunk segment due the EXO-H3's battery and hip attachment components. Such placement produces a posterior shifting of the whole-body COM which in theory should change the kinematic configurations necessary to reach certain COM states when compared to the human-only. With that said, it is unclear how the positioning of the battery theoretically impacts end-user FIP balancing capabilities (FSR size) beyond affecting the COM postion during quiet standing. To our knowledge, this question has also yet to be investigated in either an experimental or simulated setting. Therefore, in the second simulation study, we examined how fore aft shifting of the battery with respect to the end-user longitudinal axis would impact FIP FSR size. This investigation involved investigating the following three conditions within dynamic simulations:

1. Battery positioned using baseline EXO-H3 geometry from Chapter 4 (≈ -25 cm posterior to trunk longitudinal axis)
2. Battery positioned on trunk longitudinal axis (0 cm)
3. Battery positioned anterior to trunk longitudinal axis (+15 cm)

Briefly, the estimated FSR generated over the the set of AP COM positions $\{0, 0.25, ..., 1.00\}$ (normalized to foot length; 0 = COM over toe, 1 = COM over heel) are displayed for each experimental condition in Fig. 6.4. Surprisingly, there was only marginal effects on the FSR with variations in the battery's horizontal position. This result suggests that changing how the human-exoskeleton must be configured to reach a specific COM position does not have a substantial influence on the capturability of said COM position. However, we note that this does not consider how the battery position affects COM positioning and FIP perturbation recovery when the human-exoskeleton is standing quietly. The quiet stance posture adopted by a human-exoskeleton system could produce a COM state closer to an

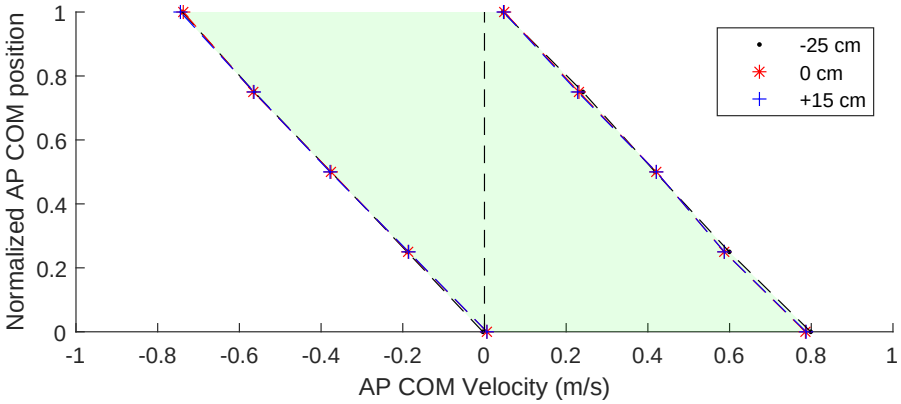


Figure 6.4: The feasible stability region (FSR) for the human-exoskeleton FIP balance model generated following repositioning of the battery rigid body with respect to the trunk-fixed longitudinal axis, i.e., -25 cm (baseline), 0 cm, +15 cm.

FSR boundary, i.e., a lower margin of stability [154], than the human-only quiet standing posture. A lower margin of stability in quiet standing implies that the COM state has less room to maneuver and is closer to requiring a change in support [154].

3) Influence of End-User Strength

In Appendix F (experiment F.3), we observed that there that there was a notable reduction in FSR size when the human-only model was restricted to 25% of their maximum possible muscle activations. Likewise, the Pareto optimization assessing the interplay between effort and COM capturability in Chapter 3 suggested that certain COM positions are far more sensitive to reductions in corrective MTG torques, e.g., trying to reduce effort when the COM is positioned over the toe with a forward velocity has a substantial negative impact on the ability to maintain upright FIP balance. Given the desired function of exoskeletons and orthoses, i.e., replacing or augmenting the end-user muscle torques, it is necessary to address whether we could restore regions of the human-only FSR lost due to muscle weakness, to the human-exoskeleton FSR via powered actuators. However, it is not certain how moderately strong exoskeleton actuators, e.g., the EXO-H3 actuators are only permitted to reach 30-35 Nm by Technaid, can really provide assistance to an end-user. Therefore, in the third simulation experiment, we examined how constrained active

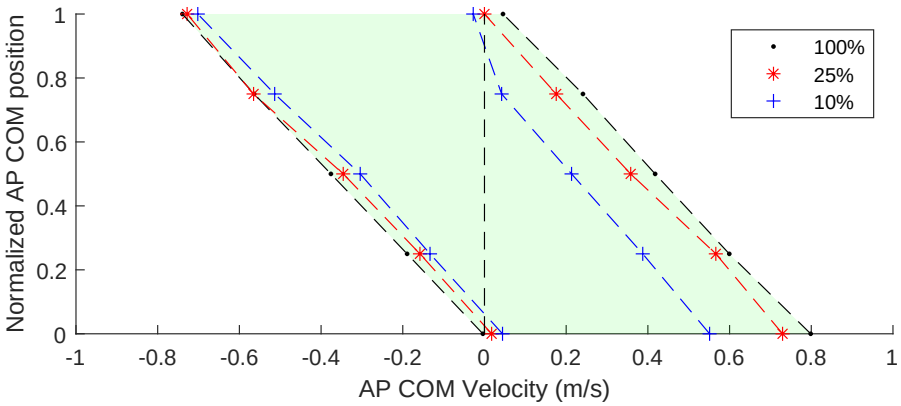


Figure 6.5: The feasible stability region (FSR) for the human-exoskeleton FIP balance model generated with different constraints imposed on the maximum muscle activation, i.e., muscle activations could not surpass 10, 25, or 100%, with the 10% condition representing the individual with the lowest muscle strength. Arm movement was restricted in these simulations.

MTG outputs affect the size and shape of the sagittal FIP FSR in a human-exoskeleton system. Equation (F.4) in Appendix F was used to impose limits on MTG activation during simulations. The following conditions were investigated with respect to influence on the FSR:

1. $\varepsilon_3 = 1.00$ (100%) – Baseline condition (full-strength)
2. $\varepsilon_3 = 0.25$ (25%) – Weakest simulated human in Appendix F
3. $\varepsilon_3 = 0.10$ (10%)

where the last condition was introduced to assess capabilities of the EXO-H3 system for a simulated user that cannot remain in a static upright configuration without assistance.

The estimated FIP FSR generated over the the set of AP COM positions $\{0, 0.25, ..., 1.00\}$ (normalized to foot length; 0 = COM over toe, 1 = COM over heel) is displayed is Fig. 6.5. In general, the powered actuators were successful in bringing the 25% strength user's posterior FSR boundary within close proximity to the 100% user's (the 10% strength user as well though less so). In the case of the anterior FSR boundary, the 25% user was once

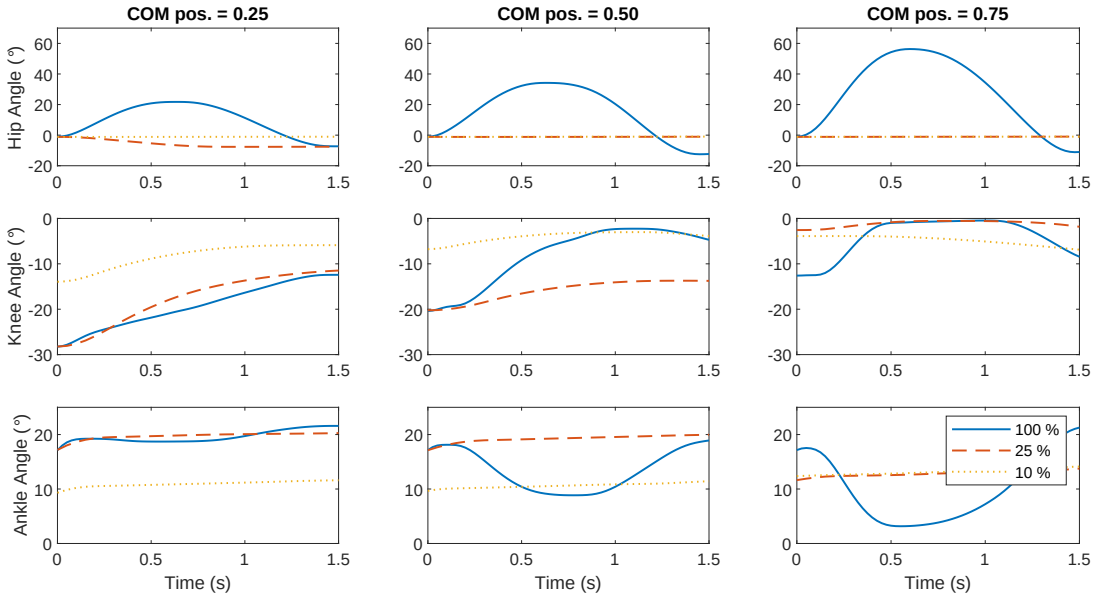


Figure 6.6: Hip, knee, and ankle joint angles that resulted in the **anterior** FSR boundary for the human-exoskeleton balance model when different constraints were imposed on the maximum muscle activation during simulations, i.e., muscle activations could not surpass 10, 25, or 100%.

again with near proximity to the 100% user's boundary, though with a larger margin of separation than in the posterior case. Most importantly, the 25% user's FSR boundaries are improved relative to the same strength of user balancing without an exoskeleton (see Fig. F.5). However, for the 10% strength user, there is still a substantial decrease in the anterior FSR boundary magnitude regardless of powered actuator assistance. In fact, the 10% strength user's FSR boundaries when wearing an exoskeleton are similar to the 25% strength user's without an exoskeleton (see Fig. F.5).

In Figs. 6.6 and 6.7, the simulated hip, knee, and ankle joint angles that yielded the maximum capturable anterior and posterior COM velocities respectively, are shown for an initial normalized COM position of 0.25, 0.50, and 0.75. When the initial COM momentum was forwards, the model would only use a hip-strategy to reach the FSR boundaries when the user had full access to MTG activations (100% condition). The 25% and 10% end-user had to rely on either a small amount of hip extension or the hips were held static. Interestingly, to halt forward COM momentum, these two categories of end-user also seemed to rely on slow motion of the knee (some *ankle* motion as well), which suggests a possible use of

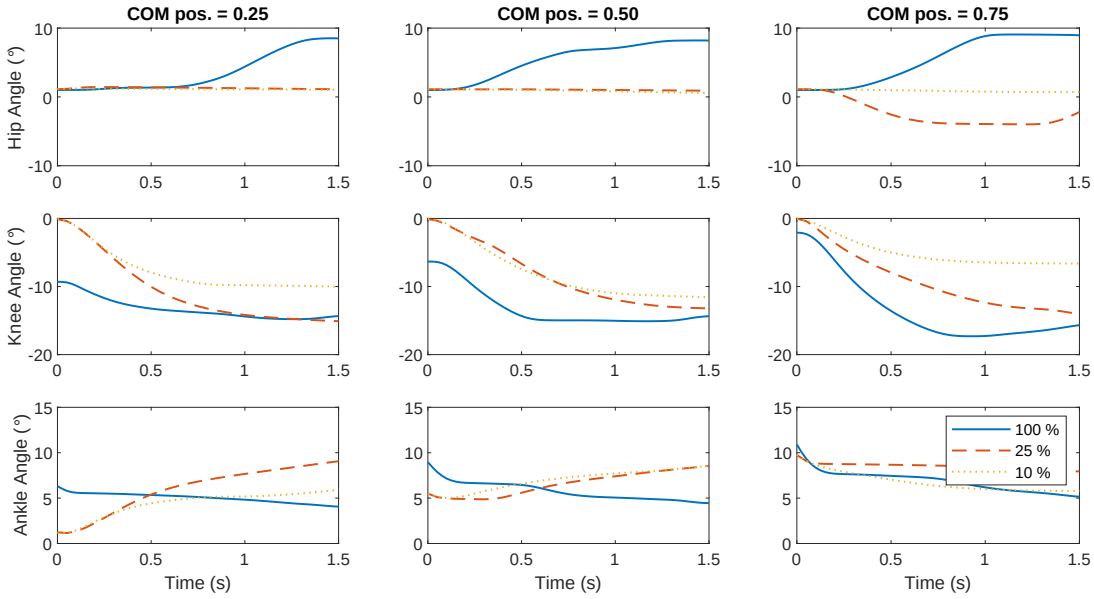


Figure 6.7: Hip, knee, and ankle joint angles that resulted in the **posterior** FSR boundary for the human-exoskeleton balance model when different constraints were imposed on the maximum muscle activation during simulations, i.e., muscle activations could not surpass 10, 25, or 100%.

isolated knee control in assisted balance recovery for weakened end-users. In Fig. 6.7, there is again a clear shift in hip motion with weakening of the MTGs; though in general hip motion is quite minimal relative to the human-only strategy in Fig. F.7. One particularly interesting observation from these plots is that knee motion is relatively consistent regardless of MTG weakness; however, ankle motion is not. Contrary to the human-only case in which MTG weakness produced a postural strategy with less ankle motion in order to initialize the COM on the FSR boundary (Fig. F.7), weakened end-users with exoskeleton assistance seem to benefit more from additional ankle motion (*dorsiflexion*) in comparison to the end-user with 100% activations. This is likely the result of the weakened users not being able to flex their hips in a controlled manner to countermove the COM forward as time progresses. Thus, posterior balance control for end-users that have substantial muscle weakness, e.g., individuals living with spinal cord injury, stroke, etc., could likely rely on inverted pendulum-based control strategies or could benefit from purely ankle-knee control like that tested by Emmens et al. [103] (exoskeleton-assisted balance recovery using ankle-knee exoskeleton).

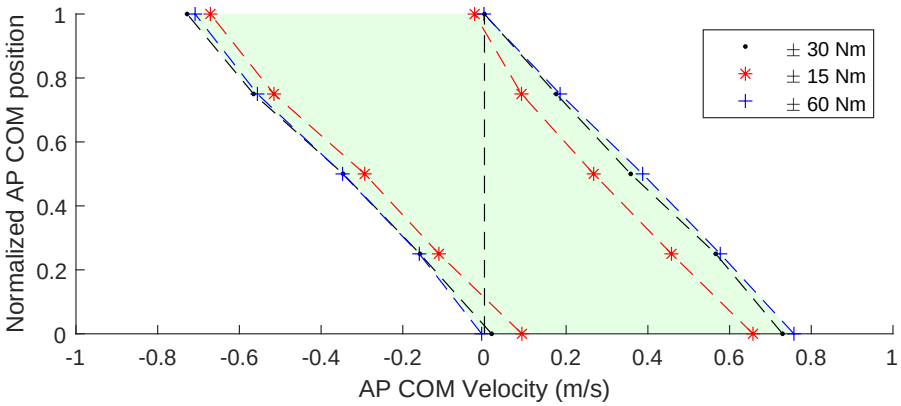


Figure 6.8: The feasible stability region (FSR) for the human-exoskeleton FIP balance model generated with different constraints imposed on the maximum amplified motor torque, i.e., τ_{mtr} for each joint could not surpass ±15 Nm, ±30 Nm (baseline), or ±60 Nm.

4) Influence of Exoskeleton Strength

In the previous simulation experiment, we observed that the weakened human FSR obtained in Chapter 3 could be restored with moderate powered actuator when that user dons the EXO-H3 model. The current experiment (and last FSR experiment in Chapter 6) thus continued this investigation but focused instead on how the weakened user (can generate 25% of active MTG torques) could benefit from actuators of different strength. The following conditions were investigated with respect to their influence on the FIP human-exoskeleton FSR:

1. $\tau_{\text{mtr}} \in [-30, 30]$ – Baseline condition used through this chapter according to Technaid's limits on the EXO-H3 actuators (±30 Nm)
2. $\tau_{\text{mtr}} \in [-15, 15]$ – 50% EXO-H3 limits (±15 Nm)
3. $\tau_{\text{mtr}} \in [-60, 60]$ – 200% EXO-H3 limits (±60 Nm)

Each condition was imposed through manipulation of the box constraints in Equation (6.9).

The estimated FIP FSR generated over the the set of AP COM positions $\{0, 0.25, ..., 1.00\}$ (normalized to foot length; 0 = COM over toe, 1 = COM over heel) is displayed is Fig. 6.8.

Surprisingly, the optimization process was not able to obtain a postural strategy that could do anything other than marginally improve the size of FSR when the absolute maximum actuator torque was increased from 30 Nm to 60 Nm. However, there was a rather notable drop-off in FSR size when the actuator output was constrained to ±15 Nm: both anterior and posterior FSR boundaries recessed by about 10 cm/s from the ±30 Nm condition. Thus, actuator output should not be reduced beyond the limits outlined by Technaid to avoid sharp reductions in the capturability of FIP balance. Likewise, pushing the actuators beyond the limit set by Technaid provided little benefit for simulated FIP balance; doing so in practice, could risk damaging the actuator hardware.

6.2 Real-Time Feet-In-Place Balance Control

The following section contains excerpts related to the paper "Assessing Control of Fixed-Support Balance Recovery in Wearable Lower-Limb Exoskeletons Using Multibody Dynamic Modelling" published/presented at the 2020 8th IEEE RAS/EMBS International Conference for Biomedical Robotics and Biomechatronics (Inkol and McPhee [169]).

The first goal in developing assistive fixed-support balance control for the EXO-H3 lower-limb exoskeleton, was to design a control architecture that could in theory autonomously drive the system if necessary. This is similar to the focus adopted by many other authors who have consider closed-loop full-state feedback control approaches that grant upright mobility to individuals with paraplegia [48, 105, 134, 138]. In the future, the application of the autonomous law could then be modified depending on the physical capabilities of the end-user as well as the intent of the user, i.e., moving towards AAN control (Chapter 2) with user-intent and/or disturbance recognition. The sections in the current Chapter will discuss the development of the control-oriented multibody dynamics models of human-exoskeleton stance in addition to the mathematical framework for real-time balance control using full-state feedback [48, 105].

6.2.1 Control-Oriented Nonlinear Dynamics

As the EXO-H3 provides no actuation of the upper-limbs, the control-oriented formulation of the integrated human-exo dynamic model assumed that the arms were locked to the

trunk. As mentioned in Chapter 3, this is often instructed or imposed in balance recovery studies [103, 344]. Furthermore, we assumed that there is no knowledge of the disturbances applied to the system, thus they are in negligible, i.e., $\mathbf{P} = \ddot{x}_{\text{plat}} = 0$. These statements are equivalent to converting the system of ODEs in (5.39) to DAEs,

$$(\mathbf{M}_{\text{h}} + \mathbf{A}_{\text{he}}^{\intercal}\mathbf{M}_{\text{e3}}\mathbf{A}_{\text{he}})\ddot{\mathbf{q}}_{\text{h}} = \boldsymbol{\Gamma}_{\text{h}} + \boldsymbol{\tau}_{\text{mtg}} + \mathbf{A}_{\text{he}}^{\intercal}\boldsymbol{\Gamma}_{\text{e3}} + 2\mathbf{A}_{\text{he}}^{\intercal}\boldsymbol{\tau}_{\text{ac}} + \nabla\Phi^{\intercal}\lambda_{\text{ctrl}} \tag{6.15}$$

$$\Phi = \begin{Bmatrix} \theta_{\text{shldr}} \\ \theta_{\text{elbow}} \end{Bmatrix} = \mathbf{0} \tag{6.16}$$

where $\Phi \in \mathbb{R}^{2\times 1}$ are the constraints the bind the arms to the trunk (imposed by constraint torques $\boldsymbol{\lambda}_{\text{ctrl}} \in \mathbb{R}^{2\times 1}$). Given $\ddot{\mathbf{q}}_{\text{h},4..5} = \mathbf{0}$, solving for $\boldsymbol{\lambda}_{\text{ctrl}}$ from Equations (6.15) and (6.16) and substituting the results back into (6.15) yields the ODEs

$$\mathbf{M}_{\text{he}}\ddot{\mathbf{q}}_{\text{he}} = \boldsymbol{\Gamma}_{\text{he}} + \boldsymbol{\tau}_{\text{mtg}} + 2\boldsymbol{\tau}_{\text{ac}} \tag{6.17}$$

where $\boldsymbol{\Gamma}_{\text{he}} \in \mathbb{R}^{3\times} = (\boldsymbol{\Gamma}_{\text{h}} + \mathbf{A}_{\text{he}}^{\intercal}\boldsymbol{\Gamma}_{\text{e3}})_{1..3}$ are the nonlinear joint torques due to gravity and quadratic velocity terms; $\mathbf{M}_{\text{he}} \in \mathbb{R}^{3\times 3}$ is the mass matrix. Although not explicitly shown, each of the terms in (6.17) are now a function of the control-oriented generalized coordinates

$$\mathbf{q}_{\text{he}} = \{\theta_{\text{hip}}, \theta_{\text{knee}}, \theta_{\text{ankle}}\}^{\intercal} \tag{6.18}$$

$$\dot{\mathbf{q}}_{\text{he}} = \{\omega_{\text{hip}}, \omega_{\text{knee}}, \omega_{\text{ankle}}\}^{\intercal} \tag{6.19}$$

where $\mathbf{q}_{\text{he}} \in \mathcal{Q}_{\text{he}}$ and $\mathcal{Q}_{\text{he}} \subseteq \mathbb{R}^3$. Note that the generalized coordinate space for the human-exoskeleton $\mathcal{Q}_{\text{he}}$ has the potential to be different than the lower-limb subset of the human-only generalized coordinate space $\mathcal{Q}_{\text{h,ll}} \subset \mathcal{Q}_{\text{h}}$; the mechanical stops reflected in the device space $\mathcal{Q}_{\text{e}}$ can result in $\mathcal{Q}_{\text{he}} \subseteq \mathcal{Q}_{\text{h,ll}}$ (see Table 4.1).

6.2.2 Balance Regulation: Full-State Feedback

The current section introduces important details regarding full-state feedback for balance control. Recently, Bayon et al. [48] reported that full-state feedback algorithms could be tuned to provide better simulations of different human balance recovery strategies when compared to controls based on angular momentum about the whole-body COM; the latter of which is employed in already proposed assistive balance control schemes [106, 105, 103]. These observations are also consistent with earlier predictive models that use optimal

feedback, e.g., Kuo [202] and van der Kooij [342]. Briefly, for assisted balance control, we wish to obtain a simple feedback control law,

$$\mathbf{u}_{\text{he}} = \mathbf{K}(\mathbf{x}_{\text{he}}(t) - \mathbf{x}_{\text{des}}(t)) + \mathbf{u}_{\text{ff}}(\mathbf{x}_{\text{he}}(t)) \tag{6.20}$$

where $\mathbf{u}_{\text{aff}}(\cdot) : \mathbb{R}^{6\times 1} \rightarrow \mathbb{R}^{n_u \times 1}$ maps the current state to n_u feedforward control inputs and $\mathbf{K} \in \mathbb{R}^{6\times 6}$ is a feedback gain matrix that regulates $\mathbf{x}_{\text{he}} \in \mathbb{R}^{6\times 1}$ about a reference function $\mathbf{x}_{\text{des}}(t) \in \mathbb{R}^{6\times 1}$. The control-oriented human-exoskeleton state was defined as

$$\mathbf{x}_{\text{he}}(t) = \begin{Bmatrix} \mathbf{q}_{\text{he}} \\ \dot{\mathbf{q}}_{\text{he}} \end{Bmatrix} \tag{6.21}$$

which further simplifies the system dynamics by ignoring MTG activations. Ideally, $\mathbf{u}_{\text{he}} = \boldsymbol{\tau}_{\text{mtr}}$ for robotic assistance, though as we show in future sections, that may not always be the case [134].

6.2.3 Optimal Balance Regulation: Linear Quadratic Regulator

To this point, much of our focus with respect to human balance recovery has been in regards to optimal control, i.e., we assume that the CNS is inherently inclined towards executing motion patterns that meet some optimality criteria. However, the baseline derivation of full-state feedback laws for FIP balance regulation using methods like computed torque control (CTC; see Appendix L) does not consider any specific performance criteria or constraints. The result is that without careful tuning, a CTC approach might not generate optimal motions and could produce unhuman balance recovery strategies. Therefore, the current subsection will discuss an approach to estimating feedback gains $\mathbf{K}$ that minimize well-established human balance recovery performance criteria (refer to Chapter 3), with the goal of developing real-time lower-limb exoskeleton FIP controllers that mimic the behaviours of the end-user CNS.

The first approach towards real-time optimal control of the multibody exoskeleton system, i.e., control of ankle, knee, and hip joints simultaneously, was based upon the model(s) of fixed-support balance control originally derived by Kuo et al. [202, 204, 203] (refer to Chapter 2 for details). The authors here generated reasonable predictions of human postural responses to lean-and-release perturbations using a linearized human-only model and a linear quadratic regulator (LQR), i.e., an optimal feedback regulator. However, these

studies were not without limitations: the human-only linear state-space model featured matrices that would explicitly map hip or ankle strategy neural inputs (*not muscle torques*) to characteristic joint accelerations [158]; the knee was always assumed to be locked. In regards to the latter, exoskeleton FIP balance controllers have been previously designed with the assumption that the knees would be restricted, e.g., Emmens et al. [103], to simplify the control problem to that of a single or double-inverted pendulum [207]. However, as we investigated in Chapter 3 and as others have studied in the literature [77, 130, 175], knee movement can theoretically improve the ability to balance with FIP and/or can reduce the balance recovery torques required to stay upright. Thus, we wished to open the possibility of knee motion within the autonomous and assistive control algorithms designed. Furthermore, humans often regulate a COM position ~ 5 cm anterior to their ankle joint [242]. The LQR designed by Kuo [202] only corrected deviations from a completely upright posture (all zero joint angles).

With these ideas in mind, the FIP balance LQR for lower-limb exoskeletons was designed such that knee movement was free to use for the controller and any non-zero equilibrium point desired by the user (*within reason*) could be stabilized. Prior to designing the control law, as the LQR approach requires a linear mathematical description of the underlying dynamical system, the nonlinear control-oriented dynamic model in Equation (6.17) had to be approximated via Taylor series expansion. To avoid approximations that could be sensitive to both the nonlinear friction model, i.e., $\tau_{\mathrm{f}}(\omega)$ in Equation (4.6) has a "spike" in the derivative at $\omega = 0$, as well as the double exponential passive muscle torques $\boldsymbol{\tau}_{\mathrm{psv}}$ near end ranges of motion, i.e. Equations (C.15– C.19), we assumed that both components were compensated for entirely within the control loop, i.e.,

$$\mathbf{M}_{\mathrm{he}}\ddot{\mathbf{q}}_{\mathrm{he}} = \boldsymbol{\Gamma}_{\mathrm{he}} + \boldsymbol{\tau}_{\mathrm{mtg}} + 2\boldsymbol{\tau}_{\mathrm{ac}} \tag{6.22}$$

$$\mathbf{M}_{\mathrm{he}}\ddot{\mathbf{q}}_{\mathrm{he}} = \boldsymbol{\Gamma}_{\mathrm{he}} + \boldsymbol{\tau}^{\mathrm{cns}}_{\mathrm{mtg}} + 2(\boldsymbol{\tau}_{\mathrm{mtr}} + \cancelto{\mathbf{0}}{\boldsymbol{\tau}_{\mathrm{psv}}} + \cancelto{\mathbf{0}}{\boldsymbol{\tau}_{\mathrm{f}}}) \tag{6.23}$$

$$\implies \mathbf{M}_{\mathrm{he}}\ddot{\mathbf{q}}_{\mathrm{he}} = \boldsymbol{\Gamma}_{\mathrm{he}} + \boldsymbol{\tau}^{\mathrm{cns}}_{\mathrm{mtg}} + 2\boldsymbol{\tau}_{\mathrm{mtr}} \tag{6.24}$$

Please refer to Chapter 7.2.3 or Hauschild and Heppler [142] for a brief overview of nonlinear friction compensation being put into practice. The remaining nonlinear state-space model was expressed as,

$$\dot{\mathbf{x}}_{\mathrm{he}} = \begin{Bmatrix} \dot{\mathbf{q}}_{\mathrm{he}} \\ \mathbf{M}^{-1}_{\mathrm{he}}(\boldsymbol{\Gamma}_{\mathrm{he}} + \boldsymbol{\tau}_{\mathrm{in}}) \end{Bmatrix} = \mathbf{f}_{\mathrm{lqr}}(\mathbf{x}_{\mathrm{he}}(t), \mathbf{u}_{\mathrm{he}}(t)) \tag{6.25}$$

where

$$\mathbf{x}_{\text{he}}(t) = \begin{Bmatrix} \mathbf{q}_{\text{he}} \\ \dot{\mathbf{q}}_{\text{he}} \end{Bmatrix}, \quad \mathbf{u}_{\text{he}}(t) = \boldsymbol{\tau}_{\text{in}} \tag{6.26}$$

and $\boldsymbol{\tau}_{\text{in}} \in \mathbb{R}^{3\times 1} = \boldsymbol{\tau}^{\text{cns}}_{\text{mtg}} + 2\boldsymbol{\tau}_{\text{mtr}}$, which allows us to generalize both human and exoskeleton inputs into a single column matrix of applied joint torques. Thus, in the proposed controller, we solve for the torque that must be provided by *both* the human user and robot concurrently to maintain upright balance. If we have no knowledge of the torques applied by the end-user, we assume that $\boldsymbol{\tau}^{\text{cns}}_{\text{mtg}} = 0$ and that the desired $\boldsymbol{\tau}_{\text{in}}$ will be directed entirely towards the exoskeleton's motors, i.e., the robotic portion of the system must fully autonomously drive FIP balance recovery. With that established, the dynamics of the human-exoskeleton system can be approximated about *any* desired static posture $\mathbf{x}_{\text{des}}$, as

$$\dot{\mathbf{x}}_{\text{he}} \approx \mathbf{A}(\mathbf{x}_{\text{he}}(t) - \mathbf{x}_{\text{des}}) + \mathbf{B}(\mathbf{u}_{\text{he}}(t) - \mathbf{u}_{\text{des}}) \tag{6.27}$$

where

$$\mathbf{f}_{\text{lqr}}(\mathbf{x}_{\text{d}}, \mathbf{u}_{\text{des}}) = \mathbf{0} \tag{6.28}$$

and

$$\mathbf{A} = \left.\frac{\partial \mathbf{f}_{\text{lqr}}}{\partial \mathbf{x}_{\text{he}}}\right|_{\substack{\mathbf{x}_{\text{he}}=\mathbf{x}_{\text{des}} \\ \mathbf{u}_{\text{he}}=\mathbf{u}_{\text{des}}}}, \quad \mathbf{B} = \left.\frac{\partial \mathbf{f}_{\text{lqr}}}{\partial \mathbf{u}_{\text{he}}}\right|_{\substack{\mathbf{x}_{\text{he}}=\mathbf{x}_{\text{des}} \\ \mathbf{u}_{\text{he}}=\mathbf{u}_{\text{des}}}} \tag{6.29}$$

i.e., the derivatives of $\mathbf{f}_{\text{lqr}}$ with respect to $\mathbf{x}_{\text{he}}$ and $\mathbf{u}_{\text{he}}$ evaluated at the static posture ($\mathbf{u}_{\text{des}}$ is the feedforward value of $\boldsymbol{\tau}_{\text{in}}$ required to maintain $\mathbf{x}_{\text{des}}$ such that $\dot{\mathbf{x}}_{\text{he}} = \mathbf{0}$).

Briefly, in the case continuous infinite-horizon LQR approach [192], we solve the continuous optimal control problem

$$\mathbf{K}_{\text{lqr}} = \underset{\mathbf{K}\in\mathbb{R}^{6\times 6}}{\operatorname{argmin}} \int_0^\infty (\mathbf{x}_{\text{he}} - \mathbf{x}_{\text{des}})^\intercal \mathbf{Q} (\mathbf{x}_{\text{he}} - \mathbf{x}_{\text{des}}) + (\mathbf{u}_{\text{he}} - \mathbf{i}_{\text{des}})^\intercal \mathbf{R} (\mathbf{u}_{\text{he}} - \mathbf{u}_{\text{des}})\, dt \tag{6.30}$$

subject to

$$\mathbf{u}_{\text{he}} = \underbrace{-\mathbf{K}}_{\mathbf{K}} (\mathbf{x}_{\text{he}} - \mathbf{x}_{\text{des}}) \underbrace{+\mathbf{u}_{\text{des}}}_{\mathbf{u}_{\text{ff}}} \tag{6.31}$$

such that we obtain optimal feedback control inputs that regulate the linear system's state about $\mathbf{x}_{\text{des}}$. In Equation (6.30), $\mathbf{Q} \in \{\mathbb{R}^{6\times 6} \,|\, \mathbb{Q} \geq 0\}$ and $\mathbf{R} \in \{\mathbb{R}^{3\times 3} \,|\, \mathbb{R} > 0\}$ are respectively positive semidefinite and definite matrices that weigh deviations of the controls or state away from equilibrium in some manner that is dependent on the tuning of specific

matrix elements. Substituting (6.31) into (6.28) converts the linear system in (6.28) to one purely dependent on its states,

$$\dot{\mathbf{x}}_{\text{he}} = (\mathbf{A} - \mathbf{B}\mathbf{K}_{\text{lqr}})(\mathbf{x}_{\text{he}} - \mathbf{x}_{\text{des}}) \tag{6.32}$$

which is marginally or asymptotically stable so long as all the eigenvalues of $\mathbf{A} - \mathbf{B}\mathbf{K}$ are located within the left-hand side of the complex plane. To prove this notion of stability, one simply needs to solve the first-order system in Equation (6.32) to reveal $\mathbf{x}_{\text{he}}$ as an exponential function with respect to these matrix eigenvalues; we leave this as an exercise to the reader. According to Kirk [192], the value of the gain $\mathbf{K}_{\text{lqr}}$ that solves (6.30) for a given cost function is obtained via the equation

$$\mathbf{K}_{\text{lqr}} = \mathbf{R}^{-1}\mathbf{B}^{\intercal}\mathbb{P} \tag{6.33}$$

where $\mathbb{P} \in \{\mathbb{R}^{6\times 6} \,|\, \mathbb{P} \geq 0\}$ is a positive semi-definite matrix that is solved from the continuous time algebraic Ricatti equation [192]:

$$\mathbf{A}^{\intercal}\mathbb{P} + \mathbb{P}\mathbf{A} - (\mathbb{P}\mathbf{B})\mathbf{R}^{-1}(\mathbf{B}^{\intercal}\mathbb{P}) + \mathbf{Q} = \mathbf{0} \tag{6.34}$$

These solutions can be obtained offline such that only (6.31) must be evaluated during run-time to obtain control-oriented exoskeleton torques for FIP balance; this is a major advantage of the LQR approach for optimal control.

As we desire a FIP controller that can provide assistance or autonomy in a human-like fashion, we again refer back to the human motor control literature to design the objective function for the human-exoskeletons [170, 202, 344]. As discussed in Chapter 3, common optimization criteria related to the human control of balance include minimizing horizontal excursions of the whole-body COM, i.e.,

$$\Delta\text{COM: } \mathcal{L}(\cdot) = (\mathbf{r}_{\text{icm}}(\mathbf{q}_{\text{he}}(t)) \cdot \hat{\imath} - \bar{r}_x)^2, \tag{6.35}$$

deviations of the trunk away from some upright reference (assuming the head and trunk are rigidly linked), i.e.,

$$\Delta\text{Trunk: } \mathcal{L}(\cdot) = (-\theta_{\text{ankle}} - \theta_{\text{knee}} - \theta_{\text{hip}} - \bar{\phi}_{\text{tr}})^2, \tag{6.36}$$

as well as minimization of effort, i.e.,

$$\Delta\text{ACT: } \mathcal{L}(\cdot) = \boldsymbol{\tau}_{\text{in}}^{\intercal}\mathbf{R}\boldsymbol{\tau}_{\text{in}} \tag{6.37}$$

where

$$\mathbf{R} = \begin{bmatrix} w_{\text{hip}} & 0 & 0 \\ 0 & w_{\text{knee}} & 0 \\ 0 & 0 & w_{\text{ankle}} \end{bmatrix} \tag{6.38}$$

is a diagonal matrix containing 3 scalar weights ($w > 0$) corresponding to the hip, knee, and ankle applied torques: w_{hip}, w_{knee}, and w_{ankle}.

Equation (6.37) is already in the appropriate quadratic form to be incorporated within the LQR cost function; however, we cannot state the same for the kinematic criteria, (6.35) and (6.36), that we wish to include. To address this issue, Taylor series expansions of the linear/nonlinear functions in question (about the static configuration) are utilized once again:

$$\mathbf{r}_{\text{icm}} \cdot \hat{\mathbf{i}} \approx \bar{r}_x(\mathbf{x}_{\text{des}}) + \mathbf{C}^x_{\text{icm}}(\mathbf{x}_{\text{he}} - \mathbf{x}_{\text{des}}) \tag{6.39}$$

$$\phi_{\text{tr}} \approx \bar{\phi}_{\text{tr}}(\mathbf{x}_{\text{des}}) + \mathbf{C}_{\text{tr}}(\mathbf{x}_{\text{he}} - \mathbf{x}_{\text{des}}) \tag{6.40}$$

where

$$\mathbf{C}^x_{\text{icm}} = \left.\frac{\partial \mathbf{r}_{\text{icm}} \cdot \hat{\mathbf{i}}}{\partial \mathbf{x}_{\text{he}}}\right|_{\mathbf{x}_{\text{he}}=\mathbf{x}_{\text{des}}}, \quad \mathbf{C}_{\text{tr}} = \left.\frac{\partial \phi_{\text{tr}}}{\partial \mathbf{x}_{\text{he}}}\right|_{\mathbf{x}_{\text{he}}=\mathbf{x}_{\text{des}}} \tag{6.41}$$

This approximation suggests that

$$(\mathbf{r}_{\text{icm}}(\mathbf{q}_{\text{he}}(t)) \cdot \hat{\imath} - \bar{r}_x)^2 \approx (\mathbf{x}_{\text{he}} - \mathbf{x}_{\text{des}})\mathbf{C}^{x\intercal}_{\text{cm}}\mathbf{C}^x_{\text{cm}}(\mathbf{x}_{\text{he}} - \mathbf{x}_{\text{des}}) \tag{6.42}$$

$$(-\theta_{\text{ankle}} - \theta_{\text{knee}} - \theta_{\text{hip}} - \bar{\phi}_{\text{tr}})^2 \approx (\mathbf{x}_{\text{he}} - \mathbf{x}_{\text{des}})\mathbf{C}^{\intercal}_{\text{tr}}\mathbf{C}_{\text{tr}}(\mathbf{x}_{\text{he}} - \mathbf{x}_{\text{des}}) \tag{6.43}$$

Therefore, we can obtain a $\mathbf{Q}$ matrix for each of the COM and trunk orientation objectives,

$$\mathbf{Q}_{\text{cm}} = \mathbf{C}^{x\intercal}_{\text{cm}}\mathbf{C}^x_{\text{cm}} \tag{6.44}$$

$$\mathbf{Q}_{\text{tr}} = \mathbf{C}^{\intercal}_{\text{tr}}\mathbf{C}_{\text{tr}} \tag{6.45}$$

and as disseminated by Kuo [202], blend between them using by defining a homotopy,

$$\mathbf{Q}_{\text{hom}} = (1 - \rho)\mathbf{Q}_{\text{cm}} + \rho\mathbf{Q}_{\text{tr}} \tag{6.46}$$

where $\rho \in [0, 1]$, to in theory allow the LQR to shift between ankle and hip strategies via end-user tuning. The final $\mathbf{Q}$ in Equation (6.30) is obtained through further parameterizations introduced by Kuo [202] for their double-pendulum model. Specifically,

$$\mathbf{Q} = \sigma^2 \frac{\mathbf{Q}_{\text{hom}}}{\max \varsigma(\mathbf{Q}_{\text{hom}})} \tag{6.47}$$

which scales the kinematic criteria against the effort criteria through a single parameter $\sigma > 0$, as well as normalizes the homotopy $\mathbf{Q}_{\text{hom}}$ to its largest singular value (reminder: singular values returned from function $\varsigma(\cdot)$). The latter operation ensures that variations of ρ do not effect the magnitude-scaling properties of σ [202].

6.2.4 Optimal Balance Regulation: Model Predictive Control

In the previous section, we noted that the proposed LQR approach to balance control was free to utilize motion of the knees to improve the stability of the end-user when donned. However, this may not be desired by all users. Likewise, the LQR is unable to consider the limits of the exoskeleton hardware (e.g., actuator torque production, mechanical joint stops limited range of motion) as well as feasibility of the resulting balance control strategy, i.e., does the ZMP remain within the support polygon. Additionally, Bayon et al. [48] recently suggested that the advantage in their momentum-based control schemes for replicating human balance recovery strategies, as opposed to a full-state feedback approach, was the ability to obtain control inputs that satisfied constraints. To this point, the CTC and LQR approaches discussed do not consider the addition of constraints; therefore, to develop a constrained optimal FIP balance regulator, we developed a novel finite-horizon model predictive control (MPC) architecture. MPC has been used previously for the control and simulation of a linear inverted pendulum with flywheel that could elicit different balance recovery strategies [25, 26]. Herein, the MPC is isolated to FIP strategies, but will generate control inputs for an explicit multibody system representation, i.e., joint torque estimations.

As discussed in Chapter 3 in regards to its nonlinear counterpart NMPC, MPC consists of projecting a dynamic model of a system of interest over some finite-horizon and determining the inputs within that horizon that minimize a given cost function. Often, for the case of real-time MPC implementation, the system dynamics are instead given by a linear state-space representation (like in the LQR). A linear system with linear-quadratic cost (with respect to $\mathbf{x}(t)$ and $\mathbf{u}(t)$) can be readily and optimally controlled using derivative-based quadratic programming (QP) methods; the gradients and Hessians required to take a desired Newton step during solving are entirely precomputed [219]. For real-time implementation, any constraints that the designer wishes to impose on the system should also be linear in $\mathbf{x}(t)$ and $\mathbf{u}(t)$ for these same reasons.

A typical way of solving MPC optimal control problems for real-time implementation, is by approximating the continuous finite-horizon optimal control problem:

$$\underset{\mathbf{x}_{\text{he}}(t),\mathbf{u}_{\text{he}}(t)}{\operatorname{argmin}} \int_{t_0}^{t_0+(N-1)\Delta t} (\mathbf{x}_{\text{he}}-\mathbf{x}_{\text{des}})^{\intercal}\mathbf{Q}(\mathbf{x}_{\text{he}}-\mathbf{x}_{\text{des}}) + (\mathbf{u}_{\text{he}}-\mathbf{u}_{\text{des}})^{\intercal}\mathbf{R}(\mathbf{u}_{\text{he}}-\mathbf{u}_{\text{des}})\, dt \quad (6.48)$$

subject to

$$\mathbf{x}_{\text{he}}(t_0) = \mathbf{x}_0 \quad (6.49)$$

$$\bar{\mathbf{C}}_{t_f}\mathbf{x}_{\text{he}}(t_0+(N-1)\Delta t) \leq \mathbf{b}_{t_f} \quad (6.50)$$

$$\dot{\mathbf{x}}_{\text{he}} = \mathbf{A}(\mathbf{x}_{\text{he}}(t)-\mathbf{x}_{\text{des}}) + \mathbf{B}(\mathbf{u}_{\text{he}}(t)-\mathbf{u}_{\text{des}}), \quad \forall\, t \in [t_0, t_0+(N-1)\Delta t] \quad (6.51)$$

$$\begin{bmatrix}\bar{\mathbf{C}} & \bar{\mathbf{D}}\end{bmatrix}\begin{Bmatrix}\mathbf{x}_{\text{he}}\\ \mathbf{u}_{\text{he}}\end{Bmatrix} \leq \mathbf{b}, \quad \forall\, t \in [t_0, t_0+(N-1)\Delta t] \quad (6.52)$$

$$\dot{\mathbf{u}}_{\min} \leq \dot{\mathbf{u}}_{\text{he}}[k] \leq \dot{\mathbf{u}}_{\max}, \quad \forall\, t \in [t_0, t_0+(N-1)\Delta t] \quad (6.53)$$

$$\begin{Bmatrix}\mathbf{x}_{\min}\\ \mathbf{u}_{\min}\end{Bmatrix} \leq \begin{Bmatrix}\mathbf{x}_{\text{he}}\\ \mathbf{u}_{\text{he}}\end{Bmatrix} \leq \begin{Bmatrix}\mathbf{x}_{\max}\\ \mathbf{u}_{\max}\end{Bmatrix}, \quad \forall\, t \in [t_0, t_0+(N-1)\Delta t] \quad (6.54)$$

as a discrete optimal control problem:

$$\underset{\{\mathbf{x}_{\text{he}}\},\{\mathbf{u}_{\text{he}}\}}{\operatorname{argmin}} \sum_{k=1}^{N} (\mathbf{x}_{\text{he}}[k]-\mathbf{x}_{\text{des}})^{\intercal}\mathbf{Q}(\mathbf{x}_{\text{he}}[k]-\mathbf{x}_{\text{des}}) + (\mathbf{u}_{\text{he}}[k]-\mathbf{u}_{\text{des}})^{\intercal}\mathbf{R}(\mathbf{u}_{\text{he}}[k]-\mathbf{u}_{\text{des}}) \quad (6.55)$$

subject to

$$\mathbf{x}_{\text{he}}[1] = \mathbf{x}_0 \quad (6.56)$$

$$\bar{\mathbf{C}}_{t_f}\mathbf{x}_{\text{he}}[N] \leq \mathbf{b}_{t_f} \quad (6.57)$$

$$\mathbf{x}_{\text{he}}[k+1] = \mathbf{x}_{\text{he}}[k] + \Delta t\mathbf{A}(\mathbf{x}_{\text{he}}[k]-\mathbf{x}_{\text{des}}) + \Delta t\mathbf{B}(\mathbf{u}_{\text{he}}[k]-\mathbf{u}_{\text{des}}), \quad \forall k = 1\ldots N-1 \quad (6.58)$$

$$\begin{bmatrix}\bar{\mathbf{C}} & \bar{\mathbf{D}}\end{bmatrix}\begin{Bmatrix}\mathbf{x}_{\text{he}}[k]\\ \mathbf{u}_{\text{he}}[k]\end{Bmatrix} \leq \mathbf{b}, \quad \forall k = 1\ldots N \quad (6.59)$$

$$\Delta\mathbf{u}_{\min} \leq \Delta\mathbf{u}_{\text{he}}[k] \leq \Delta\mathbf{u}_{\max}, \quad \forall k = 1\ldots N-1 \quad (6.60)$$

$$\begin{Bmatrix}\mathbf{x}_{\min}\\ \mathbf{u}_{\min}\end{Bmatrix} \leq \begin{Bmatrix}\mathbf{x}_{\text{he}}[k]\\ \mathbf{u}_{\text{he}}[k]\end{Bmatrix} \leq \begin{Bmatrix}\mathbf{x}_{\max}\\ \mathbf{u}_{\max}\end{Bmatrix}, \quad \forall k = 1\ldots N \quad (6.61)$$

where Δt is the sampling interval, i.e. we break the continuous finite prediction horizon into N evenly spaced nodes or knot points [188].

The following paragraph will discuss formulation of the constraints in (6.56– 6.61): because stiff ODE components like actuator friction are neglected in the control-oriented

model, the system was constrained to evolve over time intervals according to a forward Euler approximation of the continuous system dynamics (6.51) over a single sampling interval with a zero-order hold assumption on the controls $\mathbf{u}_{\text{he}}(t)$, i.e., see Equation (6.51). The limit on the magnitude of torque derivative in (6.53) was approximated for the discrete problem as a constraint on the control increment (6.60), i.e.,

$$\Delta\mathbf{u}_{\text{he}}[k] = \mathbf{u}_{\text{he}}[k+1] - \mathbf{u}_{\text{he}}[k] \tag{6.62}$$

This constraint tries to limit how noisy the resulting control signal sent to the exoskeleton is. Human motion tends towards smoothness [114, 250, 298], thus we wish for the underlying optimization to consider that when deciding how FIP balance should be optimally regulated.

At each node, box constraints (6.61) act to limit $\mathbf{q}_{\text{he}}$ to $\mathcal{Q}_{\text{he}}$, which considers the location of mechanical stops with the device actuators, $\dot{\mathbf{q}}_{\text{he}}$ to reasonable values for the actuators, as well as $\boldsymbol{\tau}_{\text{in}}$ to the combined capabilities of the end-user and exoskeleton, i.e., how much torque could these two systems generate synergistically. In addition to preserving these box constraints, we also wish for the controller to make decisions that maintain the upright control-oriented model within the FIP domain of feasibility (introduced in Chapter 3). Because we must approximate the set of nonlinear equations $\boldsymbol{\Omega}_{\text{he}}$ to enforce this condition within the MPC framework, we remove the following feasibility constraints:

$$\left\{\begin{array}{c} -\mathbf{F}_{\text{igf}} \cdot \hat{\mathbf{j}} \\ |\mathbf{F}_{\text{igf}} \cdot \hat{\mathbf{i}}| - \mu_{\text{gf}} |\mathbf{F}_{\text{igf}} \cdot \hat{\mathbf{j}}| \end{array}\right\} < \mathbf{0}, \quad \forall\, t \in [t_0, t_0 + (N-1)\Delta t] \tag{6.63}$$

as linearizations of these functions can be rather sensitive to the static equilibrium point selected. Instead, we simply consider the ZMP condition in the domain of feasibility for balanced FIP posture:

$$\boldsymbol{\Omega}_{\text{he}} = \left\{\begin{array}{c} \nu_{\text{he}} - \ell_{\text{c2t}} \\ -\ell_{\text{c2h}} - \nu_{\text{he}} \end{array}\right\} < \mathbf{0}, \quad \forall\, t \in [t_0, t_0 + (N-1)\Delta t] \tag{6.64}$$

A linear approximation of the human-exoskeleton ZMP ($\nu_{\text{he}} \in \mathbb{R}$) relative to the control input only, is obtained from Winter [359]:

$$\nu_{\text{he}} = -\frac{\tau_{\text{in},3} + \ell_{\text{ah}} \mathbf{F}_{\text{igf}} \cdot \hat{\mathrm{i}} - m_{\text{ift}} \ell_{\text{ifcx}} g}{\mathbf{F}_{\text{igf}} \cdot \hat{\mathrm{j}}} \tag{6.65}$$

$$\approx -(M_h + M_e)^{-1} g^{-1} \begin{bmatrix} 0 & 0 & 1 \end{bmatrix} \mathbf{u}_{\text{he}} \tag{6.66}$$

$$\approx \mathbf{D}_{\text{zmp}} \mathbf{u}_{\text{he}} \tag{6.67}$$

where $\tau_{\text{in},3} \in \mathbb{R}$ is the total applied ankle torque, m_{ift} is the bilateral human-exoskeleton foot mass (its COM is a horizontal distance ℓ_{ifcx} from the combined foot COM), and $\mathbf{F}_{\text{igf}} \in \mathbb{R}^{3\times 1}$ is the 3D ground-contact force. In fact, according to the ZMP equation (6.67), the ZMP could also be constrained by adjusting the boundaries provided in the box constraints, i.e., using $\nu_{\text{he}} = \ell_{\text{c2h}}$ and $\nu_{\text{he}} = \ell_{\text{c2t}}$ to solve for the ZMP ankle torque boundaries.

Like the human-only model described in Chapter 3, we also wish for the trunk kinematics to remain within values you would expect to see in balance recovery performed by a human-alone [175]. As acknowledged during LQR design, the trunk angle and angular velocity are already linear time-invariant functions of the joint kinematics:

$$\phi_{\text{tr}} = \mathbf{C}_{\text{tr}}\mathbf{x}_{\text{he}} \tag{6.68}$$

$$\dot{\phi}_{\text{tr}} = \mathbf{C}^{\omega}_{\text{tr}}\mathbf{x}_{\text{he}} \tag{6.69}$$

where

$$\mathbf{C}_{\text{tr}} = \begin{bmatrix} \frac{\partial \phi_{\text{tr}}}{\partial \mathbf{q}_{\text{he}}} & \mathbf{0}_{1\times 3} \end{bmatrix} \tag{6.70}$$

$$\mathbf{C}^{\omega}_{\text{tr}} = \begin{bmatrix} \mathbf{0}_{1\times 3} & \frac{\partial \phi_{\text{tr}}}{\partial \mathbf{q}_{\text{he}}} \end{bmatrix} \tag{6.71}$$

$$\tag{6.72}$$

With appropriate linear definitions of the domain of feasibility (ZMP constraint) and trunk motion limitation , we can then construct "feasibility" model output function

$$\mathbf{y}_{\Omega} = \bar{\mathbf{C}}\mathbf{x}_{\text{he}} + \bar{\mathbf{D}}\mathbf{u}_{\text{he}} \tag{6.73}$$

and the inequality constraint that must be satisfied at all nodes in the MPC prediction horizon,

$$\mathbf{y}_{\Omega} - \mathbf{b} \leq \mathbf{0} \tag{6.74}$$

where $\bar{\mathbf{C}} \in \mathbb{R}^{6\times 6}$ and $\bar{\mathbf{D}} \in \mathbb{R}^{6\times 3}$ are obtained from Equations (6.67), (6.68), and (6.69),

$$\bar{\mathbf{C}} = \begin{bmatrix} \mathbf{0} \\ \mathbf{0} \\ \mathbf{C}_{\text{tr}} \\ -\mathbf{C}_{\text{tr}} \\ \mathbf{C}^{\omega}_{\text{tr}} \\ -\mathbf{C}^{\omega}_{\text{tr}} \end{bmatrix}, \quad \bar{\mathbf{D}} = \begin{bmatrix} \mathbf{D}_{\text{zmp}} \\ -\mathbf{D}_{\text{zmp}} \\ \mathbf{0} \\ \mathbf{0} \\ \mathbf{0} \\ \mathbf{0} \end{bmatrix} \tag{6.75}$$

while the static inequality column matrix $\mathbf{b} \in \mathbb{R}^{6\times 1}$, i.e., the boundary enforcing term, is stated as follows:

$$\mathbf{b} = \begin{Bmatrix} \nu_{\text{he,max}} & -\nu_{\text{he,min}} & \phi_{\text{tr,max}} & -\phi_{\text{tr,min}} & \dot{\phi}_{\text{tr,max}} & -\dot{\phi}_{\text{tr,min}} \end{Bmatrix}^{\intercal} \tag{6.76}$$

Lastly, an initial equality constraint, Equation (6.56), was included to restrict the exoskeleton state at the first node to the initial measured or estimated state, i.e., the sensor or state estimator-based joint position and velocity. For terminal constraints, in Chapter 3 (human-only NMPC), multi-dimensional ellipse constraints acting at the last node in the prediction horizon were proposed with the intent of improving the convergence of the controller towards a truly stable configuration [299]. For this reason, we also elected to add terminal constraints to the finite-horizon FIP human-exoskeleton MPC problem [51, 231, 299]. However, as the ellipse equations were nonlinear, they did not fit the requirements of the real-time linear MPC approach. Instead, terminal inequality constraint that restricted the human-exoskeleton kinematics at the final node of the prediction horizon, were defined:

$$\mathbf{y}_{t_f} = \bar{\mathbf{C}}_{t_f}\mathbf{x}_{\text{he}}[N] \tag{6.77}$$

$$\mathbf{y}_{t_f} - \mathbf{b}_{t_f} \leq \mathbf{0} \tag{6.78}$$

which includes the following matrices:

$$\bar{\mathbf{C}}_{t_f} \in \mathbb{R}^{15\times 6} = \begin{bmatrix} \mathbf{C}_{\text{ixcm}} \\ -\mathbf{C}_{\text{ixcm}} \\ -\mathbf{C}^{v}_{\text{cm}} \\ \mathbf{I} \\ -\mathbf{I} \end{bmatrix}, \quad \mathbf{b}_{t_f} \in \mathbb{R}^{15\times 1} = \begin{Bmatrix} \ell_{\text{c2t}} - \bar{r}_{\text{ixcm}} \\ -(-\ell_{\text{c2h}}) + \bar{r}_{\text{ixcm}} \\ -r^{v}_{\text{icm,min}} + \bar{r}^{v}_{\text{icm}} \\ \mathbf{x}_{f,\text{max}} \\ -\mathbf{x}_{f,\text{min}} \end{Bmatrix} \tag{6.79}$$

In Equation (6.79), approximations of the nonlinear extrapolated COM equation are made [154], i.e.,

$$r_{\text{ixcm}} = \left(\mathbf{r}_{\text{icm}} + \frac{\dot{\mathbf{r}}_{\text{icm}}}{\omega_0}\right) \cdot \hat{\imath} \tag{6.80}$$

$$\approx \mathbf{C}_{\text{ixcm}}(\mathbf{x}_{\text{he}} - \mathbf{x}_{\text{des}}) + \bar{r}_{\text{ixcm}} \tag{6.81}$$

where $\bar{r}_{\text{ixcm}} = r_{\text{ixcm}}(\mathbf{x}_{\text{des}})$ and $\mathbf{C}_{\text{ixcm}} = \partial r_{\text{ixcm}}/\partial \mathbf{x}_{\text{he}}|_{\mathbf{x}_{\text{des}}}$, in addition approximations of the vertical displacement of the integrated human-exoskeleton COM:

$$\mathbf{r}_{\text{icm}} \cdot \hat{\jmath} \approx \mathbf{C}^{v}_{\text{cm}}(\mathbf{x}_{\text{he}} - \mathbf{x}_{\text{d}}) + \bar{r}^{v}_{\text{icm}} \tag{6.82}$$

where $\bar{r}^v_{\text{icm}} = r_{\text{icm}}(\mathbf{x}_{\text{des}}) \cdot \hat{\mathbf{j}}$ and $\mathbf{C}^v_{\text{cm}} = \partial(r_{\text{icm}} \cdot \hat{\mathbf{j}})/\partial \mathbf{x}_{\text{he}}|_{\mathbf{x}_{\text{des}}}$. Briefly, the conditions set in (6.78) are intended to act as follows:

a Bring the XCOM within the support polygon at the end of the prediction horizon $[-\ell_{\text{c2h}}, \ell_{\text{c2t}}]$, i.e., leave human-exoskeleton in a capturable state assuming the system is like an inverted pendulum [154],

b Set the final COM height to be above a certain threshold, i.e., avoid finishing in a squatted or pitched posture.

c Further constrain the final state if necessary according to $\mathbf{x}_{f,\max}$ and $\mathbf{x}_{f,\min}$. These states are mostly determined from tuning and can be considered the box approximation to the multi-dimensional ellipse constraint on the NMPC states. An example of their use would be to have all joint velocities zeroed at the end of the prediction horizon, similar to the simulations by Cheng et al. [77, 78].

With the discrete optimal control problem formulation delineated, the final step in designing the real-time MPC controller for FIP balance was to convert the discrete finite-horizon control problem into a quadratic programming (QP) problem:

$$\underset{\mathbf{Z}}{\text{argmin}} \ \frac{1}{2}\mathbf{Z}^\intercal \mathbf{H}_{\text{qp}} \mathbf{Z} + \mathbf{\Psi}_{\text{qp}} \mathbf{Z} \tag{6.83}$$

subject to

$$\tilde{\mathbf{D}}\mathbf{Z} \leq \tilde{\mathbf{b}} \tag{6.84}$$

$$\tilde{\mathbf{D}}_{\text{eq}}\mathbf{Z} = \tilde{\mathbf{b}}_e q \tag{6.85}$$

$$\mathbf{Z}_{\text{lb}} \leq \mathbf{Z} \leq \mathbf{Z}_{\text{ub}} \tag{6.86}$$

where $\mathbf{Z} \in \mathbb{R}^{9N \times 1} = [\mathcal{X}^\intercal, \mathcal{U}^\intercal]^\intercal = \left[\{\mathbf{x}_{\text{he}}[k]\}_{k=1}^N, \mathbf{u}_{\text{he}}[k]\}_{k=1}^N\right]^\intercal$ is the QP decision variable, which is simply a concatenation of the state/control sequences that represent the sampled continuous states/control over the prediction horizon. To construct $\mathbf{H}_{\text{qp}}$, the summation terms in the quadratic cost function in (6.55) were first expanded at any given instance k:

$$(\mathbf{x}_{\text{he}}[k] - \mathbf{x}_{\text{d}})^\intercal \mathbf{Q} (\mathbf{x}_{\text{he}}[k] - \mathbf{x}_{\text{d}}) = \mathbf{x}_{\text{he}}[k]^\intercal \mathbf{Q} \mathbf{x}_{\text{he}}[k] - \mathbf{x}_{\text{d}}^\intercal (\mathbf{Q} + \mathbf{Q}^\intercal) \mathbf{x}_{\text{he}}[k] + \mathbf{x}_{\text{d}}^\intercal \mathbf{Q} \mathbf{x}_{\text{d}} \tag{6.87}$$

$$(\mathbf{u}_{\text{he}}[k] - \mathbf{u}_{\text{d}})^\intercal \mathbf{R} (\mathbf{u}_{\text{he}}[k] - \mathbf{u}_{\text{d}}) = \mathbf{u}_{\text{he}}[k]^\intercal \mathbf{R} \mathbf{u}_{\text{he}}[k] - \mathbf{u}_{\text{d}}^\intercal (\mathbf{R} + \mathbf{R}^\intercal) \mathbf{u}_{\text{he}}[k] + \mathbf{u}_{\text{d}}^\intercal \mathbf{R} \mathbf{u}_{\text{d}} \tag{6.88}$$

Considering the form of the quadratic cost in Equations (6.87) and (6.88), and applying that pattern over the sequences $\{\mathbf{x}_{\text{he}}[k]\}_{k=1}^{N}$ and $\{\mathbf{u}_{\text{he}}[k]\}_{k=1}^{N}$ reveals the simple sparsity pattern of $\mathbf{H}_{\text{qp}}$

$$\mathbf{H}_{\text{qp}} \in \mathbb{R}^{9N\times 9N} = 2\left[\begin{array}{cccc|cccc} \mathbf{Q} & \mathbf{0} & \cdots & \mathbf{0} & \mathbf{R} & \mathbf{0} & \cdots & \mathbf{0} \\ \mathbf{0} & \mathbf{Q} & \cdots & \mathbf{0} & \mathbf{0} & \mathbf{R} & \cdots & \mathbf{0} \\ \vdots & \vdots & \ddots & \vdots & \vdots & \vdots & \ddots & \vdots \\ \underbrace{\mathbf{0}}_{x} & \mathbf{0} & \cdots & \mathbf{Q} & \underbrace{\mathbf{0}}_{u} & \mathbf{0} & \cdots & \mathbf{R} \end{array}\right] \tag{6.89}$$

as well as the structure of the linear coefficient of the QP problem, i.e.,

$$\boldsymbol{\Psi}_{\text{qp}}^{\intercal} \in \mathbb{R}^{9N\times 1} = \left\{\begin{array}{c} -(\mathbf{Q}+\mathbf{Q}^{\intercal})\mathbf{x}_{\text{d}} \\ \vdots \\ -(\mathbf{Q}+\mathbf{Q}^{\intercal})\mathbf{x}_{\text{d}} \\ \hline -(\mathbf{R}+\mathbf{R}^{\intercal})\mathbf{u}_{\text{d}} \\ \vdots \\ -(\mathbf{R}+\mathbf{R}^{\intercal})\mathbf{u}_{\text{d}} \end{array}\right\} \tag{6.90}$$

where the vertical bar delimiter in (6.89) indicates terms applied to the state or control sequence according to the definition of $\mathbf{Z}$. To obtain, the equality constraints in (6.85), the equality constraints in (6.56) and (6.58) must be vectorized over the entire prediction horizon as done for the cost function terms (6.89) and (6.90). Doing so results in the following equality constraint matrices:

$$\tilde{\mathbf{D}}_{\text{eq}} \in \mathbb{R}^{6N\times 9N} = \left[\begin{array}{ccccccc|ccccc} \mathbf{I} & \mathbf{0} & \mathbf{0} & \cdots & \mathbf{0} & \mathbf{0} & & \mathbf{0} & \mathbf{0} & \cdots & \mathbf{0} \\ \mathbf{I}+\Delta t\mathbf{A} & -\mathbf{I} & \mathbf{0} & \cdots & \mathbf{0} & \mathbf{0} & & \Delta t\mathbf{B} & \mathbf{0} & \cdots & \mathbf{0} \\ \mathbf{0} & \mathbf{I}+\Delta t\mathbf{A} & -\mathbf{I} & \cdots & \mathbf{0} & \mathbf{0} & & \mathbf{0} & \Delta t\mathbf{B} & \cdots & \mathbf{0} \\ \vdots & \vdots & \vdots & \ddots & \vdots & \vdots & & \vdots & \vdots & \ddots & \vdots \\ \mathbf{0} & \mathbf{0} & \mathbf{0} & \cdots & \mathbf{I}+\Delta t\mathbf{A} & -\mathbf{I} & & \mathbf{0} & \mathbf{0} & \cdots & \Delta t\mathbf{B} \end{array}\right] \tag{6.91}$$

and

$$\tilde{\mathbf{b}}_{\text{eq}} \in \mathbb{R}^{6N\times 1} = \left\{\begin{array}{c} \mathbf{x}_0 \\ \Delta t(\mathbf{A}\mathbf{X}_{\text{d}}+\mathbf{B}\mathbf{U}_{\text{d}}) \\ \vdots \\ \Delta t(\mathbf{A}\mathbf{X}_{\text{d}}+\mathbf{B}\mathbf{U}_{\text{d}}) \end{array}\right\} \tag{6.92}$$

which restricts changes in the state over each sampling interval within the prediction horizon such that they follow the discretized linear system dynamics in Equation (6.58).

Similar to the steps taken to develop the equality constraints in (6.85), path and terminal inequality constraints in Equations (6.57),(6.59), and (6.60) were vectorized and concatenated entirely within sparse path inequality constraint matrices,

$$\tilde{\mathbf{D}} = \left[\begin{array}{cccc|cccc} \bar{\mathbf{C}} & \mathbf{0} & \cdots & \mathbf{0} & \bar{\mathbf{D}} & \mathbf{0} & \mathbf{0} & \cdots & \mathbf{0} \\ \mathbf{0} & \bar{\mathbf{C}} & \cdots & \mathbf{0} & \mathbf{0} & \bar{\mathbf{D}} & \mathbf{0} & \cdots & \mathbf{0} \\ \vdots & \vdots & \ddots & \vdots & \vdots & \vdots & \vdots & \ddots & \vdots \\ \mathbf{0} & \mathbf{0} & \cdots & \bar{\mathbf{C}} & \mathbf{0} & \mathbf{0} & \mathbf{0} & \cdots & \bar{\mathbf{D}} \\ \hline \mathbf{0} & \mathbf{0} & \cdots & \mathbf{0} & -\mathbf{I} & \mathbf{I} & \mathbf{0} & \cdots & \mathbf{0} \\ \mathbf{0} & \mathbf{0} & \cdots & \mathbf{0} & \mathbf{0} & -\mathbf{I} & \mathbf{I} & \cdots & \mathbf{0} \\ \vdots & \vdots & \ddots & \vdots & \vdots & \vdots & \vdots & \ddots & \vdots \\ \mathbf{0} & \mathbf{0} & \cdots & \mathbf{0} & \mathbf{0} & \mathbf{0} & \mathbf{0} & \cdots & \mathbf{I} \\ \hline \mathbf{0} & \mathbf{0} & \cdots & \mathbf{0} & \mathbf{I} & -\mathbf{I} & \mathbf{0} & \cdots & \mathbf{0} \\ \mathbf{0} & \mathbf{0} & \cdots & \mathbf{0} & \mathbf{0} & \mathbf{I} & -\mathbf{I} & \cdots & \mathbf{0} \\ \vdots & \vdots & \ddots & \vdots & \vdots & \vdots & \vdots & \ddots & \vdots \\ \mathbf{0} & \mathbf{0} & \cdots & \mathbf{0} & \mathbf{0} & \mathbf{0} & \mathbf{0} & \cdots & -\mathbf{I} \\ \hline \mathbf{0} & \mathbf{0} & \cdots & \bar{\mathbf{C}}_{t_f} & \mathbf{0} & \mathbf{0} & \mathbf{0} & \cdots & \mathbf{0} \end{array}\right], \quad \tilde{\mathbf{b}} = \left\{\begin{array}{c} \mathbf{b} \\ \mathbf{b} \\ \vdots \\ \mathbf{b} \\ \hline \Delta\mathbf{u}_{\max} \\ \Delta\mathbf{u}_{\max} \\ \vdots \\ \Delta\mathbf{u}_{\max} \\ \hline -\Delta\mathbf{u}_{\min} \\ -\Delta\mathbf{u}_{\min} \\ \vdots \\ -\Delta\mathbf{u}_{\min} \\ \hline \mathbf{b}_{t_f} \end{array}\right\} \tag{6.93}$$

as were the box constraint boundaries in Equation (6.61):

$$\mathbf{Z}_{\text{lb}} \in \mathbb{R}^{9N\times 1} = \left\{\begin{array}{c} \mathbf{x}_{\min} \\ \vdots \\ \mathbf{x}_{\min} \\ \mathbf{u}_{\min} \\ \vdots \\ \mathbf{u}_{\min} \end{array}\right\}, \quad \mathbf{Z}_{\text{ub}} \in \mathbb{R}^{9N\times 1} = \left\{\begin{array}{c} \mathbf{x}_{\max} \\ \vdots \\ \mathbf{x}_{\max} \\ \mathbf{u}_{\max} \\ \vdots \\ \mathbf{u}_{\max} \end{array}\right\} \tag{6.94}$$

As a point of interest, while the MPC control formulation discussed to this point assumes that the human end-user acts passively during operation, i.e. MTGs lumped with control torques, it is also relatively simple to augment the system to solve for an optimal

control action that does consider end-user activity, e.g.,

$$\underset{\{\mathbf{x}_{\text{he}}\},\{\mathbf{u}_{\text{he}}\}}{\operatorname{argmin}} \sum_{k=1}^{N} (\mathbf{x}_{\text{he}}[k] - \mathbf{x}_{\text{d}})^{\intercal}\mathbf{Q}(\mathbf{x}_{\text{he}}[k] - \mathbf{x}_{\text{d}}) + (\mathbf{u}_{\text{he}}[k] - \mathbf{u}_{\text{d}})^{\intercal}\mathbf{R}(\mathbf{u}_{\text{he}}[k] - \mathbf{u}_{\text{d}}) \tag{6.95}$$

subject to

$$\mathbf{x}_{\text{he}}[1] = \mathbf{x}_0 \tag{6.96}$$

$$\bar{\mathbf{C}}_{t_f}\mathbf{x}_{\text{he}}[N] \leq \mathbf{b}_{t_f} \tag{6.97}$$

$$\begin{aligned}\mathbf{x}_{\text{he}}[k+1] = \mathbf{x}_{\text{he}}[k] &+ \Delta t\mathbf{A}(\mathbf{x}_{\text{he}}[k] - \mathbf{x}_{\text{d}}) + \Delta t\mathbf{B}(\mathbf{u}_{\text{he}}[k] - \mathbf{u}_{\text{d}}) \\ &+ \Delta t\mathbf{B}(\mathbf{u}_{\text{m}}[k] - \mathbf{u}_{\text{m,d}}), \quad \forall k = 1 \dots N-1\end{aligned} \tag{6.98}$$

$$\begin{bmatrix}\bar{\mathbf{C}} & \bar{\mathbf{D}}\end{bmatrix}\begin{Bmatrix}\mathbf{x}_{\text{he}}[k] \\ \mathbf{u}_{\text{he}}[k]\end{Bmatrix} \leq \mathbf{b}, \quad \forall k = 1 \dots N \tag{6.99}$$

$$\Delta\mathbf{u}_{\min} \leq \Delta\mathbf{u}_{\text{he}}[k] \leq \Delta\mathbf{u}_{\max}, \quad \forall k = 1 \dots N-1 \tag{6.100}$$

$$\begin{Bmatrix}\mathbf{x}_{\min} \\ \mathbf{u}_{\min}\end{Bmatrix} \leq \begin{Bmatrix}\mathbf{x}_{\text{he}}[k] \\ \mathbf{u}_{\text{he}}[k]\end{Bmatrix} \leq \begin{Bmatrix}\mathbf{x}_{\max} \\ \mathbf{u}_{\max}\end{Bmatrix}, \quad \forall k = 1 \dots N \tag{6.101}$$

where human muscle torques $\mathbf{u}_{\text{m}}$ are introduced separately from the original control vector $\mathbf{u}_{\text{he}}$. If the robotic system has a good understanding of how a person is likely to activate their muscles during use (perhaps using a separate prediction model [255, 258], the exoskeleton could consider these possible actions in its own decision making process, e.g., let the user drive the system or augmenting what they may desire [256, 334].

6.2.5 Nonlinear State Estimation and Intent Detection

The following section contains content related to the extended abstract "Facilitating Dynamic Balance Recovery in Lower Limb Exoskeletons with State Estimation" presented at the 11th ECCOMAS Thematic Conference on Multibody Dynamics (Inkol and McPhee [173]).

In designing full-state feedback controllers for multibody dynamic systems, it is necessary that the generalized positions and velocities be reasonably measured or estimated [260]. That being said, velocity measurements are not always available to the control engineer. In fact, we only recently gained access to velocity measurements and motor torque control with the EXO-H3 following a firmware update in March 2023. Even when these

measurements are available, there is the possibility of the signal being quantized and/or corrupted by varying degrees of noise depending on the sensor quality, controller bandwidth, etc. Both finite and infinite impulse response filters can be used in real-time to filter a noisy signal, but introduce delays into the smoothed signal. Alternatively, dynamic model-based filtering methods like the Kalman filter and moving horizon estimator (MHE; originally introduced in Chapter 4) can yield a smoothed signal with reduced lag in the outputs [360], however, they require more manual tuning and technical knowledge of the system's underlying physics [260, 310]. With that said, state estimation techniques can also provide estimations of unmeasured states so long as the system is "observable" [310]; this is particularly important for sensor configurations that measure position data, e.g., the EXO-H3 prior to firmware update.

Historically, state estimation methods have been applied to FIP balance control with great success. Linear estimation methods, i.e., the Kalman filter, accurately describe the integration of redundant sensor information by the CNS for feedback control of balance [203, 342, 341]. In humanoid robotics, both the nonlinear extension of the Kalman filter, the extended Kalman filter (EKF), in addition to nonlinear MHE have been used recently for real-time state estimation and successful walking/balance [39, 275]. The MHE is especially intriguing because it possesses the capability to handle nonlinear systems and constraints, while also offering some capability in dealing with non-Gaussian modeling errors. [39]. In lower-limb exoskeletons, the majority of the existing state-estimation literature pertains to identification of gait-states. Medrano et al. [236, 237] showed great success with EKF in real-time estimation of gait characteristics (phase, phase rate, stride length, and ground incline) and adaptations of ankle-torque assistance to allow end-users to walk on variable terrain. Notably, Tanghe et al. [323] successfully implemented MHE to both estimate future gait trajectories, i.e., where the joints need to go, and predict the onset of gait events before they occur, e.g., heel-off and toe-off.

Like estimating the joint kinematics, we also wish to investigate how we can model and estimate disturbances applied to the system. Interestingly, reasonable estimates of disturbances such as the active human muscle torques applied by the end-user could provide improved intent recognition and power augmentation by the device [53, 159, 256, 257]. It could also provide perturbation detection for improving assisted balance recovery [275]. However, control designers using commercial robotic systems are often trying to recognize disturbances from minimal sensors. In the case of biomechatronics, sensor configurations are often designed in order to be less cumbersome for the user [334]. In the literature,

force/torque estimators often rely on state-space models that also feature system states at the acceleration-level, e.g., drone technology [37, 39, 127, 234, 275]. Given the sensors we have to use currently on the EXO-H3, e.g., joint positions, velocities, and motor torques, we are interested in seeing which disturbances we can recognize given some kinematic and input observations without relying on acceleration-level observations, e.g., separate torque sensors. We were also interested in investigating how signal quantization negatively affects control performance; signals undergo substantial rounding within the CAN protocol used to interface with and run custom controllers on the EXO-H3.

The current subsection discusses our investigation into nonlinear methods of state estimation to help in the implementation of assistive/autonomous FIP balance controls. The decision to explore nonlinear methods was based on three primary reasons:

i) We want to use nonlinear dry friction compensation outside of the full-state feedback control block to simplify the underlying FIP control laws;

ii) The proposed control laws (LQR, MPC) tend to be computationally inexpensive;

iii) To explore the capabilities of modern state estimation techniques with biomechatronics in observing kinematic states and recognizing human intent.

Two approaches to estimating the multibody states of the integrated human-exoskeleton system and recognizing disturbances that could be coming from the active human muscle torques are described and tested in this section: the extended Kalman filter (EKF) and moving horizon estimator (MHE). For brevity, the derivation of the EKF is provided in Appendix M so that more focus can be placed on the novel MHE approach.

Nonlinear Moving Horizon Estimation

While the EKF is a widely used approach in the area of state-estimation for nonlinear systems, it comes with many caveats. Some of these issues include obtaining and tuning reliable process noise covariance matrices (e.g., how effective are the constant acceleration/jerk assumptions for disturbance estimation [249, 289]), sensitivity of linearizations in error covariance propagation [310], and the stability of state propagation using explicit functions and large time steps [201]. To potentially address some of these concerns, especially the latter two, we explored the using of moving horizon estimation (MHE) [310].

This method in particular was highlighted due to its limited use with robotic exoskeletons [323] despite its exciting applications in topics like vehicle maneuvering [180, 200, 321] and human biomechanics [40, 73, 127]. Furthermore, MHE also fits well with the conceptual framework of optimization and optimal control within the current dissertation.

In designing the FIP assistance MHE, we write the continuous observation-oriented state-space dynamics as the following system of ODEs:

$$\dot{\mathbf{x}}_{\text{os}} = \begin{Bmatrix} \dot{\mathbf{q}}_{\text{he}} \\ \ddot{\mathbf{q}}_{\text{he}} \\ \dot{\boldsymbol{\tau}}_{\text{mtr}} \\ \dot{\boldsymbol{\tau}}^{\text{cns}}_{\text{mtg}} \end{Bmatrix} = \begin{Bmatrix} \dot{\mathbf{q}}_{\text{he}} \\ \boldsymbol{\alpha}_{\text{he}} \\ \mathbf{w}_{\text{mtr}} \\ \mathbf{w}_{\text{mtg}} \end{Bmatrix} = \mathbf{f}_{\text{os}}(\mathbf{x}_{\text{os}}(t), \mathbf{w}(t)) \tag{6.102}$$

where the motor torques $\boldsymbol{\tau}_{\text{mtr}}$ and active MTG torques $\boldsymbol{\tau}^{\text{cns}}_{\text{mtg}}$ are now modelled as states instead of inputs so that we can estimate unobserved values, i.e., user-intent torques. Their dynamics are modelled using stochastic processes; $\mathbf{w}_{\text{mtg}} \sim \mathcal{N}(\mathbf{0}, \mathbf{Q}_{\text{mtg}})$ and $\mathbf{w}_{\text{mtr}} \sim \mathcal{N}(\mathbf{0}, \mathbf{Q}_{\text{mtr}}) \, \forall \, t$ are white Gaussian noise with constant process noise covariance matrices $\mathbf{Q}_{\text{mtr}} = \mathbb{E}[\mathbf{w}_{\text{mtr}} \mathbf{w}^{\intercal}_{\text{mtr}}]$ and $\mathbf{Q}_{\text{mtg}} = \mathbb{E}[\mathbf{w}_{\text{mtg}} \mathbf{w}^{\intercal}_{\text{mtg}}]$. Additionally, the generalized accelerations are parameterized via input $\boldsymbol{\alpha}_{\text{he}} \in \mathbb{R}^{3\times 1}$. The goal with MHE is to estimate the true value of these states at a given instant by combining the dynamic model with a series measurements,

$$\mathbf{h}(\mathbf{x}_{\text{os}}) \in \mathbb{R}^{9\times 1} = \begin{Bmatrix} \mathbf{q}_{\text{he}} \\ \dot{\mathbf{q}}_{\text{he}} \\ \boldsymbol{\tau}_{\text{mtr}} \end{Bmatrix} \tag{6.103}$$

that are corrupted by additive white noise, i.e., at a sampled instant k

$$\boldsymbol{\upsilon}[k] = \mathbf{y}[k] - \mathbf{h}(\mathbf{x}_{\text{os}}[k]) \tag{6.104}$$

where $\mathbf{y}[k] \in \mathbb{R}^{9\times 1}$ and $\boldsymbol{\upsilon}[k] \sim \mathcal{N}(\mathbf{0}, \mathbf{R})$ with measurement noise covariance $\mathbf{R}^{9\times 9}$. These variables are the same variables that can be measured in practice with the EXO-H3.

For the MHE approach, if we freeze the system at an instant i, we then want to solve the following NLP problem over the past N instances (i.e., within the moving horizon we

defined) to obtain an optimal estimate: [310]:

$$\underset{\chi_{\text{os}},\{\boldsymbol{\alpha}_{\text{he}}\},\{\mathbf{w}\},\{\boldsymbol{\upsilon}\},\boldsymbol{\eta}}{\operatorname{argmin}} \underbrace{\|\boldsymbol{\eta}\|^2_{\hat{\mathbf{P}}^{-1}[i-N|i-N]}}_{\text{arrival cost}} + \underbrace{\sum_{k=M}^{N-1} \|\mathbf{w}[k]\|^2_{\mathbf{Q}_{\text{os}}^{-1}}}_{\text{process error cost}} + \underbrace{\sum_{k=M+1}^{N} \|\boldsymbol{\upsilon}[k]\|^2_{\mathbf{R}_{\text{os}}^{-1}}}_{\text{measurement error cost}} \tag{6.105}$$

subject to:

$$\mathbf{x}_{\text{os}}[M] - \hat{\mathbf{x}}_{\text{os}}[i-N|i-N] - \boldsymbol{\eta} = \mathbf{0} \tag{6.106}$$

$$\mathbf{M}_{\text{he}}\boldsymbol{\alpha}_{\text{he}}[k] - \boldsymbol{\Gamma}_{\text{he}}[k] - \boldsymbol{\tau}^{\text{cns}}_{\text{mtg}}[k] - 2\boldsymbol{\tau}_{\text{psv}}[k] - 2\boldsymbol{\tau}_{\text{mtr}}[k] - 2\boldsymbol{\tau}_{\text{f}}[k] = \mathbf{0} \tag{6.107}$$

$$\mathbf{y}[k] - \mathbf{h}(\mathbf{x}_{\text{os}}[k]) - \boldsymbol{\upsilon}[k] = \mathbf{0} \tag{6.108}$$

$$\mathbf{x}_{\text{os}}[k] - \mathbf{x}_{\text{os}}[k+1] + \frac{\Delta t}{2}(\mathbf{f}_{\text{os}}(\mathbf{x}_{\text{os}}[k], \mathbf{w}[k]) + \mathbf{f}_{\text{os}}(\mathbf{x}_{\text{os}}[k+1], \mathbf{w}[k+1])) = \mathbf{0} \tag{6.109}$$

where we adopt the conventions of Puchaud et al. [281] once again and solve the second-order multibody dynamics in Equation (6.107) implicitly by including the generalized accelerations as a decision variable $\boldsymbol{\alpha}_{\text{he}}[k] \,\forall\, k = M \ldots N$. The trapezoidal method was implemented within the collocation constraints (6.109) to improve stability in the system projections, especially with the presence of stiff actuator friction in (6.102). Note that we can also now include box constraints within the estimation rather simply, e.g., joint angles can only be within specified ranges. In the EKF, projection methods can be used rather simply for box constraining state estimates, however, these projections are not so trivial to obtain for the estimation-error covariance [310]. For this reason, we avoided the inclusion of inequality constraints with the NLP.

Symbolic gradients and Hessians were generated in MapleSim and used to solve NLP via the interior-point solver `fmincon` in MATLAB. At iteration i, with the problem (6.105–6.109) solved, the optimal estimate of the state with respect to the output of the optimization procedure is

$$\hat{\mathbf{x}}_{\text{os}}[i|i] = \{\mathbf{x}^*_{\text{os}}[k]\}_{k=N} \tag{6.110}$$

which isolates the estimated state trajectory at the first node. To generate a new estimate of $\hat{\mathbf{P}}[i-N|i-N]$ at each new i, the EKF algorithm in Appendix M was run in parallel using previous state estimates and measurements (those at the beginning of the moving horizon [310]). Therefore, if the EKF was performing well and producing an error covariance with $\text{tr}(\hat{\mathbf{P}}) \to 0$, then this would weigh the arrival cost highly within (6.105) effectively constraining the optimization. However, if the EKF is not performing well and estimated

error covariance remains large, the MHE simply disregards the estimates by the EKF and uses local information, i.e., it uses *only* the sequence of measurements in the horizon, but does so simultaneously to come up optimal state estimate. Alternatively, one could maintain a constant error covariance matrix so that the MHE only uses the sequence of measurements provided it to over the moving window it to make an estimate (arrival cost is more or less neglected).

6.3 Proof-of-Concept Simulations

To establish the performance of the proposed full-state feedback control and state-estimation algorithms (described in the previous section), in autonomously driving upright FIP balance, a series of dynamic "what-if" simulations were performed [106]. In each proof-of-concept simulation, the plant being controlled was the control-oriented nonlinear human-exoskeleton model described in Chapter 6.2.1, i.e., the end-user arms were bound rigidly to the trunk. The same human parameters were adopted from the FSR simulations in Chapters 3 and 6 (young adult male, height = 1.80 m, weight = 75 kg), while exoskeleton parameters were those of the EXO-H3 identified in Chapter 4 via physical measurements and CAD analysis (PhyExp). The same backward and forward perturbations used in Chapter 3 to test the human model, i.e., translations of the support-surface used experimentally in [224], were used to test the proposed control/observation systems. As a reminder, the backward translations initiated a forward "fall" that the exoskeleton controller or human must respond to; forward translations induced a backward "fall". Perturbations were initiated 100 ms after the start of each simulation.

The first set of simulations were used to assess performance of the optimal full-state feedback controllers (LQR, and MPC) with perfect state measurements. Specifically, we were interested in establishing how variations in the cost function parameters and constraints (within the MPC only) altered the ideal performance of the controller, e.g., the postural strategy adopted and runtime. The second set of simulations established performance of the proposed nonlinear state estimation methods with variations in the quality of nonlinear friction compensation and onboard sensor measurements, e.g., added noise and signal quantization. Additional simulation experiments are included in the appendices as follows: Appendix L introduces and assesses baseline performance of nonlinear computed torque control algorithms in regulating upright FIP balance [315]; in Appendix N, the

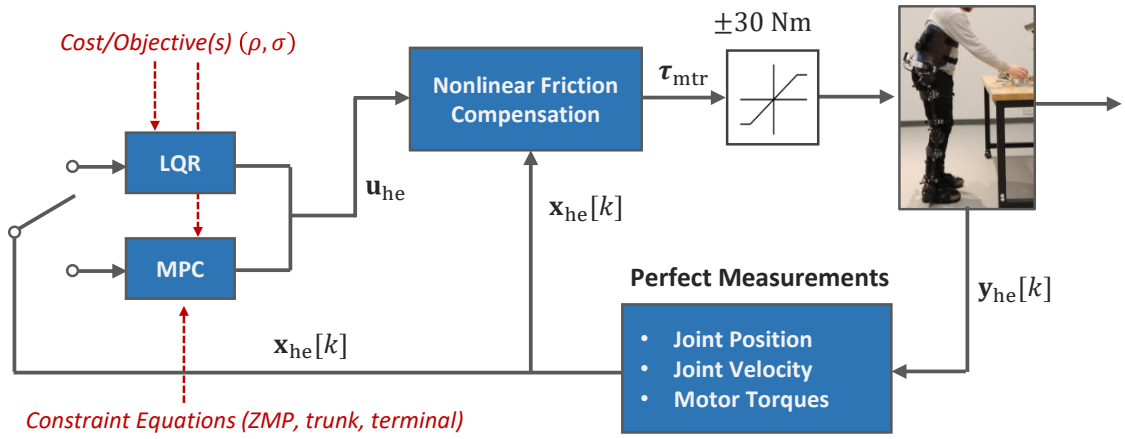


Figure 6.9: Control schematic for simulation set 2: optimal regulation of FIP balance recovery via linear quadratic regulator (LQR; unconstrained) or model predictive control (MPC; constrained).

novel MPC and MHE algorithms were applied to FIP balance assistance of an end-user of variable strength in addition to estimation of the applied active MTG torques, i.e., intent recognition. These supplementary simulations were based on the setup we had previously used in our publication, Inkol and McPhee [169].

6.3.1 Effect of Optimal Regulation Parameters and Constraints

The first set of simulations was used to assess the performance of the proposed optimal control laws in recovering FIP upright balance: LQR and MPC. The control scheme used is displayed in Fig. 6.9. Nonlinear friction compensation [142] was applied through the block described in Fig. L.2 (Appendix L). In line with manufacturer design, the exoskeleton motor torques were saturated at ±30 Nm. We assumed that friction was perfectly compensated within the loop except for torques due to viscous friction; only 80% of those torques were negated. The control-oriented model was now the linearized 3 DOF FIP model as required in the optimal control formulation (see Section 6.2.3). In all simulations, control weights were set as $\mathbf{R} = \mathbf{I}_{3\times3}$. For the MPC constraints, the support polygon was set slightly smaller than it was in the plant: $\ell_{c2t} = 19$ cm (versus 20.7 cm) and $\ell_{c2h} = 4$ cm (versus 5.9 cm). In the MPC, the ideal actuator torques (sum of passive/active MTG torques and motor torques) were still conservatively constrained to motor torque limits (±30 Nm),

while the joint states were constrained to those implemented in Chapter 6.1. Since the ideal actuator torque terms were also assumed to contain passive MTG torques, the estimated passive MTG torques at the static equilibrium configuration were subtracted from the ideal actuator signal prior to friction compensation (Fig. 6.9)

We first investigated the effect of objective tuning on real-time optimal control performance. For each of the LQR and MPC controllers (and backward and forward perturbations), three values of ρ and σ were tested: $\rho \in \{0, 0.5, 1\}$ and $\sigma \in \{5{\times}10^3, 2.5{\times}10^3, 5{\times}10^2\}$. In all simulations, a 500 ms prediction horizon was used; this value was reduced from the 800 ms used in Chapter 3.3 in order to improve computational efficiency whilst maintaining a degree of horizon length to encourage more human-like behaviours [26, 240]. Fig. 6.10 shows the balancing joint angles following a posterior and anterior support-surface translation that were generated by the LQR and MPC using different values of ρ. Fig. 6.11 shows the motor torques required to generate these joint trajectories. Additionally, Fig. 6.12 highlights the horizontal COM and ZMP positions calculated over these simulations. For the balancing joint angles following a posterior and anterior support-surface translation according to different values of σ, we refer to Fig. 6.13. Fig. 6.14 shows the motor torques generated during each simulation, while Fig. 6.15 shows the horizontal COM and ZMP positions. On average ($\pm$ SD), each call to the LQR controller required $3.33{\times}10^{-5}{\pm}1.19{\times}10^{-4}$ s of run-time while each call to the MPC required $1.91 \times 10^{-2} \pm 2.73 \times 10^{-3}$ s; the LQR gains were calculated offline. Upon inspection there was no functional difference in run-times with variations in ρ and σ.

In all simulations testing ρ and σ, the ZMP was maintained within the support polygon indicating no falling occurred. The high weighing of σ during simulations testing ρ ($\sigma = 5 \times 10^3$) produced aggressive control of the ZMP, especially during the deceleration portion of the support-surface translation. This aggressive control was reflected through large overall displacements of the ZMP with tight regulation of the COM (small displacements). Not surprisingly, setting ρ to 0 (shifting to the COM goal) led to much smaller COM displacements than that observed with $\rho = 1$ (the trunk goal). These smaller displacements were the result of greater hip flexion, which is consistent with our observations across Chapter 3 and 6. Setting $\rho = 1$ produced less hip flexion and greater ankle displacements, i.e., an ankle strategy [154, 361]. This was to be expected given the original design by Kuo [202], the more recent results by Versteeg et al. [344], in addition to our own novel NMPC-simulated results in Chapter 3.3. If we look at how the postural strategy was affected by variations of σ (for $\rho = 0$), we again see results consistent to the Pareto

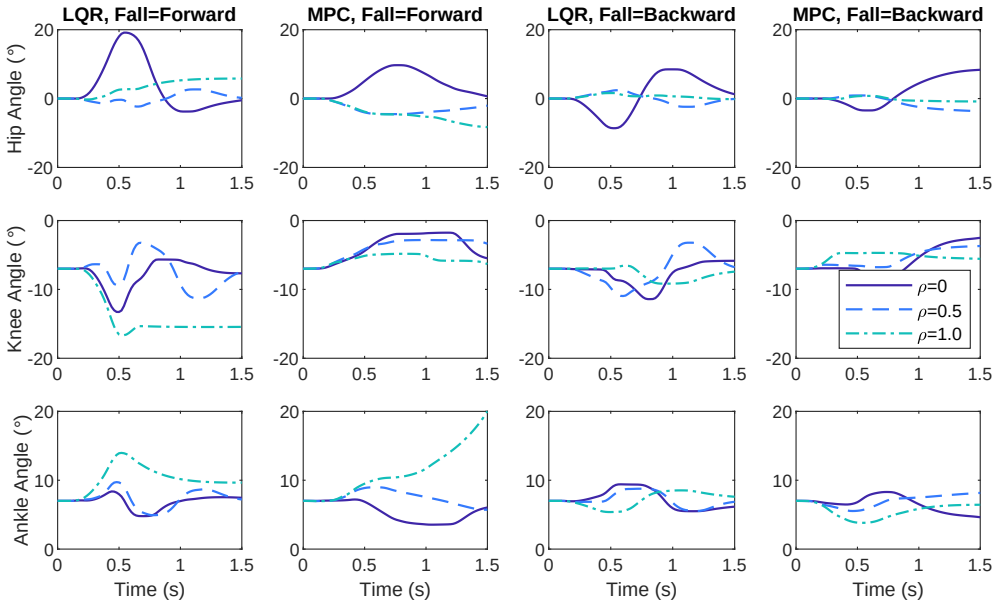


Figure 6.10: Balance recovery (with FIP) joint angle trajectories obtained with a linear quadratic regulator (LQR) and model predictive control architecture (MPC) with variations in the objective homotopy parameter ρ.

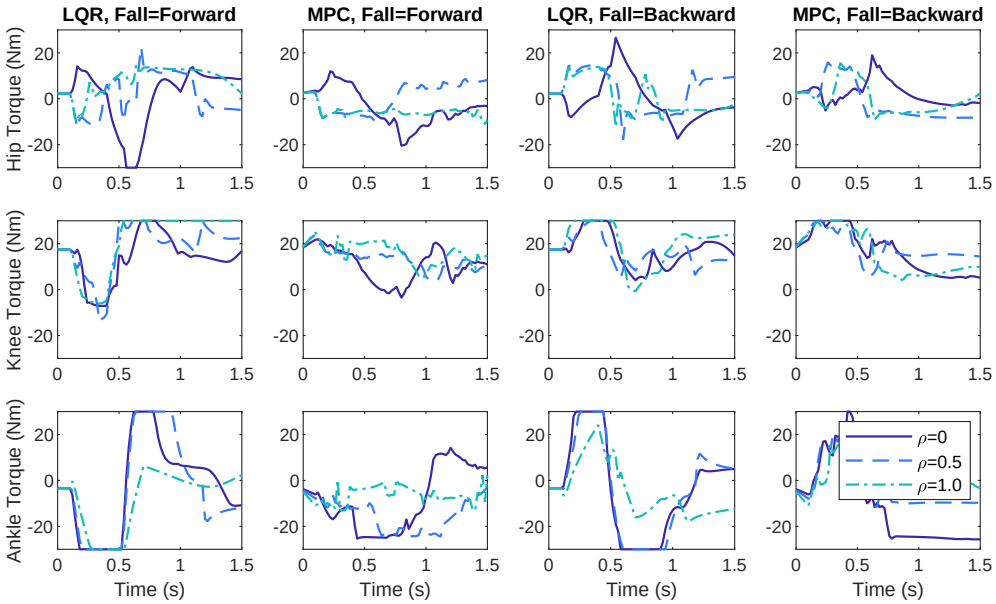


Figure 6.11: Balance recovery (with FIP) motor torque trajectories obtained with a linear quadratic regulator (LQR) and model predictive control architecture (MPC) with variations in the objective homotopy parameter ρ.

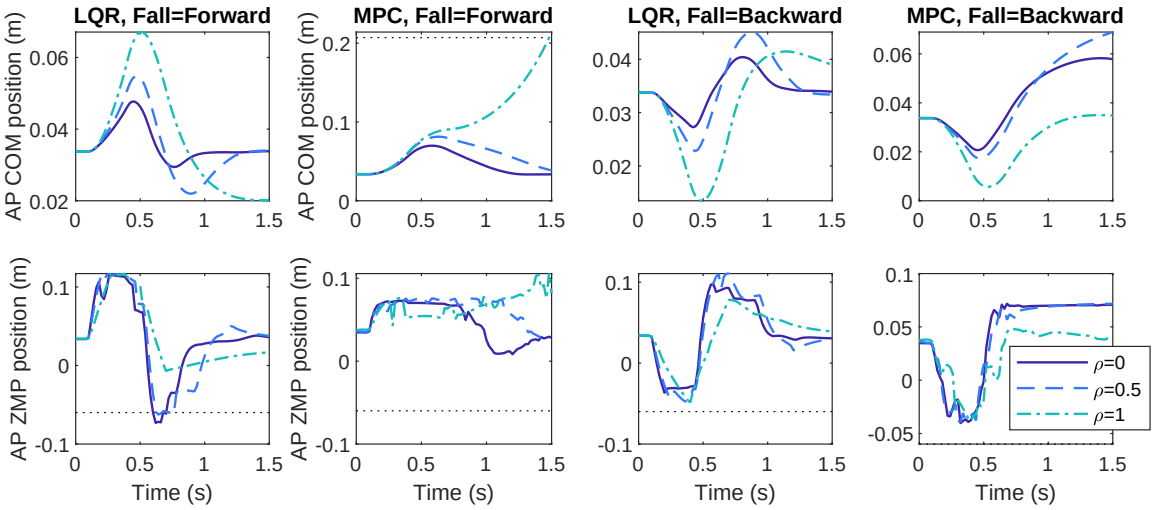


Figure 6.12: Balance recovery (with FIP) anteroposterior (AP) COM/ZMP trajectories obtained with a linear quadratic regulator (LQR) and model predictive control architecture (MPC) with variations in the objective homotopy parameter ρ. Where necessary, the relevant support polygon boundary is highlighted by a dotted line.

optimization in Chapter 3: a shift towards an ankle strategy as the squared sum of actuating torques is concurrently minimized. Looking at Fig. 6.14, we see that reducing σ did in fact tend to lower the resulting motor torques, though we note that this was a more consistent effect observed with the LQR. Both LQR and MPC had the habit of reducing the hip/ankle torque in favour of increasing the knee torques, which could also be related to friction/MTG compensation. Both LQR and MPC also caused torques to saturate during balance recovery, though MPC seemed less inclined to do so. In the MPC, torques were limited to ± 30 Nm; however, that value assumed the actuator was ideal and did not consider the torques required for friction compensation. It is likely the case that stricter box constraints in the MPC would avoid torque saturation altogether, e.g., setting torque boundaries that consider the actuator Coulomb/breakaway torques. Lastly, in comparing the LQR to the MPC across the simulations discussed to this point, we did not see differences in the magnitude of joint angles used, potentially due to the MPC being optimal over a finite-horizon and LQR over an infinite-horizon. However, the general postural strategy was similar for a given value of ρ. We did note that the MPC did show some drift with the purely trunk goal ($\rho = 1$) in comparison to the LQR, which could arise for a number

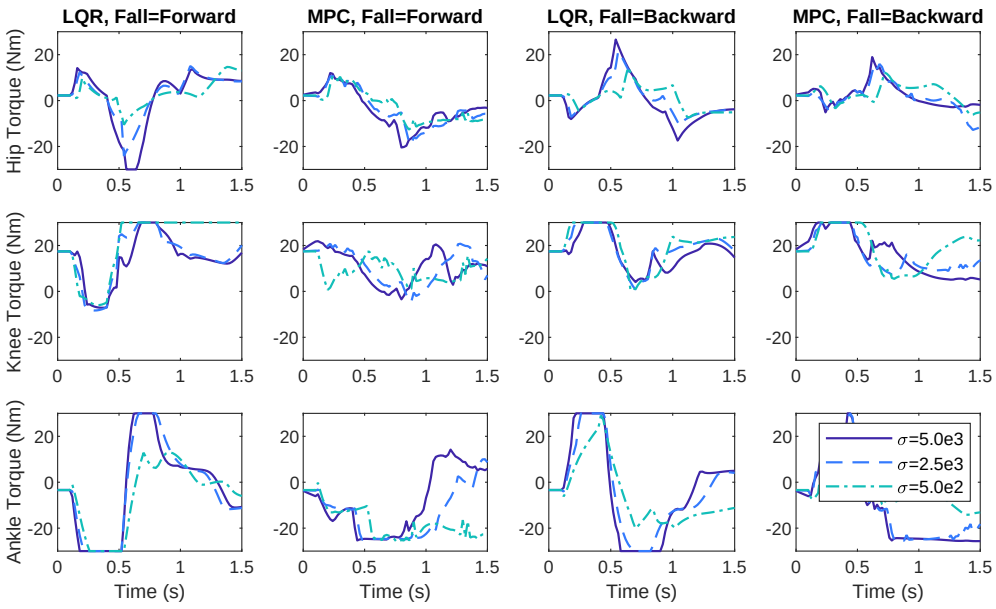


Figure 6.13: Balance recovery (with FIP) joint angle trajectories obtained with a linear quadratic regulator (LQR) and model predictive control architecture (MPC) with variations in the objective weighing parameter σ.

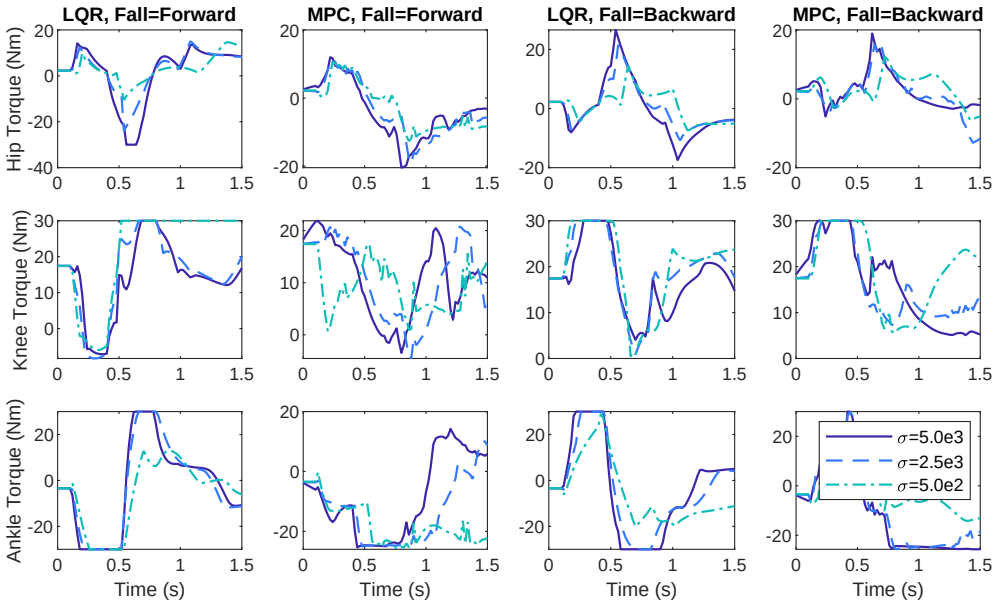


Figure 6.14: Balance recovery (with FIP) motor torque trajectories obtained with a linear quadratic regulator (LQR) and model predictive control architecture (MPC) with variations in the objective weighing parameter σ.

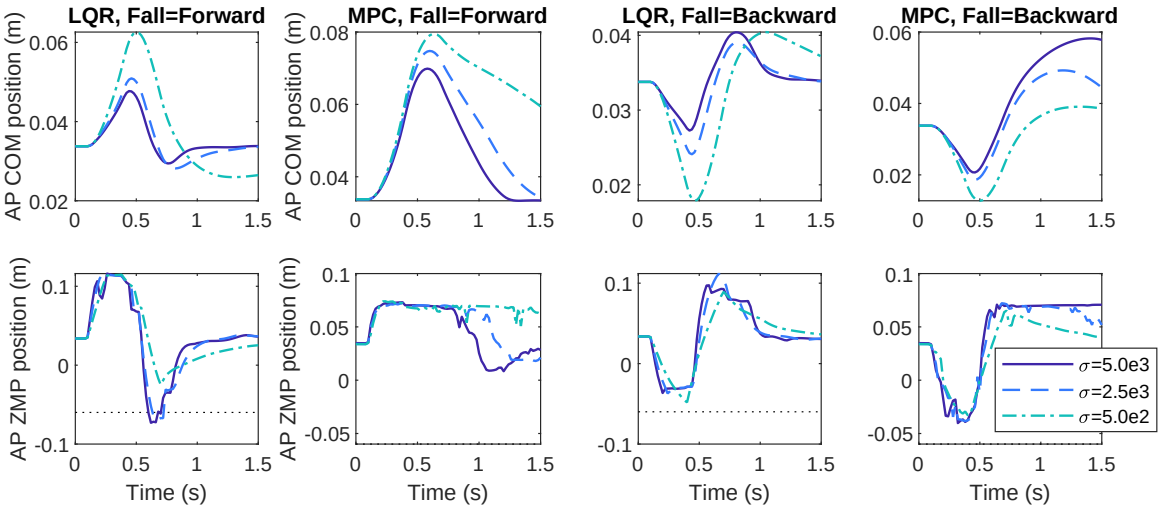


Figure 6.15: Balance recovery (with FIP) anteroposterior (AP) COM/ZMP trajectories obtained with a linear quadratic regulator (LQR) and model predictive control architecture (MPC) with variations in the objective weighing parameter σ. Where necessary, the relevant support polygon boundary is highlighted by a dotted line.

of reasons, e.g., poor scaling with σ, interactions with the terminal constraints causing issues, and limitations of the forward Euler discretization. However, as stated earlier, the real benefit of MPC over LQR is incorporating constraints into the optimal control law, addressing a key limitation of typical full-state feedback discussed by Bayon et al. [48].

Second, we investigated the effects of two constraints within the MPC framework: i) the ZMP-BOS inequality constraint (ZMP remains within support polygon [346]), and ii) the terminal inequality constraint. In each case, we performed a simulation of FIP balance recovery with full-state feedback MPC that was programmed with and without said constraint. Objective parameters were set as $\rho = 0$ and $\sigma = 2.5 \times 10^3$. Respectively, Fig. 6.16 and Fig. 6.17 show the simulated balancing joint angles and COM/ZMP trajectories that follow a posterior/anterior support-surface translation with (constrained) and without (unconstrained) the ZMP-BOS constraint. Regardless of constraint, joint trajectories were similar with a small degree of separation. Importantly, in Fig. 6.17, we see that without the constraint, the ZMP actually exits the BOS during correction for a backward fall. Interestingly, for a forward fall, the ZMP remained in the anterior portion of the foot even with the unconstrained MPC, avoiding the over-correction made by the LQR that placed

the ZMP at the posterior BOS boundary in Fig. 6.15. Shifting priority to the effects of the terminal constraints on the MPC performance, Fig. 6.18 and Fig. 6.19 show the simulated constrained/unconstrained joint angles and COM/ZMP trajectories that follow a posterior/anterior support-surface translation. Interestingly, we see that the terminal constraints actually limit the magnitude of joint deviations from the initial configuration. This result is likely due to the constraint forcing the MPC to not place the model in states that it does not think it can bring back within the terminal boundaries. For the forward fall condition, this constraint also produces a more damped COM response despite maintaining the ZMP at a forward position for longer. More research is necessary to determine the spectrum of effects that tuning the terminal constraint boundaries may have on FIP MPC performance.

Last, we briefly investigated the effect of horizon length on the resulting MPC balance control trajectories and run-time. With $\rho = 0$ and $\sigma = 2.5 \times 10^3$, MPC control of FIP balance was simulated for anterior (backward fall) and posterior (forward fall) support-surface translations, for each of the following prediction horizon durations: 300 ms, 500 ms, 700 ms. Note that in the current dissertation, we assume that the MPC prediction and control horizons are of equivalent lengths [219]. The joint angles produced for each horizon length are displayed in Fig. 6.20 generated for different values of the horizon length. In line with our observations made with use of negation of the terminal constraints, the longer prediction horizons permit postural strategies with larger joint deviations, e.g., a hip strategy to correct a forward fall with notable hip flexion and ankle plantarflexion. This observation is also in line with the postural strategies observed when using the LQR that provides an optimal feedback control gain over an infinite-horizon. With a longer prediction horizon, the MPC has a larger span of states that it can reasonably return back to the terminal constraint space (more time to reduce momenta); thus, the controller can be more aggressive in overall state/COM regulation like the LQR was, i.e., generating higher angular momentum about the COM [103, 130]. With that said, the use of larger prediction horizons also increases the computational expense of MPC. Here, the 300 ms and 500 ms horizons required an average run-time of $1.18 \times 10^{-2} \pm 7.56 \times 10^{-4}$ s and $1.82 \times 10^{-2} \pm 7.74 \times 10^{-4}$ s for each call to the MPC. However, increasing the prediction horizon to 700 ms increased the run-time to $2.54 \times 10^{-2} \pm 1.15 \times 10^{-3}$ s, which in this simulation interface, is greater than the set sampling interval. This would suggest that without further modifications, e.g., reducing the number of iterations within QP solver, a 700 ms prediction horizon is not feasible for real-time.

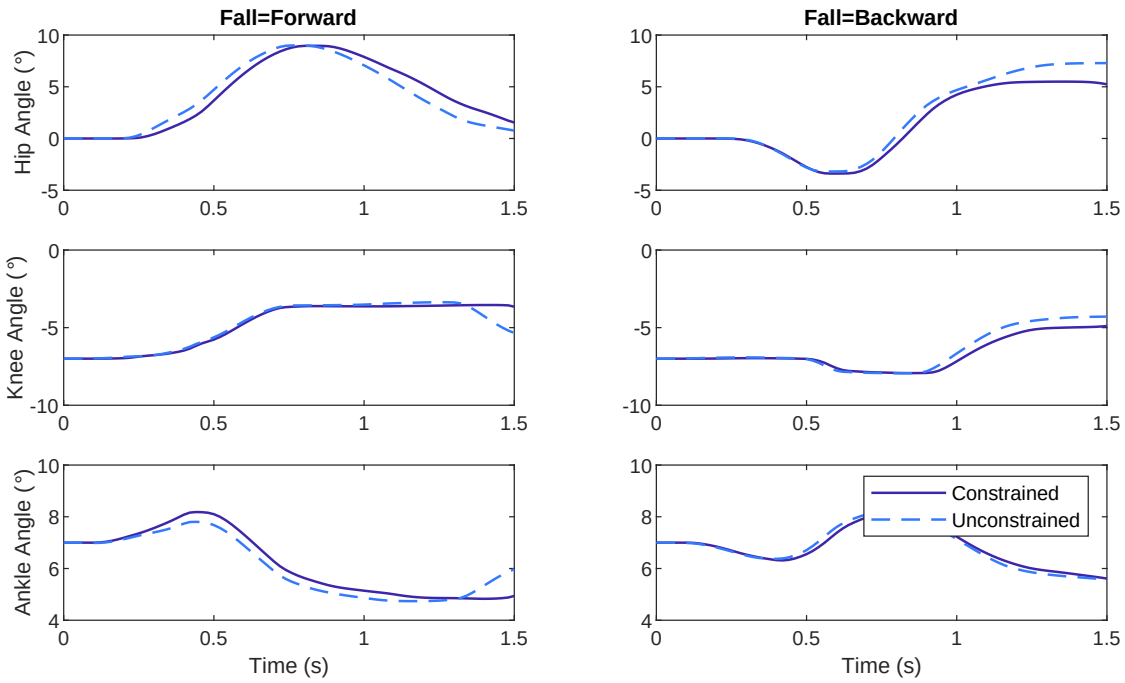


Figure 6.16: Balance recovery (with FIP) joint angle trajectories obtained via model predictive control (MPC) with (constrained) and without (unconstrained) inclusion of the ZMP-BOS constraint in Equation (6.73).

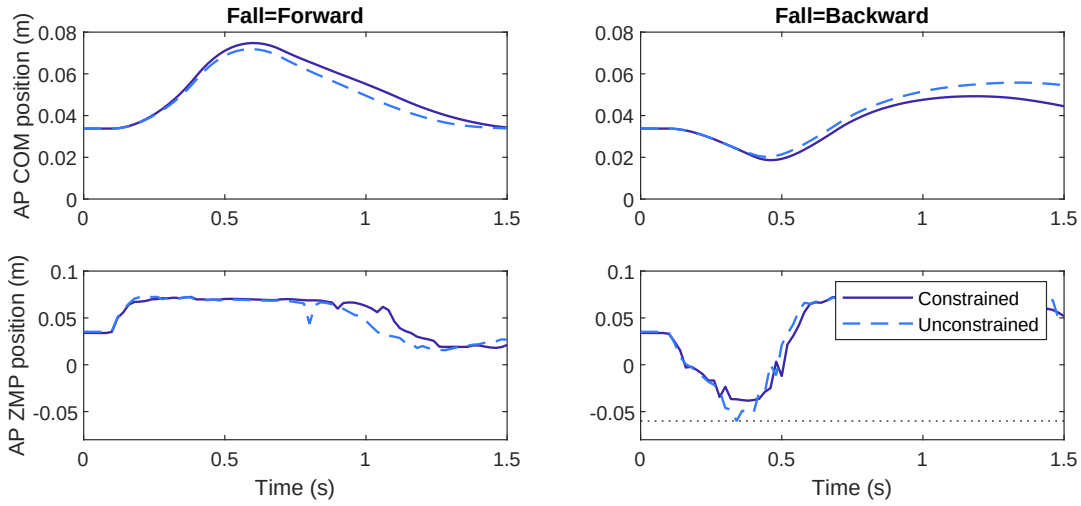


Figure 6.17: Balance recovery (with FIP) anteroposterior (AP) COM/ZMP trajectories obtained via model predictive control (MPC) with (constrained) and without (unconstrained) inclusion of the ZMP-BOS constraint in Equation (6.73).

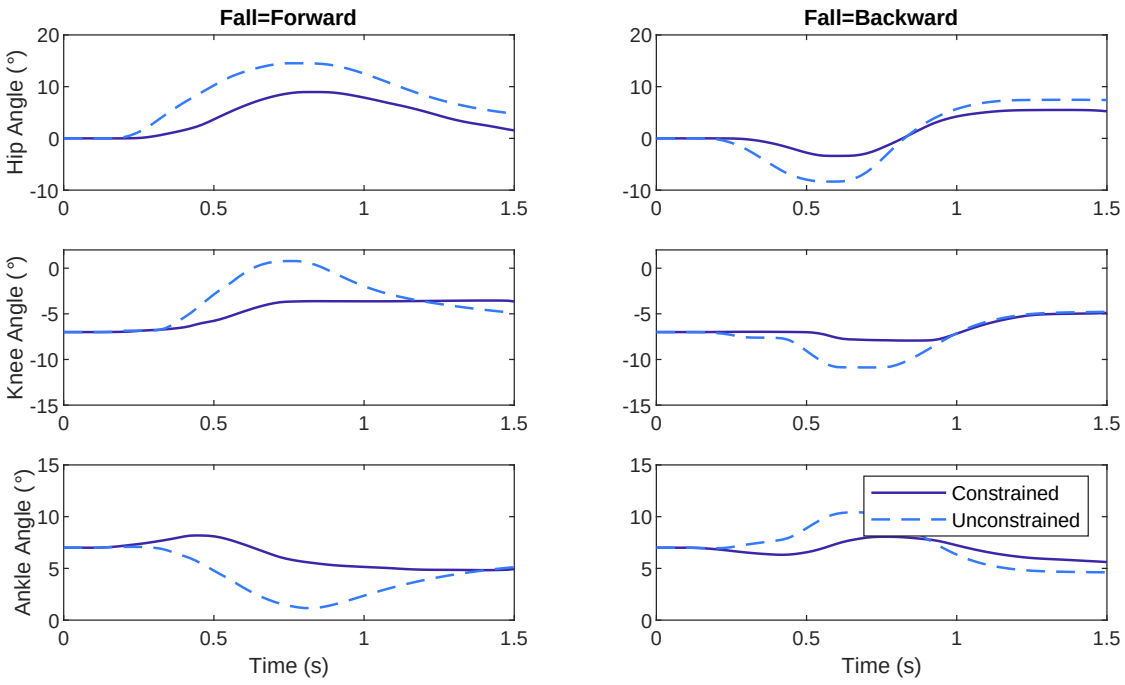


Figure 6.18: Balance recovery (with FIP) joint angle trajectories obtained via model predictive control (MPC) with (constrained) and without (unconstrained) inclusion of the terminal constraints in Equation (6.78). Support polygon boundaries exceeded the limits chose for the vertical axis.

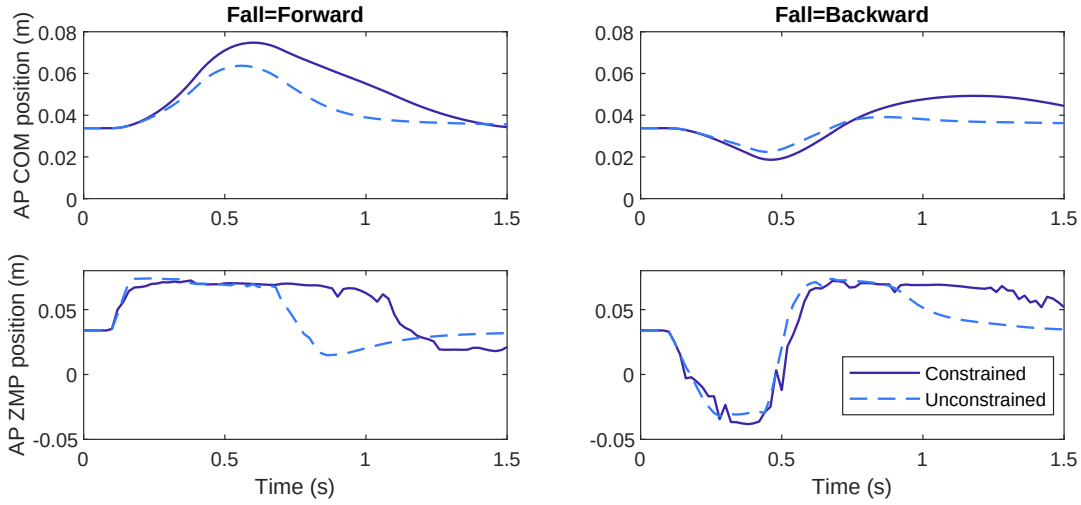


Figure 6.19: Balance recovery (with FIP) anteroposterior (AP) COM/ZMP trajectories obtained via model predictive control (MPC) with (constrained) and without (unconstrained) inclusion of the terminal constraints in Equation (6.78).

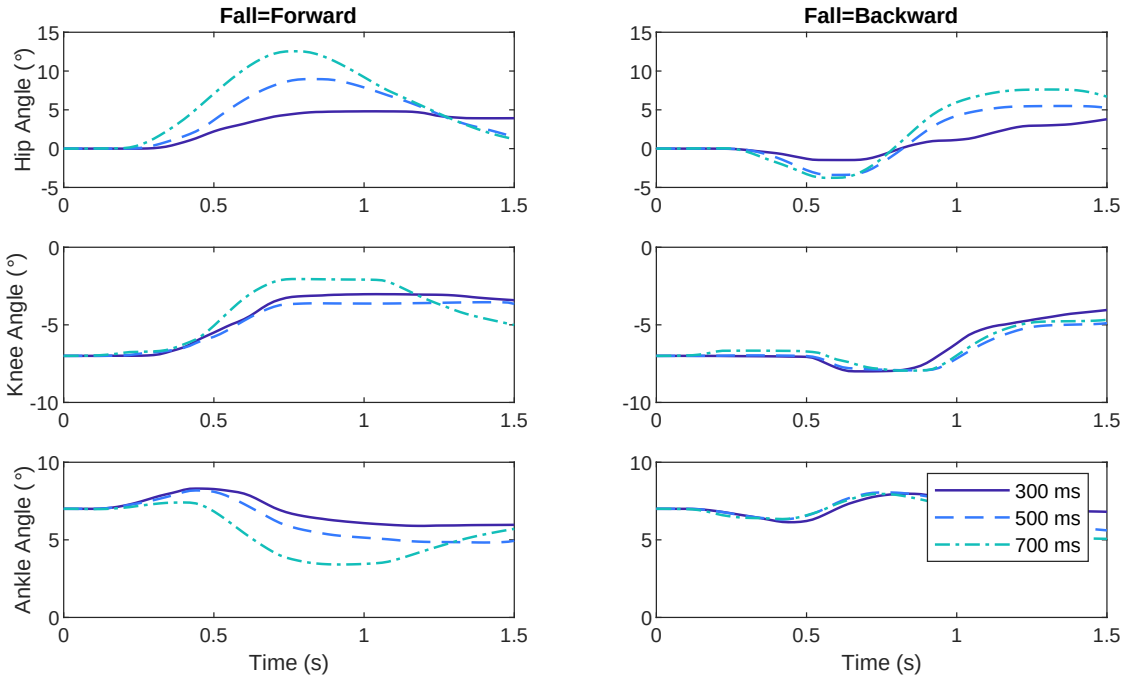


Figure 6.20: Balance recovery (with FIP) joint angle trajectories obtained via model predictive control (MPC) with variations in the prediction horizon length, i.e., 300 ms, 500 ms, or 700 ms.

6.3.2 Autonomous State Estimation during Balance Recovery

The second set of simulations was used to assess the performance of the EKF and MHE-based state and disturbance/intent estimators during MPC-automated FIP balance recovery. The control scheme used is displayed in Fig. 6.21. All simulations were controlled via MPC. As we have already highlighted the MPC controller performance under perfect full-state feedback, we elected to investigate three test cases for each of the EKF and MHE algorithms: no friction in plant/EKF (TEST 1); model-mismatch with no friction in EKF, but friction in plant (TEST 2); friction in both EKF and plant (TEST 3). For all simulations, MHE/EKF process and measurement noise covariance matrices were set as follows:

$$\mathbf{Q}_{\text{os}} = \begin{bmatrix} 10^{3}\mathbf{I}_{3\times 3} & \mathbf{0} \\ \mathbf{0} & 10^{4}\mathbf{I}_{3\times 3} \end{bmatrix}, \quad \text{and} \quad \mathbf{R}_{\text{os}} = \begin{bmatrix} 10^{-10}\mathbf{I}_{3\times 3} & \mathbf{0} & \mathbf{0} \\ \mathbf{0} & 10^{-6}\mathbf{I}_{3\times 3} & \mathbf{0} \\ \mathbf{0} & \mathbf{0} & 10\mathbf{I}_{3\times 3} \end{bmatrix} \tag{6.111}$$

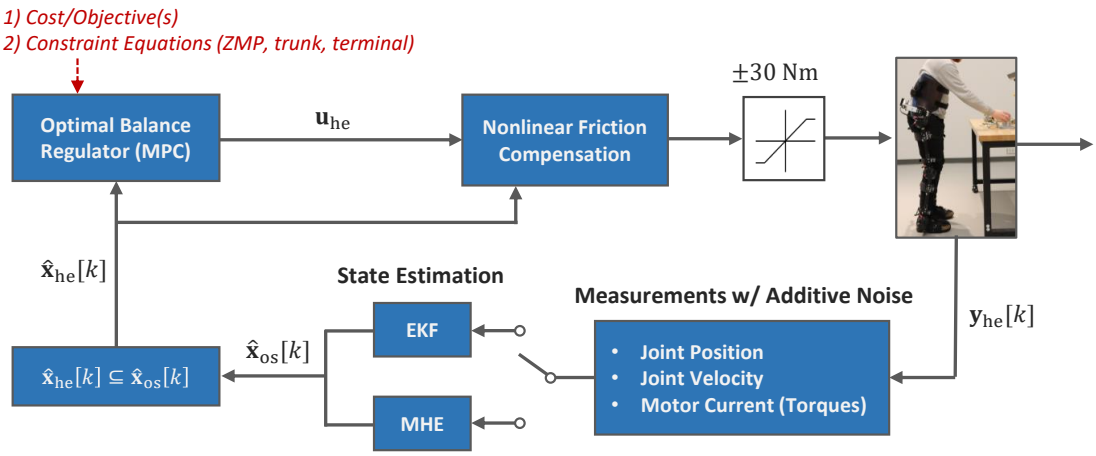


Figure 6.21: Control schematic for simulation set 3: optimal regulation of FIP balance recovery via model predictive control (MPC) with concurrent nonlinear state estimation via the extended Kalman filter (EKF) or moving horizon estimation (MHE).

Measurement covariance for the position and motor torque sensors was set according to the values reported for the sensors in [318]. The velocity measurements were corrupted by additive noise with covariance that was orders of magnitude larger than the position sensor covariance. The process noise covariance was tuned manually in order to obtain the results presented below, though we note more rigorous methods of identifying this parameter in the literature [249, 289].

In each simulation assisted via EKF and MHE, the simulated exo-assisted end-user never fell, i.e., the ZMP never exited the support polygon (Fig. 6.22). Both the EKF and MHE performed sufficiently for real-time implementation: EKF $= 4.33 \times 10^{-4} \pm 3.60 \times 10^{-4}$ s; MHE $= 1.50 \times 10^{-2} \pm 5.65 \times 10^{-3}$ s. We note here, that the combined length of the MHE and MPC as is would slightly exceed the sampling interval set; thus, a true real-time MPC-MHE implementation would require modifications of features like horizon length beforehand to avoid adding substantial/unmodeled delays into the process. Regardless, runtimes of individual components were well-feasible within the simulation interface. The MPC-EKF and plant without friction (TEST 1) struggled with state estimation, which produced poor control performance; note the rapid changes in ZMP position in Fig. 6.22 when using MPC-EKF. The MPC-MHE reliably reproduced a hip strategy in each test case (see Fig. (6.23)); it performed similar to the MPC with perfect full-state feedback

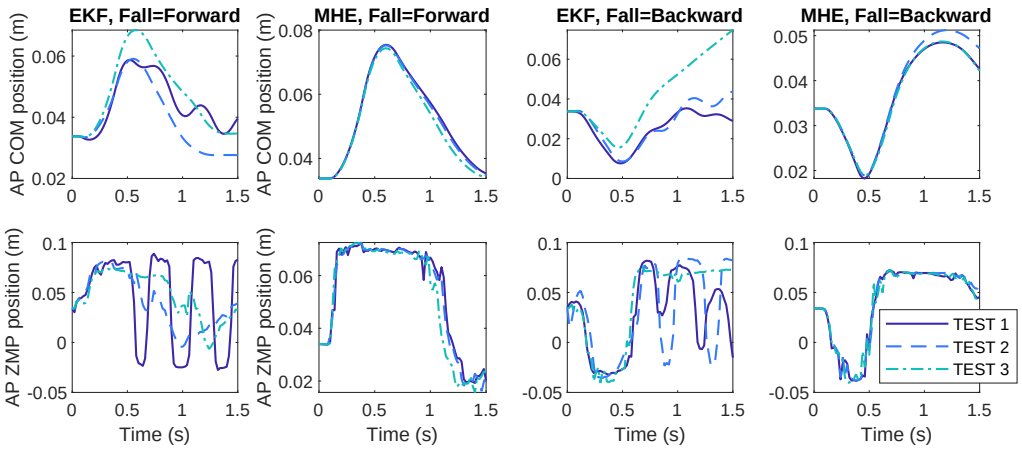


Figure 6.22: Balance recovery (with FIP) anteroposterior (AP) COM/ZMP trajectories obtained via MPC control paired with either an extended Kalman filter (EKF) or a moving horizon estimator (MHE) for each of the test cases introduced in the current section. Simulation tests were as follows: no friction in plant/EKF (TEST 1); model-mismatch with no friction in EKF, but friction in plant (TEST 2); friction in both EKF and plant (TEST 3).

(Fig. (6.10)). The MPC-EKF could provide a similar performance when nonlinear joint friction was not only included, but modelled within the EKF itself. The true motor torques required to generate the MPC-EKF and MPC-MHE postural responses are shown in Fig. 6.24.

The joint angle estimations made by both EKF and MHE within TEST 3 are shown in 6.25). Estimated versus true motor torques and human MTG torques (intent/disturbance torques) are shown in Fig. 6.26 and Fig. 6.27. Joint angle estimates were reasonable for both the EKF and MHE algorithms; however, the MHE algorithm performed better across all test cases (MHE RMSE = 0.05°; EKF RMSE = 0.22°). Note that the RMSE within each condition is averaged across the three joints and two perturbation directions. The RMSE was functionally negligible for the MHE joint angle estimations, whereas the EKF had some more exaggerated separations from the true values, especially for the backward fall case. EKF also introduced oscillations into the final simulated motions, especially when the dynamics were not damped, e.g., TEST 1. It was unable to identify the applied motor torques from the noisy measurements (RMSE = 15.21 Nm); rather, the EKF attributed changes in human-exoskeleton state to variations in the human MTG torque state (Fig. 6.27). The disturbance torques produced by the support-surface translations are also

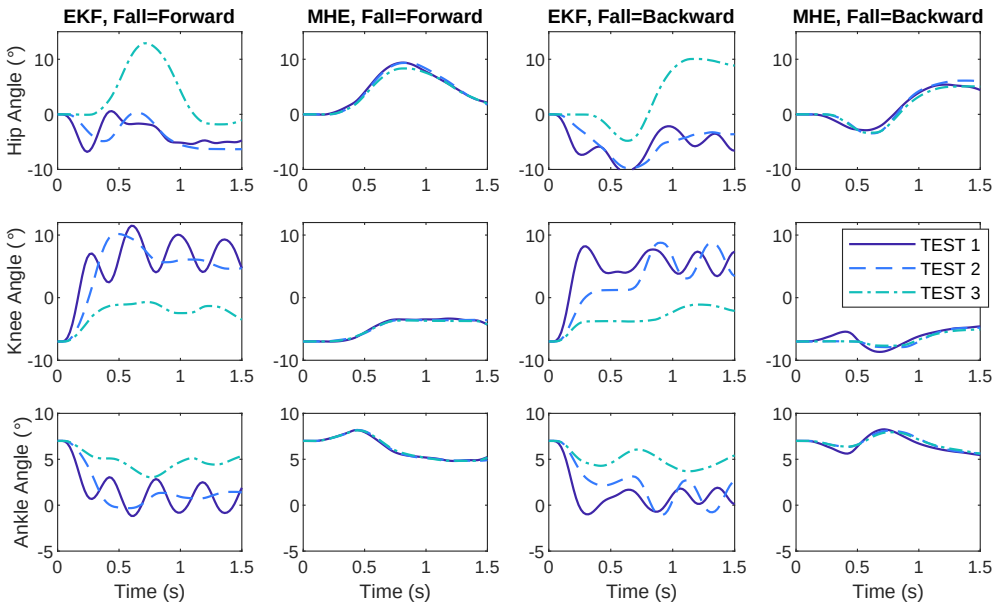


Figure 6.23: Balance recovery (with FIP) joint angle trajectories obtained via MPC control paired with either an extended Kalman filter (EKF) or a moving horizon estimator (MHE) for each of the test cases introduced in the current section.

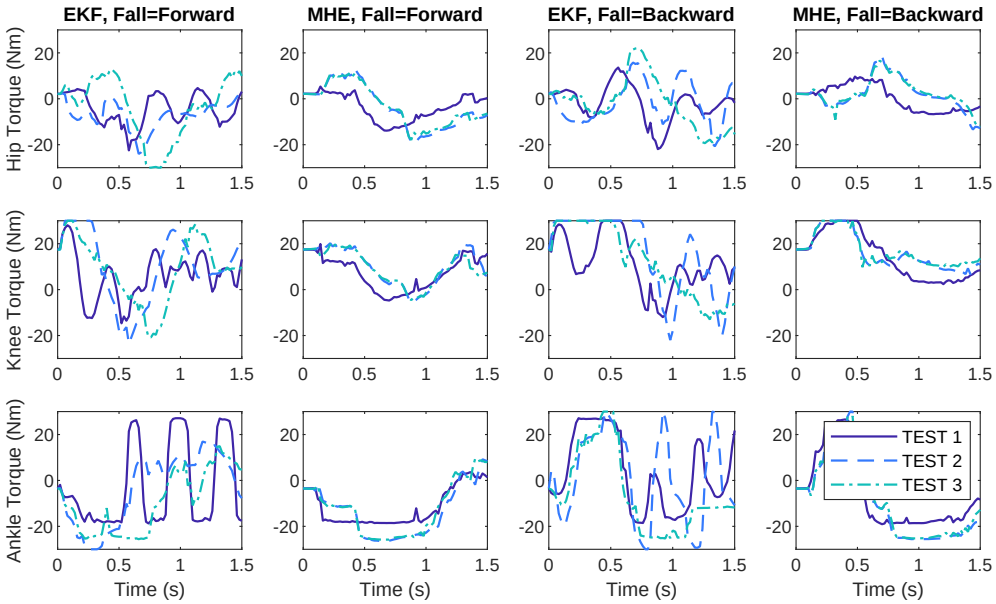


Figure 6.24: Balance recovery (with FIP) motor torque trajectories obtained via MPC control paired with either an extended Kalman filter (EKF) or a moving horizon estimator (MHE) for each of the test cases introduced in the current section.

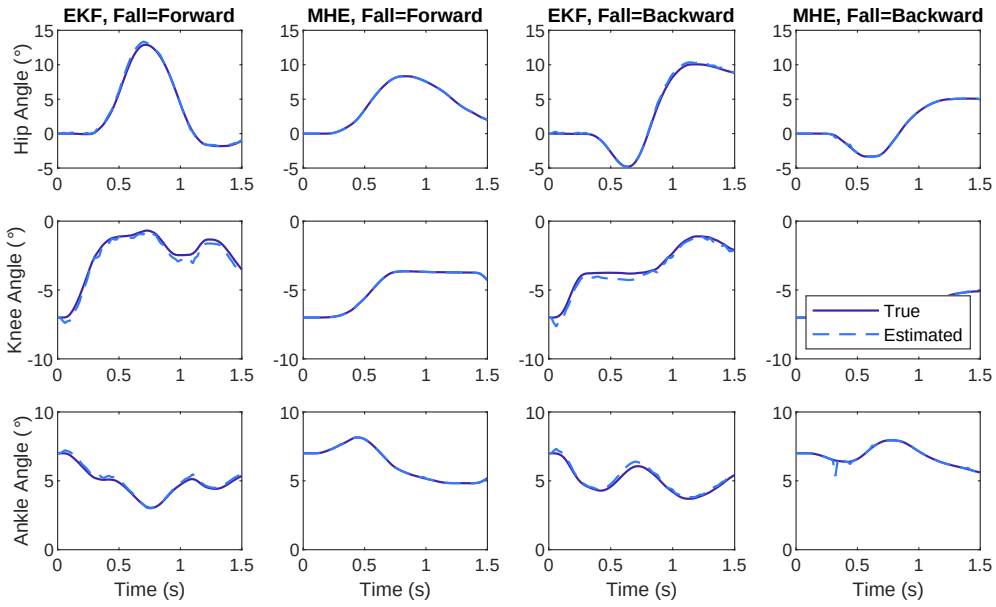


Figure 6.25: True and estimated balance recovery (with FIP) joint angle trajectories obtained via MPC control paired with either an extended Kalman filter (EKF) or a moving horizon estimator (MHE) for TEST 3.

mapped onto the human torques. This is also observed in the case of MHE observation (Fig. 6.27). However, the MHE was far superior in estimating the applied motor torques (RMSE = 3.82 Nm; Fig. 6.26).

As a small detour, we take this opportunity to highlight how signal quantization can impact performance of controls and state estimation. Often signal quantization is used to reduce the memory required to store said signal's value during transmission. On the EXO-H3 (with latest firmware updates), joint angle, angular velocity, and motor torque measurements are rounded to the nearest 0.1 deg, 0.1 deg/s, 0.1 Nm. The MPC-MHE driven simulations of balance recovery were therefore performed again, but measurements were now quantized following addition of Gaussian noise. The true and estimated joint angles are shown in Fig. 6.28; motor and human MTG torques are shown Fig. 6.29. There was a notable decrease in the quality of joint angle estimation with some large unrealistic jumps between states (RMSE = 0.95°). Motor torque estimates from the MHE also decreased in quality with measurement quantization (RMSE = 7.56 Nm), though considerably less so than the human/disturbance torque estimations, which became purely noise. There is no longer a characteristic square-waveform from the support-surface translation

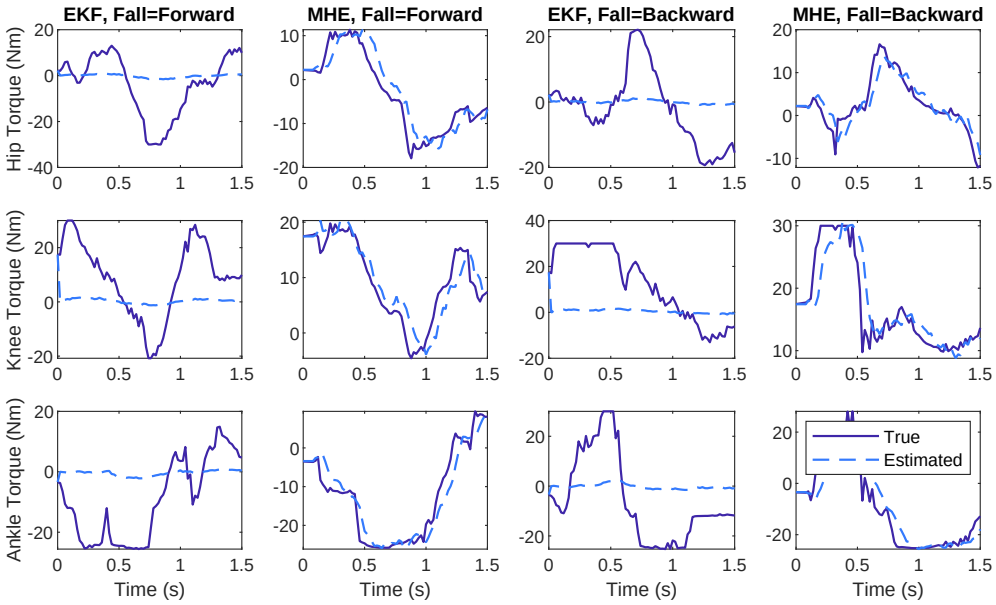


Figure 6.26: True and estimated balance recovery (with FIP) motor torque trajectories obtained via MPC control paired with either an extended Kalman filter (EKF) or a moving horizon estimator (MHE) for TEST 3.

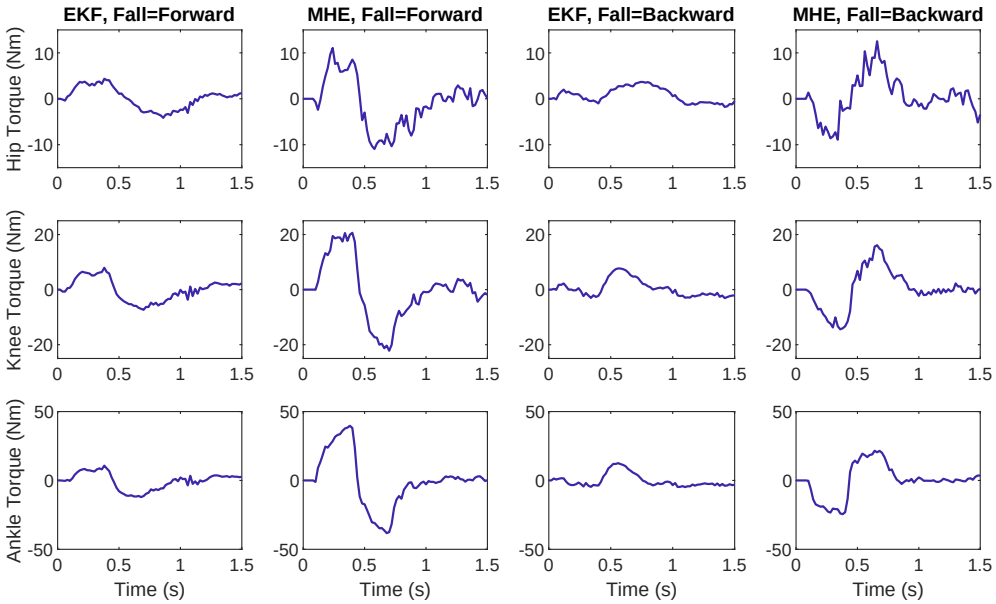


Figure 6.27: Balance recovery (with FIP) human MTG torque trajectories obtained via MPC control paired with either an extended Kalman filter (EKF) or a moving horizon estimator (MHE) for TEST 3.

appearing in the signal. Therefore, MPC-MHE state estimation and control of FIP balance is theoretically possible when measurement quantization is present; however, there are clear negative effects. It could be that further tuning of the process noise covariance could remedy these declines in performance; however, that is a point of future research.

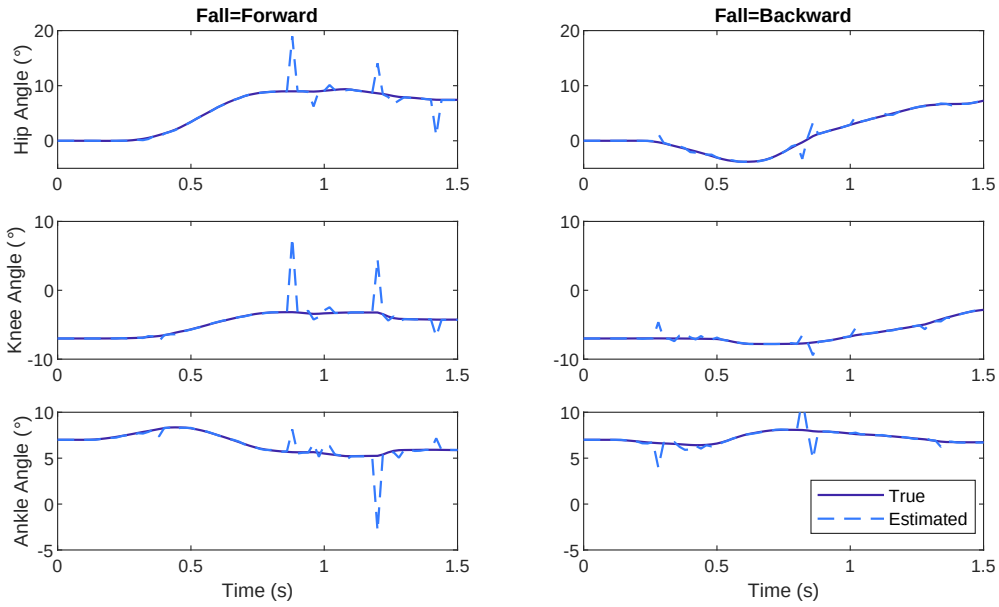


Figure 6.28: True and estimated balance recovery (with FIP) joint angle trajectories obtained via MPC control paired with either an extended Kalman filter (EKF) or a moving horizon estimator (MHE) for TEST 3. Signals were quantized for the current simulations (rounded to nearest 0.1 deg or Nm)

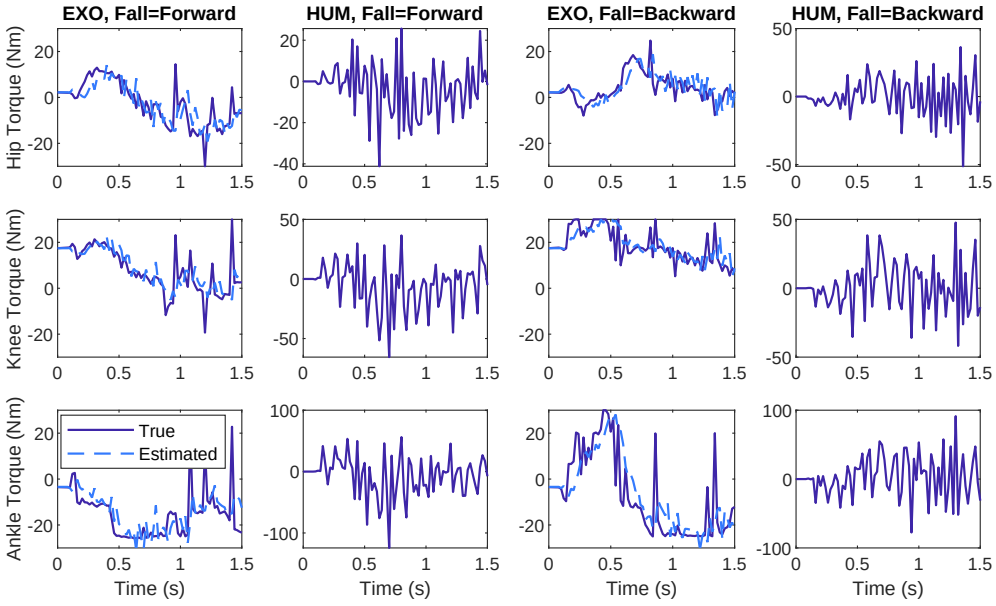


Figure 6.29: Balance recovery (with FIP) motor (EXO) and human MTG (HUM) torque trajectories obtained via MPC control paired with a moving horizon estimator (MHE) for TEST 3. Signals were quantized for the current simulations (rounded to nearest 0.1 deg or Nm)

Chapter 7

Experimental Testing of Model-Based Feet-in-Place Balance Control

7.1 Background

One flaw that many in research and clinical fields have noted regarding existing lower-limb exoskeletons is that the manufacturer-provided hardware/software does not assist the user in maintaining their balance during standing operation. Anecdotally, users often complain of feeling or being unstable while donning the device; many manufacturers require that users use an additional device for balance, e.g., crutches. In response to this feedback, there has been a push in recent years to develop and implement assistive balance controllers for these systems, as well to study the base balancing capabilities of different users while the exoskeleton operates "passively".

As detailed prior, there is evidence of higher cognitive processes and spinal/supraspinal reflex loops in the CNS being involved in executing and scaling appropriate balance recovery strategies in an optimal fashion, e.g. minimizing deviations of the whole-body center of mass from some regulated point using a hip strategy [202, 213, 223, 344]. These observations are consistent with our own observations from the simulations in Chapter 3. Despite this, optimal control methods have not yet been widely adopted for exoskeleton applications, typically due to the technical requirements necessary for implementation, e.g., designing a dynamic model, system reduction, and real-time iterative algorithm use. Previous simulation-based assessments of human and human-exoskeleton multibody dynamics

with optimal control suggest that control parameters can be tuned easily to promote particular postural strategies when applying fully to near-autonomous balance recovery to a human-exoskeleton [134, 169, 172, 202]. However, these simulations require experimental validation, especially if we are interested in factors difficult to replicate in simulation, e.g., how the end-user might adapt to certain assistive control laws [72, 256, 287]. It is well known that exoskeleton users, as they build an internal representation of the device's behaviour and can better predict its actions, will begin to "slack" in the device allowing it do as much of the work as possible [70]. Permitting this can be detrimental in rehabilitation applications where the user must be encouraged to supply as much of the power necessary as possible to improve self-mobility. In a similar vein, for users who are able to maintain their own quiet standing balance entirely, we do not wish to compete with their existing capabilities to accomplish the standing task. In fact, having an aggressive closed feedback loop running in parallel with the feedback loop within the CNS can lead to disastrous results like a fall [339].

As discussed prior in the literature review (see Chapter 2), most authors that have designed controllers to regulate FIP standing balance have not used controls based on dynamic multibody models of the device and user, instead relying on kinematic models[103, 284]. These control schemes also do not look into optimality of the control law, rather focusing on simple joint-level PD laws. The dynamic model-based controls present in the momentum-based control feature of [103] can provide control torques for a multibody system, but is limited in whether those torques optimize some objective criteria. Controllers that have used dynamic models have also focused more on stabilizing locomotion indefinitely for paraplegics [134]. To our knowledge, no authors have presented a real-time MPC-based scheme (see Chapter 6.2.4) to address the problem of assistive or autonomous balance recovery.

The primary objective of the current study was to validate whether optimal model-based control of lower-limb exoskeletons was viable in real-time for assisted FIP balance control. In the process of doing so, we wished to know whether the control law is able to provide a young adult user (without visible disabilities) with a comfortable and safe method of assistance that reasonably follows the intentions of their CNS – this would inform us of the controller's possible efficacy with disabled populations. Likewise, we wished to understand how in practice, the presence of an exoskeleton with active MPC-based controls alters the kinematic characteristics of the end-user's balance recovery. Therefore, we quantitatively assessed the performance of the constrained MPC method of exoskeleton-assisted FIP

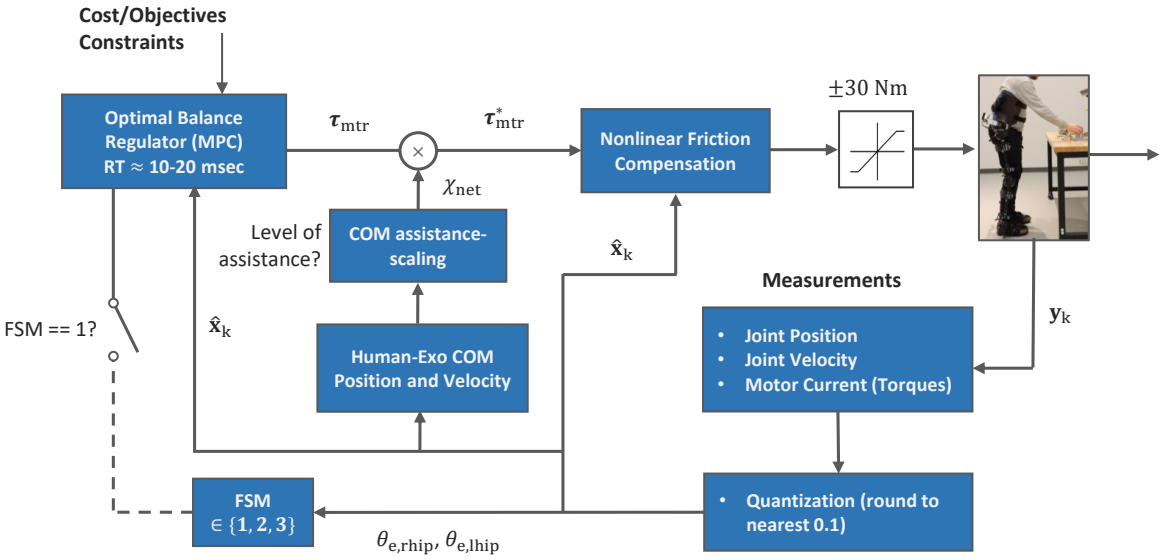


Figure 7.1: Model predictive control (MPC) and center of mass (COM) position/velocity-based assistance control architecture used in experiments. Note that the finite-state machine (FSM) used the hip angles to determine whether or not the user was in upright stance with the feet approximately symmetrical (FSM == 1).

balance recovery in experiments. The exoskeleton modelled and tested was the EXO-H3 lower limb exoskeleton (Technaid, Spain), which has DC electric motors at the right and left hip, knee, and ankle that actuate the system in the sagittal plane. Quantitative assessments were rooted in the analysis of 3D kinematic and kinetic experimental data. A robust means of maintaining balance in exoskeletons would provide the end-user with freedom to use their arms instead of requiring crutches; however, it must first be assessed in a controlled population before tested with clinical populations.

7.2 Control Architecture

The following section will outline how the autonomous MPC control architecture in 6.2.4 was augmented for the current study, i.e., scaling the amount of assistance provided according to COM kinematics in relation to the FSR. The modified control architecture is outlined in the schematic in Fig. 7.1. Note that all control algorithms involved software that were designed and implemented using a custom MATLAB interface and the CAN bus protocol designed by the exoskeleton manufacturer, Technaid.

7.2.1 Model Predictive Control

Many exoskeleton control schemes in the literature tend to be broken down into tiers, e.g., a high/medium-level tier that decides which movement patterns the robot should be trying to follow and a low-level tier that is responsible for obtaining the desired output from the onboard actuators [334]. The algorithmic component of our study is related to the high/medium-level tier of this hierarchical control, which then feeds desired actuator torques, joint positions, and/or joint velocities to the low-level controllers designed by the device manufacturer. By manufacturer design, the mode of low-level control for each actuator can be different, e.g., position control, stiffness control, and motor torque control.

The intended design of the proposed exoskeleton assistive MPC scheme is to estimate and provide the net lower-limb joint torques necessary to maintain upright balance and a fixed-base of support following a perturbation (see Chapter 6.2.4). Briefly, the model-predictive scheme consisted of using a dynamic model, outlined in Chapter 6 [169, 172], to estimate the optimal bilateral ankle, knee, and hip joint torques when recovering balance following a perturbation, i.e., those that minimize a human-like cost function. The joint torques controlled in the MPC model reflect the combined efforts of the human muscles (active and passive) and device motor torques; actuator friction is compensated for outside of the MPC. This feedback control scheme is motivated by early experimentally-validated predictive simulations of human fixed-support balance using LQR [26, 202, 203, 342] and an expansion of earlier PD control algorithms proposed for ankle and knee-ankle exoskeletons only [103, 105].

The control protocol is described in the schematic in Fig. 7.1. The MPC controller requires full-state feedback, which was met through the use of the EXO-H3's onboard

measurement system: the angle and velocity of each actuator output shaft were measured by encoders every 20 ms and quantized to the nearest 0.1 degree or degree/s. In the initial system design, a digital infinite impulse response (IIR) filter was used to smooth the measurement signals; however, the combination of filtered signal quantization and induced phase delay reduced the performance of friction compensation during runtime, i.e., it was harder to make the exoskeleton "passive". Therefore, in this early design iteration, the raw position and velocity encoding were used to facilitate full-state feedback. Note that

Table 7.1: Parameters used for real-time MPC. Parameter arrays like in the case of $\mathbf{u}_{\min}$ are written in the order hip, knee, and ankle.

Parameter	Description	Value	Units
N	Nodes	25	$\sim$
Δt	Sampling interval	0.20	s
σ	State objective weight	1	$\sim$
ρ	COM/Trunk homotopy	0.5	$\sim$
w_{hip}, w_{knee}, w_{ankle}	Control weights	0.1	$\sim$
Inequality Boundaries			
$\mathbf{u}_{\min}$	Max. ideal torque	[-352, -200, -256]	Nm
$\mathbf{u}_{\max}$	Min. ideal torque	[314, 560, 88]	Nm
$\Delta\mathbf{u}_{\min}$	Min. Torque Increment	[-2,-2,-2]	Nm
$\Delta\mathbf{u}_{\max}$	Max. Torque Increment	[2,2,2]	Nm
$\boldsymbol{\theta}_{\min}$	Min. Joint Angles	[-30, -100, -15]	degrees
$\boldsymbol{\theta}_{\max}$	Max. Joint Angles	[105, 2, 15]	degrees
$\boldsymbol{\omega}_{\min}$	Min. Joint Vel.	-150	degrees/s
$\boldsymbol{\omega}_{\max}$	Max. Joint Vel.	150	degrees/s
$\nu_{\min}$	Min. ZMP	-0.05	m
$\nu_{\max}$	Max. ZMP	0.21	m
$\text{XCOM}_{\min}$	Min. terminal XCOM	-0.03	m
$\text{XCOM}_{\max}$	Max. terminal XCOM	0.10	m
$\text{COMv}_{\min}$	Min. terminal COM vel	-0.05	m/s
$\text{COMv}_{\max}$	Max. terminal COM vel	0.05	m/s

this limitation could be improved in the future by adding the state estimation techniques discussed in Chapter 6.2.5, which can filter measurements without inducing a phase delay.

Prior to calling the MPC control element to determine what balance-control oriented torques were necessary, we had to ensure that the user was in the correct finite-state, i.e., they were in fixed-support stance with near bilateral symmetry in the sagittal plane. First, at a given sampling instant, the right-leg and left-leg joint angles were compared; if they were within 10 degrees of each other, we concluded that it was unlikely that they participant was or had taken a step and was in the fixed-support finite-state. Once that is decided, the system then generates the approximate control-oriented model state through averaging of each of the right-left joint angles and angular velocities. This state is used as the initial condition within the MPC QP problem and updated at each sampling interval.

The underlying QP problem solved in the MPC is the same one discussed in Chapter 6. Terms in the QP problem were converted into sparse matrices and column-matrices to take advantage of MATLAB's sparse linear algebra library in solving the Karush–Kuhn–Tucker (KKT) conditions [219], i.e., reduce computational expense of iterations. The QP problem itself was solved using `quadprog` in MATLAB, which used an interior-point convex solver to obtain a solution subject to equality and inequality constraints. The parameters used to define the problem are listed in Table 7.1. As mentioned prior, we assume that actuator friction is compensated for outside of the MPC model (see Chapter 7.2.3) and that the ideal joint torques solved in the MPC are the combined efforts of the human MTG (active and passive) and motor torques.

7.2.2 Novel COM-Dependent Assistance

As the participants recruited already had the ability to stand quietly and respond to perturbations, and given the challenge that exists in systems with competing feedback loops [338], we proposed and tested a COM-based assistance scaling component in this first experimental iteration of the MPC controller:

$$\tau^*_{\text{mtr}} = \chi_{\text{net}}(x_{\text{icm}}, v_{\text{icm}})\tau_{\text{mtr}} \tag{7.1}$$

where x_{icm} and v_{icm} are the horizontal integrated human-exoskeleton COM position/velocity estimated via the H3's measurements. The decision to base the AAN component of COM phase-space was motivated by the AAN-gait design by Bayon et al. [49] in addition to

the use of the XCOM within the exoskeleton literature, i.e., estimation of balanced step placement [197, 343, 348]. To our knowledge a COM-AAN approach has yet to be proposed for FIP balance; Emmens et al. [103] did however design a FIP controller around PD COM-regulation. In short, the controller was designed to provide little to no assistance during quasi-static quiet standing; however, it would increase the assistance delivered if the COM state started to approach the boundaries of the inverted pendulum FSR, i.e., a reduced margin of stability [154, 264]. We elaborate on this design below:

The COM assistance function was designed with a deadband in the quiet region of stance, and was based on the use of deadbands in electric-power steering in automobiles [239]. This quiet region is characterized by slow COM velocities around the user's equilibrium/set position [361]. When the COM is positioned close to the expected equilibrium point, e.g., 0-5 cm from Micheau et al. [242]) and Kuo [202], assistance is attenuated. As the COM is shifted away from the equilibrium point, it exits the deadband region, and enters either an anterior or posterior assistance region, i.e., we assume this change is a disruption to quiet stance. While in these assistance regions, the COM velocity is used to estimate the magnitude of disturbance and consequently, the scale of response by the exoskeleton. For example, based on the inverted pendulum model, if the COM is displaced forward and has a large velocity as it approaches the anterior BOS boundary, than assistance should be amplified due to a reduced margin of stability [154]. However, if the COM is displaced at a slower velocity, than the margin of stability will be higher and less assistance should be required by the end-user, i.e., the COM may be forward, but the end-user is not very close to the fall threshold.

To further elaborate on the proposed AAN architecture, when the COM in phase-space begins closing the distance to the boundaries of the FSR due to a perturbation, the assistance should increase. Thus, the function $\chi_{\text{net}}(\cdot)$ in Equation (7.1) can be further broken down as

$$\chi_{\text{net}} = \chi_{\max}\chi_x(x_{\text{icm}})\chi_v(x_{\text{icm}}, v_{\text{icm}}) \tag{7.2}$$

where $\chi_{\max}$ is the maximum possible percentage of assistance; the scaling functions $\chi_x(\cdot)$ and χ_v amplify assistance depending on COM position and velocity respectively. In this dissertation, position-level scaling was designed as

$$\chi_x(\cdot) = \begin{cases} f_{\text{amp}}(x_{\text{icm}}; \mathcal{B}_1, \mathcal{B}_2, \delta_{\text{ant}}) & x_{\text{icm}} \in [\mathcal{B}_1, \mathcal{B}_2) \\ f_{\text{amp}}(x_{\text{icm}}; \mathcal{B}_3, \mathcal{B}_4, \delta_{\text{post}}) & x_{\text{icm}} \in [\mathcal{B}_3, \mathcal{B}_4) \\ 0 & \text{else} \end{cases} \tag{7.3}$$

with a deadband for $x_{\text{icm}} \in [\mathcal{B}_2, \mathcal{B}_3)$ to prevent the system from trying to automate balance while the non-disabled end-user is standing quietly and close to the equilibrium point (see Fig. 7.2A). The amplification function was set using quartic Beziér polynomials as

$$f_{\text{amp}}(x, b_{\text{l}}, b_{\text{u}}, \delta) = \begin{cases} 3(1-x)x^2 + x^3 & x \in [b_{\text{l}}, b_{\text{l}} + \delta) \\ (1-x)^3 + 3(1-x)^2 x & x \in [b_{\text{u}} - \delta, b_{\text{u}}) \\ 1 & x \in [b_{\text{l}} + \delta, b_{\text{u}} - \delta) \\ 0 & \text{else} \end{cases} \tag{7.4}$$

which utilizes the parameters δ_{ant} and δ_{post} and the boundaries defined in the array $\mathcal{B} \in \mathbb{R}^{4\times 1}$ to tune how quickly χ_x approaches 1 in the respective anterior and posterior zones of assistance, i.e., $[\mathcal{B}_3, \mathcal{B}_4)$ and $[\mathcal{B}_1, \mathcal{B}_2)$ respectively. Again, due to the presence of competing feedback loops (non-disabled CNS versus MPC), if the COM is positioned very close to the toe or heel, $\chi_x(\cdot)$ reduces amplification of the control actions in case the control actions excessively compete with the person or cause too much ankle torque amplification and produce a loss of balance, i.e., there is already a low margin of stability at these positions. The intended result is the controller providing the healthy end-user with *light* assistance when they experience a perturbation from one of two directions (backward or forward); the controller then expects that the user will supply the percentage of ideal torques neglected in the scaling operation.

Scaling of balance recovery assistance with COM velocity was implemented through the function

$$\chi_v(\cdot) = \begin{cases} \frac{v_{\text{icm}}}{\mathcal{V}_{\text{for}}} & (v_{\text{icm}} < \mathcal{V}_{\text{for}}) \wedge (v_{\text{icm}} > 0) \\ \frac{v_{\text{icm}}}{\mathcal{V}_{\text{back}}} & (v_{\text{icm}} > \mathcal{V}_{\text{back}}) \wedge (v_{\text{icm}} < 0) \\ 1 & (v_{\text{icm}} > \mathcal{V}_{\text{for}}) \vee (v_{\text{icm}} \cdot \hat{\text{i}} < \mathcal{V}_{\text{back}}) \end{cases} \tag{7.5}$$

which was true if and only if the velocity bounds met the conditions $\mathcal{V}_{\text{back}} \leq 0$ or $(\vee)$ $\mathcal{V}_{\text{for}} \geq 0$; otherwise, $\chi_v = 0$ (see Fig. 7.2B). The logic "and" is denoted by $\wedge$. These velocity boundaries were calculated according to the extrapolated COM method [154]:

$$\mathcal{V}_{\text{back}} = -F\omega_0(\ell_{\text{c2h}} + x_{\text{icm}}) \tag{7.6}$$

$$\mathcal{V}_{\text{for}} = F\omega_0(\ell_{\text{c2t}} - x_{\text{icm}}) \tag{7.7}$$

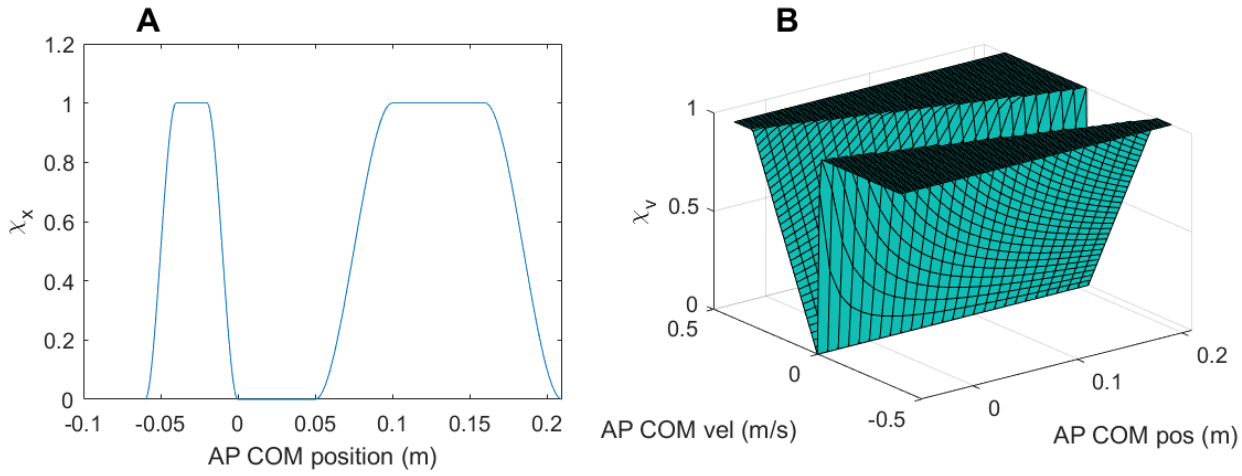


Figure 7.2: A) Anteroposterior (AP) COM position scaling function (χ_x) and B) AP COM velocity (χ_v) scaling function for $\mathcal{B} = [-0.06, 0.00, 0.05, 0.21]$ m, $\delta_{\text{ant}} = 0.05$ m, $\delta_{\text{post}} = 0.02$ m, $F = 1$, $\omega_0 = 3$ Hz, $\ell_{\text{c2h}} = 0.06$ m, and $\ell_{\text{c2t}} = 0.21$ m.

where $F \in [0, 1]$ was a parameter that defined how close to the FSR boundary the COM must be for $\chi_v = 1$. Thus, the condition $\mathcal{V}_{\text{back}} \leq 0$ and $\mathcal{V}_{\text{for}} \geq 0$ implies that the user is falling and cannot be assisted with a FIP balance recovery strategy (though this is only true for balance strategies restricted to the inverted pendulum). At this point, the controller removes any assistance for FIP balance, though ideally, the system would then switch to an assistive change-in-support controller.

7.2.3 Nonlinear Friction Compensation and Saturation

The desired control-oriented motor torques assume that the system in question only has linear, viscous damping in the actuators; nonlinear dry friction terms are assumed to be zero. To meet this condition, we must compensate for this friction outside of the MPC block. Given the use of strain-wave gearing on the EXO-H3, we elected to use the method proposed by Hauschild and Heppler [142] due to its simplicity and strong performance when used alongside a continuous velocity-dependent model of actuator friction

Table 7.2: COM-assistance parameters used in experiments.

Parameter	Description	Value	Units
$\chi_{\max}$	Maximum percentage of assistance	25	%
$\mathcal{B}$	COM-BOS intervals	[-0.06, 0, 0.05, 0.21]	m
δ_{ant}	Anterior ramp constant	0.05	m
δ_{post}	Posterior ramp constant	0.02	m
F	COM velocity scaling parameter	0.40	$\sim$

Table 7.3: Nonlinear friction compensation parameters used in experiments.

Parameter	Description	Value	Units
k_τ	Pseudovelocity torque gain	1	rad/Nms
k_υ	Velocity gain	1000	s
τ_{sat}	Pseudovelocity saturation	0.5	rad/s
α_0	Stribeck friction	1-2	Nm
α_1	Coulomb friction	5-8	Nm
α_2	Damping friction	0	Nms/rad

(see Chapter 4.1.2). Implementation of this method involved definition of a torque-based saturated/scaled pseudovelocity term,

$$\tau_{\text{nsat}} = \begin{cases} k_\tau \tau^*_{\text{mtr}} & \text{if } k_\tau |\tau^*_{\text{mtr}}| < \tau_{\text{sat}} \\ \tau_{\text{sat}} \text{sign}(\tau^*_{\text{mtr}}) & \text{if } k_\tau |\tau^*_{\text{mtr}}| \geq \tau_{\text{sat}} \end{cases} \tag{7.8}$$

alongside a velocity-based homotopy variable

$$\upsilon = \begin{cases} k_\upsilon |\omega| & \text{if } k_\upsilon |\omega| < 1 \\ 1 & \text{if } k_\upsilon |\omega| \geq 1 \end{cases}, \quad \text{st. } \upsilon \in [0, 1] \tag{7.9}$$

where k_τ and k_ν are torque and velocity-based scaling terms (see Table 7.3 for values). Recall that the torque desired as an output from the ideal actuator in our control-oriented model was defined as τ^*_{mtr}, i.e., what we received from the MPC algorithm and COM

assistance scaling. These two components allow for the calculation of a compensatory joint velocity, i.e.,

$$\breve{\omega} = \upsilon\omega + (1-\upsilon)\tau_{\text{nsat}} \tag{7.10}$$

that is subsequently fed into the regularized joint friction model. Using this augmented velocity variable instead of a raw encoder value has shown success in mimicking ideal actuator performance while also reducing some chatter when $\omega \approx 0$ and the slipping-static transition (or vice-versa) occurs [142]. The resulting torque that we provide to the joint torque controller at each sampling instant is

$$\breve{\boldsymbol{\tau}}_{\text{mtr}} = \tau^{*}_{\text{mtr}} + \alpha_0 \frac{\frac{\breve{\omega}}{\omega_{\text{t}}}}{\frac{1}{4}\left(\frac{\breve{\omega}}{\omega_{\text{t}}}\right)^2 + \frac{3}{4}} + \alpha_1 \tanh\left(4\frac{\breve{\omega}}{\omega_{\text{t}}}\right) + \alpha_2\breve{\omega} \tag{7.11}$$

where the final joint torque $\breve{\boldsymbol{\tau}}_{\text{mtr}}$ is attained by the actuators through low-level pulse-width modulation. Note that the values for each friction coefficient varied slightly from participant to participant as these parameters were tuned immediately prior to each testing session while the participant had donned the device, i.e., Table 7.3 displays the range of friction values used (set individually for each unique participant).

7.3 Methods

7.3.1 Participants

A total of 13 university-aged healthy young adults visited Prof. Andrew Laing's lab (Toby Jenkins Applied Health Research Building University of Waterloo a 3 hour testing session (7 females and 6 males; age = 19-30 years; height = 1.69 ± 0.09 m (mean $\pm$ SD); weight = 73.2 ± 14.4 kg). Participants were screened to be free of balance impairments, musculoskeletal injuries[1], evident neurological disorders, inner ear (vestibular) problems, and uncorrected vision impairment; each individual was able to stand for prolonged periods without assistance. Participants were screened as to whether they were taking common prescription medications that have been linked to impaired balance control[2] [145]. They

[1] Other injuries that affected the ability to stand like ingrown toenails, plantar fasciitis, and back pain were also defined as exclusion criteria during recruitment.

[2] "Yes" was considered an exclusion criterion.

had also confirmed that they had not been involved in any perturbation-based balance control studies prior to their study visit [212]. Each individual provided informed consent prior to participation. For their participation, they were remunerated $75 (CAD) at the end of their visit.

In addition to the aforementioned criteria, manufacturer guidelines were also followed in the recruitment process: according to the Exo-H3 (Technaid, Spain) instruction manual, participant height must be between 1.35-1.85 meters and weight must be less than 100 kg. The height restriction was based on the sets of links we had access to at the time of testing; longer and shorter links can be purchased if desired. Additionally, participants should have sufficient range of motion in the ankle, knee, and hip: approximately 90 degrees of hip flexion and 30 degrees of extension; 90 degrees of knee flexion and 0 degrees of extension; 30 degrees of ankle plantarflexion and dorsiflexion. These are the mechanical limits for the Exo-H3, so to limit the risk of injury to the participant, their range of motion should span the exoskeleton workspace. Please refer to Appendix O for a template of the screening questionnaire. Anthropometric parameters of note for the exoskeleton, e.g., segment length, are based on the physical estimates discussed in Chapter 4.2. The protocol outlined in this Chapter was reviewed and received ethics clearance through a University of Waterloo Research Ethics Board (REB#44462).

7.3.2 Experimental Protocol

Overview

The combined effects of the exoskeleton and assistive balance control algorithm in tandem were assessed using a repeated measures study design. A treatment condition was defined as when the user had donned the exoskeleton and was receiving some variable level of active assistance; the no treatment condition was the human wearing no exoskeleton and receiving no possible assistance. A total of 24 experimental trials were conducted for each of the no and with treatment conditions with each trial involving the participant responding to a single perturbation delivered using a translation of the supports-surface: 9×2 sagittal directions (forward and backward) and 3×2 frontal directions (left and right). All perturbations closely mimicked the small support-surface acceleration waveforms used in Maki et al. [224], (for parameter values, see Table 7.4). These perturbations are akin to a light push or sudden acceleration while standing on a bus and as suggested by the authors, are nearly

Table 7.4: Support-surface translation parameters

Direction	Peak Velocity	Acceleration	Final Displacement
Forward	0.285 m/s	0.950 m/s^2	0.086 m
Backward	-0.209 m/s	0.697 m/s^2	0.063 m
Right	0.278 m/s	0.927 m/s^2	0.083 m
Left	-0.278 m/s	0.927 m/s^2	0.083 m

always recoverable without requiring a step forward or backward to prevent falling. In each condition, the trials were further block-randomized into three blocks with each block containing the following perturbation direction conditions: 3 forward, 3 backward, 1 left, and 1 right (trial order in blocks was randomized). Performance in the balance recovery experiment was evaluated according to human joint angle estimates (via motion capture), upper limb kinematics, and ground reaction force data (e.g., center of pressure location); human muscle activity was also measured using lower-limb electromyography (EMG).

Preparation

Before testing, participants were outfitted with a safety harness that was tethered to a ceiling-mounted monorail. The tether length was set so that in the case of a loss of balance, the participant's knees would never impact the ground. Simultaneously, we made sure that the tether would not be tight to the point that it could be used in helping correct the participant's balance (tension was monitored via a load cell). Infrared marker clusters were then secured to the participant's skin and clothing (via two-sided tape) to capture 3D kinematics via optical motion tracking at 50 Hz (Optotrak, Northern Digital Inc., Waterloo, ON). Due to limited space with the exoskeleton, motion capture of the lower-limbs was relegated to segments of the left leg only (the right leg was used for EMG measurements). Clusters consisted of 4 markers and were fixed to each of the segments listed: the left foot, left shank, left thigh, bilateral forearms, and upper back. In total, 28 physical markers were used to track participant kinematics with one additional marker to track platform kinematics. Additional anatomical (e.g., malleoli, femoral condyles, greater trochanter) and environment landmarks (e.g., force plate corners) were also digitized with respect to

relevant/local clusters; the former were important in defining segment orientation during joint angle calculations.

Due to the limited space for sensor placement around the exoskeleton, lower-limb muscle activity in the right leg only was monitored alongside kinematics via surface electromyography (EMG). A pair of surface EMG electrodes were fixed to the skin over the following muscles: tibialis anterior (front of right lower leg); medial gastrocnemius (back of right lower leg); vastus lateralis (front of right thigh); and biceps femoris (back of right thigh) [28, 329]. The patches of skin to which the electrodes were adhered were shaved, exfoliated, and cleaned prior to electrode placement. Participants were then asked to perform four sets of four maximum voluntary contractions (MVCs), one for each muscle listed prior. Each of these MVCs involved manual isometric resistance applied by a member of the research team. During each MVC, participants were asked to try and maintain their maximal effort for 3-5 seconds; verbal encouragement was provided to the participant by the researchers to help increase participant effort [60].

Prior to moving into the experimental trials, each participant was removed from the platform and then shown each direction of support-surface translation they would experience during testing. This acted to remove some degree of uncertainty from the participant regarding what they expected to experience without having them physically respond to a perturbation prior to a block.

Data Collection

The first condition of the repeated measures experimental protocol was treatment or no treatment, i.e., exo or no exo, which was randomized between participants. The following description will pertain to the case of the treatment condition as the second set of blocks tested.

The participant not wearing the exoskeleton completed 3 blocks each containing 8 randomised trials. Each trial involved the participant maintaining standing balance following a support-surface translation in one of four directions (perturbation). Prior to each trial, the participant confirmed when they were ready and in a comfortable standing posture with feet placed symmetrically (one on each force plate collecting at 3000 Hz; AMTI OR6-7-2000, Watertown, MA, USA). They were then provided with the following set of instructions:

- "The floor will move following the countdown but we will not indicate exactly when or which direction."
- "... maintain your balance and try to do so without taking a step" (Note: stepping was allowed, but we wanted to encourage the participant's CNS to select FIP balance recovery strategies)
- "You are free to use your arms if you wish to do so."

A member of the research team would then count down until the start of data collection. Once collection had begun, the perturbation occurred with some random delay (2-5 seconds) in order to mitigate the effects of anticipatory actions. If a participant stepped during a trial, the trial was moved to the end of the block and repeated.

Once the participant had completed the 24 trials necessary, the block was finished. If the first block of trials had the participant in the treatment condition, they would then doff the device prior to moving to the next block. However, we assume the opposite in this description; the participant must don the exoskeleton for the second block. Prior to this stage, the EXO-H3 segment lengths were adjusted according to the measurements made at the beginning of the study visit using a measuring tape. The EXO-H3 was then placed on a wide stool so that the participant could sit back into the exoskeleton without disrupting the EMG electrodes or the infrared emitting diode (IRED) clusters. With the participant seated in the device, the lead researcher assessed the seated hip, knee, and ankle joint alignment between device and participant to ensure that the width of the device hip/trunk orthosis was reasonable for control performance and comfort. Once any necessary adjustments were made to the seated alignment, the dry friction parameters in Table 7.3 were tuned by having the user "backdrive" the bilateral knee and ankle joints (technically the motor is helping them drive the joint). The friction parameter values at which the actuators offered low resistance with minimal chatter for a range of velocities were logged for each joint. The participant would then stand up while the system was running with these new passive friction compensation parameters, be tethered in again, and would perform a series of squat maneuvers to further assess symmetry of friction compensation, chatter, as well as to try and verify the measurements of the on-board kinematic encoders.

With the exoskeleton calibrated and the participant harnessed and again standing in a comfortable posture of their choosing (instructed to select while in passive mode before each trial), the treatment set of blocks (3 blocks; 8 randomized trials) was performed. The

posture chosen by the participant was considered the static equilibirum point in the MPC. Each trial followed the same order of operations outlined for trials in the no treatment block. The exoskeleton balance assistive controller was roughly activated in tandem with the motion capture system by a second researcher using a desktop computer (CPU: AMD Ryzen 7 3700X 8-Core Processor, 3.60 GHz; RAM: 16 GB), MATLAB (Mathworks, MA, USA) and the H3's wired CAN protocol provided by Technaid (some buffer/delays occurred during controller launch). Internally, the CAN protocol sends and receives messages every 10 ms (100 Hz); the received messages contain sensor data (motor torques, joint positions and velocity), while the sent message contains desired input motor torques. To provide more time for the MPC to converge (thus avoiding needing to narrow the prediction horizon), the controller sampled from the CAN protocol every 20 ms (50 Hz). Prior to trials, the participant was provided the same instructions as beforehand with a slight modification: "try to maintain your balance without taking a step" and "behave as naturally as possible regardless of the presence of the device". Comfort of the participant as well as strap tightness, cable management, and the presence of occluded markers were checked throughout testing (once after every few trials).

7.3.3 Outcome Measures and Statistical Analyses

Outcome measures to assess the effect of perturbation direction and presence of exoskeleton on user balance recovery were focused around the 3D kinematic data and force plate data. Briefly, the 3D kinematic marker trajectories were interpolated (only if the gap in the data was < 7 frames, [132]) and filtered at 4 Hz. This cutoff frequency was selected after inspection of the data using FFTs. Force plate data was calibrated and filtered as well, using a 50 Hz cutoff following inspection of the signal frequency content.

From the 3D kinematics, foot, shank, thigh, and trunk segment orientation (with respect to the inertial lab frame) were calculated using ZYX Euler angles. Joint angles were subsequently calculated using these Euler angles with the Z rotation corresponding to flexion/extension of the joint in the sagittal plane. Joint velocities were calculated from these angles via central finite differentiation, inspected for frequency content, and then filtered again (10 Hz). Additionally, the XY (sagittal) position and velocity of the human and human-exoskeleton COM were estimated using the weighted marker method described in [361], but with weights determined from the anthropometrics in Chapter 3 and the physical measurements from Chapter 4. Inherently, this estimation assumes that the human and

exoskeleton are rigidly connected – future work should assess relative motion of the exoskeleton and human during operation using additional marker clusters fixed to the device itself in addition to the participant. Lastly, the norm of the velocity of each forearm was calculated using the average position of all four markers on each forearm cluster. This velocity was used to infer the speed of the participant's hand movements during balance recovery.

From the force plate data, tangential ground reactions (X and Z direction) were calculated in addition to the normal force (Y). These three were used, along with the plate origin offset provided by the manufacturer, to obtain the right and left foot COP position within a reference frame fixed to the center of each plate top. Using the methods in [361], the net COP was calculated according the distribution of body weight between the right and left legs. From this position, the velocity of the COP was also calculated (again using central finite differences and subsequent low-pass filtering following inspection).

To perform statistical analyses, we first identified the onset of each perturbation, i.e., when the norm of the platform velocity exceeded 5 mm/s for 3 consecutive frames, and windowed all time-series data sets over the two seconds following onset. In this window, we identified the following outcomes to characterize human and human-exoskeleton balance recovery:

1. Maximum hand and COP speed (the former is related to the assumption of no arm motion in the control-oriented model)
2. Maximum and minimum joint angles (hip, knee, and ankle);
3. Maximum joint speeds (hip, knee, and ankle);
4. Maximum and minimum pitch angle of the trunk;
5. Maximum absolute pitch angle of the foot (related to our assumption that the foot remains rigidly welded to the ground);
6. Maximum and minimum COM displacement along X (anteroposterior);
7. Maximum and minimum XCOM displacement along X (anteroposterior);
8. Maximum and minimum COP displacement along X and Z (anteroposterior and mediolateral);

Note that the window used to assess COM and COP kinematics was only the 1 second following the perturbation. With these metrics identified for each trial, we then obtained participant averages for each direction of perturbation when possible (backward, forward, left and right) and each treatment condition (Exo and No Exo). These participant averages were subsequently used to perform a series of one-way and two-way repeated measures ANOVA tests as outlined below:

1. **Within-Subject Effects**: Direction (Backward, Forward, Left, and Right) and Treatment (exoskeleton and no-exoskeleton); **Outcome Means Tested**: hand speed and COP speed.

2. **Within-Subject Effects**: Direction (Backward and Forward) and Treatment (exoskeleton and no-exoskeleton); **Outcome Means Tested**: max/min joint angles; max joint speeds; max/min trunk angle; and max absolute angle of the foot.

3. **Within-Subject Effects**: Direction (Backward) and Treatment (exoskeleton and no-exoskeleton); **Outcome Means Tested**: max COM displacement; max XCOM displacement; max COP displacement (all along X).

4. **Within-Subject Effects**: Direction (Forward) and Treatment (exoskeleton and no-exoskeleton); **Outcome Means Tested**: min COM displacement; min XCOM displacement; min COP displacement (all along X).

5. **Within-Subject Effects**: Direction (Left) and Treatment (exoskeleton and no-exoskeleton); **Outcome Means Tested**: max COP displacement (along Z).

6. **Within-Subject Effects**: Direction (Right) and Treatment (exoskeleton and no-exoskeleton); **Outcome Means Tested**: min COP displacement (along Z).

where the two-way ANOVA test would also test for interactions between the within-subject effects. When significance was obtained in an ANOVA (i.e., $p < 0.05$ with Greenhouse–Geisser corrections applied due to some violations of the sphericity assumption), post-hoc pairwise testing was conducted using Dunn and Sidák corrections where significance was obtained at $p < 1 - (1 - 0.05)^{1/n}$ given n unique pairwise tests [22].

7.3.4 Predictive Simulations

Predictive dynamic simulations of the backward and forward Exo/No Exo perturbation trials were performed using the human NMPC controller disseminated in Chapter 3, but modified to consider multi-objectives. Briefly, the finite-horizon discrete optimal control problem was formulated to perform simulations with either the human-only (Chapter 3) or human-exoskeleton models (Chapter 6). For example, for the human-exoskeleton simulations, the direct collocation optimal control problem was described as

$$\arg\min_{x,u} \quad \sum_{k=1}^{n} \frac{w_1}{\Pi_1}(\theta_{\text{ankle}}[k] + \theta_{\text{knee}}[k] + \theta_{\text{hip}}[k] - \bar{\phi}_{\text{tr}})^2 + \frac{w_2}{\Pi_2}(\mathbf{r}_{\text{icm}}(\mathbf{q}_{\text{h}}[k]) \cdot \hat{\imath} - \bar{r})^2 + \frac{w_3}{\Pi_3}\mathbf{a}[k]^{\intercal}\mathbf{a}[k] \tag{7.12}$$

subject to:

$$\mathbf{q}_{\text{h}}[1] = \mathbf{q}_0, \quad \dot{\mathbf{q}}_{\text{h}}[1] = \dot{\mathbf{q}}_0 \tag{7.13}$$

$$\mathbf{g}_{\text{coll}}(\mathbf{x}_{\text{he}}[k], \mathbf{u}_{\text{h}}[k], \mathbf{x}_{\text{he}}[k+1], \mathbf{u}_{\text{h}}[k+1]) \leq \mathbf{0} \quad \forall\, k = 1 \ldots n-1 \tag{7.14}$$

$$\mathbf{h}_{\text{fsr}}(\mathbf{x}_{\text{he}}[k], \mathbf{u}_{\text{h}}[k]) \leq \mathbf{0} \quad \forall\, k = 1 \ldots n \tag{7.15}$$

$$\mathbf{h}_{\text{term}}(\mathbf{x}_{\text{he}}[n], \mathbf{u}_{\text{h}}[n]) \leq \mathbf{0} \tag{7.16}$$

$$\begin{Bmatrix} \mathbf{x}_{\text{min}} \\ \mathbf{u}_{\text{min}} \end{Bmatrix} \leq \begin{Bmatrix} \mathbf{x}_{\text{he}}[k] \\ \mathbf{u}_{\text{h}}[k] \end{Bmatrix} \leq \begin{Bmatrix} \mathbf{x}_{\text{max}} \\ \mathbf{u}_{\text{max}} \end{Bmatrix} \quad \forall\, k = 1 \ldots n \tag{7.17}$$

where definitions of $\mathbf{x}_{\text{he}}$ are identical to those in Chapter 6 and $\mathbf{u}_{\text{h}}$ from Chapter 3, i.e., no actuation from the exoskeleton motors. The cost function (7.12) was defined consistently with the multi-objective cost function used in previous open-loop simulations [344], i.e., a trunk, COM, and effort objective. Equation (7.14) contains the trapezoidal collocation constraints used to solve the underlying dynamic system ODEs over the prediction horizon. Equation (7.15) constrained the trunk position/velocity at each node within the prediction horizon. Like in Chapter 3, $F_{\text{push}} = 0$ and $\ddot{x}_{\text{plat}} = 0$ within the NMPC internal model to capture a novel response to a perturbation rather than one in which the CNS is anticipating the disturbance. The terminal inequality constraint (7.16) was the XCOM - COM height ellipse from Equation (3.55), but defined instead using the integrated human-exoskeleton COM $\mathbf{r}_{\text{icm}}$. Lastly, the control signal sent from the NMPC to the plant was a linear interpolation between the first two controller actions (separated by a step duration) returned by the optimization routine. Simulations were run with weights

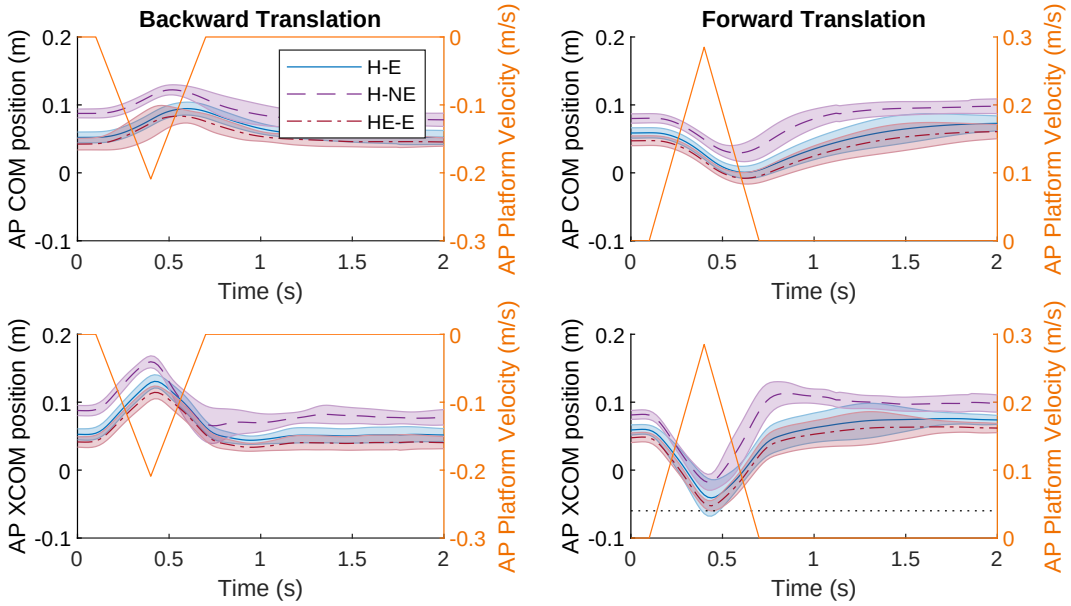


Figure 7.3: Representative mean human-only COM and XCOM position (in the Exo condition, H-E [blue], and no Exo condition, H-NE [purple], condition) as well as the combined human-exoskeleton COM and XCOM (in the Exo condition, HE-E [red]) for balance recovery in response to backward and forward support-surface translations. Shaded areas indicate ±1 SD. Also shown are the temporal profiles of the AP platform velocity for each condition, where positive values correspond to the anterior direction.

$w_1 = 2.5$, $w_2 = 2.5$, and $w_3 = 1$ in addition to normalization constants $\Pi_1 = 61.7$ rad^{-2}, $\Pi_2 = 1.07$ m^{-2}, and $\Pi_3 = 25$ (unitless). The latter values were based on the maximum possible Lagrangian value for each given cost (at a single node) multiplied by the number of prediction horizon nodes [23]. For each simulation (4 total), we compared the simulated AP COM and COP trajectories against the COM and COP trajectories obtained from the experiments (mean ± 95% confidence interval; CI). The same analysis was conducted to compare NMPC predictions of joint angle trajectories.

7.4 Experimental Results

Across all trials conducted, stepping to recover balance rarely occurred: observed in 4.64% of human-exoskeleton and 5.64 % of human-only trials (No Exo; H-NE). Given the current

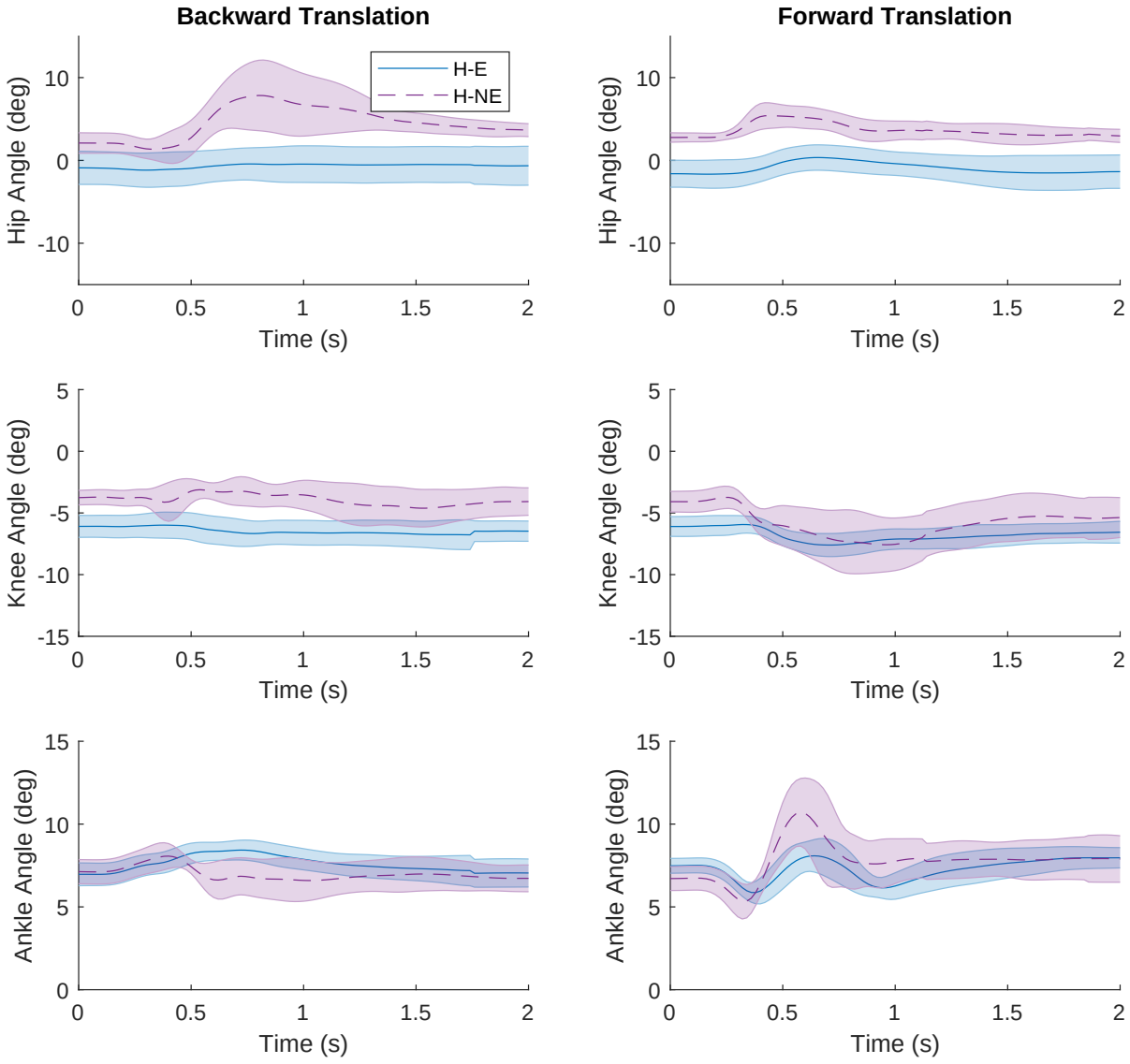


Figure 7.4: Representative mean human joint angles for balance recovery in response to backward and forward support-surface translations. Shaded areas indicate ±1 SD.

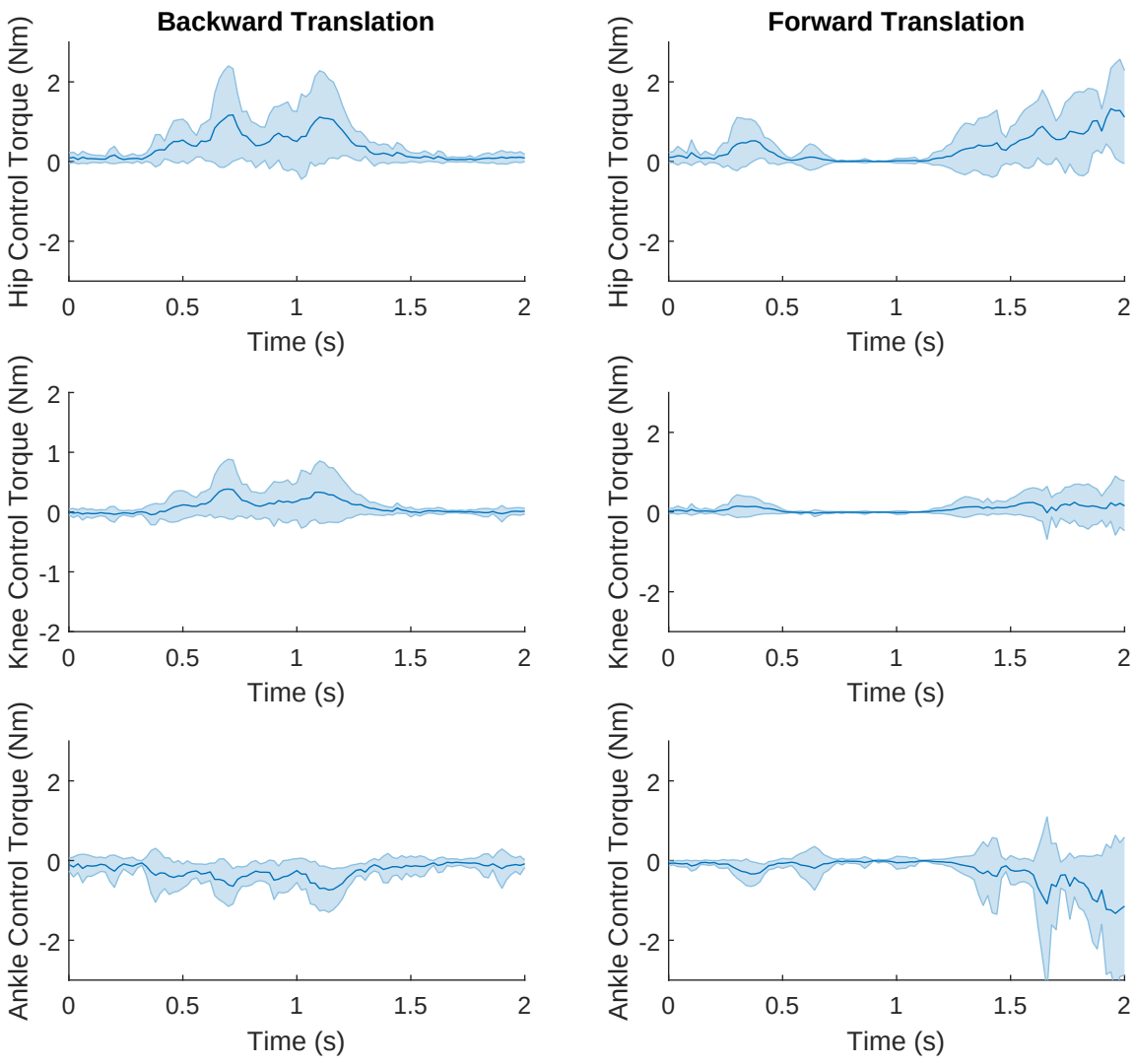


Figure 7.5: Representative mean MPC-derived assistive torque $\tau_{\text{mtr}}*$, following scaling by COM position-velocity scaling function in Section 7.2.2, for balance recovery in response to backward and forward support-surface translations. Shaded areas indicate ± 1 SD.

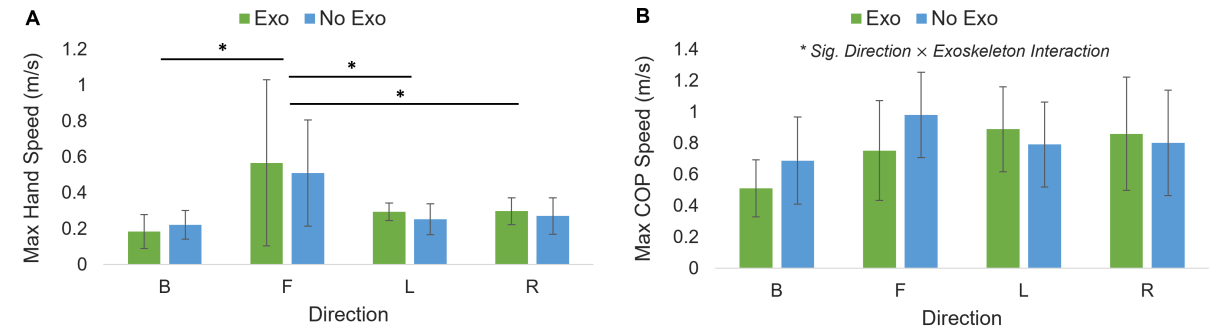


Figure 7.6: **A**) Maximum hand speed and **B**) maximum COP speed measured following each direction of perturbation (backward B, forward F, left L, right R). * indicates a statistically significant main effect ($p < 0.05$, only a direction main effect present in A).

focus on FIP strategies, these trials were excluded from analyses. Representative plots regarding balance recovery following a forward or backward perturbation, i.e., backward and forward fall respectively, were provided for a single subject. Briefly, in Fig. 7.3, the AP COM and XCOM trajectories (mean ± 1 SD) evaluated in both the Exo and No Exo conditions are shown. In human-exoskeleton trials, both the human-only and combined human-exoskeleton COM were calculated; only human COM was calculated in human-only trials. Note that the temporal profiles of the AP platform (support-surface) velocity for each condition are also included in Fig. 7.3.

In Fig. 7.4, the average (± 1 SD) joint angles are shown; this plot highlights the change in absolute joint deviations that occur after donning the exoskeleton and responding to a balance perturbation. Lastly, mean MPC-derived assistive torques $\tau_{\text{mtr}}*$, following scaling by COM position-velocity scaling function in Section 7.2.2, are shown in Fig. 7.5. These torques were then fed into the Hauschild [142] feedback friction compensation algorithm. Note that the programming of the COM-AAN function resulted in extremely small assistive torques, i.e., the participants were mainly just balancing with assistance from the nonlinear friction compensation.

Results of the repeated measures two-way ANOVAs for test 1 are highlighted in Fig. 7.6. For maximum hand speed, there was a perturbation direction main-effect only ($p = 0.024$). Pairwise comparisons following grouping of the exoskeleton (Exo; H-E) and no exoskeleton conditions (No Exo; H-NE) revealed significantly higher arm speeds following forward perturbations in comparison to backward perturbations ($p = 0.008$); however,

Table 7.5: Statistical analysis (two-way repeated measures ANOVA) of a perturbation main effect (p_{Dir}), exoskeleton main effect (p_{Exo}), and interaction (p_{Int}) for the kinematic outcome measures (mean ± SD). Note that statistical significance was reached at $p < 0.05$ (main or interaction effect indicated by *).

	Backward Translation		Forward Translation		Significance		
Outcomes	Exo	No Exo	Exo	No Exo	p_{Dir}	p_{Exo}	p_{Int}
Joint Angles							
max hip angle (°)	11.4±12.2	8.9±14.2	10.7±13.0	7.3±10.6	0.40	0.31	0.74
min hip angle (°)	3.7±8.5	-3.8±8.7	2.9±8.6	-5.5±8.3	0.15	0.01*	0.40
max knee angle (°)	-11.6±7.0	-3.9±4.8	-11.4±6.7	-4.6±5.7	0.67	<0.01*	0.25
min knee angle (°)	-16.0±8.3	-9.9±9.1	-17.2±7.5	-17.6±7.6	0.01*	0.17	<0.01*
max ankle angle (°)	11.1±3.4	9.0±2.9	14.5±3.8	16.0±4.6	<0.01*	0.74	<0.01*
min ankle angle (°)	7.1±3.4	3.4±3.1	6.0±4.6	4.8±3.2	0.92	0.11	0.05
Joint Speeds							
max hip speed (°/s)	21.5±12.6	52.2±23.4	28.1±18.8	65.3±25.0	0.04*	<0.01*	0.55
max knee speed (°/s)	16.2±8.9	25.8±14.3	24.0±14.4	69.1±38.8	0.01*	<0.01*	<0.01*
max ankle speed (°/s)	18.3±10.8	26.6±21.0	53.3±40.0	63.7±30.2	<0.01*	0.14	0.79
Segment Kinematics							
max trunk angle (°)	-0.3±7.3	1.3±6.3	3.3±7.9	8.6±9.2	<0.01*	0.08	<0.01*
min trunk angle (°)	-7.4±9.6	-9.0±9.5	-5.1±11.3	-1.7±8.8	<0.01*	0.65	0.01*
max. abs. foot angle (°)	3.9±2.1	4.2±2.9	7.1±4.7	7.0±3.6	0.02*	0.88	0.71

there was no difference between the forward perturbations and the right ($p = 0.0367$) and left ($p = 0.0324$) direction with the Dunn-Sidák corrections. For the maximum COP speed, there was a significant direction/exoskeleton interaction ($p = 0.031$). To assess where this interaction was occurring, we again used pairwise t-tests. However, the great large of tests conducted (28) combined with the variability of the data led to few significant results: COP speed was lower following backward perturbations than leftward when the participant was wearing the exoskeleton ($p = 0.001$); COP speed was significantly greater following forward perturbations when the participant was not wearing an exoskeleton in comparison to following a backward perturbation when they had donned the device ($p < 0.001$).

Results of the repeated measures two-way ANOVAs for test 2 are highlighted in Table 7.5. Representative joint angles of balance recovery following a backward or forward

Table 7.6: Statistical analyses (one-way repeated measures ANOVAs) for an exoskeleton main effect (p_{Exo}) on the COM/COP-based outcome measures (mean ± SD). Note that statistical significance was reached at $p < 0.05$ (exoskeleton main effect indicated by *).

Outcomes	Exoskeleton	No Exoskeleton	p_{Exo}
Backward			
max AP COM displacement (cm)	10.82±2.30	12.49±1.72	0.02*
max AP XCOM displacement (cm)	14.42±2.55	16.27±2.02	0.01*
max AP COP displacement (cm)	11.17±3.89	13.64±2.82	<0.01*
Forward			
min AP COM displacement (cm)	0.86±2.09	2.75±1.43	<0.01*
min AP XCOM displacement (cm)	-4.55±3.27	-2.87±1.67	0.15
min AP COP displacement (cm)	-4.71±2.73	-4.03±2.51	0.03*
Left			
max ML COP displacement (cm)	29.99±3.03	30.84±2.71	0.21
Right			
min ML COP displacement (cm)	6.34±3.89	8.64±2.52	0.04*

perturbation are shown for a single participant in Fig. 7.4. Representative scaled control trajectories for each joint (τ^*_{mtr}), i.e., what was fed into the friction compensation block, are displayed in Fig. 7.5. From Table 7.5, there was no effect of perturbation direction or exoskeleton on the magnitude of hip flexion used by the user in the 2 seconds following a perturbation. Wearing an exoskeleton with friction compensation and MPC assistance did appear to reduce the amount of trunk extension used (minimum hip angle; $p = 0.01$); however, pairwise comparisons revealed only a significant difference in minimum hip angle between forward - no Exo condition and the backward - Exo condition ($p = 0.007$). Wearing the powered exoskeleton also affected the maximum amount of knee extension used ($p < 0.01$): the exoskeleton reduced the maximum knee angle (knee more flexed) following a backward ($p = 0.002$) and forward perturbation ($p = 0.002$). However, there was an exoskeleton-perturbation direction interaction in the case of the minimum knee angle ($p < 0.01$). Using corrected pairwise comparisons to investigate this interaction, we ob-

tained a significant difference only between backward and forward knee perturbation knee angles in the No Exo condition ($p = 0.003$), i.e., the degree of knee flexion was not impacted by perturbation direction when the exoskeleton was worn. Regarding the maximum ankle angle, we again observed an exoskeleton-perturbation direction interaction ($p < 0.01$). In this case, pairwise comparisons suggested that the amount of ankle dorisflexion used following a forward perturbation was reduced when wearing the powered exoskeleton and the opposite occurred following a backward perturbation. Both Exo ($p = 0.007$) and No Exo ($p < 0.001$) conditions experienced a significant perturbation direction effect, just to a different magnitude. Lastly, there was no statistical effects observed for the minimum ankle angle suggesting that the magnitude of plantarflexion used in balance recovery was consistent across conditions.

Looking at the joint velocity-related outcome measures in Table 7.5, the following was observed: maximum hip speed was generally reduced when wearing the exoskeleton ($p < 0.01$) and higher when responding to the forward perturbations, i.e., falling backward ($p = 0.04$). The same was not observed for the knee speed – rather an interaction effect was found ($p < 0.01$). Pairwise comparisions revealed that maximum knee speed was significantly higher in the No Exo condition when the participant was responding to a forward perturbation rather than backward ($p = 0.006$). However, knee speed was not influenced by perturbation direction when the participant was wearing the exoskeleton. The maximum ankle speed also revealed a perturbation direction main effect ($p < 0.01$): ankle speeds were much larger in response to the forward perturbations. Lastly, looking at the segment kinematics in Table 7.5, there was once again a perturbation-exoskeleton interaction effect ($p \leq 0.01$). Investigating these further revealed that there was a consistent effect of perturbation direction on the maximum trunk angle: in both the No Exo ($p < 0.001$) and Exo conditions ($p < 0.001$), the degree of forward trunk pitch was always greater following a forward perturbation, though this difference was larger for the No Exo condition. Regarding the magnitude of foot pitch (maximum absolute foot angle), the degree of toe-raise following a forward perturbation was significantly greater than heel-raise following a backward perturbation ($p = 0.02$).

Results of the repeated measures one-way ANOVAs for tests 3-6 are highlighted in Table 7.6. Representative human-only and human-exoskeleton COM and XCOM trajectories following a backward or forward perturbation are shown for a single participant in Fig. 7.3. Briefly, using the exoskeleton produced smaller forward COM ($p = 0.02$), XCOM ($p = 0.01$), and COP deviations ($p < 0.01$) following a backward perturbation. Similarly,

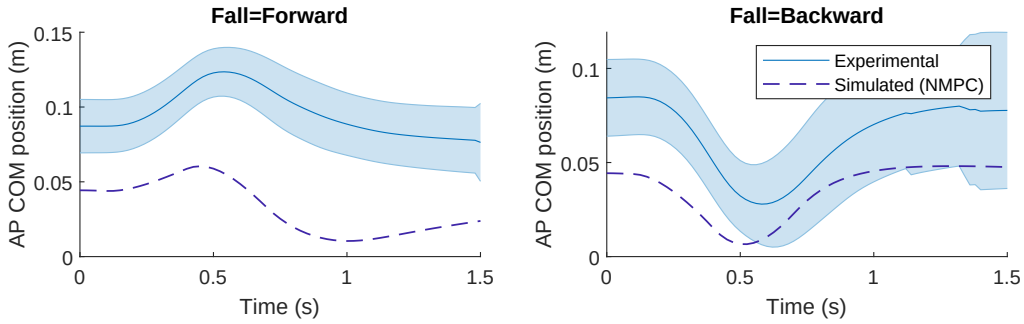


Figure 7.7: Experimental and predicted (via human-NMPC) anteroposterior (AP) COM trajectories during human-only balance recovery (No Exo), i.e., induced falling forward or backward.

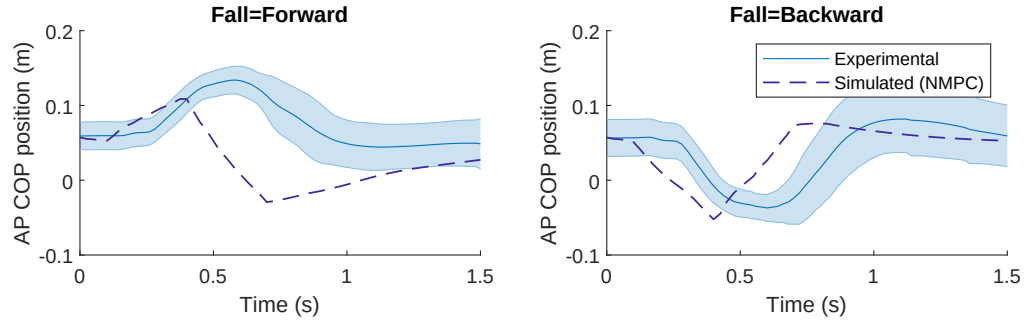


Figure 7.8: Experimental and predicted (via human-NMPC) anteroposterior (AP) COP (assumed coincident with ZMP) trajectories during human-only balance recovery (Exo), i.e., induced falling forward or backward.

the exoskeleton produced smaller backward COM ($p < 0.01$) and COP deviations ($p = 0.03$) following a forward perturbation. Lastly, the exoskeleton significantly increased the maximal leftward COP displacement following support-surface translations to the right. No effect of the exoskeleton was observed for the COP displacements following left support-surface translations.

Lastly, the predicted COM/ZMP trajectories for the backward and forward perturbations are shown against experiments (mean ±95% CI) in Fig. 7.7 and Fig. 7.8 (human-only predictive simulations) in addition to Fig. 7.9 and Fig. 7.10 (human-exoskeleton predictive simulations). A reminder that conditions with and without the exoskeleton were driven by the human MTGs; no motor torques. The predicted and experimental (mean ±95% CI) joint angle trajectories for the human-only perturbations are shown in Fig. 7.11;

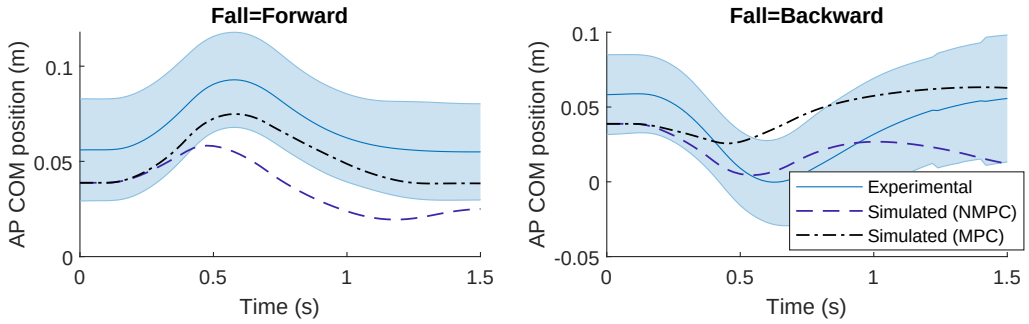


Figure 7.9: Experimental and predicted (via human-NMPC or exoskeleton-MPC) anteroposterior (AP) COM trajectories during human-exoskeleton balance recovery (No Exo), i.e., induced falling forward or backward.

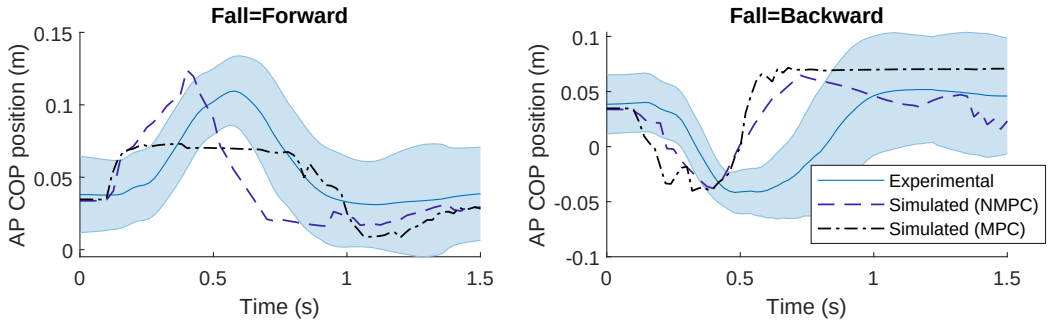


Figure 7.10: Experimental and predicted (via human-NMPC or exoskeleton-MPC) anteroposterior (AP) COP (assumed coincident with ZMP) trajectories during human-exoskeleton balance recovery (Exo), i.e., induced falling forward or backward.

human-exoskeleton predictions are shown against experiments in Fig. 7.12. Note that at the time of submitting this document, the human NMPC was unable to perform anything but a squat/hip strategy with exaggerated joint deviations, when controlling the human-exoskeleton model (Fig. 7.12); this was not the case for the human-only model (Fig. 7.11). Given that this is quite a deviation from the experimental values we observed, we decided to also plot the the simulated joint angles and COM/ZMP (COP) from MPC-driven balance recovery simulations in Chapter 6 (Figs. 7.9,7.10,7.12), which anecdotally provided a much better fit to experiments.

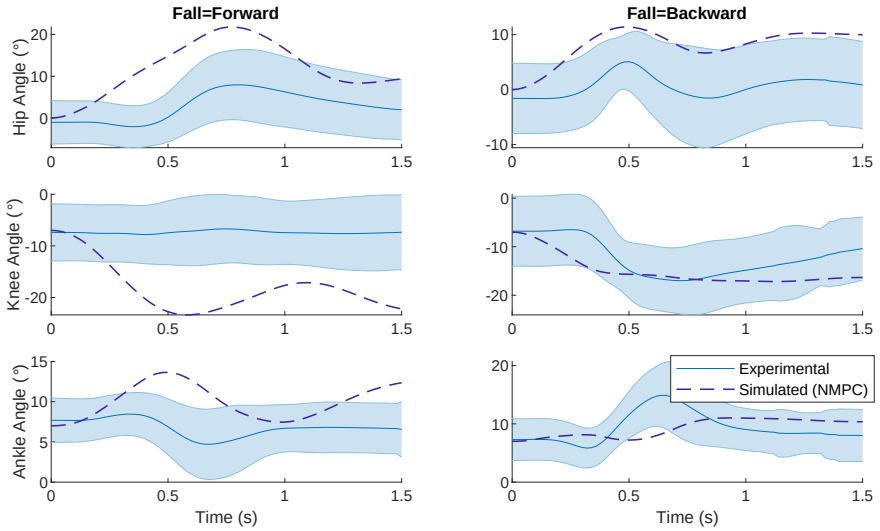


Figure 7.11: Experimental and predicted (via human-NMPC) hip, knee, and joint angle trajectories during human-only balance recovery (No Exo), i.e., induced falling forward or backward.

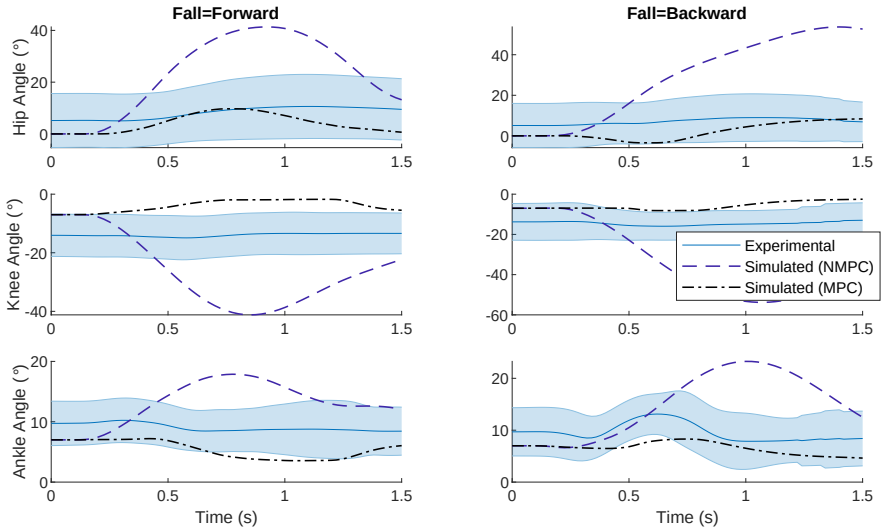


Figure 7.12: Experimental and predicted (via human-NMPC or exoskeleton-MPC) hip, knee, and joint angle trajectories during human-exoskeleton balance recovery (Exo), i.e., induced falling forward or backward.

7.5 Discussion

The goal of the current study was to assess viability of FIP balance when wearing a lower-limb exoskeleton using principles of optimal model-based control (MPC), COM-based assistance as needed (AAN), and feedback nonlinear friction compensation. To our knowledge, MPC and COM-AAN has yet to be applied to exoskeleton-assisted FIP balance control. The closest analogues exist for walking: Wang [211] proposed a gait pattern generator for exoskeletons using MPC while Bayon et al. [49] proposed a COM-AAN scheme for ankle exoskeletons to provide perturbation-correcting torques. Friction compensation has been previously applied in exoskeleton-assisted walking to assess the influence of actuator friction on metabolic expenditure [288] and some studies in the area of exoskeleton FIP balance feature "zero impedance" conditions [103, 105]. However, this appears to be the first application of it in "human-first" human-exoskeleton balance control [288] and first to use the continuous nonlinear friction model by Brown and McPhee [65] and the feedback algorithm proposed by Hauschild [142]. Ultimately, the proposed COM-AAN with the parameter values chosen provided too little assistance scaling to analyze its capabilities, and subsequently the performance of the MPC, i.e., the AAN component thought the participant did not require much assistance. On that note, that may be true – with nonlinear friction compensation alone, the healthy young adults were able to maintain FIP balance in response to all four directions of perturbations. Thus, the data presented herein better describes human balance recovery when assisted purely through friction compensation at the hip, knee, and ankle joints.

To our knowledge, this study is the second to elucidate how the baseline kinematics of young adult balance recovery, i.e., when not using a biomechatronic device, are influenced when wearing a powered hip-knee-ankle exoskeleton (EXO-H3 powered lower-limb exoskeleton). The first was performed in 2022 by Mileti et al. [243] with the EXO-H2 (previous version of EXO-H3); however, it involved full decoupling of the actuators from the rest of the hardware, i.e., the device was not powered, and perturbations that involved rotations of the support-surface, not translations. Existing studies have tested low-impedance controllers against assistive controllers, but not truly a device/no-device repeated measures design [103, 105]. In general, wearing the lower-limb exoskeleton decreased the amount of hip extension the participant maintained during quiet standing; the hip was in a flexed position when the device was worn. This posture was likely adopted due to the participant having to compensate for the mass of the battery behind them (gravitational compen-

sation not provided). Rather than flexing further during balance recovery, the hip was seemingly locked for the most part. When wearing the exoskeleton, the knees were also kept relatively locked, like in double pendulum models [202, 204]. Participants kept their knee locked when not wearing the device and responding to the backward perturbations; however, knee flexion was consistently used following the backward perturbations. This change in strategy possibly suggests CNS recruitment of knee motion with an increase in perturbation magnitude [158, 223]. This is consistent with results of simulations in Chapter 3, where knee flexion emerged for aggressive COM control when estimating the posterior FSR boundary. Lastly, based on velocity of the arms alone, it did not appear as through the arms were utilized differently when the device was donned. Arm responses were consistently evoked by the forward perturbations (falling backward), but no others. Additionally, the remaining friction in the actuators following compensation (mainly viscous) is possibly the explanation for the reduced peak joint velocity during balance recovery with the exoskeleton (consistent with simulations in Chapter 6). However, it was more likely the substantial reflected actuator inertia preventing exoskeleton joint accelerations from reaching large enough values such that human-only joint velocities were attainable.

When participants stood quietly while wearing the exoskeleton, their COM (not including the device hardware) was situated closer to the ankle than without the device. As a result, the maximum forward COM displacement following a backward perturbation was much lower when wearing the exoskeleton. On the contrary, backward net COM displacements following a forward perturbation were greater when donning the device. Further analyses should be conducted using the displacement of the COM from the initial quiet position. Wearing the exoskeleton also led to a greater posterior shift of the COP when falling backward. This difference is likely the cause of the statistically greater heel-raise than toe-raise observed in experiments. Lastly, following backward perturbations, note that the max COP was often lower than the max XCOM. According to Hof et al. [154], this suggests that a balance recovery strategy outside of the inverted pendulum may have been used; however, the trajectories in Fig. 7.12 suggest otherwise. One possibility is that participants were intuitively using the profile of support-surface accelerations (square-wave acceleration/deceleration) within their strategy to maintain upright balance their postural strategy (mathematical proof in Inkol and Vallis [174]). A more likely possibility is that the estimates of the COM were biased anteriorly, possibly due to investigator error during anatomical marker identification, shifting of marker clusters during testing (only minor deviations observed during tests), or as a deterministic error in the marker-based COM

estimation method [361]. Given the accuracy of the AMTI forces plates (often used as the gold standard in force plate validation studies [43, 196, 352]), we are more confident in the accuracy of the COP outcomes disseminated. Given that inverted pendulum models suggest that, the COM and COP are approximately coincident during quiet standing, i.e., small oscillations about a set point [154, 361], a possible correction for this data set could involve shifting the AP COM trajectories such they are initialized over the AP COP location for each trial.

In general, NMPC was relatively successful at estimating the pattern and amplitude of changes in the COP and COP (ZMP) during balance recovery in the human-only and human-exoskeleton conditions. Additionally, the exoskeleton-MPC simulations from Chapter 6 actually provided a closer estimate of COM during human-exoskeleton balance recovery than the NMPC-generated ones. It reasonable to believe that the current predictions would improve with the correction of evaluated COM trajectories (suggested in the previous paragraph), especially given the accuracy in COP estimations. From the COP estimations, it is also clear that improvements with the human NMPC architecture can be made by adding a dead-time in control response [158, 202, 344]; the NMPC responded to the perturbation immediately. Such a development could also be used to corroborate the recent experimental observations made by Beck et al. [50] in regards to ankle exoskeleton assistance, i.e., in order for exoskeleton balance assistance to be beneficial, it *must* have a smaller response delay than the CNS. As discussed in Chapter 6, the MPC runtime was just under $20ms$, which is markedly lower than the delays typically associated with human balance recovery (80-130 ms [50, 158, 344, 353]),

Regarding joint angles predictions, the NMPC performed sufficiently in human-only conditions. When falling forward (backward perturbation), the NMPC used more hip flexion and ankle dorsiflexion than participants. The NMPC also utilized changes in knee flexion unlike the participants, which may suggest that the XCOM/COM terminal constraint alone too weak to encourage convergence to an upright posture (see NMPC simulations with COM and trunk criteria in Section 3.3). The increased dorsiflexion may have emerged with the addition of effort within the NMPC objective; the plantarflexion used by participants was closer to what was simulated when obtaining the human-only FSR (Chapter 3). Therefore, a data-driven approach to identifying cost function weights could further improve fitting [55, 82, 250]. NMPC predictions of human joint angles were generally better for the forward perturbation conditions (backward fall); though, the NMPC did use slight greater hip flexion and less ankle dorsiflexion. When it came to predictive simulations of

the human-exoskeleton conditions, the NMPC was less successful. The NMPC could only adopt a hip/squatting strategy (stooped posture in Fig. 7.12) when driving the human-exoskeleton model. It could be the the NMPC was trying to minimize MTG activations by using the actuator viscous friction to help correct balance [339], but this seems unlikely given the higher-weighing of state terms. Therefore, like for the COM/ZMP validations, the exoskeleton-MPC-derived trajectories from Chapter 6 (see Fig. 6.10) were also plotted in Fig. 7.12. The simulations showed much better alignment with experimental joint angles for both categories of perturbation. In fact, these estimations further provide strength for the rationale of using MPC to derive FIP assistive torques that align well with the postural strategies selected by the CNS. Kuo [203, 202] obtained reasonable hip/ankle trajectory predictions using LQR. Given MPC is often considered an analog to constrained LQR, strong correlations to human performance are perhaps not surprising. Regardless, the results in the current dissertation support the use of MPC for assisted FIP balance.

Given the adoption of exoskeletons in the scientific community being a fairly recent event, there are relatively few existing experimental studies that focus on FIP balance. Rajasekaran et al. [284] specifically reported that ankle-hip motion (an ankle or hip strategy) was viable for postural balance assistance in hip-knee-ankle lower-limb exoskeletons; however, their approach was model-free and targeted towards rehabilitation, i.e., physically encouraging the user and helping via AAN. The investigators did not assess changes in postural kinematics and kinetics that occur when someone wears an exoskeleton. Emmens et al. [103, 105] assessed performance of their PD and momentum-based control laws in response to push perturbations; however, comparisons to their results are difficult as they primarily reported the COM sway angle, only tested forward fall conditions, and did not have hip actuation. However, they did note the following: i) forward falling produced ankle plantarflexion in both zero-impedance and assisted trials; ii) participants maintained a flexed knee [103]; though the latter was maintained through a separate PD controller. The pronounced plantarflexion observed by the authors (not observed in the current study), suggests use of a hip strategy and may indicate that the push disturbance they used created a larger perturbation to the COM than the support-surface translations used herein. Beck et al. [50] also only tested backward support-surface translations (forward falling; the other direction was used only for "catch" trials) and assistance via an ankle exoskeleton. Not surprisingly, given the larger perturbations used by these authors, they observed larger forward net COM displacements following backward surface translations (approximately 15 cm) than the values we reported (max deviation approximately 5 cm). Though this dif-

ference could also be influenced by the much bulkier hip-knee-ankle exoskeleton we tested as well as any damping associated with it. Lastly, Mileti et al. [243] recently investigated human balance recovery while wearing the EXO-H2; however, the actuators were decoupled (no actuator friction or reflected inertia). The authors were interested in how the restrictive DOF of the H2 impacted young adult balance recovery rather than testing of proposed assistive controllers. To our knowledge, this is the only other study to assess user postural kinematics with and without wearing the assistive device. While the perturbations tested by these authors were rotational, we still draw comparisons to our own results. Surprisingly, unlike herein, the authors reported no significant change in the joint range of motion spanned when recovering balance with the EXO-H2. With friction compensation alone, we saw a shift in quiet standing posture while wearing the exoskeleton (resting hip flexion to compensate for battery mass), in addition to a reduction in deviations across all joints during recovery itself (see Fig. 7.11 and Fig. 7.12). The authors did not mention the device battery (see Chapter 4), and given the decoupling of the actuators, it is reasonable to believe that it was not fixed behind the user during testing and thus did not require user compensation. The authors also did not disseminate time-series joint kinematics or EMG measurements, so it is difficult to fully ascertain how the CNS was coordinating balance recovery in those studies as a function of time. Rather, small ranges of motion outcomes suggest an ankle strategy was used in No Exo conditions in [243], whereas hip and knee motion were used by participants to recovery balance in the current study (see Fig. 7.11). Inline with our own observations however, Mileti et al. [243] did report that COP displacements while wearing the exoskeleton were increased only when the induced fall was in the backward direction. The authors infer that the increased COP deviations suggest that the exoskeleton was less stable, i.e., a reduced margin of stability. However, if we consider the margin of stability definition using XCOM from Hof [154], there was no significant difference between Exo and No Exo herein.

There were numerous limitations not yet discussed for the current investigation: foremost, assistance was scaled too low during testing to gauge how the MPC component of control influenced the general balance strategy and end-user adaptations. As stated prior, the results obtained better describe "human-first" or zero-impedance control of FIP balance while wearing a lower-limb exoskeleton (i.e., assisted by the friction compensation) [103, 105, 288]. In that sense, the study herein is closer in idea to the study by Mileti et al. [243], wherein the EXO-H2 with decoupled actuators was tested on a platform that delivered rotational perturbations. Therefore, future studies should deliver higher and con-

sistent assistance torques to non-disabled end-user to determine how the proposed MPC controller affects the end-user motor control, e.g., motor adaptations/learning, prior to studying withing clinical populations. In future studies, larger perturbations should also be investigated with a refined AAN scheme (see next section), especially for the backward direction, e.g., perturbations in Beck et al. [50]. Larger perturbations will also be necessary as we move towards controllers that can assist in maintenance of FIP and change in support balance. Lastly, the low COM-based assistance may have also been exacerbated by the toe/heel raise observed during human-exoskeleton balance recovery. In the future, inertial measurement units (IMU) should be included to provide better estimations of segment orientation in space [103, 105, 135, 138].

Possible Control Architecture Revisions

In Fig. 7.5, it is evident that the magnitude of the scaled active MPC torques was quite low relative to the joint breakaway friction (≈ 6 Nm). From this observation, we suggest that the most glaring issues in the current study stem from the overly complicated nature of the COM-scaling functions as well as the use of multiplicative COM terms. In hindsight, a better COM-based assistance system would be additive in COM position-velocity terms [154, 174]. Similarly, a simpler and more effective approach could have been employed rather than trying to incorporate and tune a novel FSR-based deadband system. Therefore, we propose the following changes to the control architecture (shown in Fig. 7.13):

Instead of scaling the MPC-derived ideal torque by an assistance variable determined by the COM state, we suggest instead separating the MPC-derived torques into a feedback and feedforward component [48]:

$$\boldsymbol{\tau}_{\text{mtr}} = \boldsymbol{\tau}_{\text{fb}} + \boldsymbol{\tau}_{\text{ff}} \tag{7.18}$$

where $\boldsymbol{\tau}_{\text{ff}} \in \mathbb{R}^3$ is the vector of ideal torques that are responsible for keeping the autonomous system upright and static (obtained from the user's starting position). Therefore, $\boldsymbol{\tau}_{\text{fb}}$ are the remaining feedback torques that emerge in response to deviations away from the equilibrium configuration. We can then reconstruct an assistive torque from $\boldsymbol{\tau}_{\text{mtr}}$ as

$$\boldsymbol{\tau}^*_{\text{fb}} = \chi_{\text{fb}}\boldsymbol{\tau}_{\text{fb}} \tag{7.19}$$

$$\boldsymbol{\tau}^*_{\text{ff}} = \chi_{\text{ff}}\boldsymbol{\tau}_{\text{ff}} \tag{7.20}$$

$$\boldsymbol{\tau}^*_{\text{mtr}} = \boldsymbol{\tau}^*_{\text{fb}} + \boldsymbol{\tau}^*_{\text{ff}} \tag{7.21}$$

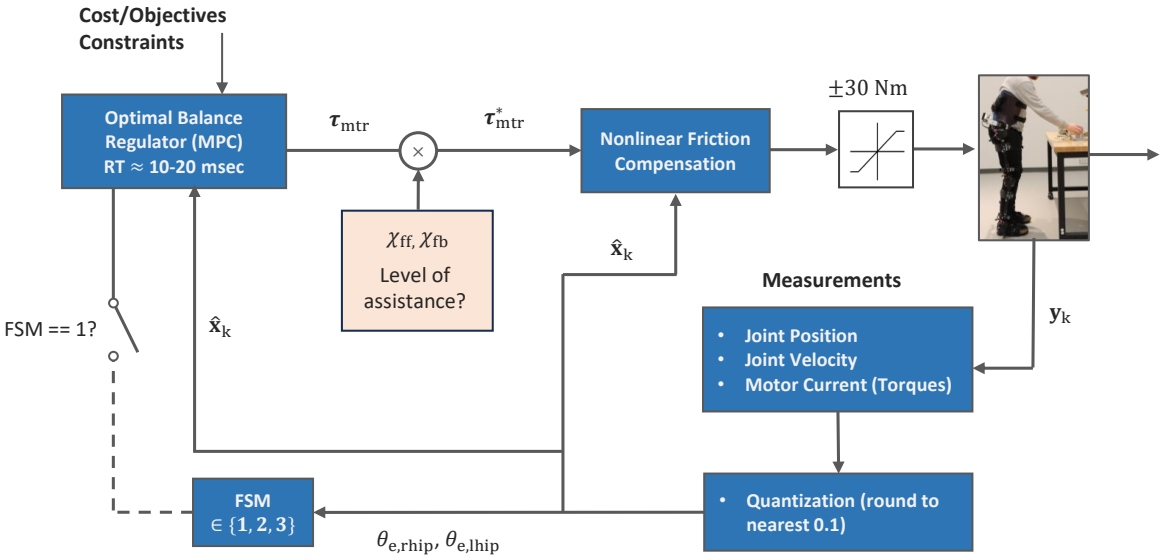


Figure 7.13: Revised model predictive control (MPC) assistance architecture using simpler assistance parameterization via χ_{ff} and χ_{fb}.

where $\chi_{\text{fb}} \in [0, 1]$ and $\chi_{\text{ff}} \in [0, 1]$ are simple assistive tuning parameters. This law assumes that the $(1-\chi_{\text{fb}})\boldsymbol{\tau}_{\text{fb}}$ and $(1-\chi_{\text{ff}})\boldsymbol{\tau}_{\text{ff}}$ torque components will be supplied by the user instead. Therefore, if $\chi_{\text{ff}} = 0$ and $\chi_{\text{fb}} \neq 0$, the user will receive assistance for deviations away from their static posture only; they must supply the torque to remain in quiet standing themselves. This draws inspiration from the much simpler PD control laws tested in experiments by [103, 105], where the authors had to include an additional feedforward torque for some paraplegic users to stand quietly in the exoskeleton.

To show how this control law may perform in experiments, we used our simulation interface in Chapter 6. In these simulations, the human CNS was modeled using the LQR outlined in 6 while the MPC output was now scaled by the new assistive control law (7.21). Three tests were conducted for balance recovery following the relatively challenging forward perturbation listed in Table 7.4:

1. TEST 1: $\chi_{\text{fb}} = 1$, $\chi_{\text{ff}} = 1$, $\tau_{\text{max\%}} = 0$

2. TEST 2: $\chi_{\text{fb}} = 0.75$, $\chi_{\text{ff}} = 0.25$, $\tau_{\text{max\%}} = 10\%$

3. TEST 3: $\chi_{\text{fb}} = 0.20$, $\chi_{\text{ff}} = 0$, $\tau_{\text{max\%}} = 100\%$

where $\tau_{\text{max\%}}$ is what percentage of the maximum isometric MTG torques that the human LQR can feasibly generate. Therefore, $\tau_{\text{max\%}} = 0\%$ when the human end-user can provide absolutely no active torques to the system, while $\tau_{\text{max\%}} = 100\%$ indicates a non-disabled end-user. In each simulation, the human-exoskeleton system was initialized with the mean joint angles shown in Fig. 7.4 and zero joint velocities. The simulated joint angles and control torques for each test, the latter from experiments being shown in Fig. 7.5, are displayed in Fig. 7.14. Note that in all cases, the ZMP's position never exceeded the posterior BOS boundary (5.99 cm posterior to the ankle), despite the integrated system being controlled by two separate controllers that have no knowledge of each other, i.e., like a person who has never experienced the exoskeleton balance control law OR perturbation beforehand. The resulting COM trajectories shown in Fig. 7.15 show quite a high agreement with the experimental human-exoskeleton COM deviations shown in Fig. 7.3 (see the red trajectory in the forward condition; HE-E), especially in the case of autonomous control (TEST 1). Not surprisingly, the other test cases show some degree of over-correction in the COM position. Lastly, we note that larger magnitude and consistent delivery of MPC torques within the revised assistive control scheme proposed (Fig. 7.14). Even in the case of a non-disabled individual (TEST 3), the magnitude of assistive torques was much higher than in experiments with the proposed COM-assistance, i.e., ankle torques reached 10 Nm compared to being $>$ 1 Nm (max 3 Nm) in experiments. While it's possible that further refining of the COM-control law could achieve similar results in simulation, again, we believe that it over-complicated the tuning and control implementation process.

There are other factors to consider when revising the control architecture. Friction compensation could in theory be achieved using a different underlying friction model such as a bristle-state model, e.g., Lugre, elastoplastic, or Gonthier [128, 142, 269]. With that said, we do not believe that doing so would improve performance; in fact, Hauschild [142] reported slightly weakened friction compensation performance when using a Lugre friction model in comparison to a purely velocity-dependent model. Another possible modification could be a separate controller that tries to keep the end-user in the upright standing state within the finite-state machine. For example, using one leg's joints for reference, a computed torque control law could be used to have the contra-lateral leg motion imitate the reference leg's. However, this controller could also be quite disruptive to the end user; any

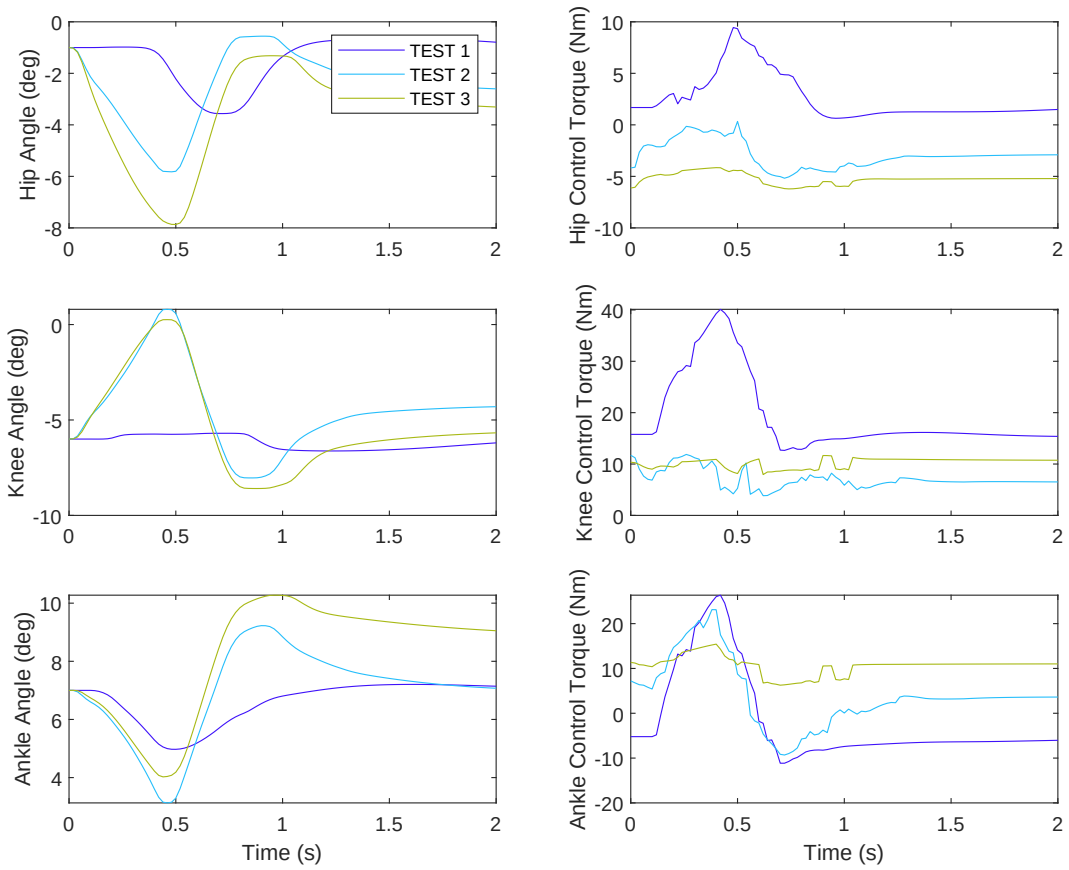


Figure 7.14: Simulated human-exoskeleton joint angles (left) and control torques (right; desired torques input to the friction compensation block) for tests 1-3 where the simulated end-user experienced a forward perturbation.

delays between the legs could exacerbate instability. Likewise, the tuning of the control law could impede a user's ability to initiate a step if a fixed BOS is no longer possible for balance maintenance. In these regards, we do also plan on adding assisted stepping strategies in the future, though these were not the focus for the current dissertation.

In addition to the revisions suggested above, we also propose the following revisions, although these are of less immediate importance: inherently, especially with a commercial unit with restricted DOF, it can be expected there will be some minor joint misalignments when fixing the end-user to the exoskeleton and during operation. In experiments, it is possible to potentially remedy this using motion capture; however, that process can still be quite challenging. Furthermore, not all research, clinical, or personal settings may have access to real-time 3D motion capture information to improve joint alignment and the

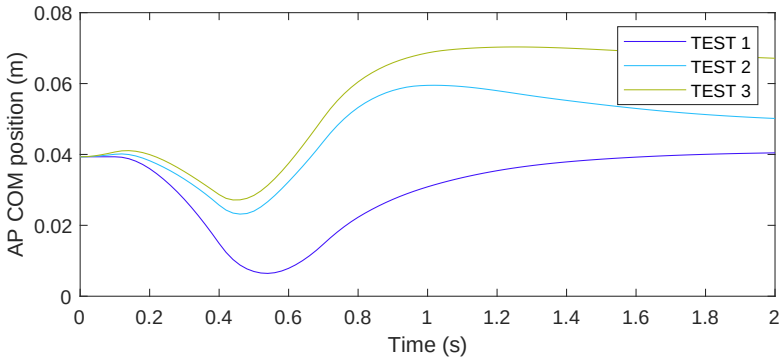


Figure 7.15: Simulated human-exoskeleton anteroposterior COM position (with respect to the ankle) for tests 1-3 where the simulated end-user experienced a forward perturbation.

matching of human and exoskeleton joint angles. The presence of elastic strapping and tissue deformation and consideration of end-user comfort can also impact device alignment. With that established, future investigations into FIP control will involve a robust MPC derivation, e.g., tube-based MPC, wherein we still use the *nominal* control law, i.e., from 6.2.4, but modify it with a separate "tube" control law that help keep the states relatively close to those being used in the MPC [68]. Likewise, with further optimization, we can incorporate the state-estimation procedures in 6.2.5 as well as investigate further state estimation procedures to improve the robustness of the finite-state machine estimation [159, 236, 237, 323], i.e., when it is appropriate to trigger the MPC. Doing so would also address the phase-delay issue encountered when testing real-time IIR filtering, could improve disturbance recognition for balance recovery, as well as active muscle torque estimation for intect recognition systems.

Chapter 8

Conclusions

8.1 Summary of Contributions

Maintaining upright balance when wearing a powered lower-limb exoskeleton can be challenging. Often, device manufacturers require the end-user to use crutches to regulate balance and stability. Thus, the current dissertation focused on the idea of *crutch-less* human-exoskeleton balance control. A novel approach to studying human-exoskeleton balance control via computationally-efficient dynamic simulations and linear/nonlinear feedback optimal control methods was presented in Sections 3 and 6. Human-exoskeleton simulations used optimized symbolic multibody dynamic models of the human musculoskeletal system and lower-limb robotic exoskeleton (based on the Technaid EXO-H3) (Chapters 3-5); a novel compliant approach to coupling these two systems using principles of contact mechanics was presented in Section 5. Methods of parameter identification with the EXO-H3 commercial lower-limb exoskeleton to help support the dynamic simulations conducted (Chapter 4). Lastly full-state feedback FIP balance regulators and nonlinear state estimation methods were designed and tested in Chapter 6, i.e., systems that ensure that sagittal plane balance is maintained (no step required) without external assistance from crutches. The most novel contribution of these, i.e., the constrained MPC, was implemented in Section 7 alongside a novel AAN COM-scaling component; though, the latter scaled the assistive torques insufficiently and requires further revisions. The following sections will briefly summarize the contributions of this dissertation:

Dynamic Simulations of Human-Only FIP Balance Recovery

- Reformulation of the FSR optimal control problem using constrained single-objective NLP: transcribed as direct collocation with symbolic derivatives [172]. Previous methods relied on direct shooting methods with a large number of objective criteria [175, 369, 370].

- First application of Pareto optimization to assess trade-offs in the anteroposterior FSR size with minimization of end-user or device "effort" [172] — an extension of previous musculoskeltal simulations that used manual tuning of cost function objectives and specific perturbations [77, 202, 344].

- Curve-fitting approximation method for piecewise MTG functions, motivated by the approach of Millard et al. [244], a useful tool for tuning the stiffness of MTG functions when utilizing derivative-based optimization methods. Note that Millard's method involved fitting the MTG functions to piecewise Bézier splines over specific intervals of the functions [244]; the method herein uses smoothing functions like in De Groote et al. [88] to ensure the splines are always C^2 continuous even with small numerical errors in the Bézier coefficients.

- Dynamic simulations of human FIP balance recovery using NMPC [170] — to our knowledge this is the first application of this method. Previous applications of MPC-driven human balance simulations have involved simple linear pendulum models [25, 26]. Other feedback human balance simulations have involved linear models, e.g., LQR [202, 203]. Nonlinear optimal control has only been applied for open-loop simulations [77, 78, 172, 175, 344].

- Investigation of arm strategies in balance recovery as they emerge from optimal control, e.g., can arm movement increase the size of the feasible stability region or do they assist in reducing other costs of balancing? [170] Arm motion is typically neglected in simulations of FIP balance [77, 202, 344]. According our simulations, countermovement arm strategies have no substantial impact on the capturability of FIP balance, i.e., the AP FIP FSR was not improved with execution of an optimal arm strategy in the sagittal plane. However, FIP balance recovery simulations driven via our novel NMPC approach suggested that arm motion may emerge when the CNS

minimizes muscle (MTG) activations while keeping the body in the FIP domain of feasibility.

Symbolic Human-Exoskeleton Multibody Dynamic Model

- Development of a lower-limb robotic exoskeleton model, joining other recent additions to the multibody dynamics literature [33, 295]. The design of the current model was based on the Technaid EXO-H3, featuring nonlinear joint impedance via a regularized friction model [65] (exoskeleton actuators are often modelled as ideal [105, 134]). The model designed herein is used to study human-exoskeleton FIP balance control, but its generalized formulation can be employed in the study of a variety of human-exoskeleton tasks, e.g., sit-to-stand, sagittal walking, change-in-support balance, etc.

- Extension of the parameter identification experiment design method by Swevers et al. [318]; mathematical approach to designing a sequence of multibody parameter identification experimental joint trajectories to be used with commercial exoskeletons (Swevers et al. proposed a method with a single experiment).

- Application of the inverse dynamics optimal exciting parameter identification method to commercial exoskeletons with their standard sensor configuration [120, 117, 282, 318]. To our knowledge, this is the first application of these methods typically used in industrial robotics to commercial lower-limb exoskeletons.

- Comparison of inverse and forward dynamics approaches, including presentation of a novel MHE method in experimental parameter identification of a commercial exoskeleton without modifications (EXO-H3). Similar to previous work done by Gautier and Poignet [121], however, these authors compared the least-squares inverse dynamics method to EKF dual-estimation on an industrial manipulator. Herein, we tested these methods with a commercial exoskeleton and investigated the standard forward dynamics approach (no EKF, [124, 300, 347]) in addition to proposing a a novel nonlinear MHE approach for parameter estimation.

- Development of a coupled human-exoskeleton model to be used within forward dynamic simulations using rigid and compliant contact principles. Rigid connections are standard practice in human-exoskeleton modelling [33, 63, 105, 103, 134, 138,

226, 295]; however, in the current dissertation, we provide a generalized derivation of reaction forces/torques at different points of application. Most novel herein was the proposed compliant coupling system; to our knowledge, this is the first application of using separate unilateral contact elements to create asymmetrical bilateral human-exoskeleton contact forces, i.e.,

  - Preliminary design of a point-contact (Hunt-Crossley [161]) human-exoskeleton contact model to capture unilateral interactions between rigid cuffing elements and soft human tissue.
  - Preliminary design of human-exoskeleton contact model to capture unilateral interactions between elastic strapping elements and soft human tissue.

  and it is the first nonlinear human-exoskeleton compliant coupling model [98, 293, 301]. Most examples of interaction models tend to assume the exoskeleton applies force equally between anterior and posterior directions or only assess one direction of loading [293, 301].

Dynamic Simulations of Human-Exoskeleton Balance Recovery

- Assessment of human-exoskeleton feasible stability region [264, 370] to quantify how certain features of the exoskeleton system design can impact the stability of the end-user under ideal scenarios. Previous dynamic simulations of human-exoskeleton motor control (specifically for lower-limb exoskeletons) have been primarily driven by experiments [295]. Herein, the dynamic simulations of human-exoskeleton were fully predictive and nonlinear; previous predictive simulations have used much simpler models [106, 211].
- Development of a multitude of model-based full-state feedback control schemes for autonomous or assistive human-exoskeleton balance recovery, including real-time control schemes based around unconstrained, i.e., linear quadratic regulator (LQR), and constrained optimal control, i.e., model predictive control (MPC). To date, constrained lower-limb exoskeleton FIP balance controllers proposed in the literature have mainly utilized centroidal momentum methods (not an optimal controller) [103, 105]; methods that could be considered close to full-state feedback have mainly

been simple PD controllers that do not consider optimality. The MPC controller proposed herein addresses both of these gaps in full-state feedback control of current FIP balance (optimal+constrained) and produces control torques for the hip, knee, and ankle. Thus, in theory, the proposed MPC should be able to produce human-like balance recovery strategies with greater fidelity than COM/centroidal momentum methods [103, 105]. This statement is based on the results of [48]: full-state feedback performed better in replicating human balance control in comparison to momentum control. MPC is both full-state feedback and optimal (over a finite horizon), which further strengthens its use [202, 344].

- Development of real-time state and disturbance estimation algorithms for standing human-exoskeleton balance; the approaches are based on Kalman filtering and nonlinear MHE [310], the latter of which is particularly novel. To our knowledge, this is the first application of nonlinear MHE for FIP state estimation in human-exoskeleton systems. The MHE has been used in humanoids for state estimation [39] and in lower-limb exoskeletons for gait event detection [323], but no applications to human-exoskeleton FIP balance with disturbance recognition. The symbolic formulation of the MHE presented herein produces rapid iterations within the NLP solver that help ensure real-time implementation.

Implementation of Assistive Model-Based Balance Controllers

- Novel model-based COM position-velocity AAN assistance profile for scaling FIP balance torques. This approach was based on the use of the COM, XCOM and FSR in scaling ankle assistance for perturbed human-exoskeleton walking [24, 49] and step-placement determination [197, 343, 348]. Unfortunately, the COM AAN approach resulted in poorly scaled MPC torques, i.e., scaled too low.

- Experimental testing of the novel MPC assistive balance control scheme (in Chapter 6) with young adult participants in Dr. Andrew Laing's laboratory at University of Waterloo [358].

- Obtained novel kinematic and kinetic data related to the human control of balance while wearing a powered hip-knee-ankle exoskeleton and provided with active compensation of the actuator friction [142] with a continuous velocity-based friction model [65]. One previous passive study of human-exoskeleton balance control

(for hip-knee-ankle exoskeletons, the EXO-H2) featured uncoupled actuators that reflected no inertia or friction onto the end-user [243]. Additionally, the authors used rotational perturbations rather than linear translations to test balance. With that said, they are the only other study aside from the one herein that investigated FIP balance with and without the exoskeleton.

8.2 Recommendations for Future Research

In this section, the following possible directions for future research are provided: i) improving models and simulations of integrated human-exoskeleton systems; ii) further development of exoskeleton-assisted balance recovery architectures; and iii) investigations into disturbance/user-intent recognition and improving observations of end-user/device states.

Modeling Human-Exoskeleton Systems

Exoskeletons are intended to assist a variety of individuals [334]. Thus, future research should be focused on creating and validating variations of the human-exoskeleton model presented herein to closer mimic the underlying physiology of clinical groups. For example, modifying the MTG model to better account for increased tonicity and other features commonly observed in those with stroke could allow for better tuning of FIP balance controllers within simulations, prior to use [271]. Likewise, older adults tend to exhibit declines in their neuromuscular physiology, such as increased reflex delays [80, 286]. Including variable delays within the simulations could greatly improve functionality of the FIP simulation interface. Additionally, this future work could be extended to assessing feasibility of subject-specific tuning, e.g., height/weight scaling terms for segmenti inertia.

Contact models of different human-device interaction elements used within biomechatronic design can provide valuable predictive information into applied pressure, possible pressure injuries, and dangerous joint loading during use [220]. Most work to date in building coupled human-exoskeleton models has used rigid connections. The novel approach herein involved principles of contact mechanics with 3D geometry; however, it still requires experimental validation. Such a validation could involve using pressure sensors during human-exoskeleton treadmill walking or standing experiments. Validating the model using data specific to human-exoskeleton interactions is important, i.e., to obtain

model parameters that consider human tissue compliance like in Sanchez-Villamañán et al. [293]. Comparisons with the kinematic constraint method would also provide clarity into the accuracy of information we can obtain from these contact forces in relation to the explicit contact models. The proposed model could also use further iterations to improve numerical stability and performance [247]. Lastly, future work should be directed to modelling and simulation of human-exoskeleton interactions when the model DOF span more than one plane, i.e., interactions in the mediolateral directions.

The EXO-H3 and many other lower-limb exoskeletons are designed to assist the user with purely sagittal plane motions (see Section 2). Any movement the end-user has within the frontal plane is due to deflections of the materials used to construct the device, i.e., no actuated DOF. As such, the model designed herein was also limited to the sagittal plane. The dynamic model used for control of the ATALANTE X was 3D but only considered inertial, motorized, and gravitational terms [134]; no consideration of the underlying muscle forces was included in the model equations. Experimentally we assessed how the EXO-H3 performed in responses to perturbations in the frontal plane in Chapter 7. Others did similar work recently with rotational perturbations, though only after uncoupling the actuators (in Chapter 7, [243]). Therefore, an interesting future direction of research for these systems with restricted DOF would be developing a coupled human-exoskeleton model wherein the human has multiple DOF that permit motion across all three anatomical planes while the exoskeleton has only sagittal DOF. However, instead of constructing the multibody dynamic model of the exoskeleton using rigid bodies, flexible bodies could be used to allow the human to deflect segments when necessary, e.g., modulating step width in the EXO-H3 for lateral gait stability. Such a model would allow simulation investigations that draw parallels to those that we and Mileti et al. [243] performed experimentally, but without any risk to the end-user or need to go through safety precautions to test.

For commercial exoskeletons like the EXO-H3, it is evident that the onboard sensors alone are not always sufficient for reliable dynamic parameter identification. Future work should continue investigating methods of non-invasive identification methods that can improve model-based control, e.g., different exciting trajectory cost functions and improving torque measurements without heavy device alterations. It would be interesting to develop a standardized approach to obtaining biomechatronic parameters for model-based assistance. Features like scan-to-CAD devices could improve biomechatronic-specific inertial parameter estimations, though still leave the engineer, clinician, or researcher the need to identify actuator parameters, which can be notably difficult (Chapter 4). A shift in the

state-of-the-art exoskeletons towards direct-drive systems would also help remedy these issues, but this requires further work in the development of small but high-torque density motors [214]. Furthermore, given the discussion on state estimation in Chapter 6, it would be interesting to test a dual-estimation approach for the FIP balance recovery MHE; however, the limited onboard sensors for the EXO-H3 would make this unreliable due to poor observability.

Lastly, future research should investigate simulations of change-in-support strategies to assess how exoskeletons affect a variety of postural responses, not just those with FIP. Inspiration can be drawn from the recent examples of perturbed human-exoskeleton walking simulations by Schemschat et al. [294]. The authors use principles of hybrid bipedal dynamics with impulse-momentum theory to model foot-ground impacts [133]. Parameter based methods could also be developed and used for permitting change-in-support motion, e.g., the Hunt-Crossley model in Gonthier et al. [128, 161], though identification of these parameters could be challenging, especially for the exoskeleton foot pad. This future work could also address sensitivity of the proposed FIP control laws when lifting of the toe or heel occurs during assistance [78] (see Chapter 7). In terms of human motor control simulations alone, future research on the FIP NMPC should investigate cost functions not considered in the current dissertation [55, 250] as well as predictions of end-user learning through manipulation of the control-oriented model, i.e., how the user updates their internal model of dynamics when donning the exoskeleton.

Exoskeleton-Assisted Balance Control

The full-state feedback approaches proposed in the current dissertation are all specialized to control/assist with FIP balance. An obvious extension to this is a controller that can assist with change-of-support balance recovery. Multiple controllers have been proposed with respect to human-exoskeleton balance control via step placement; all of these are based on the XCOM model [197, 343, 348]. Other capture point systems could be investigated for the estimation of foot placement for change-in-support balance recovery, e.g., the foot place estimator (FPE) [92, 245, 356]. Farkhatdinov et al. [109] recently proposed a simple system based on a feedforward assistive hip flexion torque profile; however, their system also required disturbance recognition through perturbations of the pelvis (see next section). The methods used by Gurriet et al. [134] involves principles of differential geometry, feedback linearization, and hybrid invariant sets to obtain model-based gait patterns that are stable.

The same approach could be used with change-in-support balance and could potentially be paired with existing NMPC or MPC methods used for stable gait/balance in humanoids [259].

A less obvious extension to the proposed assistive balance recovery architecture is the development of logic with which we use to transition between the two categories of balance recovery. Humans select between postural responses based on a multitude of complex factors [223]. A simple approach could use the COM phase-space to switch from a FIP approach to a change in support approach once that COM has entered an unstable region of the FSR, i.e., COM not capturable with FIP. However, the approach becomes less clear once the end-user enters double-support following the step(s), i.e., whether a separate controller is needed to return the system to quiet standing with bilateral symmetry between right and left legs. It may also be interesting to develop controllers that interact with environment recognition systems so that context can be used to inform the selection of postural strategy [206]. Ultimately, the choice of balance controller used in real-time may be best left to the end-user through advancements in intent recognition, though that is not without its challenges (see next section).

When discussing computational performance and future directions, it is obvious to suggest work be put into producing faster NLP algorithms, e.g., improving interior-point method speed, improving sparse linear algebra performance, solving linear equations in Newton algorithm, etc [219]. In the current dissertation, linear optimal control methods were used for assistance; nonlinear methods of exoskeleton control involved no optimization (computed torque control; Appendix L). Note that the human NMPC was both nonlinear and optimal (over a finite horizon), but was not suitable for any real-time applications (slow convergence speeds). State estimation was nonlinear, though the NLP required to solve in the MHE was much smaller in scale compared to the MPC balance regulator, i.e., moving window size versus prediction horizon size. Improvements to interior-point QP solving algorithms would allow for real-time MPC with larger prediction horizons and potentially less concern of convergence without imposing terminal constraints.

Disturbance Recognition and End-User Observation

In Chapter 6, it was difficult to identify disturbance torques and end-user MTG torques separately within the FIP balance recovery simulations. This challenge was the result of the

minimal sensors available on many commercial exoskeletons without further modifications, i.e., it is a problem of observability. The question raised is whether optimal configurations exist for high-fidelity sensor fusion in human-exoskeleton systems. Sensor fusion techniques have been used to describe how the CNS coordinates the redundant sensory information available to it to estimate body states, e.g., proprioception and vestibular information [203, 342, 341]. Ideally, the state estimation for bipeds should utilize the floating-base dynamics so that estimates are not invalidated once a change-in-support occurs (i.e., estimation not constrained to finite states [334]); however, such a model is computationally expensive and estimation requires a variety of sensors. On the EXO-H3, we originally intended to use the pressure sensors/switches located in the foot pads to construct a multi-phase MHE that could estimate joint angles/velocities for different configurations of foot contact. To date, MHE has been used to estimate gait events accurately in human-exoskeleton walking [323]. However, the sensors were faulty and could not be used in the current dissertation. Recent work in state-estimation in exoskeletons has been directed towards identifying states within phases of the gait cycle [159, 237, 236, 323], i.e., identifying the modes of the multi-phase MHE problem [133, 219]. Lastly, optimized sensor configurations could be used to improve estimations of human-exoskeleton COM for real-time control. Many proposed control architectures in the literature rely on IMUs for humanoid state estimation [39, 105, 135, 275, 314, 315]; however, herein we relied on the onboard rotary encoders with the assumption that the foot would remain flat. However, in Chapter 7, we observed the humans wearing an exoskeleton would still often raise their heel or toe during balance recovery, thus reducing the quality of the COM estimation.

According to Tucker et al. [334], ideally, the exoskeleton actions will line up exactly with the user intent provide assistance as needed, i.e., control is AAN. Systems that rely on the end-user being in charge are often seen in rehabilitative settings as they can assist in improving end-user mobility, so long as there is no slacking [287, 340]. In Chapter 7, we proposed a COM position-velocity based AAN assistance profile based on the use of the XCOM throughout the recent exoskeleton literature to either scale assistance [24, 49, 105, 103, 353] or estimate step placement [343, 345, 348]. The intention was to scale the model-based optimal torques higher when the COM was in regions of the FIP FSR that were closer to the boundaries of stability, i.e. assume the user needs assistance only when they become closer to the "fall" threshold. Assistance was based on novel COM-scaling functions designed using Bézier splines. Ultimately however, the COM AAN was sensitive to poor joint-based COM estimates and was difficult to tune such that a reliable

response was obtained. If the balance recovery response should be initiated by end-user intent, there must be further development of accurate intent recognition algorithms [255, 256, 257, 258]. Additionally, as discussed in Section 2, the average human responds to an external perturbations in approximately 100 ms [50, 158, 344]. However, certain groups of individuals, especially those in clinical populations, experience noted delays in their neuromuscular physiology [80, 221]. Thus, future research should investigate the risk-versus-reward (safety) of intent-driven AAN balance recovery across clinical end-users.

Letter of Copyright Permission

See next page.

SPRINGER NATURE LICENSE
TERMS AND CONDITIONS

Oct 26, 2023

This Agreement between Keaton Inkol ("You") and Springer Nature ("Springer Nature") consists of your license details and the terms and conditions provided by Springer Nature and Copyright Clearance Center.

License Number	5656700461928
License date	Oct 26, 2023
Licensed Content Publisher	Springer Nature
Licensed Content Publication	Multibody System Dynamics
Licensed Content Title	Muscle torque generators in multibody dynamic simulations of optimal sports performance
Licensed Content Author	Keaton A. Inkol et al
Licensed Content Date	Jun 5, 2020
Type of Use	Thesis/Dissertation
Requestor type	academic/university or research institute
Format	electronic
Portion	full article/chapter
Will you be translating?	no
Circulation/distribution	50000 or greater
Author of this Springer Nature content	yes

Title of new work	Dynamics and Model-Based Control of Balance Recovery in Humans Using Lower-Limb Exoskeletons
Institution name	University of Waterloo
Expected presentation date	Dec 2023
Requestor Location	Keaton Inkol 508 Beechwood Dr Waterloo, ON N2T 1H3 Canada Attn: Keaton Inkol
Total	0.00 USD

Terms and Conditions

Springer Nature Customer Service Centre GmbH Terms and Conditions

The following terms and conditions ("Terms and Conditions") together with the terms specified in your [RightsLink] constitute the License ("License") between you as Licensee and Springer Nature Customer Service Centre GmbH as Licensor. By clicking 'accept' and completing the transaction for your use of the material ("Licensed Material"), you confirm your acceptance of and obligation to be bound by these Terms and Conditions.

1. Grant and Scope of License

1. 1. The Licensor grants you a personal, non-exclusive, non-transferable, non-sublicensable, revocable, world-wide License to reproduce, distribute, communicate to the public, make available, broadcast, electronically transmit or create derivative works using the Licensed Material for the purpose(s) specified in your RightsLink Licence Details only. Licenses are granted for the specific use requested in the order and for no other use, subject to these Terms and Conditions. You acknowledge and agree that the rights granted to you under this License do not include the right to modify, edit, translate, include in collective works, or create derivative works of the Licensed Material in whole or in part unless expressly stated in your RightsLink Licence Details. You may use the Licensed Material only as permitted under this Agreement and will not reproduce, distribute, display, perform, or otherwise use or exploit any Licensed Material in any way, in whole or in part, except as expressly permitted by this License.

1. 2. You may only use the Licensed Content in the manner and to the extent permitted by these Terms and Conditions, by your RightsLink Licence Details and by any applicable laws.

1. 3. A separate license may be required for any additional use of the Licensed Material, e.g. where a license has been purchased for print use only, separate

References

[1] ABLE Human Motion. ABLE Exoskeleton, https://www.ablehumanmotion.com/able-human-motion-exoskeleton/.

[2] Angel Robotics. angel Suit, http://angel-robotics.com/ko/products/suit/overview.php.

[3] B-Temia. keeogo, https://b-temia.com/keeogo/.

[4] Bama Technology. RoboGait, https://www.medicalexpo.com/prod/bama-technology/product-95253-817416.html.

[5] CYBERDYNE. HAL Lower Limb, https://www.cyberdyne.jp/english/.

[6] Ekso Bionics, EksoNR, https://eksobionics.com/eksonr/?

[7] ExoAtlet. ExoAtlet II, https://exoskeletonreport.com/product/exoatlet-ii/.

[8] Fourier Intelligence International. ExoMotus, https://fftai.com/exomotus-m4-2/.

[9] GOGOA. HANK, https://www.gogoa.eu/en/exoesqueletos-medicos-hank.

[10] Hocoma. lokomat, https://www.hocoma.com/solutions/lokomat/.

[11] MyoSwiss. myosuit, https://myo.swiss/en/.

[12] Parker Hannifin (acquired by Eko Bionics). Indego, https://eksobionics.com/eksо-indego-personal/.

[13] ReWalk Robotics. ReStore Soft Exo-Suit, https://rewalk.com/restore-exo-suit/.

[14] ReWalk Robotics. ReWalk Personal, https://rewalk.com/rewalk-personal-3/.

[15] REX Bionics. REX, https://www.rexbionics.com/.

[16] SuitX (US Bionics, Inc). PheoniX, https://www.suitx.com/phoenix.

[17] Syrebo. EasyWalk Soft Exosuit, https://www.syrebo.com/assist-soft-exoskeleton-walker/.

[18] Technaid. EXO-H3, https://www.technaid.com/products/robotic-exoskeleton-exo-exoesqueleto-h3/.

[19] Wandercraft. atalante X, https://en.wandercraft.eu/.

[20] Population Projections for Canada, Provinces and Territories, 2021 to 2068, 2022. Technical report, Statistics Canada, 2022.

[21] World Health Organization, Disability, https://www.who.int/news-room/fact-sheets/detail/disability-and-health, Sept. 2023.

[22] H. Abdi. Bonferroni and Sidak corrections for multiple comparisons. In N. J. Salkind, editor, *Encyclopedia of Measurement and Statistics*, pages 103–107. Sage, Thousand Oaks, CA, 2007.

[23] A. Adelmann, P. Arbenz, A. Foster, and Y. Ineichen. A Homotopy Method for Large-Scale Multi-Objective Optimization. 2015. Publisher: arXiv Version Number: 1.

[24] M. Afschrift, E. Van Asseldonk, M. Van Mierlo, C. Bayon, A. Keemink, H. Van Der Kooij, and F. De Groote. Assisting walking balance using a bio-inspired exoskeleton controller. preprint, Biophysics, Oct. 2022.

[25] Z. Aftab, T. Robert, and P.-B. Wieber. Predicting multiple step placements for human balance recovery tasks. *J Biomech*, 45(16):2804–2809, 2012.

[26] Z. Aftab, T. Robert, and P.-B. Wieber. Balance Recovery Prediction with Multiple Strategies for Standing Humans. *PLOS ONE*, 11(3):e0151166, Mar. 2016.

[27] A. V. Alexandrov, A. A. Frolov, F. B. Horak, P. Carlson-Kuhta, and S. Park. Feedback equilibrium control during human standing. *Biol Cybern*, 93(5):309–322, 2005.

[28] J. H. J. Allum, M. G. Carpenter, F. Honegger, A. L. Adkin, and B. R. Bloem. Age-dependent variations in the directional sensitivity of balance corrections and compensatory arm movements in man. *The Journal of Physiology*, 542(2):643–663, 2002.

[29] M. Z. Amilibia, C. Cortes, A. B. Simonetti, A. Satrustegi, M. Iturburu, I. Reina, J. Finez, M. Alonso-Arce, and P. Callejo. Preliminary evaluation of an objective assessment approach from session data in exoskeleton-assisted gait rehabilitation after SCI. In *2021 43rd Annual International Conference of the IEEE Engineering in Medicine & Biology Society (EMBC)*, pages 6019–6024, Mexico, Nov. 2021. IEEE.

[30] K. N. Anakhaev. Analytical Determination of Arc Length of an Elliptic Curve. *Mech. Solids*, 54(7):1115–1118, Dec. 2019.

[31] D. E. Anderson, M. L. Madigan, and M. A. Nussbaum. Maximum voluntary joint torque as a function of joint angle and angular velocity: model development and application to the lower limb. *Journal of Biomechanics*, 40(14):3105–3113, 2007.

[32] F. C. Anderson and M. G. Pandy. A Dynamic Optimization Solution for Vertical Jumping in Three Dimensions. *Comput Methods Biomech Biomed Engin*, 2(3):201–231, 1999.

[33] A. Arami, E. Van Asseldonk, H. Van Der Kooij, and E. Burdet. A Clustering-Based Approach to Identify Joint Impedance During Walking. *IEEE Trans. Neural Syst. Rehabil. Eng.*, 28(8):1808–1816, Aug. 2020.

[34] E. M. Arnold, S. R. Ward, R. L. Lieber, and S. L. Delp. A model of the lower limb for analysis of human movement. *Ann Biomed Eng*, 38(2):269–279, Feb. 2010.

[35] M. Arquilla, I. Pisotta, F. Tamburella, N. L. Tagliamonte, M. Masciullo, A. R. Wu, C. Meijneke, H. van der Kooij, A. J. Ijspeert, and M. Molinari. Walking Assistance of Subjects with Spinal Cord Injury with an Ankle Exoskeleton and Neuromuscular Controller. In M. C. Carrozza, S. Micera, and J. L. Pons, editors, *Wearable Robotics: Challenges and Trends*, volume 22, pages 304–308. Springer International Publishing, Cham, 2019.

[36] C. G. Atkeson and B. Stephens. Multiple balance strategies from one optimization criterion. In *2007 7th IEEE-RAS International Conference on Humanoid Robots*, pages 57–64, Pittsburgh, PA, USA, Nov. 2007. IEEE.

[37] F. Augugliaro and R. D'Andrea. Admittance control for physical human-quadrocopter interaction. In *2013 European Control Conference (ECC)*, pages 1805–1810, Zurich, July 2013. IEEE.

[38] D. L. Bader and M. J. Pearcy. Material properties of Velcro fastenings. *Prosthetics & Orthotics International*, 6(2):93–96, Aug. 1982.

[39] H. Bae and J.-H. Oh. Humanoid state estimation using a moving horizon estimator. *Advanced Robotics*, 31(13):695–705, July 2017.

[40] F. Bailly, A. Ceglia, B. Michaud, D. M. Rouleau, and M. Begon. Real-Time and Dynamically Consistent Estimation of Muscle Forces Using a Moving Horizon EMG-Marker Tracking Algorithm—Application to Upper Limb Biomechanics. *Front. Bioeng. Biotechnol.*, 9:642742, Feb. 2021.

[41] G. Barbareschi, R. Richards, M. Thornton, T. Carlson, and C. Holloway. Statically vs dynamically balanced gait: Analysis of a robotic exoskeleton compared with a human. In *2015 37th Annual International Conference of the IEEE Engineering in Medicine and Biology Society (EMBC)*, pages 6728–6731, Milan, Aug. 2015. IEEE.

[42] F. Barroso, C. Santos, and J. C. Moreno. Influence of the robotic exoskeleton Lokomat on the control of human gait: An electromyographic and kinematic analysis. In *2013 IEEE 3rd Portuguese Meeting in Bioengineering (ENBENG)*, pages 1–6, Braga, Feb. 2013. IEEE.

[43] H. L. Bartlett, L. H. Ting, and J. T. Bingham. Accuracy of force and center of pressure measures of the Wii Balance Board. *Gait & Posture*, 39(1):224–228, Jan. 2014.

[44] H. Bateni, E. Heung, J. Zettel, W. E. Mcllroy, and B. E. Maki. Can use of walkers or canes impede lateral compensatory stepping movements? *Gait & Posture*, 20(1):74–83, Aug. 2004.

[45] C. E. Bauby and A. D. Kuo. Active control of lateral balance in human walking. *J Biomech*, 33(11):1433–1440, 2000.

[46] R. Baud, A. R. Manzoori, A. Ijspeert, and M. Bouri. Review of control strategies for lower-limb exoskeletons to assist gait. *J NeuroEngineering Rehabil*, 18(1):119, Dec. 2021.

[47] K. Baumgartner, A. Zanelli, and M. Diehl. A Gradient Condition for the Arrival Cost in Moving Horizon Estimation. In *2020 European Control Conference (ECC)*, pages 1286–1291, Saint Petersburg, Russia, May 2020. IEEE.

[48] C. Bayon, A. R. Emmens, M. Afschrift, T. Van Wouwe, A. Q. L. Keemink, H. Van Der Kooij, and E. H. F. Van Asseldonk. Can Momentum-Based Control Predict Human Balance Recovery Strategies? *IEEE Trans. Neural Syst. Rehabil. Eng.*, 28(9):2015–2024, Sept. 2020.

[49] C. Bayón, A. Q. L. Keemink, M. Van Mierlo, W. Rampeltshammer, H. Van Der Kooij, and E. H. F. Van Asseldonk. Cooperative ankle-exoskeleton control can reduce effort to recover balance after unexpected disturbances during walking. *J NeuroEngineering Rehabil*, 19(1):21, Dec. 2022.

[50] O. N. Beck, M. K. Shepherd, R. Rastogi, G. Martino, L. H. Ting, and G. S. Sawicki. Exoskeletons need to react faster than physiological responses to improve standing balance. *Sci Robot*, 8(75):eadf1080, Feb. 2023.

[51] A. Bemporad, L. Chisci, and E. Mosca. On the stabilizing property of SIORHC. *Automatica*, 30(12):2013–2015, Dec. 1994.

[52] E. J. Benjamin, P. Muntner, A. Alonso, M. S. Bittencourt, C. W. Callaway, A. P. Carson, A. M. Chamberlain, A. R. Chang, S. Cheng, S. R. Das, F. N. Delling, L. Djousse, M. S. Elkind, J. F. Ferguson, M. Fornage, L. C. Jordan, S. S. Khan, B. M. Kissela, K. L. Knutson, T. W. Kwan, D. T. Lackland, T. T. Lewis, J. H. Lichtman, C. T. Longenecker, M. S. Loop, P. L. Lutsey, S. S. Martin, K. Matsushita, A. E. Moran, M. E. Mussolino, M. O'Flaherty, A. Pandey, A. M. Perak, W. D. Rosamond, G. A. Roth, U. K. Sampson, G. M. Satou, E. B. Schroeder, S. H. Shah, N. L. Spartano, A. Stokes, D. L. Tirschwell, C. W. Tsao, M. P. Turakhia, L. B. VanWagner, J. T. Wilkins, S. S. Wong, S. S. Virani, and On behalf of the American

Heart Association Council on Epidemiology and Prevention Statistics Committee and Stroke Statistics Subcommittee. Heart Disease and Stroke Statistics—2019 Update: A Report From the American Heart Association. *Circulation*, 139(10), Mar. 2019.

[53] L. Bergmann, O. Lück, D. Voss, P. Buschermöhle, L. Liu, S. Leonhardt, and C. Ngo. Lower Limb Exoskeleton With Compliant Actuators: Design, Modeling, and Human Torque Estimation. *IEEE/ASME Trans. Mechatron.*, 28(2):758–769, Apr. 2023.

[54] N. Bernstein. *The co-ordination and regulation of movements*. London: Pergamon Press, 1967.

[55] B. Berret, E. Chiovetto, F. Nori, and T. Pozzo. Evidence for Composite Cost Functions in Arm Movement Planning: An Inverse Optimal Control Approach. *PLoS Comput Biol*, 7(10):e1002183, Oct. 2011.

[56] J. T. Betts. *Practical Methods for Optimal Control and Estimation Using Nonlinear Programming*. Society for Industrial and Applied Mathematics, second edition, 2010.

[57] T. Bhatt, T.-Y. Wang, F. Yang, and Y.-C. Pai. Adaptation and generalization to opposing perturbations in walking. *Neuroscience*, 246:435–450, 2013.

[58] T. Bhatt, J. D. Wening, and Y.-C. Pai. Adaptive control of gait stability in reducing slip-related backward loss of balance. *Exp Brain Res*, 170(1):61–73, 2006.

[59] N. A. Bianco, P. W. Franks, J. L. Hicks, and S. L. Delp. Coupled exoskeleton assistance simplifies control and maintains metabolic benefits: A simulation study. *PLoS One*, 17(1):e0261318, 2022.

[60] E. Binboğa, S. Tok, F. Catikkas, S. Guven, and S. Dane. The effects of verbal encouragement and conscientiousness on maximal voluntary contraction of the triceps surae muscle in elite athletes. *Journal of Sports Sciences*, 31(9):982–988, 2013.

[61] G. M. Blenkinsop, M. T. G. Pain, and M. J. Hiley. Balance control strategies during perturbed and unperturbed balance in standing and handstand. *R Soc Open Sci*, 4(7):161018, July 2017.

[62] D. A. Bolton and M. Mansour. A Modified Lean and Release Technique to Emphasize Response Inhibition and Action Selection in Reactive Balance. *JoVE*, (157):60688, Mar. 2020.

[63] J. Bottin-Noonan and M. Sreenivasa. Model based evaluation of human and lower-limb exoskeleton interaction during sit to stand motion. In *2021 IEEE International Conference on Robotics and Automation (ICRA)*, pages 2063–2069, Xi'an, China, May 2021. IEEE.

[64] S. G. Brauer, M. Woollacott, and A. Shumway-Cook. The influence of a concurrent cognitive task on the compensatory stepping response to a perturbation in balance-impaired and healthy elders. *Gait Posture*, 15(1):83–93, Feb. 2002.

[65] P. Brown and J. McPhee. A Continuous Velocity-Based Friction Model for Dynamics and Control With Physically Meaningful Parameters. *Journal of Computational and Nonlinear Dynamics*, 11(5):054502, 2016.

[66] D. Brown-Triolo, M. Roach, K. Nelson, and R. Triolo. Consumer perspectives on mobility: Implications for neuroprosthesis design. *Journal of Rehabilitation Research and Development*, 39(6):659–669, 2002.

[67] S. M. Bruijn, L. H. Sloot, I. Kingma, and M. Pijnappels. Contribution of arm movements to balance recovery after tripping in older adults. *Journal of Biomechanics*, 133:110981, Mar. 2022.

[68] P. Bumroongsri and S. Kheawhom. Robust model predictive control with time-varying tubes. *Int. J. Control Autom. Syst.*, 15(4):1479–1484, Aug. 2017.

[69] L. L. Cai, A. J. Fong, C. K. Otoshi, Y. Liang, J. W. Burdick, R. R. Roy, and V. R. Edgerton. Implications of Assist-As-Needed Robotic Step Training after a Complete Spinal Cord Injury on Intrinsic Strategies of Motor Learning. *Journal of Neuroscience*, 26(41):10564–10568, Oct. 2006.

[70] S. M. Campbell, C. P. Diduch, and J. W. Sensinger. Autonomous Assistance-as-Needed Control of a Lower Limb Exoskeleton With Guaranteed Stability. *IEEE Access*, 8:51168–51178, 2020.

[71] M. G. Carmichael, D. Liu, and K. J. Waldron. A framework for singularity-robust manipulator control during physical human-robot interaction. *The International Journal of Robotics Research*, 36(5-7):861–876, June 2017.

[72] M. Casadio and V. Sanguineti. Learning, Retention, and Slacking: A Model of the Dynamics of Recovery in Robot Therapy. *IEEE Trans. Neural Syst. Rehabil. Eng.*, 20(3):286–296, May 2012.

[73] A. Ceglia, F. Bailly, and M. Begon. Moving Horizon Estimation of Human Kinematics and Muscle Forces. *IEEE Robot. Autom. Lett.*, 8(8):5212–5219, Aug. 2023.

[74] K. Chan, J. W. Lee, J. Unger, J. Yoo, K. Masani, and K. E. Musselman. Reactive stepping after a forward fall in people living with incomplete spinal cord injury or disease. *Spinal Cord*, 58(2):185–193, Feb. 2020.

[75] F. Chassagne, P. Badel, L. Navarro, J. Molimard, N. Curt, and S. Avril. In vivo Identification of the Passive Mechanical Properties of Deep Soft Tissues in the Human Leg: In vivo Identification of Passive Mechanical Properties of Leg Soft Tissues. *Strain*, 52(5):400–411, Oct. 2016.

[76] X. Chen, X. Cheng, J. Fong, D. Oetomo, and Y. Tan. The Effect of Crutch Gait Pattern on Shoulder Reaction Force when Walking with Lower Limb Exoskeletons. In *2021 43rd Annual International Conference of the IEEE Engineering in Medicine & Biology Society (EMBC)*, pages 7574–7577, Mexico, Nov. 2021. IEEE.

[77] K. B. Cheng. Does knee motion contribute to feet-in-place balance recovery? *Journal of Biomechanics*, 49(9):1873–1880, June 2016.

[78] K. B. Cheng, H. Tanabe, W.-C. Chen, and H.-T. Chiu. Role of heel lifting in standing balance recovery: A simulation study. *Journal of Biomechanics*, 67:69–77, Jan. 2018.

[79] H. Choi, B. Na, S. Kim, J. Lee, H. Kim, D. Kim, D. Cho, J. Kim, S. Shin, D.-W. Rha, and K. Kong. Angel-suit: a Modularized Lower-limb Wearable Robot for Assistance of People with Partially Impaired Walking Ability. In *2019 Wearable Robotics Association Conference (WearRAcon)*, pages 51–56, Scottsdale, AZ, USA, Mar. 2019. IEEE.

[80] S. G. Chung, E. M. Van Rey, Z. Bai, M. W. Rogers, E. J. Roth, and L.-Q. Zhang. Aging-related neuromuscular changes characterized by tendon reflex system properties. *Archives of Physical Medicine and Rehabilitation*, 86(2):318–327, Feb. 2005.

[81] D. I. Cleather and A. M. J. Bull. Lower-extremity musculoskeletal geometry affects the calculation of patellofemoral forces in vertical jumping and weightlifting. *Proc Inst Mech Eng H*, 224(9):1073–1083, 2010.

[82] D. Clever, R. Malin Schemschat, M. L. Felis, and K. Mombaur. Inverse optimal control based identification of optimality criteria in whole-body human walking on level ground. In *2016 6th IEEE International Conference on Biomedical Robotics and Biomechatronics (BioRob)*, pages 1192–1199, Singapore, Singapore, June 2016. IEEE.

[83] T. R. Clites, M. J. Carty, J. B. Ullauri, M. E. Carney, L. M. Mooney, J.-F. Duval, S. S. Srinivasan, and H. M. Herr. Proprioception from a neurally controlled lower-extremity prosthesis. *Sci Transl Med*, 10(443), 2018.

[84] A. K. Coker. Numerical Computation. In *Fortran Programs for Chemical Process Design, Analysis, and Simulation*, pages 1–102. Elsevier, 1995.

[85] P. Corbeil, B. R. Bloem, M. van Meel, and B. E. Maki. Arm reactions evoked by the initial exposure to a small balance perturbation: A pilot study. *Gait & Posture*, 37(2):300–303, Feb. 2013.

[86] O. Cruciger, T. A. Schildhauer, R. C. Meindl, M. Tegenthoff, P. Schwenkreis, M. Citak, and M. Aach. Impact of locomotion training with a neurologic controlled hybrid assistive limb (HAL) exoskeleton on neuropathic pain and health related quality of life (HRQoL) in chronic SCI: a case study. *Disability and Rehabilitation: Assistive Technology*, pages 1–6, Nov. 2014.

[87] F. De Groote, J. L. Allen, and L. H. Ting. Contribution of muscle short-range stiffness to initial changes in joint kinetics and kinematics during perturbations to standing balance: A simulation study. *Journal of Biomechanics*, 55:71–77, Apr. 2017.

[88] F. De Groote, A. L. Kinney, A. V. Rao, and B. J. Fregly. Evaluation of Direct Collocation Optimal Control Problem Formulations for Solving the Muscle Redundancy Problem. *Ann Biomed Eng*, 44(10):2922–2936, Oct. 2016.

[89] D. De Kam, J. M. B. Roelofs, A. K. B. D. Bruijnes, A. C. H. Geurts, and V. Weerdesteyn. The Next Step in Understanding Impaired Reactive Balance Control

in People With Stroke: The Role of Defective Early Automatic Postural Responses. *Neurorehabil Neural Repair*, 31(8):708–716, Aug. 2017.

[90] P. de Leva. Adjustments to Zatsiorsky-Seluyanov's segment inertia parameters. *Journal of Biomechanics*, 29(9):1223–1230, 1996.

[91] E. De Pieri, M. E. Lund, A. Gopalakrishnan, K. P. Rasmussen, D. E. Lunn, and S. J. Ferguson. Refining muscle geometry and wrapping in the TLEM 2 model for improved hip contact force prediction. *PLoS ONE*, 13(9):e0204109, Sept. 2018.

[92] B. J. DeHart, R. Gorbet, and D. Kulic. Spherical Foot Placement Estimator for Humanoid Balance Control and Recovery. In *2018 IEEE International Conference on Robotics and Automation (ICRA)*, pages 1747–1754, Brisbane, QLD, May 2018. IEEE.

[93] S. L. Delp, F. C. Anderson, A. S. Arnold, P. Loan, A. Habib, C. T. John, E. Guendelman, and D. G. Thelen. OpenSim: Open-Source Software to Create and Analyze Dynamic Simulations of Movement. *IEEE Trans. Biomed. Eng.*, 54(11):1940–1950, Nov. 2007.

[94] J. B. Dingwell, J. P. Cusumano, P. R. Cavanagh, and D. Sternad. Local dynamic stability versus kinematic variability of continuous overground and treadmill walking. *J Biomech Eng*, 123(1):27–32, Feb. 2001.

[95] J. B. Dingwell and H. G. Kang. Differences between local and orbital dynamic stability during human walking. *J Biomech Eng*, 129(4):586–593, Aug. 2007.

[96] P. L. Ditunno, M. Patrick, M. Stineman, and J. F. Ditunno. Who wants to walk? Preferences for recovery after SCI: a longitudinal and cross-sectional study. *Spinal Cord*, 46(7):500–506, July 2008.

[97] A. M. Dollar and H. Herr. Lower Extremity Exoskeletons and Active Orthoses: Challenges and State-of-the-Art. *IEEE Trans. Robot.*, 24(1):144–158, Feb. 2008.

[98] M. K. Duong, H. Cheng, H. T. Tran, and Q. Jing. Minimizing Human-Exoskeleton Interaction Force Using Compensation for Dynamic Uncertainty Error with Adaptive RBF Network. *J Intell Robot Syst*, 82(3-4):413–433, June 2016.

[99] G. Durandau, W. Rampeltshammer, H. van der Kooij, and M. Sartori. Toward Muscle-Driven Control of Wearable Robots: A Real-Time Framework for the Estimation of Neuromuscular States During Human-Exoskeleton Locomotion Tasks. In *2018 7th IEEE International Conference on Biomedical Robotics and Biomechatronics (Biorob)*, pages 683–688, Enschede, Aug. 2018. IEEE.

[100] M. F. Eilenberg, H. Geyer, and H. Herr. Control of a Powered Ankle–Foot Prosthesis Based on a Neuromuscular Model. *IEEE Transactions on Neural Systems and Rehabilitation Engineering*, 18(2):164–173, 2010.

[101] A. Ekelem, G. Bastas, C. M. Durrough, and M. Goldfarb. Variable Geometry Stair Ascent and Descent Controller for a Powered Lower Limb Exoskeleton. *Journal of Medical Devices*, 12(3):031009, Sept. 2018.

[102] J. Emken, J. Bobrow, and D. Reinkensmeyer. Robotic Movement Training As an Optimization Problem: Designing a Controller That Assists Only As Needed. In *9th International Conference on Rehabilitation Robotics, 2005. ICORR 2005.*, pages 307–312, Chicago, IL, USA, 2005. IEEE.

[103] A. Emmens, E. van Asseldonk, M. Masciullo, M. Arquilla, I. Pisotta, N. L. Tagliamonte, F. Tamburella, M. Molinari, and H. van der Kooij. Improving the Standing Balance of Paraplegics through the Use of a Wearable Exoskeleton. In *2018 7th IEEE Int. Conf. Biomed. Robot. and Biomechatron. (Biorob)*, pages 707–712, Aug. 2018.

[104] A. Emmens, E. van Asseldonk, M. Masciullo, M. Arquilla, I. Pisotta, N. L. Tagliamonte, F. Tamburella, M. Molinari, and H. van der Kooij. Improving the Standing Balance of Paraplegics through the Use of a Wearable Exoskeleton. In *2018 7th IEEE International Conference on Biomedical Robotics and Biomechatronics (Biorob)*, pages 707–712, Enschede, Aug. 2018. IEEE.

[105] A. R. Emmens, E. H. F. van Asseldonk, and H. van der Kooij. Effects of a powered ankle-foot orthosis on perturbed standing balance. *Journal of NeuroEngineering and Rehabilitation*, 15(1):50, 2018.

[106] A. R. Emmens, G. Van Oort, E. H. F. Van Asseldonk, and H. Van Der Kooij. A comparison between control strategies for balancing with an actuated ankle orthosis: preliminary simulation results. In *Poster session presented at 2015 Dynamic Walking Conference*, Columbus, Ohio, United States., 2015.

[107] D. Erbil, G. Tugba, T. H. Murat, A. Melike, A. Merve, K. Cagla, C. C. Mehmetali, O. Akay, and D. Nigar. Effects of robot-assisted gait training in chronic stroke patients treated by botulinum toxin-a: A pivotal study. *Physiotherapy Res Intl*, 23(3):e1718, July 2018.

[108] M. Ezati, M. Khadiv, and S. A. A. Moosavian. Dynamics modeling of a biped robot with active toe joints. In *2014 Second RSI/ISM International Conference on Robotics and Mechatronics (ICRoM)*, pages 107–112, Tehran, Iran, Oct. 2014. IEEE.

[109] I. Farkhatdinov, J. Ebert, G. van Oort, M. Vlutters, E. van Asseldonk, and E. Burdet. Assisting Human Balance in Standing With a Robotic Exoskeleton. *IEEE Robot. Autom. Lett.*, 4(2):414–421, Apr. 2019.

[110] R. Feigean, C. Afroun, E. Gasnier, O. Benveniste, G. Bassez, J. Hogrel, and D. Bachasson. VP.27 Potential of the Keeogo+, a lightweight wearable powered assistive exoskeleton in patients with neuromuscular disorders: preliminary findings. *Neuromuscular Disorders*, 32:S72, Oct. 2022.

[111] R. Feigean, C. Afroun, E. Gasnier, O. Benveniste, J. Hogrel, G. Bassez, and D. Bachasson. VP.26 Potential of the MyoSuit, a lightweight wearable lower-limb cable-actuated exoskeleton in patients with neuromuscular disorders: preliminary findings. *Neuromuscular Disorders*, 32:S71–S72, Oct. 2022.

[112] J. M. Finley, A. J. Bastian, and J. S. Gottschall. Learning to be economical: the energy cost of walking tracks motor adaptation. *J Physiol*, 591(4):1081–1095, Feb. 2013.

[113] M. Firouzi, E. De Keersmaec, N. Lefeber, S. Roggeman, E. Joos, E. Kerckhofs, D. Beckwée, and E. Swinnen. Immediate Effects of the Honda Walking Assist on Spatiotemporal Gait Characteristics in Older Adults. *Topics in Geriatric Rehabilitation*, 39(1):39–46, Jan. 2023.

[114] T. Flash and N. Hogan. The coordination of arm movements: an experimentally confirmed mathematical model. *J. Neurosci.*, 5(7):1688–1703, 1985.

[115] J. Forbes, S. Munakomi, and H. Cronovich. Romberg Test. In *StatPearls*. StatPearls Publishing, Treasure Island (FL), 2023.

[116] M. Freutel, H. Schmidt, L. Dürselen, A. Ignatius, and F. Galbusera. Finite element modeling of soft tissues: Material models, tissue interaction and challenges. *Clinical Biomechanics*, 29(4):363–372, Apr. 2014.

[117] M. Gautier. Optimal motion planning for robot's inertial parameters identification. In *[1992] Proceedings of the 31st IEEE Conference on Decision and Control*, pages 70–73, Tucson, AZ, USA, 1992. IEEE.

[118] M. Gautier and W. Khalil. A direct determination of minimum inertial parameters of robots. In *Proceedings. 1988 IEEE International Conference on Robotics and Automation*, pages 1682–1687, Philadelphia, PA, USA, 1988. IEEE Comput. Soc. Press.

[119] M. Gautier and W. Khalil. Direct calculation of minimum set of inertial parameters of serial robots. *IEEE Trans. Robot. Automat.*, 6(3):368–373, June 1990.

[120] M. Gautier and W. Khalil. Exciting trajectories for the identification of base inertial parameters of robots. In *[1991] Proceedings of the 30th IEEE Conference on Decision and Control*, pages 494–499, Brighton, UK, 1991. IEEE.

[121] M. Gautier and P. Poignet. Extended Kalman filtering and weighted least squares dynamic identification of robot. *Control Engineering Practice*, 9(12):1361–1372, Dec. 2001.

[122] J. B. Geursen, D. Altena, C. H. Massen, and M. Verduin. A model of the standing man for the description of his dynamic behaviour. *Agressologie*, 17 SPECNO:63–69, 1976.

[123] B. Ghannadi, N. Mehrabi, R. S. Razavian, and J. McPhee. Nonlinear model predictive control of an upper extremity rehabilitation robot using a two-dimensional human-robot interaction model. In *2017 IEEE/RSJ International Conference on Intelligent Robots and Systems (IROS)*, pages 502–507, Vancouver, BC, 2017. IEEE.

[124] B. Ghannadi, R. Sharif Razavian, and J. McPhee. A modified homotopy optimization for parameter identification in dynamic systems with backlash discontinuity. *Nonlinear Dyn*, 95(1):57–72, Jan. 2019.

[125] S. Gibson and B. Ninness. Robust maximum-likelihood estimation of multivariable dynamic systems. *Automatica*, 41(10):1667–1682, Oct. 2005.

[126] A. Gil-Agudo, A. Megia-Garcia, J. L. Pons, I. Sinovas-Alonso, N. Comino-Suarez, V. Lozano-Berrio, and A. J. del Ama. Exoskeleton-based training improves walking independence in incomplete spinal cord injury patients: results from a randomized controlled trial. *J NeuroEngineering Rehabil*, 20(1):36, Mar. 2023.

[127] F. Girrbach. Moving horizon estimation for inertial motion tracking : algorithms and industrial applications. 2021. Publisher: Albert-Ludwigs-Universität Freiburg.

[128] Y. Gonthier, J. McPhee, C. Lange, and J.-C. Piedbœuf. A Regularized Contact Model with Asymmetric Damping and Dwell-Time Dependent Friction. *Multibody System Dynamics*, 11(3):209–233, Apr. 2004.

[129] A. M. Gordon, A. F. Huxley, and F. J. Julian. The variation in isometric tension with sarcomere length in vertebrate muscle fibres. *J. Physiol. (Lond.)*, 184(1):170–192, May 1966.

[130] A. Goswami and V. Kallem. Rate of change of angular momentum and balance maintenance of biped robots. In *IEEE International Conference on Robotics and Automation, 2004. Proceedings. ICRA '04. 2004*, pages 3785–3790 Vol.4, New Orleans, LA, USA, 2004. IEEE.

[131] E. P. Grabke, K. Masani, and J. Andrysek. Lower Limb Assistive Device Design Optimization Using Musculoskeletal Modeling: A Review. *Journal of Medical Devices*, 13(4):040801, 2019.

[132] C. Greene. interp1gap, https://www.mathworks.com/matlabcentral/fileexchange/45842-interp1gap, 2023.

[133] J. W. Grizzle, C. Chevallereau, R. W. Sinnet, and A. D. Ames. Models, feedback control, and open problems of 3D bipedal robotic walking. *Automatica*, 50(8):1955–1988, Aug. 2014.

[134] T. Gurriet, S. Finet, G. Boeris, A. Duburcq, A. Hereid, O. Harib, M. Masselin, J. Grizzle, and A. D. Ames. Towards Restoring Locomotion for Paraplegics: Realizing Dynamically Stable Walking on Exoskeletons. In *2018 IEEE International*

Conference on Robotics and Automation (ICRA), pages 2804–2811, Brisbane, QLD, May 2018. IEEE.

[135] T. Gurriet, M. Tucker, C. Kann, G. Boeris, and A. D. Ames. Stabilization of Exoskeletons through Active Ankle Compensation, Sept. 2019. arXiv:1909.11848 [cs].

[136] D. Haering, C. Pontonnier, N. Bideau, G. Nicolas, and G. Dumont. Using Torque-Angle and Torque–Velocity Models to Characterize Elbow Mechanical Function: Modeling and Applied Aspects. *Journal of Biomechanical Engineering*, 141(8):084501, Aug. 2019.

[137] L. Hao, R. Pagani, M. Beschi, and G. Legnani. Dynamic and Friction Parameters of an Industrial Robot: Identification, Comparison and Repetitiveness Analysis. *Robotics*, 10(1):49, Mar. 2021.

[138] O. Harib, A. Hereid, A. Agrawal, T. Gurriet, S. Finet, G. Boeris, A. Duburcq, M. E. Mungai, M. Masselin, A. D. Ames, K. Sreenath, and J. W. Grizzle. Feedback Control of an Exoskeleton for Paraplegics: Toward Robustly Stable, Hands-Free Dynamic Walking. *IEEE Control Syst.*, 38(6):61–87, Dec. 2018.

[139] F. Haufe, P. Wolf, and R. Riener. Human-in-the-loop optimization of a multi-joint wearable robot for movement assistance. page 2 p., Mar. 2020. Artwork Size: 2 p. Medium: application/pdf Publisher: ETH Zurich.

[140] F. L. Haufe, A. M. Kober, K. Schmidt, A. Sancho-Puchades, J. E. Duarte, P. Wolf, and R. Riener. User-driven walking assistance: first experimental results using the MyoSuit. In *2019 IEEE 16th International Conference on Rehabilitation Robotics (ICORR)*, pages 944–949, Toronto, ON, Canada, June 2019. IEEE.

[141] E. Haug. *Computational Methods in Mechanical System Dynamics*. Springer Berlin, Heidelberg, 2018.

[142] J.-P. Hauschild and G. R. Heppler. Control of Harmonic Drive Motor Actuated Flexible Linkages. In *Proceedings 2007 IEEE International Conference on Robotics and Automation*, pages 3451–3456, Rome, Italy, 2007. IEEE. ISSN: 1050-4729.

[143] S. C. Hayes, M. White, H. S. F. White, and N. Vanicek. A biomechanical comparison of powered robotic exoskeleton gait with normal and slow walking: An investigation with able-bodied individuals. *Clinical Biomechanics*, 80:105133, Dec. 2020.

[144] S. C. Hayes, M. White, C. R. J. Wilcox, H. S. F. White, and N. Vanicek. Biomechanical differences between able-bodied and spinal cord injured individuals walking in an overground robotic exoskeleton. *PLoS ONE*, 17(1):e0262915, Jan. 2022.

[145] J. Hegeman, B. van den Bemt, V. Weerdesteyn, B. Nienhuis, J. van Limbeek, and J. Duysens. Unraveling the Association Between SSRI Use and Falls: An Experimental Study of Risk Factors for Accidental Falls in Long-Term Paroxetine Users. *Clinical Neuropharmacology*, 34(6):210–215, 2011.

[146] T. L. Heiden, D. J. Sanderson, J. T. Inglis, and G. P. Siegmund. Adaptations to normal human gait on potentially slippery surfaces: the effects of awareness and prior slip experience. *Gait Posture*, 24(2):237–246, Oct. 2006.

[147] H. Hemami, K. Barin, L. Jalics, and D. G. Heiss. Dynamics, stability, and control of stepping. *Ann Biomed Eng*, 32(8):1153–1160, Aug. 2004.

[148] A. Herdt, H. Diedam, P.-B. Wieber, D. Dimitrov, K. Mombaur, and M. Diehl. Online Walking Motion Generation with Automatic Footstep Placement. *Advanced Robotics*, 24(5-6):719–737, Jan. 2010.

[149] H. Herr and A. Wilkenfeld. User-adaptive control of a magnetorheological prosthetic knee. *Industrial Robot*, 30(1):42–55, Feb. 2003.

[150] A. V. Hill. The heat of shortening and the dynamic constants of muscle. *P Roy Soc Lond B Bio*, 126(843):136–195, Oct. 1938.

[151] C. Hillermeier. Generalized Homotopy Approach to Multiobjective Optimization. *Journal of Optimization Theory and Applications*, 110(3):557–583, Sept. 2001.

[152] A. L. Hof. The equations of motion for a standing human reveal three mechanisms for balance. *J Biomech*, 40(2):451–457, 2007.

[153] A. L. Hof and C. Curtze. A stricter condition for standing balance after unexpected perturbations. *J Biomech*, 49(4):580–585, Feb. 2016.

[154] A. L. Hof, M. G. J. Gazendam, and W. E. Sinke. The condition for dynamic stability. *J Biomech*, 38(1):1–8, 2005.

[155] N. Hogan, H. I. Krebs, B. Rohrer, J. J. Palazzolo, L. Dipietro, S. E. Fasoli, J. Stein, R. Hughes, W. R. Frontera, D. Lynch, and B. T. Volpe. Motions or muscles? Some behavioral factors underlying robotic assistance of motor recovery. *J Rehabil Res Dev*, 43(5):605–618, Sept. 2006.

[156] D. P. Holland, E. J. Park, P. Polygerinos, G. J. Bennett, and C. J. Walsh. The Soft Robotics Toolkit: Shared Resources for Research and Design. *Soft Robotics*, 1(3):224–230, Sept. 2014.

[157] F. B. Horak, H. C. Diener, and L. M. Nashner. Influence of central set on human postural responses. *J. Neurophysiol.*, 62(4):841–853, 1989.

[158] F. B. Horak and L. M. Nashner. Central programming of postural movements: adaptation to altered support-surface configurations. *Journal of Neurophysiology*, 55(6):1369–1381, 1986.

[159] Y. Hua, J. Fan, G. Liu, X. Zhang, M. Lai, M. Li, T. Zheng, G. Zhang, J. Zhao, and Y. Zhu. A Novel Weight-Bearing Lower Limb Exoskeleton Based on Motion Intention Prediction and Locomotion State Identification. *IEEE Access*, 7:37620–37638, 2019.

[160] R. Huang, H. Cheng, H. Guo, X. Lin, and J. Zhang. Hierarchical learning control with physical human-exoskeleton interaction. *Information Sciences*, 432:584–595, Mar. 2018.

[161] K. H. Hunt and F. R. E. Crossley. Coefficient of Restitution Interpreted as Damping in Vibroimpact. *Journal of Applied Mechanics*, 42(2):440–445, June 1975.

[162] F. Hussain, R. Goecke, and M. Mohammadian. Exoskeleton robots for lower limb assistance: A review of materials, actuation, and manufacturing methods. *Proc Inst Mech Eng H*, 235(12):1375–1385, Dec. 2021.

[163] D. J. Hyun, H. Lim, S. Park, J. Yoon, K. Jung, K. Bae, and I. Lee. Walking propulsion generation in double stance by powered exoskeleton for paraplegics. *Robotics and Autonomous Systems*, 116:24–37, June 2019.

[164] M. Iizuka and Y. Ikeda. Regulation and innovation under the 4th industrial revolution: The case of a healthcare robot, HAL by Cyberdyne. *Technovation*, 108:102335, Dec. 2021.

[165] K. A. Inkol, C. Brown, W. McNally, C. Jansen, and J. McPhee. Muscle torque generators in multibody dynamic simulations of optimal sports performance. *Multibody Syst Dyn*, June 2020.

[166] K. A. Inkol, A. H. Huntley, and L. A. Vallis. Do perturbation-evoked responses result in higher reaction time costs depending on the direction and magnitude of perturbation? *Exp Brain Res*, 236(6):1689–1698, 2018.

[167] K. A. Inkol, A. H. Huntley, and L. A. Vallis. Modeling margin of stability with feet in place following a postural perturbation: Effect of altered anthropometric models for estimated extrapolated centre of mass. *Gait Posture*, 62:434–439, 2018.

[168] K. A. Inkol, A. H. Huntley, and L. A. Vallis. Repeated Exposure to Forward Support-Surface Perturbation During Overground Walking Alters Upper-Body Kinematics and Step Parameters. *Journal of Motor Behavior*, pages 1–13, June 2018.

[169] K. A. Inkol and J. McPhee. Assessing Control of Fixed-Support Balance Recovery in Wearable Lower-Limb Exoskeletons Using Multibody Dynamic Modelling. In *2020 8th IEEE RAS/EMBS International Conference for Biomedical Robotics and Biomechatronics (BioRob)*, pages 54–60, New York City, NY, USA, 2020. IEEE.

[170] K. A. Inkol and J. McPhee. Simulating Human Upper and Lower Limb Balance Recovery Responses Using Nonlinear Model Predictive Control. In *2021 43rd Annual International Conference of the IEEE Engineering in Medicine & Biology Society (EMBC)*, pages 4717–4721, Mexico, 2021. IEEE.

[171] K. A. Inkol and J. McPhee. Towards compliant human-exoskeleton interactions within dynamics multibody simulations of assisted human motor control. In *10th ECCOMAS Thematic Conference on Multibody Dynamics*, Budapest, Hungary, Dec. 2021.

[172] K. A. Inkol and J. McPhee. Using Dynamic Simulations to Estimate the Feasible Stability Region of Feet-In-Place Balance Recovery for Lower-Limb Exoskeleton Users. In *2022 9th IEEE RAS/EMBS International Conference for Biomedical Robotics and Biomechatronics (BioRob)*, pages 1–6, Seoul, Korea, Republic of, 2022. IEEE.

[173] K. A. Inkol and J. McPhee. Facilitating Dynamic Balance Recovery in Lower Limb Exoskeletons with State Estimation. In *11th ECCOMAS Thematic Conference on Multibody Dynamics*, Lisbon, Portugal, July 2023.

[174] K. A. Inkol and L. Vallis. Modelling the dynamic margins of stability for use in evaluations of balance following a support-surface perturbation. *J. Biomech.*, 2019.

[175] K. Iqbal and Y. Pai. Predicted region of stability for balance recovery: motion at the knee joint can improve termination of forward movement. *J Biomech*, 33(12):1619–1627, 2000.

[176] S. Jatsun, S. Savin, and A. Yatsun. Walking Pattern Generation Method for an Exoskeleton Moving On Uneven Terrain. In *Human-Centric Robotics*, pages 13–20, Porto, Portugal, Oct. 2017. World Scientific.

[177] A. Jayaraman, C. M. Gregory, M. Bowden, J. E. Stevens, P. Shah, A. L. Behrman, and K. Vandenborne. Lower extremity skeletal muscle function in persons with incomplete spinal cord injury. *Spinal Cord*, 44(11):680–687, 2006.

[178] M. Jeong, H. Woo, and K. Kong. A Study on Weight Support and Balance Control Method for Assisting Squat Movement with a Wearable Robot, Angel-suit. *Int. J. Control Autom. Syst.*, 18(1):114–123, Jan. 2020.

[179] Y. Jiang, T. Van Wouwe, F. De Groote, and C. K. Liu. Synthesis of biologically realistic human motion using joint torque actuation. *ACM Trans. Graph.*, 38(4):1–12, July 2019.

[180] C. Jin, A. Maitland, and J. McPhee. Hierarchical Nonlinear Moving Horizon Estimation of Vehicle Lateral Speed and Road Friction Coefficient. *ASME Letters in Dynamic Systems and Control*, 1(1):011005, Jan. 2021.

[181] V. Joukov, V. Bonnet, G. Venture, and D. Kulic. Constrained dynamic parameter estimation using the Extended Kalman Filter. In *2015 IEEE/RSJ International Conference on Intelligent Robots and Systems (IROS)*, pages 3654–3659, Hamburg, Germany, Sept. 2015. IEEE.

[182] Y. W. Ju, J. S. Lee, Y.-A. Choi, and Y. H. Kim. Causes and Trends of Disabilities in Community-Dwelling Stroke Survivors: A Population-Based Study. *Brain Neurorehabil*, 15(1):e5, Mar. 2022.

[183] D. M. Ka, C. Hong, T. H. Toan, and J. Qiu. Minimizing human-exoskeleton interaction force by using global fast sliding mode control. *Int. J. Control Autom. Syst.*, 14(4):1064–1073, Aug. 2016.

[184] S. Kajita and K. Tani. Study of dynamic biped locomotion on rugged terrain-derivation and application of the linear inverted pendulum mode. In *Proceedings. 1991 IEEE International Conference on Robotics and Automation*, pages 1405–1411, Sacramento, CA, USA, 1991. IEEE Comput. Soc. Press.

[185] K. Kaminishi, P. Jiang, R. Chiba, K. Takakusaki, and J. Ota. Postural control of a musculoskeletal model against multidirectional support surface translations. *PLoS ONE*, 14(3):e0212613, 2019.

[186] B. Katz. The relation between force and speed in muscular contraction. *The Journal of Physiology*, 96(1):45–64, 1939.

[187] K. R. Kaufman, M. P. Wyatt, P. H. Sessoms, and M. D. Grabiner. Task-specific fall prevention training is effective for warfighters with transtibial amputations. *Clin. Orthop. Relat. Res.*, 472(10):3076–3084, 2014.

[188] M. Kelly. An Introduction to Trajectory Optimization: How to Do Your Own Direct Collocation. *SIAM Rev.*, 59(4):849–904, Jan. 2017.

[189] Q. Khadim, M. Kiani-Oshtorjani, S. Jaiswal, M. K. Matikainen, and A. Mikkola. Estimating the Characteristic Curve of a Directional Control Valve in a Combined Multibody and Hydraulic System Using an Augmented Discrete Extended Kalman Filter. *Sensors*, 21(15):5029, July 2021.

[190] C. Khasnabis, J. Borg, and World Health Organization. *Guidelines on the provision of manual wheelchairs in less resourced settings*. World Health Organization, Geneva, 2008. OCLC: 657981948.

[191] A. Kilicarslan, S. Prasad, R. G. Grossman, and J. L. Contreras-Vidal. High accuracy decoding of user intentions using EEG to control a lower-body exoskeleton. *Conf Proc IEEE Eng Med Biol Soc*, 2013:5606–5609, 2013.

[192] D. E. Kirk. *Optimal Control Theory: an Introduction*. Dover Publications, 2012. OCLC: 868270303.

[193] H. Koch and K. Mombaur. ExoOpt - A framework for patient centered design optimization of lower limb exoskeletons. In *2015 IEEE Int. Conf. Rehabil. Robot. (ICORR)*, pages 113–118, Aug. 2015.

[194] P. A. Koljonen, A. S. Virk, Y. Jeong, M. McKinley, J. Latorre, A. Caballero, Y. Hu, Y. W. Wong, K. Cheung, and H. Kazerooni. Outcomes of a Multicenter Safety and Efficacy Study of the SuitX Phoenix Powered Exoskeleton for Ambulation by Patients With Spinal Cord Injury. *Front. Neurol.*, 12:689751, July 2021.

[195] J. R. Koller, C. David Remy, and D. P. Ferris. Comparing neural control and mechanically intrinsic control of powered ankle exoskeletons. In *2017 International Conference on Rehabilitation Robotics (ICORR)*, pages 294–299, London, July 2017. IEEE.

[196] J. Koltermann, M. Gerber, H. Beck, and M. Beck. Validation of the HUMAC Balance System in Comparison with Conventional Force Plates. *Technologies*, 5(3):44, July 2017.

[197] B. Koopman, J. H. Meuleman, E. H. F. van Asseldonk, and H. van der Kooij. Lateral balance control for robotic gait training. *IEEE Int Conf Rehabil Robot*, 2013:6650363, June 2013.

[198] B. Koopman, E. H. van Asseldonk, and H. van der Kooij. Selective control of gait subtasks in robotic gait training: foot clearance support in stroke survivors with a powered exoskeleton. *J NeuroEngineering Rehabil*, 10(1):3, 2013.

[199] S. V. Kotov, V. Y. Lijdvoy, A. B. Sekirin, K. A. Petrushanskaya, and E. V. Pismennaya. The efficacy of the exoskeleton ExoAtlet to restore walking in patients with multiple sclerosis. *Z. nevrol. psikhiatr. im. S.S. Korsakova*, 117(10):41, 2017.

[200] T. Kraus, H. Ferreau, E. Kayacan, H. Ramon, J. De Baerdemaeker, M. Diehl, and W. Saeys. Moving horizon estimation and nonlinear model predictive control for autonomous agricultural vehicles. *Computers and Electronics in Agriculture*, 98:25–33, Oct. 2013.

[201] M. Kulikova and G. Kulikov. Adaptive ODE solvers in extended Kalman filtering algorithms. *Journal of Computational and Applied Mathematics*, 262:205–216, May 2014.

[202] A. D. Kuo. An optimal control model for analyzing human postural balance. *IEEE Transactions on Biomedical Engineering*, 42(1):87–101, 1995.

[203] A. D. Kuo. An optimal state estimation model of sensory integration in human postural balance. *J Neural Eng*, 2(3):S235–249, 2005.

[204] A. D. Kuo and F. E. Zajac. Human standing posture: multi-joint movement strategies based on biomechanical constraints. *Prog. Brain Res.*, 97:349–358, 1993.

[205] B. Laschowski, K. A. Inkol, A. Mihailidis, and J. McPhee. Simulation of Energy Regeneration in Human Locomotion for Efficient Exoskeleton Actuation. preprint, Bioengineering, June 2022.

[206] B. Laschowski, W. McNally, A. Wong, and J. McPhee. Environment Classification for Robotic Leg Prostheses and Exoskeletons Using Deep Convolutional Neural Networks. *Front. Neurorobot.*, 15:730965, Feb. 2022.

[207] M. L. Latash, M. F. Levin, J. P. Scholz, and G. Schöner. Motor control theories and their applications. *Medicina (Kaunas)*, 46(6):382–392, 2010.

[208] M. S. K. Lau, S. P. Yue, K. V. Ling, and J. M. Maciejowski. A comparison of interior point and active set methods for FPGA implementation of model predictive control. In *2009 European Control Conference (ECC)*, pages 156–161, Budapest, Aug. 2009. IEEE.

[209] C. A. Laubscher, A. Goo, R. J. Farris, and J. T. Sawicki. Hybrid Impedance-Sliding Mode Switching Control of the Indego Explorer Lower-Limb Exoskeleton in able-Bodied Walking. *J Intell Robot Syst*, 104(4):76, Apr. 2022.

[210] C. Lee and S. Oh. Development, Analysis, and Control of Series Elastic Actuator-Driven Robot Leg. *Front. Neurorobot.*, 13:17, May 2019.

[211] Letian Wang, E. H. F. van Asseldonk, and H. van der Kooij. Model predictive control-based gait pattern generation for wearable exoskeletons. In *2011 IEEE International Conference on Rehabilitation Robotics*, pages 1–6, Zurich, June 2011. IEEE.

[212] X. Liu, T. Bhatt, S. Wang, F. Yang, and Y.-C. C. Pai. Retention of the "first-trial effect" in gait-slip among community-living older adults. *GeroScience*, 39(1):93–102, Feb. 2017.

[213] D. B. Lockhart and L. H. Ting. Optimal sensorimotor transformations for balance. *Nat Neurosci*, 10(10):1329–1336, 2007.

[214] G. Lv, H. Zhu, and R. D. Gregg. On the Design and Control of Highly Backdrivable Lower-Limb Exoskeletons: A Discussion of Past and Ongoing Work. *IEEE Control Systems*, 38(6):88–113, Dec. 2018.

[215] N. Maalouf, I. H. Elhajj, D. Asmar, and E. Shammas. Model-free human-like humanoid push recovery. In *2015 IEEE International Conference on Robotics and Biomimetics (ROBIO)*, pages 1560–1565, Zhuhai, Dec. 2015. IEEE.

[216] S. J. MacKenzie and E. J. Sprigings. A three-dimensional forward dynamics model of the golf swing. *Sports Eng*, 11(4):165–175, Sept. 2009.

[217] S. Maggioni, L. Lunenburger, R. Riener, and A. Melendez-Calderon. Robot-aided assessment of walking function based on an adaptive algorithm. In *2015 IEEE International Conference on Rehabilitation Robotics (ICORR)*, pages 804–809, Singapore, Singapore, Aug. 2015. IEEE.

[218] S. Maggioni, N. Reinert, L. Lünenburger, and A. Melendez-Calderon. An Adaptive and Hybrid End-Point/Joint Impedance Controller for Lower Limb Exoskeletons. *Front. Robot. AI*, 5:104, Oct. 2018.

[219] A. Maitland. *Nonlinear Model Predictive Control Reduction Strategies for Real-time Optimal Control*. PhD Thesis, University of Waterloo, 2019.

[220] A. F. Mak, M. Zhang, and E. W. Tam. Biomechanics of Pressure Ulcer in Body Tissues Interacting with External Forces during Locomotion. *Annu. Rev. Biomed. Eng.*, 12(1):29–53, July 2010.

[221] B. E. Maki, M. A. Edmondstone, and W. E. McIlroy. Age-related differences in laterally directed compensatory stepping behavior. *J. Gerontol. A Biol. Sci. Med. Sci.*, 55(5):M270–277, May 2000.

[222] B. E. Maki and W. E. McIlroy. The role of limb movements in maintaining upright stance: the "change-in-support" strategy. *Phys Ther*, 77(5):488–507, May 1997.

[223] B. E. Maki and W. E. McIlroy. Cognitive demands and cortical control of human balance-recovery reactions. *Journal of Neural Transmission*, 114(10):1279–1296, 2007.

[224] B. E. Maki, W. E. McIlroy, and S. D. Perry. Influence of lateral destabilization on compensatory stepping responses. *J Biomech*, 29(3):343–353, 1996.

[225] T. Manini. Development of physical disability in older adults. *Curr Aging Sci*, 4(3):184–191, Dec. 2011.

[226] P. Manns, M. Sreenivasa, M. Millard, and K. Mombaur. Motion Optimization and Parameter Identification for a Human and Lower Back Exoskeleton Model. *IEEE Robot. Autom. Lett.*, 2(3):1564–1570, July 2017.

[227] M. Mansouri, A. E. Clark, A. Seth, and J. A. Reinbolt. Rectus femoris transfer surgery affects balance recovery in children with cerebral palsy: A computer simulation study. *Gait & Posture*, 43:24–30, 2016.

[228] X. Mao. The truncated Euler–Maruyama method for stochastic differential equations. *Journal of Computational and Applied Mathematics*, 290:370–384, Dec. 2015.

[229] D. S. Marigold, A. J. Bethune, and A. E. Patla. Role of the unperturbed limb and arms in the reactive recovery response to an unexpected slip during locomotion. *J. Neurophysiol.*, 89(4):1727–1737, 2003.

[230] D. S. Marigold and A. E. Patla. Strategies for Dynamic Stability During Locomotion on a Slippery Surface: Effects of Prior Experience and Knowledge. *Journal of Neurophysiology*, 88(1):339–353, July 2002.

[231] O. Marjanovic and B. Lennox. Infinite horizon model predictive control with no terminal constraint. *Computers & Chemical Engineering*, 28(12):2605–2610, Nov. 2004.

[232] C. McGibbon, A. Sexton, P. Gryfe, T. Dutta, A. Jayaraman, S. Deems-Dluhy, A. Novak, E. Fabara, C. Adans-Dester, and P. Bonato. Effect of using of a lower-extremity exoskeleton on disability of people with multiple sclerosis. *Disability and Rehabilitation: Assistive Technology*, 18(5):475–482, July 2023.

[233] W. E. McIlroy, B. E. Maki, and M. Ghafouri. Initiation of rapid reach-and-grasp balance reactions: is a pre-formed visuospatial map used in controlling the initial arm trajectory? *Experimental Brain Research*, 155(4):532–536, Apr. 2004.

[234] C. D. McKinnon and A. P. Schoellig. Unscented external force and torque estimation for quadrotors. In *2016 IEEE/RSJ International Conference on Intelligent Robots and Systems (IROS)*, pages 5651–5657, Daejeon, South Korea, Oct. 2016. IEEE.

[235] J. C. Mcleod, S. J. Ward, and A. L. Hicks. Evaluation of the Keeogo™ Dermoskeleton. *Disability and Rehabilitation: Assistive Technology*, 14(5):503–512, July 2019.

[236] R. L. Medrano, G. C. Thomas, C. G. Keais, E. J. Rouse, and R. D. Gregg. Real-Time Gait Phase and Task Estimation for Controlling a Powered Ankle Exoskeleton on Extremely Uneven Terrain. *IEEE Trans. Robot.*, 39(3):2170–2182, June 2023.

[237] R. L. Medrano, G. C. Thomas, E. J. Rouse, and R. D. Gregg. Analysis of the Bayesian Gait-State Estimation Problem for Lower-Limb Wearable Robot Sensor Configurations. *IEEE Robot. Autom. Lett.*, 7(3):7463–7470, July 2022.

[238] A. Megia-Garcia, A. J. del Ama, V. Lozano-Berrio, I. Sinovas-Alonso, N. Comino-Suarez, and A. Gil-Agudo. Safety, Feasibility and Acceptance with HANK Ambulatory Robotic Exoskeleton in Incomplete Spinal Cord Injury Patients. In D. Torricelli, M. Akay, and J. L. Pons, editors, *Converging Clinical and Engineering Research on Neurorehabilitation IV*, volume 28, pages 935–939. Springer International Publishing, Cham, 2022. Series Title: Biosystems & Biorobotics.

[239] N. Mehrabi. *Dynamics and Model-Based Control of Electric Power Steering Systems*. PhD Thesis, University of Waterloo, Canada, Waterloo, Ontario, 2014.

[240] N. Mehrabi, R. Sharif Razavian, B. Ghannadi, and J. McPhee. Predictive Simulation of Reaching Moving Targets Using Nonlinear Model Predictive Control. *Frontiers in Computational Neuroscience*, 10, Jan. 2017.

[241] C. Mele. *The Physical Exoskeleton-User Interface: Investigating Modelling and Design of Coupling Surfaces*. MASc Thesis, University of Waterloo, UWSpace, 2023.

[242] P. Micheau, A. Kron, and P. Bourassa. Evaluation of the lambda model for human postural control during ankle strategy. *Biol Cybern*, 89(3):227–236, Sept. 2003.

[243] I. Mileti, J. Taborri, D. Rodriguez-Cianca, D. Torricelli, S. Rossi, and F. Patanè. Feasibility and Application of the B.E.A.T. Testbed for Assessing the Effects of Lower Limb Exoskeletons on Human Balance. *Robotics*, 11(6):151, Dec. 2022.

[244] M. Millard, A. L. Emonds, M. Harant, and K. Mombaur. A reduced muscle model and planar musculoskeletal model fit for the simulation of whole-body movements. *J Biomech*, 89:11–20, May 2019.

[245] M. Millard, J. McPhee, and E. Kubica. Foot Placement and Balance in 3D. *Journal of Computational and Nonlinear Dynamics*, 7(2):021015, 2012.

[246] M. Millard, M. Sreenivasa, and K. Mombaur. Predicting the Motions and Forces of Wearable Robotic Systems Using Optimal Control. *Frontiers in Robotics and AI*, 4:41, 2017.

[247] M. Millard, T. Uchida, A. Seth, and S. L. Delp. Flexing computational muscle: modeling and simulation of musculotendon dynamics. *J Biomech Eng*, 135(2):021005, Feb. 2013.

[248] M. Millard, D. Wight, J. McPhee, E. Kubica, and D. Wang. Human foot placement and balance in the sagittal plane. *J Biomech Eng*, 131(12):121001, Dec. 2009.

[249] S. Minsker and L. Wang. Robust Estimation of Covariance Matrices: Adversarial Contamination and Beyond. 2022. Publisher: arXiv Version Number: 1.

[250] K. Mombaur, A. Truong, and J.-P. Laumond. From human to humanoid locomotion—an inverse optimal control approach. *Autonomous Robots*, 28(3):369–383, 2010.

[251] C. D. Moore, B. C. Craven, L. Thabane, A. C. Laing, A. W. Frank-Wilson, S. A. Kontulainen, A. Papaioannou, J. D. Adachi, and L. M. Giangregorio. Lower-extremity muscle atrophy and fat infiltration after chronic spinal cord injury. *J Musculoskelet Neuronal Interact*, 15(1):32–41, Mar. 2015.

[252] P. Morasso, A. Cherif, and J. Zenzeri. Quiet standing: The Single Inverted Pendulum model is not so bad after all. *PLoS ONE*, 14(3):e0213870, Mar. 2019.

[253] P. G. Morasso and V. Sanguineti. Ankle muscle stiffness alone cannot stabilize balance during quiet standing. *J. Neurophysiol.*, 88(4):2157–2162, 2002.

[254] T. M. Morrison, P. Pathmanathan, M. Adwan, and E. Margerrison. Advancing Regulatory Science With Computational Modeling for Medical Devices at the FDA's Office of Science and Engineering Laboratories. *Front. Med.*, 5:241, Sept. 2018.

[255] A. Nasr, S. Bell, J. He, R. L. Whittaker, N. Jiang, C. R. Dickerson, and J. McPhee. MuscleNET: mapping electromyography to kinematic and dynamic biomechanical variables by machine learning. *J. Neural Eng.*, 18(4):0460d3, Aug. 2021.

[256] A. Nasr, A. Hashemi, and J. McPhee. Model-Based Mid-Level Regulation for Assist-As-Needed Hierarchical Control of Wearable Robots: A Computational Study of Human-Robot Adaptation. *Robotics*, 11(1):20, Jan. 2022.

[257] A. Nasr, J. Hunter, C. R. Dickerson, and J. McPhee. Evaluation of a machine-learning-driven active–passive upper-limb exoskeleton robot: Experimental human-in-the-loop study. *Wearable Technol.*, 4:e13, 2023.

[258] A. Nasr, K. A. Inkol, S. Bell, and J. McPhee. InverseMuscleNET: Alternative Machine Learning Solution to Static Optimization and Inverse Muscle Modeling. *Front Comput Neurosci*, 15:759489, 2021.

[259] M. Naveau, M. Kudruss, O. Stasse, C. Kirches, K. Mombaur, and P. Soueres. A Reactive Walking Pattern Generator Based on Nonlinear Model Predictive Control. *IEEE Robot. Autom. Lett.*, 2(1):10–17, Jan. 2017.

[260] M. A. Naya, E. Sanjurjo, A. J. Rodriguez, and J. Cuadrado. Kalman filters based on multibody models: linking simulation and real world. A comprehensive review. *Multibody Syst Dyn*, 58(3-4):479–521, Aug. 2023.

[261] V. Q. Nguyen, A. K. LaPre, M. A. Price, B. R. Umberger, and F. C. Sup. Inclusion of actuator dynamics in simulations of assisted human movement. *Int J Numer Meth Biomed Engng*, 36(5), May 2020.

[262] V. T. Norman-Gerum. *Predictive Dynamic Simulation of Healthy Sit-to-Stand Movement*. PhD Thesis, University of Waterloo, Waterloo, Canada, 2019.

[263] R. G. Norrie, B. E. Maki, W. R. Staines, and W. E. McIlroy. The time course of attention shifts following perturbation of upright stance. *Experimental Brain Research*, 146(3):315–321, 2002.

[264] Y. C. Pai and J. Patton. Center of mass velocity-position predictions for balance control. *J Biomech*, 30(4):347–354, 1997.

[265] C. Pais-Vieira, M. Allahdad, J. Neves-Amado, A. Perrotta, E. Morya, R. Moioli, E. Shapkova, and M. Pais-Vieira. Method for positioning and rehabilitation training with the ExoAtlet ® powered exoskeleton. *MethodsX*, 7:100849, 2020.

[266] M. G. Pandy, F. C. Anderson, and D. G. Hull. A parameter optimization approach for the optimal control of large-scale musculoskeletal systems. *J Biomech Eng*, 114(4):450–460, 1992.

[267] A. Patla. Strategies for dynamic stability during adaptive human locomotion. *IEEE Eng. Med. Biol. Mag.*, 22(2):48–52, Mar. 2003.

[268] M. A. Patterson and A. V. Rao. GPOPS-II: A MATLAB Software for Solving Multiple-Phase Optimal Control Problems Using hp-Adaptive Gaussian Quadrature Collocation Methods and Sparse Nonlinear Programming. *ACM T Math Software*, 41(1):1–37, Oct. 2014.

[269] E. Pennestrì, V. Rossi, P. Salvini, and P. P. Valentini. Review and comparison of dry friction force models. *Nonlinear Dyn*, 83(4):1785–1801, Mar. 2016.

[270] C. M. Pereira, A. L. Ramalho, and J. A. Ambrósio. A critical overview of internal and external cylinder contact force models. *Nonlinear Dyn*, 63(4):681–697, Mar. 2011.

[271] C. U. Persson, L. Holmegaard, P. Redfors, C. Jern, C. Blomstrand, and K. Jood. Increased muscle tone and contracture late after ischemic stroke. *Brain Behav*, 10(2):e01509, Feb. 2020.

[272] R. Peterka. Simplifying the complexities of maintaining balance. *IEEE Engineering in Medicine and Biology Magazine*, 22(2):63–68, Mar. 2003.

[273] S. Phu, D. L. Sturnieks, S. R. Lord, and Y. Okubo. Impact of ageing, fall history and exercise on postural reflexes following unpredictable perturbations: A systematic review and meta-analyses. *Mech Ageing Dev*, 203:111634, Apr. 2022.

[274] M. Pijnappels, I. Kingma, D. Wezenberg, G. Reurink, and J. H. Van Dieën. Armed against falls: the contribution of arm movements to balance recovery after tripping. *Exp Brain Res*, 201(4):689–699, Apr. 2010.

[275] S. Piperakis, M. Koskinopoulou, and P. Trahanias. Nonlinear State Estimation for Humanoid Robot Walking. *IEEE Robot. Autom. Lett.*, 3(4):3347–3354, Oct. 2018.

[276] S. Porsa, Y.-C. Lin, and M. G. Pandy. Direct Methods for Predicting Movement Biomechanics Based Upon Optimal Control Theory with Implementation in OpenSim. *Annals of Biomedical Engineering*, 44(8):2542–2557, 2016.

[277] N. Postol, N. J. Spratt, A. Bivard, and J. Marquez. Physiotherapy using a free-standing robotic exoskeleton for patients with spinal cord injury: a feasibility study. *J NeuroEngineering Rehabil*, 18(1):180, Dec. 2021.

[278] J. Pratt, J. Carff, S. Drakunov, and A. Goswami. Capture Point: A Step toward Humanoid Push Recovery. In *2006 6th IEEE-RAS International Conference on Humanoid Robots*, pages 200–207, University of Genova, Genova, Italy, Dec. 2006. IEEE.

[279] J. Pratt and R. Tedrake. Velocity-Based Stability Margins for Fast Bipedal Walking. In M. Diehl and K. Mombaur, editors, *Fast Motions in Biomechanics and Robotics*, volume 340, pages 299–324. Springer Berlin Heidelberg, Berlin, Heidelberg, 2006.

[280] P. Puchaud, F. Bailly, and M. Begon. Direct multiple shooting and direct collocation perform similarly in biomechanical predictive simulations. *Computer Methods in Applied Mechanics and Engineering*, 414:116162, Sept. 2023.

[281] P. Puchaud, E. Charbonneau, B. Michaud, and M. Begon. Optimality equivalence and computational advantages of free-floating base dynamics compared to full-body dynamics. *Mechanism and Machine Theory*, 181:105164, Mar. 2023.

[282] W. Rackl, R. Lampariello, and G. Hirzinger. Robot excitation trajectories for dynamic parameter estimation using optimized B-splines. In *2012 IEEE International Conference on Robotics and Automation*, pages 2042–2047, St Paul, MN, USA, May 2012. IEEE.

[283] V. Rajasekaran, J. Aranda, and A. Casals. Adaptive walking assistance based on human-orthosis interaction. In *2015 IEEE/RSJ International Conference on Intelligent Robots and Systems (IROS)*, pages 6190–6195, Hamburg, Germany, Sept. 2015. IEEE.

[284] V. Rajasekaran, J. Aranda, A. Casals, and J. L. Pons. An adaptive control strategy for postural stability using a wearable robot. *Robotics and Autonomous Systems*, 73:16–23, Nov. 2015.

[285] M. S. Redfern, R. Cham, K. Gielo-Perczak, R. Grönqvist, M. Hirvonen, H. Lanshammar, M. Marpet, C. Y. Pai, and C. Powers. Biomechanics of slips. *Ergonomics*, 44(13):1138–1166, 2001.

[286] M. S. Redfern, A. J. Chambers, J. R. Jennings, and J. M. Furman. Sensory and motoric influences on attention dynamics during standing balance recovery in young and older adults. *Exp Brain Res*, 235(8):2523–2531, 2017.

[287] D. J. Reinkensmeyer, O. Akoner, D. P. Ferris, and K. E. Gordon. Slacking by the human motor system: computational models and implications for robotic orthoses. *Conf Proc IEEE Eng Med Biol Soc*, 2009:2129–2132, 2009.

[288] R.-D. Reyes, R. Kobetic, M. Nandor, N. Makowski, M. Audu, R. Quinn, and R. Triolo. Effect of Joint Friction Compensation on a "Muscle-First" Motor-Assisted Hybrid Neuroprosthesis. *Front. Neurorobot.*, 14:588950, Dec. 2020.

[289] R. Reynolds. Robust estimation of covariance matrices. *IEEE Trans. Automat. Contr.*, 35(9):1047–1051, Sept. 1990.

[290] R. Riener and T. Edrich. Identification of passive elastic joint moments in the lower extremities. *J Biomech*, 32(5):539–544, May 1999.

[291] M. Rodrigues Da Silva, F. Marques, M. Tavares Da Silva, and P. Flores. A compendium of contact force models inspired by Hunt and Crossley's cornerstone work. *Mechanism and Machine Theory*, 167:104501, Jan. 2022.

[292] A. J. Rodriguez, E. Sanjurjo, R. Pastorino, and M. A. Naya. State, parameter and input observers based on multibody models and Kalman filters for vehicle dynamics. *Mechanical Systems and Signal Processing*, 155:107544, June 2021.

[293] M. C. Sanchez-Villamañán, D. Torricelli, and J. L. Pons. Modeling Human-Exoskeleton Interaction: Preliminary Results. In M. C. Carrozza, S. Micera, and J. L. Pons, editors, *Wearable Robotics: Challenges and Trends*, volume 22, pages 137–141. Springer International Publishing, Cham, 2019.

[294] R. M. Schemschat, D. Clever, M. L. Felis, and K. Mombaur. Optimal Push Recovery for Periodic Walking Motions. *IFAC-PapersOnLine*, 49(14):93–98, 2016.

[295] R. M. Schemschat, D. Clever, and K. Mombaur. Optimization based analysis of push recovery during walking motions to support the design of lower-limb exoskeletons. In *2016 IEEE International Conference on Simulation, Modeling, and Programming for Autonomous Robots (SIMPAR)*, pages 224–231, San Francisco, CA, USA, Dec. 2016. IEEE.

[296] D. Scherb, S. Wartzack, and J. Miehling. Modelling the interaction between wearable assistive devices and digital human models—A systematic review. *Front. Bioeng. Biotechnol.*, 10:1044275, Jan. 2023.

[297] A. L. C. Schneider, D. Wang, R. F. Gottesman, and E. Selvin. Prevalence of Disability Associated With Head Injury With Loss of Consciousness in Adults in the United States: A Population-Based Study. *Neurology*, 97(2):e124–e135, July 2021.

[298] G. Schultz and K. Mombaur. Modeling and Optimal Control of Human-Like Running. *IEEE/ASME Trans. Mechatron.*, 15(5):783–792, Oct. 2010.

[299] P. O. Scokaert and J. B. Rawlings. Infinite Horizon Linear Quadratic Control with Constraints. *IFAC Proceedings Volumes*, 29(1):5905–5910, June 1996.

[300] R. Serban and J. Freeman. Identification and identifiability of unknown parameters in multibody dynamic systems. *Multibody System Dynamics*, 5(4):335–350, 2001.

[301] G. Serrancoli, A. Falisse, C. Dembia, J. Vantilt, K. Tanghe, D. Lefeber, I. Jonkers, J. De Schutter, and F. De Groote. Subject-Exoskeleton Contact Model Calibration Leads to Accurate Interaction Force Predictions. *IEEE Trans. Neural Syst. Rehabil. Eng.*, 27(8):1597–1605, Aug. 2019.

[302] R. Sharif Razavian, N. Mehrabi, and J. McPhee. A model-based approach to predict muscle synergies using optimization: application to feedback control. *Front. Comput. Neurosci.*, 9, Oct. 2015.

[303] R. C. Sheehan, C. A. Rábago, J. H. Rylander, J. B. Dingwell, and J. M. Wilken. Use of Perturbation-Based Gait Training in a Virtual Environment to Address Mediolateral Instability in an Individual With Unilateral Transfemoral Amputation. *Phys Ther*, 96(12):1896–1904, 2016.

[304] M. A. Sherman, A. Seth, and S. L. Delp. What is a Moment Arm? Calculating Muscle Effectiveness in Biomechanical Models Using Generalized Coordinates. In *Volume 7B: 9th International Conference on Multibody Systems, Nonlinear Dynamics, and Control*, page V07BT10A052, Portland, Oregon, USA, Aug. 2013. American Society of Mechanical Engineers.

[305] C. Shirota, E. Van Asseldonk, Z. Matjačić, H. Vallery, P. Barralon, S. Maggioni, J. H. Buurke, and J. F. Veneman. Robot-supported assessment of balance in standing and walking. *J NeuroEngineering Rehabil*, 14(1):80, Dec. 2017.

[306] S. S. Shome, D. G. Beale, and D. Wang. A General Method for Estimating Dynamic Parameters of Spatial Mechanisms. *Nonlinear Dynamics*, 16(4):349–368, 1998.

[307] M. Shushtari and A. Arami. Human–Exoskeleton Interaction Force Estimation in Indego Exoskeleton. *Robotics*, 12(3):66, May 2023.

[308] T. Siebert, C. Rode, W. Herzog, O. Till, and R. Blickhan. Nonlinearities make a difference: comparison of two common Hill-type models with real muscle. *Biol Cybern*, 98(2):133–143, Feb. 2008.

[309] A. Silder, B. Whittington, B. Heiderscheit, and D. G. Thelen. Identification of passive elastic joint moment-angle relationships in the lower extremity. *J Biomech*, 40(12):2628–2635, 2007.

[310] D. Simon. Kalman filtering with state constraints: a survey of linear and nonlinear algorithms. *IET Control Theory & Applications*, 4(8):1303–1318, Aug. 2010.

[311] T. Slucock. A Systematic Review of Low-Cost Actuator Implementations for Lower-Limb Exoskeletons: a Technical and Financial Perspective. *J Intell Robot Syst*, 106(1):3, Sept. 2022.

[312] E. M. Smith, E. M. Giesbrecht, W. B. Mortenson, and W. C. Miller. Prevalence of Wheelchair and Scooter Use Among Community-Dwelling Canadians. *Phys Ther*, 96(8):1135–1142, Aug. 2016.

[313] M. Sposito, C. Di Natali, S. Toxiri, D. G. Caldwell, E. De Momi, and J. Ortiz. Exoskeleton kinematic design robustness: An assessment method to account for human variability. *Wearable Technol.*, 1:e7, 2020.

[314] B. Stephens. Humanoid push recovery. In *2007 7th IEEE-RAS International Conference on Humanoid Robots*, pages 589–595, Pittsburgh, PA, USA, Nov. 2007. IEEE.

[315] B. Stephens. Integral control of humanoid balance. In *2007 IEEE/RSJ Int. Conf. Intell. Robots and Systems*, pages 4020–4027, Oct. 2007.

[316] B. J. Stephens and C. G. Atkeson. Push Recovery by stepping for humanoid robots with force controlled joints. In *2010 10th IEEE-RAS International Conference on Humanoid Robots*, pages 52–59, Nashville, TN, USA, Dec. 2010. IEEE.

[317] G. Sung, K. Kong, and J. Choi. What Is the Proper Gait Pattern for People With Paraplegia Who Wear Powered Exoskeletons?: Re-examining gait patterns of existing powered exoskeletons. *IEEE Robot. Automat. Mag.*, pages 2–15, 2023.

[318] J. Swevers, C. Ganseman, D. Tukel, J. De Schutter, and H. Van Brussel. Optimal robot excitation and identification. *IEEE Trans. Robot. Automat.*, 13(5):730–740, Oct. 1997.

[319] N. Sylla, V. Bonnet, F. Colledani, and P. Fraisse. Ergonomic contribution of ABLE exoskeleton in automotive industry. *International Journal of Industrial Ergonomics*, 44(4):475–481, July 2014.

[320] K. Z. Takahashi, M. D. Lewek, and G. S. Sawicki. A neuromechanics-based powered ankle exoskeleton to assist walking post-stroke: a feasibility study. *J NeuroEngineering Rehabil*, 12(1):23, 2015.

[321] M. Takahashi, K. Nonaka, and K. Sekiguchi. Vehicle state estimation by moving horizon estimation considering occlusion and outlier on 3D static cameras. In *2015 IEEE Conference on Control Applications (CCA)*, pages 1211–1216, Sydney, Australia, Sept. 2015. IEEE.

[322] M. Talaty, A. Esquenazi, and J. E. Briceno. Differentiating ability in users of the ReWalk$^{\text{tm}}$ powered exoskeleton: An analysis of walking kinematics. In *2013 IEEE 13th International Conference on Rehabilitation Robotics (ICORR)*, pages 1–5, Seattle, WA, June 2013. IEEE.

[323] K. Tanghe, F. De Groote, D. Lefeber, J. De Schutter, and E. Aertbelien. Gait Trajectory and Event Prediction from State Estimation for Exoskeletons During Gait. *IEEE Trans. Neural Syst. Rehabil. Eng.*, 28(1):211–220, Jan. 2020.

[324] C. Tefertiller, K. Hays, J. Jones, A. Jayaraman, C. Hartigan, T. Bushnik, and G. F. Forrest. Initial Outcomes from a Multicenter Study Utilizing the Indego Powered Exoskeleton in Spinal Cord Injury. *Topics in Spinal Cord Injury Rehabilitation*, 24(1):78–85, Jan. 2018.

[325] D. Terrazas-Rodas, L. Rocca-Huaman, C. Ramirez-Amaya, J. Requejo-Rosales, J. Gutierrez-Atacusi, and F. Estacio-Cayetano. Control Systems in Lower-limb Exoskeletons for Rehabilitation and/or Assistance: A Brief Review. In *2022 International Conference on Smart Systems and Power Management (IC2SPM)*, pages 117–123, Beirut, Lebanon, Nov. 2022. IEEE.

[326] D. G. Thelen. Adjustment of muscle mechanics model parameters to simulate dynamic contractions in older adults. *J Biomech Eng*, 125(1):70–77, Feb. 2003.

[327] D. G. Thelen, F. C. Anderson, and S. L. Delp. Generating dynamic simulations of movement using computed muscle control. *J Biomech*, 36(3):321–328, Mar. 2003.

[328] E. Thelen. Motor development as foundation and future of developmental psychology. *International Journal of Behavioral Development*, 24(4):385–397, Dec. 2000.

[329] C. D. Tokuno, A. G. Cresswell, A. Thorstensson, and M. G. Carpenter. Age-related changes in postural responses revealed by support-surface translations with a long acceleration–deceleration interval. *Clinical Neurophysiology*, 121(1):109–117, 2010.

[330] C. M. Town, D. L. Gyemi, Z. Ellis, C. Kahelin, A. C. Laing, and D. M. Andrews. Predicting soft tissue thicknesses overlying the iliac crests and greater trochanters of younger and older adults. *PLoS ONE*, 18(3):e0283012, Mar. 2023.

[331] H. Trivedi, J. A. Leonard, L. H. Ting, and P. J. Stapley. Postural responses to unexpected perturbations of balance during reaching. *Exp Brain Res*, 202(2):485–491, 2010.

[332] K. L. Troy, S. J. Donovan, and M. D. Grabiner. Theoretical contribution of the upper extremities to reducing trunk extension following a laboratory-induced slip. *Journal of Biomechanics*, 42(9):1339–1344, June 2009.

[333] C. M. Tse, A. E. Chisholm, T. Lam, J. J. Eng, and SCIRE Research Team. A systematic review of the effectiveness of task-specific rehabilitation interventions for

improving independent sitting and standing function in spinal cord injury. *J Spinal Cord Med*, 41(3):254–266, May 2018.

[334] M. R. Tucker, J. Olivier, A. Pagel, H. Bleuler, M. Bouri, O. Lambercy, J. d. R. Millán, R. Riener, H. Vallery, and R. Gassert. Control strategies for active lower extremity prosthetics and orthotics: a review. *J NeuroEngineering Rehabil*, 12(1):1, 2015.

[335] T. Tuttle and W. Seering. Modeling a harmonic drive gear transmission. In *[1993] Proceedings IEEE International Conference on Robotics and Automation*, pages 624–629, Atlanta, GA, USA, 1993. IEEE Comput. Soc. Press.

[336] T. Tuttle and W. Seering. A nonlinear model of a harmonic drive gear transmission. *IEEE Trans. Robot. Automat.*, 12(3):368–374, June 1996.

[337] S. Ungarala. Computing arrival cost parameters in moving horizon estimation using sampling based filters. *Journal of Process Control*, 19(9):1576–1588, Oct. 2009.

[338] H. Vallery, A. Bogel, C. O'Brien, D. Li, and R. Riener. Robotic Assistance for Human Balance. In *Dynamic Walking (Conference)*, 2012.

[339] H. Vallery, A. Bögel, C. O´Brien, and R. Riener. Cooperative Control Design for Robot-Assisted Balance During Gait. *at - Automatisierungstechnik*, 60(11):715–720, Nov. 2012.

[340] E. H. F. van Asseldonk, A. Emmens, T. J. H. Brug, I. Pisotta, M. Arquilla, F. Tamburella, M. Masciullo, N. L. Tagliamonte, R. Valette, M. Molinari, and H. van der Kooij. Training Balance Recovery in People with Incomplete SCI Wearing a Wearable Exoskeleton. In M. C. Carrozza, S. Micera, and J. L. Pons, editors, *Wearable Robotics: Challenges and Trends*, volume 22, pages 334–338. Springer International Publishing, Cham, 2019.

[341] H. van der Kooij, R. Jacobs, B. Koopman, and H. Grootenboer. A multisensory integration model of human stance control. *Biol Cybern*, 80(5):299–308, May 1999.

[342] H. van der Kooij, R. Jacobs, B. Koopman, and F. van der Helm. An adaptive model of sensory integration in a dynamic environment applied to human stance control. *Biol Cybern*, 84(2):103–115, 2001.

[343] H. van der Kooij, E. H. F. van Asseldonk, and M. Vlutters. Towards Exoskeletons with Balance Capacities. In J. González-Vargas, J. Ibáñez, J. L. Contreras-Vidal, H. van der Kooij, and J. L. Pons, editors, *Wearable Robotics: Challenges and Trends*, volume 16, pages 175–179. Springer International Publishing, Cham, 2017.

[344] C. S. Versteeg, L. H. Ting, and J. L. Allen. Hip and ankle responses for reactive balance emerge from varying priorities to reduce effort and kinematic excursion: A simulation study. *J. Biomech.*, 49(14):3230–3237, 2016.

[345] M. Vlutters, E. H. F. van Asseldonk, and H. van der Kooij. Center of mass velocity-based predictions in balance recovery following pelvis perturbations during human walking. *J Exp Biol*, 219(10):1514–1523, May 2016.

[346] M. Vukobratović and B. Borovac. Zero-Moment Point — Thirty Five Years of its Life. *Int. J. Human. Robot.*, 01(01):157–173, Mar. 2004.

[347] C. P. Vyasarayani, T. Uchida, A. Carvalho, and J. McPhee. Parameter identification in dynamic systems using the homotopy optimization approach. *Multibody Syst Dyn*, 26(4):411–424, Dec. 2011.

[348] L. Wang, S. Wang, E. H. F. van Asseldonk, and H. van der Kooij. Actively controlled lateral gait assistance in a lower limb exoskeleton. In *2013 IEEE/RSJ International Conference on Intelligent Robots and Systems*, pages 965–970, Tokyo, Nov. 2013. IEEE.

[349] S. Wang, L. Wang, C. Meijneke, E. van Asseldonk, T. Hoellinger, G. Cheron, Y. Ivanenko, V. La Scaleia, F. Sylos-Labini, M. Molinari, F. Tamburella, I. Pisotta, F. Thorsteinsson, M. Ilzkovitz, J. Gancet, Y. Nevatia, R. Hauffe, F. Zanow, and H. van der Kooij. Design and Control of the MINDWALKER Exoskeleton. *IEEE Trans. Neural Syst. Rehabil. Eng.*, 23(2):277–286, Mar. 2015.

[350] X. Wang. Wiener processes with random effects for degradation data. *Journal of Multivariate Analysis*, 101(2):340–351, Feb. 2010.

[351] T. B. Weaver, M. N. Glinka, and A. C. Laing. Stooping, crouching, and standing - Characterizing balance control strategies across postures. *J Biomech*, 53:90–96, 2017.

[352] T. B. Weaver, C. Ma, and A. C. Laing. Use of the Nintendo Wii Balance Board for Studying Standing Static Balance Control: Technical Considerations, Force-Plate Congruency, and the Effect of Battery Life. *Journal of Applied Biomechanics*, 33(1):48–55, Feb. 2017.

[353] T. D. J. Welch and L. H. Ting. A Feedback Model Reproduces Muscle Activity During Human Postural Responses to Support-Surface Translations. *Journal of Neurophysiology*, 99(2):1032–1038, 2008.

[354] T. D. J. Welch and L. H. Ting. A feedback model explains the differential scaling of human postural responses to perturbation acceleration and velocity. *J. Neurophysiol.*, 101(6):3294–3309, 2009.

[355] T. D. J. Welch and L. H. Ting. Mechanisms of Motor Adaptation in Reactive Balance Control. *PLoS ONE*, 9(5):e96440, 2014.

[356] D. L. Wight, E. G. Kubica, and D. W. L. Wang. Introduction of the Foot Placement Estimator: A Dynamic Measure of Balance for Bipedal Robotics. *Journal of Computational and Nonlinear Dynamics*, 3(1):011009, Jan. 2008.

[357] T. B. Winberg. The Effects of Varying Surface Translation Acceleration and Velocity on Compensatory Forward Stepping Responses. Master's thesis, Dept. Kin., Univ. Waterloo, Waterloo, Canada, 2018.

[358] T. B. Winberg, D. R. Martel, T. B. Hoshizaki, and A. C. Laing. Evaluation of amplitude- and frequency-based techniques for attenuating inertia-based movement artifact during surface translation perturbations. *Gait & Posture*, 86:299–302, May 2021.

[359] D. Winter. Human balance and posture control during standing and walking. *Gait & Posture*, 3(4):193–214, 1995.

[360] D. A. Winter. *Biomechanics and motor control of human movement*. Wiley, Hoboken, N.J, 4th ed edition, 2009. OCLC: ocn318408191.

[361] D. A. Winter, A. E. Patla, F. Prince, M. Ishac, and K. Gielo-Perczak. Stiffness control of balance in quiet standing. *J. Neurophysiol.*, 80(3):1211–1221, 1998.

[362] J. M. Winters. Hill-Based Muscle Models: A Systems Engineering Perspective. In J. M. Winters and S. L.-Y. Woo, editors, *Multiple Muscle Systems*, pages 69–93. Springer New York, New York, NY, 1990.

[363] J. M. Winters and L. Stark. Muscle models: What is gained and what is lost by varying model complexity. *Biol. Cybern.*, 55(6):403–420, Mar. 1987.

[364] M. A. Wright, F. Herzog, A. Mas-Vinyals, A. Carnicero-Carmona, J. Lobo-Prat, C. Hensel, S. Franz, N. Weidner, J. Vidal, E. Opisso, and R. Rupp. Multicentric investigation on the safety, feasibility and usability of the ABLE lower-limb robotic exoskeleton for individuals with spinal cord injury: a framework towards the standardisation of clinical evaluations. *J NeuroEngineering Rehabil*, 20(1):45, Apr. 2023.

[365] J. Wu, J. Wang, and Z. You. An overview of dynamic parameter identification of robots. *Robotics and Computer-Integrated Manufacturing*, 26(5):414–419, Oct. 2010.

[366] F. Xia, J. Liu, H. Nie, Y. Fu, L. Wan, and X. Kong. Random Walks: A Review of Algorithms and Applications. *IEEE Trans. Emerg. Top. Comput. Intell.*, 4(2):95–107, Apr. 2020.

[367] H. Xia and F. Chen. Filtering-Based Parameter Identification Methods for Multivariable Stochastic Systems. *Mathematics*, 8(12):2254, Dec. 2020.

[368] G. T. Yamaguchi. *Dynamic modeling of musculoskeletal motion: a vectorized approach for biomechanical analysis in three dimensions*. Springer, New York, NY, 1. softcover printing edition, 2006. OCLC: 254902470.

[369] F. Yang, F. C. Anderson, and Y.-C. Pai. Predicted threshold against backward balance loss in gait. *J Biomech*, 40(4):804–811, 2007.

[370] F. Yang, D. Espy, and Y.-C. Pai. Feasible stability region in the frontal plane during human gait. *Ann Biomed Eng*, 37(12):2606–2614, Dec. 2009.

[371] M. R. Yeadon, M. A. King, and C. Wilson. Modelling the maximum voluntary joint torque/angular velocity relationship in human movement. *J Biomech*, 39(3):476–482, Jan. 2006.

[372] A. Yeaser, J. Tung, J. Huissoon, and E. Hashemi. Learning-Aided User Intent Estimation for Smart Rollators. In *2020 42nd Annual International Conference of the IEEE Engineering in Medicine & Biology Society (EMBC)*, pages 3178–3183, Montreal, QC, Canada, July 2020. IEEE.

[373] J. You, Y. Chou, C. Lin, and F. Su. Effect of slip on movement of body center of mass relative to base of support. *Clin Biomech (Bristol, Avon)*, 16(2):167–173, Feb. 2001.

[374] A. J. Young, A. M. Simon, N. P. Fey, and L. J. Hargrove. Intent Recognition in a Powered Lower Limb Prosthesis Using Time History Information. *Ann Biomed Eng*, 42(3):631–641, Mar. 2014.

[375] G. Zeilig, H. Weingarden, M. Zwecker, I. Dudkiewicz, A. Bloch, and A. Esquenazi. Safety and tolerance of the ReWalk ™ exoskeleton suit for ambulation by people with complete spinal cord injury: A pilot study. *The Journal of Spinal Cord Medicine*, 35(2):96–101, Mar. 2012.

[376] F. Zhang, M. Liu, and H. Huang. Preliminary study of the effect of user intent recognition errors on volitional control of powered lower limb prostheses. *Conf Proc IEEE Eng Med Biol Soc*, 2012:2768–2771, 2012.

[377] H. Zheng, T. Shen, M. R. Afsar, I. Kang, A. J. Young, and X. Shen. A Semi-Wearable Robotic Device for Sit-to-Stand Assistance. *IEEE Int Conf Rehabil Robot*, 2019:204–209, 2019.

APPENDICES

Appendix A

Example: Human Parameter Values

Table A.1: Example of human multibody dynamic parameters for the thigh, shank, upper arm and forearm+hand

Segment	Parameter	Value	Units
Thigh	Length	43.65	cm
	Mass	10.62	kg
	MOI (wrt COM)	$21.90 \cdot 10^{-2}$	$kg \cdot m^2$
	COM Position (wrt Hip)	17.88	cm
Shank	Length	44.87	cm
	Mass	3.25	kg
	MOI (wrt COM)	$4.05 \cdot 10^{-2}$	$kg \cdot m^2$
	COM Position (wrt Knee)	20.01	m
Upper Arm	Length	29.12	cm
	Mass	2.03	kg
	MOI (wrt COM)	$1.25 \cdot 10^{-2}$	$kg \cdot m^2$
	COM Position (wrt Shldr)	16.81	cm
Forearm+Hand	Length	36.71	cm
	Mass	1.46	kg
	MOI (wrt COM)	$2.38 \cdot 10^{-2}$	$kg \cdot m^2$
	COM Position (wrt Elbow)	18.77	cm

* Young adult male; height = 1.80 m, weight = 75 kg

Table A.2: Example of human multibody dynamic parameters for the lumped head, trunk, pelvis in addition to the lumped foot segment. The $\hat{\mathbf{j}}$-direction corresponds to the corresponding segment longitudinal axis (positive = superior); the $\hat{\mathbf{i}}$-direction describes the segment-fixed anteroposterior axis (positive = anterior).

Parameter	Value	Units
Head, Trunk, Pelvis		
Length (Hip to Top of Head)	84.46	cm
Mass	37.8	kg
MOI (wrt COM)	$200.37 \cdot 10^{-2}$	$\text{kg} \cdot \text{m}^2$
COM position (wrt Hip)	35.76	cm
Shoulder Position $\hat{\mathbf{i}}$ (wrt Hip)	-5.00	cm
Shoulder Position $\hat{\mathbf{j}}$ (wrt Hip)	51.44	cm
Foot		
Length (Toe to Heel)	26.68	cm
Mass	1.03	kg
MOI (wrt COM)	$0.67 \cdot 10^{-2}$	$\text{kg} \cdot \text{m}^2$
Toe Position $\hat{\mathbf{i}}$ (wrt Ankle)	20.70	cm
Toe Position $\hat{\mathbf{j}}$ (wrt Ankle)	-7.02	cm
Heel Position $\hat{\mathbf{i}}$ (wrt Ankle)	-5.99	cm
Heel Position $\hat{\mathbf{j}}$ (wrt Ankle)	-7.02	cm

* Scaled for young adult male; height = 1.80 m, weight = 75 kg

Appendix B

Background: Muscle Torque Generators

The following section will outline the rationale for using MTG models in place of the classical approach (i.e., muscles as redundant linear actuators) while also providing mathematical formulations that are beneficial for implementation in derivative-based optimal control simulations. Note that the following text contains excerpts from the journal paper Inkol et al. [165] published in Multibody System Dynamics (included with permission from Springer Nature; *see back of dissertation*).

To maintain reasonable fidelity within multibody dynamic simulations of human movement, it is often important to consider the limitations of muscle physiology in actuating the system. Typically, though not always, muscles are represented as linear actuators (i.e. massless cables) whose line of action is determined by anatomical origins/insertions. The experimentally observed nonlinear dependence of muscle tension on both muscle length and the rate of lengthening [129, 150, 186, 308] is then incorporated into these actuators using individual muscle model equations. Often, these muscle models take inspiration from the lumped-parameter model originally disseminated by Hill [150] with additional terms to better account for the unique input/output relationship during eccentric contractions. Muscle models can also be quite structurally varied, containing multiple elements that are distributed in series or parallel with one another [363, 362]. Although closer to the real world in theory, incorporating muscles within the multibody dynamic simulation carries several drawbacks, especially when the goal is subject- or population-specific modelling.

Some primary drawbacks include solving the actuator redundancy problem [54] and the presence of difficult-to-fit parameters for each muscle [244]. These methods also require the definition of complex musculoskeletal geometry [34, 81, 91, 304], which describes how the muscle belly interacts and slides over and around the skeletal surface. This geometry can have profound effects on factors like muscle moment-arm length, muscle length, direction of applied joint torque, etc.

Let us consider the muscle torques generated by muscles about a single revolute joint as we have in the stance model; the axis of rotation in inertial space is given as $\hat{\mathbf{n}}$. Said joint is crossed by k_i flexor or extensor muscles, each of which connect to a unique anatomical origin/insertion via tendons (note: some muscles share a common tendon). The tension generated by a musculotendon unit (combination of muscle and tendon in series) is dependent on its intrinsic physiological properties and kinematics. To capture this mathematically, we can state that the activation of a *single* muscle $\tilde{a}_{\mathrm{m},i} \in [0,1]$, in response to stimulus from the central nervous system $\tilde{u}_{\mathrm{m},i} \in [0,1]$, results in a force $F_{\mathrm{m},i}$ where:

$$F_{\mathrm{m},i} = f(\tilde{a}_{\mathrm{m},i}(t), \ell_{\mathrm{m},i}(t), \dot{\ell}_{\mathrm{m},i}, f_{\mathrm{iso}}, \alpha_{\mathrm{m},i}) \tag{B.1}$$

$$= \tilde{a}_{\mathrm{m},i}(t) F_{\mathrm{iso}} F_{\mathrm{p}}(\ell_{\mathrm{m},i}(t); \mathbf{p}_{\mathrm{p}}) F_{\mathrm{v}}(\dot{\ell}_{\mathrm{m},i}; \mathbf{p}_{\mathrm{v}}) \cos(\alpha_{\mathrm{m},i}) + F_{\mathrm{pe}}(\ell_{\mathrm{m},i}, \dot{\ell}_{\mathrm{m},i}; \mathbf{p}_{\mathrm{pe}}) \tag{B.2}$$

As highlighted in Equation (B.2), $F_{\mathrm{m},i}$ is dependent on both the muscle's time-varying length $\ell_{\mathrm{m},i}(t)$ and its time derivative $\dot{\ell}_{\mathrm{m},i}$, the muscle fiber pennation angle $\alpha_{\mathrm{m},i}$, as well as the maximum feasible isometric force F_{iso}. The muscle applies tension to the tendon, which subsequently transfers force to the bone depending on its own length ℓ_{t}, i.e. strain dependent. Each of the functions $F_{\mathrm{p}}(\cdot)$, $F_{\mathrm{v}}(\cdot)$, and $F_{\mathrm{pe}}(\cdot)$ are plotted in Fig. B.1 (*next page*) to provide the reader with an idea of the typical shape that these scaling functions take on with variations in muscle length and rate of shortening. The exact curvature that each scaling function follows is determined by the vector of parameters $\mathbf{p}_{\mathrm{p}}$, $\mathbf{p}_{\mathrm{v}}$, and $\mathbf{p}_{\mathrm{pe}}$. Various candidate functions have been proposed to capture the highly nonlinear input/output relationship observed experimentally in individual muscles [88, 247, 266, 326]; however, as these functions are not of focus in the current manuscript, we will not discuss them further.

Now, assuming muscle geometry is known, it is possible to write any given scalar flexor or extensor muscle force $F_{\mathrm{m},i}$ as a vector $\mathbf{F}_{\mathrm{m},i} \in \mathbb{R}^3$ within the inertial frame of reference. If we consider all flexors or extensors crossing the joint of interest, and control them with

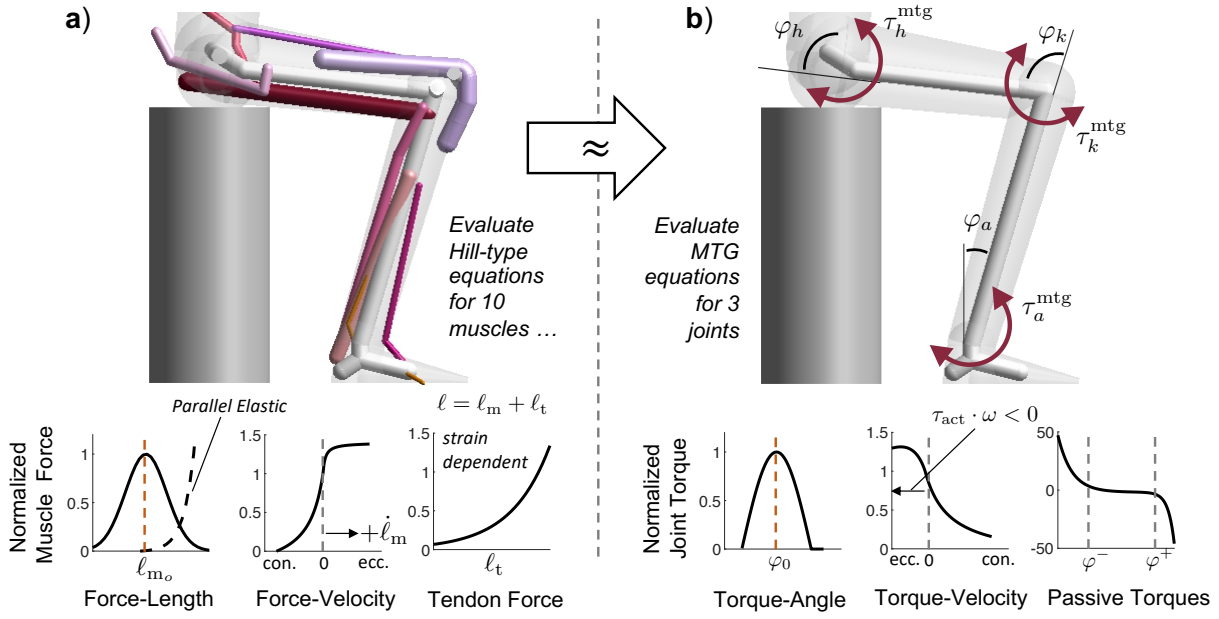


Figure B.1: Schematic of the knee, ankle, and hip joint within Norman-Gerum's sit-to-stand model [262], actuated by (a) Hill-type muscles and (b) muscle torque generators (MTGs). Note the complex wrapping geometry and redundancy encountered when using muscles. MTGs permit multibody system reduction by approximating the force-length/velocity curves and passive elements (shown *bottom*) directly at the joint level (scaling torques using joint rotations). Note the analogs between the MTG parameters and Hill-type parameters (e.g. optimal muscle length ℓ_0 and joint angle θ_0). Eccentric and concentric phases of muscle/torque scaling are indicated by "con." and "ecc." respectively. Adapted with permission from author V. Norman-Gerum [262] and Springer Nature (*see back of dissertation*).

a k_i-dimensional vector $\tilde{\mathbf{u}}$, then the joint torque produced by these muscles must be,

$$\tau_{\mathrm{m},i} = \sum_{j=1}^{k_i} [\mathbf{r}_j(\mathbf{q}_\mathrm{h}) \times \mathbf{F}_{\mathrm{m},j}(\tilde{a}_j, \ell_{\mathrm{m},j}, \dot{\ell}_{\mathrm{m},j}, \cdot)] \cdot \hat{\mathbf{n}} \tag{B.3}$$

$$= \mathbf{N}_i(\mathbf{q}_\mathrm{h})\mathbf{S}_i, \quad \mathbf{S}_i = \{F_{\mathrm{m},1}, F_{\mathrm{m},2}, ..., F_{\mathrm{m},k_i}\}^T \tag{B.4}$$

where $\mathbf{r}_i(\mathbf{q}_\mathrm{h})$ is any point along the line of action of muscle force $\mathbf{F}_{\mathrm{m},i}$ expressed in the inertial frame. The linear mapping in (B.4) projects each scalar muscle force onto the vector tangent to the corresponding muscle's moment-arm, which varies with $\mathbf{q}_\mathrm{h}$. This formulation

of τ_{m} is commonly used within the literature [32, 179, 266, 276, 304]; however, despite appearing simple, identifying the moment-arm matrix $\mathbf{N}(\mathbf{q}_{\mathrm{h}}(t))$ for each joint can become quite cumbersome when aiming for realistic muscle-wrapping geometry [304]. Furthermore, the method above requires a substantial number of operations, especially if we consider $k_1 + k_2 + \cdots + k_n \gg \dim(\mathbf{q}_{\mathrm{h}})$ in the context of muscle redundancy [54].

As a final note in this section, there is still the need to calculate each muscle ℓ_{m} and $\dot{\ell}_{\mathrm{m}}$ in order to evaluate (B.2) and subsequently τ_{m}. If the tendon is considered rigid as we have assumed, this operation requires purely algebraic manipulations using $\mathbf{q}_{\mathrm{h}}$, $\dot{\mathbf{q}}_{\mathrm{h}}$, and musculoskeletal geometry equations. Though somewhat unimposing, the additional nonlinear kinematic analyses increase the computational demands of dynamic simulations. Furthermore, the task becomes even less trivial if the tendon is compliant. Contraction dynamics must be added to the system to track changes in both muscle and tendon length as a proportion of musculotendon length [247, 266, 326]. These contraction dynamics can introduce numerical issues (e.g. singularities) that can impact performance and convergence within optimal control routines. In fact, obtaining reliable performance with these models often require substantial workarounds [247]. Additionally, in the case of specific optimal control algorithms like *direct collocation*, the increased state-space dimensionality increases the size of the control problem's search space resulting in even further reductions in computational performance.

For all the work required to implement redundant muscle actuators into biomechanical simulations, the individual designing and using these models may not even be interested in topics like predicting isolated muscle tensions or joint contact forces. In this case, we can mitigate concerns of muscle geometry and redundancy within a control framework through the use of MTGs. Functionally, an MTG produces a joint torque that mimics the behaviour of muscles crossing a given joint; this typically involves some elements of kinematic dependence on active torque generation and passive impedance. Several authors have proposed MTG functions that vary in curvature, number of parameters, and continuity [31, 136, 179, 216, 244, 368, 371]. Our focus will be on using the work disseminated in [31, 244, 368] and adapting the proposed MTG models for derivative-based optimal control simulations.

To elaborate on how MTGs work, we revisit the muscle actuation of a given revolute joint. At said joint, we assume there are k_i^{flex} flexors and k_i^{ext} extensors. By considering the joint's angle θ ($\omega = d\theta/dt$) instead of individual muscle lengths, we can in theory utilize

two rotational single-muscle equivalents to approximate the biofidelic actions of **all** muscle groups that do work about $\hat{\mathbf{n}}$:

$$\begin{aligned}\sum_{j=1}^{k_i^{\text{flex}}}[\mathbf{r}_j^{\text{flex}}\times\mathbf{F}_{\text{m},j}^{\text{flex}}(\tilde{a}_j^{\text{flex}},\ell_{\text{m},j}^{\text{flex}},\dot{\ell}_{\text{m},j}^{\text{flex}},\cdot)]\cdot\hat{\mathbf{n}}+\sum_{j=1}^{k_i^{\text{ext}}}[\mathbf{r}_j^{\text{ext}}\times\mathbf{F}_{\text{m},j}^{\text{ext}}(\tilde{a}_j^{\text{ext}},\ell_{\text{m},j}^{\text{ext}},\dot{\ell}_{\text{m},j}^{\text{ext}},\cdot)]\cdot\hat{\mathbf{n}}\\ \approx a^{\text{flex}}(t)\tau_{\text{iso}}^{\text{flex}}\tau_\theta(\theta;\mathbf{p}_\theta^{\text{flex}})\tau_\omega(\omega;\mathbf{p}_\omega^{\text{flex}})+a^{\text{ext}}(t)\tau_{\text{iso}}^{\text{ext}}\tau_\theta(\theta;\mathbf{p}_\theta^{\text{ext}})\tau_\omega(\omega;\mathbf{p}_\omega^{\text{ext}})\end{aligned} \tag{B.5}$$

where $\tau_{\text{iso}}^{\text{flex}}$ and $\tau_{\text{iso}}^{\text{ext}}$ are the maximal isometric flexion and extension torques. Note that Equation (B.5) also assumes that the tendons are rigid and that $\mathbf{F}_{\text{m}}$ contains forces arising only from the contractile element of muscle, i.e. $F_{\text{pe}}=0$. We can see that rather than requiring sets of position and velocity-scaling parameters for each individual flexor and extensor muscle (requires $[\dim(\mathbf{p}_{\text{p}})+\dim(\mathbf{p}_{\text{v}})]\times[k_i^{\text{flex}}+k_i^{\text{ext}}]$ parameters), we can instead parameterize the physiological limits of torque generation about the joint through $\dim(\mathbf{p}_\theta)+\dim(\mathbf{p}_\omega)$ MTG parameters.

An obvious limitation of Equation (B.5) is the aforementioned consideration of the contractile elements only for torque generation. If $F_{\text{pe}}\neq 0$, i.e., non-zero forces arising from passive, viscoelastic elements (e.g. epimysium, perimysium) in parallel to the active components, this approximation is no longer sufficient. Rather, the expression for active muscle torque can be combined with a nonlinear function $\tau_{\text{psv}}(\cdot)$ to capture the joint impedance resulting from deformation of not only the passives structures within the muscles, but the elements that are separate but still parallel with the muscle as well, e.g., ligaments [290, 309]). In addressing these limitations, we arrive at the full-form of single-joint MTG used within the current dissertation:

$$\begin{aligned}\tau_{\text{mtg}}(\theta,\omega,a^{\text{flex}},a^{\text{ext}})&=a^{\text{flex}}(t)\tau_{\text{iso}}^{\text{flex}}\tau_\theta(\theta;\mathbf{p}_\theta^{\text{flex}})\tau_\omega(\omega;\mathbf{p}_\omega^{\text{flex}})\\&\quad+a^{\text{ext}}(t)\tau_{\text{iso}}^{\text{ext}}\tau_\theta(\theta;\mathbf{p}_\theta^{\text{ext}})\tau_\omega(\omega;\mathbf{p}_\omega^{\text{ext}})+\tau_{\text{psv}}(\theta,\omega;\mathbf{p}_{\text{psv}})\end{aligned} \tag{B.6}$$

which now features a passive torque generator whose behaviour depends on the set of parameters $\mathbf{p}_{\text{psv}}$. In theory, a τ_{mtg} of sufficient accuracy can bypass the issues presented by muscle redundancy, geometry, and excess calculations while maintaining the important kinematic dependence of muscle force [244]. Note that in the following section, we will also briefly introduce cases in which τ_{psv} is a function of local and neighboring joint angles, i.e., passive actuation through biarticular musculature [290, 309].

Appendix C

Muscle Torque Generator Functions

To provide biofidelic actuation of the human model during predictive simulations without requiring substantial computational resources, muscle torque generators (MTGs) were implemented [31, 165, 244]. For the underlying rationale for why we use MTG models in place of the classical approach (i.e., muscles as redundant linear actuators), we refer the reader to Appendix B. Note that the text in the appendix contains excerpts from the journal paper Inkol et al. [165] published in Multibody System Dynamics.

As we assumed bilateral symmetry in our model of human upright posture, a total of $p = 10$ MTGs were implemented to drive the human: one flexor and extensor per element of $\mathbf{q}_\mathrm{h}$ (see Fig. 5.7). The resulting equation for $\boldsymbol{\tau}_\mathrm{mtg}(\cdot) \in \mathbb{R}^{5\times 1}$, as implemented in Equation (3.2), i.e., the muscle torques at each joint in the model, was thus

$$\begin{aligned}\boldsymbol{\tau}_\mathrm{mtg}(\mathbf{q}_\mathrm{h}(t), \dot{\mathbf{q}}_\mathrm{h}, \mathbf{a}(t)) = {} & 2\mathbf{a}^\mathrm{flex}(t)\boldsymbol{\tau}^\mathrm{flex}_\mathrm{iso}\boldsymbol{\tau}_\theta(\mathbf{q}_\mathrm{h}; \bar{\mathbf{p}}^\mathrm{flex}_\theta)\boldsymbol{\tau}_\omega(\dot{\mathbf{q}}_\mathrm{h}; \bar{\mathbf{p}}^\mathrm{flex}_\omega) \\ & + 2\mathbf{a}^\mathrm{ext}(t)\boldsymbol{\tau}^\mathrm{ext}_\mathrm{iso}\boldsymbol{\tau}_\theta(\mathbf{q}_\mathrm{h}; \bar{\mathbf{p}}^\mathrm{ext}_\theta)\boldsymbol{\tau}_\omega(\dot{\mathbf{q}}_\mathrm{h}; \bar{\mathbf{p}}^\mathrm{ext}_\omega) + 2\boldsymbol{\tau}_\mathrm{psv}(\mathbf{q}_\mathrm{h}, \dot{\mathbf{q}}_\mathrm{h}; \bar{\mathbf{p}}_\mathrm{psv})\end{aligned} \tag{C.1}$$

or alternatively,

$$\boldsymbol{\tau}_\mathrm{mtg}(\mathbf{q}_\mathrm{h}(t), \dot{\mathbf{q}}_\mathrm{h}, \mathbf{a}(t)) = \boldsymbol{\tau}^\mathrm{cns}_\mathrm{mtg}(\mathbf{a}, \mathbf{q}_\mathrm{h}, \dot{\mathbf{q}}_\mathrm{h}; \cdot) + 2\boldsymbol{\tau}_\mathrm{psv}(\mathbf{q}_\mathrm{h}, \dot{\mathbf{q}}_\mathrm{h}; \bar{\mathbf{p}}_\mathrm{psv}) \tag{C.2}$$

where $\boldsymbol{\tau}^\mathrm{cns}_\mathrm{mtg}(\cdot)$ is used to simply identify the torques resulting from an active neural drive and differentiate them with respect to their passive counterpart. In Equation (C.2), $\mathbf{a}(t) = [\mathbf{a}^\mathrm{flex}, \mathbf{a}^\mathrm{ext}]^\intercal$ is the concatenation of the flexor $\mathbf{a}^\mathrm{flex} \in \mathcal{A}$ and extensor activations $\mathbf{a}^\mathrm{ext} \in \mathcal{A}$ ($\mathcal{A} \subset \{\mathbb{R}^5 \,|\, a_i \in [0, 1]\}$). We also introduce isometric torque parameter vectors $\boldsymbol{\tau}^\mathrm{flex}_\mathrm{iso} =$

$[\tau^{\text{flex}}_{\text{iso},1}, \ldots, \tau^{\text{flex}}_{\text{iso},5}]^\intercal$ and $\boldsymbol{\tau}^{\text{ext}}_{\text{iso}} = [\tau^{\text{ext}}_{\text{iso},1}, \ldots, \tau^{\text{ext}}_{\text{iso},5}]^\intercal$ that control peak MTG output at zero joint-velocity. The former contains maximal isometric torques for the hip flexors, knee extensors, ankle dorsiflexors, shoulder flexors, and elbow flexors; the latter contains values for the hip extensors, knee flexors, ankle plantarflexors, shoulder extensors, and elbow extensors. Note the scaling of terms in Equation (C.1) by 2 due to the assumption of bilateral symmetry in the standing balance model, i.e., right and left groups of MTGs share the same activation profiles.

In Equation (C.1), vector-valued torque-angle and torque-velocity scaling functions were defined as follows:

$$\boldsymbol{\tau}_\theta(\mathbf{q}_\text{h}; \bar{\mathbf{p}}_\theta) = \left\{ \begin{array}{c} \tau^{\text{And.}}_\theta(\theta_\text{hip}; \mathbf{p}_{\theta_\text{hip}}) \\ \vdots \\ \tau^{\text{And.}}_\theta(\theta_\text{elbow}; \mathbf{p}_{\theta_\text{elbow}}) \end{array} \right\}, \quad \boldsymbol{\tau}_\omega(\mathbf{q}_\text{h}; \bar{\mathbf{p}}_\omega) = \left\{ \begin{array}{c} \tau^{\text{And.}}_\omega(\omega_\text{hip}; \mathbf{p}_{\omega_\text{hip}}) \\ \vdots \\ \tau^{\text{And.}}_\omega(\omega_\text{elbow}; \mathbf{p}_{\omega_\text{elbow}}) \end{array} \right\} \tag{C.3}$$

while the passive torque generator function was defined as

$$\boldsymbol{\tau}_\text{psv}(\mathbf{q}_\text{h}, \dot{\mathbf{q}}_\text{h}; \bar{\mathbf{p}}_\text{psv}) = \left\{ \begin{array}{c} \tau^{\text{SM.}}_{\text{psv,h}}(\theta_\text{hip}, \theta_\text{knee}, \omega_\text{hip}; \mathbf{p}_\text{psv,hip}) \\ \tau^{\text{SM.}}_{\text{psv,k}}(\theta_\text{hip}, \theta_\text{knee}, \theta_\text{ankle}, \omega_\text{knee}; \mathbf{p}_\text{psv,knee}) \\ \tau^{\text{SM.}}_{\text{psv,a}}(\theta_\text{knee}, \theta_\text{ankle}, \omega_\text{ankle}; \mathbf{p}_\text{psv,ankle}) \\ \tau^{\text{YM.}}_\text{psv}(\theta_\text{shldr}, \omega_\text{shldr}; \mathbf{p}_\text{psv,shldr}) \\ \tau^{\text{YM.}}_\text{psv}(\theta_\text{elbow}, \omega_\text{elbow}; \mathbf{p}_\text{psv,elbow}) \end{array} \right\} \tag{C.4}$$

where $\tau^{\text{And.}}_\theta$ and $\tau^{\text{And.}}_\omega$ are torque-angle and torque-velocity scaling functions proposed and validated for the lower-limb joints in Anderson et al. [31], $\tau^{\text{SM.}}_{\text{psv,-}}$ is the exponential passive joint torque function identified specifically for the hip, knee, ankle by Riener and Edrich [290] and Silder et al. [309], and $\tau^{\text{YM.}}_\text{psv}$ is another an exponential passive joint torque function but generalized for any hypothetical revolute joint according to the work by Yamaguchi [368] and Millard et al. [244]. Note that the equations disseminated in [290, 309] consider how biarticular musculature produces passive lower-limb joint moments, hence the inclusion of multiple joint angles as input arguments for each SM function rather than strictly local joint angles as in the YM function. Parameters that defined each individual MTGs unique shape were concatenated into separate arrays depending on whether they were flexors or

extensors, but generally followed the pattern

$$\bar{\mathbf{p}}_\theta = [\mathbf{p}_{\theta_{\text{hip}}}, \mathbf{p}_{\theta_{\text{knee}}}, \mathbf{p}_{\theta_{\text{ankle}}}, \mathbf{p}_{\theta_{\text{shldr}}}, \mathbf{p}_{\theta_{\text{elbow}}}] \tag{C.5}$$

$$\bar{\mathbf{p}}_\omega = [\mathbf{p}_{\omega_{\text{hip}}}, \mathbf{p}_{\omega_{\text{knee}}}, \mathbf{p}_{\omega_{\text{ankle}}}, \mathbf{p}_{\omega_{\text{shldr}}}, \mathbf{p}_{\omega_{\text{elbow}}}] \tag{C.6}$$

$$\bar{\mathbf{p}}_{\text{psv}} = [\mathbf{p}_{\text{psv,hip}}, \mathbf{p}_{\text{psv,knee}}, \mathbf{p}_{\text{psv,ankle}}, \mathbf{p}_{\text{psv,shldr}}, \mathbf{p}_{\text{psv,elbow}}] \tag{C.7}$$

The first functions we will examine are $\tau_\theta^{\text{And.}}(\cdot)$ and $\tau_\omega^{\text{And.}}(\cdot)$. In 2007, Anderson et al. [31] designed MTG torque-angle and torque-velocity scaling equations, specifically for leg joints, and validated their performance across a variety of populations ranging in sex and age. For position-level scaling, they proposed the equation

$$\tau_\theta^{\text{And.}}(\theta; \mathbf{p}_\theta) = \cos(\theta_{\text{rng}}(\theta - \theta_{\text{o}})) \tag{C.8}$$

$$\mathbf{p}_\theta = [\theta_{\text{o}}, \theta_{\text{rng}}] \in \mathbb{R}^2 \tag{C.9}$$

where $\theta_{\text{rng}} = \pi/(\theta_{\max} - \theta_{\min})$, i.e., the range of joint angles in which active torque is present, and θ_{o} is the joint angle at which the maximal isometric torque can be produced ($\tau_\theta(\theta_{\text{o}}) = 1$). This can be considered an analog to the optimal muscle length in muscle force production [129]. For torque-velocity scaling, Anderson [31] proposed the following piecewise equation:

$$\tau_\omega^{\text{And.}}(\omega; \mathbf{p}_\omega) = \begin{cases} \frac{2\omega_{75}\omega_{50} + \bar{\omega}(\omega_{50} - 3\omega_{75})}{2\omega_{75}\omega_{50} + \bar{\omega}(2\omega_{50} - 4\omega_{75})} & \bar{\omega} \geq 0 \\ \frac{2\omega_{75}\omega_{50} - \bar{\omega}(\omega_{50} - 3\omega_{75})}{2\omega_{75}\omega_{50} - \bar{\omega}(2\omega_{50} - 4\omega_{75})}(1 - \text{S}_e\bar{\omega}) & \bar{\omega} < 0 \end{cases} \tag{C.10}$$

$$\mathbf{p}_\omega = [\omega_{50}, \omega_{75}, \text{S}_e] \in \mathbb{R}^3 \tag{C.11}$$

where

$$\bar{\omega} \equiv k_{\text{dir}}\omega, \quad k_{\text{dir}} \in \{-1, 1\} \tag{C.12}$$

The first interval $\bar{\omega} \geq 0$ represents concentric torque generation (*muscle activated while shortening*) and $\bar{\omega} < 0$ represents eccentric torques (*muscle activated while lengthening*). Inherently, how we define these intervals will depend on the MTG of interest and the conventions defined in Fig. 3.1, e.g., an activated flexor will be in its concentric phase iff the joint is rotating in flexion, otherwise the phase will be eccentric (e.g., $k_{\text{dir}} = 1$ for the elbow flexors). The muscle-velocity relationship was approximated as piecewise hyperbola which is consistent with the classical observations by Hill [150]. Parameters include ω_{50} and ω_{75}, i.e., the angular velocities that reduce the feasible torque to 50% and 75% of

maximum isometric torque. Shaping factor S_e defines the magnitude at which torque increases in the eccentric phase relative to the concentric phase. Note that as the original publication by Anderson et al. [31] provides only lower-limb parameter values, We utilized information from the MTGs in Millard et al. [244] to generate torque-scaling parameters for the shoulder and elbow joints.

Next we examine the passive torque generator functions employed in the proposed model. First, we consider the simpler case of shoulder and elbow joint impedance given by $\tau_{\text{psv}}^{\text{YM.}}$, which combined the equations proposed by both Yamaguchi [368] and Millard [244]. Briefly, nonlinear stiffness and damping were emulated using a double exponential function,

$$\tau_{\text{psv}}^{\text{YM.}}(\theta, \omega; \mathbf{p}_{\text{psv}}) = k_{\text{f}} e^{-\beta_{\text{f}}(\theta - \theta_{\min})}(1 - \gamma_{\text{f}}\omega) - k_{\text{e}} e^{-\beta_{\text{e}}(\theta_{\max} - \theta)}(1 + \gamma_{\text{e}}\omega) - c\,\omega \tag{C.13}$$

$$\mathbf{p}_{\text{psv}} = [k_{\text{f}}, k_{\text{e}}, \beta_{\text{f}}, \beta_{\text{e}}, \theta_{\min}, \theta_{\max}, \gamma_{\text{f}}, \gamma_{\text{e}}, c] \in \mathbb{R}^9 \tag{C.14}$$

which effectively constrained the joint position within its feasible range of motion $\mathcal{Q}_{\text{h}}$ (enforced through $\theta_{\max}$ and $\theta_{\min}$) during simulations [368]. As in Yamaguchi [368], linear damping c is applied consistently regardless of the value of θ; however, like Millard et al. [244], the damping present due to γ terms is scaled accordingly with the nonlinear elastic terms. This feature draws similar parallels to some contact force models, e.g., Hunt-Crossley, where strain/deformation increases the energy dissipated for any given rate of deformation [161, 291], which can assist in suppressing vibrations during dynamic simulations [244]. Parameters for passive torques were selected to match the characteristics described in [244] such as the angles at which $\tau_{\text{psv}} = \tau_{\text{iso}}^{\text{flex}}$ or $\tau_{\text{psv}} = \tau_{\text{iso}}^{\text{ext}}$. Some values were also sourced directly from the literature, e.g., the linear damping coefficient c was set to $c = 0.1\,\text{Nm} \cdot \text{rad}^{-1}$ as recommended by Yamaguchi [368].

Second, let us consider the more complicated definitions of $\tau_{\text{psv,h}}^{\text{SM.}}(\cdot)$, $\tau_{\text{psv,k}}^{\text{SM.}}(\cdot)$, and $\tau_{\text{psv,a}}^{\text{SM.}}(\cdot)$. These three functions are based primarily upon the work in Silder et al. [309]. Briefly, the authors desired to expand upon the work by Riener and Edrich [290], e.g., adding more participants for validation, creating more physiologically meaningful parameters, etc., while still capturing the effects that biarticular muscles can have on the resulting joint impedance of the lower limbs. The specific biarticular muscles of interest were the rectus femoris, hamstrings, and gastrocnemius; the first two cross both hip and knee joints, while the latter cross the ankle and knee joint. As a result, each function considers the position of both the local and neighboring joints. By adding in nonlinear damping as done in Equation (C.14) [244, 368], we arrive as the following three sets of equations:

$$\begin{aligned}
&\tau^{\text{SM.}}_{\text{psv,h}}(\theta_{\text{hip}},\theta_{\text{knee}},\omega_{\text{hip}};\mathbf{p}_{\text{psv,hip}}) \\
&\quad= e^{\beta_{\text{RF,h}}\left(\alpha_{\text{RF}}-\theta_{\text{hip}}-\left(\frac{\beta_{\text{RF,k}}}{\beta_{\text{RF,h}}}\right)\theta_{\text{knee}}\right)} - e^{\beta_{\text{HAM,h}}\left(\theta_{\text{hip}}+\left(\frac{\beta_{\text{HAM,k}}}{\beta_{\text{HAM,h}}}\right)\theta_{\text{knee}}-\alpha_{\text{HAM}}\right)} \\
&\quad- e^{\beta_{\text{HE}}\left(\theta_{\text{hip}}-\alpha_{\text{HE}}\right)}\left(1+\gamma_{\text{HE}}\omega_{\text{hip}}\right) + e^{-\beta_{\text{HF}}\left(\theta_{\text{hip}}-\alpha_{\text{HF}}\right)}\left(1-\gamma_{\text{HF}}\omega_{\text{hip}}\right) - c_{\text{h}}\omega_{\text{hip}}
\end{aligned} \tag{C.15}$$

$$\begin{aligned}
\mathbf{p}_{\text{psv,hip}} = [&\beta_{\text{RF,h}},\beta_{\text{RF,k}},\beta_{\text{HAM,h}},\beta_{\text{HAM,k}},\beta_{\text{HF}},\beta_{\text{HE}},\ \dots \\
&\alpha_{\text{RF}},\alpha_{\text{HAM}},\alpha_{\text{HF}},\alpha_{\text{HE}},\gamma_{\text{HF}},\gamma_{\text{HE}},c_{\text{h}}] \in \mathbb{R}^{13}
\end{aligned} \tag{C.16}$$

$$\begin{aligned}
&\tau^{\text{SM.}}_{\text{psv,k}}(\theta_{\text{hip}},\theta_{\text{knee}},\theta_{\text{ankle}},\omega_{\text{knee}}) \\
&\quad= \frac{\beta_{\text{RF,k}}}{\beta_{\text{RF,h}}}e^{\beta_{\text{RF,h}}\left(\alpha_{\text{RF}}-\theta_{\text{hip}}-\left(\frac{\beta_{\text{RF,k}}}{\beta_{\text{RF,h}}}\right)\theta_{\text{knee}}\right)} - \frac{\beta_{\text{HAM,k}}}{\beta_{\text{HAM,h}}}e^{\beta_{\text{HAM,h}}\left(\theta_{\text{hip}}+\left(\frac{\beta_{\text{HAM,k}}}{\beta_{\text{HAM,h}}}\right)\theta_{\text{knee}}-\alpha_{\text{HAM}}\right)} \\
&\quad- e^{\beta_{\text{KF}}(\theta_{\text{knee}}-\alpha_{\text{KF}})}\left(1+\gamma_{\text{KF}}\omega_{\text{knee}}\right) + e^{-\beta_{\text{KE}}(\theta_{\text{knee}}-\alpha_{\text{KE}})}\left(1-\gamma_{\text{KE}}\omega_{\text{knee}}\right) \\
&\quad- e^{\beta_{\text{GAS,k}}\left(\theta_{\text{knee}}+\left(\frac{\beta_{\text{GAS,a}}}{\beta_{\text{GAS,k}}}\right)\theta_{\text{ankle}}-\alpha_{\text{GAS}}\right)} - c_{\text{k}}\omega_{\text{knee}}
\end{aligned} \tag{C.17}$$

$$\begin{aligned}
\mathbf{p}_{\text{psv,knee}} = [&\beta_{\text{RF,h}},\beta_{\text{RF,k}},\beta_{\text{HAM,h}},\beta_{\text{HAM,k}},\beta_{\text{GAS,h}},\beta_{\text{GAS,k}},\beta_{\text{KF}},\beta_{\text{KE}},\ \dots \\
&\alpha_{\text{RF}},\alpha_{\text{HAM}},\alpha_{\text{GAS}},\alpha_{\text{KF}},\alpha_{\text{KE}},\gamma_{\text{KF}},\gamma_{\text{KE}},c_{\text{k}}] \in \mathbb{R}^{16}
\end{aligned} \tag{C.18}$$

$$\begin{aligned}
&\tau^{\text{SM.}}_{\text{psv,a}}(\theta_{\text{knee}},\theta_{\text{ankle}},\omega_{\text{ankle}}) \\
&\quad= -e^{\beta_{\text{PF}}(\theta_{\text{ankle}}-\alpha_{\text{PF}})}\left(1+\gamma_{\text{PF}}\omega_{\text{ankle}}\right) + e^{-\beta_{\text{DF}}(\theta_{\text{ankle}}-\alpha_{\text{DF}})}\left(1-\gamma_{\text{DF}}\omega_{\text{ankle}}\right) \\
&\quad- \frac{\beta_{\text{GAS,a}}}{\beta_{\text{GAS,k}}}e^{\beta_{\text{GAS,k}}\left(\theta_{\text{knee}}+\left(\frac{\beta_{\text{GAS,a}}}{\beta_{\text{GAS,k}}}\right)\theta_{\text{ankle}}-\alpha_{\text{GAS}}\right)} - c_{\text{a}}\omega_{\text{ankle}}
\end{aligned} \tag{C.19}$$

$$\mathbf{p}_{\text{psv,ankle}} = [\beta_{\text{GAS,h}},\beta_{\text{GAS,k}},\beta_{\text{DF}},\beta_{\text{PF}},\alpha_{\text{GAS}},\alpha_{\text{DF}},\alpha_{\text{PF}},\gamma_{\text{DF}},\gamma_{\text{PF}},c_{\text{a}}] \in \mathbb{R}^{10} \tag{C.20}$$

Notice that while the elasticity of each lower-limb joint considers biarticular musculature, the nonlinear damping does not. Making this simplification reduced the number of parameters to be set in order to run simulations, specifically for the γ parameters which are not widely available in the literature. Another novel addition to Equation (C.19) includes the dorsiflexor elastic term, which itself was implemented using the coefficients provided in [290]. In Silder et al. [309], only plantarflexor elasticity was investigated. Lastly, we note the duplication of parameters contained between $\mathbf{p}_{\text{psv,hip}}$, $\mathbf{p}_{\text{psv,knee}}$, and $\mathbf{p}_{\text{psv,ankle}}$; this is a direct result of the biarticular musculature being modelled.

Note that the active MTG scaling functions used herein were fit to C^2-continuous Bezièr splines; spline intervals were connected via hyperbolic tangent transition smoothing functions. This approach was based on the smooth transitions in De Groote et al. [88] and the MTG Beziér splines from Millard er al. [244]. This procedure guaranteed not only that we would be able to generate and export symbolic derivatives of cost and constraint functions involving the MTGs (with respect to joint angles and velocities), but that these derivatives would be bound. The latter is particularly important as we primarily employ interior-point optimization methods to solve the NLPs within this dissertation [219]. For more information on this curve-fitting routine, please refer to Appendix D.

Appendix D

Smoothing Muscle Torque Generator Functions

D.1 Background

In Chapter 3, there were notable drawbacks and challenges in the implementation of $\tau_{\theta}^{\text{And.}}$ and $\tau_{\omega}^{\text{And.}}$ as described originally in [31]. For example, because $\cos(\cdot)$ is used to describe the torque-angle relationship, $\tau_{\theta}^{\text{And.}} < 0$ for values $\theta \notin [\theta_{\min}, \theta_{\max}]$, which is not physiologically feasible. Similarly, $\tau_{\omega}^{\text{And.}}$ can have a negative horizontal asymptote that it approaches as $\bar{\omega} \to \infty$. $\tau_{\omega}^{\text{And.}}$ can also behave unphysiologically at large $\bar{\omega} \leq 0$ due to the shape of the eccentric hyperbola, i.e., it tends back towards zero.

To address these limitations and others we utilized the notion of smoothing discussed by De Groote et al. [88] and motivated by the work of Millard et al. [244, 247]. Specifically, Millard et al. [244] used Bézier curves to create C^2 continuous MTG functions that behaved well when used in derivative-based optimization methods. The constitutive equations and parameters of the angle and angular velocity-scaling functions and were based on the model and data presented in [31] and subsequently fit to a spline of 5th-order Bezier curves. Doing so avoided issues associated with the discontinuities in [31], e.g., when scaling became negative, and yielded C^2-continuous curves with respect to $\mathbf{q}_{\text{h}}$ and $\dot{\mathbf{q}}_{\text{h}}$, which are well-suited for use in gradient-based optimization procedures, e.g., interior-point methods.

To elaborate, we parameterize some desired curve $f(t)$ over $t \in \mathbf{T}$, where $\mathbf{T} = \{T_1, T_2\}$ is a set containing the boundaries of approximation, using a vector of control points $\mathbf{b} \in \mathbb{R}^{n_b}$ as follows:

$$f(t; \mathbf{T}, \mathbf{b}) = \sum_{i=0}^{n_b} \binom{n_b}{i} (1 - \mathcal{T})^{n_b - i} \mathcal{T}^i b_{i+1} \tag{D.1}$$

$$\mathcal{T} \equiv \frac{t - T_1}{T_2 - T_1} \tag{D.2}$$

where n_b indicates the number of control points and $\mathcal{T} \in [0, 1]$ is the normalized input. Now let us say that we have a function $\mathcal{F} : t \to \mathbb{R}$ that is defined piecewise over several intervals. We can parameterize that entire function using a unique Bézier curve within each interval:

$$\mathcal{F}(t; \cdot) = \begin{cases} f(t; \mathbf{T}_1, \mathbf{b}_1) & t \in (\infty, T_{1,2}] \\ f(t; \mathbf{T}_2, \mathbf{b}_2) & t \in (T_{2,1}, T_{2,2}] \\ \vdots & \vdots \\ f(t; \mathbf{T}_{N-1}, \mathbf{b}_{N-1}) & t \in (T_{N-1,1}, T_{N-1,2}] \\ f(t; \mathbf{T}_N, \mathbf{b}_N) & t \in (T_{N,1}, \infty) \end{cases} \tag{D.3}$$

such that the domain of $\mathcal{F}$ is greater than the domain of any individual subdomain $t \in \mathbf{T}_i$. This formulation assumes that for any $\mathbf{T}_i$, $T_{i,1} = T_{i-1,2}$. A notable feature of this type of spline is that for careful selections of $\mathbf{b}_i \, \forall \, i = 1 \ldots N$, it is possible to have a C^2 piecewise continuous function [244, 247]. Such a feature permits symbolic Jacobian and Hessian use within derive-based optimization, greatly speeding up performance [219]. Thus, we can approximate curves with sharp curvature through a spline of simpler polynomials.

In programming with symbolic computing software, e.g., MapleSoft, piecewise functions can sometimes be difficult to differentiate efficiently and use for code generation. As some piecewise functions are not differentiable everywhere, i.e., the derivative does not exist for some regions of the domain, MapleSoft will try to ensure that the function can be evaluated for any given input. How the symbolic engine evaluates the function across these subintervals of the domain can then impact the ability to convert those functions into a different scripting language. Due to this issue, like De Groote et al. [87], we elected to use hyperbolic tangent smoothing functions to construct the piecewise MTG functions

discussed in Section 3. The following smoothing functions were defined:

$$\beth_{2s}(t; k_b, \mathbf{T}) = 0.5 \tanh(k_b(t - T_1)) - 0.5 \tanh(k_b(t - T_2)) \tag{D.4}$$

$$\beth_{ls}(t; k_b, \mathbf{T}) = -0.5(\tanh(k_b(t - T_2)) - 1) \tag{D.5}$$

$$\beth_{rs}(t; k_b, \mathbf{T}) = 0.5(\tanh(k_b(t - T_1)) + 1) \tag{D.6}$$

where k_b determined the rate at which the transition between intervals would occur. Thus, the smooth approximation of the piecewise curve $\mathcal{F}$, i.e., $\check{\mathcal{F}}$ is obtained through the use of the Bezier curves as basis polynomials weighed in different domains of t using the smoothing functions above:

$$\begin{aligned}\check{\mathcal{F}}(t; \cdot) = f(t; \mathbf{T}_1)\beth_{rs}(t; k_b, \mathbf{T}_N, \mathbf{b}_N) + f(t; \mathbf{T}_1, \mathbf{b}_1)\beth_{ls}(t; k_b, \mathbf{T}_1) \\ + \sum_{i=2}^{N-1} f(t; \mathbf{T}_i, \mathbf{b}_i)\beth_{2s}(t; k_b, \mathbf{T}_i)\end{aligned} \tag{D.7}$$

Compared to the standard piecewise approach, we bypass the need for logic during function evaluations and simply rely on arithmetic operations. However, the trade-off with the smoothed formulation is this increase in operations. Further work is necessary to determine whether this ultimately increases the CPU time required for evaluations. Regardless, the smoothed approximation results in consistent bounds on the evaluated derivatives and a guarantee of continuity. In fact, we can use the product rule to show that this is true for

$\check{\mathcal{F}}$ regardless of the choice of Bezier control points, i.e.,

$$\frac{d\check{\mathcal{F}}}{dt} = \dot{\check{\mathcal{F}}} = \beth_{\text{rs}}(t; k_b, \mathbf{T}_N, \mathbf{b}_N)\frac{d}{dt}f(t; \mathbf{T}_1) + f(t; \mathbf{T}_1)\frac{d}{dt}\beth_{\text{rs}}(t; k_b, \mathbf{T}_N, \mathbf{b}_N)$$
$$+ \beth_{\text{ls}}(t; k_b, \mathbf{T}_1)\frac{d}{dt}f(t; \mathbf{T}_1, \mathbf{b}_1) + f(t; \mathbf{T}_1, \mathbf{b}_1)\frac{d}{dt}\beth_{\text{ls}}(t; k_b, \mathbf{T}_1) \tag{D.8}$$
$$+ \sum_{i=2}^{N-1} \beth_{\text{2s}}(t; k_b, \mathbf{T}_i)\frac{d}{dt}f(t; \mathbf{T}_i, \mathbf{b}_i) + f(t; \mathbf{T}_i, \mathbf{b}_i)\frac{d}{dt}\beth_{\text{2s}}(t; k_b, \mathbf{T}_i)$$

$$\frac{d^2\check{\mathcal{F}}}{dt^2} = \ddot{\check{\mathcal{F}}} = 2\frac{d}{dt}\beth_{\text{rs}}(t; k_b, \mathbf{T}_N, \mathbf{b}_N)\frac{d}{dt}f(t; \mathbf{T}_1) + \beth_{\text{rs}}(t; k_b, \mathbf{T}_N, \mathbf{b}_N)\frac{d^2}{dt^2}f(t; \mathbf{T}_1) \tag{D.9}$$
$$+ 2\frac{d}{dt}\beth_{\text{ls}}(t; k_b, \mathbf{T}_1)\frac{d}{dt}f(t; \mathbf{T}_1, \mathbf{b}_1) + \beth_{\text{ls}}(t; k_b, \mathbf{T}_1)\frac{d^2}{dt^2}f(t; \mathbf{T}_1, \mathbf{b}_1) \tag{D.10}$$
$$+ f(t; \mathbf{T}_1)\frac{d^2}{dt^2}\beth_{\text{rs}}(t; k_b, \mathbf{T}_N, \mathbf{b}_N) + f(t; \mathbf{T}_1, \mathbf{b}_1)\frac{d^2}{dt^2}\beth_{\text{ls}}(t; k_b, \mathbf{T}_1) \tag{D.11}$$
$$+ \sum_{i=2}^{N-1} 2\frac{d}{dt}\beth_{\text{2s}}(t; k_b, \mathbf{T}_i)\frac{d}{dt}f(t; \mathbf{T}_i, \mathbf{b}_i) + \beth_{\text{2s}}(t; k_b, \mathbf{T}_i)\frac{d^2}{dt^2}f(t; \mathbf{T}_i, \mathbf{b}_i) \tag{D.12}$$
$$+ \sum_{i=2}^{N-1} f(t; \mathbf{T}_i, \mathbf{b}_i)\frac{d^2}{dt^2}\beth_{\text{2s}}(t; k_b, \mathbf{T}_i) \tag{D.13}$$
$$\tag{D.14}$$

D.2 Curve Fitting Routine

The goal in the current dissertation was to provide a method for rapidly generate smooth MTG curves that fit the most important characteristics of muscle behaviour. To increase the novelty of the proposed MTG modeling approach, rather than specify regions for the Bézier curve like Millard et al. [244], we used an approach based on NLP where the intervals were included as decision variables alongside the Bézier control points. The fitting of the piecewise MTG functions in Chapter 3 was thus acheived via optimization and Bézier curve

parameterization:

$$\arg\min_{\bar{\mathbf{b}},\bar{\mathbf{T}}} \int_{T_{1,2}}^{T_{N,1}} w_\varepsilon \varepsilon(t)^2 + w_\xi \xi(t)^2 \, dt \tag{D.15}$$

subject to

$$\check{\mathcal{F}}(t_{\text{ref}}) = \tau_\theta^{\text{And.}}(t_{\text{ref}}) \tag{D.16}$$

$$\mathbf{T}_{i,1} = \mathbf{T}_{i-1,2} \quad \forall\, i = 2 \ldots N \tag{D.17}$$

$$\mathbf{T}_{N,1} \geq \mathbf{T}_{N-1,1} \geq \cdots \geq \mathbf{T}_{1,1} \tag{D.18}$$

$$\dot{\check{\mathcal{F}}}(\mathbf{T}_{i,1}) = \dot{\check{\mathcal{F}}}(\mathbf{T}_{i-1,2}) \quad \forall\, i = 2 \ldots N \tag{D.19}$$

$$\ddot{\check{\mathcal{F}}}(\mathbf{T}_{i,1}) = \ddot{\check{\mathcal{F}}}(\mathbf{T}_{i-1,2}) \quad \forall\, i = 2 \ldots N \tag{D.20}$$

where w_ε weighed least-squares fitting error and w_ξ weighed the magnitude of curvature within the fit, i.e., setting this value high encouraged fit that was less stiff numerically. The inclusion of weighting terms allowed for user-desired smoothness, which could be important in the context of real-time model-based controls. Note that in this dissertation, $n_b = 4$ (quintic polynomials) and the number of intervals $N = 4$ were set identical to the parameters that Millard et al. [244] were successful with. Terms of the cost function integrand included the fitting error equation,

$$\varepsilon(t) = \tau_\theta^{\text{And.}}(t) - \check{\mathcal{F}}(t) \tag{D.21}$$

or

$$\varepsilon(t) = \tau_\omega^{\text{And.}}(t) - \check{\mathcal{F}}(t) \tag{D.22}$$

depending on the targeted function, as well as the curvature function

$$\xi(t) = \frac{\| \langle 1, \dot{\check{\mathcal{F}}}, 0 \rangle \times \langle 0, \ddot{\check{\mathcal{F}}}, 0 \rangle \|}{\| \langle 1, \dot{\check{\mathcal{F}}}, 0 \rangle \|^3} \tag{D.23}$$

where vector-operations are used to simplify notation, i.e., the cross-product.

Appendix E

Background: Feasible Stability Region and Capturability

A validated method of analyzing the balancing capabilities of a human in balance recovery is the feasible stability region (FSR) [175, 264, 370]. For balance in the sagittal plane, the concept states that so long as the *horizontal* position and velocity of the whole-body COM are within the "stable" region of COM phase-space, the biped will not fall. These boundaries are intrinsically dependent on the system dynamics and are closely related to concepts like capturability [278] and foot placement estimation [26, 245].

The following is an analytical solution for the FSR boundaries of a linearized inverted pendulum. If we make linear/small-angle approximations around $\theta = 0$:

$$\sin(\theta) \approx \theta \tag{E.1}$$

$$\cos(\theta) \approx 1 \tag{E.2}$$

and assume that the entirety of human upright stance can be modelled by an inverted pendulum [154] with a point mass located horizontally (with respect to the ankle joint centre) at $x_{\text{cm}}(t)$ such that $x_{\text{cm}}(t) = \ell\theta(t)$, we can write the equations of motion as,

$$(I + m\ell^2)\ddot{\theta} = mg\ell \sin(\theta) - \tau_{\text{mtg},3}, \quad I \to 0 \text{ (point mass approx.)} \tag{E.3}$$

$$\theta = -x_{\text{cm}}\ell^{-1} \Rightarrow \ddot{\theta} = -\ddot{x}_{\text{cm}}\ell^{-1} \tag{E.4}$$

$$\ddot{x}_{\text{cm}} = \frac{g}{\ell}x + \frac{\tau_{\text{mtg},3}}{m\ell} \tag{E.5}$$

where ℓ and m are the pendulum's length and mass respectively. Like Winter [361], if we make a linear approximation of the ZMP in (3.12) with respect to the ankle torque, i.e.,

$$\nu \approx -\frac{\tau_{\text{mtg},3}}{mg} \implies \tau_{\text{mtg},3} \approx -mg\nu \tag{E.6}$$

and swap the result into (E.5), we arrive at the final equation describing simplified human stance as utilized throughout the literature [154, 174, 361]:

$$\ddot{x}_{\text{cm}} = \omega_0^2(x_{\text{cm}}(t) - \nu(t)) \tag{E.7}$$

where $\omega_0 = \sqrt{g\ell^{-1}}$ is the pendulum's natural frequency (eigenfrequency [154]).

From Equation (E.7), we wish to parameterize the domain of feasibility discussed at the start of Chapter 3.2 by using the position (x_{cm}) and velocity ($\dot{x}_{\text{cm}}$) of the model's COM. This is conceptually similar to the idea of capture points where in we wish to identify subspaces of the COM phase space in which so long as an optimal control strategy is applied, the COM will always exist within that space [278]. In the current formulation, we will identify this space according to its potential for the halting and/or reversal of COM momentum, i.e., if the biped is falling forward, what is the largest COM momentum that can be reversed given the constraints in (3.10), Mathematically, we wish to determine when

$$\lim_{t\to\infty} x_{\text{cm}}(t) = -\infty \tag{E.8}$$

for a given $\dot{x}_{\text{cm}} > 0$. The opposite limit could be identified for the backward margin of stability, i.e., if the biped is falling backward ($\dot{x}_{\text{cm}} < 0$), what is the largest COM momentum that can be reversed given the constraints in (3.10). For (E.8), we can set a feedforward optimal control law,

$$\nu(t) = \nu_{\max} = \ell_{\text{c2t}} \tag{E.9}$$

which can then be substituted back into (E.7). Using the Laplace transform like in [153,

169], we can solve for $x_{\text{cm}}(t)$ analytically, i.e.,

$$\ddot{x}_{\text{cm}} = \omega_0^2(x_{\text{cm}}(t) - \ell_{\text{c2t}}) \tag{E.10}$$

$$\downarrow$$

$$s^2\mathcal{X}_{\text{cm}}(s) - \dot{x}_0 - sx_0 = \omega_0^2\mathcal{X}_{\text{cm}}(s) - \omega_0^2\frac{\ell_{\text{c2t}}}{s} \tag{E.11}$$

$$(s^2 - \omega_0^2)\mathcal{X}_{\text{cm}}(s) = sx_0 + \dot{x}_0 - \omega_0^2\frac{\ell_{\text{c2t}}}{s} \tag{E.12}$$

$$\downarrow$$

$$x_{\text{cm}}(t) = \ell_{\text{c2t}} + (x_0 - \ell_{\text{c2t}})\cosh(\omega_0 t) + \frac{\dot{x}_0}{\omega_0}\sinh(\omega_0 t) \tag{E.13}$$

where $\ddot{x}_0 = \ddot{x}_{\text{cm}}(0)$ and $x_0 = x_{\text{cm}}(0)$ are the systems's initial conditions (initial horizontal position and velocity of the COM). Symbolic computing software like Maple can be used to trivialize the evaluation of the limit given the optimal control law above, which reveals the following condition:

$$\lim_{t\to\infty} x_{\text{cm}}(t) = -\infty \iff x_0 + \frac{\dot{x}_0}{\omega_0} < \ell_{\text{c2t}} \tag{E.14}$$

consistent with the solution originally disseminated by Hof [154]. This result implies that for any given $x_{\text{cm}}(t)$, there are certain $\dot{x}_{\text{cm}}$ that are capturable (can theoretically remain balanced in this state) and other $\dot{x}_{\text{cm}}$ that are not, e.g., $\dot{x}_{\text{cm}} > \omega_0(\ell_{\text{c2t}} - x_{\text{cm}})$ cannot be captured for the inverted pendulum. Please refer to Inkol and Vallis [169] for a derivation related to the case in which there are platform accelerations - this can help describe the adaptive strategy some people resort to ("surfing" strategy with repeated exposure to floor translations). We now assume that the inverted pendulum is within the domain of feasibility of upright balance so long as the conditions in Equation (E.14) are met.

Based on this definition of capturability and the feasble stability region, we now wish to establish the following generalized definitions for the anterior and posterior FSR boundaries

for FIP balance control of an upright human. Mathematically, we wish to obtain

$$\dot{x}_{\text{fsr}}^{\text{ant}} = \arg \max_{\dot{\mathbf{r}}_{\text{cm}}(t)\cdot\hat{\imath}} \{\dot{\mathbf{r}}_{\text{cm}}(t) \cdot \hat{\imath}\} \tag{E.15}$$

$$\dot{x}_{\text{fsr}}^{\text{pos}} = \arg \min_{\dot{\mathbf{r}}_{\text{cm}}(t)\cdot\hat{\imath}} \{\dot{\mathbf{r}}_{\text{cm}}(t) \cdot \hat{\imath}\} \tag{E.16}$$

subject to

$$\boldsymbol{\Omega}(\cdot) < \mathbf{0}, \quad \forall\, t \in [0, \infty) \tag{E.17}$$

$$\mathbf{r}_{\text{cm}}(t) \cdot \hat{\imath} = x_{\text{cm}} \tag{E.18}$$

where $\dot{x}_{\text{fsr}}^{\text{ant}}$ and $\dot{x}_{\text{fsr}}^{\text{pos}}$ are the anterior and posterior boundaries of the FSR respectively. As eluded to in the previous paragraphs, the boundaries of the system's FSR could be estimated using the linear inverted pendulum model by Hof et al. [154] replicating the ankle strategy observed by Horak and Nashner [158], i.e.,

$$\dot{x}_{\text{fsr}}^{\text{ant}} \approx \omega_0(\ell_{\text{c2t}} - \mathbf{r}_{\text{cm}}(t) \cdot \hat{\imath}) \tag{E.19}$$

$$\dot{x}_{\text{fsr}}^{\text{pos}} \approx -\omega_0(\ell_{\text{c2h}} + \mathbf{r}_{\text{cm}}(t) \cdot \hat{\imath}) \tag{E.20}$$

where pendulum length ℓ was set to 1.10 m for the human-only [154] and ℓ_{c2t} (distance from ankle to toe) and ℓ_{c2h} (distance from ankle to heel) were set according to the values in Table A.1. For more complex models of human stance, we must rely on computer simulations to inform us of the theoretical boundaries of stability and how they may be affected by certain model parameters. For example, Pai and Patton [264] evaluated the boundaries for a nonlinear inverted pendulum model using forward dynamics simulations. Yang et al. [369, 370] continued this work by expanding their examinations of postural stability using computer simulations of a walking model with one foot on the ground (single-support). However, rather than introducing constraints into their optimization routines, the authors of most recent simulations have relied on careful tuning of cost functions containing a large number of terms within a direct shooting-formulated optimal control problem.

Appendix F

F.1 Effect of Different FSR Candidate Functions

The current simulation experiment was designed to investigate the performance of different cost functions in obtaining (3.19). To date, despite the numerous formulations in the literature [174, 175, 264, 370], no research has been published on how different functions might perform in the estimation of a human or humanoid FSR. Therefore, the following three functions were tested herein:

$$\text{Lin: } J = -d\dot{\mathbf{r}}_{\text{cm}}[1] \cdot \hat{\imath} + \epsilon^{-1} \tag{F.1}$$

$$\text{Rec: } J = (d\dot{\mathbf{r}}_{\text{cm}}[1] \cdot \hat{\imath} + \epsilon)^{-1} \tag{F.2}$$

$$\text{Exp: } J = e^{-dk\dot{\mathbf{r}}_{\text{cm}}[1]\cdot\hat{\imath}} + (1-\epsilon)\epsilon^{-1} \tag{F.3}$$

and were based on those available previously in the literature [174, 369, 370]. To our knowledge, no author has yet proposed the exponential variant (Exp) of the cost function in (F.3). The FSR was assessed using each cost function (swapped in to Equation (3.19)) given the following parameter values: $k = 1$, $\epsilon = 1$. Note that ϵ was included primarily as a means of permitting a static posture initial guess to the NLP solver when using the reciprocal (Rec) function, i.e., singularity when $\epsilon = -d\dot{\mathbf{r}}_{\text{cm}}[1] \cdot \hat{\imath}$ that was not considered by Yang et al. [369, 370]. The anterior FSR boundary was estimated when $d = 1$, while the posterior boundary was obtained when $d = -1$.

The estimated FSR generated over the the set of COM positions $\{0, 0.25, ..., 1.00\}$ (normalized to foot length; 0 = COM over toe, 1 = COM over heel) for each of the candidate FSR functions (linear = Lin, reciprocal = Rec, and exponential = Exp) is

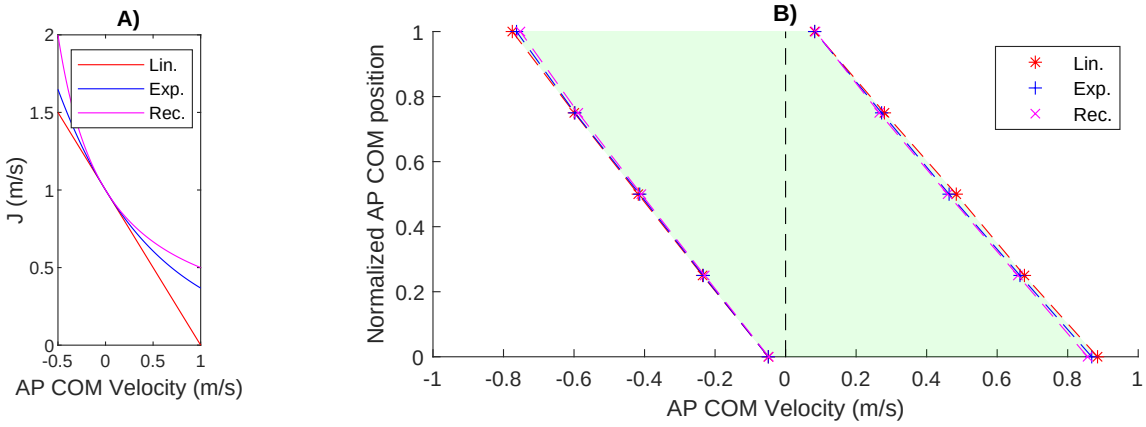


Figure F.1: A) Plots of the three feasible stability region (FSR) candidate functions introduced in F.1 (experiment 1; $k = 1$, $d = 1$, $\epsilon = 1$) in addition to B) the FSR for the human-only FIP balance model generated using each function candidate (arm movement was restricted). As a reminder, for a given COM position normalized to foot length (vertical axis; 0 = toe, 1 = heel), if the COM velocity is within the FSR boundaries (shaded region), then the biped can terminate this velocity such that quiet, upright stance can still be captured. If the velocity goes beyond these boundaries, then the model must take a step (not analyzed herein) or fall. The rightmost and leftmost boundary represent the anterior (forward) and posterior (backward) fall limit respectively.

displayed is Fig. F.1. The linear cost function Lin resulted in the largest FSR; exponential and reciprocal functions yielded basically identical estimates. With that said, the maximum absolute difference between the linear and exponential FSRs was only approximately 2 cm/s (considering both the anterior and posterior boundaries). These differences were especially negligible when, for a forward fall, the COM began over the toes and, for a backward fall, when the COM began over the heels.

While the differences between the three FSR functions were small in terms of the resulting size of FSR, larger differences were evident in simulation performance. A single simulation with the an initial normalized AP COM of 0 (beginning over the heel) using the exponential FSR candidate function (Exp) typically required a 600 second runtime (2080 iterations required by interior-point algorithm). The reciprocal function (Rec) required only 563 seconds over 1993 iterations for Rec, but provided a lower FSR estimate; 0.84

m/s vs 0.86 m/s in the Exp condition. However, using the Lin function increased the time required to obtain convergence in the optimization (e.g., 740 seconds of runtime with 2600 iterations), but obtained the highest FSR boundary estimate (0.88 m/s) Because the FSR size was very similar between the three functions, the Exp function was utilized for all further FSR simulation experiments in this dissertation. This choice was made primarily due to the Exp functions relative speed and reliability in obtaining convergence compared to the linear function, while requiring less time to obtain the estimation. The Rec was not used due to it having the poorest estimate of the linear function results despite providing the quickest convergence.

F.2 Influence of Adding Degrees of Freedom for Initial COM Velocity

The current simulation experiment was designed to investigate how imposing different constraints on the initial joint velocities, i.e., which joints could contribute to generating the maximal COM velocity at onset. While briefly investigated for the knee movement in [175], the current experiment extended this investigation into restrictions on the hip velocity in addition to the upper limbs. Thus, we considered four conditions for the current simulation experiment:

1. Only ankle velocity permitted at the onset of balance recovery (DOF=1)
2. Only ankle and hip velocities permitted at the onset of balance recovery (DOF=2)
3. Only ankle, knee, and hip velocities permitted at the onset of balance recovery (DOF=3)
4. Ankle, knee, hip, and upper limb velocities permitted at the onset of balance recovery (DOF=3)

The onset of balance recovery was coincident with the first node of the discrete simulation horizon. In all conditions, the optimal control algorithm had access to all 5-DOF of the human model, i.e., arm motion could be used if desired. Restrictions on the initial velocities used were imposed through manipulation of the initial inequality constraints in Equation

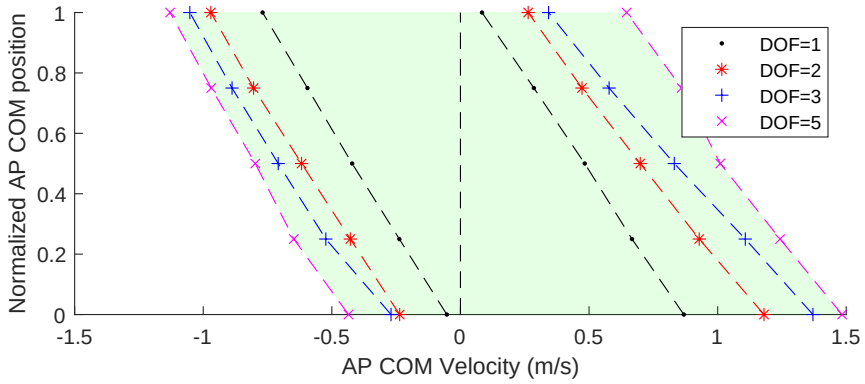


Figure F.2: The feasible stability region (FSR) for the human-only FIP balance model generated with different constraints on the initial velocity, i.e., which joints could contribute to generating the maximal COM velocity at onset. Arm movement was **NOT** restricted in these simulations. Conditions are as follows: only ankle velocity (DOF=1); ankle+hip permitted (DOF=2); ankle+knee+hip permitted (DOF=3); ankle+knee+hip and upper limbs permitted (DOF=5).

(3.28), i.e., restricted initial joint velocities could never exceed $\pm 0.005\,^{\circ}/\mathrm{s}$ according to $\boldsymbol{\omega}_{\max,0}$ and $\boldsymbol{\omega}_{\min,0}$.

The estimated FSR generated over the the set of anteroposterior (AP) COM positions $\{0, 0.25, ..., 1.00\}$ (normalized to foot length; 0 = COM over toe, 1 = COM over heel) is displayed is Fig. F.2. In Figs. F.3 and F.4, the simulated joint angle trajectories that yielded the maximum capturable anterior and posterior COM velocities respectively, are shown for an initial normalized COM position of 0.25, 0.50, and 0.75. According to Fig. F.2, each successive condition within the current simulation experiment yielded an increase in FSR size, i.e., each restriction removed on the initial joint velocities increases the theoretical range of capturable COM velocities [175].

First, we discuss the effects of each condition on the joint trajectories utilized to halt forward COM momentum. To increase the initial capturable COM velocity from DOF=1 to DOF=2, ankle dorsiflexion velocity was increased with simultaneous hip extension (Fig. F.3); this is similar to the change in body kinematics induced by a forward push applied to the pelvis [103, 169]. The same upper limb strategy observed in Experiment 2) was observed

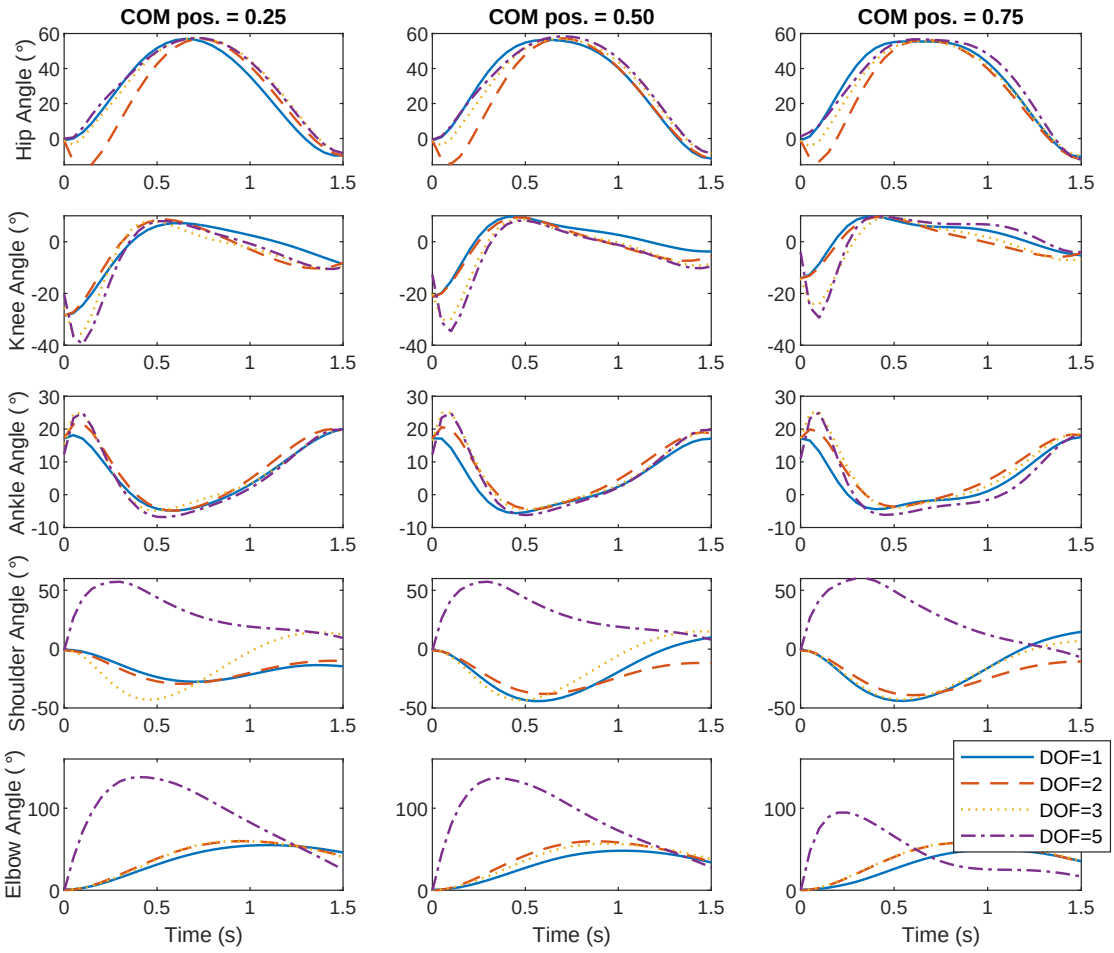


Figure F.3: Joint angles that result in the **anterior** FSR boundary for the human-only balance model when different constraints are imposed on the initial velocity, i.e., which joints could contribute to generating the maximal COM velocity at onset (right boundary in Fig. F.2). Shown are the results for simulations in which the initial normalized COM position is 0.25 (*left*), 0.50 (*middle*), and 0.75 units (*right*). Arm movement was **NOT** restricted in these simulations. Conditions are as follows: only ankle velocity (DOF=1); ankle+hip permitted (DOF=2); ankle+knee+hip permitted (DOF=3); ankle+knee+hip and upper limbs permitted (DOF=5).

for this DOF=2 condition. Once the initial knee velocity was unrestricted (DOF=3), the optimal motor strategy switched to initial hip flexion velocity with initial knee flexion. These lower limb strategies were maintained into the DOF=5 condition (initial upper limb velocities permitted); however, we did note that optimal upper limb strategy changed

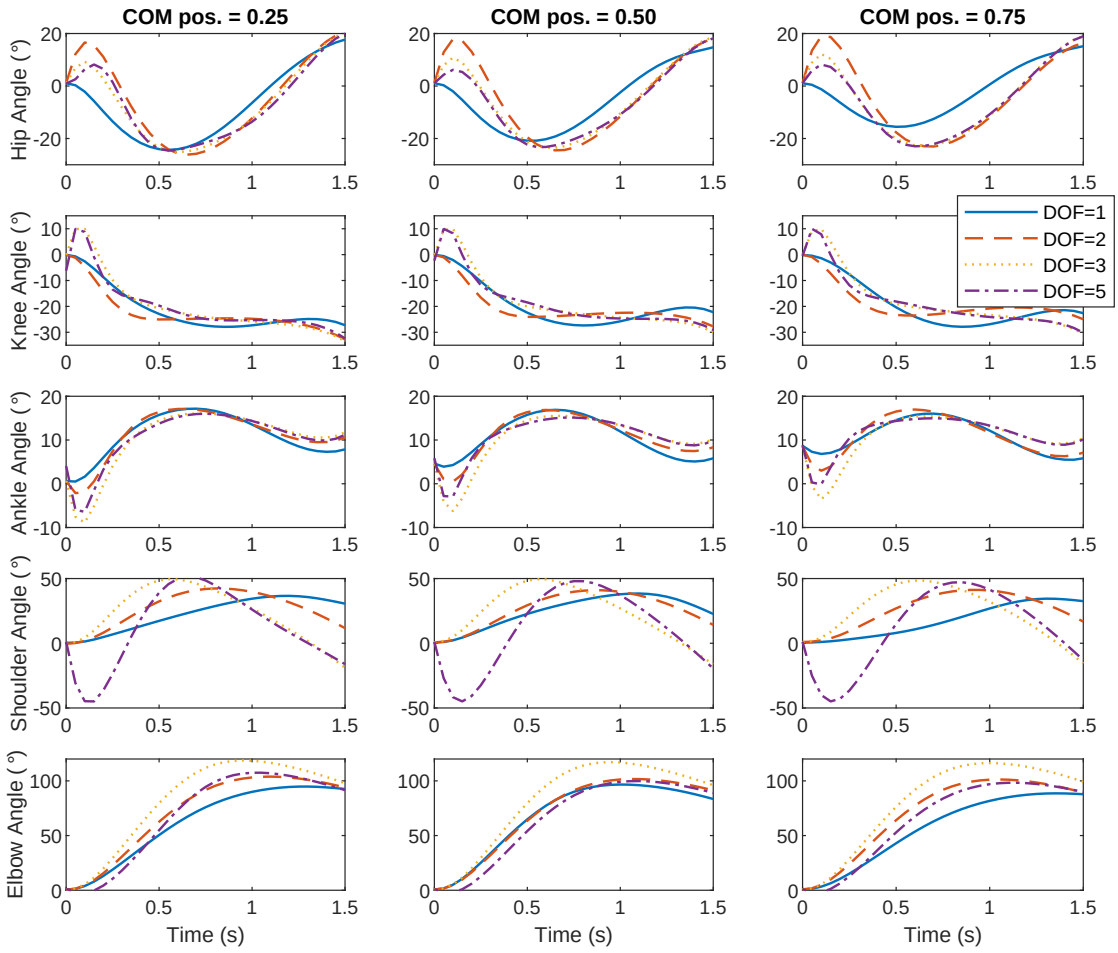


Figure F.4: Joint angles that result in the **posterior** FSR boundary for the human-only balance model when different constraints are imposed on the initial velocity, i.e., which joints could contribute to generating the maximal COM velocity at onset (left boundary in Fig. F.2). Shown are the results for simulations in which the initial normalized COM position is 0.25 (*left*), 0.50 (*middle*), and 0.75 units (*right*). Arm movement was **NOT** restricted in these simulations.

drastically. Instead, a shoulder/elbow flexion strategy was used to not only increase the initial COM velocity, but to eventually halt the COM momentum. Interestingly, this type of arm strategy may be closer in relation to those observed in experiments involving induced trips [67, 274], where the arms are stretch forward and out despite that being the direction of fall; however, these strategies have been suggested to assist more with control of momentum within the transverse plane.

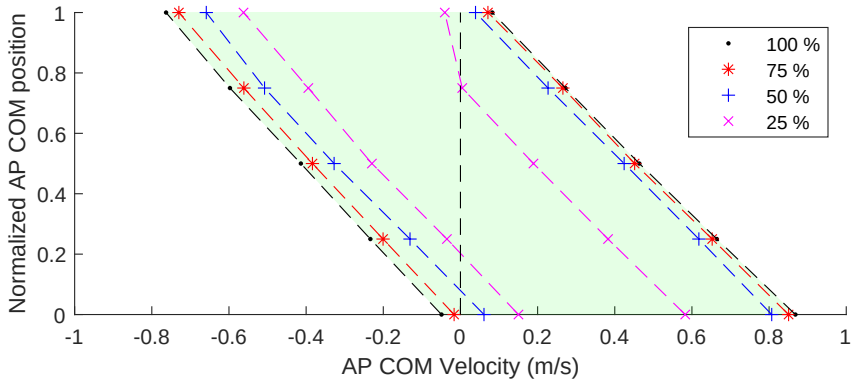


Figure F.5: The feasible stability region (FSR) for the human-only FIP balance model generated with different constraints imposed on the maximum muscle activation, i.e., muscle activations could not surpass 25, 50, 75, or 100%, with the 25% condition representing the individual with the lowest muscle strength. Arm movement was restricted in these simulations.

Looking into the effects of each condition on the joint trajectories utilized to halt backward COM momentum (Fig. F.4), we observed that increases in the initial capturable COM velocity from DOF=1 to DOF=2 were produced by an increased ankle plantarflexion velocity and hip flexion velocity. This trend was maintained switching from the DOF=2 to the DOF=3 condition, though with the addition of an initial burst of knee extension prior to flexion to improve COM capturability. The same upper limb strategy observed for the posterior FSR boundary in Experiment 2) was observed for the DOF=1, DOF=2, and DOF=3 condition. The only shift in postural strategy was observed in the DOF=5 condition. The lower limb strategies were very similar between DOF=3 and DOF=5; however, there was the addition of initial shoulder extension not observed in other conditions. This initial shoulder extension was clearly used to increase the initial backward COM momentum, with the shoulder eventually transitioning into flexion as in experiment 2 to assist in balance recovery.

F.3 Influence of Muscle Strength

In the current simulation experiment, we examined how constrained active MTG outputs affect the size and shape of the sagittal FIP FSR. Like the delays in experiment 5, this limitation was incorporated through the box constraints in Equation (3.27) as

$$\mathbf{a}[k] < \varepsilon_3 \; \forall \, k = 1 \ldots n \tag{F.4}$$

where the value of parameter $\varepsilon_3 \in [0, 1]$ dictated what level of MTG activation was feasible by the simulated human. The following conditions were investigated with respect to influence on the FIP FSR:

1. $\varepsilon_3 = 1.00$ (100%) – Baseline condition (full-strength)
2. $\varepsilon_3 = 0.75$ (75%)
3. $\varepsilon_3 = 0.50$ (50%)
4. $\varepsilon_3 = 0.25$ (25%)

The last two conditions featuring the lowest activation limits were based on the experimental work by Jayaraman [177], where study participants with an incomplete spinal cord injury could generate approximately 30-40% of the active ankle torque magnitude that able-bodied participants could produce. Again, as arm movement had little impact on the FSR size in experiments 1-3, it was restricted within each of the conditions listed above, i.e., the standing model contained 3-DOF.

The estimated FSR generated over the the set of AP COM positions $\{0, 0.25, ..., 1.00\}$ (normalized to foot length; 0 = COM over toe, 1 = COM over heel) is displayed is Fig. F.5. In Figs. F.6 and F.7, the simulated hip, knee, and ankle joint angles that yielded the maximum capturable anterior and posterior COM velocities respectively, are shown for an initial normalized COM position of 0.25, 0.50, and 0.75. When the initial COM momentum was forwards, the model always aimed to use a hip-strategy to estimate the FSR regardless of MTG constraints. To expand, all four conditions plotted in Fig. F.6 utilized a similar magnitude and timing of hip flexion regardless of initial COM position. However, with each successive condition that weakened the MTG activations (from 100% to 25%), the ankle trajectories shifted from a plantarflexion strategy to a dorsiflexion strategy. In the

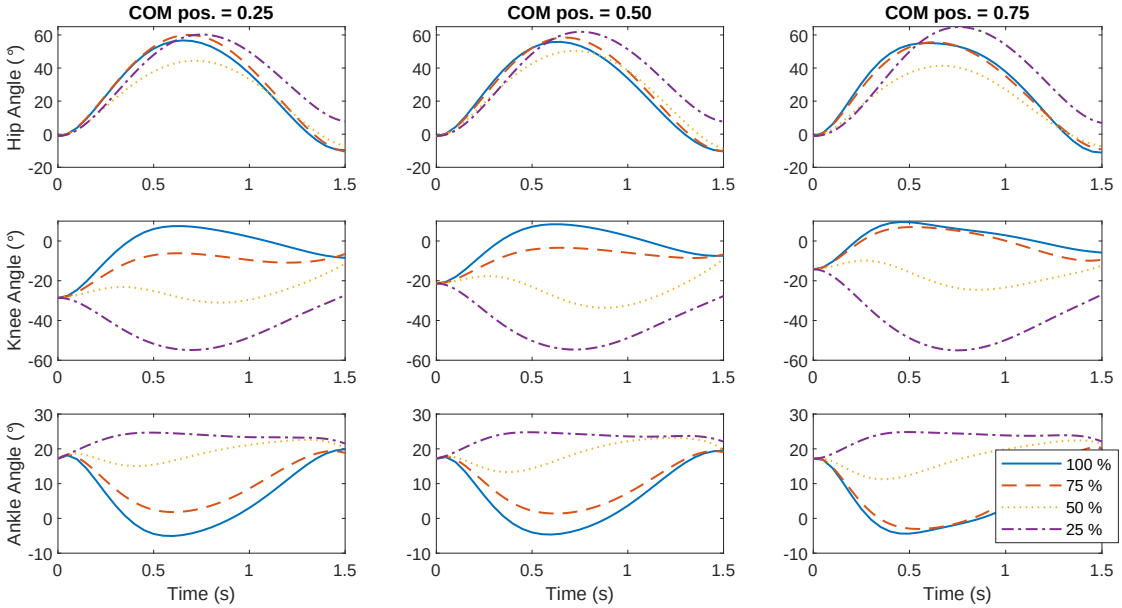


Figure F.6: Active hip, knee, and ankle muscle torques that resulted in the **anterior** FSR boundary for the human-only balance model when different time delays (dead time, δ) were imposed during simulations (right boundary in Fig. 3.7).

same vein, the knee trajectories shifted from an extension strategy to a flexion strategy as the MTGs were weakened. When the initial COM momentum was backwards, a hip strategy was used regardless of MTG constraint condition; however, this trend was different than that observed for the forward/anterior case. In Fig. F.7, there is a clear shift in hip motion with weakening of the MTGs; the hip trajectory transitions away from an extension strategy to a flexion strategy suggesting that hip *extension* maneuvers are costly in terms of torque-requirements. In general, a knee flexion and ankle dorsiflexion strategy was maintained across conditions, with some surprising exceptions: at the 50% condition, the magnitude of knee flexion was reduced substantially in exchange for shifting of the ankle towards plantarflexion. However, examining results from the 25% condition reveals increased knee flexion and ankle dorsiflexion that is closer in shape to the trajectories observed in the 75%, though with a greater degree of hip flexion used.

To our knowledge, Kuo [202] was the first to suggest through optimal control that the hip strategy uses the largest magnitude of joint torques (relative to the ankle strategy at the same "neural effort") to subsequently have a large influence over individual joint accelerations relative to the ankle strategy. The authors validated this assessment against

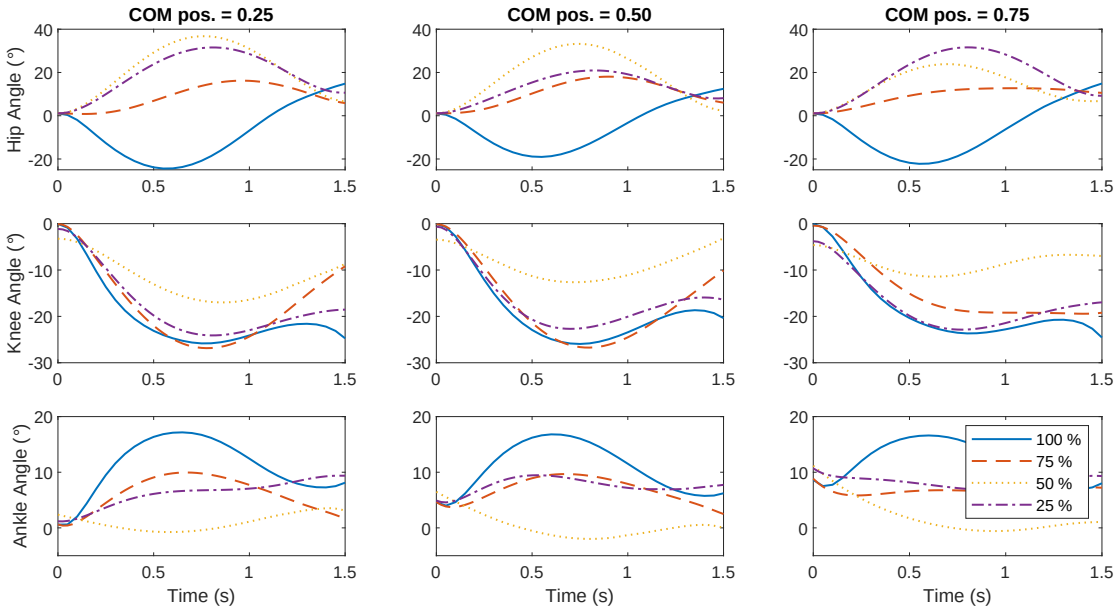


Figure F.7: Hip, knee, and ankle joint angles that resulted in the **posterior** FSR boundary for the human-only balance model with different constraints imposed on the maximum muscle activation simulations (left boundary in Fig. F.5).

experiment postural responses to lean-and-release perturbations [62]. However, in Versteeg et al. [344], the authors noted that for a forward loss of balance, increasing the weighing of muscle stress (not activations or force) had the general trend of increasing the maximum degree of trunk pitch used in simulations. The authors also suggested that "there may be multiple muscle recruitment patterns that similarly minimize COM excursion with varying levels of effort, whereas maintaining vertical trunk orientation may require specific and energetically costly muscle recruitment patterns" [344]. Herein, it is clear that for a forward loss of balance, a hip strategy in a weakened human was still optimal in maximizing the capturable COM velocities. The primary changes in postural strategy that occur with increasing MTG constraints include a shift to a predominant knee-flexion, ankle-dorsiflexion strategy (seen clearly in the 25% and 50% condition; Fig. F.6). Evidently, the components requiring the most substantial MTG activations include concurrent ankle-plantarflexion and knee-extension with the characteristic hip flexion and forward trunk pitch (seen in the 100% condition; Fig. F.6). In the more recent lean-and-release perturbation simulations by Cheng [78], active MTG activations and the final COM position were incorporated in the objective function similar to [344]. However, without variations in the weighing of the ac-

tivation term, all simulations consistently produced an exaggerated hip strategy, i.e., large magnitude of hip flexion to recover balance. In fact, the magnitude of trunk rotation in these simulations would likely have violated the constraints in Equation (3.35) that were included to make the resulting simulations more reasonable in relation to experimental observations [175, 344].

Appendix G

Obtaining the Set of Minimum Parameters

The first assumption made in designing and optimizing the parameter identification experiment for the EXO-H3 is that one leg is completely locked, e.g., right-leg motion is restricted to a static configuration:

$$\mathbf{q}_{\mathrm{e,rl}} = \mathbf{0} \tag{G.1}$$

$$\dot{\mathbf{q}}_{\mathrm{e,rl}} = \mathbf{0} \tag{G.2}$$

$$\ddot{\mathbf{q}}_{\mathrm{e,rl}} = \mathbf{0} \tag{G.3}$$

By assuming that the right and left leg share identical parameter values, the underlying mathematical model can be greatly simplified. We further assume that there is explicit knowledge of the exoskeleton floating-base kinematics ($\mathbf{q}_{\mathrm{e,fb}}$ and its derivatives) such that they can be treated as inputs to the multibody dynamic system. Substituting Equations (G.1), (G.2), and (G.3) into (4.3) results in the single-leg equations of motion

$$\mathbf{M}_{\mathrm{JJ}}\ddot{\mathbf{q}}_{\mathrm{e,ll}} = \boldsymbol{\Gamma}_{\mathrm{BJ}}(\cdot) + \boldsymbol{\tau}_{\mathrm{ac}}(\cdot) - \mathbf{M}_{\mathrm{BJ}}^{T}\ddot{\mathbf{q}}_{\mathrm{e,fb}} \tag{G.4}$$

$$\mathbf{M}_{\mathrm{JJ}}\ddot{\mathbf{q}}_{\mathrm{e,ll}} = \boldsymbol{\Gamma}_{\mathrm{FB}}(\cdot, \mathbf{u}_{\mathrm{inertial}}) + \boldsymbol{\tau}_{\mathrm{ac}}(\cdot) \tag{G.5}$$

where $\mathbf{u}_{\mathrm{inertial}} = \{\mathbf{q}_{\mathrm{e,fb}}^{\intercal}, \dot{\mathbf{q}}_{\mathrm{e,fb}}^{\intercal}, \ddot{\mathbf{q}}_{\mathrm{e,fb}}^{\intercal}\}^{\intercal}$ are the inertial inputs related to the floating-base DOF. In Equation (G.5), $\boldsymbol{\Gamma}_{\mathrm{FB}} \in \mathbb{R}^{3\times 1}$ is the modified nonlinear applied torque vector that results from addition of floating-base accelerations as inputs, i.e., $\boldsymbol{\Gamma}_{\mathrm{FB}} = \boldsymbol{\Gamma}_{\mathrm{BJ}} - \mathbf{M}_{\mathrm{BJ}}^{T}\ddot{\mathbf{q}}_{\mathrm{e,fb}}$.

To further simplify the equations of motion from (G.5), as well as to allow for easier manual inspection of the linear independence of the dynamic parameters with respect to the applied torques [119, 306, 318], the second-order dynamic joint-space ODEs in (G.5) were transitioned into the segment angle space. In short, this transfer was made via specification of virtual constraints:

$$\boldsymbol{\phi}(t) = \mathbf{J}\mathbf{q}_{\mathrm{e,ll}}(t) + \boldsymbol{\gamma}(t) \tag{G.6}$$

where $\boldsymbol{\phi}(t) = \{\phi_{\mathrm{th}}(t), \phi_{\mathrm{sh}}(t), \phi_{\mathrm{ft}}(t)\}^{\intercal} \in \mathbb{R}^{3\times 1}$ are the angles of the left thigh, shank, and foot segment respectively, with respect to the vertical of the inertial-frame $\mathcal{F}_{\mathrm{I}}$ (see Fig. 4.1). Additional terms in Equation (G.6) include

$$\mathbf{J} \in \mathbb{R}^{3\times 3} = \begin{bmatrix} 1 & 0 & 0 \\ 1 & 1 & 0 \\ 1 & 1 & 1 \end{bmatrix} \quad \text{and} \quad \boldsymbol{\gamma}(t) \in \mathbb{R}^{3\times 1} = \mathbf{1}\phi_{\mathrm{tr}}(t) + \begin{Bmatrix} 0 \\ 0 \\ \frac{1}{2}\pi \end{Bmatrix} \tag{G.7}$$

where $\mathbf{1} \in \mathbb{R}^{3\times 1}$ is a column matrix of ones and $\phi_{\mathrm{tr}} \in \mathbb{R}$ is the orientation of the floating exoskeleton trunk within the inertial frame. Because $\mathbf{J}$ is full-rank, the inverse expression to (G.6) can also be obtained as

$$\mathbf{q}_{\mathrm{e,ll}}(t) = \mathbf{J}^{-1}(\boldsymbol{\phi}(t) - \boldsymbol{\gamma}(t)) \tag{G.8}$$

such that we can easily map variables back and forth between segment- and joint-angle kinematic space.

From the principle of virtual work [141], we know that any virtual work δW done along $\delta\boldsymbol{\phi}$ can be expressed as:

$$\delta W = Q_{\mathrm{th}}\delta\phi_{\mathrm{th}} + Q_{\mathrm{sh}}\delta\phi_{\mathrm{sh}} + Q_{\mathrm{ft}}\delta\phi_{\mathrm{ft}} \tag{G.9}$$

where

$$Q_k = \sum_{i=1}^{3} \tau_i \cdot \frac{\partial \mathbf{q}_{\mathrm{e,ll},i}}{\partial \phi_k} \tag{G.10}$$

According to Equation (G.8), $\partial\mathbf{q}_{\mathrm{e,ll},i}/\partial\phi_{\mathrm{th}}$ is simply the i^{th} column of $\mathbf{J}^{-1}$; therefore, we simply state that

$$\begin{Bmatrix} Q_{\mathrm{th}} \\ Q_{\mathrm{sh}} \\ Q_{\mathrm{ft}} \end{Bmatrix} = \mathbf{J}^{-\intercal}\boldsymbol{\tau} \tag{G.11}$$

where $\boldsymbol{\tau} \in \mathbb{R}^{3\times 1}$ is any applied torque column matrix expressed in joint-space and $\mathbf{J}^{-\intercal} \equiv (\mathbf{J}^{-1})^{\intercal}$. Using D'Alembert s principle (adding work due to inertial forces) with Equation (G.5), we set variable $\boldsymbol{\tau}$ as follows:

$$\begin{aligned}\boldsymbol{\tau} &= \mathbf{M}_{\mathrm{JJ}}\ddot{\mathbf{q}}_{\mathrm{e,ll}} - \boldsymbol{\Gamma}_{\mathrm{FB}}(\cdot, \mathbf{u}_{\mathrm{inertial}}) - \boldsymbol{\tau}_{\mathrm{ac}}(\cdot) \\ &= \mathbf{0}\end{aligned} \tag{G.12}$$

Substituting the joint-segment kinematic relations from Equation (G.8) into Equation (G.12) and substituting (G.12) into (G.11), we arrive at a set of multibody dynamic equations representing EXO-H3 single-leg dynamics within the segment-angle coordinate space:

$$\mathbf{J}^{-\intercal}\mathbf{M}_{\mathrm{JJ}}\ddot{\mathbf{q}}_{\mathrm{e,ll}} - \mathbf{J}^{-\intercal}\boldsymbol{\Gamma}_{\mathrm{FB}}(\cdot, \mathbf{u}_{\mathrm{inertial}}) - \mathbf{J}^{-\intercal}\boldsymbol{\tau}_{\mathrm{ac}}(\cdot) = \mathbf{0} \tag{G.13}$$

$$\mathbf{J}^{-\intercal}\mathbf{M}_{\mathrm{JJ}}\mathbf{J}^{-1}\ddot{\boldsymbol{\phi}} - \mathbf{J}^{-\intercal}\boldsymbol{\Gamma}_{\mathrm{FB}}(\cdot, \mathbf{u}_{\mathrm{inertial}}) - \mathbf{J}^{-\intercal}\boldsymbol{\tau}_{\mathrm{ac}}(\cdot) = \mathbf{0} \tag{G.14}$$

$$\tilde{\mathbf{M}}_{\mathrm{e}}\ddot{\boldsymbol{\phi}} = \tilde{\boldsymbol{\Gamma}}_{\mathrm{FB}}(\cdot, \mathbf{u}_{\mathrm{inertial}}) + \tilde{\boldsymbol{\tau}}_{\mathrm{ac}}(\cdot, \mathbf{u}_{\mathrm{inertial}}) \tag{G.15}$$

where $\tilde{\mathbf{M}}_{\mathrm{e}} \in \mathbb{R}^{3\times 3}$ is the simplified exoskeleton leg mass matrix (now in segment angle space) and like previously, $\tilde{\boldsymbol{\Gamma}}_{\mathrm{FB}} \in \mathbb{R}^{3\times 1}$ contains velocity-dependent, gravitational, and floating-base-induced inertial torques. Note that the segment actuator friction torques $\tilde{\boldsymbol{\tau}}_{\mathrm{ac}}$ are now a function of $\mathbf{u}_{\mathrm{inertial}}$; hip actuator friction is dependent on the relative velocity of the thigh and trunk segments.

With the system dynamics written, at baseline there exists a set of 15 *redundant* parameters (some shown in Fig. 4.1A) that we assume are unknown but are required for dynamic simulation. These parameters can be organized into their own vector as follows:

$$\mathbf{p}_{\mathrm{r}} = \{\underbrace{m_{\mathrm{th}}, m_{\mathrm{sh}}, m_{\mathrm{ft}}}_{\text{Mass}}, \underbrace{I_{\mathrm{th}}, I_{\mathrm{sh}}, I_{\mathrm{ft}}}_{\text{MOI wrt COM}}, \underbrace{\ell_{\mathrm{th}}, \ell_{\mathrm{sh}}, \ell_{\mathrm{ft}}}_{\text{Length}}, \underbrace{{}_{x}c_{\mathrm{th}}, {}_{x}c_{\mathrm{sh}}, {}_{x}c_{\mathrm{ft}}}_{\text{COM x (Local)}}, \underbrace{{}_{y}c_{\mathrm{th}}, {}_{y}c_{\mathrm{sh}}, {}_{y}c_{\mathrm{ft}}}_{\text{COM y (Local)}}\}^{\intercal} \tag{G.16}$$

where the under-bracket text in Equation (G.16) was included to highlight what each group of parameters was related to. Note that the subscript "x" indicates that the parameter belongs to rigid body "x" (th = thigh; sh = shank; ft = foot). As introduced prior, a problem in identifying these redundant parameters is that often variations in different ones can result in similar variances within the measured torque signal. For example, we may have difficulties in identifying segment lengths and MOIs separately using motor torque measurements; both types of parameters are responsible for scaling acceleration terms within the equations of motion (G.15). Alternatively, we can identify a *minimal* set of

parameters [119, 306, 318] for which the segment torques $\tilde{\boldsymbol{\tau}}_{\text{ac}}$ obtained from the inverse dynamic equations (G.15) are linear in.

The minimal set of linear parameter for the EXO-H3 leg ODEs (G.15) were manually identified and extracted. For the reader's interest, they are expressed in terms of the redundant parameters $\mathbf{p}_{\text{r}}$ below:

$$\mathbf{p}_{\text{Md}} = \begin{Bmatrix} (m_{\text{ft}} + m_{\text{sh}})\ell_{\text{th}}^2 + ({}_x c_{\text{th}}^2 + {}_y c_{\text{th}}^2)m_{\text{th}} + I_{\text{th}} \\ m_{\text{ft}}\ell_{\text{th}}^2 + ({}_x c_{\text{sh}}^2 + {}_y c_{\text{sh}}^2)m_{\text{sh}} + I_{\text{sh}} \\ ({}_x c_{\text{ft}}^2 + {}_y c_{\text{ft}}^2)m_{\text{ft}} + I_{\text{ft}} \end{Bmatrix} \tag{G.17}$$

$$\mathbf{p}_{\text{Mod}} = \begin{Bmatrix} m_{\text{ft}}\ell_{\text{sh}}\ell_{\text{th}} - {}_y c_{\text{sh}} m_{\text{sh}}\ell_{\text{th}} \\ {}_x c_{\text{sh}} m_{\text{sh}}\ell_{\text{th}} \\ {}_y c_{\text{ft}} m_{\text{ft}}\ell_{\text{th}} \\ {}_x c_{\text{ft}} m_{\text{ft}}\ell_{\text{th}} \\ {}_y c_{\text{ft}} m_{\text{ft}}\ell_{\text{sh}} \\ {}_x c_{\text{ft}} m_{\text{ft}}\ell_{\text{sh}} \end{Bmatrix} \tag{G.18}$$

$$\mathbf{p}_{\text{g}} = \begin{Bmatrix} -(m_{\text{ft}} + m_{\text{sh}})\ell_{\text{th}} + {}_y c_{\text{th}} m_{\text{th}} \\ -{}_y c_{\text{th}} m_{\text{th}} \\ -m_{\text{ft}}\ell_{\text{sh}} + {}_y c_{\text{sh}} m_{\text{sh}} \\ -{}_x c_{\text{sh}} m_{\text{sh}} \\ {}_y c_{\text{sh}} m_{\text{ft}} \\ -{}_x c_{\text{ft}} m_{\text{ft}} \end{Bmatrix} \tag{G.19}$$

where $\mathbf{p}_{\text{Md}} \in \mathbb{R}^{3\times 1}$ are the parameters contained along the diagonal of $\tilde{\mathbf{M}}_{\text{e}}$, $\mathbf{p}_{\text{Mod}} \in \mathbb{R}^{6\times 1}$ contains off-diagonal $\tilde{\mathbf{M}}_{\text{e}}$ terms and velocity-dependent torque parameters found in $\tilde{\boldsymbol{\Gamma}}_{\text{FB}}$, and $\mathbf{p}_{\text{g}} \in \mathbb{R}^{6\times 1}$ contains parameters related to the presence of conservative torques (both floating-base and gravitational effects). Interestingly, the system was found to have the same number of redundant and minimal parameters. The equations of motion can be

rewritten in terms of these linear parameters as follows:

$$\tilde{\boldsymbol{\tau}}_{\text{ac}}(\cdot) = \tilde{\mathbf{M}}_{\text{e}}\ddot{\boldsymbol{\phi}} - \tilde{\boldsymbol{\Gamma}}_{\text{FB}}(\cdot, \mathbf{u}_{\text{inertial}}) \tag{G.20}$$

$$\mathbf{J}^{-\intercal}\boldsymbol{\tau}_{\text{mtr}} + \mathbf{J}^{-\intercal}\boldsymbol{\tau}_{\text{f}} = \tilde{\mathbf{M}}_{\text{e}}\ddot{\boldsymbol{\phi}} - \tilde{\boldsymbol{\Gamma}}_{\text{FB}}(\cdot, \mathbf{u}_{\text{inertial}}) \tag{G.21}$$

$$\tilde{\boldsymbol{\tau}}_{\text{mtr}} = \tilde{\mathbf{M}}_{\text{e}}\ddot{\boldsymbol{\phi}} - \tilde{\boldsymbol{\Gamma}}_{\text{FB}}(\cdot, \mathbf{u}_{\text{inertial}}) - \tilde{\boldsymbol{\tau}}_{\text{f}} \tag{G.22}$$

$$= \boldsymbol{\Lambda}_{\text{Md}}\mathbf{p}_{\text{Md}} + \boldsymbol{\Lambda}_{\text{Mod}}\mathbf{p}_{\text{Mod}} + (\boldsymbol{\Lambda}_{\text{g}} + \boldsymbol{\Lambda}_{\text{fb}})\mathbf{p}_{\text{g}} + \boldsymbol{\Lambda}_{\text{f}}\mathbf{p}_{\text{f}} \tag{G.23}$$

where $\boldsymbol{\Lambda}_{\text{Md}} \in \mathbb{R}^{3\times3}$ and $\boldsymbol{\Lambda}_{\text{Md}} \in \mathbb{R}^{6\times3}$ are matrices that map the minimal parameters to the acceleration and quadratic-velocity-based torques experienced by the system; $\boldsymbol{\Lambda}_{\text{g}} \in \mathbb{R}^{6\times3}$ and $\boldsymbol{\Lambda}_{\text{fb}} \in \mathbb{R}^{6\times3}$ produce gravitational and floating-base inertial terms; and $\boldsymbol{\Lambda}_{\text{f}}\mathbf{p}_{\text{f}}$ maps segment friction torques from the linear friction parameters in Equation (4.7). As a reminder, τ_{f} is linear in 3 parameters: α_0, α_1, and α_2. As the simplest case, we assumed that each joint shared the same friction parameter values as EXO-H3 actuators are identical between joints, i.e., the total linear friction parameters are

$$\mathbf{p}_{\text{f}} = \begin{Bmatrix} \alpha_0 \\ \alpha_1 \\ \alpha_2 \end{Bmatrix} \tag{G.24}$$

However, we can also set $\mathbf{p}_{\text{f}}$ such that each joint does in fact have its own unique friction parameters that must be identified:

$$\mathbf{p}_{\text{f}} = \{\underbrace{\alpha_{\text{h},0}, \alpha_{\text{h},1}, \alpha_{\text{h},2}}_{\text{hip}}, \underbrace{\alpha_{\text{k},0}, \alpha_{\text{k},1}, \alpha_{\text{k},2}}_{\text{knee}}, \underbrace{\alpha_{\text{a},0}, \alpha_{\text{a},1}, \alpha_{\text{a},2}}_{\text{ankle}}\}^{\intercal} \tag{G.25}$$

For the purpose of experiment design, we assumed the first case was true, i.e., joints share same friction parameter values. However, as we discuss later, this assumption as well as the general presence of dry gearing friction can make the process of parameter identification quite challenging.

As a final note, Equation (G.23) can be written more succinctly as

$$\tilde{\boldsymbol{\tau}}_{\text{mtr}} = \boldsymbol{\Lambda}_{\text{obs}}\mathbf{p} \tag{G.26}$$

where $\boldsymbol{\Lambda}_{\text{obs}} \in \mathbb{R}^{3\times p}$ (i.e., the observation matrix) maps the full set of EXO-H3 minimal parameters $\mathbf{p} \in \mathbb{R}^{p\times1}$ to segment motor torques $\tilde{\boldsymbol{\tau}}_{\text{mtr}} \in \mathbb{R}^{3\times1}$. Note that $\mathbf{p} = \{\mathbf{p}_{\text{Md}}, \mathbf{p}_{\text{Mod}}, \mathbf{p}_{\text{g}}, \mathbf{p}_{\text{f}}\}^{\intercal}$; therefore, the choice of $\mathbf{p}_{\text{f}}$ from (G.24) and (G.25) will affect the value of p. Please refer to Appendix H for further details on the individual elements of the linear parameter matrices.

Appendix H

Minimal Parameter Equations of Motion (Exoskeleton Leg)

The following equations detail the individual elements of the parameter minimum matrices introduced in Equation (G.23):

$$\mathbf{\Lambda}_{\mathrm{Md}} = \begin{bmatrix} \ddot{\phi}_{\mathrm{th}} & 0 & 0 \\ 0 & \ddot{\phi}_{\mathrm{sh}} & 0 \\ 0 & 0 & \ddot{\phi}_{\mathrm{ft}} \end{bmatrix} \tag{H.1}$$

$$\mathbf{\Lambda}_{\mathrm{g}} = \begin{bmatrix} -g\sin(\phi_{\mathrm{th}}) & -g\cos(\phi_{\mathrm{th}}) & 0 & 0 & 0 & 0 \\ 0 & 0 & -g\sin(\phi_{\mathrm{sh}}) & -g\cos(\phi_{\mathrm{sh}}) & 0 & 0 \\ 0 & 0 & 0 & 0 & -g\sin(\phi_{\mathrm{ft}}) & -g\cos(\phi_{\mathrm{ft}}) \end{bmatrix} \tag{H.2}$$

$$\begin{aligned}\mathbf{\Lambda}_{\mathrm{Mod};(1,1)} =& -\cos(\phi_{\mathrm{th}})\sin(\phi_{\mathrm{sh}})\dot{\phi}_{\mathrm{sh}}^2 + \cos(\phi_{\mathrm{sh}})\sin(\phi_{\mathrm{th}})\dot{\phi}_{\mathrm{sh}}^2 \\ &+ \cos(\phi_{\mathrm{th}})\cos(\phi_{\mathrm{sh}})\ddot{\phi}_{\mathrm{sh}} + \sin(\phi_{\mathrm{th}})\sin(\phi_{\mathrm{sh}})\ddot{\phi}_{\mathrm{sh}}\end{aligned} \tag{H.3}$$

$$\begin{aligned}\mathbf{\Lambda}_{\mathrm{Mod};(2,1)} =& \cos(\phi_{\mathrm{th}})\sin(\phi_{\mathrm{sh}})\dot{\phi}_{\mathrm{th}}^2 - \cos(\phi_{\mathrm{sh}})\sin(\phi_{\mathrm{th}})\dot{\phi}_{\mathrm{th}}^2 \\ &+ \cos(\phi_{\mathrm{th}})\cos(\phi_{\mathrm{sh}})\ddot{\phi}_{\mathrm{th}} + \sin(\phi_{\mathrm{th}})\sin(\phi_{\mathrm{sh}})\ddot{\phi}_{\mathrm{th}}\end{aligned} \tag{H.4}$$

$$\begin{aligned}\mathbf{\Lambda}_{\mathrm{Mod};(1,2)} =& -\sin(\phi_{\mathrm{th}})\sin(\phi_{\mathrm{sh}})\dot{\phi}_{\mathrm{sh}}^2 - \cos(\phi_{\mathrm{th}})\dot{\phi}_{\mathrm{sh}}^2\cos(\phi_{\mathrm{sh}}) \\ &+ \sin(\phi_{\mathrm{th}})\ddot{\phi}_{\mathrm{sh}}\cos(\phi_{\mathrm{sh}}) - \ddot{\phi}_{\mathrm{sh}}\cos(\phi_{\mathrm{th}})\sin(\phi_{\mathrm{sh}})\end{aligned} \tag{H.5}$$

$$\begin{aligned}\mathbf{\Lambda}_{\mathrm{Mod};(2,2)} =& \cos(\phi_{\mathrm{th}})\dot{\phi}_{\mathrm{th}}^2\cos(\phi_{\mathrm{sh}}) + \sin(\phi_{\mathrm{sh}})\dot{\phi}_{\mathrm{th}}^2\sin(\phi_{\mathrm{th}}) \\ &- \cos(\phi_{\mathrm{th}})\sin(\phi_{\mathrm{sh}})\ddot{\phi}_{\mathrm{th}} + \cos(\phi_{\mathrm{sh}})\sin(\phi_{\mathrm{th}})\ddot{\phi}_{\mathrm{th}}\end{aligned} \tag{H.6}$$

$$\begin{aligned}\mathbf{\Lambda}_{\mathrm{Mod};(1,3)} =& \sin(\phi_{\mathrm{ft}})\dot{\phi}_{\mathrm{ft}}^2\cos(\phi_{\mathrm{th}}) - \cos(\phi_{\mathrm{ft}})\dot{\phi}_{\mathrm{ft}}^2\sin(\phi_{\mathrm{th}}) \\ &- \sin(\phi_{\mathrm{ft}})\ddot{\phi}_{\mathrm{ft}}\sin(\phi_{\mathrm{th}}) - \cos(\phi_{\mathrm{ft}})\ddot{\phi}_{\mathrm{ft}}\cos(\phi_{\mathrm{th}})\end{aligned} \tag{H.7}$$

$$\begin{aligned}\mathbf{\Lambda}_{\mathrm{Mod};(1,4)} =& -\sin(\phi_{\mathrm{ft}})\dot{\phi}_{\mathrm{ft}}^2\sin(\phi_{\mathrm{th}}) - \dot{\phi}_{\mathrm{ft}}^2\cos(\phi_{\mathrm{ft}})\cos(\phi_{\mathrm{th}}) \\ &- \sin(\phi_{\mathrm{ft}})\ddot{\phi}_{\mathrm{ft}}\cos(\phi_{\mathrm{th}}) + \cos(\phi_{\mathrm{ft}})\ddot{\phi}_{\mathrm{ft}}\sin(\phi_{\mathrm{th}})\end{aligned} \tag{H.8}$$

$$\begin{aligned}\mathbf{\Lambda}_{\mathrm{Mod};(3,3)} =& \sin(\phi_{\mathrm{th}})\cos(\phi_{\mathrm{ft}})\dot{\phi}_{\mathrm{th}}^2 - \sin(\phi_{\mathrm{ft}})\cos(\phi_{\mathrm{th}})\dot{\phi}_{\mathrm{th}}^2 \\ &- \sin(\phi_{\mathrm{th}})\sin(\phi_{\mathrm{ft}})\ddot{\phi}_{\mathrm{th}} - \cos(\phi_{\mathrm{th}})\cos(\phi_{\mathrm{ft}})\ddot{\phi}_{\mathrm{th}}\end{aligned} \tag{H.9}$$

$$\begin{aligned}\mathbf{\Lambda}_{\mathrm{Mod};(3,4)} =& \sin(\phi_{\mathrm{th}})\dot{\phi}_{\mathrm{th}}^2\sin(\phi_{\mathrm{ft}}) + \cos(\phi_{\mathrm{ft}})\dot{\phi}_{\mathrm{th}}^2\cos(\phi_{\mathrm{th}}) \\ &+ \sin(\phi_{\mathrm{th}})\cos(\phi_{\mathrm{ft}})\ddot{\phi}_{\mathrm{th}} - \sin(\phi_{\mathrm{ft}})\cos(\phi_{\mathrm{th}})\ddot{\phi}_{\mathrm{th}}\end{aligned} \tag{H.10}$$

$$\begin{aligned}\mathbf{\Lambda}_{\mathrm{Mod};(2,5)} =& -\sin(\phi_{\mathrm{sh}})\cos(\phi_{\mathrm{ft}})\dot{\phi}_{\mathrm{ft}}^2 + \sin(\phi_{\mathrm{ft}})\cos(\phi_{\mathrm{sh}})\dot{\phi}_{\mathrm{ft}}^2 \\ &- \sin(\phi_{\mathrm{sh}})\sin(\phi_{\mathrm{ft}})\ddot{\phi}_{\mathrm{ft}} - \cos(\phi_{\mathrm{sh}})\cos(\phi_{\mathrm{ft}})\ddot{\phi}_{\mathrm{ft}}\end{aligned} \tag{H.11}$$

$$\begin{aligned}\mathbf{\Lambda}_{\mathrm{Mod};(3,5)} =& \cos(\phi_{\mathrm{ft}})\sin(\phi_{\mathrm{sh}})\dot{\phi}_{\mathrm{sh}}^2 - \sin(\phi_{\mathrm{ft}})\cos(\phi_{\mathrm{sh}})\dot{\phi}_{\mathrm{sh}}^2 \\ &- \cos(\phi_{\mathrm{ft}})\cos(\phi_{\mathrm{sh}})\ddot{\phi}_{\mathrm{sh}} - \sin(\phi_{\mathrm{ft}})\sin(\phi_{\mathrm{sh}})\ddot{\phi}_{\mathrm{sh}}\end{aligned} \tag{H.12}$$

$$\begin{aligned}\mathbf{\Lambda}_{\mathrm{Mod};(2,6)} =& -\sin(\phi_{\mathrm{sh}})\sin(\phi_{\mathrm{ft}})\dot{\phi}_{\mathrm{ft}}^2 - \cos(\phi_{\mathrm{ft}})\cos(\phi_{\mathrm{sh}})\dot{\phi}_{\mathrm{ft}}^2 \\ &+ \sin(\phi_{\mathrm{sh}})\cos(\phi_{\mathrm{ft}})\ddot{\phi}_{\mathrm{ft}} - \sin(\phi_{\mathrm{ft}})\cos(\phi_{\mathrm{sh}})\ddot{\phi}_{\mathrm{ft}}\end{aligned} \tag{H.13}$$

$$\begin{aligned}\mathbf{\Lambda}_{\mathrm{Mod};(3,6)} =& \cos(\phi_{\mathrm{ft}})\cos(\phi_{\mathrm{sh}})\dot{\phi}_{\mathrm{sh}}^2 + \sin(\phi_{\mathrm{ft}})\sin(\phi_{\mathrm{sh}})\dot{\phi}_{\mathrm{sh}}^2 \\ &+ \cos(\phi_{\mathrm{ft}})\sin(\phi_{\mathrm{sh}})\ddot{\phi}_{\mathrm{sh}} - \sin(\phi_{\mathrm{ft}})\cos(\phi_{\mathrm{sh}})\ddot{\phi}_{\mathrm{sh}}\end{aligned} \tag{H.14}$$

$$\tag{H.15}$$

Appendix I

Offline Moving Horizon Estimation

I.1 Overview

It is often possible to improve performance of interior-point NLP methods by supplying the solver with symbolic gradients and Hessians of the cost/constraint functions with respect to the decision variable(s) [219]. While obtaining and using symbolic derivatives is a relatively trivial process in the case of inverse dynamics identification (the equations are purely algebraic), the forward dynamics approach requires that we solve for states (from ODEs) and dynamic parameters at the same time [124, 300, 347]. Solving the state trajectories and parameters simultaneously can be rather cumbersome, especially when there are a substantial number of measured samples and number of underlying equations to be solved [124, 226].

To improve tractability of the symbolic forward dynamics NLP, we designed a parameter identification approach using principles of dual estimation [181, 260] and moving horizon estimation(MHE; [310]). First, the EXO-H3 leg multibody system was converted to state-space as

$$\mathbf{x}_{\mathrm{p}} = \{\boldsymbol{\phi}^{\intercal}, \dot{\boldsymbol{\phi}}^{\intercal}\}^{\intercal}, \quad \mathbf{u}_{\mathrm{p}} = \{\tilde{\boldsymbol{\tau}}_{\mathrm{mtr}}^{\intercal}, \mathbf{u}_{\mathrm{inertial}}^{\intercal}\}^{\intercal} \tag{I.1}$$

with

$$\dot{\mathbf{x}}_{\mathrm{p}} = \mathbf{f}_{\mathrm{p}}(\mathbf{x}_{\mathrm{p}}, \mathbf{u}_{\mathrm{p}}; \mathbf{p}) = \left\{ \begin{array}{c} \dot{\boldsymbol{\phi}} \\ \tilde{\mathbf{M}}_{\mathrm{lin}}^{-1}(\tilde{\boldsymbol{\tau}}_{\mathrm{mtr}} + \tilde{\boldsymbol{\tau}}_{\mathrm{f}} + \tilde{\boldsymbol{\Gamma}}_{\mathrm{lin}}) \end{array} \right\}. \tag{I.2}$$

with state $\mathbf{x}_\mathrm{p} \in \mathbb{R}^{6\times 1}$ and input $\mathbf{u}_\mathrm{p} \in \mathbb{R}^{6\times 1}$. The forward dynamics NLP over N_e experiments was then reformulated to a least-squares optimization over a window of measurements, defined as $k \in [N, N+1, \ldots, M]$, within a *single* experimental trial:

$$\underset{\mathbf{p},\mathbf{p}_\mathrm{r},\{\mathbf{x}_\mathrm{p}\},\{\boldsymbol{\upsilon}\},\boldsymbol{\eta}}{\operatorname{argmin}} \quad \|\boldsymbol{\eta}\|^2_{\mathbf{P}^{-1}} + \sum_{k=M+1}^{N} \|\boldsymbol{\upsilon}[k]\|^2_{\mathbf{I}_{3\times 3}} \tag{I.3}$$

subject to:

$$\mathbf{R}_{\mathbf{p}_\mathrm{r}}\mathbf{p}_\mathrm{r} - \mathbf{p}_\mathrm{meas} = \mathbf{0} \tag{I.4}$$

$$\mathbf{g}_\mathbf{p}(\mathbf{p}_\mathrm{r}) - \mathbf{p} = \mathbf{0} \tag{I.5}$$

$$\mathbf{p}_\mathrm{r,min} \leq \mathbf{p}_\mathrm{r} \leq \mathbf{p}_\mathrm{r,max} \tag{I.6}$$

$$\mathbf{x}_\mathrm{p}[M] - \mathbf{x}_0 = \mathbf{0} \tag{I.7}$$

$$\mathbf{p} - \hat{\mathbf{p}}[M|M] - \boldsymbol{\eta} = \mathbf{0} \tag{I.8}$$

$$\mathbf{y}(\mathbf{x}_\mathrm{p}[k]) - \boldsymbol{\phi}_\mathrm{exp}[k] - \boldsymbol{\upsilon}[k] = \mathbf{0}, \quad \forall\, k = M+1 \ldots N \tag{I.9}$$

$$\mathbf{x}_\mathrm{p}[k] - \mathbf{x}_\mathrm{p}[k+1] + \frac{\Delta t}{2}(\mathbf{f}_\mathrm{p}(\mathbf{x}_\mathrm{p}[k], \cdot) + \mathbf{f}_\mathrm{p}(\mathbf{x}_\mathrm{p}[k+1], \cdot)) = \mathbf{0}, \quad \forall\, k = M \ldots N-1 \tag{I.10}$$

where $\{x\} \equiv \{x\}_{k=M}^{N}$ is an (N-M+1)-length sequence containing evenly-spaced samples of $x(t)$, $\{\boldsymbol{\upsilon}\}$ was a sequence of Gaussian measurement error/noise in which we assume $\boldsymbol{\upsilon}[k] \sim \mathcal{N}(\mathbf{0}, \mathbf{I})$ ($\boldsymbol{\upsilon}[k]$ and $\boldsymbol{\upsilon}[k+1]$ are uncorrelated). Likewise, $\boldsymbol{\eta} \sim \mathcal{N}(\mathbf{0}, \mathbf{P})$ was the Gaussian parameter estimation-error with covariance $\mathbf{P} = \mathbb{E}[(\mathbf{p} - \hat{\mathbf{p}}[M|M])(\mathbf{p} - \hat{\mathbf{p}}[M|M])^\intercal]$, i.e., how reliable is the initial guess for the parameters. Assuming $\mathbf{P} \in \mathbb{R}^{p\times p}$ is effectively updated at prior to each call of the MHE, this term in theory allows the estimator to weigh how well previous parameters estimations have gone as the window continually shifts forward. The first term in Equation (I.3) is also referred to as an "arrival" cost; identifying suitable arrival cost functions is an active area of research in MHE development [47, 310, 337]. The notation $\hat{\mathbf{p}}[M|M]$ indicates the estimation of $\mathbf{p}$ at instance M (the start of the moving window) given measurements up to and including those taken at instant M. Initial conditions for the states at M, i.e., $\mathbf{x}_0$, were obtained directly from the processed 3D motion capture data (assumed to be perfect measurements of the NLP initial conditions). The NLP displayed above was solved using `fmincon` (interior-point algorithm) with symbolic gradients/Hessians obtained through in MapleSim .

As we were not specifically interested in real-time implementation for the current MHE design, we used an unscented Kalman filter (UKF) described in detail in [260, 310] to

update the error covariance. This method requires discretized system dynamics explicit in $\mathbf{x}_{\mathrm{p}}[k+1]$; however, as discussed prior, explicit ODE solving formulations have been avoided in the current dissertation due to their instability when the continuous dynamics are stiff. In an attempt to address this issue, we consider the single-step method of solving stiff ODEs disseminated by Rosenbrock [141]: the continuous state-space system was first modified by adding the parameters as states undergoing a stationary process:

$$\mathbf{f}_{\mathrm{p2}}(\mathbf{x}_{\mathrm{p2}}, \mathbf{u}_{\mathrm{p2}}) = \begin{Bmatrix} \dot{\boldsymbol{\phi}} \\ \ddot{\boldsymbol{\phi}} \\ \dot{\mathbf{p}} \end{Bmatrix} = \begin{Bmatrix} \dot{\boldsymbol{\phi}} \\ \tilde{\mathbf{M}}_{\mathrm{lin}}^{-1}(\tilde{\boldsymbol{\tau}}_{\mathrm{mtr}} + \tilde{\boldsymbol{\tau}}_{\mathrm{f}} + \tilde{\boldsymbol{\Gamma}}_{\mathrm{lin}}) \\ \mathbf{0} \end{Bmatrix} \tag{I.11}$$

with

$$\mathbf{x}_{\mathrm{p2}} = \{\boldsymbol{\phi}^{\intercal}, \dot{\boldsymbol{\phi}}^{\intercal}, \mathbf{p}^{\intercal}\}^{\intercal}, \quad \mathbf{u}_{\mathrm{p2}} = \{\tilde{\boldsymbol{\tau}}_{\mathrm{mtr}}^{\intercal}, \mathbf{u}_{\mathrm{inertial}}^{\intercal}\}^{\intercal} \tag{I.12}$$

where $\dot{\mathbf{p}}$ is the time derivative of the true parameters [260]. The equation $\dot{\mathbf{x}}_{\mathrm{p2}} = \mathbf{f}_{\mathrm{p2}}(\mathbf{x}_{\mathrm{p2}}, \cdot)$ is then approximately solved over $t \in [t_0, t_f]$, where $\Delta t = t_f - t_0$, by

$$\mathbf{x}_{\mathrm{p2}}(t_0 + \Delta t) = \mathbf{x}_{\mathrm{p2}}(t_0) + [\mathbf{I} - \Delta t \nabla_{\mathbf{x}} \mathbf{f}_{\mathrm{p2}}(t_0)] \cdot \Delta t \mathbf{f}_{\mathrm{p2}}(t_0) \tag{I.13}$$

or equivently,

$$\mathbf{x}_{\mathrm{p2}}[k+1] = \mathbf{x}_{\mathrm{p2}}[k] + [\mathbf{I} - \Delta t \nabla_{\mathbf{x}} \mathbf{f}_{\mathrm{p2}}[k]] \cdot \Delta t \mathbf{f}_{\mathrm{p2}}[k] \tag{I.14}$$

$$= \mathbf{f}_{\zeta}(\mathbf{x}_{\mathrm{p2}}[k], \mathbf{u}_{\mathrm{p2}}[k]) \tag{I.15}$$

where

$$\nabla_{\mathbf{x}} \mathbf{f}_{\mathrm{p2}}[k] = \left. \frac{\partial \mathbf{f}_{\mathrm{p2}}}{\mathbf{x}_{\mathrm{p2}}} \right|_{\mathbf{x}_{\mathrm{p2}}[k]} \tag{I.16}$$

Briefly, the UKF uses unscented transformations to yield 3$^{\mathrm{rd}}$ order accurate state estimations in comparison to the first-order accurate predictions in the extended Kalman filter (EKF) [181, 260]. Unscented transforms are a method of calculating the statistical parameters (mean and covariance) of a random variable undergoing a given nonlinear transformation, i.e., knowing the variable $\mathbf{x}_{\mathrm{p2}}[k]$ and wanting to estimate the statistical parameters of $\mathbf{x}_{\mathrm{p2}}[k+1]$ following transformation by $\mathbf{f}_{\zeta}(\cdot)$. Sampling points (sigma points) are obtained through perturbations of $\mathbf{x}_{\mathrm{p2}}$; these perturbed sigma points are propagated through the nonlinear transformation and are subsequently used to estimate the mean and covariance of $\mathbf{x}_{\mathrm{p}}[k+1]$ through additional operations [260]; a subset of this estimated error covariance matrix is used in each solving the MHE NLP. In the current dissertation, the UKF component of parameter estimation was implemented using MATLAB's Control System Toolbox and Unscented Kalman Filter algorithm.

I.2 Results

To test performance of the novel MHE approach of estimating multibody dynamic parameters, we used the same data used in the forward step validations. For this MHE design, we elected to test how two factors would influence convergence of the algorithm to a set of parameters: i) variations in the length of moving window (EXP 1) and ii) variations in the measurement noise relative to the initial estimation error covariance (EXP 2), i.e., how strongly to weigh the parameters at arrival versus the high-resolution segment angle measurements. These two factors were selected as there can often be a high degree of manual tuning in obtaining reliable performance of state estimation algorithms; we elected to tune measurement noise covariance [181, 310]. The conditions in EXP 1 involved setting the MHE window length differently (M=2, M=5, M=10) for a given measurement noise covariance ($\text{cov}(\upsilon) = 10^{-6}\mathbf{I}$), whereas in EXP 2 the measurement noise covariance was adjusted ($\upsilon) = 10^{-6}\mathbf{I}$, $\text{cov}(\upsilon) = 10^{-6}\mathbf{I}$, $\text{cov}(\upsilon) = 10^{-1}\mathbf{I}$) for a set MHE window length (M=5). Fig. I.1 shows how the minimal segment MOI from $\mathbf{p}_{\text{Md}}$ were adjusted with each MHE iteration under each condition. In Fig. I.2, the changes in hip, knee, and ankle joint friction (Coulomb) are shown with successive iterations. Fig. I.3 shows the trace of the estimation covariance matrix $\mathbf{P}$ over MHE iterations for each of the conditions tested; a summary table of the final segment angle RMSE for each condition (not joint angles) can be found in Table I.1.

From Fig. I.1, it can be seen that in general, the three minimal MOI parameters highlighted would converge after 100-200 iterations, regardless of the MHE parameters tested. The only exception here is the high measurement covariance condition in EXP 2; the unreliable position measurements caused sudden changes in parameter estimates towards the 300^{th} iteration. The poor quality of measurements in general results in poor parameter estimates, i.e., the trace of the error covariance diverges in final iterations (Fig. I.3B). This result is somewhat surprising given the expectation that high measurement noise would weigh the arrival term in the MHE cost function higher (see Equation (I.3)). Furthermore, the converged MOI values varied greatly between conditions; though, this could be more representative of poor parameter identifiabililty given the tested motion and inputs [300]. From Fig. I.2, the identified Coulomb friction torques only seemed to converge with a small MHE window and low measurement noise covariance; increasing the window length even slightly was largely detrimental to algorithm performance for these parameters. This idea is supported by the segment angle RMSE presented in Table I.1, where the first condition

in EXP 1 (M = 2, $\text{cov}(\upsilon) = 10^{-6}\mathbf{I}$) yielded the lowest RMSE in addition to the steadiest progression towards a final estimate of all parameters (Fig. I.3A). Thus, in its current state, the proposed MHE estimation algorithm seems capable of obtaining a set of constrained parameters, like in [181], following careful selection of estimation parameters. Even with that, convergence does not seem guaranteed, like in the case of the friction parameters in Fig. I.2. To amend these problems, we propose some possible adjustments: first, in a true dual-estimation format, uncertainty could be added to the state at the beginning of the moving window (not just the parameters) in addition to process noise covariance, i.e., uncertainity in the dynamic equations [260, 310]. Herein, we assumed that the dynamics were perfect as in the forward dynamics identification papers in the literature [124, 300, 347]. Likewise, it may be beneficial to test different explicit ODE solvers in establishing system equations for the UKF component. Herein, we proposed novel explicit integration of stiff dynamic equations within a state estimator via the Rosenbrock method; however, other stiff methods like the adaptive trapezoidal method recently proposed by Kulikova et al. [201] may perform more reliably. Lastly, additional measurements with uncertainty could be added to output equations, e.g., include the quantized motor torques in the estimation, in addition to adding box constraints to the UKF as well as the MHE during updates to estimation error covariance, i.e., using only the sigma points located within the box constraints in updating the estimation error covariance.

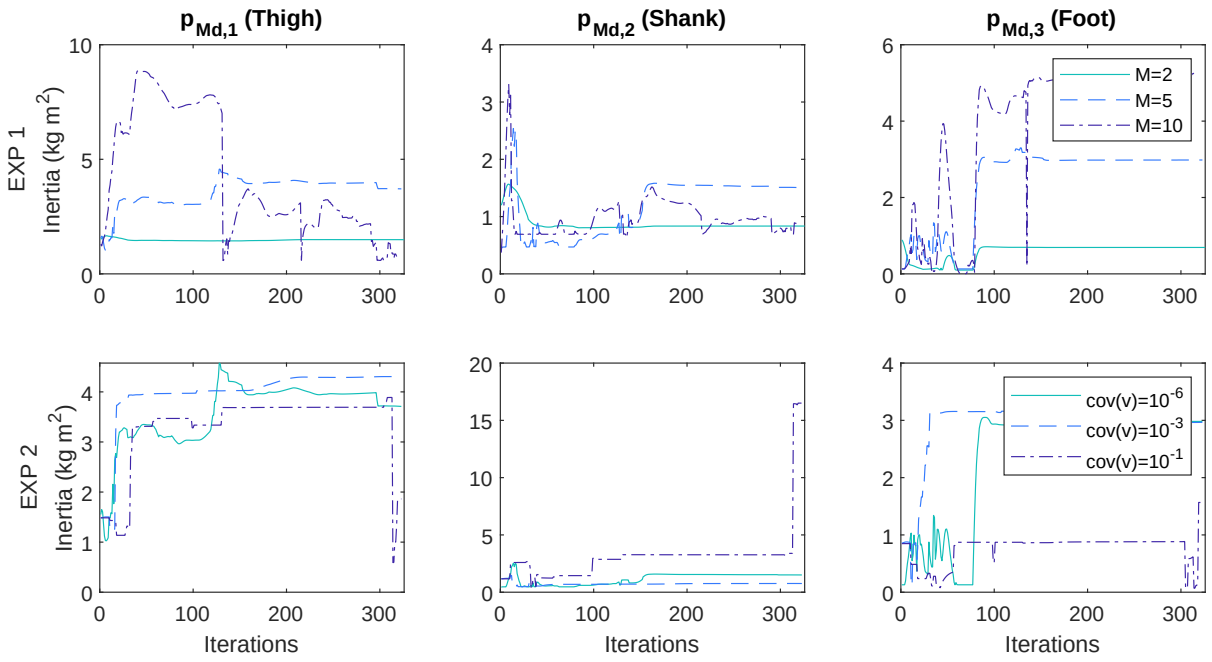


Figure I.1: Estimated minimal MOI parameters, i.e., $\mathbf{p}_{\mathrm{Md},1}$ (*left*; thigh), $\mathbf{p}_{\mathrm{Md},2}$ (*centre*; shank), and $\mathbf{p}_{\mathrm{Md},3}$ (*right*; foot), using the proposed MHE scheme over multiple iterations. The MHE algorithm was tested under two conditions: EXP 1 (*top*), the MHE window length was adjusted (M=2, M=5, M=10) for a given measurement noise covariance ($\mathrm{cov(v)} = 10^{-6}$); EXP 2 (*bottom*), the measurement noise covariance was adjusted ($\mathrm{cov(v)} = 10^{-6}$, $\mathrm{cov(v)} = 10^{-6}$, $\mathrm{cov(v)} = 10^{-1}$) for a given MHE window (M=5).

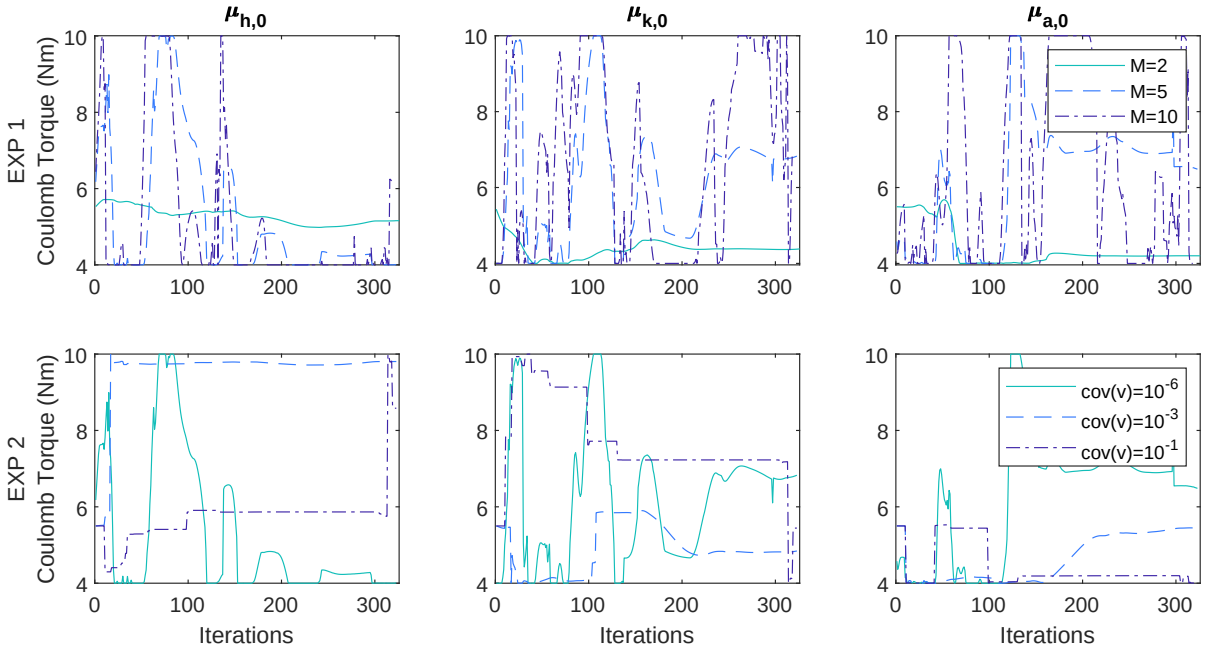


Figure I.2: Estimated Coulomb friction parameters, i.e., $\mu_{\mathrm{h},0}$ (*left*; hip), $\mu_{\mathrm{k},0}$ (*centre*; knee), and $\mu_{\mathrm{a},0}$ (*right*; ankle), using the proposed MHE scheme over multiple iterations. The MHE algorithm was tested under two conditions: EXP 1 (*top*), the MHE window length was adjusted (M=2, M=5, M=10) for a given measurement noise covariance (cov(v) = 10^{-6}); EXP 2 (*bottom*), the measurement noise covariance was adjusted (cov(v) = 10^{-6}, cov(v) = 10^{-6}, cov(v) = 10^{-1}) for a given MHE window (M=5).

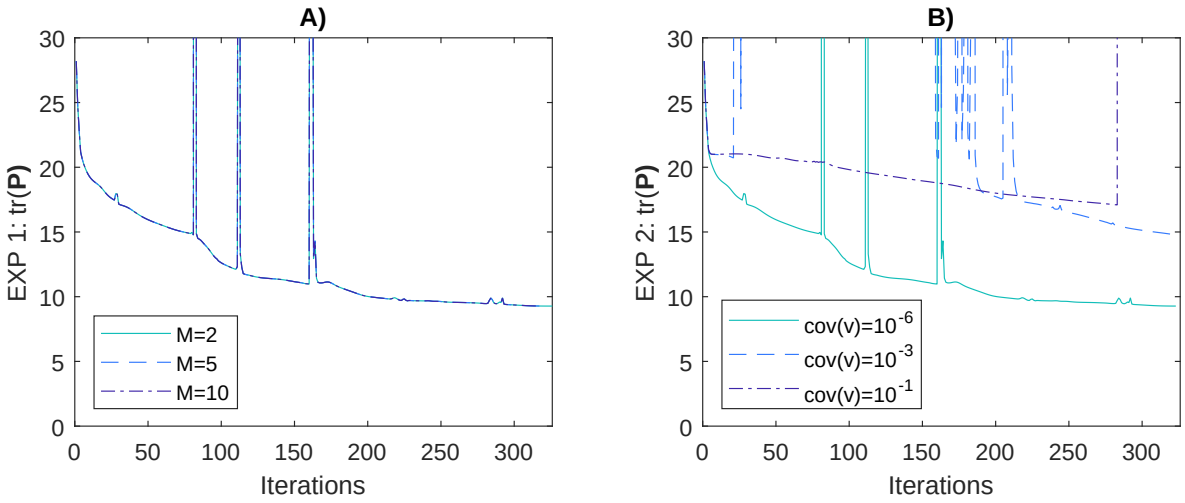


Figure I.3: Trace of the estimated parameter error covariance **P** using the proposed MHE scheme over multiple iterations. The MHE algorithm was tested under two conditions: **A)** EXP 1, the MHE window length was adjusted (M=2, M=5, M=10) for a given measurement noise covariance (cov(v) = 10^{-6}); **B)** EXP 2, the measurement noise covariance was adjusted (cov(v) = 10^{-6}, cov(v) = 10^{-6}, cov(v) = 10^{-1}) for a given MHE window (M=5).

Table I.1: Root mean square error (RMSE) between the experimental step validation segment angles and values estimated using the MHE scheme iteratively under the conditions outlined in the leftmost columns.

		Identification Method		
Window Length (M)	Measurement Covariance (cov(v))	Thigh	Shank	Foot
EXP 1				
M=2	cov(v)=10^{-6}	0.02°	0.07°	0.08°
M=5	cov(v)=10^{-6}	0.09°	0.23°	0.33°
M=10	cov(v)=10^{-6}	0.56°	0.79°	0.89°
EXP 2				
M=5	cov(v)=10^{-6}	0.09°	0.23°	0.33°
M=5	cov(v)=10^{-3}	0.10°	0.53°	0.31°
M=5	cov(v)=10^{-1}	0.14°	0.37°	0.47°

Appendix J

Background: Interactions via Kinematic Constraints

It is most commonly assumed that the human and biomechatronic device models are rigidly connected through a set of kinematic constraints. Using this assumption, we avoid the need to define parameters related to the human-device contact mechanics and are no longer, and as described by Grizzle et al. [133], "obliged to *guess* reasonable values" for these parameters. For example, let us consider the case of merging the human 5-DOF inverted pendulum model with the floating-base exoskeleton , i.e., combining Equation (3.2) and Equation (4.4) to obtain the following second-order ODEs:

$$\begin{bmatrix} \mathbf{M}_{\mathrm{h}} & \mathbf{0} \\ \mathbf{0} & \mathbf{M}_{\mathrm{e}} \end{bmatrix} \begin{Bmatrix} \ddot{\mathbf{q}}_{\mathrm{h}} \\ \ddot{\mathbf{q}}_{\mathrm{e}} \end{Bmatrix} = \begin{Bmatrix} \boldsymbol{\Gamma}_{\mathrm{h}} + \boldsymbol{\tau}_{\mathrm{mtg}} + \mathbf{P} \\ \boldsymbol{\Gamma}_{\mathrm{e}} + \mathbf{T}_{\mathrm{ac}} \end{Bmatrix} + (\nabla \Phi)^{\intercal} \boldsymbol{\lambda}_{\mathrm{he}} \tag{J.1}$$

where we introduce human-exoskeleton reaction (interaction) forces and torques in the equations of motion as Lagrange multipliers $\boldsymbol{\lambda}_{\mathrm{he}}$. Reactions are mapped to the generalized coordinate space via the constraint Jacobian ($\nabla \Phi$). The purpose of $\boldsymbol{\lambda}_{\mathrm{he}}$ is to maintain the equality constraint equations $\boldsymbol{\Phi} = \mathbf{0}$ that are predefined by the system designer. The simple case of coupling the human-exoskeleton systems defined in the current dissertation

together involves the following nonlinear kinematic constraint equations:

$$\boldsymbol{\Phi} = \begin{Bmatrix} \theta_{\text{e,lhip}} - \theta_{\text{hip}} \\ \theta_{\text{e,rhip}} - \theta_{\text{hip}} \\ \theta_{\text{e,lknee}} - \theta_{\text{knee}} \\ \theta_{\text{e,rknee}} - \theta_{\text{knee}} \\ \theta_{\text{e,lankle}} - \theta_{\text{ankle}} \\ \theta_{\text{e,rankle}} - \theta_{\text{ankle}} \\ x_{\text{tr}} - \mathbf{r}_{\text{hip}}(\mathbf{q}_{\text{h}}) \cdot \hat{\imath} \\ y_{\text{tr}} - \mathbf{r}_{\text{hip}}(\mathbf{q}_{\text{h}}) \cdot \hat{\jmath} \\ \phi_{\text{tr}} + (\theta_{\text{hip}} + \theta_{\text{knee}} + \theta_{\text{ankle}}) \end{Bmatrix} = \mathbf{0} \tag{J.2}$$

where $\mathbf{r}_{\text{hip}}(\cdot) \in \mathbb{R}^3$ is the position of the human hip joint center that we wish to connect to the insertion of the planar joint in the exoskeleton model. In Equation (J.2), it is assumed that the human and device joint centers are perfectly aligned and that the human-exoskeleton joint coordinates share identical values. By adding these algebraic equations to our system of ODEs in Equation (J.1), we obtain a set of differential algebraic equations (DAEs) that can be solved in order to obtain human-device interaction torques/forces in addition to $\mathbf{q}_{\text{h}}(t)$ and $\mathbf{q}_{\text{e}}(t)$:

$$\begin{bmatrix} \mathbf{M}_{\text{h}} & \mathbf{0} \\ \mathbf{0} & \mathbf{M}_{\text{e}} \end{bmatrix} \begin{Bmatrix} \ddot{\mathbf{q}}_{\text{h}} \\ \ddot{\mathbf{q}}_{\text{e}} \end{Bmatrix} = \begin{Bmatrix} \boldsymbol{\Gamma}_{\text{h}} + \boldsymbol{\tau}_{\text{mtg}} + \mathbf{P} \\ \boldsymbol{\Gamma}_{\text{e}} + \mathbf{T}_{\text{ac}} \end{Bmatrix} + (\nabla\Phi)^{\intercal} \boldsymbol{\lambda}_{\text{he}} \tag{J.3}$$
$$\boldsymbol{\Phi} = \mathbf{0}$$

Note that by defining a 9 scalar constraint equations, i.e., $\boldsymbol{\Phi}(\cdot) : \mathbb{R}^{14} \rightarrow \mathbb{R}^9$, we have effectively reduced the 14-DOF coupled multibody dynamic system in Equation (J.3) to a 5-DOF system, i.e., one that is based entirely around the human DOF in Chapter 3.

Equation (J.3) can be further expanded to solve for $\boldsymbol{\lambda}_{\text{he}}$ at any instant in terms of the generalized positions and velocities alone [141]. First, we convert the index-2 DAEs in (J.3) to ODEs by twice differentiating the kinematic constraints in Equation (J.2), i.e.,

$$\ddot{\boldsymbol{\Phi}} = (\nabla\Phi) \begin{Bmatrix} \ddot{\mathbf{q}}_{\text{h}} \\ \ddot{\mathbf{q}}_{\text{e}} \end{Bmatrix} + \left(\frac{d}{dt} \nabla\Phi \right) \begin{Bmatrix} \dot{\mathbf{q}}_{\text{h}} \\ \dot{\mathbf{q}}_{\text{e}} \end{Bmatrix} = \mathbf{0} \tag{J.4}$$

where $\nabla\Phi = \begin{bmatrix} \partial\Phi/\partial\mathbf{q}_{\text{h}} & \partial\Phi/\partial\mathbf{q}_{\text{e}} \end{bmatrix}$ is the aforementioned constraint Jacobian. Solving for $\{\ddot{\mathbf{q}}_{\text{h}}, \ddot{\mathbf{q}}_{\text{e}}\}^{\intercal}$ from (J.1) and substituting the result into Equation (J.4), allows us to isolate

and solve for $\boldsymbol{\lambda}_{\text{he}}$ algebraically:

$$
\begin{aligned}
-\left(\nabla\Phi\right)\begin{bmatrix}\mathbf{M}_{\text{h}}^{-1} & \mathbf{0}\\ \mathbf{0} & \mathbf{M}_{\text{e}}^{-1}\end{bmatrix}\left(\nabla\Phi\right)^{\intercal}\boldsymbol{\lambda}_{\text{he}} = \left(\nabla\Phi\right)\begin{bmatrix}\mathbf{M}_{\text{h}}^{-1} & \mathbf{0}\\ \mathbf{0} & \mathbf{M}_{\text{e}}^{-1}\end{bmatrix}\begin{Bmatrix}\boldsymbol{\Gamma}_{\text{h}}+\boldsymbol{\tau}_{\text{mtg}}+\mathbf{P}\\ \boldsymbol{\Gamma}_{\text{e}}+\mathbf{T}_{\text{ac}}\end{Bmatrix}\\
+\left(\frac{d}{dt}\nabla\Phi\right)\begin{Bmatrix}\dot{\mathbf{q}}_{\text{h}}\\ \dot{\mathbf{q}}_{\text{e}}\end{Bmatrix}
\end{aligned}
\tag{J.5}
$$

Note that in solving for $\boldsymbol{\lambda}_{\text{he}}$, we assume that the left-hand side term in Equation (J.5) is well-conditioned, e.g., the constraint Jacobian has full row-rank, a solution exists, etc.

Prior to moving forward we address two concerns common in using kinematic constraints: i) convergence of the constraint error during dynamic simulations; ii) how altering the kinematic constraint definitions can affect evaluations of the human-device interaction forces. In regards to i), numerical methods have been published in the literature that limit propagation of integration error when solving a system of DAEs converted to ODEs. For example, the Baumgarte stabilization method [141] involves rewriting the acceleration term in Equation (J.4) as

$$
\ddot{\boldsymbol{\Phi}}+2\alpha_{\text{bm}}\dot{\boldsymbol{\Phi}}+\beta_{\text{bm}}^{2}\boldsymbol{\Phi}=\mathbf{0}
\tag{J.6}
$$

which effectively reconstructs the algebraic constraints into a mass-spring-damper system that oscillates around $\boldsymbol{\Phi}=\mathbf{0}$. Regarding point ii), system designers should strive to formulate the constraint equations in a manner that aligns most effectively with their specific requirements and objectives. For example, if we instead desired purely reactions forces to be generated in $\boldsymbol{\lambda}_{\text{he}}$ (no torques), we must define the kinematic constraints in the (x,y,z) space. An example would be to specify the following nine constraints instead of the nine in Equation (J.2):

$$
\boldsymbol{\Phi}=\mathbf{0}=\left\{\begin{array}{l}
\left.\begin{array}{l}(\mathbf{r}_{\text{tr}}^{\text{exo}}-\mathbf{r}_{\text{tr}}^{\text{h}})\cdot\hat{\text{i}}\end{array}\right\}\text{- connect exoskeleton trunk to human trunk}\\
\left.\begin{array}{l}(\mathbf{r}_{\text{lth}}^{\text{exo}}-\mathbf{r}_{\text{th}}^{\text{h}})\cdot\hat{\text{i}}\\ (\mathbf{r}_{\text{rth}}^{\text{exo}}-\mathbf{r}_{\text{th}}^{\text{h}})\cdot\hat{\text{i}}\end{array}\right\}\text{- connect right/left thigh}\\
\left.\begin{array}{l}(\mathbf{r}_{\text{lsh}}^{\text{exo}}-\mathbf{r}_{\text{h}}^{\text{h}})\cdot\hat{\text{i}}\\ (\mathbf{r}_{\text{rsh}}^{\text{exo}}-\mathbf{r}_{\text{sh}}^{\text{h}})\cdot\hat{\text{i}}\end{array}\right\}\text{- connect right/left shank}\\
\left.\begin{array}{l}(\mathbf{r}_{\text{lft}}^{\text{exo}}-\mathbf{r}_{\text{ft}}^{\text{h}})\cdot\hat{\text{i}}\\ (\mathbf{r}_{\text{rft}}^{\text{exo}}-\mathbf{r}_{\text{ft}}^{\text{h}})\cdot\hat{\text{i}}\\ (\mathbf{r}_{\text{lft}}^{\text{exo}}-\mathbf{r}_{\text{ft}}^{\text{h}})\cdot\hat{\text{j}}\\ (\mathbf{r}_{\text{rft}}^{\text{exo}}-\mathbf{r}_{\text{ft}}^{\text{h}})\cdot\hat{\text{j}}\end{array}\right\}\text{- connect right/left foot}
\end{array}\right.
\tag{J.7}
$$

where the notation $\mathbf{r}_x^{\text{exo}} \in \mathbb{R}^3$ indicates the location of the segment-x-fixed human-exoskeleton point of interaction, fixed to the exoskeleton, and expressed in the inertial frame. Variable $\mathbf{r}_x^{\text{h}} \in \mathbb{R}^3$ is therefore the corresponding point of interaction on human segment x (fixed to the human). Descriptions to the right of the column matrix in Equation (J.7) provide a high-level interpretation of each element of $\mathbf{\Phi}$, i.e., what each term is responsible for maintaining during simulations. The main consideration to make in setting these constraints is to avoid defining equations that could over-constrain the desired DOF. Likewise, too few or poorly defined constraints could rather permit too many (or undesired) DOF within computer simulations. The system designer should avoid defining redundant constraints, i.e., the constraint Jacobian should ideally be full row rank, otherwise, a least-square pseudoinverse approach may be required to consistently evaluate $\boldsymbol{\lambda}_{\text{he}}$. An example of redundant constraints could be prescribing weld joint kinematic constraints for each human-exoskeleton point of interaction, e.g., (7 segments $\times$ 3 scalar constraints) = 14 constraint equations and 14 generalized coordinates, yet we still effectively would have a 5-DOF system (not a 0-DOF system).

Appendix K

Supplementary Human-Exoskeleton FSR Simulations

K.1 Influence of Adding Degrees of Freedom to Pendulum: Human-Exoskeleton

The current set of simulation experiments in this current chapter was identical to the second simulation experiment in Chapter 3. To reiterate, this experiment was designed to investigate how imposing different constraints on the model degrees of freedom, i.e., which joints were to be "locked" during simulations, would impact the estimated human-exoskeleton FIP FSR boundaries. Again, we considered the following three conditions for the current simulation experiment:

1. Only ankle movement permitted during balance recovery (DOF=1, i.e., inverted pendulum)
2. Ankle, knee, and hip movements permitted during balance recovery (DOF=3, i.e., triple inverted pendulum)
3. Ankle, knee, and hip movements in addition to upper limbs movements are permitted during balance recovery (DOF=5)

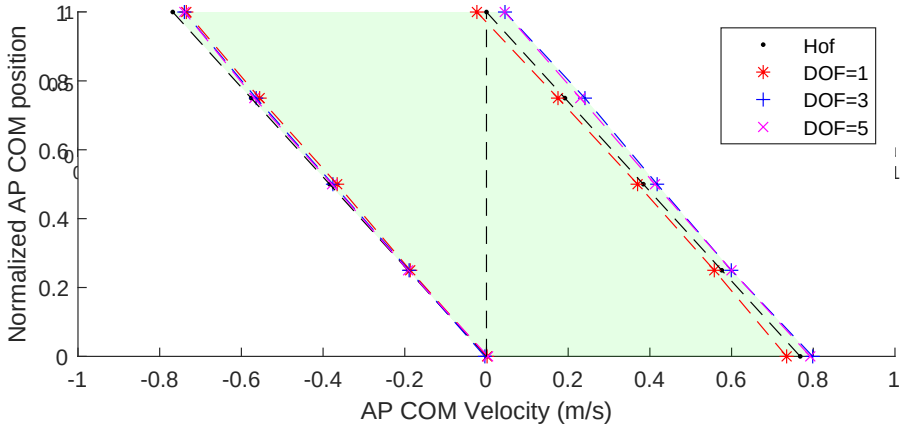


Figure K.1: The feasible stability region (FSR) for the human-exoskeleton FIP balance model generated with different constraints on the model degrees of freedom, i.e., which joints were to be "locked" during simulations. Conditions are as follows: only ankle movement (DOF=1); ankle+knee+hip movement permitted (DOF=3); ankle+knee+hip and upper limbs movement permitted (DOF=5). Additionally, the analytical results from Hof et al. [154] are shown (FSR derived from linear inverted pendulum) to validate the results of the DOF=1 simulation, i.e., the nonlinear inverted pendulum FSR.

Additionally, the analytical results from Hof et al. [154] were calculated (FSR derived from linear inverted pendulum, according to Equations (E.19) and (E.20)) with an adjusted eigenfrequency to account for a lowered COM, i.e., $\omega = 2.88$ Hz. Like in Chapter 3, Restrictions on the DOF used were imposed through manipulation of the box constraints in Equation (3.27), i.e., constrained joint velocities could never exceed $\pm 0.005\,^{\circ}/\mathrm{s}$

The estimated FSR generated over the the set of anteroposterior (AP) COM positions $\{0, 0.25, ..., 1.00\}$ (normalized to foot length; 0 = COM over toe, 1 = COM over heel) is displayed is Fig. K.1. In Figs. K.2 and K.3, the simulated whole-body human-exoskeleton COM and ZMP trajectories that yielded the maximum capturable anterior and posterior COM velocities respectively, are shown for an initial normalized COM position of 0.25, 0.50, and 0.75. The joint angles that generated these COM/ZMP trajectories are shown in Figs. K.4 and K.5. As was the case for the human-only, the DOF=3 system was able to capture larger anterior and posterior COM velocities for balance recovery in comparison to the DOF=1 system. Again, there was no notable increase in FSR size for the DOF=5 system, suggesting that sagittal motion of the arms does not make notable contributions to COM

capturability when hip and knee motion is already available. Additionally, improvements in the FSR with increased DOF were only observed for the anterior FSR boundary (right boundary in Fig. K.1); the added DOF had little influence on the posterior FSR boundary. This interesting result suggests that the human-exoskeleton should optimally balance itself like an inverted pendulum when "falling" backwards; though, forward fall cessation can still be improved through counter rotations of the superior segments relative to the COM [130, 152]. This is in contrast to observations from Chapter 3 where both anterior and posterior FSR boundaries for the human-only model benefited from increasing the number of DOF. In general, the DOF=3 and DOF=5 human-only FSRs in Fig. 3.2 were larger than their human-exoskeleton equivalent in Fig. K.1. For example, for DOF=3 systems, the human-exoskeleton anterior FSR boundary values were 55-92% of the human-only values (on average, capturable velocities were 4.99 cm/s less); for the posterior boundary, they were 79-96% of human-only values (on average, capturable velocities were 3.68 cm/s greater).

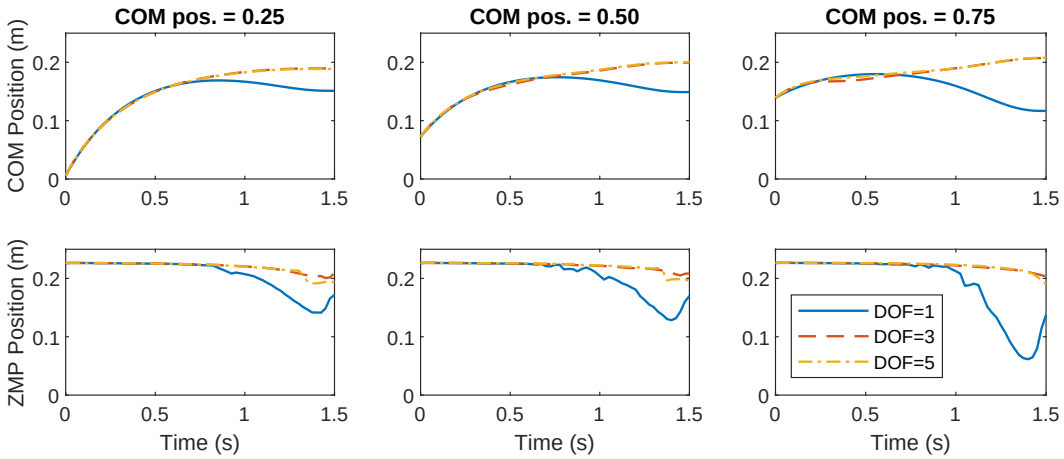


Figure K.2: COM and ZMP position that result in the **anterior** FSR boundary for the human-exoskeleton balance model when different constraints are imposed on the model degrees of freedom, i.e., which joints were to be "locked" during simulations.

Like in the case of human-only balance recovery, simulated human-exoskeleton balance to estimate the FIP FSR boundaries often involved positioning of the COP at the outermost boundaries of the support polygon (see Figs. K.2 and K.3). Again, like the human-only,

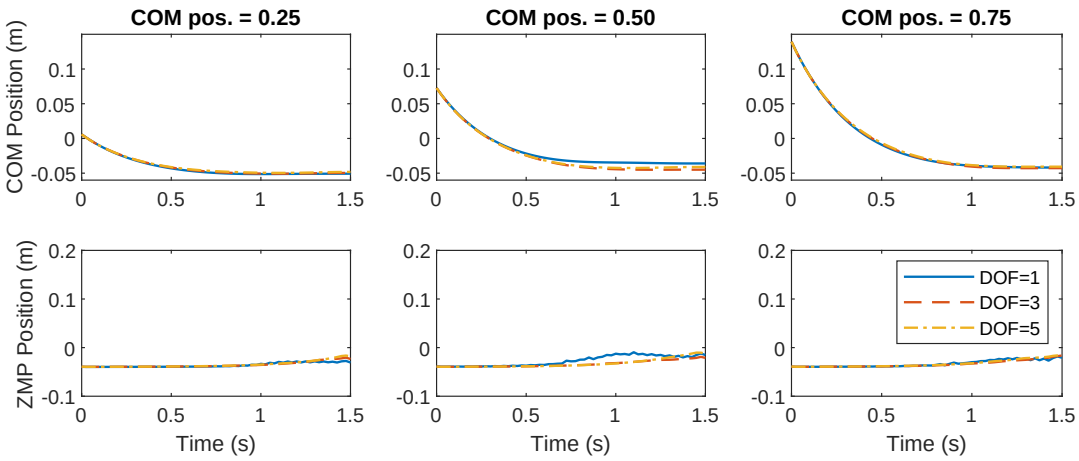


Figure K.3: COM and ZMP position that result in the **posterior** FSR boundary for the human-exoskeleton balance model when different constraints are imposed on the model degrees of freedom, i.e., which joints were to be "locked" during simulations.

the postural strategy used to estimate the anterior boundary of FIP balance involved a hip strategy (hip flexion and ankle plantarflexion, [158]); however, the amplitude of hip flexion used by the human-exoskeleton was less. Compared to the human-only, there was also often a much slower extension of the knee, likely due to the actuator impedance. Interestingly, from the knee motion displayed under the COM pos. = 0.75 condition of Fig. K.4, the NLP algorithm applied to the DOF=5 system obtained a motion in which the DOF=3 knee extension was absent; however, from Fig. K.1, we know that the DOF=3 and DOF=5 boundaries were extremely similar. This suggests that the added arm motion, which was similar to the arm motion observed for human-only simulations, allowed for improved COM capturability form the DOF=1 case.

For the postural strategies obtained while solving for the posterior human-exoskeleton FIP FSR boundary, we noted that DOF=3 and DOF=5 systems displayed similar ankle, hip and knee trajectories between each other (Fig. K.5). The DOF=5 again involved similar arm motion to the human-only simulations in Fig. 3.6, though with no real tangible improvement to the FSR. It is possible that this motion helped increase the magnitude of hip flexion used to balance [332]. With that said, unlike the human-only, the presence of the exoskeleton prevented the human-exoskeleton model from using trunk extension to

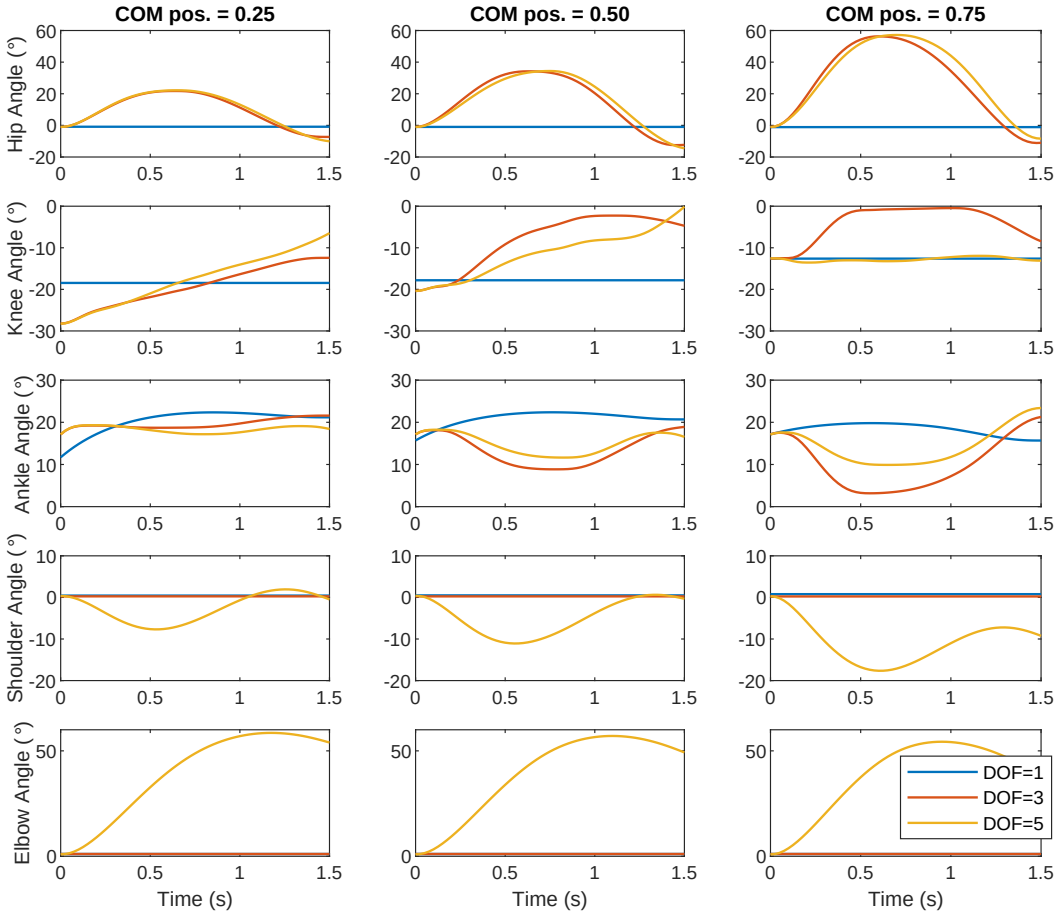


Figure K.4: Joint angles that result in the **anterior** FSR boundary for the human-exoskeleton balance model when different constraints are imposed on the model degrees of freedom, i.e., which joints were to be "locked" during simulations. Conditions are as follows: only ankle movement (DOF=1); ankle+knee+hip movement permitted (DOF=3); ankle+knee+hip and upper limbs movement permitted (DOF=5).

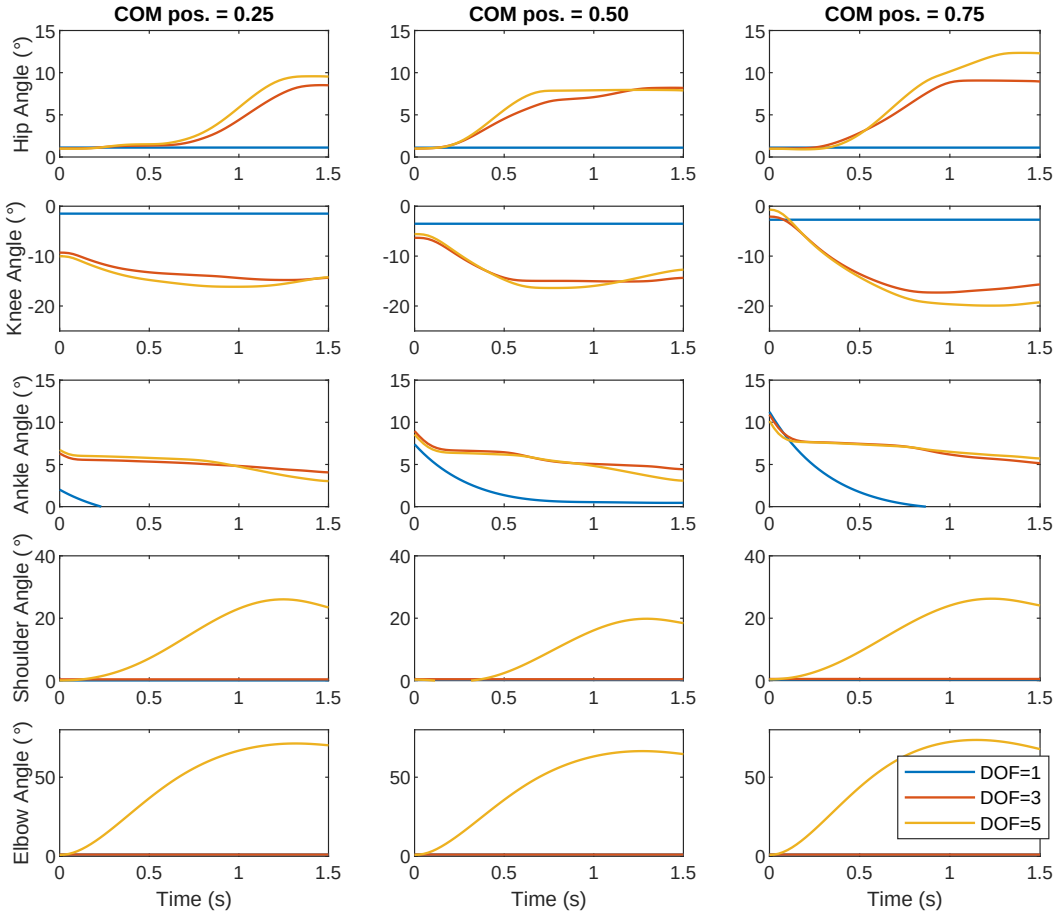


Figure K.5: Joint angles that result in the **posterior** FSR boundary for the human-exoskeleton balance model when different constraints are imposed on the model degrees of freedom, i.e., which joints were to be "locked" during simulations. Conditions are as follows: only ankle movement (DOF=1); ankle+knee+hip movement permitted (DOF=3); ankle+knee+hip and upper limbs movement permitted (DOF=5).

help correct balance. Human-only ankle motion was especially reduced for the DOF=3 and DOF=5 systems; knee motion was reduced though mainly only in the COM pos. = 0.25 condition (Fig. K.5).

K.2 Effect of Added Mass at Different Locations

The added weight of a lower-limb exoskeleton and its distribution often produces a human-exoskeleton COM position lower than that of the human end-user alone. According to Hof et al. [154], lowering of the COM corresponds to a reduction of the inverted pendulum length, which in turn suggests an increase in FIP FSR size (see Chapter 3). With that said, we observed in simulation experiment 1 of the Chapter that the benefits of lowering the COM were outweighed by the presence of high actuator impedance. Therefore, in the third simulation study, we examined the effects of adding a 5 kg mass to different bilateral segments (total added = 10 kg) to assess whether an added mass could offset the limitations introduced by the actuators and whether there was an optimal placement for said mass. The following five conditions and their effects on the human-exoskeleton FIP FSR were studied:

1. Baseline: EXO-H3 mass distribution based on physical measurements/estimations of parameters in Chapter 4 (PhyExp).
2. Trunk: 10 kg point mass added at location of orthosis COM (along trunk longitudinal axis).
3. Thigh: 5 kg point mass added at location of right and left primary thigh link COM (along each thigh's longitudinal axis).
4. Shank: 5 kg point mass added at location of right and left primary shank link COM (along each shank's longitudinal axis).
5. Foot: 5 kg point mass added at location of right and left foot pad COM (along each foot's longitudinal axis).

Briefly, the estimated FSR generated over the the set of AP COM positions $\{0, 0.25, ..., 1.00\}$ (normalized to foot length; 0 = COM over toe, 1 = COM over heel) are displayed for each

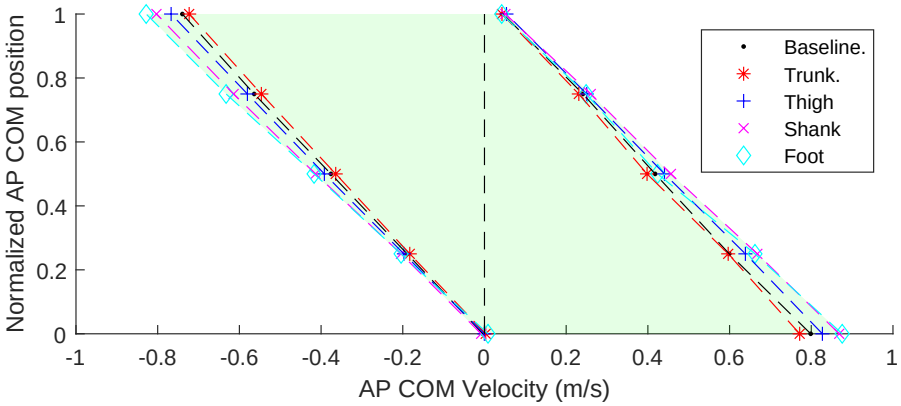


Figure K.6: The feasible stability region (FSR) for the human-exoskeleton FIP balance model generated following addition of 10 kg mass to the centroid of different segments (5 kg to left and right segments; along the longitudinal axis). Mass was added to the following segments: the trunk, thighs, shanks, and feet. The baseline condition used the EXO-H3 multibody parameters obtained in Chapter 4.

experimental condition in Fig. K.6. In line with Hof et al. [154], there were progressive improvements in the FSR size following addition of the point mass and repositioning of it inferiorly (anatomically). Specifically, the anterior FIP FSR boundary increased though only for more posterior COM positions; where the COM was near or over the toe, there was basically no added benefit from the 10 kg mass. This observation could suggest a possible improvement in human-exoskeleton walking slip recovery with the addition of weight, especially during double-support where the COM is posterior or close to the leading limb's heel [373, 369]. With that said, the addition of mass distally with respect to the hip also would increase the metabolic demand of gait itself. Thus, it may be necessary to perform separate analyses wherein we assess trade-offs in metabolic expenditure with features meant to improve end-user stability and balancing capabilities. Lastly, in similar fashion, the posterior FIP FSR boundary increased for only anterior COM positions, i.e., the mass provided no improvement to COM capturability when the COM was positioned near or over the heel. In fact, the segments of FSR boundaries that were improved by added mass were very similar in magnitude to the human-only FSR boundaries at those same COM positions.

Appendix L

Full-State Feedback: Computed Torque Control)

L.1 Overview

Computed torque control (CTC) is an impedance-based control law often used in exoskeleton-assisted gait control [46, 334]. It is notably been extrapolated to multi-joint balance recovery by Stephens for the case of unstable humanoid robots [315]. To elaborate on how the CTC method can be used for exoskeleton balance control, we begin in the control-oriented joint space (JCTC). By setting $\boldsymbol{\tau}_{\text{mtr}} = \mathbf{u}_{\text{he}}$, $\ddot{\mathbf{q}}_{\text{he}} = -\mathbf{K}_{\text{j}}(\mathbf{q}_{\text{he}} - \mathbf{q}_{\text{des}}) - \mathbf{D}_{\text{j}}(\dot{\mathbf{q}}_{\text{he}} - \dot{\mathbf{q}}_{\text{des}})$, it is feasible to derive a nonlinear control law to stabilize certain configurations and joint trajectories, i.e., rewriting the multibody equations of motion in (6.17) as

$$\mathbf{u}_{\text{he}} = \underbrace{-\frac{1}{2}\mathbf{M}_{\text{he}}\begin{bmatrix}\mathbf{K}_{\text{j}} & \mathbf{D}_{\text{j}}\end{bmatrix}}_{\mathbf{K}}(\mathbf{x}_{\text{he}}(t) - \mathbf{x}_{\text{des}}(t)) \underbrace{-\frac{1}{2}\boldsymbol{\Gamma}_{\text{he}}(\mathbf{q}_{\text{he}}, \dot{\mathbf{q}}_{\text{he}}) - \frac{1}{2}\boldsymbol{\tau}_{\text{mtg}}}_{\mathbf{u}_{\text{ff}}} \tag{L.1}$$

where $\mathbf{K}_j$ and $\mathbf{D}_j$ are coupled stiffness and damping matrices respectively. In the case of FIP balance, it is usually the case that the desired configuration is static [315]. Therefore, for the current investigation, a reasonable choice of $\mathbf{x}_{\text{des}}(t)$ may be $\{\mathbf{q}_{\text{des}}^{\intercal}, \mathbf{0}^{\intercal}\}^{\intercal}$ where $\mathbf{q}_{\text{des}} \in \mathbb{R}^{3\times 1}$ is a constant desired upright joint angle configuration. From Equation L.1, we see that this control approach in essence reduces the multibody dynamic system to a mass-spring-damper system. As desired in (6.20), the CTC method provides both a feedforward torque

(the $\mathbf{u}_{\text{ff}}$ term) that compensates for quadratic velocity effects and gravitational toppling, as well as a feedback torque ($\mathbf{K}$ term) intended to correct any deviations from the desired states. Additionally, we assume that the controller has knowledge to the joint torques applied by the human $\boldsymbol{\tau}_{\text{mtg}}$, however, these can be incredibly challenging to estimation [255, 258, 307]. In the case of autonomous exoskeleton control [103, 105, 134, 138], these torques are set to 0, i.e., the muscles exert no force back onto the device.

As discussed throughout this dissertation, human balance recovery is often framed within the context of the COM task-space. As such, a nonlinear computed torque control law can also be formulated within that space (CCTC) [314]. In this example, the horizontal and vertical components of the human-exoskeleton COM position $\mathbf{r}_{\text{ccm}} \in \mathbb{R}^{2\times 1} = \{\mathbf{r}_{\text{icm}} \cdot \mathbf{i}, \mathbf{r}_{\text{icm}} \cdot \mathbf{j}\}^{\intercal}$, calculated according to Equation (6.12), are controlled according to a desired COM trajectory. To obtain a law that meets this criteria, we first define the COM Jacobian $\mathbf{C}_{\text{ccm}} = \partial \mathbf{r}_{\text{ccm}}/\partial \mathbf{q}_{\text{he}}$ as well as the following relationships from $\mathbf{r}_{\text{ccm}} \equiv \mathbf{r}_{\text{ccm}}(\mathbf{q}_{\text{he}})$:

$$\dot{\mathbf{q}}_{\text{he}} = \mathbf{C}_{\text{ccm}}^{-1}\dot{\mathbf{r}}_{\text{ccm}} \tag{L.2}$$

$$\ddot{\mathbf{q}}_{\text{he}} = \mathbf{C}_{\text{ccm}}^{-1}(\ddot{\mathbf{r}}_{\text{ccm}} - \dot{\mathbf{C}}_{\text{icm}}\dot{\mathbf{q}}_{\text{he}}) \tag{L.3}$$

where $\mathbf{C}_{\text{cm}}^{-1}$ is the damped least-squares pseudoinverse [71], i.e.,

$$\mathbf{C}_{\text{cm}}^{-1} = \mathbf{C}_{\text{cm}}^{\intercal}(\mathbf{C}_{\text{cm}}\mathbf{C}_{\text{cm}}^{\intercal} + \psi^2\mathbf{I})^{-1} \tag{L.4}$$

where $\psi \in \{\mathbb{R} \,|\, \psi \neq 0\}$ is a damping constant that improves the matrix conditioning around singularities of $\mathbf{C}_{\text{cm}}\mathbf{C}_{\text{cm}}^{\intercal}$. By using the relationships (L.2) and (L.3), we then rewrite the open-chain equations of motion from (6.17) in COM space:

$$\mathbf{C}_{\text{ccm}}^{\intercal}\mathbf{F}_{\text{ccm}} = \mathbf{M}_{\text{he}}\mathbf{C}_{\text{ccm}}^{-1}(\ddot{\mathbf{r}}_{\text{ccm}} - \dot{\mathbf{C}}_{\text{ccm}}\dot{\mathbf{q}}_{\text{he}}) - \boldsymbol{\Gamma}_{\text{he}}(\mathbf{q}_{\text{he}}, \dot{\mathbf{q}}_{\text{he}}) - \boldsymbol{\tau}_{\text{mtg}} \tag{L.5}$$

$$\mathbf{F}_{\text{ccm}} = \mathbf{C}_{\text{ccm}}^{-\intercal}[\mathbf{M}_{\text{he}}\mathbf{C}_{\text{ccm}}^{-1}(\ddot{\mathbf{r}}_{\text{ccm}} - \dot{\mathbf{C}}_{\text{ccm}}\dot{\mathbf{q}}_{\text{he}}) - \boldsymbol{\Gamma}_{\text{he}}(\mathbf{q}_{\text{he}}, \dot{\mathbf{q}}_{\text{he}}) - \boldsymbol{\tau}_{\text{mtg}}] \tag{L.6}$$

where $\mathbf{C}_{\text{ccm}}^{-\intercal} \equiv (\mathbf{C}_{\text{ccm}}^{\intercal})^{-1}$. Like for the joint-space control law, if we say that $\ddot{\mathbf{r}}_{\text{ccm}} = -\mathbf{K}_{\text{c}}(\mathbf{r}_{\text{ccm}} - \mathbf{r}_{\text{des}}(t)) - \mathbf{D}_{\text{c}}(\dot{\mathbf{r}}_{\text{ccm}} - \dot{\mathbf{r}}_{\text{des}}(t))$, a closed-loop control law can be designed according to these COM equations of motion:

$$\mathbf{u}_{\text{he}} = \underbrace{-\frac{1}{2}\mathbf{M}_{\text{he}}\mathbf{C}_{\text{icm}}^{-1}\begin{bmatrix}\mathbf{K}_{\text{c}} & \mathbf{D}_{\text{c}}\end{bmatrix}}_{\mathbf{K}}\begin{Bmatrix}\mathbf{r}_{\text{ccm}} - \mathbf{r}_{\text{des}}(t) \\ \dot{\mathbf{r}}_{\text{ccm}} - \dot{\mathbf{r}}_{\text{des}}(t)\end{Bmatrix}\underbrace{-\frac{1}{2}\left(\mathbf{M}_{\text{he}}\mathbf{C}_{\text{ccm}}^{-1}\dot{\mathbf{C}}_{\text{icm}}\dot{\mathbf{q}}_{\text{he}} - \boldsymbol{\Gamma}_{\text{he}}(\mathbf{q}_{\text{he}}, \dot{\mathbf{q}}_{\text{he}}) - \boldsymbol{\tau}_{\text{mtg}}\right)}_{\mathbf{u}_{\text{ff}}} \tag{L.7}$$

where $\mathbf{r}_{\text{des}}(t) \in \mathbb{R}^{2\times 1}$ and $\dot{\mathbf{r}}_{\text{des}}(t) \in \mathbb{R}^{2\times 1}$ are the reference COM position/velocity trajectories that we wish for the system to follow; $\mathbf{K}_{\text{c}} \in \mathbb{R}^{2\times 2}$ and $\mathbf{D}_{\text{c}} \in \mathbb{R}^{2\times 2}$ are COM gain matrices that regulate COM kinematics. Again, for the case of FIP control, we often wish to maintain a static reference [315]; therefore $\dot{\mathbf{r}}_{\text{des}}(t)$ can reasonably be set to zero. According to Micheau et al. [242], an acceptable value of $\mathbf{r}_{\text{des}}(t)$ may be a constant 5 cm anterior to the ankle joint center; the desired height will vary with user height.

Alternatively, the controller implemented in the lower-limb exoskeleton could combine both the JCTC and CCTC feedback laws through summation (COMB):

$$\begin{aligned}\mathbf{u}_{\text{he}} = &\underbrace{-\frac{1}{2}\mathbf{M}_{\text{he}}\begin{bmatrix}\mathbf{K}_{\text{j}} & \mathbf{D}_{\text{j}}\end{bmatrix}}_{\mathbf{K}\text{ (Joint)}}(\mathbf{x}_{\text{he}}(t) - \mathbf{x}_{\text{des}}(t)) \\ &\underbrace{-\frac{1}{2}\mathbf{M}_{\text{he}}\mathbf{C}_{\text{icm}}^{-1}\begin{bmatrix}\mathbf{K}_{\text{c}} & \mathbf{D}_{\text{c}}\end{bmatrix}}_{\mathbf{K}\text{ (COM)}}\begin{Bmatrix}\mathbf{r}_{\text{ccm}} - \mathbf{r}_{\text{des}}(t) \\ \dot{\mathbf{r}}_{\text{ccm}} - \dot{\mathbf{r}}_{\text{des}}(t)\end{Bmatrix} \\ &\underbrace{-\frac{1}{2}\left(\mathbf{M}_{\text{he}}\mathbf{C}_{\text{ccm}}^{-1}\dot{\mathbf{C}}_{\text{icm}}\dot{\mathbf{q}}_{\text{he}} - \boldsymbol{\Gamma}_{\text{he}}(\mathbf{q}_{\text{he}}, \dot{\mathbf{q}}_{\text{he}}) - \boldsymbol{\tau}_{\text{mtg}}\right)}_{\mathbf{u}_{\text{ff}}}\end{aligned} \tag{L.8}$$

This method is similar to that employed in a humanoid COM control architecture [315]. Here, the authors combined joint-space linear quadratic regulator (LQR) with a CTCC-like controller for fixed point stabilization (controlled only horizontal COM position). The joint-space feedback torques provided restoration to a specific postural configuration, while the COM feedback torques could generate human-like counterbalance strategies, e.g. the hip strategy [158, 202, 315, 344]. Methods combining joint and task space impedance control in lower-limb exoskeletons have also been recently proposed for assisted walking [218].

L.2 Balance Recovery Simulations

The first set of simulations was used to assess the performance of the CTC-based control laws in recovering upright balance autonomously, i.e., without simultaneous active inputs from the user (only passive MTG torques). The control scheme used herein is displayed in Fig. L.1; nonlinear friction compensation [142] was applied through the block described in

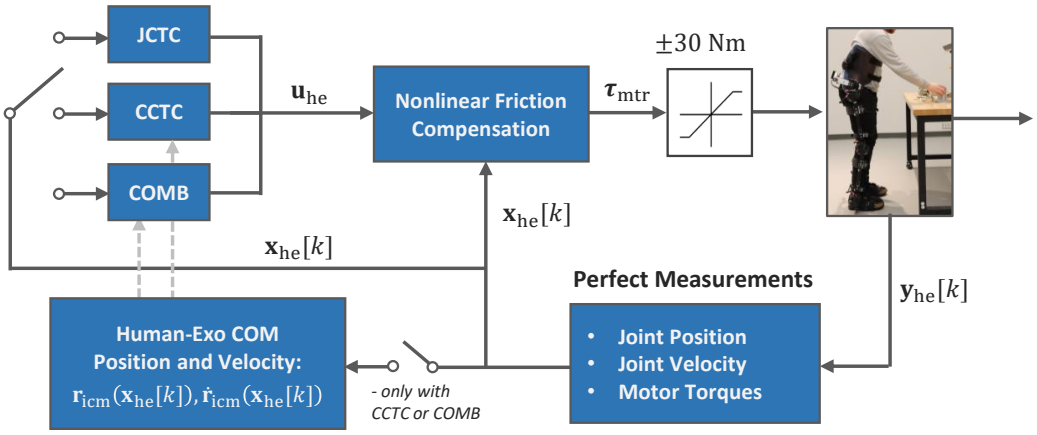


Figure L.1: Control schematic for simulation set 1: computed torque control (CTC) of FIP balance recovery in joint space (JCTC), COM-space (CCTC), or a combination of the two (COMB).

Fig. L.2. In line with manufacturer design, the exoskeleton motor torques were saturated at ±30 Nm. We assumed that friction was perfectly compensated within the loop except for torques due to viscous friction; only 80% of those torques were negated. The CCTC and COMB approaches required separate estimation of the whole-body COM kinematics from the perfect joint angle and velocity measurements, i.e., full-state feedback. Each of the three different CTC variations were tested separately with the following set of parameters: $\mathbf{K}_{\text{j}} = \text{diag}([8, 8, 8])$, $\mathbf{D}_{\text{j}} = \text{diag}([5, 5, 5])$, $\mathbf{K}_{\text{c}} = \text{diag}([7, 7, 7])$, $\mathbf{D}_{\text{c}} = \text{diag}(5, 5, 5)$. Simulations were performed under the assumption that the control-oriented model, i.e., that utilized by the controller to make a decision, was a perfect replication of the plant. Note that for the combined CTC (COMB), the gains used for each controller were the gains listed above scaled by 50% (for $\mathbf{K}_{\text{j}}$ and $\mathbf{D}_{\text{j}}$) and 40% (for $\mathbf{K}_{\text{c}}$ and $\mathbf{D}_{\text{c}}$).

Fig. L.3 shows the joint angles generated using each of the CTC control laws (JCTC, CCTC, COMB) in performing balance recovery following a posterior and anterior support-surface translation (forward and backward fall respectively). Fig. L.4 shows the motor torques generated during each simulation. Additionally, Fig. L.5 highlights the horizontal (anteroposterior; AP) COM and ZMP positions calculated during simulations. For all simulations the ZMP was maintained within the support polygon (-5.9 cm $\leq$ ZMP $\leq$ 20.7 cm) indicating no actual loss-of-balance occurred.

In general, the CTC controllers maintained the human-exoskeleton joint angles within reasonable values (anatomically). Within the first 500 ms of forward and backward sim-

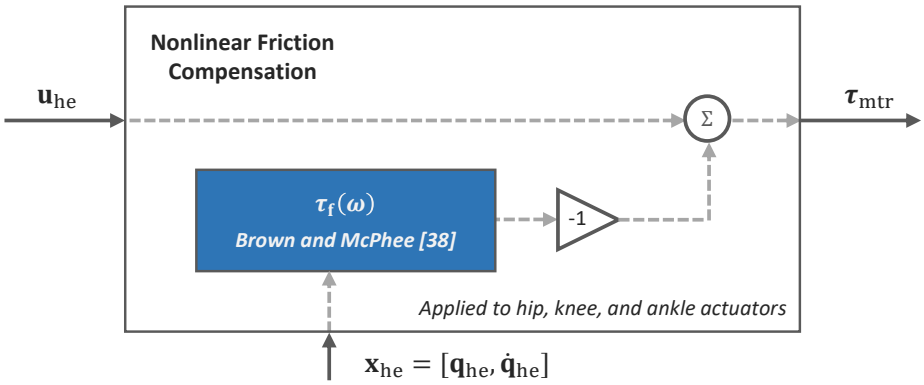


Figure L.2: Feed-forward nonlinear friction compensation block incorporated in the simulated control schemes in Chapter 6.

ulations, the joint angles were similar between CTC controllers. Later into the postural response, the CCTC controller used greater hip flexion, knee extension, and ankle plantarflexion, like a hip strategy [158, 359]. This was expected given the simulated results in humanoid robots [315]. With that said, the regulating term in the CCTC law did have some trouble returning the system to upright in addition to drift; though this drift did demand less of the actuators as suggested by the simulated motor torques in Fig. L.4. The COMB strategy appeared to remedy this issue with the CCTC [202, 315], though the COMB gains were not able to generate any more hip flexion than the JCTC controller. The COM and ZMP trajectories in Fig. L.5 also interestingly suggest that the choice of control law had minimal effect on the net COM and ZMP displacements experienced by the human-exoskeleton, i.e., backward ΔCOM ≈ 3 cm, forward ΔCOM ≈ -2 cm.

The main drawback of the CTC controllers was that they were very sensitive to choice of gains, i.e., CTC can be difficult to tune without external or data-driven methods [33, 169]. Ideally, the gains selected would produce a control law that optimizes some desired performance criteria. While that is possible with CTC, the optimized gains are still quite challenging to attain. Rather, the advantage of these nonlinear CTC controllers is their computational efficiency: between forward and backward falling conditions, the mean $\pm$ SD computational run-time for the JCTC was $5.62 \times 10^{-5} \pm 1.19 \times 10^{-4}$ s. The CCTC ($9.77 \times 10^{-5} \pm 1.94 \times 10^{-4}$ s) and COMB ($9.59 \times 10^{-5} \pm 2.07 \times 10^{-4}$ s) controllers required slightly elevated run-times with respect to the JCTC; however, in all cases, these run-times were substantially under the time provided with the 20 ms sampling interval.

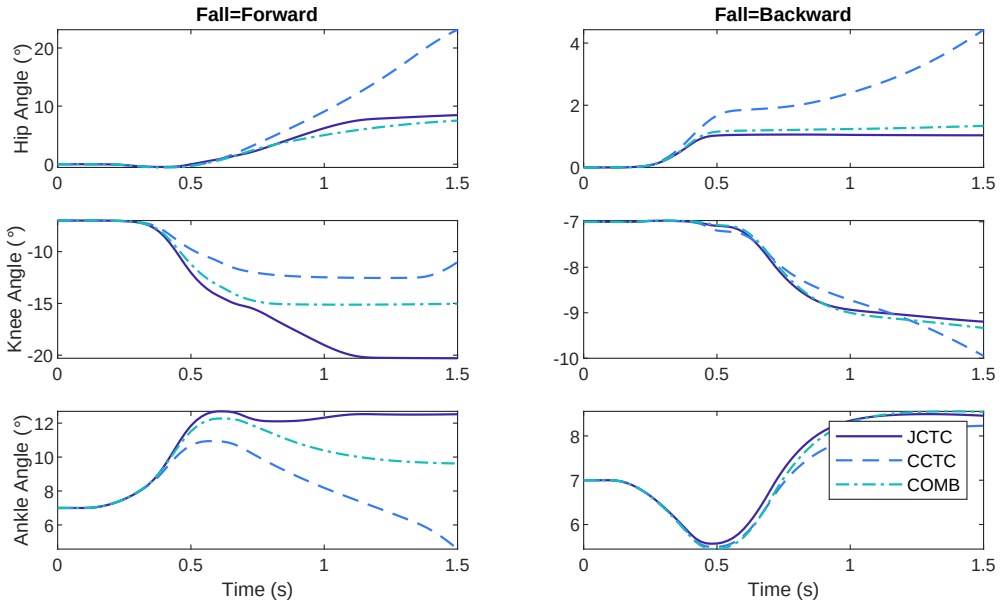


Figure L.3: Balance recovery (with FIP) joint angle trajectories obtained for each variation of computed torque control formulated in joint space (JCTC), COM-space (CCTC), or a combination of the two (COMB).

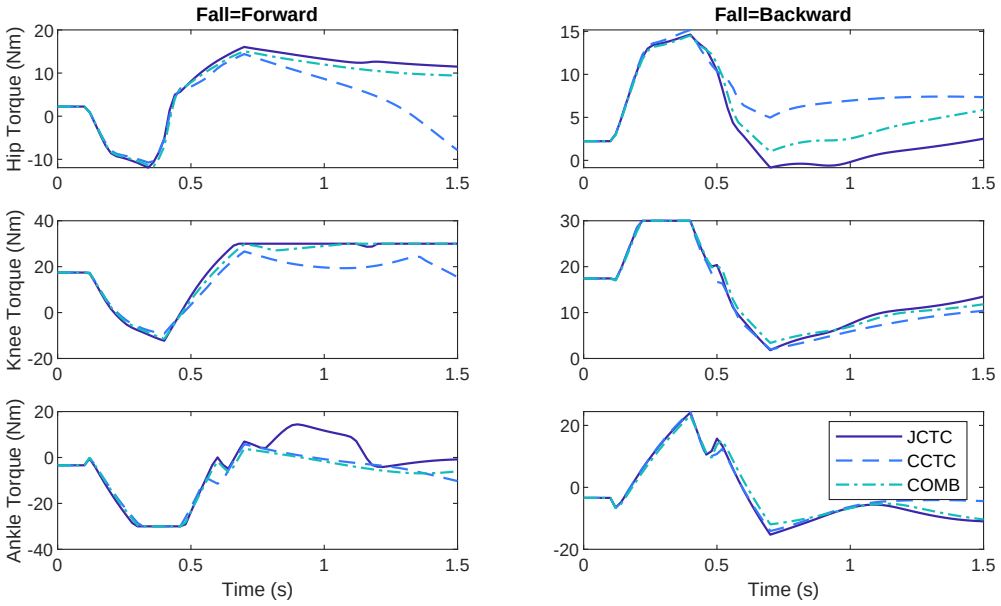


Figure L.4: Balance recovery (with FIP) motor torque trajectories obtained for each variation of computed torque control formulated in joint space (JCTC), COM-space (CCTC), or a combination of the two (COMB).

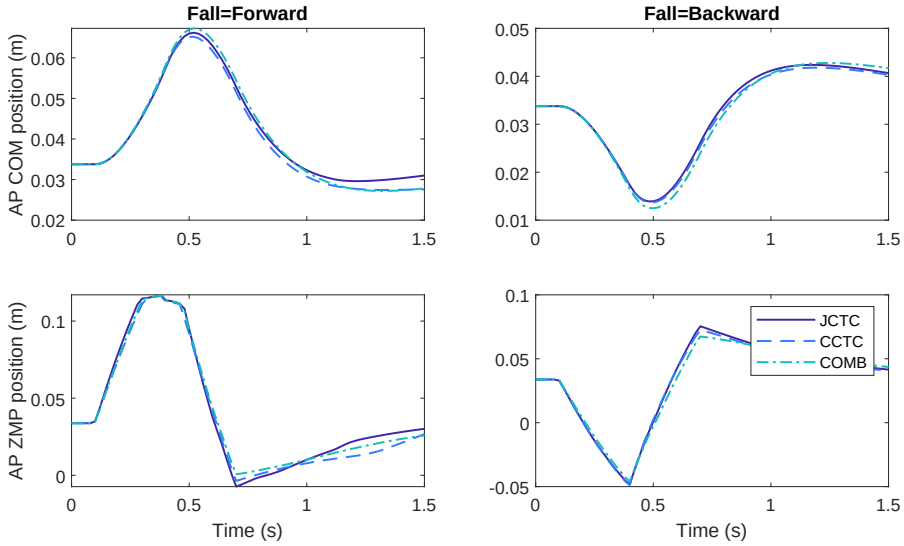


Figure L.5: Balance recovery (with FIP) anteroposterior (AP) COM/ZMP trajectories obtained for each variation of computed torque control formulated in joint space (JCTC), COM-space (CCTC), or a combination of the two (COMB).

Appendix M

Extended Kalman Filtering for FIP Balance

As mentioned prior, the primary idea behind Kalman filtering is to combine knowledge of the underlying physics of the system with statistical methods of processing of noisy measurements [310]. The extended Kalman filter (EKF) is a relatively simple and computationally inexpensive example in this category of estimation algorithms for nonlinear systems [260, 310]. To derive an EKF for the FIP balance regulator, we first derive observation-oriented multibody dynamics by expanding the control-oriented dynamics from (6.17):

$$\mathbf{M}_{\text{he}}(\mathbf{q}_{\text{he}})\ddot{\mathbf{q}}_{\text{he}} = \boldsymbol{\Gamma}_{\text{he}}(\mathbf{q}_{\text{he}}, \dot{\mathbf{q}}_{\text{he}}) + \boldsymbol{\tau}_{\text{mtg}}(t, \mathbf{q}_{\text{he}}, \dot{\mathbf{q}}_{\text{he}}) + \boldsymbol{\tau}_{\text{ac}}(\dot{\mathbf{q}}_{\text{he}}) \tag{M.1}$$

$$= \boldsymbol{\Gamma}_{\text{he}}(\mathbf{q}_{\text{he}}, \dot{\mathbf{q}}_{\text{he}}) + \boldsymbol{\tau}_{\text{mtg}}^{\text{cns}} + 2(\boldsymbol{\tau}_{\text{mtr}} + \boldsymbol{\tau}_{\text{psv}} + \boldsymbol{\tau}_{\text{f}}) \tag{M.2}$$

We then create a state-space representation of this observation-oriented system where $\boldsymbol{\tau}_{\text{mtr}}$ and $\boldsymbol{\tau}_{\text{mtg}}^{\text{cns}}$ are now included as states that must be estimated rather than inputs:

$$\mathbf{x}_{\text{os}} \in \mathbb{R}^{12\times 1} = \begin{Bmatrix} \mathbf{q}_{\text{he}} \\ \dot{\mathbf{q}}_{\text{he}} \\ \boldsymbol{\tau}_{\text{mtr}} \\ \boldsymbol{\tau}_{\text{mtg}}^{\text{cns}} \end{Bmatrix}, \quad \dot{\mathbf{x}}_{\text{os}} = \begin{Bmatrix} \dot{\mathbf{q}}_{\text{he}} \\ \ddot{\mathbf{q}}_{\text{he}} \\ \dot{\boldsymbol{\tau}}_{\text{mtr}} \\ \dot{\boldsymbol{\tau}}_{\text{mtg}}^{\text{cns}} \end{Bmatrix}. \tag{M.3}$$

The state-space dynamics then follow from (M.2) as

$$\dot{\mathbf{x}}_{\text{os}} = \left\{ \begin{array}{c} \dot{\mathbf{q}}_{\text{e3}} \\ \mathbf{M}_{\text{he}}(\mathbf{q}_{\text{he}})^{-1}(\boldsymbol{\Gamma}_{\text{he}}(\mathbf{q}_{\text{he}}, \dot{\mathbf{q}}_{\text{he}}) + \boldsymbol{\tau}_{\text{mtg}}^{\text{cns}} + 2(\boldsymbol{\tau}_{\text{mtr}} + \boldsymbol{\tau}_{\text{psv}} + \boldsymbol{\tau}_{\text{f}})) \\ \mathbf{0} \\ \mathbf{0} \end{array} \right\} = \mathbf{f}_{\text{os}}(\mathbf{x}_{\text{os}}(t)) \tag{M.4}$$

where $\boldsymbol{\tau}_{\text{mtg}}^{\text{cns}}(t)$ and $\boldsymbol{\tau}_{\text{mtr}}(t)$ are deterministically considered to be stationary processes.

In order to generate state estimations for the model outlined, the dynamics must first be discretized before introducing stochastic processes. These processes can help describe important variance in the noisy measurements not described by the deterministic components of the dynamics (M.4). In saying that, we must also do so in a way that reasonably captures how a change in the hidden user and motor torque states may result in a change in the observed kinematic states. In these regards, we introduce the concept of scaled random walks [366]. To elaborate, we suggest that $\boldsymbol{\tau}_{\text{mtr}}$ and $\boldsymbol{\tau}_{\text{mtg}}^{\text{cns}}$ evolve over Δt according to a stationary deterministic term in addition to a stochastic component, i.e.,

$$\boldsymbol{\tau}_{\text{mtg}}^{\text{cns}}[k+1] = \boldsymbol{\tau}_{\text{mtg}}^{\text{cns}}[k] + \Delta t \mathbf{w}_{\text{mtg}}[k] \tag{M.5}$$

$$\boldsymbol{\tau}_{\text{mtr}}[k+1] = \underbrace{\boldsymbol{\tau}_{\text{mtr}}[k]}_{\text{Deterministic}} + \underbrace{\Delta t \mathbf{w}_{\text{mtr}}[k]}_{\text{Stochastic}} \tag{M.6}$$

where the Gaussian processes $\mathbf{w}_{\text{mtg}}[k] \sim \mathcal{N}(\mathbf{0}, \mathbf{Q}_{\text{mtg}})$ and $\mathbf{w}_{\text{mtr}}[k] \sim \mathcal{N}(\mathbf{0}, \mathbf{Q}_{\text{mtr}}) \, \forall \, k$ can thought of as the derivative of $\boldsymbol{\tau}_{\text{mtg}}$ and $\boldsymbol{\tau}_{\text{mtr}}$ sampled at k with constant process noise covariance matrices $\mathbf{Q}_{\text{mtr}} = \mathbb{E}[\mathbf{w}_{\text{mtr}}[k]\mathbf{w}_{\text{mtr}}^{\intercal}[k]]$ and $\mathbf{Q}_{\text{mtg}} = \mathbb{E}[\mathbf{w}_{\text{mtg}}[k]\mathbf{w}_{\text{mtg}}^{\intercal}[k]]$. Equations (M.5) and (M.6) can be considered an approximate solution, i.e., an Euler-Maruyama approximation, to the underlying stochastic differential equations describing torque dynamics over the span Δt (from Itô calculus [228]). Inherently, this assumption dictates that the derivatives are constant over that span. Note that $\mathbf{w} \sim \mathcal{N}(\mathbf{0}, \mathbf{Q}) \implies \Delta t \mathbf{w} \sim \mathcal{N}(\mathbf{0}, \Delta t^2 \mathbf{Q})$ which further implies that $\sqrt{\Delta t^{-1}}\sqrt{\mathbf{Q}^{-1}}\Delta t \mathbf{w} \sim \mathcal{N}(\mathbf{0}, \Delta t \mathbf{I})$, i.e., $\sqrt{\Delta t^{-1}}\sqrt{\mathbf{Q}^{-1}}\Delta t \mathbf{w}$ is simply a Wiener process [350].

For the purpose of the EKF equations, we assume over the sampling interval $t \in [t_0, t_0 + \Delta t]$ the human-exoskeleton system undergoes a constant acceleration, i.e.,

$$\begin{aligned} \ddot{\mathbf{q}}_{\text{he}}(t) \approx \; & \mathbf{M}_{\text{he}}^{-1}(\mathbf{q}_{\text{he}}(t_0))(\boldsymbol{\Gamma}_{\text{he}}(\mathbf{q}_{\text{he}}(t_0), \dot{\mathbf{q}}_{\text{he}}(t_0)) + 2\boldsymbol{\tau}_{\text{psv}}(\mathbf{q}_{\text{he}}(t_0), \dot{\mathbf{q}}_{\text{he}}(t_0))) \\ & + 2\mathbf{M}_{\text{he}}^{-1}(\mathbf{q}_{\text{he}}(t_0))\boldsymbol{\tau}_{\text{f}}(\dot{\mathbf{q}}_{\text{he}}(t_0)) \\ & \forall \, t \in [t_0, t_0 + \Delta t] \end{aligned} \tag{M.7}$$

and a linearly increasing acceleration due to the change in applied torques (M.5– M.6). These assumptions were used to assemble the discretized acceleration equation used for EKF state predictions:

$$\begin{aligned}\ddot{\mathbf{q}}_{\text{he}}(t) \approx\ & \mathbf{M}_{\text{he}}^{-1}(\mathbf{q}_{\text{he}}(t_0))(\boldsymbol{\Gamma}_{\text{he}}(\mathbf{q}_{\text{he}}(t_0), \dot{\mathbf{q}}_{\text{he}}(t_0)) + 2\boldsymbol{\tau}_{\text{psv}}(\mathbf{q}_{\text{he}}(t_0), \dot{\mathbf{q}}_{\text{he}}(t_0)) + 2\boldsymbol{\tau}_{\text{f}}(\dot{\mathbf{q}}_{\text{he}}(t_0))) \\ & + \mathbf{M}_{\text{he}}^{-1}(\mathbf{q}_{\text{he}}(t_0))(\boldsymbol{\tau}_{\text{mtg}}^{\text{cns}}(t_0) + 2\boldsymbol{\tau}_{\text{mtr}}(t_0) + (t - t_0)\mathbf{w}_{\text{mtg}}(t_0) + 2(t - t_0)\mathbf{w}_{\text{mtr}}(t_0)) \\ & + \mathbf{w}_{\alpha}\end{aligned} \tag{M.8}$$

$\forall\, t \in [t_0, t_0 + \Delta t]$

By integrating this acceleration equation over the sampling interval,

$$\dot{\mathbf{q}}_{\text{he}}[k+1] = \dot{\mathbf{q}}_{\text{he}}[k] + \int_{t_0}^{t_0+\Delta t} \ddot{\mathbf{q}}_{\text{he}}(t)\, dt, \tag{M.9}$$

$$\mathbf{q}_{\text{e3}}[k+1] = \mathbf{q}_{\text{he}}[k] + \int_{t_0}^{t_0+\Delta t} \int \ddot{\mathbf{q}}_{\text{he}}(t)\, dt\, dt \tag{M.10}$$

the discrete state-space representation of the human-exoskeleton dynamics with unknown motor and active muscle torques being applied was obtained:

$$\mathbf{x}_{\text{os}}[k+1] = \mathbf{f}_{\text{d}}(\mathbf{x}_{\text{os}}[k]) + \mathbf{G}(\mathbf{x}_{\text{os}}[k])\mathbf{w}[k] \tag{M.11}$$

$$\mathbf{y}_{\text{os}}[k] = \mathbf{h}(\mathbf{x}_{\text{os}}[k]) + \boldsymbol{\upsilon}[k] \tag{M.12}$$

where $\mathbf{w} = [\mathbf{w}_{\text{mtr}}^{\intercal}, \mathbf{w}_{\text{mtg}}^{\text{cns}\intercal}]^{\intercal}$ includes the motor and muscle torque process noise and $\boldsymbol{\upsilon} = [\boldsymbol{\upsilon}_{\theta}^{\intercal}, \boldsymbol{\upsilon}_{\omega}^{\intercal}, \boldsymbol{\upsilon}_{\text{mtg}}^{\intercal}]^{\intercal}$ is the concatenation of additive joint position, velocity, and motor torque noise, with the symmetric noise covariance matrices

$$\mathbf{Q}_{\text{os}} \in \mathbb{R}^{6\times 6} = \begin{bmatrix} \mathbf{Q}_{\text{m}} & \mathbf{0} \\ \mathbf{0} & \mathbf{Q}_{\text{mtg}} \end{bmatrix} \quad \text{and} \quad \mathbf{R}_{\text{os}} \in \mathbb{R}^{9\times 9} = \begin{bmatrix} \mathbf{R}_{\theta} & \mathbf{0} & \mathbf{0} \\ \mathbf{0} & \mathbf{R}_{\omega} & \mathbf{0} \\ \mathbf{0} & \mathbf{0} & \mathbf{R}_{\tau} \end{bmatrix}. \tag{M.13}$$

Terms within the dynamic Equation (M.11) include the functions

$$\mathbf{f}_{\mathrm{d}}(\mathbf{x}_{\mathrm{os}}[k]) = \begin{Bmatrix} \mathbf{q}_{\mathrm{he}}[k] + \Delta t \dot{\mathbf{q}}_{\mathrm{he}}[k] + \frac{1}{2}\Delta t^2 \mathbf{M}_{\mathrm{he}}^{-1}[k](\boldsymbol{\Gamma}_{\mathrm{he}}[k] + \boldsymbol{\tau}_{\mathrm{mtg}}^{\mathrm{cns}}[k] + 2\boldsymbol{\tau}_{\mathrm{psv}}[k] + 2\boldsymbol{\tau}_{\mathrm{mtr}}[k] + 2\boldsymbol{\tau}_{\mathrm{f}}[k]) \\ \dot{\mathbf{q}}_{\mathrm{he}}[k] + \Delta t \mathbf{M}_{\mathrm{he}}^{-1}[k](\boldsymbol{\Gamma}_{\mathrm{he}}[k] + \boldsymbol{\tau}_{\mathrm{mtg}}^{\mathrm{cns}}[k] + 2\boldsymbol{\tau}_{\mathrm{psv}}[k] + 2\boldsymbol{\tau}_{\mathrm{mtr}}[k] + 2\boldsymbol{\tau}_{\mathrm{f}}[k]) \\ \mathbf{0} \\ \mathbf{0} \end{Bmatrix}, \tag{M.14}$$

$$\mathbf{G}(\mathbf{x}_{\mathrm{os}}[k]) = \begin{bmatrix} \frac{1}{6}\Delta t^3 \mathbf{M}_{\mathrm{he}}^{-1}(\mathbf{q}_{\mathrm{he}}[k]) & \frac{1}{6}\Delta t^3 \mathbf{M}_{\mathrm{he}}^{-1}(\mathbf{q}_{\mathrm{he}}[k]) \\ \frac{1}{2}\Delta t^2 \mathbf{M}_{\mathrm{he}}^{-1}(\mathbf{q}_{\mathrm{he}}[k]) & \frac{1}{2}\Delta t^2 \mathbf{M}_{\mathrm{he}}^{-1}(\mathbf{q}_{\mathrm{he}}[k]) \\ \Delta t \mathbf{I} & 0 \\ 0 & \Delta t \mathbf{I} \end{bmatrix} \tag{M.15}$$

where $\mathbf{f}_{\mathrm{d}}$ is responsible for producing the discrete deterministic changes in state over Δt; $\mathbf{G} \in \mathbb{R}^{12\times 6}$ maps the process noise $\mathbf{w}$ to joint accelerations (multiplicative noise). The nonlinear output equation (M.12) was in reality a linear function with respect to the state variables:

$$\mathbf{h}(\mathbf{x}_{\mathrm{os}}[k]) \in \mathbb{R}^{9\times 1} = \begin{Bmatrix} \mathbf{q}_{\mathrm{he}}[k] \\ \dot{\mathbf{q}}_{\mathrm{he}}[k] \\ \boldsymbol{\tau}_{\mathrm{mtr}}[k] \end{Bmatrix} \tag{M.16}$$

These variables output from the model are the same variables that can be measured in practice with the EXO-H3. With that said, during initial testing of this EKF design, we observed that the algorithm sometimes behaved poorly with the presence of the cubic Δt term in (M.15). This outcome was likely due to poor conditioning of $\mathbf{G}\mathbf{Q}_{\mathrm{os}}\mathbf{G}^{\intercal}$ during Kalman recursion, which effects predictions of changes in estimation-error covariance over Δt [310]. Instead, due to its more reliable performance in kinematic variable estimation, the following $\mathbf{G}$ matrix was supplied during EKF implementation:

$$\mathbf{G}(\mathbf{x}_{\mathrm{os}}[k]) = \begin{bmatrix} \frac{1}{4}\Delta t^2 \mathbf{M}_{\mathrm{he}}^{-1}(\mathbf{q}_{\mathrm{he}}[k]) & \frac{1}{4}\Delta t^2 \mathbf{M}_{\mathrm{he}}^{-1}(\mathbf{q}_{\mathrm{he}}[k]) \\ \frac{1}{2}\Delta t^2 \mathbf{M}_{\mathrm{he}}^{-1}(\mathbf{q}_{\mathrm{he}}[k]) & \frac{1}{2}\Delta t^2 \mathbf{M}_{\mathrm{he}}^{-1}(\mathbf{q}_{\mathrm{he}}[k]) \\ \Delta t \mathbf{I} & 0 \\ 0 & \Delta t \mathbf{I} \end{bmatrix} \tag{M.17}$$

where the cubic Δt terms were exchanged for quadratic terms, and the leading coefficients were scaled by 2/3.

With the state-space representation of the observation-oriented human-exoskeleton system defined, the EKF-based FIP estimator could be constructed. Briefly, the EKF method

recursively generates estimates of the state at a given sampling instant by weighing predictions of the change-in-state made by the observation-oriented dynamic model against the state of the system as implied by noisy measurements [310]. As each iteration proceeds, the algorithm effectively weighs the quality of the previous predictions made by the system model through concurrent propagation and correction of the estimated state and estimation-error covariance matrix $\hat{\mathbf{P}} = \mathbb{E}[\boldsymbol{\eta}[k]\boldsymbol{\eta}^{\intercal}[k]]$ where $\boldsymbol{\eta}[k] = \hat{\mathbf{x}}_{\text{os}}[k|k] - \mathbf{x}_{\text{os}}[k]$ [260, 310]; the notation $\hat{\mathbf{x}}[k|k]$ indicates the estimate of the true variable $\mathbf{x}$ at k given measurements up until and including those at instant k. For the classical Kalman Filter, the use of a linear system produces an optimal state estimation, i.e, one the minimizes the mean square estimation error at a given iteration (equivalent to minimizing the trace of $\hat{\mathbf{P}}[k|k]$). In the case of EKF, to keep the system propagation model as nonlinear, we lose this guarantee of optimality. Error covariance propagation continues to rely on linearizations, i.e.,

$$\mathbf{F}_{\text{d}}[k] = \left.\frac{\partial \mathbf{f}_{\text{d}}}{\partial \mathbf{x}_{\text{os}}}\right|_{\hat{\mathbf{x}}_{\text{os}}[k-1|k-1]}, \quad \mathbf{H}[k] = \left.\frac{\partial \mathbf{h}}{\partial \mathbf{x}_{\text{os}}}\right|_{\hat{\mathbf{x}}_{\text{os}}[k|k-1]} \tag{M.18}$$

in order to make near- though still sub-optimal estimates of $\hat{\mathbf{x}}_{\text{os}}[k|k]$. Two steps are required to perform a single iteration of recursion within the EKF algorithm:

Stage 1: Predict

$$\text{1): } \hat{\mathbf{x}}_{\text{os}}[k|k-1] = \mathbf{f}_{\text{d}}(\hat{\mathbf{x}}_{\text{os}}[k-1|k-1]) \tag{M.19}$$

$$\text{2): } \hat{\mathbf{P}}[k|k-1] = \mathbf{F}_{\text{d}}[k]\hat{\mathbf{P}}[k-1|k-1]\mathbf{F}_{\text{d}}[k]^{\intercal} + \mathbf{G}[k]\bar{\mathbf{Q}}\mathbf{G}[k]^{\intercal} \tag{M.20}$$

Stage 2: Correct

$$\text{3): } \boldsymbol{\varepsilon}[k] = \mathbf{y}_{\text{os}}[k] - \mathbf{h}(\hat{\mathbf{x}}_{\text{os}}[k|k-1]) \tag{M.21}$$

$$\text{4): } \boldsymbol{\mathcal{S}}[k] = \mathbf{H}[k]\hat{\mathbf{P}}[k|k-1]\mathbf{H}[k]^{\intercal} + \bar{\mathbf{R}} \tag{M.22}$$

$$\text{5): } \mathbf{K}_{\text{kf}}[k] = \hat{\mathbf{P}}[k|k-1]\mathbf{H}[k]^{\intercal}\boldsymbol{\mathcal{S}}^{-1}[k] \tag{M.23}$$

$$\text{6): } \hat{\mathbf{x}}_{\text{os}}[k|k] = \hat{\mathbf{x}}_{\text{os}}[k|k-1] + \mathbf{K}_{\text{kf}}[k]\boldsymbol{\varepsilon}[k] \tag{M.24}$$

$$\text{7): } \hat{\mathbf{P}}[k|k] = (\mathbf{I} - \mathbf{K}_{\text{kf}}[k]\mathbf{H}[k])\hat{\mathbf{P}}[k|k-1] \tag{M.25}$$

where $\varepsilon[k] \in \mathbb{R}^{9\times 1}$ is measurement residual error at instance k, $\boldsymbol{\mathcal{S}}[k] \in \mathbb{R}^{9\times 9}$ is the corresponding residual covariance, and $\mathbf{K}_{\text{kf}} \in \mathbb{R}^{12\times 9}$ is typically referred to as the "Kalman gain" [310]. This gain is responsible for correcting errors introduced into the estimated state during the prediction state. This process is repeated for as long as the system designer desires.

Appendix N

Supplementary Human-Exoskeleton Simulations of Assisted Balance

The current set of simulations was used to assess the performance of the MPC-MHE-based balance recovery when paired with an existing feedback control law representing the CNS of the end-user that has no knowledge of the device control law. The basis of this investigation was to establish how the the controller might either augment or compete with an end-user if their goals did not match, i.e., assistance without intent recognition. Vallery et al. [338, 339] discussed this issue faced in biomechatronics: the human and device represent two closed feedback loops that could have competing interests. Herein, the simulations represent a worst-case scenario in which both CNS and exoskeleton controllers enact FIP balancing actions but do so slightly differently from each other. In the real-world, such competing feedback laws could appear when the end-user does not have a strong internal model of the device assistive law [340]. Given the differences in trajectories observed between MPC and LQR in the second set of simulations, we thus elected to simulate the exoskeleton MPC-MHE controller acting in coordination with the human CNS, i.e., an LQR with ideal actuators [202, 169, 342]. The LQR torques were saturated to the maximum isometric torques to keep them within reasonable values (see Chapter 3). Both LQR and MPC were run with $\rho = 0.5$, $\sigma = 2.5 \times 10^3$, and a 500 ms prediction horizon. The control scheme used is shown in Fig. N.1. The human CNS component received perfect full-state feedback, which we assumed was true given previous validated models of CNS-based sensor fusion [203, 341, 342].

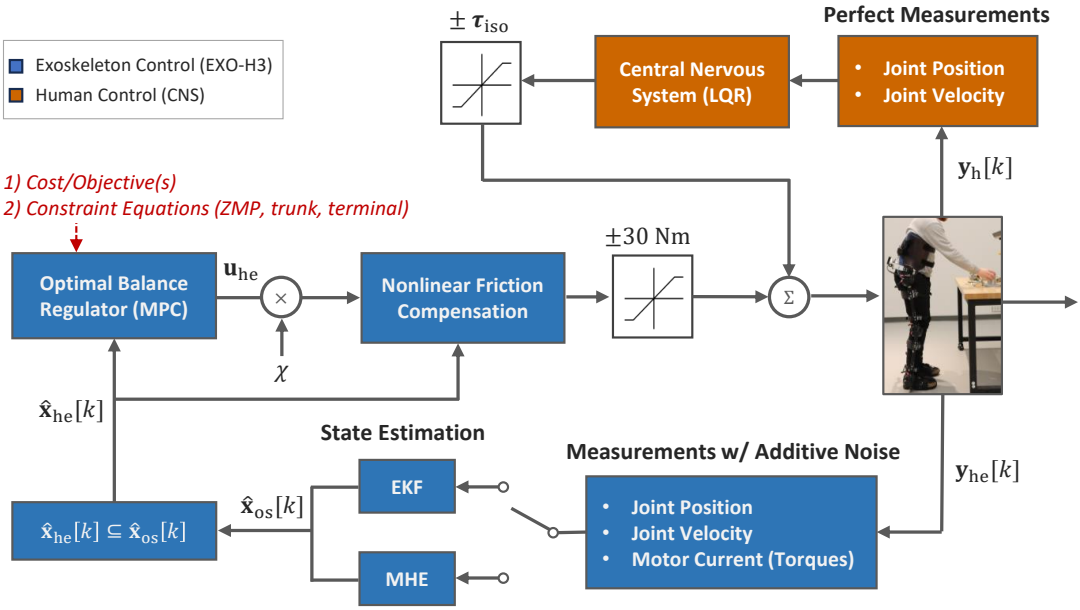


Figure N.1: Control schematic for simulation set 4: assisted FIP balance recovery via model predictive control (MPC) with concurrent nonlinear state estimation (moving horizon estimation; MHE). The human end-user CNS is modelled using the LQR from Chapter 6 to capture performance of the MHE when there is a mismatch between the exoskeleton and human feedback control law. Assistive torques derived from the MPC were scaled by factor $\chi \in [0, 1]$

Two cases were tested in this last set of simulations:

1. The first case involved FIP balance recovery simulations with an end-user who could only generate 40% of the maximal isometric muscle torques of a healthy young adult (from Inkol and McPhee [169]). This percentage was taken from the work by Jayaraman et al. [177], where study participants with an incomplete spinal cord injury (SCI) could generate approximately 30-40% of the active ankle torque magnitude that participants without disability could produce. From simulations not shown, we found that without assistance from the device actuators, this end-user would lose their balance and fall following the support-surface translations used.

2. Simulations of FIP balance recovery with an end-user user that can produce 70% of the maximal isometric muscle torques of a healthy young adult. In this case, the saturation of force was included to mimic the decline in muscle force generation that can emerge with aging [31, 264]. Aging is characterized by a multitude of physiological

processes not isolated to muscle strength, and thus this case is not a strict model of assisted older adult balance. Rather it is incorporating a symptom of aging to test exoskeleton assistance. Note that the 70%-strength end-user was able to stay upright following the support-surface translations without assistance from the exoskeleton.

Assistance was delivered by scaling the net applied ideal torque derived from the MPC by a factor χ that was set differently for each case, i.e., $\chi = 0.6$ for the 40%-strength end-user and $\chi = 0.3$ for the 70%-strength end-user (these values were determined through manual tuning).

In each simulation, the assisted 40%-strength end-user never truly lost their balance according to the FIP domain of feasibility, i.e., the ZMP was always with boundaries of the support polygon (Fig. N.2). However, the combined actions of the MPC and LQR without knowledge of each other resulted in aggressive COM regulation (displacements on the scale of 1-2 cm). While the ZMP did not exit the support boundaries, it became close to the posterior boundary for both directions of perturbations. Not surprisingly, when the 70%-strength end-user was included in simulations, the concurrent actions of the device and human caused the net ZMP position to exit the BOS (Fig. N.2). Specifically, during forward fall correction, the ZMP shifted posteriorly past the heel boundary to reverse COM motion following the initial correction of forward momentum (from 0.5-0.75 seconds). The ZMP did not exit the support polygon for the backward fall correction. Despite these over-corrections, the MHE provided good estimates of joint angles in simulations with both the 40%-strength end-user (RMSE = 0.10°; Fig. N.4)) and the 70%-strength user (RMSE = 0.03°; Fig. N.6)). Likewise, the MHE was able to obtain reasonable estimates of the applied motor torques: 40% user, RMSE = 2.95 Nm (hip), 9.80 Nm (knee), and 13.14 Nm (ankle; see Fig. N.5); 70% user, RMSE = 2.67 Nm (hip), 9.39 Nm (knee), and 12.59 Nm (ankle; see Fig. N.7). However, the presence of the support-surface perturbations resulted in rather poor estimates of the human MTG torques: 40% user, RMSE = 3.82 Nm (hip), 16.52 (knee), and 25.06 Nm (ankle; see Fig. N.5); 70% user, RMSE = 4.41 Nm (hip), 18.82 Nm (knee), and 29.33 Nm (ankle; see Fig. N.7).

Foremost, it is evident that the current proposed sensor configuration imposes limitations on our ability to distinguish active human muscle torques indicating CNS intent from external disturbance torques. At its core, this problem is one of poor observability; without additional measurements, there is no way to separate human torques from perturbation torques, i.e., these elements act in parallel. The EXO-H3 does also feature applied torque

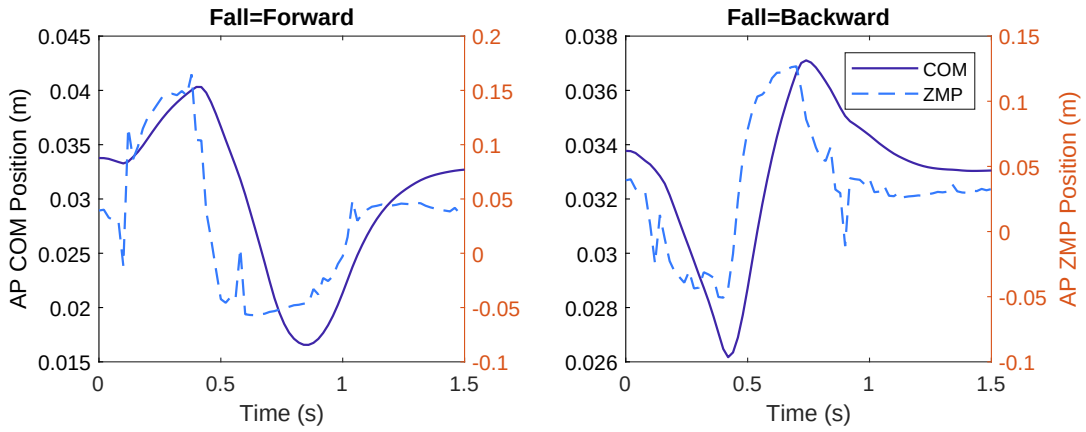


Figure N.2: Anteroposterior (AP) COM/ZMP trajectories obtained via MPC control paired with a moving horizon estimator (MHE) to assist a simulated 40%-strength end-user with FIP balance recovery.

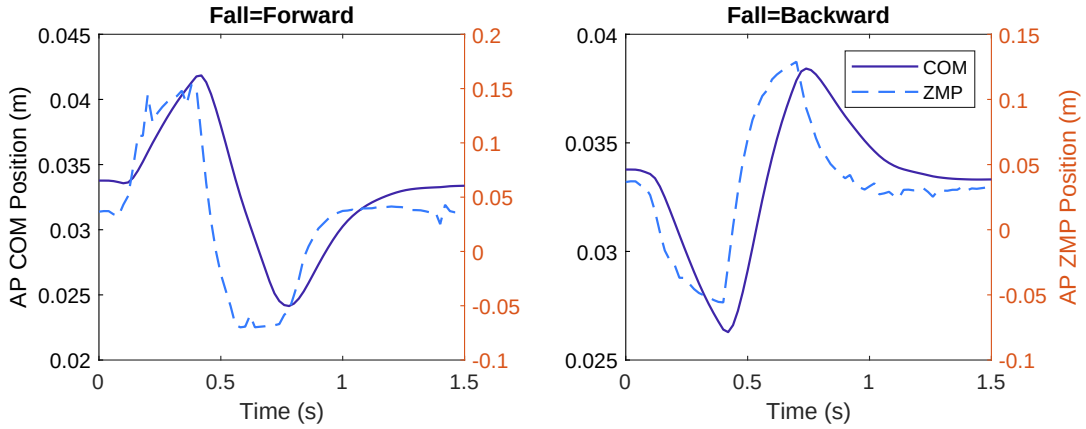


Figure N.3: Anteroposterior (AP) COM/ZMP trajectories obtained via MPC control paired with a moving horizon estimator (MHE) to assist a simulated 70%-strength end-user with FIP balance recovery.

sensors, but further work is necessary to devise a mathematical relation that links their outputs to the model states. Even so, it is unlikely that these sensors would be able to isolate external disturbances from human torques. Additionally, at the time of conducting

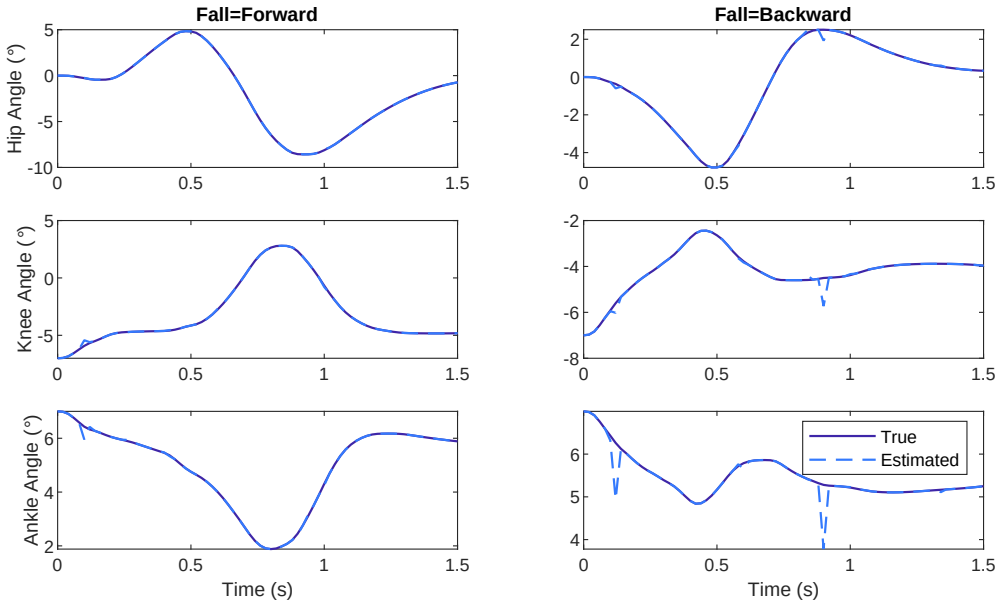


Figure N.4: True and estimated joint angle trajectories obtained via MPC control paired with a moving horizon estimator (MHE) to assist a simulated 40%-strength end-user with FIP balance recovery.

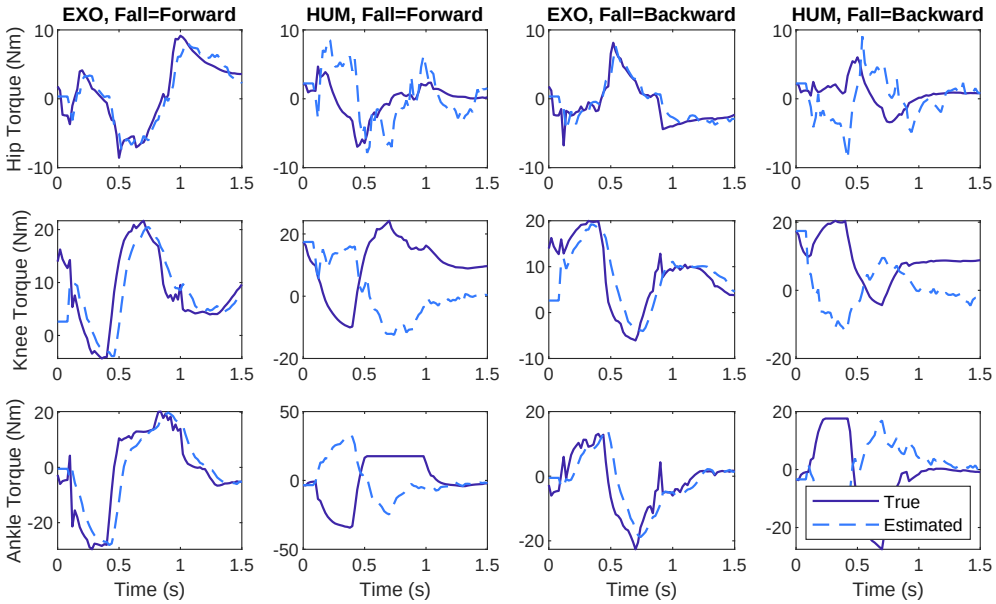


Figure N.5: True and estimated motor (EXO) and human MTG (HUM) torque trajectories obtained via MPC control paired with a moving horizon estimator (MHE) to assist a simulated 40%-strength end-user with FIP balance recovery.

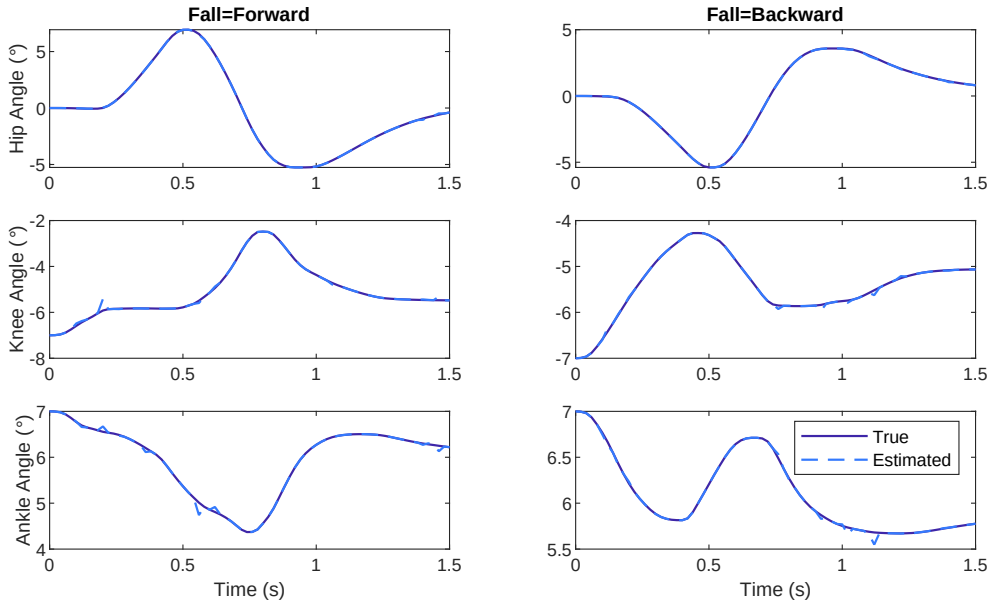


Figure N.6: True and estimated joint angle trajectories obtained via MPC control paired with a moving horizon estimator (MHE) to assist a simulated 70%-strength end-user with FIP balance recovery.

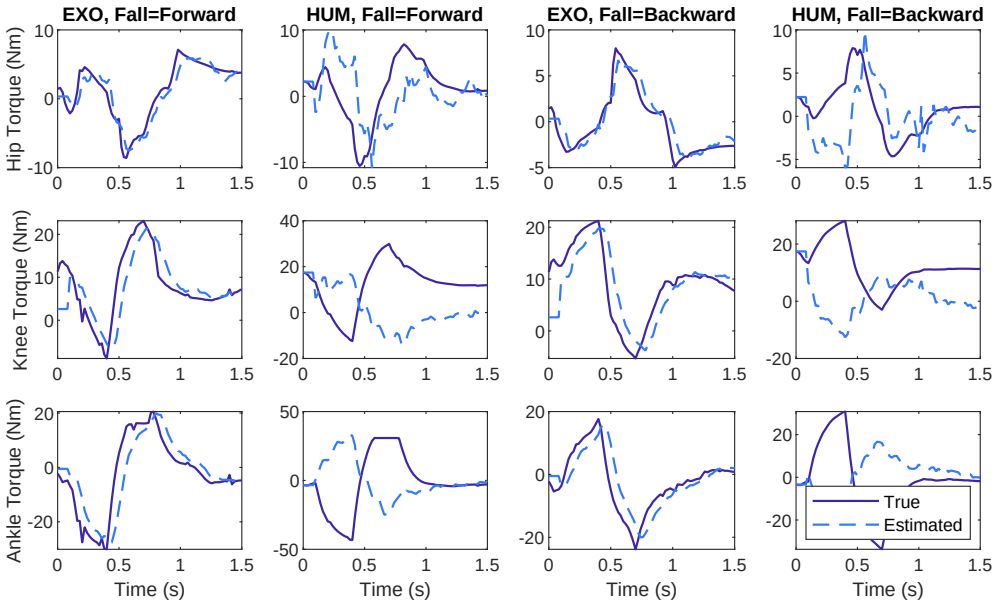


Figure N.7: True and estimated motor (EXO) and human MTG (HUM) torque trajectories obtained via MPC control paired with a moving horizon estimator (MHE) to assist a simulated 70%-strength end-user with FIP balance recovery.

this research, these sensors were faulty on our EXO-H3 and required repairs from the manufacturer Technaid. Since the perturbations were delivered through the tangential ground reaction force, transducers in the exoskeleton foot pad with reasonable fidelity would likely provide better results [215]. Regardless, further work on the intent/disturbance recognition component is important for perturbation observation, i.e., devising when to effectively initiate assistance to a user that can stand quietly unassisted [109]. As discussed in the derivation of the MPC in Chapter 6.2.4, improved human MTG torque estimation could also permit modulation of the MPC control law to augment end-user intent and better regulate the ZMP with the support polygon. Note that this model and simulation interface could also be applied towards investigations on hardware configurations that optimize sensor fusion. For example, once a model is designed and validated for the EXO-H3 applied torque sensors, this interface can be used to assess their performance in the MHE. Likewise, force transducer positioning could be investigated for improved detection of a physical push from the environment [316]. Inertial measurement units (IMUs) have also seen considerable attention in the human-exoskeleton balance space for feedback control [103, 105, 135, 138]; the simulation interface herein could be used to investigate minimal and less-invasive IMU setups for full-state feedback without requiring any physical experiments. Moving to the final point of discussion, humans exhibit some degree of COM sway during quiet standing [361]. Over these small regions of sway about the equilibrium point, an AAN control architecture should in theory avoid over-controlling the human-exoskeleton and possibly inducing a fall so long as the user can support themselves in quiet standing unassisted. Such a system could involve introduction of a deadzone into the state, torque, or COM space feedback law, similar to concepts used in powered electric steering [239]. In Chapter 7, we investigate performance of a novel approach of model-based COM-based scaling of MPC-assistance given the recent work on exoskeleton-assisted walking by Bayon et al. [49] and previous models suggesting that muscle activity in postural responses scales with COM kinematics [353, 354]. Given the use of the XCOM in exoskeleton-assisted step placement [343, 348] and it role in the FIP margin of stability (related to the FSR; see Chapter 3), we approached assistive-scaling from the COM position-velocity phase space.

Appendix O

Participant Screening Questionnaire

See next page.

Screening Questionnaire **Date:** _____

ID: _____



Dept. Systems Design Engineering
Dept. Kinesiology and Health Sciences

Thank you for your interest in participating in our study! We will give you a quick description of what you will be doing for the study. We will be analyzing how you respond to an unexpected movement of the floor with and without assistance from a robotic lower-limb exoskeleton. The exoskeleton uses electric motors attached compliantly to the user to apply assistive forces. All testing will take place in our lab in the CCCARE facility (Toby Jenkins Applied Health Research Building)

To ensure that you will be comfortable participating in this study and that you meet the necessary inclusion criteria, we would like to fill out the following questions:

General Survey

1. What is your age? (must 18-30 years old) _____
2. What is your height? (must be 1.35-1.85 m or 4'5"-6'0" to use exo) _____
3. What is your weight? (must be less than 100 kg or 220 lbs to use exo) _____

Answer the following by circling yes (Y) or no (N):

Question	Response:
1. Are you able to perform all activities of daily living independently?	Y N
2. Are you able to stand and walk freely without a walking aid?	Y N
3. Have you ever participated in a postural balance study before?	Y N
4. Are you willing and able to follow study instructions?	Y N

Screening Questionnaire **Date:** _____

ID: _____

Health Information and Screening

Sex: M F Prefer not to say

(Note: We inquire as we wish to maintain a balanced sample of individuals)

Question	Response:
1. Do you have any allergies to isopropyl alcohol, adhesives, or gels?	Y N
If no, do you have *any* skin sensitivities to these substances?	Y N
2. Do you have any uncorrected visual problems?	Y N
3. Have you ever been diagnosed with any neuromuscular disorders? e.g., diabetic neuropathy	Y N
If yes, please specify (write N/A if you do not wish to disclose): _____	
_____	
4. Have you ever had any muscular or skeletal injuries, e.g., fractures, muscle strains, sprains, etc.)	Y N
If yes, please specify what and when: _____	
_____	
In your opinion, does this injury still impact function? _____	
5. Have you ever been diagnosed with any vestibular (inner ear) problems?	Y N
6. Do you ever feel dizzy or nauseous when you do the following:	
a. Look at the sky?	Y N
b. Look at the ceiling/floor?	Y N
c. Take the elevator?	Y N
d. Are sitting down and reading?	Y N
e. Are riding in an automobile?	Y N
f. Pass from indoors to outdoors?	Y N
g. Pass from outdoors to indoors?	Y N
h. Are washing your hair in the shower?	Y N
7. Do you have any open wounds, fragile skin, or skin lesions that may hinder or prevent the application of force by the exoskeleton?	Y N

Screening Questionnaire **Date:** _____

ID: _____

8. Are you on contact precautions for any infections? Y N

9. Are you pregnant? Y N

10. To your knowledge, do you have limited passive range of motion in the ankle, knee, or hip joints? If not sure, write "maybe" on the line below and we will verify that you have a sufficient range of motion during your study visit. Note: If range is in fact limited, the study visit may be discontinued for your safety. Y N

_____

11. Are currently taking any medications? Y N

If yes, please specify indicate whether they appear in the table on the next page (do not specify the medication). Y N

8. Do you have any of the following conditions that may affect your ability to stand and walk safely: plantar fasciitis, back soreness, metatarsalgia (pain on ball of foot), or ingrown toenails? Y N

** For your personal safety, only medications that may affect your balance control exclude you from being able to participate within this study. These include any from the chart below:

MEDICATIONS	
Tranquilizers	*chlorpromazine, flupenthixol, fluphenazine, fluspirilene, haloperidol, loxapine Mesoridazine, pericyazine, perphenazine, pimozide, pipotiazine, prochlorperazine, thioridazine, thiothixene, trifluoperazine*
Sedatives	*Benzodiazepenes: alprazolam, bromazepam, Chlordiazepoxide, clorazepate (choral hydrate),diazepam/valium, flurazepam, lorazepam, meprobamate, methotrimeprazine nitrazepam, oxazepam, temazepam, triazolam,* *Barbiturates: amobarbital, butabarbital, pentobarbital, secobarbital*
Antidepressants	*Tricyclics: amitryptyline, desipramine, doxepin, Imipramine, nortriptyline, protriptyline, trimipramine,.* *SSRIs: sertraline, paroxetine,* *M-Ox In: fluoxetine, fluvoxamine, phenelzine, tranylcypromine* *Other: amoxapine, maprotiline, trazodone*